frontiers | Research Topics

Algal photosynthesis

Edited by
Weimin Ma, Luning Liu, Qiang Wang, Deqiang Duanmu
and Bao-Sheng Qiu

Published in
Frontiers in Microbiology

ISSN 1664-8714
ISBN 978-2-83251-352-1
DOI 10.3389/978-2-83251-352-1

About Frontiers

Frontiers is more than just an open access publisher of scholarly articles: it is a pioneering approach to the world of academia, radically improving the way scholarly research is managed. The grand vision of Frontiers is a world where all people have an equal opportunity to seek, share and generate knowledge. Frontiers provides immediate and permanent online open access to all its publications, but this alone is not enough to realize our grand goals.

Frontiers journal series

The Frontiers journal series is a multi-tier and interdisciplinary set of open-access, online journals, promising a paradigm shift from the current review, selection and dissemination processes in academic publishing. All Frontiers journals are driven by researchers for researchers; therefore, they constitute a service to the scholarly community. At the same time, the *Frontiers journal series* operates on a revolutionary invention, the tiered publishing system, initially addressing specific communities of scholars, and gradually climbing up to broader public understanding, thus serving the interests of the lay society, too.

Dedication to quality

Each Frontiers article is a landmark of the highest quality, thanks to genuinely collaborative interactions between authors and review editors, who include some of the world's best academicians. Research must be certified by peers before entering a stream of knowledge that may eventually reach the public - and shape society; therefore, Frontiers only applies the most rigorous and unbiased reviews. Frontiers revolutionizes research publishing by freely delivering the most outstanding research, evaluated with no bias from both the academic and social point of view. By applying the most advanced information technologies, Frontiers is catapulting scholarly publishing into a new generation.

What are Frontiers Research Topics?

Frontiers Research Topics are very popular trademarks of the *Frontiers journals series*: they are collections of at least ten articles, all centered on a particular subject. With their unique mix of varied contributions from Original Research to Review Articles, Frontiers Research Topics unify the most influential researchers, the latest key findings and historical advances in a hot research area.

Find out more on how to host your own Frontiers Research Topic or contribute to one as an author by contacting the Frontiers editorial office: frontiersin.org/about/contact

Algal photosynthesis

Topic editors

Weimin Ma — Shanghai Normal University, China
Luning Liu — University of Liverpool, United Kingdom
Qiang Wang — Henan University, China
Deqiang Duanmu — Huazhong Agricultural University, China
Bao-Sheng Qiu — Central China Normal University, China

Citation

Ma, W., Liu, L., Wang, Q., Duanmu, D., Qiu, B.-S., eds. (2023). *Algal photosynthesis*. Lausanne: Frontiers Media SA. doi: 10.3389/978-2-83251-352-1

Table of contents

frontiers | Frontiers in Microbiology

TYPE Editorial
PUBLISHED 04 January 2023
DOI 10.3389/fmicb.2022.1112301

OPEN ACCESS

EDITED AND REVIEWED BY
Marc Strous,
University of Calgary, Canada

*CORRESPONDENCE
Weimin Ma
✉ wma@shnu.edu.cn
Lu-Ning Liu
✉ luning.liu@liverpool.ac.uk
Qiang Wang
✉ wangqiang@henu.edu.cn
Deqiang Duanmu
✉ duanmu@mail.hzau.edu.cn
Bao-Sheng Qiu
✉ bsqiu@mail.ccnu.edu.cn

SPECIALTY SECTION
This article was submitted to Microbial Physiology and Metabolism, a section of the journal Frontiers in Microbiology

RECEIVED 30 November 2022
ACCEPTED 13 December 2022
PUBLISHED 04 January 2023

CITATION
Ma W, Liu L-N, Wang Q, Duanmu D and Qiu B-S (2023) Editorial: Algal photosynthesis.
Front. Microbiol. 13:1112301.
doi: 10.3389/fmicb.2022.1112301

Editorial: Algal photosynthesis

Weimin Ma[1]*, Lu-Ning Liu[2]*, Qiang Wang[3]*, Deqiang Duanmu[4]* and Bao-Sheng Qiu[5]*

[1]College of Life Sciences, Shanghai Normal University, Shanghai, China, [2]Institute of Systems, Molecular and Integrative Biology, University of Liverpool, Liverpool, United Kingdom, [3]State Key Laboratory of Crop Stress Adaptation and Improvement, School of Life Sciences, Henan University, Kaifeng, China, [4]State Key Laboratory of Agricultural Microbiology, College of Life Science and Technology, Shenzhen Institute of Nutrition and Health, Huazhong Agricultural University, Wuhan, China, [5]Hubei Key Laboratory of Genetic Regulation and Integrative Biology, School of Life Sciences, Central China Normal University, Wuhan, China

KEYWORDS

algae, light energy harvesting, photosynthetic membrane complexes, photosynthetic electron transfer, carbon dioxide-concentrating mechanism, carbon fixation, antioxidant mechanism, evolution

Editorial on the Research Topic
Algal photosynthesis

Algae are a diverse group of predominantly aquatic photosynthetic organisms, including cyanobacteria, green algae and other eukaryotic algae. They account for more than 50% of the photosynthesis that takes place on Earth. Photosynthetic efficiency is generally higher in algae than in higher plants, because of a wide range of antenna pigments to harvest more solar energy and a variety of carbon dioxide-concentrating systems to increase carbon dioxide (CO_2) concentration around ribulose-1,5-bisphosphate carboxylase/oxygenase (Rubisco). Apart from their natural role as primary producers in the global carbon cycle, algae also feature in biotechnology for the production of a range of high-value natural products and a sustainable source of protein. This Research Topic aims to gather knowledge on understanding the working mechanisms of efficient photosynthesis in algae and contains 12 papers of which 8 are original research, 3 are reviews or mini-reviews, and one is a perspective.

The oligomeric states of cyanobacterial photosystem I (PSI) are diverse and at least consist of its monomer, dimer, trimer and tetramer. Such diversity is of significant importance for the survival of cyanobacterial cells under changing ecological environments. Chen, Liu, et al. review the implications of structural and oligomeric diversity among cyanobacterial PSI supercomplexes. Through biochemical and biophysical characterization and cryo-EM single-particle analysis, Chen, He, et al. further identified two novel oligomeric states of PSI, hexamer and octamer, from the filamentous cyanobacterium *Anabaena* sp. PCC 7120 grown in a low light environment. Du et al. construct a photo-bio-electrochemical system and in this system, purified reaction center-light harvesting (RC-LH) complex as a mediator can accept the electron from hydroxymethylferrocene (FcMeOH) and transfer to the overlapped fluorine-doped tin oxide (FTO) electrode, being composed of a FTO glass as the front electrode and a Pt-coated FTO glass as the counter electrode. This indicates that purified RC-LH

complex can operate in this *in vitro* system. In addition, the activity and stability of PSI are significantly reduced and phototropic growth is significantly attenuated in a *Chlamydomonas reinhardtii* heme oxygenase 1 mutant (*hmox1*) that is deficient in bilin biosynthesis. Zhang et al. reveal the presence of an alternative bilin biosynthetic pathway independent of heme oxygenase 1 in the chloroplast by a *hmox1* suppressor screening in *Chlamydomonas* cells.

Photosynthetic ferredoxin:plastoquinone oxidoreductase (NDH-1) is predominantly, if not totally, located in the thylakoid membrane, accepts electrons from reduced ferredoxin by PSI, and participates in a variety of bio-energetic reactions, including cyclic electron transfer around PSI, CO_2 acquisition, and cellular respiration. Mi describes the current advances and possible regulatory mechanisms of cyanobacterial NDH-1 in photosynthesis. Translocation of chloroplast-located genes to mitochondria or nucleus is considered to be a safety strategy that impedes mutation of photosynthetic genes and maintains their household function during evolution. Yu et al. propose that the organelle translocation strategy of photosynthetic NDH-1 genes during evolution is necessary to maintain the function of photosynthetic NDH-1 as an important antioxidant mechanism for efficient photosynthesis.

Cyanobacteria use an inorganic carbon-concentrating mechanism (CCM) to increase inorganic carbon concentration around Rubisco for efficient CO_2 fixation. Tang et al. reveal distinct molecular components and organization of CCM in thermophilic cyanobacteria using the comparative genomic analysis. Their findings provide insights into the CCM components of thermophilic cyanobacteria and fundamental knowledge for further research regarding photosynthetic improvement and biomass yield of thermophilic cyanobacteria with important biotechnological potentials. In addition, through structural analyses and molecular dynamic simulations, Min et al. reveal a previously unrecognized mechanism for the uncommon intermolecular Coenzyme A (CoA) transfer reaction, a key reaction intermediate for carbon fixation. This discovery not only broadens the knowledge on the catalytic mechanisms of CoA transferases, but also contributes to enzyme engineering of the 3-hydroxypropionate cycle for synthesis of high-value chemicals.

During algal evolution, a variety of antioxidant mechanisms are developed to protect algal photosynthesis under harsh environment conditions. Iron-stress-induced protein A (IsiA) is the major chlorophyll-containing protein in iron-starved cyanobacteria, binding up to 50% of the chlorophyll in these cells. Jia et al. describe progress in understanding the regulation and functions of IsiA based on laboratory research using model cyanobacteria. Abscisic acid (ABA) is known as a stress related hormone and plays a critical role in the regulation of various types of stress responses. Yang et al. propose that ABA is synthesized in *Neopyropia yezoensis* possibly *via* the carotenoid, mevalonate (MVA) and 2-C-methyl-D-erythritol 4-phosphate (MEP) pathways and the up-regulation of antioxidase genes under high salinity is mediated by the ABA signaling pathway.

A greater plasticity of metabolic pathways in response to the trophic growth mode is of significant importance for cyanobacterial growth and environmental acclimation. Muth-Pawlak et al. propose the regulatory patterning of carbon metabolism in cyanobacterial cells grown under different trophic modes (including low-carbon autotrophy, carbon-rich autotrophy, photomixotrophy and light-activated heterotrophy) *via* a comparative proteomic strategy. On Earth, far-red light derived photosynthesis occurs in cyanobacteria living in environments where visible light is strongly attenuated. Billi et al. identify the endolithic, extremotolerant cyanobacterium *Chroococcidiopsis* sp. CCMEE 010 capable of far-red light photoacclimation (FaRLiP) with a significantly reduced FaRLiP cluster, which has implications for the possibility of oxygenic photosynthesis on exoplanets.

Collectively, this volume of the Research Topic provides exiting works in the area of the catalytic and antioxidant mechanisms of algal photosynthesis, ranging from the structure, biogenesis, metabolism, signaling, regulation and evolution of photosynthesis in algae to the molecular components and modules of efficient photosynthesis in algae. With the efforts of many researchers worldwide, the frontiers of this topic keep evolving at a rapid pace.

Author contributions

All authors listed have made a substantial, direct, and intellectual contribution to the work and approved it for publication.

Funding

WM was supported by the National Natural Science Foundation of China (Grant No. 32170257).

Acknowledgments

We thank all the authors and reviewers that have contributed to this Research Topic.

Conflict of interest

The authors declare that the research was conducted in the absence of any commercial or financial relationships that could be construed as a potential conflict of interest.

Publisher's note

frontiers in Microbiology

REVIEW
published: 17 November 2021
doi: 10.3389/fmicb.2021.774107

Regulation and Functional Complexity of the Chlorophyll-Binding Protein IsiA

*Anqi Jia, Yanli Zheng, Hui Chen and Qiang Wang**

State Key Laboratory of Crop Stress Adaptation and Improvement, School of Life Sciences, Henan University, Kaifeng, China

As the oldest known lineage of oxygen-releasing photosynthetic organisms, cyanobacteria play the key roles in helping shaping the ecology of Earth. Iron is an ideal transition metal for redox reactions in biological systems. Cyanobacteria frequently encounter iron deficiency due to the environmental oxidation of ferrous ions to ferric ions, which are highly insoluble at physiological pH. A series of responses, including architectural changes to the photosynthetic membranes, allow cyanobacteria to withstand this condition and maintain photosynthesis. Iron-stress-induced protein A (IsiA) is homologous to the cyanobacterial chlorophyll (Chl)-binding protein, photosystem II core antenna protein CP43. IsiA is the major Chl-containing protein in iron-starved cyanobacteria, binding up to 50% of the Chl in these cells, and this Chl can be released from IsiA for the reconstruction of photosystems during the recovery from iron limitation. The pigment–protein complex (CPVI-4) encoded by *isiA* was identified and found to be expressed under iron-deficient conditions nearly 30 years ago. However, its precise function is unknown, partially due to its complex regulation; *isiA* expression is induced by various types of stresses and abnormal physiological states besides iron deficiency. Furthermore, IsiA forms a range of complexes that perform different functions. In this article, we describe progress in understanding the regulation and functions of IsiA based on laboratory research using model cyanobacteria.

Keywords: CP43, cyanobacteria, iron deficiency, IsiA, photosynthesis

OPEN ACCESS

Edited by:
Hidetoshi Urakawa, Florida Gulf Coast University, United States

Reviewed by:
Tanai Cardona, Imperial College London, United Kingdom
Zhengke Li, Dalhousie University, Canada

****Correspondence:***
Qiang Wang
wangqiang@henu.edu.cn

Specialty section:
This article was submitted to Microbial Physiology and Metabolism, a section of the journal Frontiers in Microbiology

Received: *11 September 2021*
Accepted: *25 October 2021*
Published: *17 November 2021*

Citation:
Jia A, Zheng Y, Chen H and Wang Q (2021) Regulation and Functional Complexity of the Chlorophyll-Binding Protein IsiA. Front. Microbiol. 12:774107. doi: 10.3389/fmicb.2021.774107

INTRODUCTION

Cyanobacteria are the oldest known lineage of oxygen-releasing photosynthetic organisms (Fournier et al., 2021). Oxygenic photosynthesis, which was first invented by cyanobacteria, is widely thought to have led to the ancient conversion of the reducing atmosphere into an oxidizing one (Nealson and Myers, 1990; Wang et al., 2017; Catling and Zahnle, 2020). Then, oxidative phosphorylation provides energy support for the evolution of larger individuals and the formation of the ozone layer made it possible for life to come ashore (Vik, 2007; Jie et al., 2019). Cyanobacteria are evolutionary ancestors to chloroplasts, and the comparison of chloroplasts and cyanobacteria showed their similarities (Tomitani, 1999). Thus, cyanobacteria helped shaping the ecology of this blue planet more than any other group of organisms until humans developed modern technologies.

Fe, the fourth most common elements in the earth's crust, mostly exists in the form of ferrous iron. Iron can have multiple, coordination-dependent electrical potentials (−2 to +6), making it an ideal transition metal for redox reactions in biological systems (Guerinot and Yi, 1994). Iron involved in basic biochemical functions in early life, including nitrogen reduction, pigment synthesis and degradation, fatty acid metabolism, and DNA synthesis, which created an irreversible link between Fe and life (Wrigglesworth and Baum, 1980). Accordingly, cyanobacteria have heavily incorporated iron into their basic electron transport systems for photosynthesis. The photosynthetic apparatus therefore represents one of the most iron-enriched cellular systems, requiring 23 to 24 atoms of iron in a single linear electron transport chain, including 12 iron atoms in the 4Fe-4S centers of PSI (Ferreira and Straus, 1994; Raven et al., 1999; Behrenfeld and Milligan, 2013; Guowei et al., 2021).

During oxidization, ferrous iron is oxidized to ferric iron, which is hardly soluble in water and has low bioavailability at a physiological pH (Guerinot and Yi, 1994). Iron deficiency is therefore a common stress encountered by cyanobacteria, which can lead to a significant decrease in their chlorophyll (Chl)-binding protein contents (Guikema and Sherman, 1984). Cyanobacteria have evolved several responses that allow them to withstand this physiological crisis and maintain photosynthesis under iron deficiency. In response to limited iron bioavailability, the phycocyanin (PC) and Chl a contents of cyanobacteria are reduced, along with a large decrease in the number of phycobilisomes, the main light harvesting proteins of PSII embedded in the thylakoid membrane (Guikema and Sherman, 1983; Sherman and Sherman, 1983; Guikema and Sherman, 1984; Pakrasi et al., 1985a; Odom et al., 1993; Falk et al., 1995). As the number of iron-containing proteins, such as Fd and Cytc553, decreases, the iron-stress-induced proteins, such as flavodoxin, PC, IsiA, IdiA (iron deficiency induced protein A), and OCP (orange carotenoid protein), become more abundant (Laudenbach and Straus, 1988; Odom et al., 1993; Exss-Sonne et al., 2000; Sandström et al., 2002; Wilson et al., 2006). Iron deficiency also results in carotenoid (Car) accumulation and enhances fatty acid desaturation (Ivanov et al., 2007). Along with these diverse structural and compositional changes, iron deficiency affects many photochemical properties of PSII and PSI, resulting in a decrease in the PSI/PSII ratio. This decrease inhibits linear intersystem electron transport but enhances cyclic electron transport around PSI (Ivanov et al., 2000; Sandström et al., 2002) and reduces the capacity for state transitions, locking the cyanobacteria in state I, in which PSI absorbs more light energy than PSII, and more excitation energy is transferred to PSII (Ivanov et al., 2006).

Among the proteins involved in the response to limited iron bioavailability, IsiA is an excellent marker of iron deficiency, as it is strongly induced and becomes the most abundant Chl-binding protein in iron-starved cells (Burnap et al., 1993). Over the past 30 years, extensive research has been performed on IsiA, but its exact function has not been determined. **Table 1** lists the nine most highly co-cited articles and the main findings of these articles. From these top-cited publications, we clearly observed the evolution of IsiA research over time. The *isiA* gene was first reported by Laudenbach and Straus in 1988 (Laudenbach and Straus, 1988), with the protein product identified in 1993 (Burnap et al., 1993). IsiA was initially proposed to protect PSII from excessive excitation (Park et al., 1999; Sandström et al., 2001); however, two groups simultaneously identified the $IsiA_{18}$-PSI trimer complex in two model cyanobacteria species (Bibby et al., 2001a; Boekema et al., 2001), with later studies demonstrating that IsiA was efficiently coupled to the PSI reaction center core (Andrizhiyevskaya

TABLE 1 | The nine most highly co-cited references published before 2021.

Rank	Number of co-citations	References	Main results
1	275	Bibby et al. (2001a) *Nature*, 412, 743–745	Iron deficiency induces the formation of $IsiA_{18}$-PSI_3 in *Synechocystis* sp. PCC 6803
2	260	Boekema et al. (2001) *Nature*, 412, 745–748	Iron deficiency induces the formation of $IsiA_{18}$–PSI_3 in *Synechococcus* sp. PCC 7942
3	107	Yeremenko et al. (2004) *Biochemistry*, 43, 10,308–10,313	IsiA forms various complexes and functions as an energy collector and dissipater during prolonged iron stress
4	99	Park et al. (1999) *Molecular Microbiology*, 32, 123–129	IsiA protects photosystem II from excess light under iron-limited conditions
5	95	Havaux et al. (2005) *FEBS Letters*, 579, 2,289–2,292	IsiA protects cyanobacteria from photooxidative stress and plays a photoprotective role
6	74	Melkozernovet al. (2003) *Biochemistry*, 42, 3,893–3,903	The IsiA antenna ring is efficiently coupled to the PSI reaction center core
7	73	Andrizhiyevskaya et al. (2002) *BBA-Bioenergetics*, 1,556, 265–272	The IsiA ring increases the absorption cross section of PSI by about 100%
8	69	Sandström et al. (2001) *Photochemistry and Photobiology*, 74, 431–437	IsiA functions as an excitation energy dissipator that protects photosystem II from excess light under iron-limited conditions
9	52	Jeanjean et al. (2003) *FEBS Letters*, 549, 52–56	IsiA is induced by oxidative stress, suggesting it plays a role in photoprotection

et al., 2002; Melkozernov et al., 2003). Subsequently, it was discovered that IsiA formed various complexes and had dual functions as an energy collector and an energy dissipater under prolonged iron deficiency (Yeremenko et al., 2004). These results represent the intellectual base of IsiA research.

The aim of this article is to provide a detailed review of IsiA research that will help research groups focus their studies on the key issues. Also, it highlights the issues that remain to be addressed.

EXPRESSION AND REGULATION OF *isiA*

Induction of *isiA* Expression Under Environmental Stresses

A Chl-protein complex, designated CPVI-4, is the major pigment-protein complex in cyanobacteria under iron-starved conditions, which was first described in 1985 (Pakrasi et al., 1985b). Burnap et al. (1993) provided evidence that the CPVI-4 complex was encoded by *isiA*, an iron-stress-induced gene. The *isiA* gene is widely distributed in most cyanobacteria, but no homologs were found in plants (González et al., 2018). It is cotranscribed from the *isiAB* operon containing the *isiB* (flavodoxin gene), *isiC* and *isiD* (unknown functions) in *Synechococcus* sp. PCC 7942, *Synechococcus* sp. PCC 7002, and *Synechocystis* sp. PCC 6803 (Laudenbach and Straus, 1988; Leonhardt and Straus, 1992; Vinnemeier et al., 1998; Kojima et al., 2006). In *Anabaena* sp. PCC 7120, however, *isiA* and *isiB* were found to be separately transcribed (Leonhardt and Straus, 1994). The IsiA protein is often called CP43' because its amino acid sequence is homologous to that of PsbC, the CP43 protein in cyanobacterial PSII. IsiA, like CP43, is predicted to comprise six transmembrane helices, but it lacks the large hydrophilic loop that joins the luminal ends of helices V and VI in CP43 (Laudenbach and Straus, 1988).

Li et al. (2019) reported that cyanobacterial *IsiA* had a predictable biogeographical distribution in the marine environment, consistent with the perceived biological role of IsiA as an adaptation to low-iron conditions. However, *isiA* transcription was initially discovered in iron-starved cells, it is also found to be induced by other environmental stresses, including salt, heat, oxidative stress, and high levels of light (Vinnemeier et al., 1998; Yousef et al., 2003; Havaux et al., 2005). Vinnemeier et al. (1998) observed that the salt-induced accumulation of *isiA* mRNA was not repressed by the addition of iron; thus, it was unlikely that the salt-dependent induction of *isiA* was due to a reduced iron uptake in the salt-stressed cells. A reasonable explanation for this is that there may be a common signal for the induction of *isiA* generated by salt stress and iron deficiency. Iron deficiency and other stress conditions all eventually lead to a secondary oxidative response (Xu et al., 2014a; Xiao et al., 2018; Yu et al., 2018). Moreover, hydrogen peroxide was found to induce *isiA* transcription much faster than other stresses (Yousef et al., 2003; Dühring et al., 2006); therefore, it is tempting to hypothesize that the oxidative response may be the common downstream signal that regulates *isiA* transcription. In agreement with this hypothesis, *isiA* expression was abolished when iron-stressed cells were grown in the presence of the antioxidant tempol (Latifi et al., 2005). It was also observed that *isiA* transcription was not induced by iron deficiency in cells acclimated to low Mn levels, which had a low PSII activity and decreased electron transport, minimizing the downstream oxidative damage (Salomon and Keren, 2015). This hypothesis explains why *isiA* is expressed in some mutants; for example, the deletion of *psaFJ* or *petJ* resulted in the accumulation of electrons at PSI, with the resulting higher levels of reactive oxygen species triggering the expression of the *isiAB* operon (Ardelean et al., 2002; Jeanjean et al., 2003). The biosynthesis of the IsiA protein was also induced by high light, protecting cyanobacteria from photooxidative stress (Havaux et al., 2005), although the IsiA levels remained much less abundant than in cyanobacteria experiencing iron deficiency.

However, no studies have provided evidence that *isiA* transcription is accompanied by protein biosynthesis under salt, heat, or oxidative stress (Vinnemeier et al., 1998; Hagemann et al., 1999). Mutants lacking *isiA* treated with high salt had only a slightly reduced salt tolerance (Karandashova et al., 2002) and were more resistant to hydrogen peroxide while being more susceptible to sublethal heat stress (Singh et al., 2005; Kojima et al., 2006). This suggests that IsiA functions at an undetectable or very low level under these stress conditions compared to high light and iron deficiency stresses. Indeed, the accumulation of *isiA* mRNA was transiently induced by salt, heat, and oxidative stress, with levels peaking and then immediately decreasing sharply or even disappearing. By contrast, the *isiA* mRNA maximum prevailed for a longer period under high light and iron deficiency stresses (Vinnemeier et al., 1998; Yousef et al., 2003; Dühring et al., 2006). The modification of *isiA* mRNA stability likely also affects the levels of IsiA in cells.

Overall, although the oxidative response could be a secondary signal triggering *isiA* (or *isiAB* operon) transcription, there are some differences in the mechanisms by which iron deficiency stress and oxidative stress (e.g., salt, heat, hydrogen peroxide, and high light stress) induce *isiA* expression. These differences are reflected in the stability of the *isiA* mRNA and ultimately in IsiA accumulation in cells.

Regulation of *isiA* Expression

The negative regulation of *isiA* is achieved at both the transcriptional and post-transcriptional levels by FurA (ferric uptake regulator A) protein and *isrR* (iron stress-repressed RNA) microRNA, respectively. It is widely accepted that FurA is a global transcription repressor that uses iron as a cofactor, which binds specifically to arrays of A/T-rich sequences known as Fur boxes. Once iron becomes scarce in the environment, FurA is inactivated by the release of iron, triggering the derepression of genes regulated by FurA (Mills and Marletta, 2005). The inactive FurA detaches from the upstream region of the *isiAB* operon; subsequently, the *isiA*/*isiB* genes are transcribed under the iron-deficient conditions. *furA* is an essential gene and was never completely inactivated by insertional

mutation; however, heteroallelic *furA* mutants exhibited a blue shift in the main red Chl absorption band under iron-deficient conditions, which is a characteristic symptom of iron deficiency resulting from the appearance of IsiA proteins (Ghassemian and Straus, 1996; Kunert et al., 2003).

Recently, it was reported that the FtsH1/FtsH3 protease heterocomplex mediates the degradation of the FurA repressor and thus promotes IsiA accumulation, which was important for the acclimation of cells to iron deficiency (Krynicka et al., 2014). These results indicate that both the modification of the activity and abundance of FurA influence *isiA* transcription. Other studies have shown that antisense RNAs interfere with the translation of *furA* transcripts, post-transcriptionally affecting the levels of FurA in cyanobacteria (Hernández et al., 2006; Sevilla et al., 2011). Moreover, the *furA* antisense RNA was upregulated as a consequence of oxidative stress (Martin-Luna et al., 2011), suggesting that the induction of *isiA* expression under stress environmental may result from the subsequent oxidative response reducing the level of *furA* mRNA by upregulating its antisense RNA and removing its inhibition of *isiA* expression.

isrR is an antisense RNA transcribed from the noncoding strand of *isiA*. Under optimal growth conditions, *isrR* is highly abundant, while *isiA* mRNA is not detectable (Dühring et al., 2006; Xu et al., 2014b). By contrast, *isrR* is degraded and *isiA* mRNA becomes more abundant upon iron deficiency (Dühring et al., 2006), suggesting that the degradation of *isrR* and *isiA* mRNA is linked and could be a reversible switch that responds to iron deficiency. In addition, the degradation of *isrR* was induced by high light and hydrogen peroxide stress (Dühring et al., 2006), indicating another possible mechanism by which *isiA* is induced by various environmental stresses. These stresses caused an oxidative response, which may promote the degradation of *isrR* by unknown regulators and derepress the accumulation of *isiA* mRNA.

Iron deficiency and oxidative stress both stimulate the biosynthesis of IsiA by repressing the levels of *isrR* and FurA; however, iron deficiency has a much greater effect on the induction of *isiA* expression than does oxidative stress. On the one hand, oxidative stress may not effectively repress the activity of FurA mediated by the loss of iron compared to iron-deficient stress itself, although reactive oxygen species can also detach ferrous iron from FurA. On the other hand, this difference could result from the more rapid decrease of *isiA* mRNAs under hydrogen peroxide stress than under iron-deficient stress (Dühring et al., 2006). Mathematical modeling and quantitative experimental analyses showed that *isrR* restricted the accumulation of *isiA* mRNA under prolonged, severe, and unremitting stress conditions, and it was found to be responsible for the rapid decline in *isiA* mRNA levels once the stress was removed (Legewie et al., 2008). Thus, Legewie et al. (2008) speculates that iron deficiency may stimulate a longer oxidative response than oxidative stress in the repression of *isrR*, which maintains the stability of *isiA* mRNA for translation, promoting the accumulation of IsiA protein. Consistent with this hypothesis, IsiA was found to accumulate during the transition from the exponential phase to the stationary phase of growth when PSII photoprotection occurred (Durham et al., 2002; Singh and Sherman, 2006; Foster et al., 2007).

In addition to negative regulation, *isiA* transcription has also been shown to be positively regulated. As a transcriptional repressor, FurA binds to Fur-boxes near the promoter sequences of the *isiA* gene, blocking the entry of RNA polymerase and thereby inhibiting the initiation of transcription. In *Synechocystis* cells, an assay of modified *isiA* promoters fused with GFP showed that only those lacking the Fur motif region did not generate the maximum GFP fluorescence. Kunert et al. (2003) proposed that additional sequence elements in a 90-bp region upstream of the putative −35 box in the *isiA* promoter could be recognized by RNA polymerase, with an unidentified activator affecting its transcriptional activity.

Model of the Expression and Regulation of *isiA*

The link between iron homeostasis and the redox stress response on the expression of *isiA* highlights the complexity of its regulation, as indicated by multiple studies (Xu et al., 2003; Balasubramanian et al., 2006; Jantaro et al., 2006). The expression and regulation of *isiA* by iron deficiency and oxidative stress may partially overlap. It is probable that the regulation of *isiA* occurs at both the transcriptional and post-transcriptional levels and involves at least two regulators, FurA, the prokaryotic transcriptional regulators that integrate iron metabolism under stress environment, and *isrR*, the only RNA known so far to regulate a photosynthesis component (Dühring et al., 2006; Hernández et al., 2006). A working model is based on studies in *Synechocystis* sp. PCC 6803 (**Figure 1**). Northern blot analysis showed that more than four different transcripts originated in the *isiAB* operon (Vinnemeier et al., 1998; Dühring et al., 2006): a cis-encoded antisense RNA, *isrR*, transcribed from the *isiA* noncoding strand under optimal growth conditions; the dicistronic *isiAB* transcript; the *isiA* monocistronic transcript; and the 5′ untranslated region transcript (not shown in our model), which was observed but not further analyzed under iron deficiency or oxidative stress.

Briefly, under optimal growth conditions, the iron-binding FurA protein and the *isrR* antisense RNA corepress the biosynthesis of IsiA. It assumed that the equilibrium between iron-bound and nonbound FurA was easily disturbed by variations in environmental conditions, allowing *isiA* to be expressed at very low levels in the cell. It is therefore crucial that *isrR* expression under iron-replete conditions controls the degradation of *isiA* mRNA at the post-transcriptional level. Under iron deficiency or oxidative stress, the level of FurA was downregulated by either stress-induced antisense RNA or FtsH1/FtsH3 protease, allowing RNA polymerase to function in combination with an unknown activator to initiate *isiA* transcription (Krynicka et al., 2014). Under iron-limited conditions, *isrR* expression is repressed by an unknown mechanism, leading to the further accumulation of *isiA* mRNA and IsiA protein (**Figure 1**). As noted above, it is possible that the effective inactivation of FurA by a loss of iron, as well as the longer oxidative response that represses *isrR*

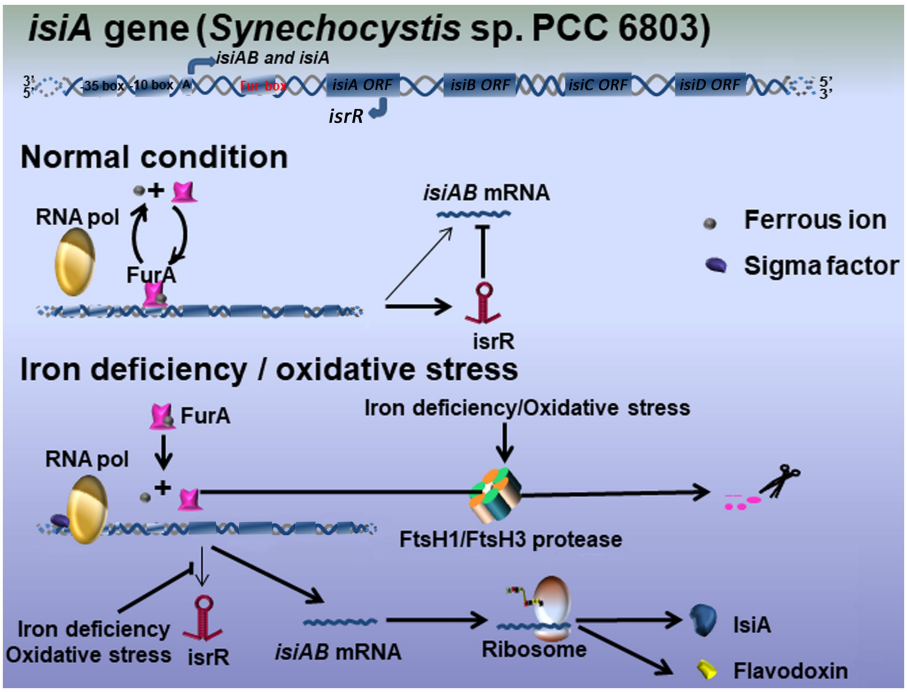

FIGURE 1 | Hypothetical model for the IsiA regulatory mechanisms in *Synechocystis* sp. PCC 6803. Three main transcripts originate in the operon *isiAB*: the bicistronic *isiAB* transcript, the *isiA* monocistronic transcript, and *isrR* microRNA. Under optimal growth conditions, iron-binding FurA represses the expression of *IsiA* at the transcriptional level. The equilibrium between iron-bound and unbound FurA is easily disturbed by variation in the environmental conditions, meaning *isiA* mRNA tends to be continuously expressed at very low levels. The antisense RNA *isrR* mediates the degradation of *isiA* mRNA at the post-transcriptional level. Under iron-limited or oxidative stress conditions, FurA is downregulated by either stress-induced antisense RNA or the FtsH1/FtsH3 protease, leaving RNA polymerase to interact with an unknown activator to initiate *isiA* transcription. *isrR* is also repressed, leading to the further accumulation of *isiA* mRNA and the biosynthesis of IsiA.

transcription, may be important for the accumulation of IsiA in the cell.

Besides the overlapping regulatory networks mentioned above, it cannot rule out the possibility that iron deficiency stress and other environmental changes or stresses regulate *isiA* expression through different signaling pathways. Lopez-Gomollon et al. (2007) pointed out that nitrogen regulation was present upstream of the *isiA* gene in the N_2-fixing heterotrophic *Anabaena* sp. PCC 7120. Moreover, Pilla et al. (2013) reported that a heat-responsive transcriptional regulator, Sll1130, might bind to a conserved inverted repeat (GGCGATCGCC) and negatively regulate *isiA* transcription in *Synechocystis* sp. PCC 6803. Thus, additional cis-acting factors might regulate *isiA* transcription to enable cyanobacteria to withstand a variable environment. The model will likely be refined by future research.

Structure and Function of IsiA Complexes

Structural Organization of IsiA Complexes

In 2001, two groups simultaneously reported a supercomplex, $IsiA_{18}$-PSI trimer, consisting of a trimeric PSI surrounded by a closed ring comprising 18 IsiA subunits in two model cyanobacterial species, *Synechocystis* sp. PCC 6803 and *Synechococcus* sp. PCC 7942 (Bibby et al., 2001a; Boekema et al., 2001). Subsequently, electron microscopy and image analyses of IsiA complexes in *Synechocystis* cells under prolonged iron stress conditions revealed a highly flexible interaction between PSI and IsiA or between the IsiA subunits in this complex (Kouril et al., 2005a).

Recently, the overall structure of the IsiA-PSI supercomplex was resolved as a disk of 3-fold rotational symmetry, and the angle is about 120°. The higher-resolution map showed that the supercomplex comprises four helices, each facing PSI, with each IsiA monomer rotated by approximately 60° relative to its neighbor. 18 IsiA monomers form a ring around the PSI trimer, and 6 IsiA monomers around a PSI monomer (Toporik et al., 2019; Cao et al., 2020). In 2020, Zhao et al. had visualized the native organization of the $IsiA_{18}$-PSI trimer in *Synechococcus* sp. PCC 7942 cells by high-resolution atomic force microscopy (Zhao et al., 2020). They found that the diameter of PSI trimer is 21 nm, the distance between two adjacent highest positions of PSI monomers in PSI trimer is 11 nm (**Figure 2**). The distance between two adjacent $IsiA_{18}$-PSI trimer supercomplexes is 25.7 nm, and the distance between two close $IsiA_{18}$-PSI trimer supercomplexes is 60.2 nm (Zhao et al., 2020). They found that IsiA has multiple assembly methods on the thylakoid membrane, which are helical, "S"-shape, strom-like and IsiA fibres insert into the core of an IsiA-PSI supercomplex (Zhao et al., 2020). The typical $IsiA_{18}$-PSI trimer complex is formed during short-term iron-deficient conditions. When the PSI trimers were depolymerized into monomers by prolonged iron deficiency, the IsiA proteins assembled into single rings or double rings

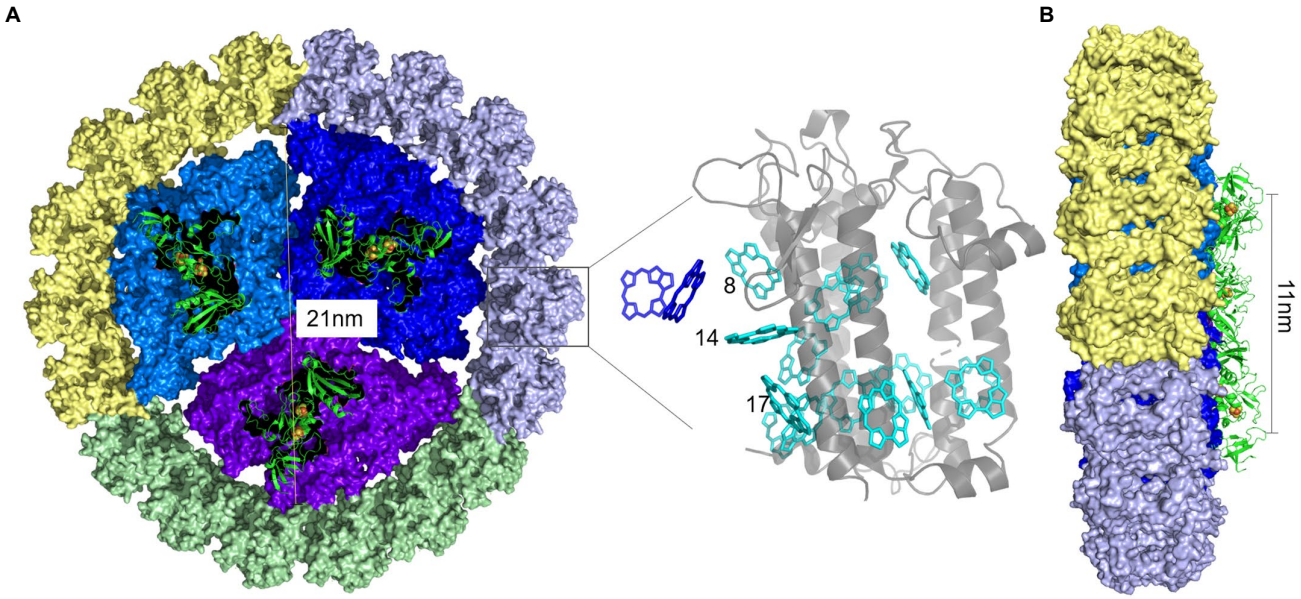

FIGURE 2 | PSI-IsiA supercomplex structure (Drawn according to the study by Toporik et al. (2019) and Cao et al. (2020). A. The IsiA18 –PSI trimer supercomplex structure. 18 IsiA monomers form a ring around the PSI trimer. PSI monomers were colored in blue, dark blue and purple, respectively. 6 IsiA proteins surrounding each PSI monomer were colored grey, green and yellow, respectively. The diameter of PSI trimer is 21 nm, and the distance between two adjacent highest positions of PSI monomers in PSI trimer is 11 nm (B). Chlorophylls around IsiA is cyan, and the Chlorophylls near the PSI trimer is dark blue. Grey is the IsiA protein.

surrounding a PSI monomer (Kouril et al., 2005b). Moreover, single, double, triple or multimeric IsiA rings surrounded the PSI trimers, dimers and monomers, and forming IsiA-PSI supercomplex of different structures (Zhao et al., 2020).

Under iron-deficient conditions, the majority of unbound IsiA proteins form IsiA aggregates of different sizes. These IsiA aggregates exist in single rings or double rings, which are similar to the shapes and sizes of those with a central PSI monomer. The existence of the IsiA aggregates demonstrates that the self-assembly of IsiA proteins does not require the presence of either PSI trimers or monomers (Ihalainen et al., 2005). It is often argued that the observed larger IsiA aggregates, with or without PSI monomers, are simply an artifact of severe iron starvation, which leads to chlorosis. By contrast, van der Weij-de Wit et al. (2007) reported that the IsiA aggregates appeared *in vivo* during the early stages of iron stress, which was confirmed by our subsequent finding that the IsiA aggregates formed before the IsiA-PSI trimers (Ma et al., 2017). Furthermore, a sizable pool of uncoupled IsiA aggregates was found in cells grown in a steady-state iron stress condition with replete macronutrients mimicking natural high-nitrate, low-Chl environments (Schrader et al., 2011). By using chlorophyll fluorescence analysis, the IsiA aggregates elevated the Fo (initial fluorescence levels) and decreased the apparent Fv/Fm (the maximum quantum yield of PSII photochemistry), which was consistent with the results of earlier non-steady-state studies (Guikema and Sherman, 1983; Pakrasi et al., 1985a; Falk et al., 1995). Therefore, the significant pool of energetically uncoupled IsiA aggregates is a reality in modern iron-limited environments. Chauhan et al. (2011) observed that the exposure of *Thermosynechococcus elongatus* cells to nanomolar concentrations of iron induced the formation of the largest IsiA-PSI supercomplex, consisting of a PSI trimer surrounded by two complete IsiA rings, with the inner ring comprised of 18 IsiA subunits and the outer ring containing 25 IsiA subunits.

Our previous study suggested that the IsiA proteins seemed to preferentially encircle trimeric PSI when both the PSI trimers and monomers were present in cells exposed to short-term iron deficiency (Ma et al., 2017). The binding preference of IsiA is similar to IdiA, another iron-stress-induced protein that is not homologous to IsiA and binds only to dimeric, not monomeric, PSII (Lax et al., 2007); however, the trimeric organization of PSI was not necessary for the binding of the IsiA protein, as noted above. Moreover, IsiA still had a strong tendency to form complexes with the PSI monomer in a *psaL* deletion mutant lacking PSI trimers, even in short-term iron-deficient conditions (Aspinwall et al., 2004; Kouril et al., 2005b). In the *psaL* deletion mutant, incomplete single or double rings of IsiA proteins specifically bound next to the PsaF/J subunits in the PSI monomer, indicating that these subunits might be responsible for the binding of IsiA. Interactions were observed between IsiA's "a" "c" "d" "e" positions and PSI subunits PsaF, PsaJ, and PsaK, revealing that these protein–protein interactions involved the C terminus of IsiA (**Figure 2**; Toporik et al., 2019). Nevertheless, in the mutant strain lacking the PsaF and PsaJ subunits, IsiA was still capable of binding the PSI trimer as a ring of 17 units (Kouřil et al., 2003). These results clarified that the PsaL and PsaF/J subunits facilitated the binding of IsiA to PSI but were not obligatory structural components in the formation of the IsiA-PSI complexes. The observation that

IsiA proteins specifically associate with PSI monomers next to the PsaF/J subunits suggests that the IsiA docking site is located near these subunits. In plants, PsaG acts as a linker protein that anchors a belt of four light-harvesting proteins, Lhca1–4, to the side of the PsaF/J subunits of the PSI core complex *via* its two tilting transmembrane helices (Ben-Shem et al., 2003). In cyanobacteria, an accessory protein factor similar to PsaG plays a role in the assembly of the IsiA-PSI complex, but whether it is absent in the resulting complex is unknown (Boichenko, 2004). Schoffman and Keren (2019) demonstrated that the biodilution of intercellular Fe was the main factor that controlled the formation of IsiA pigment–protein complexes.

There are 591 Chls on $IsiA_{18}$-PSI trimer supercomplex, 306 Chls with the IsiA ring and 298 Chls in PSI trimer in *Synechocystis* sp. PCC 6803. However, in different cyanobacterium, the $IsiA_{18}$-PSI trimer supercomplex combines different Chl a and Car, such as the $IsiA_{18}$-PSI trimer of *Synechococcus* sp. PCC 7942 binds to 3 Chl a and 3 Car more than *Synechocystis* sp. PCC 6803 in the core part (Toporik et al., 2019; Cao et al., 2020). Feng et al. (2011) have reported that IsiA most likely bound to 13 Chls, in agreement with the number of Chls in CP43 of PS II. Toporik et al. (2019) pointed out each IsiA monomer bound to 17 Chls, of which 13 are in a similar position to their location on CP43 and four are specific to IsiA. Ihalainen et al. (2005) showed that four Cars were present in each IsiA monomer, including two β-carotenoids, one echinaceone, and one zeaxanthin. However, Toporik et al. (2019) identified three Cars at the IsiA-IsiA interface, and another Car, B1, bound to the interface between IsiA and PSI. Cao et al. (2020) reported the structures of the PSI_3–$IsiA_{18}$–Fld_3 and PSI_3–$IsiA_{18}$ supercomplexes from *Synechococcus sp*. PCC 7942, revealing features that are different from the previously reported PSI structures, and a sophisticated pigment network that involves previously unobserved pigment molecules. Pigment analysis results showed that, when compared with the trimeric PSI core alone, the PSI_3–$IsiA_{18}$ supercomplex contains higher amounts of zeaxanthin (Zea), a molecule that is essential for quenching excessive absorbed energy.

The prochlorophytes, such as the marine phytoplankton *Prochlorococcus*, are a class of cyanobacteria that do not use phycobilisomes, but instead use intrinsic light-collecting proteins, known as Pcb proteins, which contain Chl a/b as light-harvesting systems. There are six transmembrane helices, and highly homology with the chlorophyll-binding protein that includes the Chl a-binding proteins CP43, CP47 of PSII and the iron stress-induced protein IsiA. Some constitutively expressed Pcbs form light-harvesting structures in *Prochlorococcus* strains, including the $PcbG_{18}$-PSI trimer in the low-light-adapted strain SS120, the $PcbA_8$-PSII dimer in the moderate low-light-adapted strain *Prochlorococcus* sp. MIT9313 and in the high-light-adapted strain MED4 (Bibby et al., 2003). In *Prochlorococcus* sp. MIT 9313, iron deficiency could induce the formation of $PcbB_{18}$-PSI trimer complexes similar to the $IsiA_{18}$-PSI trimer (Bibby et al., 2003). MED4 PSI domains were loosely packed in the thylakoid membrane of *Prochlorococcus* sp. MIT 9313, while in the low-light condition, PSI was organized into a tightly packed pseudo-hexagonal lattice to maximize harvesting and trapping of light. The low-light-adapted algal strain SS120 has a different strategy for coping with low-light levels, and SS120 thylakoids contained hundreds of tightly packed Pcb-PSI supercomplexes, saving the extra iron and nitrogen required to PSI-only domains (MacGregor-Chatwin et al., 2019). These results indicated that it was a common phenomenon to express iron-deficiency induced antenna pigment protein and assemble to maintain photosynthesis under iron deficiency conditions.

Diversity of IsiA Function

As mentioned above, IsiA shares high sequence similarity with CP43 in PSII but lacks the large hydrophilic loop between helices V and VI of CP43 (Chen and Bibby, 2005). In *Synechocystis* sp. PCC 6803, deletion mutations in the long hydrophilic loop of CP43 led to the disappearance of oxygen evolution activity (Kuhn and Vermaas, 1993), suggesting that IsiA cannot functionally replace CP43 under iron-deficient conditions, as was proposed by Burnap et al. (1993). Using mutants lacking the long hydrophilic loop of CP43, it was confirmed that no detectable differences were present in the light-dependent evolution of oxygen under iron deficiency and salt stress conditions (Vinnemeier et al., 1998). A high-resolution crystal structure of PSII at a resolution of 1.9 Å showed that the CP43-Glu 354 residue was located in the hydrophilic loop in the Mn_4CaO_5 cluster of the water-splitting reaction center, where it functions as a bidentate ligand for Mn_2 and Mn_3 (Umena et al., 2011). As the loss of the hydrophilic loop leads to the loss of hydrolysis ability, IsiA cannot replace CP43.

When iron becomes readily available in the environment, iron-starved cells recover quickly, resynthesizing the thylakoid membranes and reassembling their Chl-containing protein complexes (Sherman and Sherman, 1983; Odom et al., 1993). Using a Chl biosynthesis inhibitor, some studies have shown that the reassembly of Chl-containing protein complexes occurred before Chl biosynthesis (Riethman and Sherman, 1988; Troyan et al., 1989). IsiA is the major Chl-containing protein, binding up to 50% of the Chl in iron-starved cells (Burnap et al., 1993). In iron-limited cultures, transfer of half of the chlorophyll in the cell from PSI to IsiA had negligible effects on energy transfer from antenna systems to PSII *in vivo* (Schoffman and Keren, 2019). Therefore, the IsiA pigment-protein complex not only plays a key role when cells transition into iron limitation, but also supports the efficient recovery of photosynthetic apparatus during cells transition back out of iron limit-phase (Schoffman and Keren, 2019). However, the above content may not be the main function of IsiA, it should only be a cost-effective way of supplying preexisting Chl in IsiA for the reassembly of PSII and PSI complexes after the addition of iron.

Due to its high level of Chl binding, IsiA was also hypothesized to serve as an alternative light-harvesting complex, compensating for the decrease in phycobilisomes in iron-starved cells (Burnap et al., 1993; Schoffman and Keren, 2019). Cheng et al. (2020) showed the deletion of *isiA* in *Synechocystis* sp. PCC 6803 affected the genes expression that are involved in photosynthesis, phycobilisome, and the proton-transporting ATPase complex. A 77 K fluorescence spectrum revealed that the characteristic

peak of isolated IsiA aggregates at around 685 nm was very high but was weak in the $IsiA_{18}$-PSI trimer complex (Bibby et al., 2001a). Furthermore, treating the $IsiA_{18}$-PSI trimer complex with Triton X-100 caused this weak peak to become the dominant emission (Bibby et al., 2001b), indicating that PSI trimer coupling IsiA in such a way is to efficiently transfer light energy to the PSI reaction center. In another report, Toporik et al. (2019) proposed that the large amount of chlorophyll in the stromal layer meant that photons would be absorbed by this layer and then converted into excitation energy to be transferred to PSI through the luminal layer. Chlorophyll at position 17 (chlorophyll 17) through chlorophyll at position 8 (chlorophyll 8) combined with the main pigment cluster, with chlorophyll 8 being unique to IsiA (**Figure 2**). The specific position of chlorophyll 17 and 8 molecules showed that they were the terminal emitters of IsiA and thus played a key role in the process of energy transfer. More chlorophyll was distributed on the stromal side of the membrane, where it formed a continuous pigment layer around PSI, which is different from what was observed in eukaryotes; therefore, Toporik et al. (2019) speculated that this phenomenon plays an important role in the photoprotective process.

Using different spectroscopic measurements, such as time-resolved absorption and emission spectroscopy, the energy transfer and trapping processes in the $IsiA_{18}$-PSI trimers in *Synechocystis* sp. PCC 6803, *Synechococcus* sp. PCC 7942 and *Thermosynechococcus vulcanus* were studied (Andrizhiyevskaya et al., 2002; Melkozernov et al., 2003; Andrizhiyevskaya et al., 2004; Akita et al., 2020). For the largest $IsiA_{43}$-PSI supercomplex, identified in *T. elongatus*, fluorescence-decay-associated spectra also indicated that IsiA was energetically strongly associated with the PSI trimer (Chauhan et al., 2011). Based on calculations of the optimal energy transfer within the $IsiA_{18}$-PSI trimer, IsiA was proposed to bind 15 Chls in *Synechocystis* sp. PCC 6803 (Zhang et al., 2010); however, Feng et al. (2011) showed that IsiA most likely possessed 13 Chls in *Synechocystis* sp. PCC 6803 in agreement with the number in CP43 of PSII, as determined from a crystal structure with a resolution of 1.9 Å. Recently, Toporik et al. (2019) pointed out each IsiA monomer bound to 17 Chls. As 96 Chl molecules are present in the PSI monomer, determined from a crystal structure with a higher resolution of 2.5 Å (Jordan et al., 2001), the theoretical cross sections of the $IsiA_{18}$-PSI complex should increase by approximately 81% compared to the PSI trimer alone (Bibby et al., 2001a). Using a light saturation curve in *Synechococcus* sp. PCC 7942, the light-harvesting ability of the $IsiA_{18}$-PSI trimer was only found to be about 44% higher than that of PSI (Boekema et al., 2001). In addition to *in vitro* measurements, Ryan-Keogh et al. (2012) demonstrated an increase of 60% in the absorption cross section of PSI in iron-starved *Synechocystis* sp. PCC 6803 cells. Another report provided evidence that the increased absorption cross section provided by the IsiA proteins led to an enhanced rate of electron transfer through PSI in the marine strain *Synechococcus* sp. PCC 7002 (Sun and Golbeck, 2015).

In the $IsiA_{18}$-PSI trimer structural model, the 18 IsiA proteins did not form a perfect ring and were instead distorted by the 3-fold rotational symmetry of the PSI trimer (Nield et al., 2003; Feng et al., 2011). Only the regions where PSI Chl a molecules are located close to the IsiA Chl a molecules were believed to be involved in transferring energy from IsiA to the PSI trimer. It was also proposed that not all IsiA proteins transfer energy directly to the inner PSI molecules, due to their nonequivalent positions relative to PSI. Akita et al. (2020) recently report a 2.7-Å resolution cryo-electron microscopic structure of a supercomplex between PSI core trimer and IsiA from a thermophilic cyanobacterium *Thermosynechococcus vulcanus*, and time-resolved fluorescence spectra of the $IsiA_{18}$-PSI trimers supercomplex showed clear excitation-energy transfer from IsiA to PSI, strongly indicating that IsiA functions as an energy donor, but not an energy quencher, in the supercomplex.

Toporik et al. (2019) demonstrated that the crystal structure of IsiA has been resolved, the Chl in the IsiA loop is unequally distributed, and the stromal side of the membrane contains nearly twice as many pigments as the lumenal side. In the PSI-IsiA supercomplex at the stromal side, only one chlorophyll pair is located close to 18 Å, and the next pair is at 21–25 Å. These distances are enough to mediate energy transfer, but much larger than most Chl distances between internal IsiA and PSI, further indicating that the IsiA loop and PSI are independently present on the stromal side. On the luminal side, where there is little pigment, 10 Chl pairs were observed below 20 Å, linking IsiA and PSI, most of which involved Chl 17, 14, and 8 on the IsiA subunit (**Figure 2**). Due to their abundance in the stromal layer, photons are more likely to be absorbed by the stromal layer, but the excitation energy is more likely to be transferred to the PSI through the lumenal side. The location of Chl 8 and 17 at the interface between the adjacent IsiA subunit and PSI strongly indicates that these Chl molecules are terminal emitters of IsiA and should play a key role in their function (Toporik et al., 2019).

In addition, steady-state and time-resolved fluorescence measurements indicated that isolated IsiA aggregates dissipated excitation energy, after which they were in a strongly fluorescence-quenched state (Ihalainen et al., 2005). The IsiA aggregates are present in the early stages of iron starvation, and their fluorescence quenching is similar to that observed under long-term iron starvation (van der Weij-de Wit et al., 2007). Therefore, IsiA might mediate the thermal dissipation of absorbed energy and thereby protect PSII from excessive excitation under iron-limited conditions, as predicted in previous studies (Park et al., 1999; Sandström et al., 2001). It is well established that Car can quench the excited state of Chl, and a similar mechanism appears to operate in IsiA aggregates (Berera et al., 2009); for example, a high-performance liquid chromatography analysis revealed that IsiA aggregates contain Chl a, β-carotene, echinenone, and zeaxanthin (Ihalainen et al., 2005; Berera et al., 2009). In a mutant strain lacking *CrtO*, which encodes β-carotene ketolase, the enzyme mediating the conversion of β-carotene to echinenone, the IsiA aggregates lacking echinenone were not deficient in their fluorescence quenching ability (Dhaene et al., 2008).

Model of the Structures and Functions of IsiA Complexes

Under iron-replete conditions, the PSI/PSII ratio is high and sufficient phycobilisomes can move between the two photosynthetic systems, which together maintain an electron flow balance between PSI and PSII. Under iron-limited conditions, the PSI/PSII ratio drops and the phycobiliprotein content is significantly reduced, perturbing the electron balance between the photosystems and resulting in serious oxidative damage. In the electron transport chain, PSII is more labile and vulnerable to oxidative damage (Allakhverdiev et al., 2008). The importance of defending PSII from oxidative damage under iron-deficient conditions has been confirmed based on several observations, including the rapid increase in thermal dissipation at the level of the antenna associated with an orange carotenoid protein (OCP; Wilson et al., 2006; Wilson et al., 2007) and the induction of another iron stress protein, IdiA, that protects the acceptor side of PSII against photodamage (Exss-Sonne et al., 2000; Lax et al., 2007). The transcription of *idiA* precedes that of *isiA*, and the deletion of *idiA* promotes the formation of IsiA-PSI complexes under iron starvation (Tölle et al., 2002; Yousef et al., 2003), indicating that the expression of *isiA* cannot be effectively prevented when PSII is damaged.

Recently, using immunoblot and 77 K fluorescence analyses performed with thylakoid membranes and fractions from a sucrose gradient ultracentrifugation, we observed that free IsiA proteins preferentially encircled the PSI trimer to efficiently transfer energy to the PSI cores, even without an IsiA-originated fluorescence peak, a state of IsiA-PSI trimer that had not previously been reported (Ma et al., 2017). IsiA-PSI complexes formed and gradually accumulated throughout the iron deficiency period, providing more convincing evidence that the original role of IsiA bound to PSI was as an energy collector for PSI. Not all energy absorbed by IsiA is transferred to PSI, especially during prolonged iron deficiency, possibly because the increased *in vivo* cross section of PSI is lower than the theoretical increased cross section of the $IsiA_{18}$-PSI trimer (Ma et al., 2017). As already noted, the IsiA aggregates likely appeared before the formation of the $IsiA_{18}$-PSI trimer and became larger following prolonged iron deficiency, dissipating excess energy throughout the course of iron deficiency.

Thus, a scenario for the dynamic change in IsiA complex structures and the roles of IsiA in these complexes during long-term periods of iron deficiency under laboratory conditions was presented (**Figure 3**). In the early stages of iron-limited stress, the IdiA proteins are produced and located at the acceptor side of PSII, where they prevent photodamage. In the middle stage, the IsiA proteins possibly appear as small aggregates, but later begin to associate with the PSI trimer to efficiently transfer energy to the PSI cores by IsiA-PSI supercomplex. In the late stage of iron-limited stress, the PSI trimers depolymerize to monomers, leaving the IsiA proteins to be incorporated into larger IsiA aggregates or form IsiA-PSI monomer complexes, in which the IsiA proteins have the primary function of being energy collectors and the secondary function of dissipating energy to provide photoprotection for PSI. Chen et al. found that IsiA quench excitation energy by a novel cysteine-mediated process for the photoprotection (Chen et al., 2021). The IsiA aggregates dissipate excess energy, providing photoprotection for the whole photosynthetic apparatus, especially PSII. The dynamic changes in IsiA and its associations with PSI and PSII may be an optimal adaptation to the degree of iron deficiency, enabling flexible light harvesting and balancing electron transfer between PSI and PSII to minimize photodamage, and ensuring the cells survive. By contrast, Toporik et al. (2019) observed that, besides the light-harvesting and photoprotection functions of IsiA, the IsiA dimer can also maintain the effective transfer of excitation energy in the IsiA ring.

The function of the IsiA–PSI supercomplex that favour energy transfer towards the central PSI was confirmed recently by structure analysis of membrane complexes in the cyanobacterial thylakoid membrane using high-resolution atomic force microscopy (Zhao et al., 2020). However, although

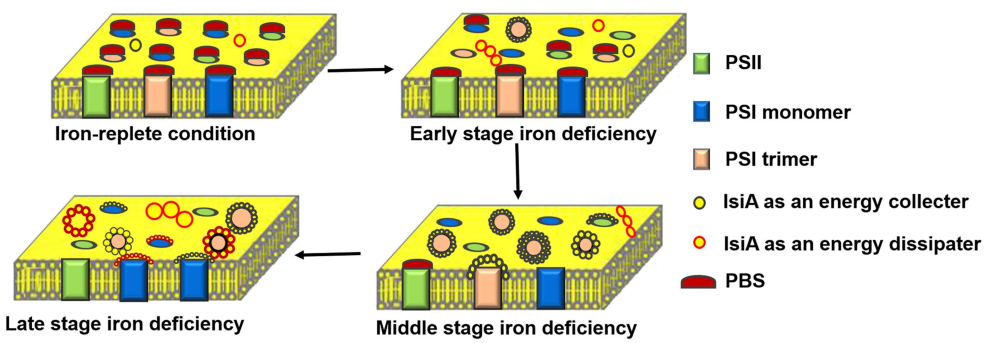

FIGURE 3 | Schematic representation of the dynamic changes in the structure and function of IsiA-containing complexes during a long period of iron deficiency. Under the iron-replete condition, phycobilisome (PBS) acts as a light-harvesting complex for both PSII and PSI. In the early stages of iron deficiency, IsiA forms small aggregates and $IsiA_{18}$-PSI trimers, in which the IsiA proteins serve as energy collectors and efficiently transfer energy to the PSI cores. In the middle stage of iron deficiency, the levels of PSB, PSI, and PSII all decline, with PSB still serving PSII. An IsiA-PSI low fluorescence supercomplex (ILFS) is formed, in which IsiA acts an energy collector. In the late stage of iron deficiency, the IsiA-PSI high fluorescence supercomplex (IHFS) and plentiful IsiA aggregates are formed. The IsiA proteins serve as an energy dissipater, providing photoprotection for the entire photosynthetic apparatus, especially PSII.

significant progress has been made in our understanding of the IsiA complexes (**Figure 3**), many questions remain, and further verification is required. For example, whether IsiA and PSII can associate with each other is still under debate. It was clear that accumulated IsiA did not contribute to light capture by PSII (Falk et al., 1995; Fraser et al., 2013); however, energy transfer was observed between PBS and the IsiA aggregates (Rakhimberdieva et al., 2007; Wilson et al., 2007). This supports the proposal that IsiA displays a remarkable mobility (Sarcina and Mullineaux, 2004), enabling it to be located between PSII and PBS within the membrane and thereby compete with the energy transfer from PBS to PSII (or PSI; Huner et al., 2001). Notably, Toporik et al. (2019) demonstrated that the IsiA ring interacted with soluble PBS. Using BN-SDS-PAGE, immunoblot, and 77 K fluorescence analyses, Wang et al. (2010) demonstrated that a IsiA-PSI-PSII supercomplex was present in long-term iron-starved cells, which is inconsistent with the result that no potential structural information about the IsiA-PSII complex was detected under long-term iron-deficient conditions using electron microscopy (Kouril et al., 2005a).

Within the IsiA-PSI-PSII supercomplexes, IsiA was proposed to be a regulator or assembler, rather than physically encircling the complexes. In addition, it was previously shown that the IsiA protein was enriched in HLIP (high light inducible protein)-containing PSI trimers prepared from *Synechocystis* sp. PCC 6803 cells treated with high-intensity light (Wang et al., 2008). Further studies using a *PsaL*-deleted mutant lacking the PSI trimers showed that IsiA was a component of the novel high-light-inducible carotenoid-binding protein complex (HLCC), consisting of Slr1128, IsiA, PsaD, and high-light-induced proteins A/B (HliA/B; Daddy et al., 2015). In the latter study, the authors hypothesized that the HLCC is also induced by iron deficiency and oxidative stress. In this case, IsiA, together with other components, might be localized at the stromal side of PSI, mediated by PsaD, to stabilize trimeric PSI and protect PSI from direct or indirect oxidative stresses, probably by scavenging reactive oxygen species produced at ferredoxin (Fd). The assembly of IsiA in the HLCC appeared to be a more accepted explanation of the role of IsiA under oxidative stress, despite its much lower abundance under oxidative stress than iron-deficient stress. The revelation of the IsiA-PSI-PSII supercomplex and HLCC further expands our understanding of the structure and function of the IsiA complexes.

CONCLUSION AND PROSPECTS

Over the almost 30 years since its discovery, there has been tremendous progress in our understanding of the iron-stressed *isiA* gene. The induction of *isiA* expression by various unfavorable environmental stresses or abnormal physiological states (such as in genetic mutants) reflects the complexity of the regulation of *isiA* expression. While the oxidative response could be considered a superior downstream trigger for *isiA* transcription, it is not enough to strongly induce the translation of IsiA proteins. Therefore, the regulation of IsiA function occurs at both the transcriptional and translational levels, involving at least FurA and the *isrR* antisense RNA, respectively. Moreover, it is likely that the effective inactivity of FurA by the loss of iron and the stabilization of *isiA* mRNA by the repression of *isrR* expression following an extended oxidative response are both closely related to the accumulation of IsiA proteins in cyanobacteria.

As described above, the model of the regulation of *IsiA* expression should be improved upon in the future. Physiological and functional analyses demonstrated that IsiA acts as an energy collector or an energy dissipater, depending on the functions of the complexes it forms. While structural models of the $IsiA_{18}$-PSI trimer have been presented, a high-resolution crystal structure of this complex would be helpful for determining which domains and subunits of PSI are crucial for IsiA binding and which Chls are crucial for the energy transfer network. Similarly, further studies are required to establish whether zeaxanthin or β-carotene acts as an energy quencher in these complexes or if another factor is involved. Moreover, the factors that initiate or facilitate the binding of IsiA to the PSI trimer are not currently known and should be identified. In addition, the existence of the IsiA-PSI-PSII supercomplex is yet to be verified, and further studies of HLCC will greatly enhance our knowledge of the physiological functions of IsiA.

AUTHOR CONTRIBUTIONS

AJ, YZ, and QW conceptualized the idea for manuscript. AJ, YZ, and HC drafted the manuscript. AJ and YZ made the figures. QW evaluated the manuscript and improvised the content. All authors contributed to the article and approved the submitted version.

FUNDING

This work was supported jointly by the National Key Research and Development Program of China (2020YFA0907600), the National Natural Science Foundation of China (31,770,128, 91,851,103 and 31,870,041), and the Natural Science Foundation of Henan Province (212300410024).

REFERENCES

Akita, F., Nagao, R., Kato, K., Nakajima, Y., Yokono, M., Ueno, Y., et al. (2020). Structure of a cyanobacterial photosystem I surrounded by octadecameric IsiA antenna proteins. *Communications Biology* 3, 232. doi: 10.1038/s42003-020-0949-6

Allakhverdiev, S. I., Kreslavski, V. D., Klimov, V. V., Los, D. A., Carpentier, R., and Mohanty, P. (2008). Heat stress: an overview of molecular responses in photosynthesis. *Photosynth Research* 98, 541–550. doi: 10.1007/s11120-008-9331-0

Andrizhiyevskaya, E. G., Frolov, D., Van Grondelle, R., and Dekker, J. P. (2004). Energy transfer and trapping in the photosystem I complex of *Synechococcus*

PCC 7942 and in its supercomplex with IsiA. *Biochim. Biophys. Acta* 1656, 104–113. doi: 10.1016/j.bbabio.2004.02.002

Andrizhiyevskaya, E. G., Schwabe, T. M., Germano, M., D'Haene, S., Kruip, J., van Grondelle, R., et al. (2002). Spectroscopic properties of PSI–IsiA supercomplexes from the cyanobacterium *Synechococcus* PCC 7942. *Biochimica et Biophysica Acta (BBA)-Bioenergetics* 1556, 265–272. doi: 10.1016/S0005-2728(02)00371-7

Ardelean, I., Matthijs, H., Havaux, M., Joset, F., and Jeanjean, R. (2002). Unexpected changes in photosystem I function in a cytochrome c6-deficient mutant of the cyanobacterium *Synechocystis* PCC 6803. *FEMS Microbiol. Lett.* 213, 113–119. doi: 10.1111/j.1574-6968.2002.tb11294.x

Aspinwall, C. L., Duncan, J., Bibby, T., Mullineaux, C. W., and Barber, J. (2004). The trimeric organisation of photosystem I is not necessary for the iron-stress induced CP43 protein to functionally associate with this reaction Centre. *FEBS Lett.* 574, 126–130. doi: 10.1016/j.febslet.2004.08.016

Balasubramanian, R., Shen, G., Bryant, D. A., and Golbeck, J. H. (2006). Regulatory roles for IscA and SufA in iron homeostasis and redox stress responses in the cyanobacterium *Synechococcus* sp. strain PCC 7002. *Journal of Bacteriol* 188, 3182–3191. doi: 10.1128/jb.188.9.3182-3191.2006

Behrenfeld, M. J., and Milligan, A. J. (2013). Photophysiological expressions of iron stress in phytoplankton. *Annu. Rev. Mar. Sci.* 5, 217–246. doi: 10.1146/annurev-marine-121211-172356

Ben-Shem, A., Frolow, F., and Nelson, N. (2003). Crystal structure of plant photosystem I. *Nature* 426, 630–635. doi: 10.1038/nature02200

Berera, R., van Stokkum, I. H., d'Haene, S., Kennis, J. T., van Grondelle, R., and Dekker, J. P. (2009). A mechanism of energy dissipation in cyanobacteria. *Biophys. J.* 96, 2261–2267. doi: 10.1016/j.bpj.2008.12.3905

Bibby, T., Mary, I., Nield, J., Partensky, F., and Barber, J. (2003). Low-light-adapted *Prochlorococcus* species possess specific antennae for each photosystem. *Nature* 424, 1051–1054. doi: 10.1038/nature01933

Bibby, T. S., Nield, J., and Barber, J. (2001a). Iron deficiency induces the formation of an antenna ring around trimeric photosystem I in cyanobacteria. *Nature* 412, 743–745. doi: 10.1038/35089098

Bibby, T. S., Nield, J., and Barber, J. (2001b). Three-dimensional model and characterization of the iron stress-induced CP43′-photosystem I supercomplex isolated from the cyanobacterium *Synechocystis* PCC 6803. *J. Biol. Chem.* 276, 43246–43252. doi: 10.1074/jbc.M106541200

Boekema, E., Hifney, A., Yakushevska, A., Piotrowski, M., Keegstra, W., Berry, S., et al. (2001). A giant chlorophyll–protein complex induced by iron deficiency in cyanobacteria. *Nature* 412, 745–748. doi: 10.1038/35089104

Boichenko, V. A. (2004). Photosynthetic units of phototrophic organisms. *Biochemistry-Moscow* 69, 471–484. doi: 10.1023/b:biry.0000029844.31857.40

Burnap, R. L., Troyan, T., and Sherman, L. A. (1993). The highly abundant chlorophyll-protein complex of iron-deficient *Synechococcus* sp. PCC7942 (CP43 [prime]) is encoded by the isiA Gene. *Plant Physiol.* 103, 893–902. doi: 10.1104/pp.103.3.893

Cao, P., Cao, D. F., Si, L., Su, X. D., Tian, L. J., Chang, W. R., et al. (2020). Structural basis for energy and electron transfer of the photosystem I-IsiA-flavodoxin supercomplex. *Nature Plants* 6, 167–176. doi: 10.1038/s41477-020-0593-7

Catling, D.C., and Zahnle, K.J. (2020). The Archean atmosphere. *Science advances* 6:16. doi: 10.1126/sciadv.aax1420

Chauhan, D., Folea, I. M., Jolley, C. C., Kouril, R., Lubner, C. E., Lin, S., et al. (2011). A novel photosynthetic strategy for adaptation to low-iron aquatic environments. *Biochemistry* 50, 686–692. doi: 10.1021/bi1009425

Chen, H., Niedzwiedzki, D. M., Bandyopadhyay, A., Biswas, S., and Pakrasi, H. B. (2021). *A Novel Mode of Photoprotection Mediated by a Cysteine Residue in the Chlorophyll Protein IsiA. microbiology* 12:14. doi: 10.1128/mBio.03663-20.

Chen, M., and Bibby, T. S. (2005). Photosynthetic apparatus of antenna-reaction centres supercomplexes in oxyphotobacteria: insight through significance of Pcb/IsiA proteins. *Photosynth. Res.* 86, 165–173. doi: 10.1007/s11120-005-1330-9

Cheng, Y. R., Zhang, T. Y., Wang, L., and Chen, W. L. (2020). Transcriptome analysis reveals IsiA-regulatory mechanisms underlying iron depletion and oxidative-stress acclimation in Synechocystis sp. strain PCC 6803. *Applied and environmental microbiology*. 86. doi: 10.1128/AEM.00517-20

Daddy, S., Zhan, J., Jantaro, S., He, C., He, Q., and Wang, Q. (2015). A novel high light-inducible carotenoid-binding protein complex in the thylakoid membranes of *Synechocystis* PCC 6803. *Sci. Rep.* 5. doi: 10.1038/srep09480

Dhaene, S., Tsoukatos, K., Lampoura, S.S., Matthijs, H.C., and Dekker, J.P. (2008). "role of echinenone in fluorescence quenching in IsiA aggregates from cyanobacteria," in *photosynthesis. Energy from the Sun*. Springer. 253-256.

Dühring, U., Axmann, I. M., Hess, W. R., and Wilde, A. (2006). An internal antisense RNA regulates expression of the photosynthesis gene isiA. *Proc. Natl. Acad. Sci.* 103, 7054–7058. doi: 10.1073/pnas.0600927103

Durham, K. A., Porta, D., Twiss, M. R., McKay, R. M. L., and Bullerjahn, G. S. (2002). Construction and initial characterization of a luminescent *Synechococcus* sp. PCC 7942 Fe-dependent bioreporter. *FEMS Microbiol. Lett.* 209, 215–221. doi: 10.1016/s0378-1097(02)00567-0

Exss-Sonne, P., Tolle, J., Bader, K. P., Pistorius, E. K., and Michel, K. P. (2000). The IdiA protein of *Synechococcus* sp. PCC 7942 functions in protecting the acceptor side of photosystem II under oxidative stress. *Photosynth. Res.* 63, 145–157. doi: 10.1023/a:1006322925324

Falk, S., Samson, G., Bruce, D., Huner, N. P., and Laudenbach, D. E. (1995). Functional analysis of the iron-stress induced CP 43′ polypeptide of PS II in the cyanobacterium *Synechococcus* sp. PCC 7942. *Photosynth. Res.* 45, 51–60. doi: 10.1007/BF00032235

Feng, X., Neupane, B., Acharya, K., Zazubovich, V., Picorel, R., Seibert, M., et al. (2011). Spectroscopic study of the CP43′ complex and the PSI–CP43′ Supercomplex of the Cyanobacterium *Synechocystis* PCC 6803. *J. Phys. Chem. B* 115, 13339–13349. doi: 10.1021/jp206054b

Ferreira, F., and Straus, N. A. (1994). Iron deprivation in cyanobacteria. *J. Appl. Phycol.* 6, 199–210. doi: 10.1007/BF02186073

Foster, J. S., Singh, A. K., Rothschild, L. J., and Sherman, L. A. (2007). Growth-phase dependent differential gene expression in *Synechocystis* sp. strain PCC 6803 and regulation by a group 2 sigma factor. *Arch. Microbiol.* 187, 265–279. doi: 10.1007/s00203-006-0193-6

Fournier, G. P., Moore, K. R., Rangel, L. T., Payette, J. G., Momper, L., and Bosak, T. (2021). The Archean origin of oxygenic photosynthesis and extant cyanobacterial lineages. *Proc. Biol. Sci.* 288, 20210675. doi: 10.1098/rspb.2021.0675

Fraser, J. M., Tulk, S. E., Jeans, J. A., Campbell, D. A., Bibby, T. S., and Cockshutt, A. M. (2013). Photophysiological and photosynthetic complex changes during iron starvation in *Synechocystis* sp. PCC 6803 and *Synechococcus* elongatus PCC 7942. *PloS one* 8:11. doi: 10.1371/journal.pone.0059861

Ghassemian, M., and Straus, N. A. (1996). Fur regulates the expression of iron-stress genes in the cyanobacterium *Synechococcus* sp. strain PCC 7942. *Microbiology* 142, 1469–1476. doi: 10.1099/13500872-142-6-1469

González, A., Fillat, M.F., Bes, M.-T., Peleato, M.-L., and Sevilla, E. (2018). "The challenge of iron stress in cyanobacteria," in *Cyanobacteria*. ed. A. Tiwari. 109–138.

Guerinot, M. L., and Yi, Y. (1994). Iron: nutritious, noxious, and not readily available. *Plant Physiol.* 104, 815–820. doi: 10.1104/pp.104.3.815

Guikema, J. A., and Sherman, L. A. (1983). Organization and function of chlorophyll in membranes of cyanobacteria during iron starvation. *Plant Physiol.* 73, 250–256. doi: 10.1104/pp.73.2.250

Guikema, J. A., and Sherman, L. A. (1984). Influence of iron deprivation on the membrane-composition of anacystis-nidulans. *Plant Physiol.* 74, 90–95. doi: 10.1104/pp.74.1.90

Guowei, Q., Koedooder, C., Qiu, B.-S., Shaked, Y., and Keren, N. (2021). Iron transport in cyanobacteria -from molecules to communities. *Trends Microbiol.* doi: 10.1016/j.tim.2021.06.001

Hagemann, M., Jeanjean, R., Fulda, S., Havaux, M., Joset, F., and Erdmann, N. (1999). Flavodoxin accumulation contributes to enhanced cyclic electron flow around photosystem I in salt-stressed cells of *Synechocystis* sp. strain PCC 6803. *Physiol. Plant.* 105, 670–678. doi: 10.1034/j.1399-3054.1999.105411.x

Havaux, M., Guedeney, G., Hagemann, M., Yeremenko, N., Matthijs, H. C., and Jeanjean, R. (2005). The chlorophyll-binding protein IsiA is inducible by high light and protects the cyanobacterium *Synechocystis* PCC6803 from photooxidative stress. *FEBS Lett.* 579, 2289–2293. doi: 10.1016/j.febslet.2005.03.021

Hernández, J. A., Muro-Pastor, A. M., Flores, E., Bes, M. T., Peleato, M. L., and Fillat, M. F. (2006). Identification of a furA cis antisense RNA in the cyanobacterium *anabaena* sp. PCC 7120. *J. Mol. Biol.* 355, 325–334. doi: 10.1016/j.jmb.2005.10.079

Huner, N.P., Krol, M., Ivanov, A., Sveshnikov, D., and Oquist, G. (2001). CP43'induced under Fe-stress in *Synechococcus* sp. PCC 7942 is associated with PSI. *Science Access* 3, 3–61. doi: 10.1071/sa0403111

Ihalainen, J. A., D'Haene, S., Yeremenko, N., van Roon, H., Arteni, A. A., Boekema, E. J., et al. (2005). Aggregates of the chlorophyll-binding protein IsiA (CP43') dissipate energy in cyanobacteria. *Biochemistry* 44, 10846–10853. doi: 10.1021/bi0510680

Ivanov, A., Park, Y.-I., Miskiewicz, E., Raven, J., Huner, N., and Öquist, G. (2000). Iron stress restricts photosynthetic intersystem electron transport in *Synechococcus* sp. PCC 7942. *FEBS Lett.* 485, 173–177. doi: 10.1016/S0014-5793(00)02211-0

Ivanov, A. G., Krol, M., Selstam, E., Sane, P. V., Sveshnikov, D., Park, Y. I., et al. (2007). The induction of CP43' by iron-stress in *Synechococcus* sp. PCC 7942 is associated with carotenoid accumulation and enhanced fatty acid unsaturation. *Biochimica et Biophysica Acta (BBA)* 1767, 807–813. doi: 10.1016/j.bbabio.2007.02.006

Ivanov, A. G., Krol, M., Sveshnikov, D., Selstam, E., Sandström, S., Koochek, M., et al. (2006). Iron deficiency in cyanobacteria causes monomerization of photosystem I trimers and reduces the capacity for state transitions and the effective absorption cross section of photosystem I in vivo. *Plant Physiol.* 141, 1436–1445. doi: 10.1104/pp.106.082339

Jantaro, S., Ali, Q., Lone, S., and He, Q. (2006). Suppression of the lethality of high light to a quadruple HLI mutant by the inactivation of the regulatory protein PfsR in *Synechocystis* PCC 6803. *J. Biol. Chem.* 281, 30865–30874. doi: 10.1074/jbc.M606252200

Jeanjean, R., Zuther, E., Yeremenko, N., Havaux, M., Matthijs, H. C., and Hagemann, M. (2003). A photosystem 1 psaFJ-null mutant of the cyanobacterium *Synechocystis* PCC 6803 expresses the isiAB operon under iron replete conditions. *FEBS Lett.* 549, 52–56. doi: 10.1016/S0014-5793(03)00769-5

Jie, W., Wei, Z., Hui, C., Jiao, Z., He, C., and Wang, Q. (2019). Ammonium nitrogen tolerant chlorella strain screening and its damaging effects on photosynthesis. *Front. Microbiol.* 9:03250. doi: 10.3389/fmicb.2018.03250

Jordan, P., Fromme, P., Witt, H. T., Klukas, O., Saenger, W., and Krauss, N. (2001). Three-dimensional structure of cyanobacterial photosystem I at 2.5 A resolution. *Nature* 411, 909–917. doi: 10.1038/35082000

Karandashova, I., Elanskaya, I., Marin, K., Vinnemeier, J., and Hagemann, M. (2002). Identification of genes essential for growth at high salt concentrations using salt-sensitive mutants of the cyanobacterium *Synechocystis* sp. strain PCC 6803. *Curr. Microbiol.* 44, 184–188. doi: 10.1007/s00284-001-0035-3

Kojima, K., Suzuki-Maenaka, T., Kikuchi, T., and Nakamoto, H. (2006). Roles of the cyanobacterial isiABC operon in protection from oxidative and heat stresses. *Physiol. Plant.* 128, 507–519. doi: 10.1111/j.1399-3054.2006.00781.x

Kouril, R., Arteni, A. A., Lax, J., Yeremenko, N., D'Haene, S., Rogner, M., et al. (2005a). Structure and functional role of supercomplexes of IsiA and photosystem I in cyanobacterial photosynthesis. *FEBS Lett.* 579, 3253–3257. doi: 10.1016/j.febslet.2005.03.051

Kouril, R., Yeremenko, N., D'Haene, S., Oostergetel, G. T., Matthijs, H. C., Dekker, J. P., et al. (2005b). Supercomplexes of IsiA and photosystem I in a mutant lacking subunit PsaL. *Biochimica et Biophysica Acta (BBA)* 1706, 262–266. doi: 10.1016/j.bbabio.2004.11.008

Kouřil, R., Yeremenko, N., D'Haene, S., Yakushevska, A. E., Keegstra, W., Matthijs, H. C. P., et al. (2003). Photosystem I trimers from *Synechocystis* PCC 6803 lacking the PsaF and PsaJ subunits bind an IsiA ring of 17 units. *Biochimica et Biophysica Acta (BBA) - Bioenergetics* 1607, 1–4. doi: 10.1016/j.bbabio.2003.08.002

Krynicka, V., Tichy, M., Krafl, J., Yu, J., Kana, R., Boehm, M., et al. (2014). Two essential FtsH proteases control the level of the fur repressor during iron deficiency in the cyanobacterium *Synechocystis* sp. PCC 6803. *Mol. Microbiol.* 94, 609–624. doi: 10.1111/mmi.12782

Kuhn, M. G., and Vermaas, W. F. J. (1993). Deletion mutations in a long hydrophilic loop in the photosystem-ii chlorophyll-binding protein CP43 in the cyanobacterium *Synechocystis* sp. PCC 6803. *Plant Mol. Biol.* 23, 123–133. doi: 10.1007/bf00021425

Kunert, A., Vinnemeier, J., Erdmann, N., and Hagemann, M. (2003). Repression by fur is not the main mechanism controlling the iron-inducible isiAB operon in the cyanobacterium *Synechocystis* sp. PCC 6803. *FEMS Microbiol. Lett.* 227, 255–262. doi: 10.1016/S0378-1097(03)00689-X

Latifi, A., Jeanjean, R., Lemeille, S., Havaux, M., and Zhang, C.-C. (2005). Iron starvation leads to oxidative stress in *anabaena* sp. strain PCC 7120. *J. Bacteriol.* 187, 6596–6598. doi: 10.1128/JB.187.18.6596-6598.2005

Laudenbach, D. E., and Straus, N. A. (1988). Characterization of a cyanobacterial iron stress-induced gene similar to psbC. *J. Bacteriol.* 170, 5018–5026. doi: 10.1128/jb.170.11.5018-5026.1988

Lax, J. E.-M., Arteni, A. A., Boekema, E. J., Pistorius, E. K., Michel, K.-P., and Rögner, M. (2007). Structural response of photosystem 2 to iron deficiency: characterization of a new photosystem 2–IdiA complex from the cyanobacterium *Thermosynechococcus elongatus* BP-1. *Biochimica et Biophysica Acta (BBA)-Bioenergetics* 1767, 528–534. doi: 10.1016/j.bbabio.2007.01.003

Legewie, S., Dienst, D., Wilde, A., Herzel, H., and Axmann, I. M. (2008). Small RNAs establish delays and temporal thresholds in gene expression. *Biophys. J.* 95, 3232–3238. doi: 10.1529/biophysj.108.133819

Leonhardt, K., and Straus, N. A. (1992). An iron stress operon involved in photosynthetic electron transport in the marine cyanobacterium *Synechococcus* sp. PCC 7002. *J. Gen. Microbiol.* 138, 1613–1621. doi: 10.1099/00221287-138-8-1613

Leonhardt, K., and Straus, N. A. (1994). Photosystem II genes isiA, psbDI and psbC in *anabaena* sp. PCC 7120: cloning, sequencing and the transcriptional regulation in iron-stressed and iron-repleted cells. *Plant Mol. Biol.* 24, 63–73. doi: 10.1007/BF00040574

Li, Q., Huisman, J., Bibby, T. S., and Jiao, N. Z. (2019). Biogeography of Cyanobacterial isiA genes and their link to iron availability in the ocean. *Front. Microbiol.* 10. doi: 10.3389/fmicb.2019.00650

Lopez-Gomollon, S., Hernandez, J. A., Pellicer, S., Angarica, V. E., Peleato, M. L., and Fillat, M. F. (2007). Cross-talk between iron and nitrogen regulatory networks in *anabaena* (Nostoc) sp. PCC 7120: identification of overlapping genes in FurA and NtcA regulons. *J. Mol. Biol.* 374, 267–281. doi: 10.1016/j.jmb.2007.09.010

Ma, F., Zhang, X., Zhu, X., Li, T., Zhan, J., Chen, H., et al. (2017). Dynamic changes of IsiA-containing complexes during long-term iron deficiency in *Synechocystis* sp. PCC 6803. *Mol. Plant* 10, 143–154. doi: 10.1016/j.molp.2016.10.009

MacGregor-Chatwin, C., Jackson, P. J., Sener, M., Chidgey, J. W., Hitchcock, A., Qian, P., et al. (2019). Membrane organization of photosystem I complexes in the most abundant phototroph on earth. *Nature Plants* 5, 879–889. doi: 10.1038/s41477-019-0475-z

Martin-Luna, B., Sevilla, E., Gonzalez, A., Bes, M. T., Fillat, M. F., and Peleato, M. L. (2011). Expression of fur and its antisense α-fur from Microcystis *aeruginosa* PCC7806 as response to light and oxidative stress. *J. Plant Physiol.* 168, 2244–2250. doi: 10.1016/j.jplph.2011.08.006

Melkozernov, A. N., Bibby, T. S., Lin, S., Barber, J., and Blankenship, R. E. (2003). Time-resolved absorption and emission show that the CP43'antenna ring of iron-stressed *Synechocystis* sp. PCC6803 is efficiently coupled to the photosystem I reaction center core. *Biochemistry* 42, 3893–3903. doi: 10.1021/bi026987u

Mills, S. A., and Marletta, M. A. (2005). Metal binding characteristics and role of iron oxidation in the ferric uptake regulator from Escherichia coli. *Biochemistry* 44, 13553–13559. doi: 10.1021/bi0507579

Nealson, K. H., and Myers, C. R. (1990). Iron reduction by bacteria - a potential role in the genesis of banded iron formations. *Am. J. Sci.* 290A, 35–45.

Nield, J., Morris, E. P., Bibby, T. S., and Barber, J. (2003). Structural analysis of the photosystem I supercomplex of cyanobacteria induced by iron deficiency. *Biochemistry* 42, 3180–3188. doi: 10.1021/bi026933k

Odom, W. R., Hodges, R., Chitnis, P. R., and Guikema, J. A. (1993). Characterization of Synechocystis sp. PCC 6803 in iron-supplied and iron-deficient media. *Plant Mol. Biol.* 23, 1255–1264. doi: 10.1007/BF00042358

Pakrasi, H. B., Goldenberg, A., and Sherman, L. A. (1985a). Membrane development in the cyanobacterium, Anacystis nidulans, during recovery from iron starvation. *Plant Physiol.* 79, 290–295. doi: 10.1104/pp.79.1.290

Pakrasi, H. B., Riethman, H. C., and Sherman, L. A. (1985b). Organization of pigment proteins in the photosystem II complex of the cyanobacterium Anacystis nidulans R2. *Proc. Natl. Acad. Sci.* 82, 6903–6907. doi: 10.1073/pnas.82.20.6903

Park, Y. I., Sandström, S., Gustafsson, P., and Öquist, G. (1999). Expression of the isiA gene is essential for the survival of the cyanobacterium *Synechococcus*

sp. PCC 7942 by protecting photosystem II from excess light under iron limitation. *Mol. Microbiol.* 32, 123–129. doi: 10.1046/j.1365-2958.1999.01332.x

Pilla, S. K., Balaga, R. R., Iwane, S., Sisinthy, S., and Jogadhenu, S. (2013). A novel transcriptional regulator, Sll1130, negatively regulates heat-responsive genes in *Synechocystis* sp. PCC6803. *Biochem. J.* 449, 751–760. doi: 10.1042/BJ20120928

Rakhimberdieva, M. G., Vavilin, D. V., Vermaas, W. F., Elanskaya, I. V., and Karapetyan, N. V. (2007). Phycobilin/chlorophyll excitation equilibration upon carotenoid-induced non-photochemical fluorescence quenching in phycobilisomes of the cyanobacterium *Synechocystis* sp. PCC 6803. *Biochimica et Biophysica Acta (BBA)* 1767, 757–765. doi: 10.1016/j.bbabio.2006.12.007

Raven, J. A., Evans, M. C., and Korb, R. E. (1999). The role of trace metals in photosynthetic electron transport in O2-evolving organisms. *Photosynth. Res.* 60, 111–150. doi: 10.1023/A:1006282714942

Riethman, H. C., and Sherman, L. A. (1988). Immunological characterization of iron-regulated membrane proteins in the cyanobacterium Anacystis nidulans R2. *Plant Physiol.* 88, 497–505. doi: 10.1104/pp.88.2.497

Ryan-Keogh, T. J., Macey, A. I., Cockshutt, A. M., Moore, C. M., and Bibby, T. S. (2012). The cyanobacterial chlorophyll-binding-protein IsiA acts to increase the in vivo effective absorption cross-section of PSI under iron limitation. *J. Phycol.* 48, 145–154. doi: 10.1111/j.1529-8817.2011.01092.x

Salomon, E., and Keren, N. (2015). Acclimation to environmentally relevant Mn concentrations rescues a cyanobacterium from the detrimental effects of iron limitation. *Environ. Microbiol.* 17, 2090–2098. doi: 10.1111/1462-2920.12826

Sandström, S., Ivanov, A. G., Park, Y. I., Öquist, G., and Gustafsson, P. (2002). Iron stress responses in the cyanobacterium *Synechococcus* sp. PCC7942. *Physiol. Plant.* 116, 255–263. doi: 10.1034/j.1399-3054.2002.1160216.x

Sandström, S., Park, Y. I., Öquist, G., and Gustafsson, P. (2001). CP43′, the isiA gene product, functions as an excitation energy Dissipator in the Cyanobacterium *Synechococcus* sp. PCC 7942. *Photochem. Photobiol.* 74, 431–437. doi: 10.1562/0031-8655(2001)074<0431:CTIGPF>2.0.CO;2

Sarcina, M., and Mullineaux, C. W. (2004). Mobility of the IsiA chlorophyll-binding protein in cyanobacterial thylakoid membranes. *J. Biol. Chem.* 279, 36514–36518. doi: 10.1074/jbc.M405881200

Schoffman, H., and Keren, N. (2019). Function of the IsiA pigment-protein complex in vivo. *Photosynth. Res.* 141, 343–353. doi: 10.1007/s11120-019-00638-5

Schrader, P. S., Milligan, A. J., and Behrenfeld, M. J. (2011). Surplus photosynthetic antennae complexes underlie diagnostics of iron limitation in a cyanobacterium. *PLoS One* 6, e18753. doi: 10.1371/journal.pone.0018753

Sevilla, E., Martín-Luna, B., González, A., Gonzalo-Asensio, J. A., Peleato, M. L., and Fillat, M. F. (2011). Identification of three novel antisense RNAs in the fur locus from unicellular cyanobacteria. *Microbiology* 157, 3398–3404. doi: 10.1099/mic.0.048231-0

Sherman, D., and Sherman, L. (1983). Effect of iron deficiency and iron restoration on ultrastructure of Anacystis nidulans. *J. Bacteriol.* 156, 393–401. doi: 10.1128/jb.156.1.393-401.1983

Singh, A. K., Li, H., Bono, L., and Sherman, L. A. (2005). Novel adaptive responses revealed by transcription profiling of a *Synechocystis* sp. PCC 6803 ΔisiA mutant in the presence and absence of hydrogen peroxide. *Photosynth. Res.* 84, 65–70. doi: 10.1007/s11120-004-6429-x

Singh, A. K., and Sherman, L. A. (2006). Iron-independent dynamics of IsiA production during the transition to stationary phase in the cyanobacterium *Synechocystis* sp. PCC 6803. *FEMS Microbiol. Lett.* 256, 159–164. doi: 10.1111/j.1574-6968.2006.00114.x

Sun, J., and Golbeck, J. H. (2015). The presence of the IsiA-PSI Supercomplex leads to enhanced photosystem I electron throughput in iron-starved cells of *Synechococcus* sp. PCC 7002. *J. Phys. Chem. B* 119, 13549–13559. doi: 10.1021/acs.jpcb.5b02176

Tölle, J., Michel, K.-P., Kruip, J., Kahmann, U., Preisfeld, A., and Pistorius, E. K. (2002). Localization and function of the IdiA homologue Slr1295 in the cyanobacterium *Synechocystis* sp. strain PCC 6803. *Microbiology* 148, 3293–3305. doi: 10.1099/00221287-148-10-3293

Tomitani, A. (1999). Chlorophyll b and phycobilins in the common ancestor of cyanobacteria and chloroplasts. *Nature* 400, 159–162. doi: 10.1038/22101

Toporik, H., Li, J., Williams, D., Chiu, P.-L., and Mazor, Y. (2019). The structure of the stress-induced photosystem I-IsiA antenna supercomplex. *Nat. Struct. Mol. Biol.* 26, 443–449. doi: 10.1038/s41594-019-0228-8

Troyan, T., Bullerjahn, G., and Sherman, L. (1989). "Assembly of Chl-protein complexes in membranes of iron-stressed *Synechococcus* SP. PCC7942 proceeds in the absence of chlorophyll synthesis," in *Techniques and New Developments in Photosynthesis Research*. (Springer), 601-604.

Umena, Y., Kawakami, K., Shen, J. R., and Kamiya, N. (2011). Crystal structure of oxygen-evolving photosystem II at a resolution of 1.9 A. *Nature* 473, 55–60. doi: 10.1038/nature09913

van der Weij-de Wit, C. D., Ihalainen, J. A., van de Vijver, E., D'Haene, S., Matthijs, H. C., van Grondelle, R., et al. (2007). Fluorescence quenching of IsiA in early stage of iron deficiency and at cryogenic temperatures. *Biochimica et Biophysica Acta (BBA)* 1767, 1393–1400. doi: 10.1016/j.bbabio.2007.10.001

Vik, S. (2007). ATP synthesis by oxidative phosphorylation. *EcoSal Plus* 2, 177–231. doi: 10.1128/ecosalplus.3.2.3

Vinnemeier, J., Kunert, A., and Hagemann, M. (1998). Transcriptional analysis of the isiAB operon in salt-stressed cells of the cyanobacterium *Synechocystis* sp. PCC 6803. *FEMS Microbiol. Lett.* 169, 323–330. doi: 10.1111/j.1574-6968.1998.tb13336.x

Wang, Q., Hall, C. L., Al-Adami, M. Z., and He, Q. (2010). IsiA is required for the formation of photosystem I supercomplexes and for efficient state transition in synechocystis PCC 6803. *PLoS One* 5. doi: 10.1371/journal.pone.0010432

Wang, Q., Jantaro, S., Lu, B., Majeed, W., Bailey, M., and He, Q. (2008). The high light-inducible polypeptides stabilize trimeric photosystem I complex under high light conditions in Synechocystis PCC 6803. *Plant Physiol.* 147, 1239–1250. doi: 10.1104/pp.108.121087

Wang, Q., Sun, H., and Huang, J. L. (2017). Re-analyses of "algal" genes suggest a complex evolutionary history of Oomycetes. *Front. Plant Sci.* 8. doi: 10.3389/fpls.2017.01540

Wilson, A., Ajlani, G., Verbavatz, J.-M., Vass, I., Kerfeld, C. A., and Kirilovsky, D. (2006). A soluble carotenoid protein involved in phycobilisome-related energy dissipation in cyanobacteria. *The Plant Cell Online* 18, 992–1007. doi: 10.1105/tpc.105.040121

Wilson, A., Boulay, C., Wilde, A., Kerfeld, C. A., and Kirilovsky, D. (2007). Light-induced energy dissipation in iron-starved cyanobacteria: roles of OCP and IsiA proteins. *The Plant Cell Online* 19, 656–672. doi: 10.1105/tpc.106.045351

Wrigglesworth, J. M., and Baum, H. (1980). The biochemical functions of iron. *Iron in Biochemistry and Medicine*, 29–86.

Xiao, T. W., Mi, M. M., Wang, C. Y., Qian, M., Chen, Y. H., Zheng, L. Q., et al. (2018). A methionine-R-sulfoxide reductase, OsMSRB5, is required for rice defense against copper toxicity. *Environ. Exp. Bot.* 153, 45–53. doi: 10.1016/j.envexpbot.2018.04.006

Xu, L. H., Wang, W. Y., Guo, J. J., Qin, J., Shi, D. Q., Li, Y. L., et al. (2014a). Zinc improves salt tolerance by increasing reactive oxygen species scavenging and reducing Na+ accumulation in wheat seedlings. *Biol. Plant.* 58, 751–757. doi: 10.1007/s10535-014-0442-5

Xu, W.-L., Jeanjean, R., Liu, Y.-D., and Zhang, C.-C. (2003). pkn22 (alr2502) encoding a putative Ser/Thr kinase in the cyanobacterium *anabaena* sp. PCC 7120 is induced by both iron starvation and oxidative stress and regulates the expression of isiA. *FEBS Lett.* 553, 179–182. doi: 10.1016/s0014-5793(03)01019-6

Xu, W., Chen, H., He, C.-L., and Wang, Q. (2014b). Deep sequencing-based identification of small regulatory RNAs in *Synechocystis* sp. PCC 6803. *PloS one*. 9:e92711. doi: 10.1371/journal.pone.0092711

Yeremenko, N., Kouril, R., Ihalainen, J. A., D'Haene, S., van Oosterwijk, N., Andrizhiyevskaya, E. G., et al. (2004). Supramolecular organization and dual function of the IsiA chlorophyll-binding protein in cyanobacteria. *Biochemistry* 43, 10308–10313. doi: 10.1021/bi048772l

Yousef, N., Pistorius, E. K., and Michel, K. P. (2003). Comparative analysis of idiA and isiA transcription under iron starvation and oxidative stress in *Synechococcus elongatus* PCC 7942 wild-type and selected mutants. *Arch. Microbiol.* 180, 471–483. doi: 10.1007/s00203-003-0618-4

Yu, J. J., Zhang, Y. X., Liu, J. M., Wang, L., Liu, P. P., Yin, Z. P., et al. (2018). Proteomic discovery of H2O2 response in roots and functional characterization of PutGLP gene from alkaligrass. *Planta* 248, 1079–1099. doi: 10.1007/s00425-018-2940-8

Zhang, Y., Chen, M., Church, W. B., Lau, K. W., Larkum, A. W. D., and Jermiin, L. S. (2010). The molecular structure of the IsiA–photosystem I supercomplex, modelled from high-resolution, crystal structures of photosystem I and the CP43 protein. *Biochimica et Biophysica Acta (BBA) - Bioenergetics* 1797, 457–465. doi: 10.1016/j.bbabio.2010.01.002

Zhao, L. S., Huokko, T., Wilson, S., Simpson, D. M., Wang, Q., Ruban, A. V., et al. (2020). Structural variability, coordination and adaptation of a native photosynthetic machinery. *Nature Plants* 6, 869–882. doi: 10.1038/s41477-020-0694-3

Conflict of Interest: The authors declare that the research was conducted in the absence of any commercial or financial relationships that could be construed as a potential conflict of interest.

Publisher's Note: All claims expressed in this article are solely those of the authors and do not necessarily represent those of their affiliated organizations, or those of the publisher, the editors and the reviewers. Any product that may be evaluated in this article, or claim that may be made by its manufacturer, is not guaranteed or endorsed by the publisher.

frontiers in Microbiology

ORIGINAL RESEARCH
published: 10 January 2022
doi: 10.3389/fmicb.2021.775710

Synthesis of Abscisic Acid in *Neopyropia yezoensis* and Its Regulation of Antioxidase Genes Expressions Under Hypersaline Stress

Jiali Yang[1,4], Wenhui Gu[1,2,3], Zezhong Feng[1,5], Bin Yu[1,4], Jianfeng Niu[1,2,3] and Guangce Wang[1,2,3]**

[1] Key Laboratory of Experimental Marine Biology, Institute of Oceanology, Chinese Academy of Sciences (IOCAS), Qingdao, China, [2] Laboratory for Marine Biology and Biotechnology, Pilot National Laboratory for Marine Science and Technology, Qingdao, China, [3] Center for Ocean Mega-Science, Chinese Academy of Sciences (CAS), Qingdao, China, [4] College of Earth and Planetary Sciences, University of Chinese Academy of Sciences, Beijing, China, [5] Marine Science and Engineering College, Qingdao Agricultural University, Qingdao, China

OPEN ACCESS

Edited by:
Qiang Wang,
Henan University, China

Reviewed by:
Manoj Kumar,
University of Technology Sydney, Australia
Qingfang He,
University of Arkansas at Little Rock, United States
Yandu Lu,
Hainan University, China

***Correspondence:**
Jianfeng Niu
jf_niu@qdio.ac.cn
Guangce Wang
gcwang@qdio.ac.cn

Specialty section:
This article was submitted to Microbial Physiology and Metabolism, a section of the journal Frontiers in Microbiology

Received: *14 September 2021*
Accepted: *02 December 2021*
Published: *10 January 2022*

Citation:
Yang J, Gu W, Feng Z, Yu B, Niu J and Wang G (2022) Synthesis of Abscisic Acid in Neopyropia yezoensis and Its Regulation of Antioxidase Genes Expressions Under Hypersaline Stress. Front. Microbiol. 12:775710. doi: 10.3389/fmicb.2021.775710

Abscisic acid (ABA) is regarded as crucial for plant adaptation to water-limited conditions and it functions evolutionarily conserved. Thus, insights into the synthesis of ABA and its regulation on downstream stress-responsive genes in *Neopyropia yezoensis*, a typical Archaeplastida distributed in intertidal zone, will improve the knowledge about how ABA signaling evolved in plants. Here, the variations in ABA contents, antioxidant enzyme activities and expression of the target genes were determined under the presence of exogenous ABA and two specific inhibitors of the ABA precursor synthesis. ABA content was down-regulated under the treatments of each or the combination of the two inhibitors. Antioxidant enzyme activities like SOD, CAT and APX were decreased slightly with inhibitors, but up-regulated when the addition of exogenous ABA. The quantitative assays using real-time PCR (qRT-PCR) results were consistent with the enzyme activities. All the results suggested that ABA can also alleviate oxidative stress in *N. yezoensis* as it in terrestrial plant. Combined with the transcriptome assay, it was hypothesized that ABA is synthesized in *N. yezoensis* via a pathway that is similar to the carotenoid pathway in higher plants, and both the MVA and that the MEP pathways for isoprenyl pyrophosphate (IPP) synthesis likely exist simultaneously. The ABA signaling pathway in *N. yezoensis* was also analyzed from an evolutionary standpoint and it was illustrated that the emergence of the ABA signaling pathway in this alga is an ancestral one. In addition, the presence of the ABRE motif in the promoter region of antioxidase genes suggested that the antioxidase system is regulated by the ABA signaling pathway.

Keywords: abscisic acid, antioxidase, ABRE motif, ABA signaling pathway, *Neopyropia yezoensis*

INTRODUCTION

Abscisic acid (ABA) is a phytohormone that is found in all photosynthetic organisms (Cutler and Krochko, 1999; Hunter, 2007). In higher plants, ABA is known as a stress related hormone and plays a critical role in the regulation of various stress responses, including cold, salt, and drought stresses (Nogueira et al., 2003; Tijero et al., 2016; Jiang et al., 2019). The environmental stress factors

mentioned above inevitably cause oxidative damage to cells (Kaur and Pati, 2016). Guan et al. (2000) discovered that exogenously applied ABA and H_2O_2 reinforced the expression of the antioxidant *Cat1* gene in maize and proposed that H_2O_2 was an intermediary that was involved ABA regulation of *Cat1* gene expression during osmotic stress. Jiang and Zhang (2002) also reported that ABA levels significantly increased under water stress in maize leaves. Furthermore, reactive oxygen species (ROS), such as O_2^- and H_2O_2, and antioxidant enzymes, such as superoxide dismutase (SOD), catalase (CAT), ascorbate peroxidase (APX), and glutathione reductase (GR), were also strongly up-regulated after 12 h of osmotic stress. Recently, several studies have reported that ROS levels increased under alkaline osmotic stress in higher plants, and that the application of ABA effectively reduced ROS levels. Other studies have shown that ABA significantly enhanced SOD, CAT, peroxidase (POD), and APX activity (Sahu and Kar, 2018; Liu et al., 2019).

It is believed that ABA contents in algae are usually lower than in higher plants, but it plays a more important role in physiological activity (Huang et al., 2010; Yokoya et al., 2010). Hirsch et al. (1989) determined the ABA contents in 64 algal species and found that its content increased under hyperosmotic salinity stress. The oxidative stress response has been a very active research field, not only in higher plants, but also in algae. Under oxidative stress, ABA is involved in regulating algal morphogenesis during the transformation from vegetative to cyst cells in the unicellular green alga *Haematococcus pluvialis* (Kobayashi et al., 1997). Yoshida et al. (2003) added exogenous ABA to *Chlamydomonas reinhardtii* and measured the changes to key enzyme activities in the antioxidant system and found that SOD, CAT, and APX activities significantly increased.

The stress responsive pathway mediated by ABA has been deciphered in the model plant *Arabidopsis thaliana*. It is usually controlled by several core components, namely, ABA receptors (PYLs), type 2C protein phosphatases (PP2Cs), and class III sucrose-non-fermenting 1 (SNF1)-related protein kinase 2 (SnRK2). In the presence of ABA, PYL protein binds to PP2C and prevents activity. Thus, SnRK2 is released and the phosphorylated SnRK2 activates the ABA response element-binding factors (ABFs), which initiates downstream expression of ABA-responsive element genes in an ABRE-dependent manner (Soon et al., 2012; Fujita et al., 2013). Collectively, the ABA signaling pathway belongs to a sophisticated and intricate responsive pathway and it seems to be conserved across plants, including higher plants, bryophytes, and algae (Komatsu et al., 2020). However, parts of these core components have not been reported in algae (Komatsu et al., 2020).

The same is true for the synthesis of ABA (Hauser et al., 2011). The first biosynthetic pathway for ABA was discovered in a plant mutant (Linforth et al., 1987; Taylor et al., 1988). Since then, ABA biosynthesis and its metabolic pathways in higher plants have been extensively studied. Now, it is generally accepted that there are two ABA synthesis pathways, including the carotenoid pathway (indirect pathway) which is present in higher plants, and the direct pathway, which is mainly found in two fungi, *Cercospora rosicola* and *Cercospora cruenta* (Bennett et al., 1984; Inomata et al., 2004; Takino et al., 2019). In both pathways, ABA is derived from the five carbon precursor, isoprenyl pyrophosphate (IPP) (Nambara and Marion-Poll, 2005). Isoprenyl pyrophosphate can be biosynthesized *via* two pathways: (1) the mevalonate (MVA) pathway, where it is synthesized in the cytoplasm using acetyl-CoA as a substrate, and (2) the methylerythritol phosphate (MEP) pathway, where it is synthesized in the plastids using pyruvate and glyceraldehyde 3-phosphate (GA-3P) as substrates (Jomaa et al., 1999; Lichtenthaler, 2000; Yang et al., 2012). The MEP pathway is the main synthesis pathway for the IPP in higher plants and also operates in bacteria and green algae (Hunter, 2007; Phillips et al., 2008). Several studies have shown that 1-deoxy-D-xylulose 5-phosphate synthase (DXS) is one of the most important rate-limiting enzymes in the MEP pathway (Estevez et al., 2001; Cordoba et al., 2011), and it can be inhibited by clomazone (2-[(2-chlorophenyl) methyl]-4,4-dimethyl-3- isoxazolidinone) (Carretero-Paulet et al., 2006; Han et al., 2013). However, the MVA pathway, mainly found in the cytoplasm, is the only synthetic pathway for IPP in many fungi and animals. In this pathway, 3-hydroxy-3-methylglutaryl coenzyme A reductase is the rate-limiting enzyme and it can be inhibited by mevinolin (Mev) (Jomaa et al., 1999). Studies have suggested that some green algae, such as *C. reinhardtii* and *Scenedesmus obliquus*, only have an MEP pathway (Schwender et al., 1996; Disch et al., 1998). However, there are different opinions about red algae (Rhodophyta) (Schwender et al., 1997; Grauvogel and Petersen, 2007), especially *N. yezoensis* where the IPP synthesis pathway has not yet been elucidated.

Neopyropia yezoensis is a typical intertidal macroalgae that belongs to the Bangiales and represents an ancient lineage of red algae with simple morphology (Sutherland et al., 2011). At low tide, *N. yezoensis* lose as much as 90% of their cellular water due to desiccation stress (Blouin et al., 2011), but their activities can completely recover when rehydrated. Therefore, *N. yezoensis* has been suggested as a model organism for investigating the stress tolerance mechanisms in intertidal seaweed (Blouin et al., 2011; Sun et al., 2015). Previous results showed that the activities of some antioxidant enzymes were significantly up-regulated under hypersaline stress (Yu et al., 2020). However, it is not known whether ABA is involved in regulating the expression of antioxidant enzymes.

Here, we applied exogenous ABA to *N. yezoensis* thalli and/or treated them with two specific inhibitors of ABA synthesis. Then the photosynthetic parameters, the ABA content, and the variation in antioxidant enzymes activity were determined under high salinity stress conditions (120‰). The samples under the designed conditions were collected and subjected to a transcriptome analysis. Based on the results, a theoretical synthesis pathway for ABA was analyzed and the possible regulation of related antioxidant enzymes by ABA was investigated. These results improve our understanding of ABA-mediated stress resistance in *N. yezoensis* and will improve understanding about the evolution of the ABA signaling pathway. The results also provide a theoretical foundation for the cultivation of new strains with excellent resistance.

MATERIALS AND METHODS

Algae Preparation

The *N. yezoensis* thalli samples were collected from an algae culture farm in the offshore cultivation area of Jimo, Shandong Province, China. The selected algae were cultured in fresh seawater with PES medium at 10°C under 50 μmol photons m^{-2} s^{-1} light provided by halogen lamps with a photoperiod of 12 h light/12 h dark. The culture medium was constantly filled with filter-sterilized air and replaced every day.

Inhibitor and Hyperosmolarity Stress Treatments

The stock solutions of inhibitors clomazone (Clo) and mevinolin (Mev) were prepared in DMSO at concentration 50 and 25 μM, respectively, in the dark at 4°C. The ABA was dissolved in methanol to a concentration of 100 mg mL^{-1} and stored at −20°C with light preservation. All the stock solution was diluted 1,000 times before it was used in the inhibitor treatment experiments. The 120‰ high salinity seawater was prepared by adding the sea salt to fresh seawater and the salinity was monitored by a salinity meter.

Fresh seaweed samples were treated in 120‰ salinity seawater at 10°C under 50 μmol photons m^{-2} s^{-1} of artificial light for 1 h. Then, the high salinity treated samples were recovered in seawater containing the one or both of the inhibitors, or the two inhibitors combined with ABA for 4 h. This procedure allowed the inhibitors to enter the algae when it was rehydrated after the high salinity treatment. The control (C) was just subjected to the high salinity treatment and was recovered in normal seawater. About 1 g (fresh weight) recovered *N. yezoensis* of each treatment was treated again with 120‰ salinity seawater containing the chemicals in subsequent experiments (**Supplementary Figure 2**). All the samples under each treatment were collected separately, immediately frozen with liquid nitrogen, and stored at −80°C. Three parallel samples were processed for each treatment.

Determination of the Photosynthetic Parameters

The recovered *N. yezoensis* was treated again with 120‰ salinity seawater containing the different chemicals for 4 h and rehydrated for another 4 h. The photosynthetic parameters for the samples after 4 h dehydration (S4h), and 0.5, 2, or 4 h of rehydration (R0.5h, R2h, and R4h, respectively) were determined using a Dual-PAM-100 measuring system (Heinz Walz, Effeltrich, Germany). All the samples were kept in the dark for 10 min before determining the chlorophyll fluorescence parameters. The procedure followed (Xie et al., 2020) and used actinic light at 57 μmol m^{-2} s^{-1}. Maximal PS II quantum yield, F_v/F_m, and the quantum yield of non-regulated energy dissipation in PS II [Y(NO)] were automatically calculated by the software provided. Here, Y(NO) values were increased indicated that the algae had been damaged to a certain extent, and a decrease indicates that the algae has recovered.

Determination of the ABA Content in the Samples

Four inhibitor treatments, which were Clo, Mev, Clo + Mev (MC), and Clo + Mev + ABA (CMA) were applied to explore the effects of the inhibitors on ABA content. The treated samples (about 100 mg fresh weight) were frozen in liquid nitrogen and ground by grinders (Jingxin Technology, Shanghai) in 2 ml grinding tubes. A total of 10 ng d6-ABA was added to monitor the ABA losses from the samples during extraction and purification (Dobrev et al., 2005). Next, 500 μL ABA extraction solvent (methanol:H_2O:CH3COOH = 89:10:1, vol/vol/vol) was added and incubated for 30 min at 120 rpm at 4°C. The supernatant was obtained through centrifugation at 13,000 *g* for 5 min at 4°C and an equal volume of petroleum ether was added to remove the components affecting ABA determination. Then, the ABA crude extract was enriched and eluted through a C_{18}-SPE column (Waters, Milford, MA, United States) (Oh et al., 2018) and the elute was concentrated with pre-cooled nitrogen (not completely dried to avoid any ABA losses). The ABA samples were made up to 50 μL using methanol:H_2O:CH3COOH = 20:79:1 (vol/vol/vol). Finally, the obtained ABA extract was injected into an HPLC–MS/MS system (Bruker, Compact II, Germany) and determined (Lopez-Carbonell et al., 2009; Pan et al., 2010; Fu et al., 2012).

Determination of the H_2O_2 Concentration in Each Sample

Based on the ABA content results for each sample, the MC, CMA and the control (C) were further selected to investigate the effects of ABA on the expression of antioxidant enzymes. Firstly, the H_2O_2 contents in the C, MC and CMA treated *N. yezoensis* thalli were determined using the corresponding assay kits from Sigma-Aldrich (St. Louis, MO, United States). The samples were extracted according to Yu et al. (2020).

Activities of Enzymes Associated With the Anti-oxidative System

The SOD, CAT, and GPX enzyme activities in the C, MC, and CMA treated *N. yezoensis* thalli were determined using the corresponding assay kits from Sigma-Aldrich. The APX, POD, and NOX activities were determined using an assay kit supplied by Jian Cheng (Nanjing Jiancheng Institute of Biological Engineering, China). The protein extractions were carried out according to Yu et al. (2020).

RNA Extraction, cDNA Library Construction, Sequencing and Annotation

The MC, CMA, and C samples were used to carry out the transcriptome assay. The total RNA from each sample was extracted using an RNAprep Pure Plant kit (Tiangen, Beijing, China) according to manufacturer's instructions. The RNA integrity was checked by 1% agarose gel electrophoresis, and the concentration and purity of the RNA was detected by a NanoPhotometer NP80 Touch (Implen Gmbh, Munich,

Germany). A total of 3 μg RNA was used to construct the cDNA library, which was sequenced on an Illumina HiSeq 2500 system at Wuhan Frasergen Bioinformatics Technology Co., Ltd., Wuhan, China.

The expression level of the genes was ascertained from the fragments per kilobase per million bases (FPKM) value, and screened using RSEM and bowtie2 (Trapnell et al., 2010; Li and Dewey, 2011). DESeq2 (1.22.2) was used to determine the differentially expressed genes (DEGs) and all DEGs reached the conditions of FDR < 0.05, log2FC > 1, or log2FC < -1 (Love et al., 2014).

Functional annotation of the DEGs was performed by Blast[1] against the NCBI non-redundant protein sequences (NR), Kyoto Encyclopedia of Genes and Genomes (KEGG), Swiss-Prot, Gene Ontology (GO), and Clusters of euKaryotic Orthologous Groups of proteins (KOG) databases. The statistical enrichment analyses of DEGs in the KEGG pathway were performed using KOBAS software (Mao et al., 2005) and FDR values less than or equal to 0.05 were defined as differentially expressed metabolic pathways.

Validation of Gene Expression Using the Quantitative Assays Using Real-Time PCR Method

Based on the variation recorded for the annotated transcripts, nine DEGs, consisting of three genes related to the biosynthesis of ABA and six enzyme genes associated with the anti-oxidative system, were selected to perform the quantitative assays using real-time PCR (qRT-PCR). The feasibility of the transcriptome data was validated, and the effects of inhibitors on the synthesis of ABA precursors and the expression of antioxidant enzymes under hypersaline conditions were studied. The *Actin* gene was used as the internal control (**Supplementary Table 1**). The qRT-PCR assays were carried out using 2× SG Fast qPCR Master Mix (High Rox, B639273, Japan) on a StepOne Plus Multicolor Real-Time PCR Detection System (ABI, Foster City, CA, United States). Each gene in the different samples was determined using three technical replicates. The relative gene expression value was calculated by the $2^{-\Delta\Delta Ct}$ method (Livak and Schmittgen, 2001).

Analysis of the Core Components of the Abscisic Acid Signaling Pathway in *N. yezoensis*

Abscisic acid is regarded as crucial for plant adaptation to water-limited conditions and it functions evolutionarily conserved among terrestrial plants, bryophytes, and algae. The Rhodophyta, *N. yezoensis*, is a typical Archaeplastida that is found in intertidal zone, which represents a transition habitat for plant evolution and colonization of terrestrial environments. Thus, we screened the sequence information about core components of the ABA signaling pathway from the transcriptome data and made comparisons with those published in other species. Since ABA activates the expression of downstream target genes by binding AREB to the ABA-responsive elements (ABREs) in the promoter regions, we also investigated the target sequence for AREB on the promoter of several antioxidase genes, including *SOD, CAT, APX, GPX,* and *POD*.

Data and Statistical Analysis

All experimental data were derived from three independent measurements (±SD). Statistical analysis was performed using SPSS 26.0[2], and significances differences were determined using analysis of variance (Duncan's test; $P < 0.05$).

RESULTS

Changes to the Photosynthetic Parameters Under the Different Treatments

The F_v/F_m and Y(NO) values for the control, the Clo, Mev, MC, and CMA chemical treatments showed different trends. Before hypersaline stress treatment, F_v/F_m was not significantly different among the samples ($P > 0.05$) (**Figure 1A**). However, after severe high salinity (120‰) stress for 4 h (S4h), the F_v/F_m value for each sample decreased to about 42.1, 27.0, 20.3, 25.6, and 36.4%, respectively, of the values recorded for the algae before hypersaline stress. During rehydration, all the F_v/F_m values in the different treatments recovered rapidly, but the recovery speed for the samples treated with inhibitors was slower than the control. At R2h, the F_v/F_m values of all the samples were restored to their original levels before the treatments.

The Y(NO) values for the different inhibitor treatments were higher than that of the control before hypersaline stress (**Figure 1B**). At S4h, the Y(NO) values in all treatments were close to 1. However, there were no statistically significant differences between the ABA addition treatment (CMA) and the other treatments (**Figure 1B**). In a similar way to F_v/F_m, Y(NO) also rapidly decreased when the samples were subjected to normal seawater, but the recovery period was longer in the inhibitor treatments.

Impact of Inhibitors on Abscisic Acid Content Under High-Salinity Stress

The ABA content was 0.082 ng g^{-1} under 120‰ hypersaline stress only (control, C) (**Figure 2**). However, it was 0.019, 0.029, and 0.037 ng g^{-1} after the Clo, Mev, and MC treatments, respectively. Therefore, ABA level decreased significantly ($P < 0.5$) under the different inhibitor treatments by 2–4 times compared to C (**Figure 2**). While adding of exogenous ABA (CMA treatment) significantly increased the ABA content to almost 1.5 times of that in the control.

Variations in H_2O_2 Content

As showed in **Figure 3**, the H_2O_2 content in the CMA treatment was lower than that in C before hypersaline stress. At S4h, it was up-regulated in the different groups, but there were no significant differences ($P > 0.05$) among C, MC, and CMA. During the hydration process, the H_2O_2 level in the MC samples were higher

[1]http://blast.ncbi.nlm.nih.gov/Blast.cgi

[2]https://www.ibm.com

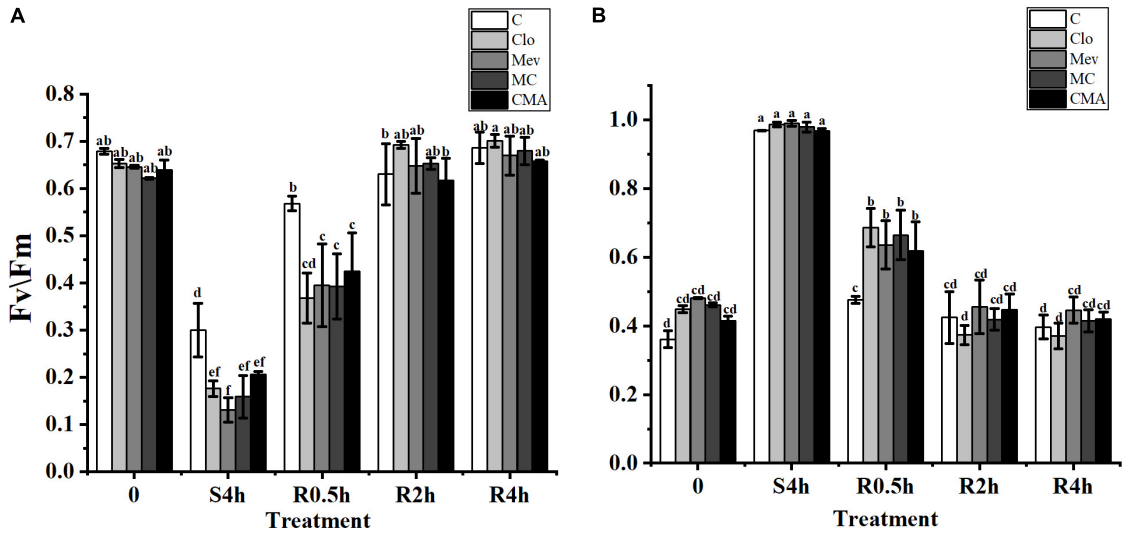

FIGURE 1 | The change of F_v/F_m **(A)** and Y(NO) **(B)** in different treatments of *Neopyropia yezoensis*. The abscissa, respectively, represented before hypersaline stress (0), under severe high salinity (120‰) stress 4 h (S4h), normal seawater recovery at 0.5, 2, and 4 h with different inhibitor treatments (R0.5h, R2h, and R4h). C, control; Clo, clomazone; Mev, mevinolin; MC, Mev + Clo; CMA, Clo + Mev + ABA. F_v/F_m, maximal PS II quantum yield; Y(NO), quantum yield of non-regulated energy dissipation. Data were Mean ± SD (n = 3). Different letters indicate significant differences ($P < 0.05$).

than that in C, and it was lower than that of the control after the CMA treatment.

Activity Assay of Enzymes Related to the Antioxidant System

As showed in **Figure 4**, SOD, CAT, POD, and NOX activities were increased significantly after high salinity stress. However, high salinity had little effect on APX and GPX activities in the C and CMA samples. With the exception of the down-regulation of APX, other enzyme activities were up-regulated when the MC inhibitors were present under high salinity treatment. More importantly, the addition of exogenous ABA to the MC treatments usually enhanced the activities of SOD, CAT, APX, and GPX under the high salinity conditions.

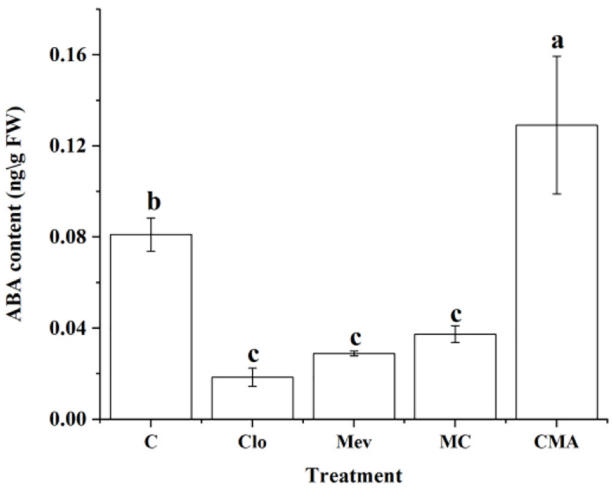

FIGURE 2 | Abscisic acid (ABA) content under hypersaline (120‰) stress 4 h (S4h) in *N. yezoensis* after different inhibitor treatments. C, treatment of 120‰ hypersaline stress; Clo, clomazone treatment under hypersaline stress; Mev, mevinolin treatment under hypersaline stress; MC, Mev and Clo treatment under hypersaline stress; CMA, Clo, Mev and ABA treatment under hypersaline stress simultaneously. Data were Mean ± SD (n = 3). Different letters indicate significant differences ($P < 0.05$).

Transcriptome Analysis of the Samples Treated With the Different Chemical Treatments

To investigate the changes in the genes associated with ABA synthesis and the expression of antioxidant enzymes in *N. yezoensis* thalli under 120‰ hypersaline stress, we constructed three cDNA libraries, which were control, MC, and CMA. A total of 11,973 genes were obtained by comparing them to the reference genome for the *N. yezoensis* thallus (Wang et al., 2020). Overall, 2614 DEGs were detected with an FDR < 0.05, log2FC > 1, or log2FC < −1. Compared to C, 1039 and 761 genes were up-regulated, and 1,149 and 712 genes were down regulated in MC and CMA, respectively (**Figure 5A**). In addition, 323 genes were up-regulated and 204 genes were down-regulated in CMA compared to MC (**Figure 5B**).

Differentially Expressed Genes Related to Abscisic Acid Biosynthesis and the Anti-oxidative Enzymes

A KEGG enrichment search identified the pathways related to ABA biosynthesis and the anti-oxidative system. These included the terpenoid backbone biosynthesis (ko00900), glutathione metabolism (ko00480), and peroxisome (ko04146) pathways

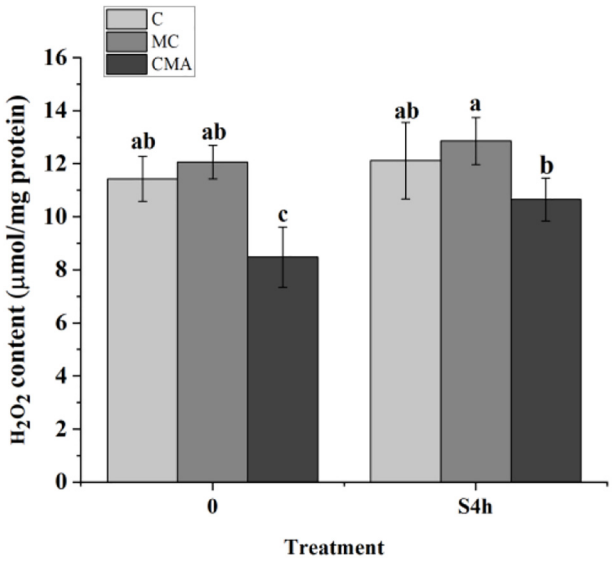

FIGURE 3 | The fluctuation of hydrogen peroxide (H_2O_2) content in different treatments of *N. yezoensis*. C, control; MC, Clo + Mev; CMA, Clo + Mev + ABA. The ordinate represented the content of H_2O_2. Data were Mean ± SD (n = 3). Different letters indicated significant differences ($P < 0.05$).

(**Supplementary Table 2**). We screened the DEGs related to anti-oxidative enzyme genes and found that the glutathione peroxidase (*GPX*), superoxide dismutase (*SOD*), and catalase (*CAT*) genes had a similar variation tendency after the chemical treatments. Compared to C, the gene expression levels were down-regulated under the MC treatment and up-regulated when exogenous ABA was added (CMA).

The DEGs related to ABA biosynthesis, which belonged to the terpenoid backbone biosynthesis (ko00900) pathway, including 1-dehydro-D-xylulose-5-phosphate synthase (*DXS*), farnesyl pyrophosphate synthase (*FPS*), and xanthoxin dehydrogenase (*XanDH*), were screened. Under the MC inhibitor treatment, the expression levels of the *DXS* and *XanDH* genes were down-regulated, but the addition of exogenous ABA increased their gene expression levels.

A heatmap clustering analysis of the DEGs associated with the anti-oxidative enzymes and ABA biosynthesis is shown in **Figure 5C**. A total of 15 DEGs were divided into two expression modes in the different treatment groups. The expression levels of the genes were either down-regulated or up-regulated in MC and CMA compared to C (**Figure 5C**).

Validation of the Gene Expression Profiles by Quantitative Assays Using Real-Time PCR

A total of nine crucial genes were analyzed by qRT-PCR and the results showed that their expression levels were basically consistent with the transcriptome data, which indicated that the RNA-seq results were reliable (**Figure 6**).

Annotation of Key Genes in the Abscisic Acid and Isoprenyl Pyrophosphate Synthesis Pathways

A total of 17 genes associated with the synthesis of ABA and IPP, a precursor of ABA, were identified (**Supplementary Table 3**). A specific synthesis pathway for ABA and its precursor IPP in *N. yezoensis* is suggested (**Supplementary Figure 1**) based on our transcriptome data and several previous studies (Hemmerlin et al., 2012; Lohr et al., 2012; Mikami et al., 2016). Among the 17 genes, a total of seven genes were annotated in the MEP pathway for IPP, but only one gene was annotated in the MVA pathway. In addition, nine major genes in the indirect ABA biosynthesis pathway were also annotated (**Supplementary Table 3**). The DEGs among these included *NyDXS*, *NyFPS*, and *Ny XanDH*.

Analysis of the Core Components of the Abscisic Acid Signaling Pathway in *N. yezoensis*

All the annotated genes related to the core components of the ABA signaling pathway are summarized in **Table 1**. Although the PYR/PYL/RCAR-type ABA receptor genes were not found, the other core components, such as protein phosphatase 2C (PP2C), SNF1-related protein kinase 1 (SnRK1), and ABA responsive element-binding transcription factors (AREB/ABF) were identified in *N. yezoensis*. However, a similarity search for the *nyPP2C* sequence in the NCBI database did not match the model *PP2C-A* gene in terrestrial plants. Furthermore, only one SNF1-related protein kinase 1 (SnRK1) transcript, which is believed to be the ancestral member of the SnRK protein family, was annotated in *N. yezoensis*. Additionally, there were 69 different transcripts annotated as the bZIP transcription factor detected, which implied the existence of gene expression regulation by ABA in *N. yezoensis*. And a computer search indicated that *CAT, APX, GPX,* and *POD* harbored the ABRE motif on the upstream 2 kb sequences of the transcription start code, which illustrated that expression of these antioxidant enzymes was regulated by the ABA-signaling pathway.

DISCUSSION

Inhibitor Treatments Under Hypersaline Conditions

Here, we employed two inhibitor treatments to investigate the synthesis of ABA and the potential ABA regulation of antioxidase expression. The samples were first incubated with the inhibitors for a complete dehydration and rehydration cycle. During the process, the originally ABA contained in the cell is probably consumed due to the stress response by *N. yezoensis*. This eliminated the influence of background ABA on the determinations of various parameters. Furthermore, rehydration with inhibitors ensured that the chemicals were fully absorbed and infiltrated the cell. This favored the accurate determination of ABA content and other determinations during the second round of stress treatments.

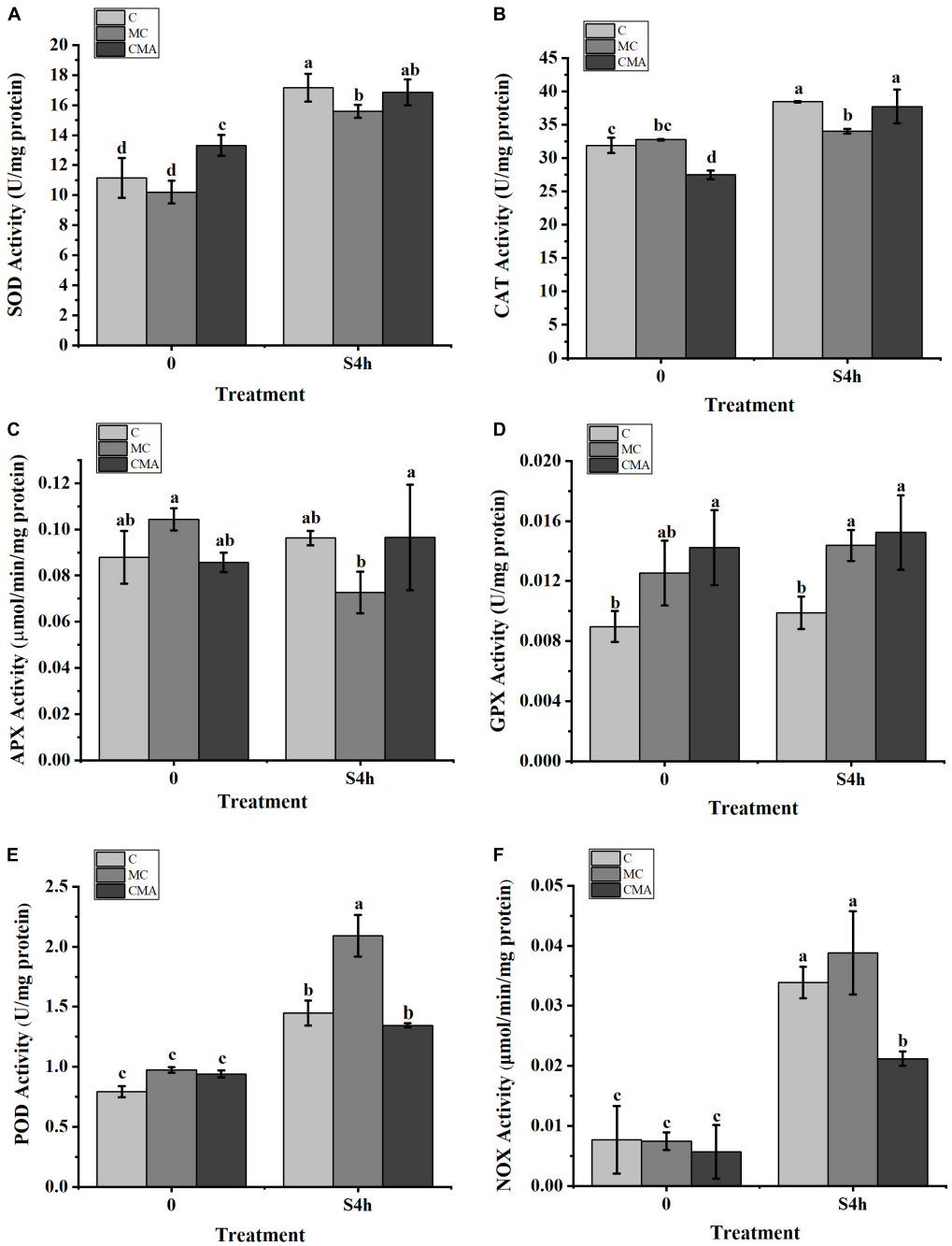

FIGURE 4 | Variation of enzyme activities related to the anti-oxidation system with different inhibitors treatment under hypersaline stress in *N. yezoensis*. **(A)** Superoxide dismutase (SOD); **(B)** catalase (CAT); **(C)** ascorbate peroxidase (APX); **(D)** glutathione peroxidase (GPX); **(E)** peroxidases (POD); **(F)** NADPH oxidase (NOX). The abscissa represented treatment time under hypersaline (120‰) stress conditions. The ordinate represented variation of enzymes activity. C, control; MC, Clo + Mev; CMA, Clo + Mev + ABA. Data were Mean ± SD (n = 3). Different letters indicated significant differences ($P < 0.05$).

Analysis of a Possible Pathway for Abscisic Acid Synthesis in *N. yezoensis*

Neopyropia yezoensis is a type of Archaeplastida and it is supposed to possess ancestral features of primary photosynthetic eukaryotes (Mikami et al., 2016). Usually, the alga are distributed along the intertidal zones and thus it must have evolved special stress response pathways to survive the extremely variable environments. Although many studies have reported that ABA may play an important role in stress responses by this alga, its endogenous biosynthesis remains poorly understood. A gene survey using EST information showed the existence of genes encoding zeaxanthin epimerase and a xanthoxin dehydrogenase

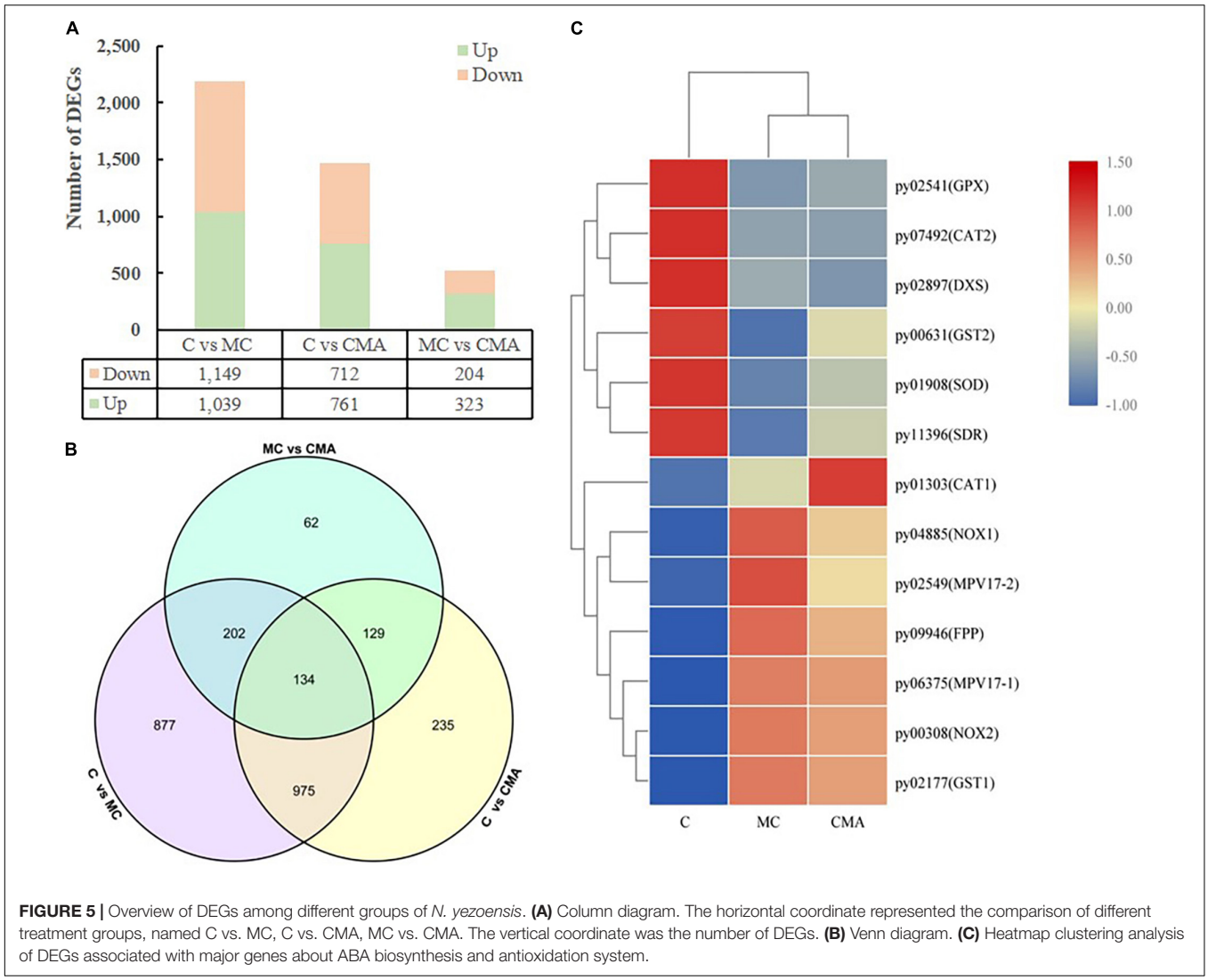

FIGURE 5 | Overview of DEGs among different groups of *N. yezoensis*. **(A)** Column diagram. The horizontal coordinate represented the comparison of different treatment groups, named C vs. MC, C vs. CMA, MC vs. CMA. The vertical coordinate was the number of DEGs. **(B)** Venn diagram. **(C)** Heatmap clustering analysis of DEGs associated with major genes about ABA biosynthesis and antioxidation system.

homolog in *N. yezoensis*. Mikami et al. (2016) combined these results with liquid chromatography-mass spectrometry results and strongly suggested that *N. yezoensis* can produce ABA *via* pathways similar to the indirect pathway in terrestrial plants. However, as for the metabolic process prior to carotene synthesis, there have been no previous reports addressed in *N. yezoensis*.

It is well known that carotene is derived from isoprenyl pyrophosphate (IPP) in plants. The synthesis of IPP is prerequisite for ABA biosynthesis, regardless of whether the direct or indirect pathways are used. There are two pathways for the biosynthesis of IPP, the mevalonate (MVA) pathway in the cytoplasm and the methylerythritol phosphate (MEP) pathway in the plastids (Bick and Lange, 2003). Either one or both of these two pathways have been found to exist in cells depending on the organism (Lohr et al., 2012). In brief, it appears that the MEP pathway is essential for plastid-bearing organisms since carotenoids are synthesized in plastids *via* IPP (Lohr et al., 2012). The cytosolic MVA pathway in algae with secondary plastids is considered to be a genetic patchwork, although all the extant algae with secondary plastids that have been investigated contain the MVA pathway (Lohr et al., 2012). Our transcription data revealed the presence of all the key enzyme genes associated with the MEP pathway, among which, the *NyDXS* (py02897) gene was down-regulated when treated with inhibitors (**Figure 6**). However, only one gene, *NyAACT* of the MVA pathway was identified. Meanwhile, the ABA content decreased under specific inhibition of the MVA pathway by Mev (**Figure 2**). Meanwhile, the Clo, inhibitor of key *DXS* enzymes in the MEP pathway could effectively reduce the ABA content during high salinity treatment (**Figure 2**). This suggests that both the MVA and the MEP pathways may be operative in *N. yezoensis*. When the MEP pathway was suppressed, the MVA pathway was activated to compensate for the reduction in IPP supply. Similar findings have also been reported for other phototrophic algae. For example, studies have showed that *Galdieria sulphuraria* and *Cyanidium caldarium* have both the MVA and MEP pathways (Schwender et al., 1997; Disch et al., 1998; Grauvogel and Petersen, 2007; Lohr et al., 2012). Therefore, cooperation between the MVA

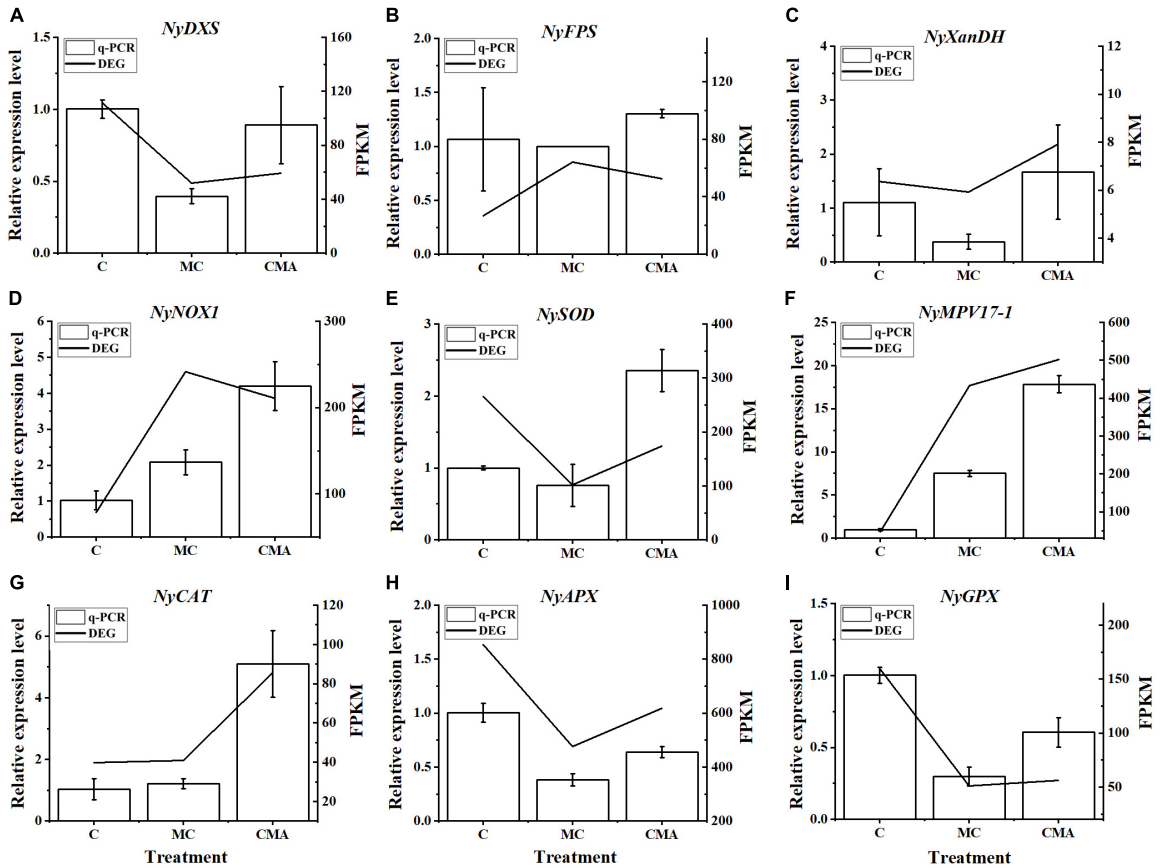

FIGURE 6 | Comparison of qRT-PCR results with those of RNA-Seq data from selected DEGs, including **(A)** *NyDXS* (py02897), **(B)** *NyFPS* (py09946), **(C)** *NyXanDH* (py11396), **(D)** *NyNOX1* (py00308), **(E)** *NySOD* (py01908), **(F)** *NyMPV17-1* (py06375), **(G)** *NyCAT* (py01303), **(H)** *NyAPX* (py06229), and **(I)** *NyGPX* (py02541). The horizontal coordinate represents the treatment of different inhibitors, named C, MC, and CMA. The vertical coordinate represents the relative expression levels of different DEGs and FPKM, respectively. FPKM, fragments per kilobase per million.

and MEP pathways in *N. yezoensis* is likely to occur to fine tune the IPP supply.

Effects of Abscisic Acid on Photosynthetic Efficiency Under Hypersaline Conditions

Both the individual IPP synthesis inhibitors and a combination of the inhibitors significantly reduced the F_v/F_m of the samples under high salinity stress conditions. Even in the followed rehydration, the recovery rates of photosynthetic parameters were clearly slower than that of the control, but the treatment samples did eventually recover. The results indicated that treatment with the inhibitors did not cause substantial damage to the seaweed photosynthetic elements and thus the experiments designed in this study can be used to investigate the role of ABA in the regulation of antioxidant enzyme expressions.

Earlier studies showed that ABA promoted the repair of photo-induced inactivation of the photosystem II complex in *C. reinhardtii* under low temperature stress, and that it played a protective role in the photosynthetic system (Saradhi et al., 2000). Our results showed that the ABA synthesis inhibitors significantly reduced the ABA content in *N. yezoensis* (**Figure 2**) and simultaneously decreased F_v/F_m (**Figure 1A**) under hypersaline conditions. In contrast, the application of exogenous ABA (CMA treatment), significantly increased the ABA content (**Figure 2**) and slightly increased the F_v/F_m values, although the change was not significant ($P > 0.05$) (**Figure 1A**). Other studies suggested that ABA may not directly improve photosynthetic activity, but may protect the photosynthetic system from damage by ROS (Yoshida et al., 2003). Consequently, ABA may play a vital role in alleviating the effect of hypersaline stress on photosynthesis through the antioxidation system in *N. yezoensis*, but the specific regulatory mechanism needs further study.

Significance of NADPH Oxidase in the Induction of the Abscisic Acid Signaling Pathway

For a long time, it is not clear whether the synthesis of ROS is necessary for the ABA signaling pathway. While the results in *Arabidopsis* using the mutant illustrated that when the NADPH oxidase gene (*NOX*) was disrupted, the ABA signaling pathway became impaired, whereas exogenous addition of H_2O_2 rescued

TABLE 1 | The core genes of the abscisic acid (ABA) signaling pathway identified in different organisms.

Gene name	Seed plants	Bryophytes	Streptophyte algae	*N. yezoensis*	Gene function description
PYR/PYL/RCAR	+	+	*PYL* ortholog	–	Soluble ABA receptor
PP2C	*PP2C-A*	*PP2C-A*	*PP2C-A*-like genes	Ancient *PP2C*	Protein phosphatase 2C, releasing SnRK2 from PP2C inhibition
SnRK2	+	+	+	*SnRK1*	SNF1-related protein kinase 2, phosphorylates downstream substrates such as ABF
AREB/ABF	+	+	+	+	Leucine zipper (bZIP) transcription factor, recognize the ABA-responsive elements in promoters of stress responsive genes

the physiological response in the mutant (Kwak et al., 2003). The central positive inductor of ROS to the ABA signal transduction was constructed. The NOX enzyme is a type of plasma membrane protein and NOX activity may be the main ROS source when the plant is subjected to stress (Lamb and Dixon, 1997). This shows that the transplasma membrane NOX (O_2^- synthases) might be crucially important to ABA signaling.

In this study, two *NOX* transcripts were identified and the results of the qRT-PCR analysis showed that their expression was up-regulated when the inhibitors were applied, but the addition of exogenous ABA reduced the magnitude of the up-regulation compared to that of the control. We also found that the NOX activity analysis produced the same profile as the qRT-PCR results (**Figures 4**, **6**). Based on the current results for NOX alone, we suggested that ABA may down-regulate the expression of the *NOX* gene and reduce the synthesis of O_2^- species. However, it is a paradox since that ROS produced by NOX has been proposed to play a role in the induction of the ABA signaling pathway (Kwak et al., 2003). In fact, ROS scavenging enzyme genes, such as *SOD*, *CAT*, *GPX*, *APX*, and *POD*, may be regulated by ABA and thus contribute to the maintenance of proper redox homeostasis in plant cells (Mittler, 2002; Kwak et al., 2003). **Figure 4** shows that the activities of several antioxidase enzymes were up-regulated when exogenous ABA was added compared to the MC inhibitor treatment. Therefore, we propose that the ROS scavenging enzymes, in both C and CMA were induced when the samples were recovered prior to the second round of high salinity stress. The up-regulation of the ROS scavenging enzymes maintained the cell redox homeostasis state and this alleviated the effects of stress on NOX and which decreased the induction of ROS. All these results illustrated the potential interrelationship between *NOX* expression and ABA signaling. On the other hand, the significant upregulation of *NOX* expression and enzyme activity in the inhibitor treatments (MC) demonstrated that the algal cell was in a more severe oxidation state, which triggered the formation of ROS.

Effects of Abscisic Acid on H_2O_2 Production

Hydrogen peroxide is considered to be a byproduct of environmental stress metabolism and is thought to induce cellular damage (Neill et al., 2002; Miller et al., 2010). Here, the H_2O_2 content was significantly down-regulated after adding of exogenous ABA compared to the MC and C under the high salinity conditions (**Figure 3**). It is worth noting that H_2O_2 accumulation is also alleviated as ABA content increases in higher plants. For example, Jiang and Zhang (2002) reported that the ABA content in maize leaf cells increased continuously with water stress, while the H_2O_2 level increased at first and then decreased. Thus, we speculate that it caused an increase in H_2O_2 during the first rehydration period of the algae in the control and the samples with added exogenous ABA. The increase in H_2O_2 during the first round of high salinity stress and recovery up-regulated the ROS scavenging system, which constrained H_2O_2 accumulation when the samples were subjected to the second round of high salinity treatment. In brief, H_2O_2 was induced by ABA at first, but was then removed by the activated antioxidation system. This may be a universal process that is present in all organisms.

Potential Correlation Between Abscisic Acid and the Antioxidant Enzymes

The effects of ABA on the induction of antioxidant responses in *Pyropia orbicularis* and other intertidal seaweed species have been evaluated and the results showed that ABA regulated the activation of antioxidant enzymes activities during desiccation (Guajardo et al., 2016). Additionally, ABA can significantly increase GR activity in *Platycladus orientalis* (Yao et al., 2020). Similar results were obtained in this study. The CAT, SOD, APX, and GPX activities were up-regulated under hypersaline stress (**Figure 4**). Furthermore, adding chemicals to inhibit the synthesis of ABA under high salinity conditions decreased antioxidant enzyme activities in the MC treatments compared to C. In contrast, the application of exogenous ABA (CMA) recovered the activities of most antioxidant enzymes. These findings suggest that there is a correlation between ABA and the antioxidant system under high salinity stress in *N. yezoensis*.

Additionally, the transcriptomic data showed that there were two KEGG pathways associated with the oxidation stress response, which were the glutathione metabolism and peroxisome pathways (**Supplementary Table 2**). There were 10 DEGs related to the anti-oxidative system, including *CAT, SOD, GPX, NOX*, and *glutathione S-transferase* (*GST*) (**Figure 5C** and **Supplementary Table 2**). The expression levels of *NyCAT* (py01303) and *NySOD* (py01908) had similar enzyme activity

tendencies under hypersaline stress (**Figure 6**). Previous studies have shown that ABA increases the transcription levels of *Mn-SOD* genes during maize embryo maturation (Zhu and Scandalios, 1994). Our results showed that exogenous ABA could significantly increase expression of the *NySOD* gene in *N. yezoensis* under high salinity stress, which was consistent with the change in SOD enzyme activity (**Figures 4A**, **6E**). Mittler and Zilinskas (1992) found that the cytosolic *ApxI* transcript increased dramatically in response to drought, high temperature, and ABA stress in pea. Williamson and Scandalios (1992) discovered that ABA significantly induced the expression of *Cat-1* in the dark. Our results indicated the *NyAPX* and *NyCAT* genes expressions had the same profiles and were similar to *NySOD*.

However, the change in *NyGPX* (py02541) expression level was inconsistent with its variation in enzyme activity. Glutathione peroxidase is an important antioxidant enzyme that catalyzes the conversion of H_2O_2 into water using reduced GSH, thioredoxin (Trx), or other electron donors (Ursini et al., 1995; Bela et al., 2015; Passaia and Margis-Pinheiro, 2015). A number of studies have shown that there are different GPX homologs in organisms (Passaia et al., 2013). Some homologs are up-regulated under certain abiotic stresses, while other homologs may be down-regulated (Zhou et al., 2018). Thus, our transcriptome and qRT-PCR results did not cover all the contributions made by the transcripts with a GPX function. The expression of *NyGPX* was up-regulated when exogenous ABA was added. Therefore, it is reasonable to propose that ABA at least partly regulates *NyGPXs* expression under high salinity stress conditions. The up-regulation of the enzyme activity under the normal conditions could be explained by the induction of ABA during the rehydration prior to high salinity stress with the chemicals.

It is well known that salinity stress can induce ROS accumulation and activate the antioxidant system, which plays an important role in protecting algal cells from oxidative damage (Luo and Liu, 2011; Wang et al., 2019). It has also been shown that ABA is considered to be a common constituent in Rhodophyta where it is involved in regulating physiological processes (Yoshida et al., 2003; Yokoya et al., 2010). Our previous study found that ABA content significantly increased under high salinity stress in *N. yezoensis* (Yu et al., 2018) and that there was also a significant change in antioxidant enzyme activities (Yu et al., 2020). However, whether ABA regulates the expression of antioxidant enzymes in this alga is unknown.

Signaling Pathway for the Abscisic Acid-Mediated Expression of Antioxidant Enzymes in *N. yezoensis*

Acquisition of the ABA signaling pathway is widely regarded as one of the crucial factors for successful land colonization by terrestrial plants (Komatsu et al., 2020). The mechanism underlying the ABA signaling pathway has been determined in the model plant *A. thaliana*. Under osmotic stress conditions, researchers found that ABA can protect cells from multiple environmental stress factors. Functional genomic studies have suggested that the same signaling components are induced in bryophytes under desiccation conditions as those in angiosperms (Xiao et al., 2018). Indeed, the core ABA signaling components seem to be evolutionarily conserved among land plants (Komatsu et al., 2020). Therefore, the ABA signaling pathway must have existed in a common ancestor of land plants around 400–500 million years ago (Takezawa et al., 2011).

Previous studies have suggested that the ABA receptor gene for PYR/PYL/RCAR was laterally transferred from bacteria to the ancestral genome of the *Zygnematophyceae*, which are believed to be the closest algal relatives of land plants (Wickett et al., 2014; Cheng et al., 2019). Thus, the corresponding pathway in algae before *Zygnematophyceae* was defined as a kind of prototype ABA signaling pathway that might have consisted of different molecules but with similar functions to those in higher plants (Komatsu et al., 2020). Major ABA signaling components other than PYR/PYL/RCAR-type receptor genes have been identified in the streptophyte algae *Klebsormidium nitens* and *Chara braunii* (Hori et al., 2014; Nishiyama et al., 2018). As a core protein in ABA signaling, *PP2C* inhibits *SnRK2* kinase activity by dephosphorylation. It is thought to have emerged early in evolutionary life and is widely distributed in archaea, bacteria, plants, and even animals (Komatsu et al., 2020). During evolution from prokaryotes to terrestrial plants, *PP2C*s diversified and formed different subgroups with increased total gene numbers (Fuchs et al., 2013). The *PP2C* family has been classified into several different groups based on their amino acid sequence characteristics (Fuchs et al., 2013; Bhaskara et al., 2019), of which, group A *PP2C* (*PP2C-A*) may play a crucial role in the ABA signaling pathway. In bryophytes, the PP2C-A gene may have been evolutionarily conserved and could have functioned as a negative regulator that was analogous to that in angiosperms. However, there does not seem to be any *PP2C-A* genes in the algal *PP2C* family except for the *PP2C-A*-like genes found in the chlorophyte genome (Komatsu et al., 2020). In this study, a full length *PP2C* gene was obtained from *N. yezoensis*. However, a similarity search in the NCBI database showed that the *nyPP2C* gene was not an analog of *PP2C-A* but belonged to an ancestral *PP2C* gene.

The SnRK2s phosphorylated AREB transcription factors (AREB/ABFs) and these activated AREB/ABFs recognized the conserved ABA-responsive elements (ABREs) in the promoters of downstream target genes. Based on their C-terminal domain structure, the SnRK family in plants can be defined as SnRK1, SnRK2, and SnRK3 (Hrabak et al., 2003). SnRK1, a SnRK2-like kinase, has also been detected in the green alga *C. reinhardtii*, which is located at the base of the green plant phylogenetic tree (Komatsu et al., 2020). In contrast, only one copy of *SnRK1*-related kinase was found in the genome of *Cyanidioschyzon merolae*, a red alga that emerged before green algae (Komatsu et al., 2020). These results imply that SnRK1 is an older SnRK than SnRK2. Thus, it is reasonable to believe that the association between ancestral PP2C and SnRK1 occurred long before the emergence of PP2C-A/SnRK2. Recent published *Porphyra* genome showed that there was no SnRK proteins with similarity to the SnRK2 subfamily, but it encoded SnRK1 and SnRK3. Furthermore, several members of the SnRK3/CIPK clade contain the similar motifs to the C-terminal domain of SnRK2 (Brawleya

et al., 2017). Similarly, there was no *SnRK2* gene was found in our transcriptome data, but one *SnRK1* transcript was annotated in *N. yezoensis*.

Many studies have reported that the AREB/ABFs play a central role in osmotic stress inducible adaptive pathways (Nakashima et al., 2014) and that the transcriptions of stress related genes are enhanced by ABA accumulation. During this process, the most important and well-characterized regulator of AREB/ABFs is the basic leucine zipper (bZIP) transcription factor (Fujita et al., 2013). The named ABRE is constituted by the ACGTGG/TC sequence (Guiltinan et al., 1990; Busk and Pages, 1998). It has been shown that the interaction between the ACGT-box and a so-called coupling element (CE) in higher plants is sufficient to confer ABA induction (Shen et al., 1996; Narusaka et al., 2003) and that an ACGT-box can interact with different CESs, which usually leads to a synergistic effect on the absolute expression levels of the target genes (Shen et al., 1996). A pair of ABREs has been found to form such an ABA-responsive complex (Hattori et al., 2002). In addition, promoter analyses have revealed that multiple ABREs will enhance the expression of the related genes under drought or ABA accumulation (Shen et al., 1996; Narusaka et al., 2003). Several bZIP transcription factors were also identified in our transcriptome. In addition, we also identified at least one ABRE motif in the promoter region of some *N. yezoensis* genes related to the antioxidant system, including *CAT, APX, GPX, POD,* and *NOX*.

Although several core component genes were identified, studies on the ABA signaling pathway in Rhodophyta are still fragmented. Together with the ABA stress response factor, the AREB/ABF-SnRK2 signaling and the ABRE sequence in the promoters of downstream genes are believed to be conserved from bacteria to mammals (Takezawa et al., 2011). This implies the possibility of a mechanistic analogy among the ABA signaling pathways in organisms from different kingdoms. Thus, it is reasonable to assume that ABA signal transduction occurs in *N. yezoensis* and the up-regulation of antioxidase genes under high salinity conditions could be attributed to ABRE-mediated activation.

Although none of the genes for the core components in ABA signaling were identified as DEGs under the MC and the CMA treatments according to our transcriptome analysis. The up-regulation of most antioxidation-related enzymes under high salinity conditions with the addition of exogenous ABA in the inhibitors treatment illustrated the induction of these genes.

CONCLUSION

Based on our transcriptome results and analyses of the related molecular information that has been published, we suggest that ABA is synthesized *via* the carotenoid pathway in *N. yezoensis* in a similar manner to terrestrial plants. We also suggest that both the MVA and MEP pathways likely exist simultaneously due to the inhibition of ABA synthesis under the corresponding specific inhibitor treatments. Both the activity and the expression of the antioxidases significantly increased after the addition of exogenous ABA. Except for the PYR/PYL/RCAR-type receptor genes, the other core components of the ABA signaling pathway were identified in *N. yezoensis*. However, these molecules showed evolutionary differences to those in terrestrial plants. This showed that the ABA signaling pathway in *N. yezoensis* is an ancestral one. Taking into account the ABRE motif in the promoter region of genes related to the antioxidant system, we propose that the up-regulation of antioxidase genes under high salinity conditions is mediated by the ABA signaling pathway.

DATA AVAILABILITY STATEMENT

The data presented in the study are deposited in the Oceanographic Data Center, accession number PAPER2021120050-01.

AUTHOR CONTRIBUTIONS

JN and GW conceived and designed the research. JY, ZF, WG, and JN conducted the experiments. JN, JY, and WG analyzed the data. JN, JY, and BY wrote the manuscript. GW checked and revised the manuscript. JN and GW served as the author who were responsible for contact and ensuring communication. All authors contributed to the article and approved the submitted version.

FUNDING

This study was funded by the National Natural Science Foundation of China (Nos. 41776150 and 41476140), China Agriculture Research System of MOF and MARA, the Key Deployment Project of the Centre for Ocean Mega-Research of Science, the Chinese Academy of Sciences (COMS2019Q02), and the Major Scientific and Technological Innovation Project of Shandong Provincial Key Research and Development Program (2019JZZY010815).

SUPPLEMENTARY MATERIAL

The Supplementary Material for this article can be found online at: https://www.frontiersin.org/articles/10.3389/fmicb.2021.775710/full#supplementary-material

Supplementary Figure 1 | Hypothetical synthetic route of ABA and precursor IPP in *N. yezoensis*. Enzymes marked in red indicated that had been annotated in our transcriptome data. The red five-pointed star represents the genes were expressed differentially. GA-3P, glyceraldehyde 3-phosphate; DXP, 1-deoxy-D-xylulose 5-phosphate; MEP, 2-C-Methyl-D-erythritol-4-phosphate; CDP-ME, 4-(cytidines5-diphospho)-2-C-methylerythritol; CDP-MEP, 2-phospho-4-(cytidines5-diphospho)-2-C-methylerythritol; ME-cPP, 2-C-methyl-D-erythritol-2, 4-cyclodiphosphate; HMBPP, hydroxymethyl-2-(E)-butenyl 4-diphosphate; IPP, isopentenyl diphosphate; GPP, Geranyl diphosphate; FPP, Farnesyl diphosphate; GGPP, Geranylgeranyl

diphosphate; NSY, neoxanthin synthase; NCED, 9-cis -epoxycarotenoid dioxygenases; AAO, abscisic aldehyde oxidase; ACC, acetoacetyl-CoA; HMGS, 3-hydroxy-3-rnethylglutaryl-CoA synthase; HMG-CoA, 3-hydroxy-3-methylglutaryl-CoA; HMGR, 3-hydroxy-3-methylglutaryl-CoA reductase; MVA, mevalonic acid;. MK, mevalonatekinase; MVAP, mevalonate 5-phosphate; PMK, phosphomevalonate kinase; MVAPP, mevalonate 5-diphosphate; MDC, mevalonate-5-diphosphate decarboxylase. Other abbreviations in this figure were described in **Supplementary Table 3**.

Supplementary Figure 2 | Flow chart of samples treatment.

Supplementary Table 1 | Information about the nine genes and primers used in this study.

Supplementary Table 2 | Annotate the major KEGG metabolic pathways of DEGs between different sample groups in *N. yezoensis*.

Supplementary Table 3 | The genes relevant to ABA synthesis.

REFERENCES

Bela, K., Horvath, E., Galle, A., Szabados, L., Tari, I., and Csiszar, J. (2015). Plant glutathione peroxidases: emerging role of the antioxidant enzymes in plant development and stress responses. *J. Plant Physiol.* 176, 192–201. doi: 10.1016/j.jplph.2014.12.014

Bennett, R. D., Norman, S. M., and Maier, V. P. (1984). Biosynthesis of abscisic-acid from farnesol derivatives in cercospora-rosicola. *Phytochemistry* 23, 1913–1915.

Bhaskara, G. B., Wong, M. M., and Verslues, P. E. (2019). The flip side of phospho-signalling: regulation of protein dephosphorylation and the protein phosphatase 2Cs. *Plant Cell Environ.* 42, 2913–2930. doi: 10.1111/pce.13616

Bick, J. A., and Lange, B. M. (2003). Metabolic cross talk between cytosolic and plastidial pathways of isoprenoid biosynthesis: unidirectional transport of intermediates across the chloroplast envelope membrane. *Arch. Biochem. Biophys.* 415, 146–154. doi: 10.1016/s0003-9861(03)00233-9

Blouin, N. A., Brodie, J. A., Grossman, A. C., Xu, P., and Brawley, S. H. (2011). Porphyra: a marine crop shaped by stress. *Trends Plant Sci.* 16, 29–37. doi: 10.1016/j.tplants.2010.10.004

Brawleya, S. H., Blouina, N. A., Ficko-Blean, E., Wheeler, G. L., Lohre, M., Goodson, H. V., et al. (2017). Insights into the red algae and eukaryotic evolution from the genome of *Porphyra umbilicalis* (Bangiophyceae, Rhodophyta). *Proc. Natl. Acad. Sci. U.S.A.* 114, E6361–E6370. doi: 10.1073/pnas.1703088114

Busk, P. K., and Pages, M. (1998). Regulation of abscisic acid-induced transcription. *Plant Mol. Biol.* 37, 425–435. doi: 10.1023/a:1006058700720

Carretero-Paulet, L., Cairo, A., Botella-Pavia, P., Besumbes, O., Campos, N., Boronat, A., et al. (2006). Enhanced flux through the methylerythritol 4-phosphate pathway in Arabidopsis plants overexpressing deoxyxylulose 5-phosphate reductoisomerase. *Plant Mol. Biol.* 62, 683–695. doi: 10.1007/s11103-006-9051-9

Cheng, S. F., Xian, W. F., Fu, Y., Marin, B., Keller, J., Wu, T., et al. (2019). Genomes of Subaerial Zygnematophyceae Provide Insights into Land Plant Evolution. *Cell* 179, 1057–1067. doi: 10.1016/j.cell.2019.10.019

Cordoba, E., Porta, H., Arroyo, A., San Roman, C., Medina, L., Rodriguez-Concepcion, M., et al. (2011). Functional characterization of the three genes encoding 1-deoxy-D-xylulose 5-phosphate synthase in maize. *J. Exp. Bot.* 62, 2023–2038. doi: 10.1093/jxb/erq393

Cutler, A. J., and Krochko, J. E. (1999). Formation and breakdown of ABA. *Trends Plant Sci.* 4, 472–478.

Disch, A., Schwender, J., Muller, C., Lichtenthaler, H. K., and Rohmer, M. (1998). Distribution of the mevalonate and glyceraldehyde phosphate/pyruvate pathways for isoprenoid biosynthesis in unicellular algae and the cyanobacterium Synechocystis PCC 6714. *Biochem. J.* 333, 381–388. doi: 10.1042/bj3330381

Dobrev, P. I., Havlicek, L., Vagner, M., Malbeck, J., and Kaminek, M. (2005). Purification and determination of plant hormones auxin and abscisic acid using solid phase extraction and two-dimensional high performance liquid chromatography. *J. Chromatogr. A* 1075, 159–166. doi: 10.1016/j.chroma.2005.02.091

Estevez, J. M., Cantero, A., Reindl, A., Reichler, S., and Leon, P. (2001). 1-deoxy-D-xylulose-5-phosphate synthase, a limiting enzyme for plastidic isoprenoid biosynthesis in plants. *J. Biol. Chem.* 276, 22901–22909. doi: 10.1074/jbc.M100854200

Fu, J., Chu, J., Sun, X., Wang, J., and Yan, C. (2012). Simple, rapid, and simultaneous assay of multiple carboxyl containing phytohormones in wounded tomatoes by UPLC-MS/MS using single SPE purification and Isotope Dilution. *Anal. Sci.* 28, 1081–1087. doi: 10.2116/analsci.28.1081

Fuchs, S., Grill, E., Meskiene, I., and Schweighofer, A. (2013). Type 2C protein phosphatases in plants. *FEBS J.* 280, 681–693. doi: 10.1111/j.1742-4658.2012.08670.x

Fujita, Y., Yoshida, T., and Yamaguchi-Shinozaki, K. (2013). Pivotal role of the AREB/ABF-SnRK2 pathway in ABRE-mediated transcription in response to osmotic stress in plants. *Physiol. Plant.* 147, 15–27. doi: 10.1111/j.1399-3054.2012.01635.x

Grauvogel, C., and Petersen, J. (2007). Isoprenoid biosynthesis authenticates the classification of the green alga *Mesostigma viride* as an ancient streptophyte. *Gene* 396, 125–133. doi: 10.1016/j.gene.2007.02.020

Guajardo, E., Correa, J. A., and Contreras-Porcia, L. (2016). Role of abscisic acid (ABA) in activating antioxidant tolerance responses to desiccation stress in intertidal seaweed species. *Planta* 243, 767–781. doi: 10.1007/s00425-015-2438-6

Guan, L. Q. M., Zhao, J., and Scandalios, J. G. (2000). Cis-elements and trans-factors that regulate expression of the maize Cat1 antioxidant gene in response to ABA and osmotic stress: H2O2 is the likely intermediary signaling molecule for the response. *Plant J.* 22, 87–95. doi: 10.1046/j.1365-313x.2000.00723.x

Guiltinan, M. J., Marcotte, W. R., and Quatrano, R. S. (1990). A plant leucine zipper protein that recognizes an abscisic-acid response element. *Science* 250, 267–271. doi: 10.1126/science.2145628

Han, M., Heppel, S. C., Su, T., Bogs, J., Zu, Y. G., An, Z. G., et al. (2013). Enzyme inhibitor studies reveal complex control of Methyl-D-Erythritol 4-Phosphate (MEP) pathway enzyme expression in *Catharanthus roseus*. *PLoS One* 8:e0062467. doi: 10.1371/journal.pone.0062467

Hattori, T., Totsuka, M., Hobo, T., Kagaya, Y., and Yamamoto-Toyoda, A. (2002). Experimentally determined sequence requirement of ACGT-containing abscisic acid response element. *Plant Cell Physiol.* 43, 136–140. doi: 10.1093/pcp/pcf014

Hauser, F., Waadtl, R., and Schroeder, J. I. (2011). Evolution of abscisic acid synthesis and signaling mechanisms. *Curr. Biol.* 21, R346–R355. doi: 10.1016/j.cub.2011.03.015

Hemmerlin, A., Harwood, J. L., and Bach, T. J. (2012). A raison d'etre for two distinct pathways in the early steps of plant isoprenoid biosynthesis? *Prog. Lipid Res.* 51, 95–148. doi: 10.1016/j.plipres.2011.12.001

Hirsch, R., Hartung, W., and Gimmler, H. (1989). Abscisic-acid content of algae under stress. *Bot. Acta* 102, 326–334.

Hori, K., Maruyama, F., Fujisawa, T., Togashi, T., Yamamoto, N., Seo, M., et al. (2014). *Klebsormidium flaccidum* genome reveals primary factors for plant terrestrial adaptation. *Nat. Commun.* 5:3978. doi: 10.1038/ncomms4978

Hrabak, E. M., Chan, C. W. M., Gribskov, M., Harper, J. F., Choi, J. H., Halford, N., et al. (2003). The Arabidopsis CDPK-SnRK superfamily of protein kinases. *Plant Physiol.* 132, 666–680. doi: 10.1104/pp.102.011999

Huang, X., Ke, C. H., and Wang, W. X. (2010). Cadmium and copper accumulation and toxicity in the macroalga *Gracilaria tenuistipitata*. *Aquat. Biol.* 11, 17–26. doi: 10.3354/ab00288

Hunter, W. N. (2007). The non-mevalonate pathway of isoprenoid precursor biosynthesis. *J. Biol. Chem.* 282, 21573–21577. doi: 10.1074/jbc.r700005200

Inomata, M., Hirai, N., Yoshida, R., and Ohigashi, H. (2004). The biosynthetic pathway to abscisic acid via ionylideneethane in the fungus Botrytis cinerea. *Phytochemistry* 65, 2667–2678. doi: 10.1016/j.phytochem.2004.08.025

Jiang, D., Zhou, L., Chen, W., Ye, N., Xia, J., and Zhuang, C. (2019). Overexpression of a microRNA-targeted NAC transcription factor improves drought and salt tolerance in Rice via ABA-mediated pathways. *Rice* 12:76. doi: 10.1186/s12284-019-0334-6

Jiang, M. Y., and Zhang, J. H. (2002). Water stress-induced abscisic acid accumulation triggers the increased generation of reactive oxygen species and

up-regulates the activities of antioxidant enzymes in maize leaves. *J. Exp. Bot.* 53, 2401–2410. doi: 10.1093/jxb/erf090

Jomaa, H., Wiesner, J., Sanderbrand, S., Altincicek, B., Weidemeyer, C., Hintz, M., et al. (1999). Inhibitors of the nonmevalonate pathway of isoprenoid biosynthesis as antimalarial drugs. *Science* 285, 1573–1576. doi: 10.1126/science.285.5433.1573

Kaur, G., and Pati, P. K. (2016). Analysis of cis-acting regulatory elements of Respiratory burst oxidase homolog (Rboh) gene families in Arabidopsis, and rice. (provides)clues for their diverse functions. *Comput. Biol. Chem.* 62, 104–118. doi: 10.1016/j.compbiolchem.2016.04.002

Kobayashi, M., Hirai, N., Kurimura, Y., Ohigashi, H., and Tsuji, Y. (1997). Abscisic acid-dependent algal morphogenesis in the unicellular green alga *Haematococcus pluvi*alis. *Plant Growth Regul.* 22, 79–85.

Komatsu, K., Takezawa, D., and Sakata, Y. (2020). Decoding ABA and osmostress signalling in plants from an evolutionary point of view. *Plant Cell Environ.* 43, 2894–2911. doi: 10.1111/pce.13869

Kwak, J. M., Mori, I. C., Pei, Z. M., Leonhardt, N., Torres, M. A., Dangl, J. L., et al. (2003). NADPH oxidase AtrbohD and AtrbohF genes function in ROS-dependent ABA signaling in Arabidopsis. *EMBO J.* 22, 2623–2633. doi: 10.1093/emboj/cdg277

Lamb, C., and Dixon, R. A. (1997). The oxidative burst in plant disease resistance. *Annu. Rev. Plant Physiol. Plant Mol. Biol.* 48, 251–275.

Li, B., and Dewey, C. N. (2011). RSEM: accurate transcript quantification from RNA-Seq data with or without a reference genome. *BMC Bioinformatics* 12:323. doi: 10.1186/1471-2105-12-323I

Lichtenthaler, H. K. (2000). Non-mevalonate isoprenoid biosynthesis: enzymes, genes and inhibitors. *Biochem. Soc. Trans.* 28, 785–789.

Linforth, R. S. T., Bowman, W. R., Griffin, D. A., Marples, B. A., and Taylor, I. B. (1987). 2-trans-ABA alcohol accumulation in the wilty tomato mutants flacca and sitiens. *Plant Cell Environ.* 10, 599–606. doi: 10.1111/1365-3040.ep11604117

Liu, X. L., Zhang, H., Jin, Y. Y., Wang, M. M., Yang, H. Y., Ma, H. Y., et al. (2019). Abscisic acid primes rice seedlings for enhanced tolerance to alkaline stress by upregulating antioxidant defense and stress tolerance-related genes. *Plant Soil* 438, 39–55.

Livak, K. J., and Schmittgen, T. D. (2001). Analysis of relative gene expression data using real-time quantitative PCR and the 2(T)(-Delta Delta C) method. *Methods* 25, 402–408. doi: 10.1006/meth.2001.1262

Lohr, M., Schwender, J., and Polle, J. E. W. (2012). Isoprenoid biosynthesis in eukaryotic phototrophs: a spotlight on algae. *Plant Sci.* 185, 9–22. doi: 10.1016/j.plantsci.2011.07.018

Lopez-Carbonell, M., Gabasa, M., and Jauregui, O. (2009). Enhanced determination of abscisic acid (ABA) and abscisic acid glucose ester (ABA-GE) in *Cistus albidus* plants by liquid chromatography-mass spectrometry in tandem mode. *Plant Physiol. Biochem.* 47, 256–261. doi: 10.1016/j.plaphy.2008.12.016

Love, M. I., Huber, W., and Anders, S. (2014). Moderated estimation of fold change and dispersion for RNA-seq data with DESeq2. *Genome. Biol.* 15:550. doi: 10.1186/s13059-014-0550-8

Luo, M. B., and Liu, F. (2011). Salinity-induced oxidative stress and regulation of antioxidant defense system in the marine macroalga Ulva prolifera. *J. Exp. Mar. Biol. Ecol.* 409, 223–228. doi: 10.1016/j.jembe.2011.08.023

Mao, X. Z., Cai, T., Olyarchuk, J. G., and Wei, L. P. (2005). Automated genome annotation and pathway identification using the KEGG Orthology (KO) as a controlled vocabulary. *Bioinformatics* 21, 3787–3793. doi: 10.1093/bioinformatics/bti430

Mikami, K., Mori, I. C., Matsuura, T., Ikeda, Y., Kojima, M., Sakakibara, H., et al. (2016). Comprehensive quantification and genome survey reveal the presence of novel phytohormone action modes in red seaweeds. *J. Appl. Phycol.* 28, 2539–2548.

Miller, G., Suzuki, N., Ciftci-Yilmaz, S., and Mittler, R. (2010). Reactive oxygen species homeostasis and signalling during drought and salinity stresses. *Plant Cell Environ.* 33, 453–467. doi: 10.1111/j.1365-3040.2009.02041.x

Mittler, R. (2002). Oxidative stress, antioxidants and stress tolerance. *Trends Plant Sci.* 7, 405–410.

Mittler, R., and Zilinskas, B. A. (1992). Molecular-coloning and characterization of a gene encoding pea cytosolic ascorbate peroxidase. *J. Biol. Chem.* 267, 21802–21807. doi: 10.1016/s0021-9258(19)36683-9

Nakashima, K., Yamaguchi-Shinozaki, K., and Shinozaki, K. (2014). The transcriptional regulatory network in the drought response and its crosstalk in abiotic stress responses including drought, cold, and heat. *Front. Plant Sci.* 5:170. doi: 10.3389/fpls.2014.00170

Nambara, E., and Marion-Poll, A. (2005). Abscisic acid biosynthesis and catabolism. *Annu. Rev. Plant Biol.* 56, 165–185.

Narusaka, Y., Nakashima, K., Shinwari, Z. K., Sakuma, Y., Furihata, T., Abe, H., et al. (2003). Interaction between two cis-acting elements, ABRE and DRE, in ABA-dependent expression of Arabidopsis rd29A gene in response to dehydration and high-salinity stresses. *Plant J.* 34, 137–148. doi: 10.1046/j.1365-313x.2003.01708.x

Neill, S. J., Desikan, R., Clarke, A., Hurst, R. D., and Hancock, J. T. (2002). Hydrogen peroxide and nitric oxide as signalling molecules in plants. *J. Exp. Bot.* 53, 1237–1247. doi: 10.1093/jexbot/53.372.1237

Nishiyama, T., Sakayama, H., de Vries, J., Buschmann, H., Saint-Marcoux, D., Ullrich, K. K., et al. (2018). The Chara genome: secondary complexity and implications for plant Terrestrialization. *Cell* 174, 448–464. doi: 10.1016/j.cell.2018.06.033

Nogueira, F. T. S., De Rosa, V. E., Menossi, M., Ulian, E. C., and Arruda, P. (2003). RNA expression profiles and data mining of sugarcane response to low temperature. *Plant Physiol.* 132, 1811–1824. doi: 10.1104/pp.102.017483

Oh, H. D., Yu, D. J., Chung, S. W., Chea, S., and Lee, H. J. (2018). Abscisic acid stimulates anthocyanin accumulation in 'Jersey' highbush blueberry fruits during ripening. *Food Chem.* 244, 403–407. doi: 10.1016/j.foodchem.2017.10.051

Pan, X., Welti, R., and Wang, X. (2010). Quantitative analysis of major plant hormones in crude plant extracts by high-performance liquid chromatography-mass spectrometry. *Nat. Protoc.* 5, 986–992. doi: 10.1038/nprot.2010.37

Passaia, G., Fonini, L. S., Caverzan, A., Jardim-Messeder, D., Christoff, A. P., Gaeta, M. L., et al. (2013). The mitochondrial glutathione peroxidase GPX3 is essential for H2O2 homeostasis and root and shoot development in rice. *Plant Sci.* 208, 93–101. doi: 10.1016/j.plantsci.2013.03.017

Passaia, G., and Margis-Pinheiro, M. (2015). Glutathione peroxidases as redox sensor proteins in plant cells. *Plant Sci.* 234, 22–26. doi: 10.1016/j.plantsci.2015.01.017

Phillips, M. A., Leon, P., Boronat, A., and Rodriguez-Concepcion, M. (2008). The plastidial MEP pathway: unified nomenclature and resources. *Trends Plant Sci.* 13, 619–623. doi: 10.1016/j.tplants.2008.09.003

Sahu, M., and Kar, R. K. (2018). Possible interaction of ROS, antioxidants and ABA to survive osmotic stress upon acclimation in *Vigna radiata* L. Wilczek seedlings. *Plant Physiol. Biochem.* 132, 415–423. doi: 10.1016/j.plaphy.2018.09.034

Saradhi, P. P., Suzuki, I., Katoh, A., Sakamoto, A., Sharmila, P., Shi, D. J., et al. (2000). Protection against the photo-induced inactivation of the photosystem II complex by abscisic acid. *Plant Cell Environ.* 23, 711–718.

Schwender, J., Seemann, M., Lichtenthaler, H. K., and Rohmer, M. (1996). Biosynthesis of isoprenoids (carotenoids, sterols, prenyl side-chains of chlorophylls and plastoquinone) via a novel pyruvate/glyceraldehyde 3-phosphate non-mevalonate pathway in the green alga *Scenedesmus obliquus*. *Biochem. J.* 316, 73–80. doi: 10.1042/bj3160073

Schwender, J., Zeidler, J., Groner, R., Muller, C., Focke, M., Braun, S., et al. (1997). Incorporation of 1-deoxy-D-xylulose into isoprene and phytol by higher plants and algae. *FEBS Lett.* 414, 129–134. doi: 10.1016/s0014-5793(97)01002-8

Shen, Q. X., Zhang, P. N., and Ho, T. H. D. (1996). Modular nature of abscisic acid (ABA) response complexes: composite promoter units that are necessary and sufficient for ABA induction of gene expression in barley. *Plant Cell* 8, 1107–1119. doi: 10.1105/tpc.8.7.1107

Soon, F.-F., Ng, L.-M., Zhou, X. E., West, G. M., Kovach, A., Tan, M. H. E., et al. (2012). Molecular mimicry regulates ABA signaling by SnRK2 kinases and PP2C phosphatases. *Science* 335, 85–88. doi: 10.1126/science.1215106

Sun, P. P., Mao, Y. X., Li, G. Y., Cao, M., Kong, F. N., Wang, L., et al. (2015). Comparative transcriptome profiling of *Pyropia yezoensis* (Ueda) MS Hwang & HG Choi in response to temperature stresses. *BMC Genomics* 16:463. doi: 10.1186/s12864-015-1586-1

Sutherland, J. E., Lindstrom, S. C., Nelson, W. A., Brodie, J., Lynch, M. D. J., Hwang, M. S., et al. (2011). a new look at an ancient order: generic revision of the Bangiales (rhodophyta). *J. Phycol.* 47, 1131–1151. doi: 10.1111/j.1529-8817.2011.01052.x

Takezawa, D., Komatsu, K., and Sakata, Y. (2011). ABA in bryophytes: How a universal growth regulator in life became a plant hormone? *J. Plant Res.* 124, 437–453. doi: 10.1007/s10265-011-0410-5

Takino, J., Kozaki, T., Ozaki, T., Liu, C., Minami, A., and Oikawa, H. (2019). Elucidation of biosynthetic pathway of a plant hormone abscisic acid in phytopathogenic fungi. *Biosci. Biotechnol. Biochem.* 83, 1642–1649. doi: 10.1080/09168451.2019.1618700

Taylor, I. B., Linforth, R. S. T., Alnaieb, R. J., Bowman, W. R., and Marples, B. A. (1988). The wilty tomato mutants flacca and sitiens are impaired in the oxidation of ABA-aldehyde to ABA. *Plant Cell Environ.* 11, 739–745. doi: 10.1111/j.1365-3040.1988.tb01158.x

Tijero, V., Teribia, N., Munoz, P., and Munne-Bosch, S. (2016). Implication of Abscisic acid on ripening and quality in sweet cherries: differential effects during pre- and post-harvest. *Front. Plant Sci.* 7:602. doi: 10.3389/fpls.2016.00602

Trapnell, C., Williams, B. A., Pertea, G., Mortazavi, A., Kwan, G., van Baren, M. J., et al. (2010). Transcript assembly and quantification by RNA-Seq reveals unannotated transcripts and isoform switching during cell differentiation. *Nat. Biotechnol.* 28, 511–174. doi: 10.1038/nbt.1621

Ursini, F., Maiorino, M., Brigelius-Flohe, R., Aumann, K. D., Roveri, A., Schomburg, D., et al. (1995). Diversity of glutathione peroxidases. *Methods Enzymol.* 252, 38–53. doi: 10.1016/0076-6879(95)52007-4

Wang, D., Yu, X., Xu, K., Bi, G., Cao, M., Zelzion, E., et al. (2020). *Pyropia yezoensis* genome reveals diverse mechanisms of carbon acquisition in the intertidal environment. *Nat. Commun.* 11:4028. doi: 10.1038/s41467-020-17689-1

Wang, W., Xu, Y., Chen, T., Xing, L., Xu, K., Xu, Y., et al. (2019). Regulatory mechanisms underlying the maintenance of homeostasis in *Pyropia haitanensis* under hypersaline stress conditions. *Sci. Total Environ.* 662, 168–179. doi: 10.1016/j.scitotenv.2019.01.214

Wickett, N. J., Mirarab, S., Nguyen, N., Warnow, T., Carpenter, E., Matasci, N., et al. (2014). Phylotranscriptomic analysis of the origin and early diversification of land plants. *Proc. Natl. Acad. Sci. U.S.A.* 111, E4859–E4868. doi: 10.1073/pnas.1323926111

Williamson, J. D., and Scandalios, J. G. (1992). Differential response of maize catalases to abscisic-acid VP1 transcriptional activator is not required for abscisic acid regulated CAT1 expression. *Proc. Natl. Acad. Sci. U.S.A.* 89, 8842–8846. doi: 10.1073/pnas.89.18.8842

Xiao, L., Yobi, A., Koster, K. L., He, Y., and Oliver, M. J. (2018). Desiccation tolerance in Physcomitrella patens: rate of dehydration and the involvement of endogenous abscisic acid (ABA). *Plant Cell Environ.* 41, 275–284. doi: 10.1111/pce.13096

Xie, X. J., Lu, X. P., Wang, L. P., He, L. W., and Wang, G. C. (2020). High light intensity increases the concentrations of j3-carotene and zeaxanthin in marine red macroalgae. *Algal Res.* 47, 1–12.

Yang, D., Du, X., Liang, X., Han, R., Liang, Z., Liu, Y., et al. (2012). Different roles of the mevalonate and methylerythritol phosphate pathways in cell growth and tanshinone production of *Salvia miltiorrhiza* Hairy Roots. *PLoS One* 7:e0046797. doi: 10.1371/journal.pone.0046797

Yao, X. M., Ji, J., Yue, J. Y., Shi, S. Q., Ou, C., Jiang, Z. P., et al. (2020). Exogenous abscisic acid modulates reactive oxygen metabolism and related gene expression in *Platycladus orientalis* under H2O2-Induced Stress. *Russ. J. Plant Physiol.* 67, 85–93. doi: 10.1134/s1021443720010264

Yokoya, N. S., Stirk, W. A., van Staden, J., Novak, O., Tureckova, V., Pencik, A., et al. (2010). Endogenous cytokinins, auxins and absicsic acid in red algae from Brazil. *J. Phycol.* 46, 1198–1205.

Yoshida, K., Igarashi, E., Mukai, M., Hirata, K., and Miyamoto, K. (2003). Induction of tolerance to oxidative stress in the green alga, *Chlamydomonas reinhardtii*, by abscisic acid. *Plant Cell Environ.* 26, 451–457.

Yu, B., Yang, J., Niu, J., and Wang, G. (2018). Synthesis of abscisic acid in *Pyropia yezoensis* and its protection on photosynthesis under high-salinity stress. *Mar. Sci.* 42, 83–90.

Yu, B., Yang, J. L., Niu, J. F., and Wang, G. (2020). Antioxidant responses to hyperosmolarity stress in the intertidal *Pyropia yezoensis* (Bangiales, Rhodophyta). *Algal Res.* 48:101930. doi: 10.1016/j.algal.2020.101930

Zhou, Y., Hu, L. F., Ye, S. F., Jiang, L. W., and Liu, S. Q. (2018). Genome-wide identification of glutathione peroxidase (GPX) gene family and their response to abiotic stress in cucumber. *3 Biotech* 8:159. doi: 10.1007/s13205-018-1185-3

Zhu, D. H., and Scandalios, J. G. (1994). Differential accumulation of manganese-superoxide dismutase transcripts in maize in response to abscisic-acid and high osmoticum. *Plant Physiol.* 106, 173–178. doi: 10.1104/pp.106.1.173

Conflict of Interest: The authors declare that the research was conducted in the absence of any commercial or financial relationships that could be construed as a potential conflict of interest.

Publisher's Note: All claims expressed in this article are solely those of the authors and do not necessarily represent those of their affiliated organizations, or those of the publisher, the editors and the reviewers. Any product that may be evaluated in this article, or claim that may be made by its manufacturer, is not guaranteed or endorsed by the publisher.

frontiers in Microbiology

MINI REVIEW
published: 24 February 2022
doi: 10.3389/fmicb.2021.781826

Diversity Among Cyanobacterial Photosystem I Oligomers

Ming Chen[1], Xuan Liu[1], Yujie He[2], Ningning Li[1,3,4], Jun He[2,5] and Ying Zhang[1,3,4]**

[1] The Seventh Affiliated Hospital, Sun Yat-sen University, Shenzhen, China, [2] Center for Cell Fate and Lineage (CCLA), Bioland Laboratory (Guangzhou Regenerative Medicine and Health Guangdong Laboratory), Guangzhou, China, [3] China–UK Institute for Frontier Science, Shenzhen, China, [4] Tomas Lindahl Nobel Laureate Laboratory, The Seventh Affiliated Hospital, Sun Yat-sen University, Shenzhen, China, [5] Center for Cell Lineage and Development, Guangzhou Institutes of Biomedicine and Health, Chinese Academy of Sciences, Guangzhou, China

Unraveling the oligomeric states of the photosystem I complex is essential to understanding the evolution and native mechanisms of photosynthesis. The molecular composition and functions of this complex are highly conserved among cyanobacteria, algae, and plants; however, its structure varies considerably between species. In cyanobacteria, the photosystem I complex is a trimer in most species, but monomer, dimer and tetramer arrangements with full physiological function have recently been characterized. Higher order oligomers have also been identified in some heterocyst-forming cyanobacteria and their close unicellular relatives. Given technological progress in cryo-electron microscope single particle technology, structures of PSI dimers, tetramers and some heterogeneous supercomplexes have been resolved into near atomic resolution. Recent developments in photosystem I oligomer studies have largely enriched theories on the structure and function of these photosystems.

Keywords: photosystem I, structure, cyanobacteria (blue-green algae), oligomers states, supercomplexes organization

OPEN ACCESS

Edited by:
Bao-Sheng Qiu,
Central China Normal University, China

Reviewed by:
Xiaochun Qin,
University of Jinan, China
Weimin Ma,
Shanghai Normal University, China

****Correspondence:***
Jun He
he_jun@gibh.ac.cn
Ying Zhang
zhangy856@mail.sysu.edu.cn

Specialty section:
This article was submitted to Microbial Physiology and Metabolism, a section of the journal Frontiers in Microbiology

Received: *23 September 2021*
Accepted: *06 December 2021*
Published: *24 February 2022*

Citation:
Chen M, Liu X, He Y, Li N, He J and Zhang Y (2022) Diversity Among Cyanobacterial Photosystem I Oligomers. Front. Microbiol. 12:781826. doi: 10.3389/fmicb.2021.781826

INTRODUCTION

Photosystem I (PSI) is a light-driven membrane protein complex that transfers electrons from plastocyanin/cytochrome C to ferredoxin/flavodoxin in oxygenic photosynthetic organisms (Amunts and Nelson, 2009). In cyanobacterial species, the PSI consists of 11 or 12 proteins coordinating approximately 127 cofactors that are responsible for the initial steps of light energy-induced electron transfer during photosynthesis. The current detailed understanding of the 3D structure of PSI originated from a study in cyanobacteria, in which a structure with 2.5Å resolution was established using X-ray crystallography (Jordan et al., 2001). Novel structural features, such as molecular interfaces, subcomplex organization, cofactors, pigment binding and functional relatives have been recently identified using cryo-electron microscope (EM) single particle analysis in oxygenic organisms (Pan et al., 2018, 2021; Suga et al., 2019; Zheng et al., 2019).

The native assembly of the PSI complex is of broad scientific interest in photosynthesis research owing to its considerable variability. The predominant state of the PSI complex is a trimer in most cyanobacterial species (Jordan et al., 2001; Malavath et al., 2018; Hamaguchi et al., 2021), whereas monomer (El-Mohsnawy et al., 2010), dimer, tetramer (Watanabe et al., 2010; Li et al., 2014; Zheng et al., 2019) and some undefined higher order oligomers (Watanabe et al., 2014; Li et al., 2019) have been detected in some subclasses. Unraveling the oligomeric diversity among PSI complexes is essential to understanding photosynthesis and the evolution of photosystems. For instance, in *Thermosynechococcus elongatus*, PSI trimers can absorb more photons than monomers under low light intensities owing to its higher optical cross-section (Baker et al., 2014). PSI dimers

are regarded as an evolutionary intermediate between the trimers in cyanobacteria and monomers in eukaryotic photosynthetic organisms. This review discusses the implications of structural and oligomeric diversity among cyanobacterial PSI supercomplexes.

PHOTOSYSTEM I SUBUNITS

The subunit composition of PSI complexes is highly conserved between cyanobacteria and plants. The structural and functional details of PSI proteins have previously been discussed in depth (Xu et al., 2001; Grotjohann and Fromme, 2005; Amunts and Nelson, 2009), and in this section of the review, a brief introduction to this topic is given. As shown in **Figure 1**, twelve subunits have been identified in cyanobacteria, nine of which (PsaA, PsaB, PsaF, PsaJ, PsaI, PsaK, PsaL, PsaM, and PsaX) are transmembrane proteins, and three of which (PsaC, PsaD and PsaE) are membrane extrinsic proteins, located on the stromal side of the PSI complex (Jordan et al., 2001).

PsaA, PsaB, and PsaC coordinate the major pigments for light reaction in photosynthesis, with central roles in light energy absorption and conversion; these proteins therefore comprise the core of the PSI complex (Nechushtai et al., 1983). PsaA and PsaB are transmembrane proteins with eleven transmembrane helices each. They share homology with each other and form a heterodimer in the redox center of PSI. These two subunits play essential roles in both light harvesting and electron transfer (Chitnis, 1996; Jordan et al., 2001). The main cofactors in the electron transfer chain (ETC)—P700, A, A0, A1 and Fx—are surrounded by the five C-terminal α-helices of the PsaA/PsaB subunits. These ETC cofactors are surrounded by the core antenna chlorophylls, also coordinated by PsaA/PsaB. The structure shows that most of chlorophyll A molecules in the reaction center bind with subunits PsaA and PsaB hydrophobically (Jordan et al., 2001). PsaC is an 8.8 KDa ferredoxin-like protein; together with PsaA and PsaB, this protein comprises the central core of PSI complex, harboring the ETC. Using biochemical reconstitution experiments, it has been shown that the PsaC polypeptide binds two [Fe_4S_4] clusters, F_A and F_B, which are the terminal electron acceptors in PSI complex (Vassiliev et al., 1998). Interruption of the *psaC* gene in the filamentous cyanobacteria *Anabaena* sp. PCC 29413 led to the complete loss of the PsaC protein and its associated cofactors F_A and F_B and thus resulted in the absence of PSI-mediated electron transfer from P700 to ferredoxin (Mannan et al., 1991). PsaC is thought to mediate terminal electron transfer in the reaction center of the PSI complex (Klukas et al., 1999). Interestingly, a recent study in cyanobacteria revealed that PsaC interacts with ferredoxin in a similar way to a multi-protein complex-NDH-1L, which accepts electrons from ferredoxin (Zhang et al., 2020). This supports a role for PsaC as a core protein that mediates electron transfer from the reaction center of PSI to the outer electron acceptor chains.

PsaD and PsaE are peripheral proteins on the reducing side of PSI and are both involved in electron transfer (Yu et al., 1993; Chitnis et al., 1996). In biochemical studies in cyanobacteria, it has been demonstrated that PsaD provides a ferredoxin docking site, PsaE is also involved in ferredoxin binding to the PSI complex (Yu et al., 1993; Xu et al., 1994; Klukas et al., 1999). A high-resolution structure of the plastocyanin (Pc)–photosystem I (PSI)–ferredoxin oxidoreductase (Fd) supercomplex was recently resolved in the pea plant *Pisum sativum*, which clearly revealed a model for Fd–PSI binding (Caspy et al., 2020). From the structure, it has been concluded that the positively-charged amino acids in PsaD and PsaE composite a part of electrostatic interactions for the binding of ferredoxin to PSI complex. PsaF is an integral membrane protein with a molecular weight of 15.6 kDa. In green algae, PsaF is proposed to be a docking site for soluble electron donors, while in cyanobacteria, deletion of PsaF has no effect on photoautotrophic growth, as this protein is not essential for docking and electron transfer (Chitnis et al., 1991; Fischer et al., 1999). Structural studies revealed that a positively charged patch composed of Lys93, Lys96 and Lys100 in PsaF may be involved in correctly orienting Pc, aligning Cu^{2+} directly over P700 (Jordan et al., 2001). PsaI, PsaJ, PsaM, and PsaX are small transmembrane proteins in the cyanobacterial PSI complex, which stabilize the whole complex by interacting with the core subunits (Xu et al., 1995, 2001; Chitnis, 1996; Naithani et al., 2000).

PsaL is a hydrophobic protein that is critical for the oligomerization of the PSI complex. The deletion of PsaL results in disassembly of PSI trimer in *Synechocystis* sp. PCC 6803 (Chitnis et al., 1993). The structure of PsaL subunits varies a little between monomeric, dimeric and trimeric states of the PSI; detailed structure differences are shown in **Figure 2**. An α-helix fragment at the luminal side (**Figure 2B**), which is involved in PSI trimer connections in *Thermosynechococcus elongatus*, was found to be missing when the PSI complex was biochemically monomerized (Jordan et al., 2001; Çoruh et al., 2021). Sequence alignments showed that the region involved in oligomerization is comprised of a 16 amino acid peptide, from Leu140 to Asn155 (**Supplementary Figure 1B**). In dimeric PSI, a similar α-helix fragment (**Figure 2A**) can be detected in the C-terminal of PsaL both from structural (**Figure 2A**) and sequence (**Supplementary Figure 1A**) data. As shown in **Figure 2C**, one additional structural variation in PsaL is that the dimer has a shorter C-terminal than the trimer by four amino acids (**Supplementary Figure 1C**). This may prevent the trimeric complex from forming, thus stabilizing the dimer (Jordan et al., 2001; Kato et al., 2019; Zheng et al., 2019; Chen et al., 2020). Interestingly, an extended loop is present in the dimer (**Figures 2A,C**); sequence alignments revealed that the loop is composed of six amino acids (**Supplementary Figures 1A,C**). The function of this loop in the oligomerization of the PSI dimer is currently unclear.

MONOMERS

For decades, the PSI trimer was recognized as the only form with full physiological function in the model species of cyanobacteria (Boekema et al., 1987; Ford and Holzenburg, 1988; Kruip et al., 1994). The theory was challenged by El-Mohsnawy and coworkers, who isolated an intact monomeric form in which all subunits and photochemical activities of trimer

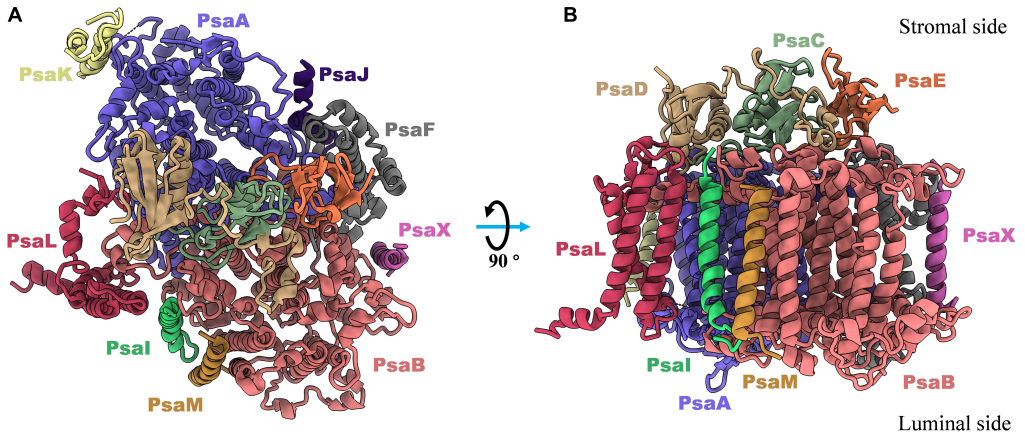

FIGURE 1 | Top **(A)** and side **(B)** views of subunits composition in monomeric photosystem I complex from thermophilic cyanobacterium *Thermosynechococcus elongatus* (PDB: 1JB0). There are nine transmembrane proteins (PsaA, PsaB, PsaF, PsaJ, PsaK, PsaL, PsaM, PsaI, and PsaX) in which most of cofactors are non-charged bonded to perform light harvesting, light-to-electron energy conversion, and excitation transport. And three out membrane proteins (PsaC, PsaD, and PsaE) are located in stromal side and responsible for the electron transfer from PSI complex to the soluble acceptors.

were preserved (El-Mohsnawy et al., 2010). The monomeric state is recognized as a structural and functional intermediate during PSI trimer biogenesis and assembly. More importantly, the dynamic equilibrium between monomers and trimers may be critical for cyanobacteria to adapt to changing ecological environments (El-Mohsnawy et al., 2010; Yang et al., 2015). Most recently, high resolution structures of monomeric PSI complexes were resolved in *Synechocystis* sp. PCC 6803 and *Thermosynechococcus elongatus* using X-ray crystallography and cryo-EM single particle analysis, respectively (Netzer-El et al., 2019; Çoruh et al., 2021). Both structures clearly revealed that the subunit composition of monomers are highly identical to trimeric PSI. In *Thermosynechococcus elongatus*, the major difference was in the cofactors, in which 14 chlorophyll molecules detected in trimer were not be able to be built in atomic model of monomer. However, very few chlorophylls (aC-M1601 of PsaM and aC-K1401 of PsaK) at the monomer–monomer interface in the PSI trimer were found to be missing from the structure. This is an unexpected feature, as monomer isolation and purification preparation can result in the disassociation of cofactors located near the interface in the trimer.

Surprisingly, the chlorophylls that were located in the PsaL trimerization domain were present in the monomeric structure in *Thermosynechococcus elongatus*. However, through resolving the PSI monomeric structure from a PsaL modified strain of *Synechocystis* sp. PCC6803, Çoruh and coworkers found that disruption of a short helix in the PsaL C-terminus region, which stabilizes trimerization, can result in monomerization and loss of PsaL-associated pigments (Çoruh et al., 2021). One of the most important pieces of information to be drawn from studies of PSI monomers is the structural basis for the loss of red chlorophylls in cyanobacteria, which have essential functions for energy absorption and excitation of the complex under low light conditions. In *Thermosynechococcus elongatus*, between nine and eleven chlorophylls, with a red shift spectroscopic absorption of over 700 nm (long wavelength), were detected in each monomer unit of the PSI trimer (Pålsson et al., 1998; Jordan et al., 2001). Spectroscopic and structural characterization of both monomeric and trimeric PSI complexes strongly indicate that chlorophyll B1233 and PsaX-adjacent chlorophylls are long-wavelength chlorophylls (Skandary et al., 2015; Toporik et al., 2020).

DIMERS

The PSI dimer is one of the predominant oligomeric states in heterocystous cyanobacteria, and the high-resolution structure of the PSI dimer has been resolved in *Anabaena* sp. PCC 7120 (Zheng et al., 2019; Chen et al., 2020). As shown in **Figure 3A**, the dimer is composed of two monomers connected *via* specific interfaces. The interfaces are composed of subunits PsaL and PsaK from monomer1, PsaL and PsaB from monomer2 (Zheng et al., 2019). In contrast to the PSI trimer, four residues in PsaL at the C-terminus are missing from the luminal side in *Anabaena* sp. PCC 7120, resulting in a conformational change and slight movement of PsaL protein out from the C-terminal domain at the interface. Thus, it has thus been suggested that PSI dimerization occurs mainly *via* the stromal helices of PsaL (Chen et al., 2020). As a result, the connection between the two adjacent monomers is weaker compared with the trimeric state. Structurally, the distance between two chlorophylls that form the energetic coupling of the two monomers is greater, which suggests that the adjacent monomers in the dimer function more independently than in the trimer, owing to looser connections and longer distances.

Even though the PSI dimer has been intensively characterized in cyanobacteria, it was first observed in spinach, and was suggested to be an artificial aggregation of monomers resulting from membrane solubilization (van Roon et al., 2000). Large amounts of PSI–light harvesting complex I (LHCI) dimers were observed in the stromal lamellae of dark-adapted spinach thylakoids using atomic force microscopy (AFM) technology (Wood et al., 2018). A high-resolution structure (2.97Å) of the

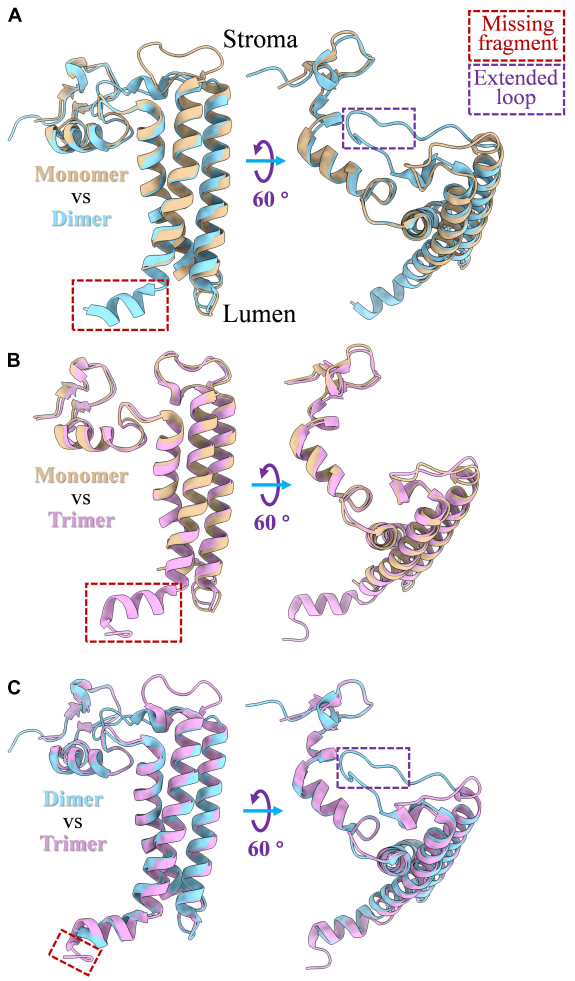

FIGURE 2 | PsaL structure comparison among monomeric, dimeric and trimeric states of PSI complex. **(A)** Structure differences of PsaL between PSI monomer and dimer; **(B)** structure differences between of PsaL between PSI monomer and trimer; **(C)** structure differences of PsaL between PSI dimer and trimer. The losing fragments and extended loop regions were marked by red and purple rectangles, respectively. PSI monomer (PDB code: 6LU1) and trimer (PDB code: 1JB0) from *Thermosynechococcus elongatus* and PSI tetramer (PDB code: 6K61) from *Anabaena* sp. PCC 7120 were source molecules from which PsaL structures were extracted.

chloroplast PSI–LHCI dimeric supercomplex has been resolved very recently (Naschberger et al., 2021). It was clearly shown in this structure that the interface in the PSI–LHCI dimer is composed of the LHC9 protein and its associated bound lipids and pigments, which is a distinct molecular link for PSI oligomerization from that of cyanobacteria. The physiological function of the PSI–LHCI dimer complex is not well defined in higher plants; however, the dimeric arrangement seems to be dark-responsive (Wood et al., 2018).

TRIMERS

In most species of cyanobacteria, PSI complexes assemble as a cloverleaf-shaped trimer with a diameter of 220Å (**Figure 3B**) in the native thylakoid membrane, in which the linker peptide is PsaL. Boekema and coworkers (Boekema et al., 1987) obtained the very first evidence for trimerization of the PSI reaction center from a thermophilic cyanobacterial species. The PsaL subunit plays a pivotal role in forming the interface between PsaL are the key force to link monomers to form trimer were detected on experimental deletion of the PsaL subunits. High resolution (2.5Å) structure (PDB entry: 1JB0) of the PSI trimer has been obtained from *Thermosynechococcus elongatus* using X-ray crystallography (Jordan et al., 2001), in which details of the complex architecture, molecular locations, compositions, and interactions were presented clearly for the first time. Nine transmembrane subunits (PsaA, PsaB, PsaF, PsaI, PsaJ, PsaK, PsaL, PsaM, and PsaX) and three stromal attached subunits (PsaC, PsaD, and PsaE) were present in this structure (**Figure 1**). The positions of all subunits were revealed in the core structure, which were consistent with biochemical and biophysical evidences (Boekema et al., 1987; Li et al., 1991; Chitnis et al., 1993; Vassiliev et al., 1998; Fischer et al., 1999; Klukas et al., 1999).

Unlike the PSI dimer, the interface between monomeric units in the PSI trimer complex mainly consists of the PsaL subunit. The cofactor framework for light energy conversion and transfer was also drawn clearly from this model. In 2018, Malavath and coworkers resolved a structure with 2.5Å resolution (PDB entry: 5OY0) for the PSI trimer from the mesophilic cyanobacterium *Synechocystis* sp. PCC 6803 using X-ray crystallography (Malavath et al., 2018; Netzer-El et al., 2019). The molecular composition, positions, and interfaces in this structure were mostly identical to that of *Thermosynechococcus elongatus*; however, more detailed information could be derived from this model. There were found to be several novel structural features compared with the PSI trimer from *Thermosynechococcus elongatus*, including the absence of nine chlorophylls in the trimeric model, the replacement of PsaX with chlorophyll F1302, and several new carotenoids and lipids were determined for the first time from this structure.

In recent years, new PSI complex structures have been resolved in some cyanobacterial species that utilize far-red light (Gisriel et al., 2020; Hamaguchi et al., 2021) and are adapted to extremely high light intensities (Dobson et al., 2021). The assembled PSI trimers in these species has a similar shape to the trimers from *Thermosynechococcus elongatus* and *Synechocystis* sp. PCC 6803. Further, PSI trimers has been established as the most predominant oligomeric state in cyanobacteria *via* the structural analyses described here.

TETRAMERS

Tetrameric PSI complexes are novel supercomplexes that were first detected in *Anabaena* and *Cyanophora paradoxa* using blue native polyacrylamide gel electrophoresis (BN-PAGE); (Watanabe et al., 2010). Molecular weight and sodium dodecylsulfate (SDS)-PAGE-based molecular composition assays have strongly suggested that the larger detected band on the BN-PAGE is a tetrameric PSI complex. The existence

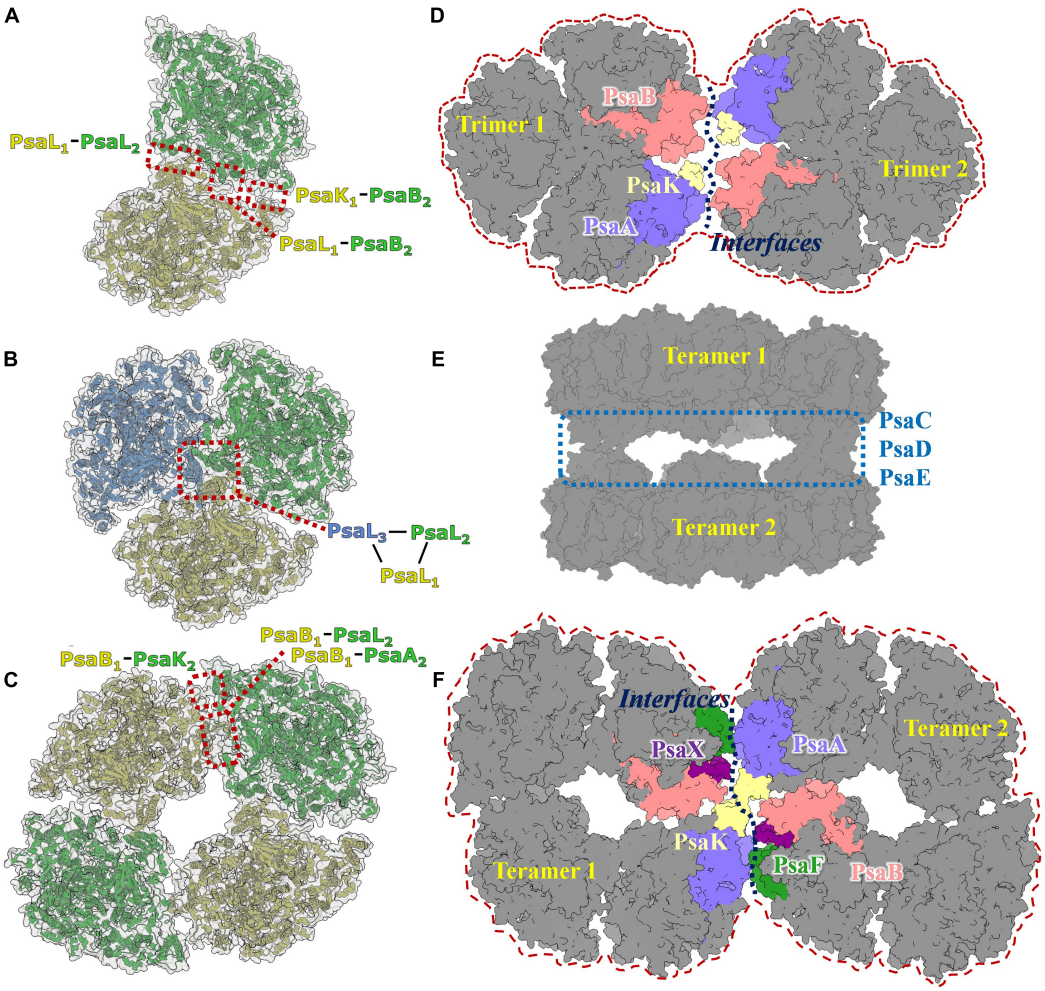

FIGURE 3 | Photosystem I diversities in cyanobacteria. **(A)** Model of PSI dimer in *Anabaena* sp. PCC 7120 (PDB code: 6K61). **(B)** Model of PSI trimer in *Thermosynechococcus elongatus* (PDB code:1JB0). **(C)** Model of PSI tetramer in *Anabaena* sp. PCC 7120 (PDB code: 6TCL). **(D)** Predicted 3D map of PSI hexamer architecture. The interface involves subunits of PsaA, PsaB, Psak, Psal, PsaM, and PsaL were colored and labeled separately. **(E)** Cryo-EM single particle density map of two face-to-face associated PSI tetramer complex. **(F)** Predicted 3D map of PSI octamer architecture. It should be realized that the models revealed in **Figures 3A–C,E** are experimental resolved and reported in the literature, while models revealed in **Figures 3D,F** are speculated according to the acknowledged structure basis of PSI dimer, trimer and tetramer.

of the PSI tetramer was demonstrated in the heterocystous cyanobacterium *Anabaena* sp. PCC 7120 using single particle transmission electron microscopy analysis (TEM; Watanabe et al., 2014). The first cryo-EM structure of the PSI tetramer was obtained by Semchonok and coworkers from the thermophilic cyanobacterium *Chroococcidiopsis* sp. TS-821 (Semchonok et al., 2016). This 11.5Å resolution revealed that the PSI tetramer is a pseudotetramer, consisting of a dimer of dimers (**Figure 3C**). Two types of interfaces were presented in PSI oligomerization based on the electron density map, including one novel type. Interface features have been shown using rigid body-fitting for the monomers within the crystal structure of the PSI trimer from *Thermosynechococcus elongatus*. The subunits PsaA, PsaB, PsaI, PsaL, and PsaM are involved in the interface I, while PsaA, PsaB, and PsaL are the mainly proteins in interface II. Recently, high-resolution structures of PSI tetramers have been resolved from *Anabaena* sp. PCC 7120 using cryo-EM single particle analysis (Kato et al., 2019; Zheng et al., 2019; Chen et al., 2020). The monomeric models from *Thermosynechococcus elongatus* and *Synechocystis* sp. PCC 6803 were used as initial models to build and refine atomic models of the PSI tetramer. No significant conformational variations in the interacting protein subunits of monomer complexes were detected among these models. Interface I is present in $PsaL_1$–$PsaB_2$, $PsaL_1$–$PsaL_2$, and $PsaK_1$–$PsaB_2$ interactions; this is similar to the interfaces in the trimeric PSI from *Thermosynechococcus elongatus*. Unlike interface I, the interface II occurs in the $PsaB_1$–$PsaA_2$, $PsaB_1$-$PsaL_2$, and $PsaB_1$-$PsaA_2$ interactions. A tight hydrophobic interaction between adjacent PsaL subunits is the primary connection in the formation of dimer units, as was observed in trimeric complexes. PsaL subunits also have a vital role in the assembly of tetramers. Research revealed two additional polar contact sites in interface I; one between Arg85 of PsaK from one monomer and Ser214 of PsaB' from the adjacent monomer, and one between the two

stromal side residues of PsaL and the two C-terminal residues of the adjacent subunit PsaL' (Zheng et al., 2019).

To explore why monomers form dimers instead of trimers given the structural similarities in interface I, Kato and coworkers superimposed a monomeric unit of the PSI tetramer onto the corresponding site in the PSI trimer (Kato et al., 2019). Several steric hindrances were found to prevent formation of the trimeric core, which were contributed mainly by the N-terminal, middle and C-terminal regions of the PsaL subunit. Among these residues, Thr58, Phe60, Arg61, Asn140, and Ser144 were found to be conserved in species in which the PSI tetramer was formed. Some interface variations were detected in the validated model of the PSI tetramer. For instance, a short luminal C-terminal residue in PsaL was found to be missing in *Anabaena* and this was reported to form a coordination site for Ca^{2+} ions that stabilize the trimer (Chen et al., 2020). One interesting finding is that a tilting was detected in both PsaI and PsaL subunits, introducing 5–6Å movements away from the interface that stabilized the oligomerization of monomers. This tilting ultimately resulted in a shift of the monomer and a loosening of PsaL-mediated monomer interactions that generate the internal connections within PSI dimer. Another significant structural variation is that the distance between chlorophylls forming exitonic couplings in the PSI trimer was increased from 17.0 to 20.7Å in the dimer, supporting the functional variation in PSI dimer where each monomer functions more independently than in the trimer (Chen et al., 2020).

HIGHER ORDER OLIGOMERS

Higher order oligomeric PSI complexes are rarely reported in cyanobacteria, algae, or green plants. Through negative staining single particle TEM analysis, Watanabe and coworkers averaged a projection map of shoulder-to-shoulder associated PSI tetramer (Watanabe et al., 2014). Further biochemical and biophysical studies are needed to evaluate whether this is a PSI octamer. In our previous work, a novel structure of a dimer of PSI tetramers was reconstructed and refined to resolution of 6–8Å (Chen et al., 2020). In this complex, two PSI tetramers are present with face-to-face stromal domains formed *via* direct interactions between PsaC, PsaD, and PsaE modules (**Figure 3E**). This indicates that such a complex is probably not physiologically relevant, and thus not a PSI octamer complex. In these studies, the major doubt for the existence of native higher order PSI complexes comes from a lack of biochemical evidence, such as the presence of PSI complex bands with molecular weight larger than that of the tetramer on native blue PAGE, and purification of the stable complex from cyanobacteria.

In a recent study, Li and coworkers identified a possible PSI hexamer in *Chroococcidiopsis* sp. PCC 6712 using BN-PAGE technology (Li et al., 2019). No high-resolution structure has been resolved for these supercomplexes so far; however, assembly models for PSI hexamer and octamer can still be hypothesized based on reported structural details of molecular interfaces in PSI dimers and tetramers, and on the negatively stained image of a possible PSI hexamer in *Chroococcidiopsis* (Li et al., 2019) and PSI octamer in *Anabaena* (Watanabe et al., 2014). As shown in **Figures 3D,F**, theoretical models of the PSI hexamer and octamer can be drawn based on the interfaces involved in dimer and tetramer formation between PsaA, PsaB, PsaF, PsaK, PsaL, PsaM, PsaI, and PsaX subunits (Zheng et al., 2019; Chen et al., 2020). Using newly developed isolation methods, we obtained a pure sample of PSI-like supercomplexes with molecular weights between 2000 and 2800 kDa. Structural and functional characterization of these supercomplexes are underway, from which further details of these complexes may be inferred.

An interesting study on the biogenesis of cyanobacterial thylakoid membranes was recently published (Huokko et al., 2021), in which it was shown that the assembly of photosynthetic membrane complexes respond dynamically to changing light strength. The assembly of PSI complexes in cyanobacterial cells are largely improved during a 5-day dark adaptation period. The photosynthetic complexes may be reorganized under such dynamic circumstances. Recent atomic force microscopy results clearly show that the photosynthetic complexes attach to each other to form megacomplexes with dynamic architectural reorganization of the native thylakoid membrane (Zhao et al., 2020). Such dynamic rearrangements in membrane complexes have been regarded as an important mechanism for living cells to adapt to variations in ecological environments, as in the phycobilisome (PBS)-iron stress-induced protein A (isiA)-NADH dehydrogenase-like complex type-1 (NDH-1) supercomplex (Zhang et al., 2010; Casella et al., 2017; MacGregor-Chatwin et al., 2017; Zhao et al., 2020). PSI tetramers have been presented as highly light-responsive complexes in *Chroococcidiopsis* sp. TS-821. PSI oligomer state equilibrium is considered as one means by which energetic metabolism is balanced in living cyanobacterial cells (Li et al., 2014). Taking the above into account, higher order PSI supercomplexes in native membranes may be structurally and functionally important for efficient energy metabolism and even survival in cyanobacteria under stress condition. All these studies have indicated that unknown oligomer states of PSI supercomplexes with specific physiological functions can be detected, especially in cells faced with variable ecological environments.

CONCLUSION

Photosystem I is one of the most important multiprotein membrane complexes in oxygenic photosynthetic organisms. An understanding of homogenous and heterogenous PSI supercomplexes is required to understand the native mechanisms of photosynthesis. The diversity in PSI oligomeric states among cyanobacteria has garnered considerable interest recently, because resolving high resolution structure of these supercomplexes is now technically feasible. At least four different kinds of oligomer have been functionally and structurally demonstrated in cyanobacteria. Such diversity in oligomeric states is now acknowledged to be functionally important, helping cells to survive under changing ecological environments. Monomeric PSI exhibits a complete range of physiological functions in cyanobacteria compared with the previously-established range for the trimer. Meanwhile the

trimer harvests light more efficiently under low light conditions, and the tetramer is more prevalent in high-light conditions. The tetramer is composed of a dimer of dimers; the dimer is now regarded as an evolutionary intermediate state between the trimer in cyanobacteria and the monomer in green algae and higher plants. Given the advantages of cryo-EM single particle structural analysis of supercomplexes, novel molecular features, including conformers, assembly models, interfaces, and even ligand binding were acknowledged to help unravel energy-trapping and electron transfer in PSI complexes. Furthermore, some newly higher order PSI oligomers have also been detected in cyanobacteria, algae and higher plants. This indicates that the assembly of native PSI complexes is more complicated than previously thought, and its characterization is key to understanding the role of these complexes in photosynthesis.

AUTHOR CONTRIBUTIONS

MC, XL,YH, and YZ wrote the manuscript with adding from NL, JH, and YZ supported the research with funding acquisition. All authors read and approved the manuscript.

FUNDING

This work was supported by China Postdoctoral Science Foundation (Grant No. 2020T130747), and by 100 Top Talents Program of Sun Yat-sen University (Grant No. 392009).

ACKNOWLEDGMENTS

The authors want to thank the reviewers for their very careful reading and grateful suggestions to this manuscript. And we appreciate Lijin Tian for his critical reading and improving to the scientific point of this manuscript.

SUPPLEMENTARY MATERIAL

The Supplementary Material for this article can be found online at: https://www.frontiersin.org/articles/10.3389/fmicb.2021.781826/full#supplementary-material

REFERENCES

Amunts, A., and Nelson, N. (2009). Plant photosystem I design in the light of evolution. *Structure* 17, 637–650. doi: 10.1016/j.str.2009.03.006

Baker, D. R., Manocchi, A. K., Lamicq, M. L., Li, M., Nguyen, K., Sumner, J. J., et al. (2014). Comparative photoactivity and stability of isolated cyanobacterial monomeric and trimeric photosystem I. *J. Phys. Chem. B* 118, 2703–2711. doi: 10.1021/jp407948p

Boekema, E. J., Dekker, J. P., van Heel, M. G., Rögner, M., Saenger, W., Witt, I., et al. (1987). Evidence for a trimeric organization of the photosystem I complex from the thermophilic cyanobacterium *Synechococcus* sp. *FEBS Lett.* 217, 283–286. doi: 10.1016/0014-5793(87)80679-8

Casella, S., Huang, F., Mason, D., Zhao, G. Y., Johnson, G. N., Mullineaux, C. W., et al. (2017). Dissecting the native architecture and dynamics of cyanobacterial photosynthetic machinery. *Mol. Plant* 10, 1434–1448. doi: 10.1016/j.molp.2017.09.019

Caspy, I., Borovikova-Sheinker, A., Klaiman, D., Shkolnisky, Y., and Nelson, N. (2020). The structure of a triple complex of plant photosystem I with ferredoxin and plastocyanin. *Nat. Plants* 6, 1300–1305. doi: 10.1038/s41477-020-00779-9

Chen, M., Perez-Boerema, A., Zhang, L., Li, Y., Yang, M., Li, S., et al. (2020). Distinct structural modulation of photosystem I and lipid environment stabilizes its tetrameric assembly. *Nat. Plants* 6, 314–320. doi: 10.1038/s41477-020-0610-x

Chitnis, P. R. (1996). Photosystem I. *Plant Physiol.* 111, 661–669.

Chitnis, P. R., Purvis, D., and Nelson, N. (1991). Molecular cloning and targeted mutagenesis of the gene psaF encoding subunit III of Photosystem I from the cyanobacterium *Synechocystis* sp. PCC 6803. *J. Biol. Chem.* 266, 20146–20151. doi: 10.1016/s0021-9258(18)54902-4

Chitnis, V. P., Jungs, Y. S., Albee, L., Golbeck, J. H., and Chitnis, P. R. (1996). Mutational analysis of photosystem I polypeptides. Role of PsaD and the lysyl 106 residue in the reductase activity of the photosystem I. *J. Biol. Chem.* 271, 11772–11780. doi: 10.1074/jbc.271.20.11772

Chitnis, V. P., Xu, Q., Yu, L., Golbeck, J. H., Nakamoto, H., Xie, D. L., et al. (1993). Targeted inactivation of the gene psaL encoding a subunit of photosystem I of the cyanobacterium *Synechocystis* sp. PCC 6803. *J. Biol. Chem.* 268, 11678–11684. doi: 10.1016/s0021-9258(19)50253-8

Çoruh, O., Frank, A., Tanaka, H., Kawamoto, A., El-Mohsnawy, E., Kato, T., et al. (2021). Cryo-EM structure of a functional monomeric photosystem I from *Thermosynechococcus elongatus* reveals red chlorophyll cluster. *Commun. Biol.* 4:304. doi: 10.1038/s42003-021-01808-9

Dobson, Z., Ahad, S., Vanlandingham, J., Toporik, H., Vaughn, N., Vaughn, M., et al. (2021). The structure of photosystem I from a high-light-tolerant cyanobacteria. *Elife* 10:e67518. doi: 10.7554/eLife.67518

El-Mohsnawy, E., Kopczak, M. J., Schlodder, E., Nowaczyk, M., Meyer, H. E., Warscheid, B., et al. (2010). Structure and function of intact photosystem 1 monomers from the cyanobacterium *Thermosynechococcus elongatus*. *Biochemistry* 49, 4740–4751. doi: 10.1021/bi901807p

Fischer, N., Boudreau, E., Hippler, M., Drepper, F., Haehnel, W., and Rochaix, J. D. (1999). A large fraction of PsaF is nonfunctional in photosystem I complexes lacking the PsaJ subunit. *Biochemistry* 38, 5546–5552. doi: 10.1021/bi982821a

Ford, R. C., and Holzenburg, A. (1988). Investigation of the structure of trimeric and monomeric photosystem I reaction centre complexes. *EMBO J.* 7, 2287–2293. doi: 10.1002/j.1460-2075.1988.tb03071.x

Gisriel, C., Shen, G., Kurashov, V., Ho, M.-Y., Zhang, S., Williams, D., et al. (2020). The structure of photosystem I acclimated to far-red light illuminates an ecologically important acclimation process in photosynthesis. *Sci. Adv.* 6:eaay6415. doi: 10.1126/sciadv.aay6415

Grotjohann, I., and Fromme, P. (2005). Structure of cyanobacterial photosystem I. *Photosynth. Res.* 85, 51–72.

Hamaguchi, T., Kawakami, K., Shinzawa-Itoh, K., Inoue-Kashino, N., Itoh, S., Ifuku, K., et al. (2021). Structure of the far-red light utilizing photosystem I of *Acaryochloris marina*. *Nat. Commun.* 12:2333. doi: 10.1038/s41467-021-22502-8

Huokko, T., Ni, T., Dykes, G. F., Simpson, D. M., Brownridge, P., Conradi, F. D., et al. (2021). Probing the biogenesis pathway and dynamics of thylakoid membranes. *Nat. Commun.* 12:3475. doi: 10.1038/s41467-021-23680-1

Jordan, P., Fromme, P., Witt, H. T., Klukas, O., Saenger, W., and Krauß, N. (2001). Three-dimensional structure of cyanobacterial Photosystem I at 2.5 Å resolution. *Nature* 411, 909–917. doi: 10.1038/35082000

Kato, K., Nagao, R., Jiang, T.-Y., Ueno, Y., Yokono, M., Chan, S. K., et al. (2019). Structure of a cyanobacterial photosystem I tetramer revealed by cryo-electron microscopy. *Nat. Commun.* 10:4929. doi: 10.1038/s41467-019-12942-8

Klukas, O., Schubert, W.-D., Jordan, P., Krauß, N., Fromme, P., Witt, H. T., et al. (1999). Photosystem I, an improved model of the stromal subunits PsaC, PsaD, and PsaE *. *J. Biol. Chem.* 274, 7351–7360. doi: 10.1074/jbc.274.11.7351

Kruip, J., Bald, D., Boekema, E., and Rögner, M. (1994). Evidence for the existence of trimeric and monomeric photosystem I complexes in thylakoid membranes from cyanobacteria. *Photosynth. Res.* 40, 279–286. doi: 10.1007/BF00034777

Li, M., Calteau, A., Semchonok, D. A., Witt, T. A., Nguyen, J. T., Sassoon, N., et al. (2019). Physiological and evolutionary implications of tetrameric photosystem I in cyanobacteria. *Nat. Plants* 5, 1309–1319. doi: 10.1038/s41477-019-0566-x

Li, M., Semchonok, D. A., Boekema, E. J., and Bruce, B. D. (2014). Characterization and evolution of tetrameric photosystem I from the thermophilic cyanobacterium *Chroococcidiopsis* sp TS-821. *Plant Cell* 26, 1230–1245. doi: 10.1105/tpc.113.120782

Li, N., Zhao, J., Warren, P. V., Warden, J. T., Bryant, D. A., and Golbeck, J. H. (1991). PsaD is required for the stable binding of PsaC to the photosystem I core protein of *Synechococcus* sp. PCC 6301. *Biochemistry* 30, 7863–7872. doi: 10.1021/bi00245a028

MacGregor-Chatwin, C., Sener, M., Barnett, S. F. H., Hitchcock, A., Barnhart-Dailey, M. C., Maghlaoui, K., et al. (2017). Lateral segregation of photosystem I in cyanobacterial thylakoids. *Plant Cell* 29, 1119–1136. doi: 10.1105/tpc.17.00071

Malavath, T., Caspy, I., Netzer-El, S. Y., Klaiman, D., and Nelson, N. (2018). Structure and function of wild-type and subunit-depleted photosystem I in *Synechocystis*. *Biochim. Biophys. Acta Bioenerg.* 1859, 645–654. doi: 10.1016/j.bbabio.2018.02.002

Mannan, R. M., Whitmarsh, J., Nyman, P., and Pakrasi, H. B. (1991). Directed mutagenesis of an iron-sulfur protein of the photosystem I complex in the filamentous cyanobacterium *Anabaena variabilis* ATCC 29413. *Proc. Natl. Acad. Sci. U. S. A.* 88, 10168–10172. doi: 10.1073/pnas.88.22.10168

Naithani, S., Hou, J. M., and Chitnis, P. R. (2000). Targeted inactivation of the psaK1, psaK2 and psaM genes encoding subunits of photosystem I in the cyanobacterium *Synechocystis* sp. PCC 6803. *Photosynth. Res.* 63, 225–236. doi: 10.1023/A:1006463932538

Naschberger, A., Mosebach, L., Tobiasson, V., Kuhlgert, S., Scholz, M., Perez-Boerema, A., et al. (2021). Chloroplast photosystem I dimer and high resolution model of the complex with plastocyanin. *bioRxiv* [Preprint] doi: 10.1101/2021.08.30.458224

Nechushtai, R., Muster, P., Binder, A., Liveanu, V., and Nelson, N. (1983). Photosystem I reaction center from the thermophilic cyanobacterium *Mastigocladus laminosus*. *Proc. Nat. Acad. Sci. U. S. A.* 80, 1179–1183. doi: 10.1073/pnas.80.5.1179

Netzer-El, S. Y., Caspy, I., and Nelson, N. (2019). Crystal structure of photosystem I monomer from *Synechocystis* PCC 6803. *Front. Plant Sci.* 9:1865. doi: 10.3389/fpls.2018.01865

Pålsson, L. O., Flemming, C., Gobets, B., van Grondelle, R., Dekker, J. P., and Schlodder, E. (1998). Energy transfer and charge separation in photosystem I: P700 oxidation upon selective excitation of the long-wavelength antenna chlorophylls of *Synechococcus elongatus*. *Biophys. J.* 74, 2611–2622. doi: 10.1016/S0006-3495(98)77967-6

Pan, X., Ma, J., Su, X., Cao, P., Chang, W., Liu, Z., et al. (2018). Structure of the maize photosystem I supercomplex with light-harvesting complexes I and II. *Science* 360, 1109–1113. doi: 10.1126/science.aat1156

Pan, X., Tokutsu, R., Li, A., Takizawa, K., Song, C., Murata, K., et al. (2021). Structural basis of LhcbM5-mediated state transitions in green algae. *Nat. Plants* 7, 1119–1131. doi: 10.1038/s41477-021-00960-8

Semchonok, D. A., Li, M., Bruce, B. D., Oostergetel, G. T., and Boekema, E. J. (2016). Cryo-EM structure of a tetrameric cyanobacterial photosystem I complex reveals novel subunit interactions. *Biochim. Biophys. Acta* 1857, 1619–1626. doi: 10.1016/j.bbabio.2016.06.012

Skandary, S., Konrad, A., Hussels, M., Meixner, A. J., and Brecht, M. (2015). Orientations between red antenna states of photosystem I monomers from *Thermosynechococcus elongatus* revealed by single-molecule spectroscopy. *J. Phys. Chem. B* 119, 13888–13896. doi: 10.1021/acs.jpcb.5b04483

Suga, M., Ozawa, S.-I., Yoshida-Motomura, K., Akita, F., Miyazaki, N., and Takahashi, Y. (2019). Structure of the green algal photosystem I supercomplex with a decameric light-harvesting complex I. *Nat. Plants* 5, 626–636. doi: 10.1038/s41477-019-0438-4

Toporik, H., Khmelnitskiy, A., Dobson, Z., Riddle, R., Williams, D., Lin, S., et al. (2020). The structure of a red-shifted photosystem I reveals a red site in the core antenna. *Nat. Commun.* 11:5279.

van Roon, H., van Breemen, J. F., de Weerd, F. L., Dekker, J. P., and Boekema, E. J. (2000). Solubilization of green plant thylakoid membranes with n-dodecyl-alpha,D-maltoside. Implications for the structural organization of the photosystem II, photosystem I, ATP synthase and cytochrome b6 f complexes. *Photosynth. Res.* 64, 155–166. doi: 10.1023/A:1006476213540

Vassiliev, I. R., Jung, Y. S., Yang, F., and Golbeck, J. H. (1998). PsaC subunit of photosystem I is oriented with iron-sulfur cluster F(B) as the immediate electron donor to ferredoxin and flavodoxin. *Biophys. J.* 74, 2029–2035. doi: 10.1016/S0006-3495(98)77909-3

Watanabe, M., Kubota, H., Wada, H., Narikawa, R., and Ikeuchi, M. (2010). Novel supercomplex organization of photosystem I in *Anabaena* and *Cyanophora paradoxa*. *Plant Cell Physiol.* 52, 162–168. doi: 10.1093/pcp/pcq183

Watanabe, M., Semchonok, D. A., Webber-Birungi, M. T., Ehira, S., Kondo, K., Narikawa, R., et al. (2014). Attachment of phycobilisomes in an antenna–photosystem I supercomplex of cyanobacteria. *Proc. Nat. Acad. Sci. U. S. A.* 111, 2512–2517. doi: 10.1073/pnas.1320599111

Wood, W. H. J., MacGregor-Chatwin, C., Barnett, S. F. H., Mayneord, G. E., Huang, X., Hobbs, J. K., et al. (2018). Dynamic thylakoid stacking regulates the balance between linear and cyclic photosynthetic electron transfer. *Nat. Plants* 4, 116–127.

Xu, Q., Hoppe, D., Chitnis, V. P., Odom, W. R., Guikema, J. A., and Chitnis, P. R. (1995). Mutational analysis of photosystem I polypeptides in the cyanobacterium *Synechocystis* sp. PCC 6803. Targeted inactivation OF psaI reveals the function of PsaI in the structural orgnization of PsaL. *J. Biol. Chem.* 270, 16243–16250. doi: 10.1074/jbc.270.27.16243

Xu, Q., Jung, Y. S., Chitnis, V. P., Guikema, J. A., Golbeck, J. H., and Chitnis, P. R. (1994). Mutational analysis of photosystem I polypeptides in Synechocystis sp. PCC 6803. Subunit requirements for reduction of $NADP^+$ mediated by ferredoxin and flavodoxin. *J. Biol. Chem.* 269, 21512–21518. doi: 10.1016/s0021-9258(17)31834-3

Xu, W., Tang, H., Wang, Y., and Chitnis, P. R. (2001). Proteins of the cyanobacterial photosystem I. *Biochim. Biophys. Acta* 1507, 32–40. doi: 10.1016/s0005-2728(01)00208-0

Yang, H., Liu, J., Wen, X., and Lu, C. (2015). Molecular mechanism of photosystem I assembly in oxygenic organisms. *Biochim. Biophys. Acta Bioenerg.* 1847, 838–848. doi: 10.1016/j.bbabio.2014.12.011

Yu, L., Zhao, J., Muhlenhoff, U., Bryant, D. A., and Golbeck, J. H. (1993). PsaE is required for in vivo cyclic electron flow around photosystem I in the cyanobacterium *Synechococcus* sp. PCC 7002. *Plant Physiol.* 103, 171–180. doi: 10.1104/pp.103.1.171

Zhang, C., Shuai, J., Ran, Z., Zhao, J., Wu, Z., Liao, R., et al. (2020). Structural insights into NDH-1 mediated cyclic electron transfer. *Nat. Commun.* 11:888. doi: 10.1038/s41467-020-14732-z

Zhang, Y., Chen, M., Church, W. B., Lau, K. W., Larkum, A. W., and Jermiin, L. S. (2010). The molecular structure of the IsiA-Photosystem I supercomplex, modelled from high-resolution, crystal structures of photosystem I and the CP43 protein. *Biochim. Biophys. Acta* 1797, 457–465. doi: 10.1016/j.bbabio.2010.01.002

Zhao, L.-S., Huokko, T., Wilson, S., Simpson, D. M., Wang, Q., Ruban, A. V., et al. (2020). Structural variability, coordination and adaptation of a native photosynthetic machinery. *Nat. Plants* 6, 869–882. doi: 10.1038/s41477-020-0694-3

Zheng, L., Li, Y., Li, X., Zhong, Q., Li, N., Zhang, K., et al. (2019). Structural and functional insights into the tetrameric photosystem I from heterocyst-forming cyanobacteria. *Nat. Plants* 5, 1087–1097. doi: 10.1038/s41477-019-0525-6

Conflict of Interest: The authors declare that the research was conducted in the absence of any commercial or financial relationships that could be construed as a potential conflict of interest.

Publisher's Note: All claims expressed in this article are solely those of the authors and do not necessarily represent those of their affiliated organizations, or those of the publisher, the editors and the reviewers. Any product that may be evaluated in this article, or claim that may be made by its manufacturer, is not guaranteed or endorsed by the publisher.

frontiers | Frontiers in Microbiology

ORIGINAL RESEARCH
published: 06 May 2022
doi: 10.3389/fmicb.2022.876272

Comparative Genomic Analysis Revealed Distinct Molecular Components and Organization of CO_2-Concentrating Mechanism in Thermophilic Cyanobacteria

*Jie Tang[1], Huizhen Zhou[1], Dan Yao[1], Sadaf Riaz[2], Dawei You[2], Anna Klepacz-Smółka[3] and Maurycy Daroch[2]**

[1] School of Food and Bioengineering, Chengdu University, Chengdu, China, [2] School of Environment and Energy, Peking University Shenzhen Graduate School, Shenzhen, China, [3] Department of Bioprocess Engineering, Faculty of Process and Environmental Engineering, Łódź University of Technology, Łódź, Poland

OPEN ACCESS

Edited by:
Qiang Wang,
Henan University, China

Reviewed by:
John Albert Raven,
University of Dundee, United Kingdom
Jianhua Fan,
East China University of Science and Technology, China

***Correspondence:**
Maurycy Daroch
m.daroch@pkusz.edu.cn

Specialty section:
This article was submitted to Microbial Physiology and Metabolism, a section of the journal Frontiers in Microbiology

Received: 15 February 2022
Accepted: 04 April 2022
Published: 06 May 2022

Citation:
Tang J, Zhou H, Yao D, Riaz S, You D, Klepacz-Smółka A and Daroch M (2022) Comparative Genomic Analysis Revealed Distinct Molecular Components and Organization of CO_2-Concentrating Mechanism in Thermophilic Cyanobacteria. Front. Microbiol. 13:876272. doi: 10.3389/fmicb.2022.876272

Cyanobacteria evolved an inorganic carbon-concentrating mechanism (CCM) to perform effective oxygenic photosynthesis and prevent photorespiratory carbon losses. This process facilitates the acclimation of cyanobacteria to various habitats, particularly in CO_2-limited environments. To date, there is limited information on the CCM of thermophilic cyanobacteria whose habitats limit the solubility of inorganic carbon. Here, genome-based approaches were used to identify the molecular components of CCM in 17 well-described thermophilic cyanobacteria. These cyanobacteria were from the genus *Leptodesmis*, *Leptolyngbya*, *Leptothermofonsia*, *Thermoleptolyngbya*, *Thermostichus*, and *Thermosynechococcus*. All the strains belong to β-cyanobacteria based on their β-carboxysome shell proteins with 1B form of Rubisco. The diversity in the C_i uptake systems and carboxysome composition of these thermophiles were analyzed based on their genomic information. For C_i uptake systems, two CO_2 uptake systems (NDH-1_3 and NDH-1_4) and BicA for HCO_3^- transport were present in all the thermophilic cyanobacteria, while most strains did not have the Na^+/HCO_3^- Sbt symporter and HCO_3^- transporter BCT1 were absent in four strains. As for carboxysome, the β-carboxysomal shell protein, ccmK2, was absent only in *Thermoleptolyngbya* strains, whereas ccmK3/K4 were absent in all *Thermostichus* and *Thermosynechococcus* strains. Besides, all *Thermostichus* and *Thermosynechococcus* strains lacked carboxysomal β-CA, ccaA, the carbonic anhydrase activity of which may be replaced by ccmM proteins as indicated by comparative domain analysis. The genomic distribution of CCM-related genes was different among the thermophiles, suggesting probably distinct expression regulation. Overall, the comparative genomic analysis revealed distinct molecular components and organization of CCM in

thermophilic cyanobacteria. These findings provided insights into the CCM components of thermophilic cyanobacteria and fundamental knowledge for further research regarding photosynthetic improvement and biomass yield of thermophilic cyanobacteria with biotechnological potentials.

Keywords: thermophilic cyanobacteria, inorganic carbon uptake, CO_2-concentrating mechanisms (CCMs), carboxysomes, photosynthesis, Rubisco

INTRODUCTION

Thermophilic cyanobacteria are photoautotrophic prokaryotes with a cosmopolitan distribution in diverse thermal environments (Tang et al., 2018a,b; Alcorta et al., 2020). With the increase of studies on these unique microorganisms and their niches, their importance as primary photosynthetic producers of the geothermal ecosystems becomes apparent. The thermophilic cyanobacteria account for a large part of the thermal ecosystem biomass and productivity. From an applicative perspective, thermophilic cyanobacteria can be explored for high value-added products relevant to agricultural, pharmaceutical, nutraceutical, and industrial applications (Patel et al., 2019). Particularly, the potential contribution of thermophilic cyanobacteria to mitigating carbon dioxide becomes attractive to researchers in the context of global warming and greenhouse gas emissions. Thermophilic cyanobacteria may facilitate the collection of CO_2 right from locations where it was generated, e.g., fossil fuels power plants, thanks to their higher thermostability of photosynthetic apparatus and resistance to photosynthetic inhibitors such as NO_x and SO_x found in high levels in the flue gases (Liang et al., 2019; Chen and Wang, 2020).

The CO_2-concentrating mechanism (CCM) is a vital biological process for CO_2 utilization by cyanobacteria under conditions of CO_2 limitation. Cyanobacterial CCM enables adequate photosynthetic CO_2 fixation by elevating the CO_2 level near the active site of Rubisco, thus providing adaptation to various CO_2-limited niches (Clement et al., 2016; Raven et al., 2017). For most thermophilic cyanobacteria, the aquatic environments where they live suffer from low availability of inorganic carbon (Ci), primarily due to external factors, e.g., temperature, pH and gas exchange (Durall and Lindblad, 2015).

The dissolution of gaseous CO_2 in water starts from CO_2 (g) transferring to CO_2 (aq), i.e., CO_2 mass transfer from gas to liquid phase (**Figure 1A**). Further, the small fraction of dissolved CO_2 reacts in the liquid phase *via* two parallel paths depending on pH and subsequent availability of OH^-. One leads to H^+ and HCO_3^- formation with the unstable intermediate product – carbonic acid H_2CO_3*, while the second with hydroxide ions also forms bicarbonate ions which further can dissociate into H^+ and CO_3^-. When the pH of the aqueous solution is lower than 8, CO_2 hydration follows the first path, and due to the very low value of the dissociation constant of the bicarbonate, the formation of carbonate ions can be neglected (Kierzkowska-Pawlak et al., 2022). The direct data on CO_2 dissociation and different species of inorganic carbon present in hot springs have not been much discussed in the literature yet. However, the known equations of dissociation constants of CO_2 in water and saline solutions are sufficient approximations to understand what inorganic carbon species are available across different pH ranges of those hot springs. The most commonly used equations for dissociation constants of CO_2 in water (both fresh and saline) are applicable up to 40–50°C (Mook, 2000; Woosley, 2021). Based on those works, Bjerrum plot (**Figure 1**) of the carbonate system can be further extrapolated to 72°C and adjusted for salinity (Mook, 2000; Solomon, 2001; Tremaine et al., 2004). The solubility of CO_2 in water is a function of temperature and do lower extend salinity (**Figure 1**), the higher the temperature, the lower the carbon dioxide solubility, elevating the temperature from 30 to 60°C results in 40% lower availability of CO_2. Further decrease of that solubility occurs due to increased salinity or presence of other dissolved elements ubiquitous in hot springs. Meanwhile the distribution of carbon species across different pH is also affected by the temperature and to lesser extend salinity (**Figure 1**). Whilst bicarbonate (HCO_3^-) remains a dominant dissolved inorganic specie between pH 6 and 10; its ratio with other carbon species is temperature sensitive. The equilibrium between carbonic acid, bicarbonate and carbonate species is acid-shifted with an increase of temperature. Therefore, to survive in their unique aquatic habitat, the thermophilic cyanobacteria utilize CCM to ensure that the Rubisco with low affinity for CO_2 is surrounded by high CO_2 levels and regularly function regardless of thermal stress.

Prior studies on the effect of temperature on Rubisco, including that of thermophilic origin revealed that the maximal of rates of carboxylation reaction are typically higher than optimal growth temperatures of an organism (Galmés et al., 2015, 2016). This discrepancy in is partially due to the decreased affinity of Rubisco and lower specificity of carboxylation versus oxidation reaction at higher temperatures ($S_{c/o}$) (Gubernator et al., 2008; Galmés et al., 2015, 2016). All in all thermophilic cyanobacteria must operate carbon concentration mechanisms to mitigate both challenges associated with lower carbon availability resulting from its poor solubility, and lower specificity of Rubisco toward CO_2 at elevated temperatures.

In general, the cyanobacterial CCM comprises two primary components: C_i uptake systems and carboxysomes. Cyanobacteria have been reported to have up to five different systems to actively acquire and transport C_i into the cells, namely two for uptake of CO_2 and three for transport of HCO_3^- (Pronina et al., 2017). The two CO_2 uptake systems that convert cytosolic CO_2 into HCO_3^- rely on plastoquinone oxidoreductase NADPH dehydrogenase respiratory complexes (Price, 2011). The complexes include NDH-1_3, a low-CO_2 inducible high-affinity CO_2 uptake system encoded by *ndhD3*, *ndhF3* and *cupA* (*chpY*) genes, and NDH-1_4, a constitutive low-affinity CO_2

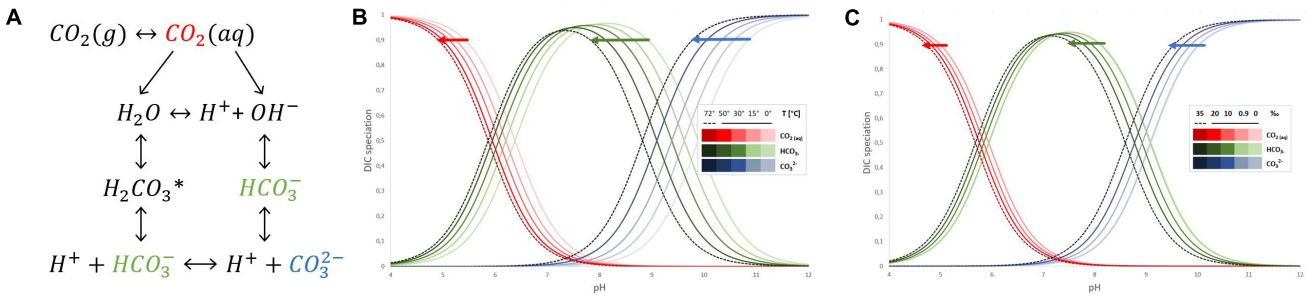

FIGURE 1 | Interconversions of inorganic carbon species in aqueous solution **(A)**. The effect of temperature on inorganic carbon species distribution across different pH in aqueous solution **(B)**. The effect of salinity in ‰ on inorganic carbon species distribution across different pH in aqueous solution **(C)**.

uptake system encoded by *ndhD4*, *ndhF4*, and *cupB* (*chpX*) genes (Kaplan, 2017). The transport of HCO_3^- takes place at the plasma membrane and is performed by three transporters, including *bicA* (a *sulP*-type sodium-dependent HCO_3^- transporter), *sbtA* (a sodium-dependent HCO_3^- symporter), and *BCT1* (an ATP-binding cassette ABC-type HCO_3^- transporter) (Raven et al., 2017). Inside the cyanobacterial cell, the HCO_3^- is further transported into the carboxysomes that comprise protein shells and two encapsulated enzymes, Rubisco and carbonic anhydrase (CA) (Kerfeld and Melnicki, 2016). CA catalyzes the conversion of HCO_3^- into CO_2, which is a substrate for Rubisco. Rubisco consisting in cyanobacteria of eight small (*rbcS*) and eight large (*rbcL*) subunits, catalyzes CO_2 fixation reaction to generate 3-phosphoglycerate for subsequent rearrangement through the Calvin-Benson-Bassham cycle (Hill et al., 2020). There are two types of shell proteins encoded by *cso* operon and *ccmKLMNO* operon, termed α-carboxysomes and β-carboxysomes, respectively. Based on this criterion, the cyanobacterial species carrying form 1A of Rubisco within α-carboxysomes are classified as α-cyanobacteria, while the species containing form 1B of Rubisco within β-carboxysomes as β-cyanobacteria (Melnicki et al., 2021). The *ccmP* was another β-carboxysome component, forming a bilayered shell protein (Cai et al., 2013). In addition, various carboxysomal CAs have been reported, including β-CA (*ccaA*) and γ-CA (*ccmM*) in β-cyanobacteria and β-CA (*csoSCA*) in α-cyanobacteria (MacCready et al., 2020). Two types of non-carboxysomal CAs were also reported in β-cyanobacteria, namely *ecaB* (β-CA) and *ecaA* (α-CA) (Sun et al., 2019).

Although CCM of freshwater, marine and alkaliphilic cyanobacteria have been reported (Burnap et al., 2015; Kupriyanova and Samylina, 2015; Klanchui et al., 2017), no comprehensive investigation on CCM of thermophilic cyanobacteria have been performed. Moreover, previous studies mainly focused on cyanobacterial CCM related to environments with distinct C_i content, salinity and especially pH that strongly influenced the CCM due to the equilibrium of C_i species (Mangan et al., 2016). Therefore, it is indispensable to survey the CCM of thermophilic strains in relation to their habitats that limit the solubility of inorganic carbon (Kamennaya et al., 2012). In recent years, next-generation sequencing (NGS) has been extensively employed to investigate the cyanobacterial genomes in thermal environments (Walter et al., 2017; Alcorta et al., 2020; Chen et al., 2021). This offers an opportunity to explore the thermophilic cyanobacterial CCM and the relationship with their niches at the genomic level. Furthermore, the studies on the molecular components of cyanobacterial CCM in relation to their specific habitats may improve photosynthetic CO_2 fixation and biomass production in cyanobacteria (Noreña-Caro and Benton, 2018) and crop plants (Hennacy and Jonikas, 2020) through genetic engineering.

In the present study, genome sequences of 17 thermophilic cyanobacterial strains were used to investigate the molecular basis of CCM by computational identification. The relationship between CCM components and adaptations of these thermophilic cyanobacteria were further discussed. The insights into the CCM components lay a solid foundation for future research regarding photosynthetic improvement and biomass yield of thermophilic cyanobacteria with biotechnological potentials.

MATERIALS AND METHODS

Genome Collection of Thermophilic Cyanobacteria

According to the genomic resources of the NCBI at the time of this study (2021/05/20), cyanobacteria with available genomes and closely related to thermophilic or hot-spring strains were first retrieved as a preliminary dataset. To ensure the accurate collection of thermophilic cyanobacteria, these strains were further filtered by conducting literature searches, contacting culture collections, leading authors of the manuscripts and submissions to retain thermophilic cyanobacteria with definite information about their thermophilic characteristics. Then, quality control for all genomes was performed based on the following criteria to reduce data redundancy and biased genome representation of cyanobacteria. First, the whole-genome average nucleotide identity (ANI) for each pair of genomes was calculated using the ANI calculator with default settings[1]. Genomes with an ANI value greater than 99.9% were considered as redundant genomes, and then only one of

[1]http://enve-omics.ce.gatech.edu/ani/

these genomes was randomly kept for the analysis. Second, the quality of the genomes was evaluated using CheckM (Parks et al., 2015) to ensure a more reliable genome dataset with near completeness (≥95%) and low contamination (<5%). These analyses finally generated a dataset comprising 16 thermophilic cyanobacteria. The genome, protein sequences and genomic annotations of the thermophilic cyanobacteria studied were downloaded from the database of NCBI. The genomes with no or incomplete annotations were annotated using the RAST annotation system (Aziz et al., 2008), provided in **Supplementary Table 1**.

Information regarding the 16 thermophilic strains was summarized in **Table 1**. Briefly, the 16 thermophiles were affiliated to four families of order Pseudanabaenales and Synechococcales, including Leptolyngbyaceae: *Leptodesmis sichuanensis* A121 (Tang et al., 2022a), *Leptolyngbya* sp. JSC-1 (Brown et al., 2010), *Leptothermofonsia sichuanensis* E412 (Tang et al., 2022b); Oculatellaceae: *Thermoleptolyngbya* sp. O-77 (Yoon et al., 2017), *T. sichuanensis* A183 (Tang et al., 2021); Synechococcaceae: *Synechococcus* sp. 60AY4M2, 63AY4M2, 65AY6A5, and 65AY6Li (Olsen et al., 2015), *Thermostichus* sp. JA-2-3B and JA-3-3Ab (Bhaya et al., 2007); Thermosynechococcaceae: *Thermosynechococcus* sp. CL-1 (Cheng et al., 2020) and TA-1 (Leu et al., 2013), *T. vestitus* BP-1 (Nakamura et al., 2002) and E542 (Liang et al., 2019), *T. vulcanus* NIES-2134 (Liang et al., 2018).

TABLE 1 | Ecological information and genome characteristics of thermophilic cyanobacteria studied.

Species	Isolation source	Niche temperature (°C)	Niche pH	Genome completeness (%)	Genome contamination (%)	Accession number	References
Leptodesmis sichuanensis A121	Hot spring, Erdaoqiao, Sichuan, China	40.8°C	6.32	99.53	0.94	GCA_021379005	Tang et al., 2022a
Leptolyngbya sp. JSC-1	La Duke Hot Springs, Montana, United States	60°C	6.85	99.53	1.30	GCA_000733415	Brown et al., 2010
Leptothermofonsia sichuanensis E412	Hot spring, Lotus Lake, Sichuan, China	42.7°C	8.61	99.29	0.00	GCA_019891175	Tang et al., 2022b
Thermoleptolyngbya sichuanensis A183	Hot spring, Erdaoqiao, Sichuan, China	40.8°C	6.32	98.94	0.94	GCA_013177315	Tang et al., 2021
Thermoleptolyngbya sp. O-77	Hot spring, Kumamoto, Japan	35–60°C	NA	98.70	1.53	GCA_001548395	Yoon et al., 2017
Thermostichus sp. 60AY4M2	Mushroom Spring, Yellowstone National Park, United States	60°C	alkaline	100.00	0.88	GCA_002760375	Olsen et al., 2015
Thermostichus sp. 63AY4M2	Mushroom Spring, Yellowstone National Park, United States	63°C	alkaline	100.00	0.00	GCA_002760475	Olsen et al., 2015
Thermostichus sp. 65AY6A5	Mushroom Spring, Yellowstone National Park, United States	65°C	alkaline	100.00	0.88	GCA_002760415	Olsen et al., 2015
Thermostichus sp. 65AY6Li	Mushroom Spring, Yellowstone National Park, United States	65°C	alkaline	99.61	1.32	GCA_002760345	Olsen et al., 2015
Thermostichus sp. JA-2-3Ba	Octopus Spring, Yellowstone National Park, United States	58–65°C	8.5	100.00	0.00	GCA_000013225	Bhaya et al., 2007
Thermostichus sp. JA-3-3Ab	Octopus Spring, Yellowstone National Park, United States	58–65°C	8.5	100.00	1.32	GCA_000013205	Bhaya et al., 2007
Thermosynechococcus lividus PCC 6715	Hot spring, Yellowstone National Park, United States	NA	NA	98.86	0.12	GCA_002754935	This study
Thermosynechococcus sp. CL-1	Chin-Lun hot spring, Taiwan, China	62°C	9.3	100.00	0.12	GCA_008386235	Cheng et al., 2020
Thermosynechococcus sp. TA-1	Taian hot springs, Taiwan, China	50°C	7–9	100.00	0.12	GCA_017086385	Leu et al., 2013
Thermosynechococcus vestitus BP-1	Hot spring, Beppu, Japan	52°C	7.5	99.76	0.12	GCA_000011345	Nakamura et al., 2002
Thermosynechococcus vestitus E542	Hot spring, Lotus lake, Sichuan, China	67.2°C	7.95	100.00	0.12	GCA_003555505	Liang et al., 2019
Thermosynechococcus vulcanus NIES-2134	Yunomine Hot Spring, Wakayama, Japan	50–57°C	NA	99.76	0.12	GCA_003990665	Liang et al., 2018

Genome Sequencing and *de novo* Assembly

Additional to the 16 downloaded genomes, we sequenced the genome of another thermophilic cyanobacterium, purchased from Pasteur Culture Collection of Cyanobacteria as *Synechococcus lividus* PCC 6715. Whole-genome sequencing was carried out using integrated sequencing strategies, including PacBio and Illumina HiSeq Technology. The PacBio SMRT sequencing of PCC 6715 yielded 96,587 adapter-trimmed reads (subreads) with an average read length of approximately 11 kbp, corresponding to 400-fold coverage. *De novo* assembly was performed using the hierarchical genome assembly process (HGAP) method implemented in SMRT analysis v2.3.0 (Chin et al., 2013), generating two contigs. The Illumina sequencing of PCC 6715 generated 5,566,668 filtered paired-end reads (clean data), providing approximately 520-fold coverage of the genome. The clean data of short reads generated by Illumina were assembled into contigs using SOAPdenovo v2.04 (Luo et al., 2012) with default parameters. Based on the contigs from SOAPdenovo assembler, the contigs derived from the HGAP method were comparatively examined to determine their continuity and concatenated into one closed circular chromosome. The genome obtained was mapped with Illumina reads using BWA v0.7.17 (Li and Durbin, 2009) and then Pilon v1.23 (Walker et al., 2014) to correct any assembly and sequence errors. The genome of PCC 6715 was annotated as described above and deposited in the NCBI under the accession number CP018092.

Identification of Orthologous Proteins

Amino acid sequences of 28 proteins involved in CCM of *Synechocystis* sp. PCC 6803 were downloaded from the CyanoBase[2] as a reference protein set. Based on the bidirectional best hit (BBH) criterion (Brilli et al., 2010), orthologous proteins involved in CCM of the studied species were identified using BLASTP with the following thresholds: *E*-value cut-off of 1E-6, ≥30% identity and 70% coverage. The identified proteins were homologous to these proteins in *Synechocystis* PCC 6803, namely *bicA1* (*sll0834*), *bicA2* (*slr0096*), *ccaA* (*slr1347*), *ccmK1* (*sll1029*), *ccmK2* (*sll1028*), *ccmK3* (*slr1838*), *ccmK4* (*slr1839*), *ccmL* (*sll1030*), *ccmM* (*sll1031*), *ccmN* (*sll1032*), *ccmO* (*slr0436*), *ccmP* (*slr0169*), *cmpA* (*slr0040*), *cmpB* (*slr0041*), *cmpC* (*slr0043*), *cmpD* (*slr0044*), *cupA* (*sll1734*), *cupB* (*slr1302*), *ecaB* (*slr0051*), *ndhD3* (*sll1733*), *ndhD4* (*sll0027*), *ndhF3* (*sll1732*), *ndhF4* (*sll0026*), *rbcL* (*slr0009*), *rbcS* (*slr0012*), *rbcX* (*slr0011*), *sbtA* (*slr1512*), and *SbtB* (*slr1513*). The homologs of *ecaA* protein were searched using the experimentally confirmed protein *ecaA* (*all2929*) of *Anabaena* PCC 7120 (Soltes-Rak et al., 1997) as a query. The italic number in bracket mentioned above refers to the gene ID in CyanoBase (see text footnote 2). The accession numbers of orthologous proteins identified in each genome of the thermophilic cyanobacteria studied was summarized in **Supplementary Table 2**.

Phylogeny

Amino acid sequences of Rubisco large subunit (*rbcL*) were collected for the studied species and reference cyanobacteria. The phylogram of *rbcL* was used to infer the protein function and classification among the strains. Protein sequences of genes *ccmK*, *-L*, *-M*, *-N*, *-O*, and *-P* encoding carboxysome shell proteins, *cmpA*, *-B*, *-C*, and *-D* encoding the HCO_3^- transporter BCT1 and *nrtA*, *-B*, *-C*, and *-D* of the nitrite/nitrate assimilation were also collected for phylogenetic reconstruction. All the protein sequences used were retrieved from the public databases, CyanoBase (see text footnote 2) or the NCBI[3]. All the phylogenetic analyses were performed using the following pipeline: multiple sequence alignments by Muscle complemented in Mega7 (Kumar et al., 2016) and Maximum-Likelihood (ML) inference of phylogenies by PhyML v3.3 (Guindon et al., 2010). Parameter settings in PhyML and bootstrap analysis of phylogenies were followed as described (Tang et al., 2019).

RESULTS AND DISCUSSION

Thermophilic Cyanobacteria and Classification of Their Carbon-Concentrating Mechanism

The 17 thermophilic cyanobacteria collected in this study all originated from hot springs (**Table 1**). Although the niche temperatures showed significant variation, these thermophilic cyanobacteria were defined based on their ability to grow above 50°C. Two types of morphology were characterized for these thermophilic cyanobacteria, comprising unicellular *Synechococcus*, *Thermostichus* and *Thermosynechococcus*, and filamentous *Leptodesmis*, *Leptolyngbya*, *Leptothermofonsia*, and *Thermoleptolyngbya*. In addition, strains JA-2-3Ba and JA-3-3Ab, previously known as *Synechococcus* strains, have been reclassified into a newly delineated taxon, genus *Thermostichus* (Komárek et al., 2020). According to the suggested values for species (ANI > 96%, AAI ≥ 95%) and genus (ANI < 83%, AAI ≤ 70%) delimitation (Jain and Rodriguez, 2018), the result of genome-wide ANI and AAI indicated that strain JA-2-3Ba and JA-3-3Ab were different species (ANI = 85.6%, AAI = 87.8%) within *Thermostichus*, while strain JA-3-3Ab, plus the other four strains from Yellowstone National Park (**Table 1**), belong to the same species (ANI/AAI > 98%) also within *Thermostichus*. However, the case of *S. lividus* PCC 6715 was contradictory. Between *S. lividus* PCC 6715 and the five *Thermosynechococcus* strains, the values of ANI and ANI were ∼ 77 and ∼ 81% (**Supplementary Table 3**), respectively. To resolve the dilemma, a third approach was employed to determine the percentages of conserved proteins (POCP) between genomes. The POCP values (**Supplementary Table 3**) between *S. lividus* PCC 6715 and the *Thermosynechococcus* strains ranged from 83.4 to 84.0%, all far beyond the threshold (50%) for the definition of a prokaryotic genus (Qin et al., 2014). Taken together, strain PCC 6715 might be a member of *Thermosynechococcus*, and was proposed

[2]http://genome.kazusa.or.jp/cyanobase

[3]https://www.ncbi.nlm.nih.gov/

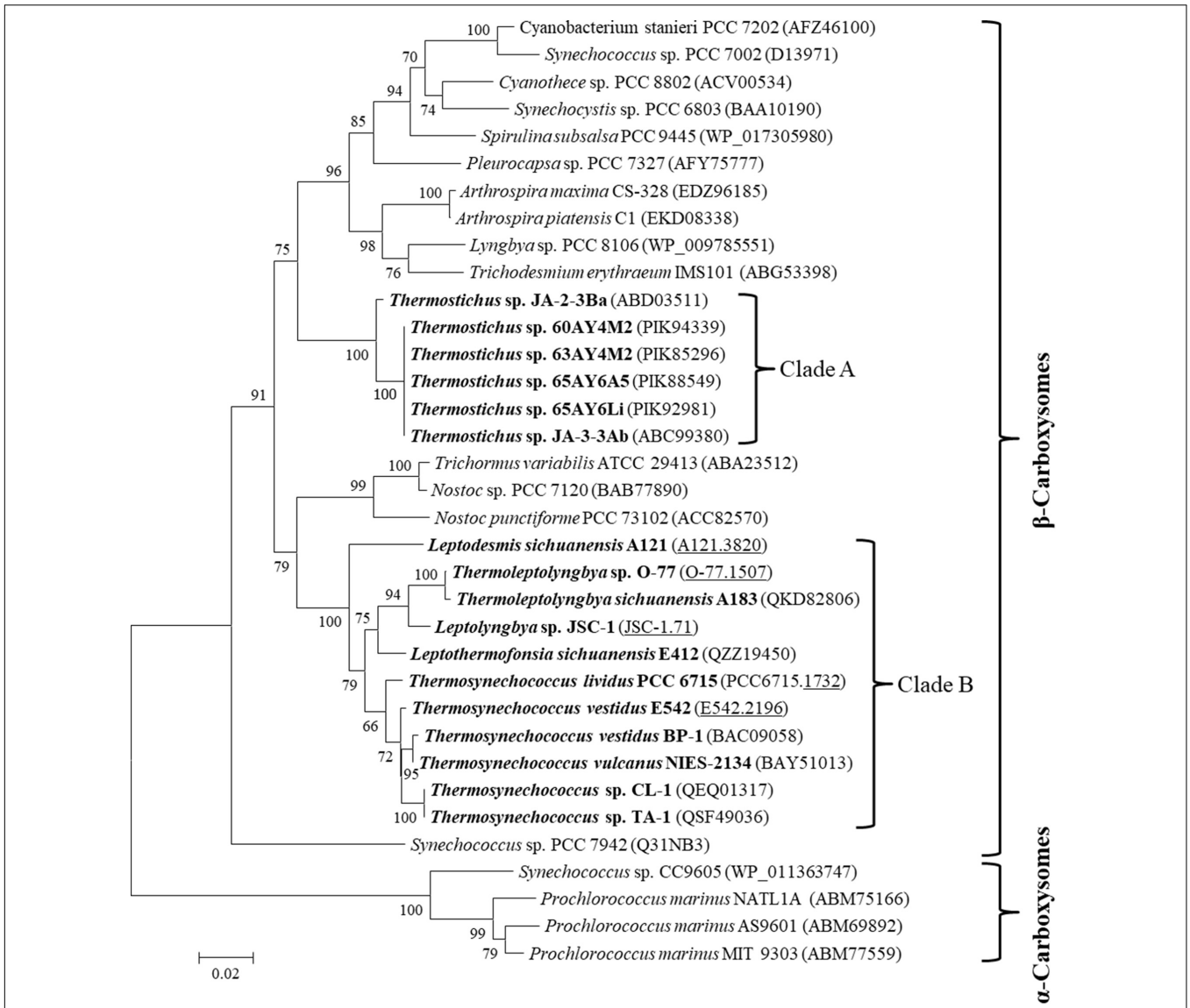

FIGURE 2 | Phylogenetic inference of Rubisco large subunit protein sequences. The thermophilic cyanobacteria investigated in this study are indicated in bold. The accession numbers underscored refers to the gene IDs in **Supplementary Table 1**. Only bootstrap values > 50% are indicated at nodes. Scale bar = 1% substitutions per site.

to be *Thermosynechococcus lividus*. However, this conclusion requires validation with comprehensive investigation beyond the genomic data.

The carboxysome type of the 17 thermophilic cyanobacteria was investigated based on the phylogenetic analysis of a frequently used molecular marker, *rbcL* (Klanchui et al., 2017). The ML phylogram of *rbcL* categorized the 35 cyanobacteria into two categories (**Figure 2**), α-cyanobacteria and β-cyanobacteria, according to their Rubisco forms. There was only one exception that *Synechococcus* PCC 7942 was solely placed in a separate branch. The 17 thermophilic cyanobacteria surveyed were all grouped into the β-cyanobacteria category, indicating the presence of Rubisco 1B form in these thermophiles. However, considerable genetic diversity of *rbcL* amino acid sequences was also shown among these thermophilic cyanobacteria, distributing the strains into two clades (**Figure 2**). Clade A included only *Thermostichus* strains, also known as early-branching or early-divergent *Synechococcus* (Blank and Sánchez-Baracaldo, 2010), whereas clade B contained thermophiles from a different genus. In addition, the clustering of strains did not completely comply with morphology, e.g., filamentous strains clustered with unicellular strains (clade B). Intriguingly, the 17 thermophilic strains did not group with any non-thermophilic strains, suggesting *rbcL* specificity of thermophiles. Although phylogenetic analysis of *rbcL* sequences can be used for the classification of cyanobacterial types, the evolutionary relationship based on habitats or morphology cannot be elucidated from the present *rbcL* phylogram. This is consistent

with the conclusions in previous studies that phylogenetic inference of molecular markers may be improper for the elaboration of evolutionary relationship with cyanobacterial habitat and environments (Komárek, 2016; Klanchui et al., 2017).

Genes Encoding C_i Uptake Systems in Thermophilic Cyanobacteria

Five different transport systems (**Table 2**) have been identified in the 17 thermophilic cyanobacteria. The two CO_2 uptake systems, NDH-1_3 and NDH-1_4 complex, were present in all the surveyed thermophilic cyanobacteria. Both CO_2 uptake systems in these thermophilic cyanobacteria were consistent with the previous reports that both CO_2 transporters were present in β-cyanobacteria living in freshwater, brackish or eutrophic lakes (Sandrini et al., 2014; Durall and Lindblad, 2015). In contrast, oceanic α-cyanobacteria (e.g., *Prochlorococcus* species) and marine β-cyanobacteria (e.g., *Trichodesmium* species) contained only one or even lacked them entirely (Price et al., 2007; Pronina et al., 2017). These results strongly indicated that the presence of NDH-1_3 and NDH-1_4 might be relevant to the environments where these cyanobacteria live. Thermophilic cyanobacteria, similar to freshwater and estuarine strains, contained essential components of CO_2 uptake and bicarbonate transport genes. Both constitutive systems NDH-1_4 complex and *bic*A were ubiquitous in all known thermophilic strains. The inducible NDH-1_3 complex is also universal suggesting that these strains are prepared for occasional carbon dioxide shortages. Unfortunately, it was not verified based on the current data that the niche temperature directly affected the existence of the two CO_2 uptake systems in light of their near-ubiquity in non-thermophilic cyanobacteria. The protein sequences of five genes encoding the two systems showed different identities with the sequences of non-thermophilic reference cyanobacteria (*Synechocystis* PCC 6803), ranging from 50.4 to 64.7% (**Table 2**), but a high degree of homology (≥70% identity) was noticed only among *cupA* genes. In addition, intragenus and intergenic variations of protein sequences were revealed by the different identities (**Table 2**). Moreover, the distinct property of the two complexes, a low-CO_2 inducible high-affinity CO_2 uptake system (NDH-1_3 complex) and a constitutive low-affinity CO_2 uptake system (NDH-1_4 complex), may confer the thermophilic cyanobacteria with more alternative strategies to survive in environments with significant CO_2 fluctuation, particularly in hot springs.

More variations among the 17 thermophilic cyanobacteria were noticed in HCO_3^- transport systems than in CO_2 uptake systems (**Table 2** and **Figure 3**). Association of the abundance of these mechanisms with their respective environmental niches is inconclusive. Similar repertoires of CO_2 and bicarbonate uptake genes were observed in *L. sichuanensis* A121 with the lowest habitat temperature and the most thermophilic strains of genus *Thermostichus* (**Table 2** and **Figure 3**). When it comes to the pH of the environmental niches, no evident niches preference of genes was observed. Genetic repertoire of strains isolated from acidic and alkaline niches appeared to be unrelated to the niche pH. For *bicA* transporter, only *Leptothermofonsia* E412 and *Thermoleptolyngbya* A183 possessed both *bicA1* and *bicA2*, while

TABLE 2 | Availability of genes encoding Ci uptake systems of thermophilic cyanobacteria studied.

Strain	Ci uptake systems													
	CO_2 uptake						HCO_3^- transport							
	NDH-1_4 complex			NDH-1_3 complex			BicA		Sbt regulator		BCT1			
	ndhD4	*ndhF4*	*cupB*	*ndhD3*	*ndhF3*	*cupA*	*bicA1*	*bicA2*	*sbtA*	*sbtB*	*cmpA*	*cmpB*	*cmpC*	*cmpD*
Leptodesmis A121	√ (60.9)	√ (59.7)	√ (62.7)	√ (61.5)	√ (57.2)	√ (71.8)	√ (65.8)	x	x	x	√ (69.2)	√ (70.9)	√ (73.6)	√ (67.2)
Leptolyngbya JSC-1	√ (62.6)	√ (56.9)	√ (62.9)	√ (59.6)	√ (59.0)	√ (81.7)	√ (57.3)	x	√ (75.9)	√ (79.1)	√ (63.9)	√ (65.2)	√ (70.8)	√ (72.2)
Leptothermofonsia E412	√ (63.8)	√ (59.3)	√ (64.7)	√ (62.8)	√ (60.8)	√ (84.2)	√ (64.8)	√ (59.2)	x	x	√ (63.0)	√ (64.5)	√ (70.8)	√ (73.6)
Thermoleptolyngbya A183	√ (60.3)	√ (55.6)	√ (62.3)	√ (58.8)	√ (57.8)	√ (85.7)	√ (65.5)	√ (62.3)	√ (70.7)	√ (62.5)	x	x	x	x
Thermoleptolyngbya O-77	√ (59.0)	√ (56.1)	√ (61.3)	√ (57.7)	√ (57.7)	√ (84.7)	√ (65.5)	x	√ (71.9)	√ (63.4)	√ (68.7)	√ (64.8)	√ (78.2)	√ (75.8)
Thermostichus 60AY4M2	√ (57.6)	√ (54.5)	√ (56.8)	√ (58.6)	√ (53.8)	√ (75.8)	√ (60.2)	x	x	x	√ (65.8)	√ (65.9)	√ (72.2)	√ (66.8)
Thermostichus 63AY4M2	√ (57.4)	√ (54.5)	√ (56.8)	√ (58.6)	√ (53.9)	√ (75.8)	√ (60.2)	x	x	x	√ (65.8)	√ (66.2)	√ (72.1)	√ (66.8)
Thermostichus 65AY6A5	√ (57.4)	√ (54.5)	√ (56.8)	√ (58.6)	√ (53.8)	√ (75.8)	√ (59.8)	x	x	x	√ (65.8)	√ (66.2)	√ (72.2)	√ (66.8)
Thermostichus 65AY6Li	√ (57.4)	√ (54.5)	√ (56.8)	√ (58.4)	√ (53.9)	√ (75.3)	√ (60.0)	x	x	x	√ (65.4)	√ (66.2)	√ (72.2)	√ (67.1)
Thermostichus JA-2-3Ba	√ (57.6)	√ (53.6)	√ (59.6)	√ (58.1)	√ (53.4)	√ (76.0)	√ (59.8)	x	x	x	√ (68.2)	√ (67.0)	√ (71.7)	√ (63.3)
Thermostichus JA-3-3Ab	√ (57.4)	√ (54.5)	√ (56.8)	√ (58.4)	√ (53.9)	√ (75.3)	√ (60.2)	x	x	x	√ (67.5)	√ (66.2)	√ (71.8)	√ (65.0)
Thermosynechococcus PCC 6715	√ (56.8)	√ (55.5)	√ (59.7)	√ (59.2)	√ (50.4)	√ (70.7)	x	√ (57.1)	√ (81.6)	√ (80.9)	x	x	x	x
Thermosynechococcus CL-1	√ (59.3)	√ (56.7)	√ (61.9)	√ (61.5)	√ (58.1)	√ (70.6)	x	√ (57.2)	√ (74.1)	√ (80.9)	√ (66.5)	√ (59.5)	√ (73.1)	√ (71.2)
Thermosynechococcus TA-1	√ (60.2)	√ (56.8)	√ (62.6)	√ (61.1)	√ (58.0)	√ (70.8)	x	√ (56.8)	x	√ (80.2)	x	x	x	x
Thermosynechococcus BP-1	√ (60.3)	√ (56.8)	√ (61.4)	√ (61.4)	√ (57.7)	√ (70.7)	x	√ (56.1)	x	x	√ (67.7)	√ (61.0)	√ (73.3)	√ (66.8)
Thermosynechococcus E542	√ (59.9)	√ (57.4)	√ (62.0)	√ (62.9)	√ (59.0)	√ (70.4)	x	√ (56.4)	√ (72.7)	√ (81.8)	x	x	x	x
Thermosynechococcus NIES-2134	√ (59.9)	√ (56.8)	√ (61.4)	√ (61.6)	√ (58.3)	√ (70.7)	x	√ (53.2)	x	x	√ (67.5)	√ (68.1)	√ (73.0)	√ (68.1)

√ and x refers to the presence and absence of the gene, respectively. The number in brackets indicates the identity (%) between the identified protein and the corresponding sequence of Synechocystis PCC 6803.

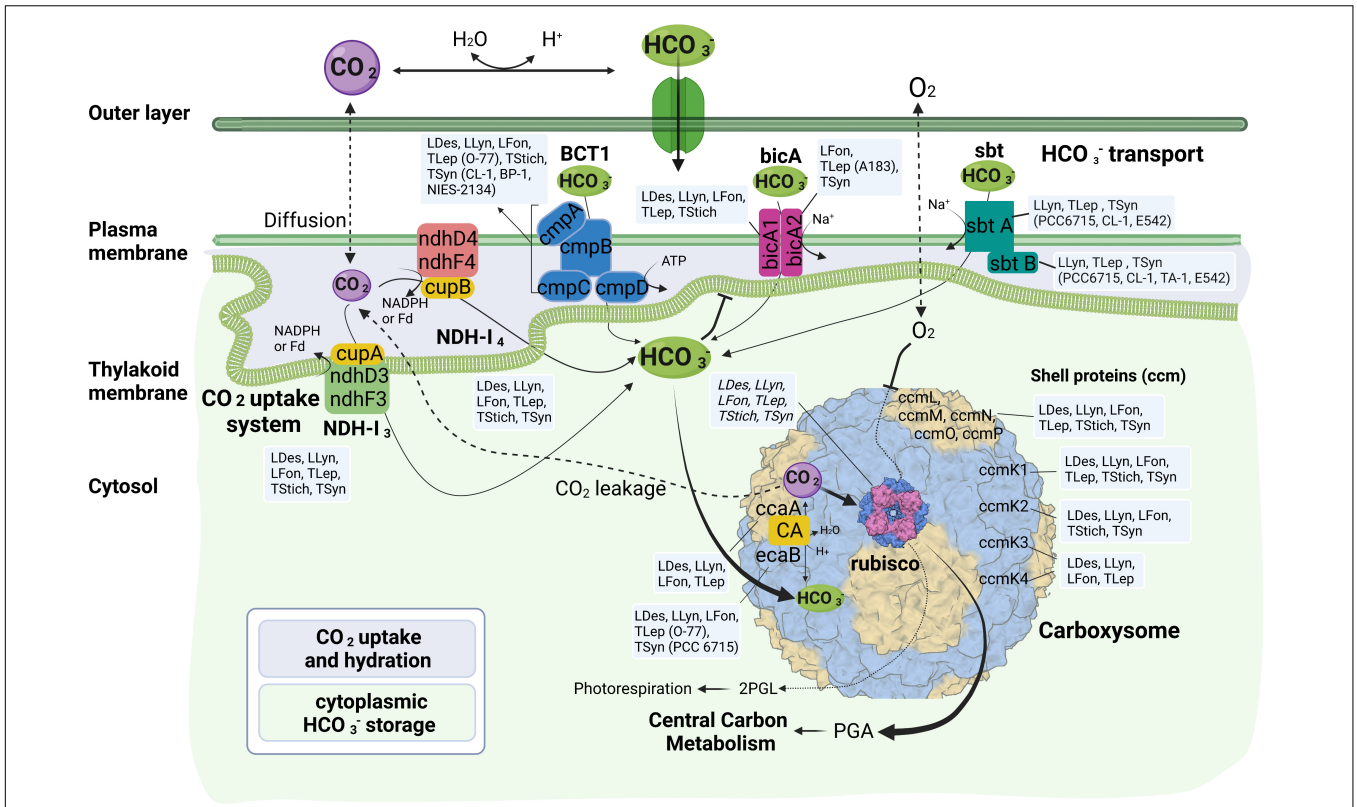

FIGURE 3 | Molecular components of CCM characteristic for various strains of thermophilic cyanobacteria divided according to their function. LDes – *Leptodesmis*, LLyn – *Leptolyngbya*, LFon – *Leptothermofonsia*, TLep – *Thermoleptolyngbya*, TStich – *Thermostichus*, TSyn – *Thermosynechococcus*; 2PGL – 2-phosphoglycolate; PGA – phosphoglyceric acid. Figure created with BioRender.com.

the other strains contained *bicA1* or *bicA2* (**Table 2**). The amino acid sequence identities of *bicA* genes were around 60% between the thermophilic cyanobacteria and *Synechocystis* PCC 6803. The presence of *bicA1* and/or *bicA2* was consistent within each genus except for *Thermoleptolyngbya* (strain A183 and O-77). Sequence analysis suggested that a putative protein-coding gene of O-77 (O-77.5066, **Supplementary Table 1**) showed very low amino acid coverage (46.9%) to *bicA2* of A183, but the aligned region was almost identical to each other (**Supplementary Figure 1**), indicating this short CDS might be a partial region of *bicA2*. Such discrepancy in CDS length of *bicA2* within *Thermoleptolyngbya* requires future studies to elucidate the possible causes, e.g., mutations, gene lost, or sequencing errors. For *sbt* regulator, both *sbtA* and *sbtB* were found only in six thermophilic cyanobacteria (**Table 2**). Furthermore, considerable variations existed within the genus *Thermosynechococcus*. Strain E542, PCC 6715 and CL-1 possessed both *sbtA* and *sbtB*. TA-1 had only *sbtB*, while the other two *Thermosynechococcus* strains contained none. This result implied that the *sbt* genes of these *Thermosynechococcus* strains might be acquired by horizontal gene transfer or vertically inherited but lost during the evolutionary process. In addition, it appeared that the thermophilic cyanobacteria typically have *bicA* rather than *sbt* as revealed by the dominant presence (**Table 2**). This could be ascribed to the distinct traits of the two transporters and the habitat of these cyanobacteria. First, *bicA* shows low affinity and high flux rate to HCO_3^- and the genes encoding *bicA* were found to be primarily constitutively expressed (Price et al., 2004). Second, *sbt* was highly inducible under carbon-limited conditions and had a relatively high affinity to HCO_3^- (Price, 2011). The *sbt* may therefore become accessory when cyanobacteria live in alkaline ecosystems typically rich in HCO_3^-, which was in accordance with most cases in this study (**Table 1**), e.g., *Thermostichus* strains. Meanwhile, it was evident that thermophilic cyanobacteria with both transporters might be advantageous to acclimatize to the highly dynamic shift of exogenous HCO_3^- by selective utilization of the two HCO_3^- transport systems.

As for the third HCO_3^- transporter, BCT1 encoded by *cmpA*, *-B*, *-C*, and *-D* and with high affinity for HCO_3^- was induced under low levels of C_i and enhanced by high light conditions (Omata et al., 2002). The *cmp* genes were detected in all thermophilic cyanobacteria except for *Thermoleptolyngbya* A183 and *Thermosynechococcus* E542, PCC 6715 and TA-1 (**Table 2**). Intriguingly, strains without *cmp* genes all possessed *sbt*, which might to some extent compensate the function of *cmp* genes for adaptation to thermal environments limited in inorganic carbon (Kamennaya et al., 2012). The identified *cmp* genes showed amino acid sequence identity of 59.5–75.8% with the reference proteins (**Table 2**). In addition, it was reported that *nrtA*, *-B*, *-C*, and *-D* (nitrate/nitrite transport system) shared high sequence similarity

with *cmpA*, *-B*, *-C*, and *-D* (Omata, 1995). Therefore, we also identified the *nrt* genes in the 17 thermophilic cyanobacteria, and phylogenetic analysis based on amino acid sequences of *cmp* and *nrt* genes was performed to verify the annotations with the help of experimentally confirmed *cmp* proteins of *Synechococcus* PCC 7942 (Omata et al., 1999). As shown in **Figure 4**, the *cmp* proteins of thermophilic cyanobacteria clustered with that of *Synechococcus* PCC 7942 and other reference strains, while the *nrt* proteins grouped into clades or clusters separated from *cmp* proteins. Furthermore, sequence conservation was low, as suggested by long branches among the clusters formed in the phylogram (**Figure 4**). Surprisingly, the genome of *Thermoleptolyngbya* O-77 was the only genome without the complete set of *nrtA*, *-B*, *-C*, and *-D*, *nrtC* of which was not found by BLASTP. However, sequence analysis (**Supplementary Figure 2**) showed that two putative genes both shared high similarity of protein sequence with *nrtC* of *Thermoleptolyngbya* A183, suggesting unknown interruption within CDS of *nrtC* in O-77 genome. This might be ascribed to mutations, partial gene lost, or sequencing errors. Intriguingly, the discrepancy of the presence of *cmp* genes within genus *Thermoleptolyngbya* and *Thermosynechococcus* again suggested that these genes might be acquired by horizontal gene transfer or vertically inherited but lost during the evolutionary process.

In summary, the C_i uptake systems could assign the 17 thermophilic cyanobacteria into three genotypes: (I) strains comprising NDH-1_3, NDH-1_4, *bicA*, *sbt*, and BCT1; (II) NDH-1_3, NDH-1_4, *bicA*, and *sbt*; and (III) NDH-1_3, NDH-1_4, *bicA*, and BCT1. This result suggested that the same CO_2 uptake systems and different HCO_3^- transport systems were shared by these thermophilic cyanobacteria. Different genotypes were primarily attributed to the presence/absence of *sbt* and BCT1 (**Table 2**). Only three strains, namely *Leptolyngbya* JSC-1, *Thermoleptolyngbya* O-77, and *Thermosynechococcus* CL-1, contained both types of high-affinity HCO_3^- transporters, indicating that these strains may have a higher capacity for HCO_3^- uptake under various growth environments. Definitely, owning one of *sbt* and BCT1 appeared to be sufficient for thermophilic strains to cope with extremely low inorganic carbon and ions in thermal aquatic environments. Future experimental studies should be carried out to elucidate the function of these *in silico* identified proteins in thermophilic cyanobacteria.

Genes Encoding Carboxysomes in Thermophilic Cyanobacteria

Carboxysomes in cyanobacteria are bacterial microcompartments (BMCs) that provide an environment for enhancing the catalytic capabilities of the CO_2 fixing enzyme, Rubisco (Cai et al., 2009). A typical β-cyanobacterial genome usually contains *ccmK1-4* (MacCready et al., 2020). However, only three out of 17 thermophilic cyanobacteria studied showed such diversity of the shell proteins, while *Thermoleptolyngbya* strains lacked *ccmk2*, and *Thermostichus* and *Thermosynechococcus* strains contained none of *ccmk3* and *ccmK4* (**Table 3**). Previous studies showed that *ccmK1* and *ccmK2* were the main structural proteins of the carboxysome shell (Kerfeld et al., 2005; Rae et al., 2013). Phylogenetic analysis and identity calculation suggested particularly high sequence conservation between the two homologs of *ccmK1/2*, as revealed by low amino acid substitution rates and short branches (**Figure 5A**) and high identity (**Table 3**). In contrast, phylogenetic branches of the *ccmK3* and *ccmK4* proteins were much longer, and residues were less conserved (**Figures 5B,C** and **Table 3**). Although deletion of the *ccmK2* gene in *Synechococcus* PCC 7942 that lacked *ccmK1* caused a carboxysome-less phenotype (Rae et al., 2012), this experiment did not verify whether normal phenotype can be achieved with the presence of sole *ccmK1* homolog. Besides, the main distinguishing feature between *ccmK1* and *ccmK2* was the ∼10 amino acid long C-terminal extension of *ccmK1* (Kerfeld et al., 2005), which has been proven to show limited structural relevance for shell assembly (Cai et al., 2016). Instead, it might be just the genomic proximity of the two *ccmK* genes, as indicated by its high degree of conservation (15/17 genomes, **Table 3**). Future studies are required to carefully investigate the specificity regarding the structure and function of *ccmk1* in the *Thermoleptolyngbya* strains. Regarding *ccmK3* and *ccmK4*, the widespread absence of the two genes was not surprising. The previous studies showed they are similar molecular components (Sommer et al., 2017) and suggested functional redundancy that play only a minor structural role (Rae et al., 2012). On the other hand, a recent study proposed a functional scenario in which minor *ccmK3/K4* incorporation in shells would introduce sufficient local disorder to allow shell remodeling (Garcia-Alles et al., 2019). Another study indicated that *ccmK3-ccmK4* heterohexamers potentially expand the range of permeability properties of metabolite channels in carboxysome shells (Sommer et al., 2019). Taken together, these findings suggested that *ccmK3/K4* present in *Leptodesmis* A121, *Leptolyngbya* JSC-1, *Leptothermofonsia* E412, and *Thermoleptolyngbya* A183 and O-77 may be utilized to adjust the properties of carboxysome for rapid adaptation to environmental changes that happen in thermal regions. In addition to *ccmK*, other genes encoding carboxysome shell proteins, *ccmL*, *-M*, *-N*, *-O*, and *-P* were also found to be present in all 17 thermophilic cyanobacteria (**Table 3**). Only *ccmN* exhibited weak homologs (<40%). All the surveyed thermophilic cyanobacteria showed a high degree of homology (67.6–76.1%) with the *ccmP* of *Synechocystis* PCC 6803, and similarly identity range of 65.8–75.5% to the *ccmP* of *Synechococcus* PCC 7942, an experimentally confirmed protein (Cai et al., 2013). Further phylogenetic analysis suggested extensive genetic diversity in these genes as indicated by the assignments of these thermophilic cyanobacteria into different clusters or clades (**Supplementary Figure 3**).

The subunits of Rubisco, *rbcL* and *rbcS*, and Rubisco assembly chaperone, *rbcX*, were present in all the 17 thermophilic cyanobacteria (**Table 3**). The protein sequences of *rbcL* in thermophilic cyanobacteria were highly conserved to the reference protein (>83% identity), while that of *rbcS* was moderately conserved (∼ 65% identity). The protein sequences of *rbcX* were more variable, showing ∼ 45% identity with the reference protein. In regards to β-CA, carboxysomal *ccaA* and/or non-carboxysomal *ecaB* proteins with low sequence identity (38.1–49.7%) were detected only in six thermophilic

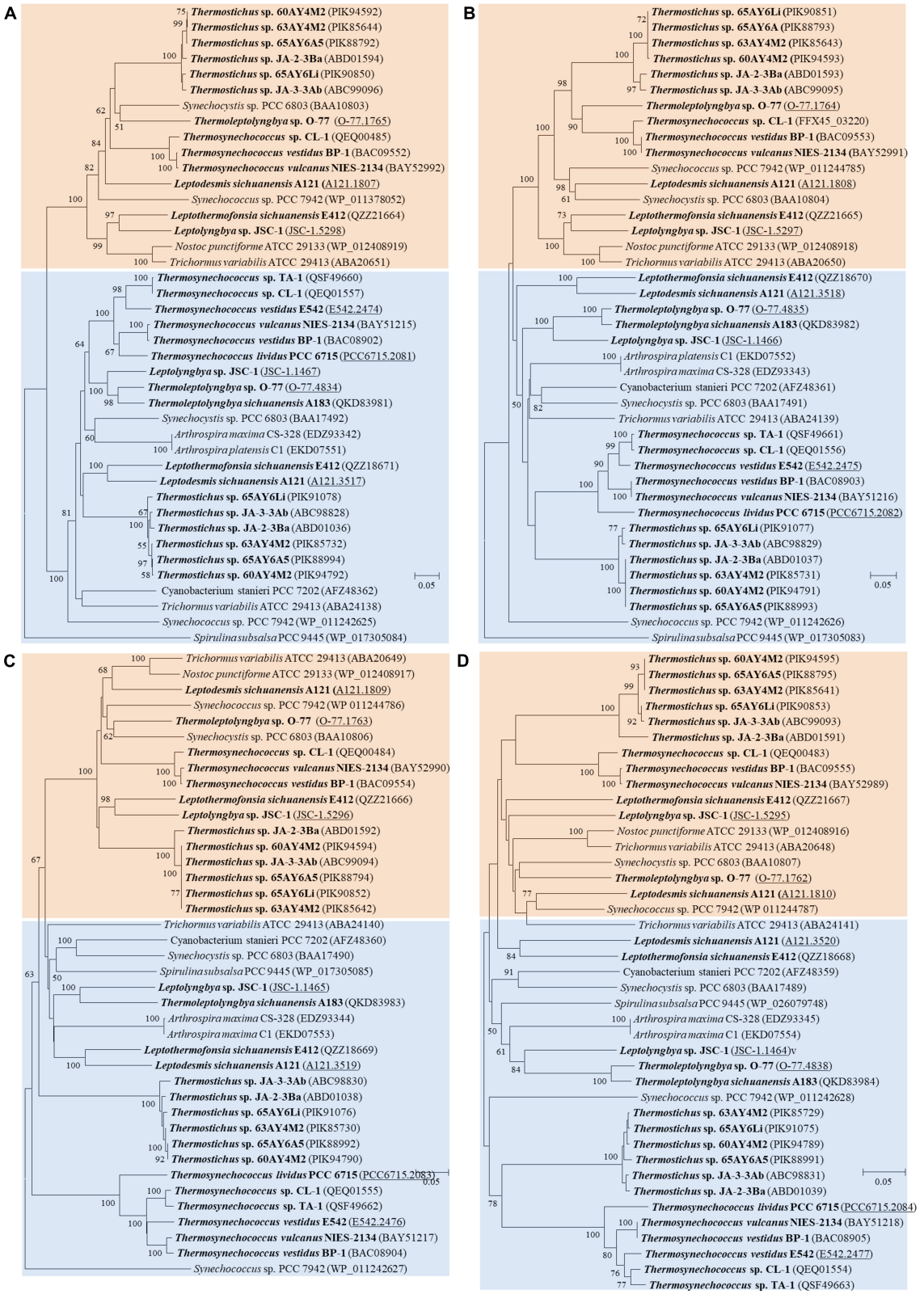

FIGURE 4 | Phylogenetic inference of protein sequences of *cmp* and *nrt* genes. **(A)** *cmpA* and *nrtA*; **(B)** *cmpB* and *nrtB*; **(C)** *cmpC* and *nrtC*; **(D)** *cmpD* and *nrtD*. The thermophilic cyanobacteria investigated in this study are indicated in bold. The accession numbers underscored refers to the gene IDs in **Supplementary Table 1**. Only bootstrap values > 50% are indicated at nodes.

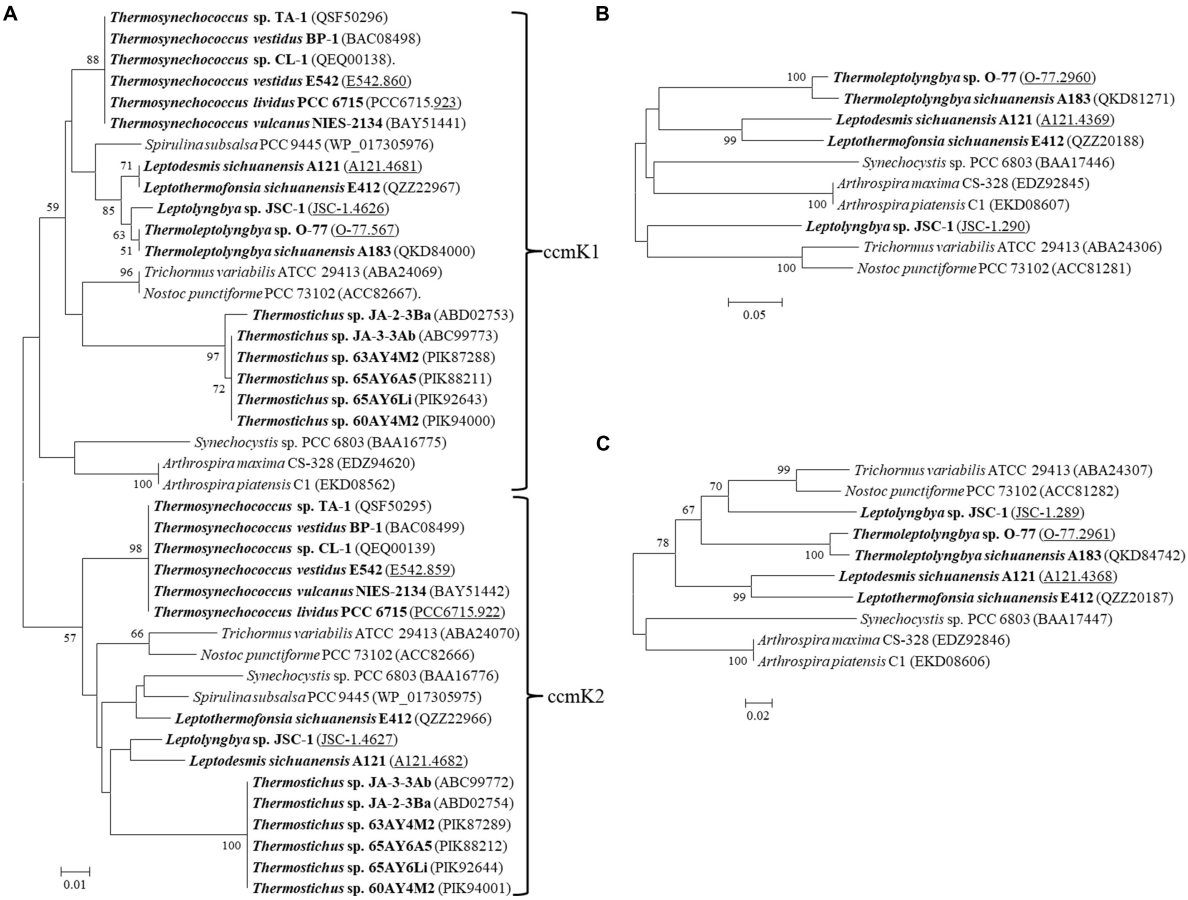

FIGURE 5 | Phylogenetic inference of protein sequences of *ccmK1/2* **(A)**, *ccmK3* **(B)** and *ccmK4* **(C)**. The thermophilic cyanobacteria investigated in this study are indicated in bold. The accession numbers underscored refers to the gene IDs in **Supplementary Table 1**. Only bootstrap values > 50% are indicated at nodes.

strains (**Table 3**), respectively. Apart from the functions as shell protein, an additional function of *ccmM* (γ-CA) as CA activity was reported in cyanobacteria lacking *ccaA* (Peña et al., 2010; de Araujo et al., 2014). Thus, we compared γ-CA-like domain in N-terminal of *ccmM* in thermophilic cyanobacteria to the functional γ-CA in *Thermosynechococcus* BP-1 (Peña et al., 2010) and *Nostoc* PCC 7120 (de Araujo et al., 2014) as well as non-functional γ-CA in *Synechocystis* PCC 6803 (Cot et al., 2008) and *Synechococcus* PCC 7942 (So and Espie, 2005). As shown in **Figure 6**, strains from *Thermostichus* and *Thermosynechococcus* exhibited similar primary structure of amino acid residues in γ-CA-like domain of *ccmM* to that with CA activity in *Thermosynechococcus* BP-1 and *Nostoc* PCC 7120. The result suggested that these *ccmM* proteins may play a role in CA activity in light of the absence of a carboxysomal CA (*ccaA*) (**Table 3**) in these thermophilic cyanobacteria. Although strains from *Leptodesmis*, *Leptolyngbya*, *Leptothermofonsia*, and *Thermoleptolyngbya* had both *ccmM* and *ccaA*, it is likely that only *ccaA* function as CA activity as indicated by the primary structure analysis, which was consistent with the result found in haloalkaliphilic cyanobacteria *Microcoleus* sp. IPPAS B-353 (Kupriyanova et al., 2016). In addition, strains living in high temperatures above 50°C (**Table 1**) appeared to tend to lose *ccaA*. Meanwhile, high pH conditions were speculated to be an important factor in *ccaA* absence (Klanchui et al., 2017). However, the reasons were still unclear. Certainly, the co-evolution of *ccmM* and *ccaA* is crucial for carboxysome to regularly function in extreme environments regardless of high temperature or alkalinity. As for α-CA, non-carboxysomal *ecaA* was not found in all the 17 thermophilic cyanobacteria.

Genomic Distribution Pattern of Carbon-Concentrating Mechanism-Related Genes in Thermophilic Cyanobacteria

The genomic location of CCM-related genes in thermophilic cyanobacteria may provide insights into the function and evolution of these genes. In the present study, the genomic organization of CCM-related genes was illustrated in **Figure 7**. Genes encoding each NDH-1 complex were all clustered together, except for the *ndhD4* of *Thermosynechococcus* TA-1. This gene was remote from the other genes of NDH-1_4 complex (**Figure 7**). In light of the coordination of *NDH* and *cup* proteins in CO_2

TABLE 3 | Availability of genes encoding carboxysomes of thermophilic cyanobacteria studied.

Strain	Carboxysome													
	Shell proteins									Encapsulated enzymes				
	β-Carboxysomal shell proteins									Rubisco			β-CA	
	ccmK1	*ccmK2*	*ccmK3*	*ccmK4*	*ccmL*	*ccmM*	*ccmN*	*ccmO*	*ccmP*	*rbcL*	*rbcS*	*rbcX*	*ccaA*	*ecaB*
Leptodesmis A121	√ (85.2)	√ (91.3)	√ (56.9)	√ (64.8)	√ (56.4)	√ (49.5)	√ (35.0)	√ (54.2)	√ (72.0)	√ (85.1)	√ (63.9)	√ (41.7)	√ (49.7)	√ (39.5)
Leptolyngbya JSC-1	√ (84.3)	√ (91.3)	√ (62.9)	√ (61.5)	√ (67.6)	√ (47.1)	√ (37.9)	√ (58.6)	√ (73.7)	√ (84.3)	√ (68.1)	√ (42.2)	√ (48.1)	√ (41.0)
Leptothermofonsia E412	√ (85.2)	√ (94.2)	√ (63.8)	√ (61.8)	√ (57.8)	√ (48.9)	√ (38.2)	√ (54.0)	√ (72.8)	√ (83.9)	√ (63.9)	√ (42.9)	√ (48.6)	√ (38.1)
Thermoleptolyngbya A183	√ (85.2)	x	√ (63.1)	√ (63.1)	√ (66.0)	√ (44.9)	√ (37.8)	√ (55.6)	√ (75.6)	√ (83.7)	√ (67.8)	√ (39.4)	√ (39.5)	x
Thermoleptolyngbya O-77	√ (85.2)	x	√ (63.6)	√ (63.1)	√ (66.0)	√ (41.3)	√ (37.4)	√ (54.9)	√ (76.1)	√ (83.5)	√ (67.8)	√ (38.9)	√ (39.3)	√ (42.8)
Thermostichus 60AY4M2	√ (82.6)	√ (88.3)	x	x	√ (60.4)	√ (49.9)	√ (37.8)	√ (52.4)	√ (67.6)	√ (86.3)	√ (65.0)	√ (44.7)	x	x
Thermostichus 63AY4M2	√ (82.6)	√ (88.3)	x	x	√ (60.4)	√ (49.5)	√ (37.8)	√ (52.1)	√ (67.6)	√ (86.3)	√ (65.0)	√ (44.7)	x	x
Thermostichus 65AY6A5	√ (82.6)	√ (88.3)	x	x	√ (60.4)	√ (49.7)	√ (38.1)	√ (52.4)	√ (67.6)	√ (86.3)	√ (65.0)	√ (44.7)	x	x
Thermostichus 65AY6Li	√ (82.6)	√ (88.3)	x	x	√ (60.4)	√ (49.6)	√ (37.8)	√ (52.1)	√ (67.6)	√ (86.3)	√ (65.0)	√ (44.7)	x	x
Thermostichus JA-2-3Ba	√ (81.7)	√ (88.3)	x	x	√ (63.7)	√ (50.3)	√ (37.7)	√ (53.9)	√ (69.0)	√ (87.2)	√ (64.2)	√ (43.9)	x	x
Thermostichus JA-3-3Ab	√ (82.6)	√ (88.3)	x	x	√ (60.4)	√ (49.6)	√ (37.6)	√ (52.1)	√ (67.6)	√ (86.3)	√ (65.0)	√ (44.7)	x	x
Thermosynechococcus PCC 6715	√ (86.1)	√ (90.3)	x	x	√ (53.0)	√ (42.7)	√ (37.5)	√ (54.6)	√ (67.3)	√ (83.9)	√ (62.7)	√ (44.7)	x	√ (42.8)
Thermosynechococcus CL-1	√ (86.1)	√ (90.3)	x	x	√ (54.1)	√ (46.0)	√ (38.8)	√ (54.3)	√ (72.8)	√ (84.9)	√ (63.1)	√ (46.0)	x	x
Thermosynechococcus TA-1	√ (86.1)	√ (90.3)	x	x	√ (54.1)	√ (46.0)	√ (38.7)	√ (54.9)	√ (72.8)	√ (84.9)	√ (61.9)	√ (45.3)	x	x
Thermosynechococcus BP-1	√ (86.1)	√ (90.3)	x	x	√ (56.3)	√ (45.8)	√ (35.7)	√ (55.0)	√ (72.3)	√ (84.1)	√ (63.3)	√ (46.3)	x	x
Thermosynechococcus E542	√ (86.1)	√ (90.3)	x	x	√ (54.1)	√ (45.7)	√ (36.4)	√ (54.4)	√ (72.8)	√ (84.7)	√ (63.9)	√ (45.3)	x	x
Thermosynechococcus NIES-2134	√ (86.1)	√ (90.3)	x	x	√ (54.1)	√ (45.8)	√ (35.7)	√ (53.9)	√ (72.3)	√ (84.3)	√ (63.3)	√ (46.3)	x	x

√ and x refers to the presence and absence of the gene, respectively. The number in brackets indicates the identity (%) between the identified protein and the corresponding sequence of Synechocystis PCC 6803.

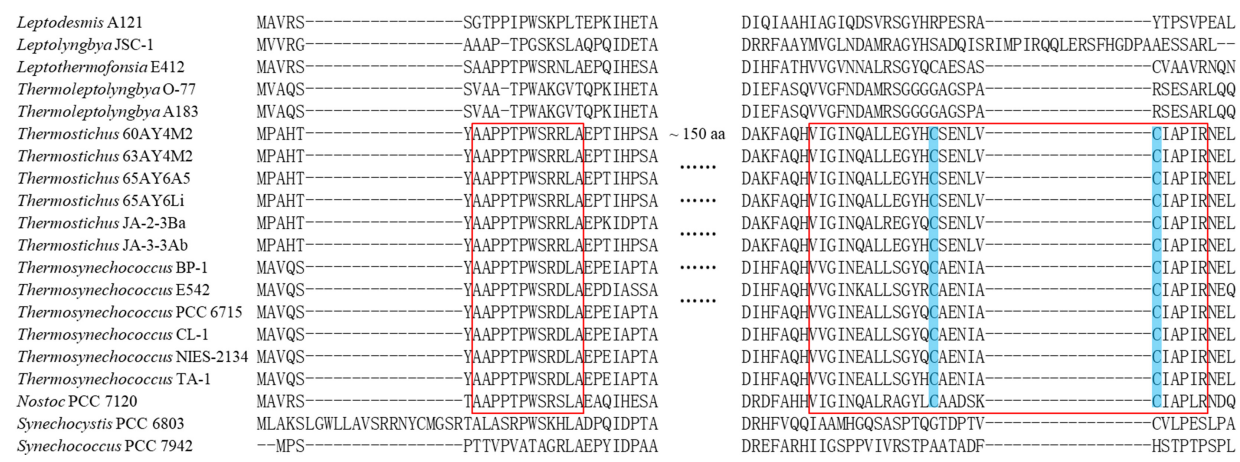

FIGURE 6 | Partial alignments of *ccmM* amino acid sequences representing 17 thermophilic cyanobacteria, *Nostoc* PCC 7120, and *Synechocystis* PCC 6803 and *Synechococcus* PCC 7942 as outgroup. As suggested by Peña et al. (2010), red boxes refer to conserved regions of the N-terminal domain of *ccmM* necessary for CA activity, while shaded cysteine amino acids indicate essential residues participating in the disulfide bond in the C-termini of active *ccmM* protein.

uptake (Han et al., 2017), whether and how such organization in *Thermosynechococcus* TA-1 affects the co-regulation requires further experimental elucidation. In addition, the genes encoding *bicA1* and *bicA2* were positionally scattered in the genomes of *Leptothermofonsia* E412 and *Thermoleptolyngbya* A183, whereas genes encoding *cmpABCD* and *sbtA/B* were located together in genomes (**Figure 7**), respectively.

Focusing on the gene organization of the carboxysome, there appeared to be the main carboxysome locus (MCL) in the genomes of all the studied thermophilic cyanobacteria, comprising one to two *ccmK1/2* genes, always followed by *ccmL*, *-M*, *-N* and in the majority of genomes (11 out of 17), *ccmO* (**Figure 7**). The sequential arrangement of *ccmK2* and *ccmK1* in the MCL might facilitate protein complex assembly or help

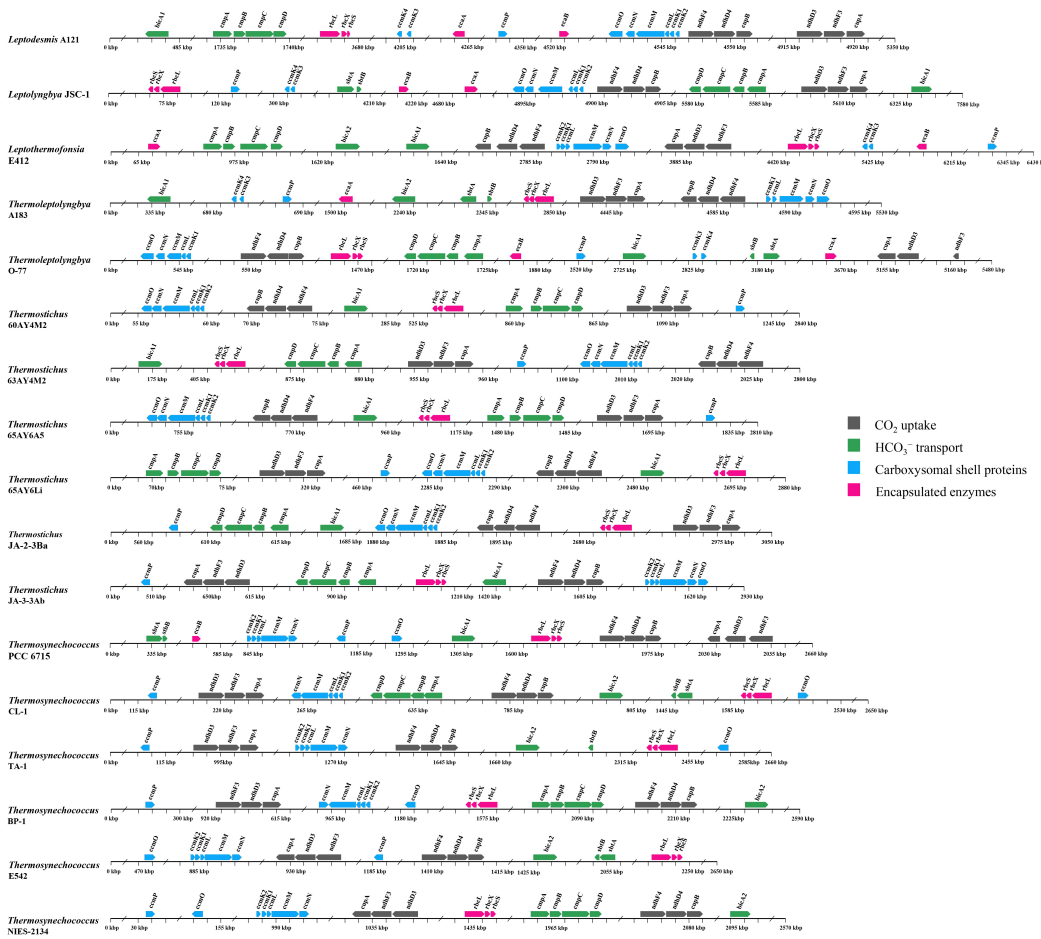

FIGURE 7 | Genomic organization of CCM-related genes in the 17 thermophilic cyanobacteria studied. Solid arrow boxes refer to genes and the direction of transcription.

to balance the shell protein stoichiometry during translation of MCL genes (Cai et al., 2016). Moreover, previous studies suggested that *ccmK*, *-L*, *-M*, and *-N* were co-regulated in an MCL as an operon (Rae et al., 2013; Billis et al., 2014). In addition to the MCL, satellite loci were found in several genomes. Satellite locus encoding the *ccmP* protein was found in all the 17 thermophilic cyanobacteria. The satellite loci formed by *ccmK3* and *ccmK4* was present only in five genomes (**Figure 7**). The organization of *K1*/*K2* and *K3*/*K4* paralogs in separated operons might relate to structural segregation of the two groups (Sommer et al., 2019). Although *ccmK3* and *ccmK4* clustered in operon, it was reported that the stoichiometry of incorporation of *ccmK3* in associations with *ccmK4* was low in *Synechocystis* PCC6803 (Garcia-Alles et al., 2019). However, the expression of *ccmK3* and *ccmK4* from a satellite locus may increase the flexibility of carboxysome shell assembly and permeability (Sommer et al., 2019), and may provide differing metabolite selectivities (Sommer et al., 2017). Another satellite locus, *ccmO*, was positionally variable (**Figure 7**). In 11 genomes, *ccmO* was the terminal gene in the MCL. However, *ccmO* in six *Thermosynechococcus* genomes was located as a satellite locus, remote from other carboxysome genes, and this *ccmO* formed a distinct clade as revealed by the phylogenetic analysis (**Supplementary Figure 3D**). Previous transcriptome analysis demonstrated that the *ccmO* gene was co-regulated with MCL genes only when it was associated with the MCL (Sommer et al., 2017). Therefore, the dispersal of *ccmO* as well as other carboxysome genes across the genome may increase the plasticity of individual regulation of their expression, perhaps in response to changes in environmental conditions, and vice versa, diverse environmental conditions appear to promote relocation of these genes driven by evolutionary force (Cai et al., 2012; Shih et al., 2013).

Genes encoding *rbcL*, *rbcS*, and *rbcX* for Rubisco were localized together in all of the 17 thermophilic cyanobacteria, which was in line with the previous consensus that the three genes were clustered in an operon in β-cyanobacteria (Badger et al., 2002). The Rubisco gene cluster was all apart from the MCL in each genome, indicating that it, as satellite loci to MCL, might regulate its expression independently. This was supported by the results reported by Billis et al. (2014) that *ccmO*, *rbcL*, and *rbcS* were less strictly co-regulated with the MCL genes. As for the chaperone *rbcX*, sometimes it was non-essential for the

assembly of an active Rubisco enzyme, e.g., in *Synechococcus* PCC 7942 (Emlyn-Jones et al., 2006). The role of *rbcX* in these thermophilic cyanobacteria requires future investigations. In regards to β-CAs, scattered distribution of *ccaA* and *ecaB* was present in the genomes.

Functional and Comparative Analysis of Carbon-Concentrating Mechanism Components Among β-Cyanobacteria

The overall composition of the CCM system presented in **Figure 3** contains all typical components found in other cyanobacteria, including the complete set of genes for carboxysome assembly. A comparison of these components among β-cyanobacteria was performed between thermophilic cyanobacteria and non-thermophilic cyanobacteria. For a precise comparison, we divided the non-thermophilic cyanobacteria into three groups: freshwater, marine, and alkaliphilic cyanobacteria. The overall compositions of CCM components in thermophilic cyanobacteria were more similar to the freshwater and alkaliphilic than the marine groups (Klanchui et al., 2017). The thermophilic, freshwater and alkaliphilic cyanobacteria possessed both CO_2 uptake systems, NDH-1_3 and NDH-1_4, whereas most marine cyanobacteria lacked the NDH-1_3. In light of the HCO_3^- uptake, marine and some thermophilic/alkaliphilic cyanobacteria lacked the BCT1 transporter. Although freshwater cyanobacteria consistently possessed BCT1 transporter, some thermophilic cyanobacteria with freshwater origins lacked that. The relatively high diversity of bicarbonate transporters is a distinguishing factor for certain thermophilic strains probably as indicator of their specific location and not their thermophilic character. However, there is no apparent correlation between the pH of the isolation sources of these strains and the presence or absence of specific bicarbonate uptake systems (**Figure 3** and **Table 1**). More thorough studies are required to characterize the functions of these transporters in the future. In addition, the freshwater cyanobacteria possessed the highest abundance of CAs, β-CA (*ccaA* and *ecaB*), α-CA (*ecaA*), and γ-CA (*ccmM*), while the thermophilic cyanobacteria with freshwater origins were likely to possess up to two CAs (**Table 3** and **Figure 3**). Notably, 11 out of the 17 investigated thermophiles appeared to have only γ-CA (*ccmM*). On the other hand, the diversity of carboxysome shell proteins appears to be lower in thermophilic strains than many of their mesophilic counterparts, with multiple strains lacking at least one of the four *ccmK* genes.

CONCLUSION

In the present study, we investigated the molecular components and distribution of CCM in 17 thermophilic cyanobacteria. The diversity in the C_i uptake systems and carboxysome of these thermophiles were observed. Particularly, the presence of HCO_3^- transporters, *ccmK2/3/4* and CAs tremendously varied among these thermophiles. Several strains have more C_i uptake-related components, indicating the capabilities of these strains to acclimate and establish competitive growth by using different C_i uptake strategies in response to environmental fluctuation. The distinct genomic distribution of CCM-related genes among the thermophiles probably suggested various regulations of expression. Overall, the comparative genomic analysis revealed distinct molecular components and organization of CCM in thermophilic cyanobacteria. These findings provided insights into the CCM components of thermophilic cyanobacteria and fundamental knowledge for further research regarding photosynthetic improvement and biomass yield of thermophilic cyanobacteria with biotechnological potentials.

DATA AVAILABILITY STATEMENT

The datasets presented in this study can be found in online repositories. The names of the repository/repositories and accession number(s) can be found below: https://www.ncbi.nlm.nih.gov/, CP018092.

AUTHOR CONTRIBUTIONS

JT: conceptualization, methodology, validation, formal analysis, investigation, data curation, writing – original draft, writing, review, editing, visualization, supervision, project administration, and funding acquisition. HZ: formal analysis, investigation, data curation, and visualization. DYa: formal analysis, investigation, and data curation. SR: formal analysis, data curation, and visualization. DYo: formal analysis, visualization, writing, review, and editing. AK-S: formal analysis, investigation, and funding acquisition. MD: conceptualization, methodology, resources, data curation, writing – original draft, writing, review, editing, supervision, project administration, and funding acquisition. All authors contributed to the article and approved the submitted version.

FUNDING

This research was funded by the National Natural Science Foundation of China (31970092 and 32071480), Shenzhen Fundamental Research Program (GXWD20201231165807007-20200806170221001), National Science Centre (Poland) through project no. 2018/31/B/ST8/00822, and Tenure-Track Fund to MD. Funding bodies had no influence over the design and execution of this research.

ACKNOWLEDGMENTS

We would like to thank Dr. Igor Brown and the culture collections of PCC and NIES for the assistance in verifying the actual thermophilicity of certain strains.

SUPPLEMENTARY MATERIAL

The Supplementary Material for this article can be found online at: https://www.frontiersin.org/articles/10.3389/fmicb.2022.876272/full#supplementary-material

REFERENCES

Alcorta, J., Alarcón-Schumacher, T., Salgado, O., and Díez, B. (2020). Taxonomic novelty and distinctive genomic features of hot spring cyanobacteria. *Front. Genet.* 11:568223. doi: 10.3389/fgene.2020.568223

Aziz, R. K., Bartels, D., Best, A. A., DeJongh, M., Disz, T., Edwards, R. A., et al. (2008). The RAST Server: Rapid annotations using subsystems technology. *BMC Genom.* 9:75. doi: 10.1186/1471-2164-9-75

Badger, M. R., Hanson, D., and Price, G. D. (2002). Evolution and diversity of CO_2 concentrating mechanisms in cyanobacteria. *Funct. Plant Biol.* 29, 161–173. doi: 10.1071/PP01213

Bhaya, D., Grossman, A. R., Steunou, A.-S., Khuri, N., Cohan, F. M., Hamamura, N., et al. (2007). Population level functional diversity in a microbial community revealed by comparative genomic and metagenomic analyses. *ISME J.* 1, 703–713. doi: 10.1038/ismej.2007.46

Billis, K., Billini, M., Tripp, H. J., Kyrpides, N. C., and Mavromatis, K. (2014). Comparative transcriptomics between *Synechococcus* PCC 7942 and *Synechocystis* PCC 6803 provide insights into mechanisms of stress acclimation. *PLoS One* 9:e109738. doi: 10.1371/journal.pone.0109738

Blank, C. E., and Sánchez-Baracaldo, P. (2010). Timing of morphological and ecological innovations in the cyanobacteria–a key to understanding the rise in atmospheric oxygen. *Geobiology* 8, 1–23. doi: 10.1111/j.1472-4669.2009.00220.x

Brilli, M., Fondi, M., Fani, R., Mengoni, A., Ferri, L., Bazzicalupo, M., et al. (2010). The diversity and evolution of cell cycle regulation in alpha-*proteobacteria*: a comparative genomic analysis. *BMC Syst. Biol.* 4:52. doi: 10.1186/1752-0509-4-52

Brown, I. I., Bryant, D. A., Casamatta, D., Thomas-Keprta, K. L., Sarkisova, S. A., Shen, G., et al. (2010). Polyphasic characterization of a thermotolerant siderophilic filamentous cyanobacterium that produces intracellular iron deposits. *Appl. Environ. Microbiol.* 76, 6664–6672. doi: 10.1128/aem.00662-10

Burnap, R. L., Hagemann, M., and Kaplan, A. (2015). Regulation of CO_2 concentrating mechanism in cyanobacteria. *Life* 5, 348–371. doi: 10.3390/life5010348

Cai, F., Bernstein, S. L., and Wilson, S. C. (2016). Production and characterization of synthetic carboxysome shells with incorporated luminal proteins. *Plant Physiol.* 170, 1868–1877. doi: 10.1104/pp.15.01822

Cai, F., Kerfeld, C. A., and Sandh, G. (2012). "Bioinformatic identification and structural characterization of a new carboxysome shell protein," in *Functional Genomics and Evolution of Photosynthetic Systems*, eds R. Burnap and W. Vermaas (Dordrecht: Springer Netherlands), 345–356. doi: 10.1016/j.jmb.2009.03.056

Cai, F., Menon, B. B., Cannon, G. C., Curry, K. J., Shively, J. M., and Heinhorst, S. (2009). The pentameric vertex proteins are necessary for the icosahedral carboxysome shell to function as a CO_2 leakage barrier. *PLoS One* 4:e7521. doi: 10.1371/journal.pone.0007521

Cai, F., Sutter, M., Cameron, J. C., Stanley, D. N., Kinney, J. N., and Kerfeld, C. A. (2013). The structure of CcmP, a tandem bacterial microcompartment domain protein from the β-Carboxysome, forms a subcompartment within a microcompartment. *J. Biol. Chem.* 288, 16055–16063. doi: 10.1074/jbc.M113.456897

Chen, H., and Wang, Q. (2020). Microalgae-based nitrogen bioremediation. *Algal Res.* 46:101775. doi: 10.1016/j.algal.2019.101775

Chen, M.-Y., Teng, W.-K., Zhao, L., Hu, C.-X., Zhou, Y.-K., Han, B.-P., et al. (2021). Comparative genomics reveals insights into cyanobacterial evolution and habitat adaptation. *ISME J.* 15, 211–227. doi: 10.1038/s41396-020-00775-z

Cheng, Y.-I., Chou, L., Chiu, Y.-F., Hsueh, H.-T., Kuo, C.-H., and Chu, H.-A. (2020). Comparative genomic analysis of a novel strain of Taiwan hot-spring cyanobacterium *Thermosynechococcus* sp. CL-1. *Front. Microbiol.* 11:82. doi: 10.3389/fmicb.2020.00082

Chin, C.-S., Alexander, D. H., Marks, P., Klammer, A. A., Drake, J., Heiner, C., et al. (2013). Nonhybrid, finished microbial genome assemblies from long-read SMRT sequencing data. *Nat. Meth.* 10, 563–569. doi: 10.1038/nmeth.2474

Clement, R., Dimnet, L., Maberly, S. C., and Gontero, B. (2016). The nature of the CO_2-concentrating mechanisms in a marine diatom, *Thalassiosira pseudonana*. *New Phytol.* 209, 1417–1427. doi: 10.1111/nph.13728

Cot, S. S. W., So, A. K. C., and Espie, G. S. (2008). A multiprotein bicarbonate dehydration complex essential to carboxysome function in cyanobacteria. *J. Bacteriol.* 190, 936–945. doi: 10.1128/jb.01283-07

de Araujo, C., Arefeen, D., Tadesse, Y., Long, B. M., Price, G. D., Rowlett, R. S., et al. (2014). Identification and characterization of a carboxysomal γ-carbonic anhydrase from the cyanobacterium *Nostoc* sp. PCC 7120. *Photosynth. Res.* 121, 135–150. doi: 10.1007/s11120-014-0018-4

Durall, C., and Lindblad, P. (2015). Mechanisms of carbon fixation and engineering for increased carbon fixation in cyanobacteria. *Algal Res.* 11, 263–270. doi: 10.1016/j.algal.2015.07.002

Emlyn-Jones, D., Woodger, F. J., and Whitney, P. S. M. (2006). RbcX can function as a rubisco chaperonin, but is non-essential in *Synechococcus* PCC7942. *Plant Cell Physiol.* 47, 1630–1640. doi: 10.1093/pcp/pcl028

Galmés, J., Hermida Carrera, C., Laanisto, L., and Niinemets, Ü (2016). A compendium of temperature responses of Rubisco kinetic traits: variability among and within photosynthetic groups and impacts on photosynthesis modeling. *J. Exp. Bot.* 67:erw267. doi: 10.1093/jxb/erw267

Galmés, J., Kapralov, M. V., Copolovici, L. O., Hermida-Carrera, C., and Niinemets, Ü (2015). Temperature responses of the Rubisco maximum carboxylase activity across domains of life: phylogenetic signals, trade-offs, and importance for carbon gain. *Photosynth. Res.* 123, 183–201. doi: 10.1007/s11120-014-0067-8

Garcia-Alles, L., Root, K., Maveyraud, L., Aubry, N., Lesniewska, E., Mourey, L., et al. (2019). Occurrence and stability of hetero-hexamer associations formed by β-carboxysome CcmK shell components. *PLoS One* 14:e0223877. doi: 10.1101/730861

Gubernator, B., Bartoszewski, R., Kroliczewski, J., Wildner, G., and Szczepaniak, A. (2008). Ribulose-1,5-bisphosphate carboxylase/oxygenase from thermophilic cyanobacterium Thermosynechococcus elongatus. *Photosynth. Res.* 95, 101–109. doi: 10.1007/s11120-007-9240-7

Guindon, S., Dufayard, J.-F., Lefort, V., Anisimova, M., Hordijk, W., and Gascuel, O. (2010). New algorithms and methods to estimate Maximum-Likelihood phylogenies: assessing the performance of PhyML 3.0. *Syst. Biol.* 59, 307–321. doi: 10.1093/sysbio/syq010

Han, X., Sun, N., Xu, M., and Mi, H. (2017). Co-ordination of NDH and Cup proteins in CO_2 uptake in cyanobacterium *Synechocystis* sp. PCC 6803. *J. Exp. Bot.* 68, 3869–3877. doi: 10.1093/jxb/erx129

Hennacy, J. H., and Jonikas, M. C. (2020). Prospects for engineering biophysical CO_2 concentrating mechanisms into land plants to enhance yields. *Annu. Rev. Plant Biol.* 71, 461–485. doi: 10.1146/annurev-arplant-081519-040100

Hill, N. C., Tay, J. W., Altus, S., Bortz, D. M., and Cameron, J. C. (2020). Life cycle of a cyanobacterial carboxysome. *Sci. Adv.* 6:eaba1269. doi: 10.1126/sciadv.aba1269

Jain, C., and Rodriguez, R. L. (2018). High throughput ANI analysis of 90K prokaryotic genomes reveals clear species boundaries. *Nat. Commun.* 9:5114. doi: 10.1101/225342

Kamennaya, N. A., Ajo-Franklin, C. M., Northen, T., and Jansson, C. (2012). Cyanobacteria as biocatalysts for carbonate mineralization. *Minerals* 2, 338–364. doi: 10.3390/min2040338

Kaplan, A. (2017). On the cradle of CCM research: discovery, development, and challenges ahead. *J. Exp. Bot.* 68, 3785–3796. doi: 10.1093/jxb/erx122

Kerfeld, C. A., and Melnicki, M. R. (2016). Assembly, function and evolution of cyanobacterial carboxysomes. *Curr. Opin. Plant Biol.* 31, 66–75. doi: 10.1016/j.pbi.2016.03.009

Kerfeld, C. A., Sawaya, M. R., Tanaka, S., Nguyen, C. V., Phillips, M., Beeby, M., et al. (2005). Protein structures forming the shell of primitive bacterial organelles. *Science* 309, 936–938. doi: 10.1126/science.1113397

Kierzkowska-Pawlak, H., Kruszczak, E., and Tyczkowski, J. (2022). Catalytic activity of plasma-deposited Co_3O_4-based thin films for CO_2 hydration – A new approach to carbon capture applications. *Appl. Catal. B Environ.* 304:120961. doi: 10.1016/j.apcatb.2021.120961

Klanchui, A., Cheevadhanarak, S., Prommeenate, P., and Meechai, A. (2017). Exploring components of the CO_2-concentrating mechanism in alkaliphilic cyanobacteria through genome-based analysis. *Comput. Struct. Biotechnol. J.* 15, 340–350. doi: 10.1016/j.csbj.2017.05.001

Komárek, J. (2016). A polyphasic approach for the taxonomy of cyanobacteria: principles and applications. *Eur. J. Phycol.* 51, 346–353. doi: 10.1080/09670262.2016.1163738

Komárek, J., Johansen, J., Smarda, J., and Strunecký, O. (2020). Phylogeny and taxonomy of *Synechococcus*-like cyanobacteria. *Fottea* 20, 171–191. doi: 10.5507/fot.2020.006

Kumar, S., Stecher, G., and Tamura, K. (2016). MEGA7: molecular evolutionary genetics analysis version 7.0 for bigger datasets. *Mol. Biol. Evol.* 33, 1870–1874. doi: 10.1093/molbev/msw054

Kupriyanova, E. V., Cho, S. M., Park, Y.-I., Pronina, N. A., and Los, D. A. (2016). The complete genome of a cyanobacterium from a soda lake reveals the presence of the components of CO_2-concentrating mechanism. *Photosynth. Res.* 130, 151–165. doi: 10.1007/s11120-016-0235-0

Kupriyanova, E. V., and Samylina, O. S. (2015). CO_2-concentrating mechanism and its traits in haloalkaliphilic cyanobacteria. *Microbiology* 84, 112–124. doi: 10.1134/S0026261715010075

Leu, J.-Y., Lin, T.-H., Selvamani, M. J. P., Chen, H.-C., Liang, J.-Z., and Pan, K.-M. (2013). Characterization of a novel thermophilic cyanobacterial strain from Taian hot springs in Taiwan for high CO_2 mitigation and C-phycocyanin extraction. *Process Biochem.* 48, 41–48. doi: 10.1016/j.procbio.2012.09.019

Li, H., and Durbin, R. (2009). Fast and Accurate Short Read Alignment with Burrows-Wheeler Transform. *Bioinformatics* 25, 1754–1760. doi: 10.1093/bioinformatics/btp324

Liang, Y., Kaczmarek, M. B., Kasprzak, A. K., Tang, J., Shah, M. M. R., Jin, P., et al. (2018). Thermosynechococcaceae as a source of thermostable C-phycocyanins: properties and molecular insights. *Algal Res.* 35, 223–235. doi: 10.1016/j.algal.2018.08.037

Liang, Y., Tang, J., Luo, Y., Kaczmarek, M. B., Li, X., and Daroch, M. (2019). *Thermosynechococcus* as a thermophilic photosynthetic microbial cell factory for CO_2 utilisation. *Bioresour. Technol.* 278, 255–265. doi: 10.1016/j.biortech.2019.01.089

Luo, R., Liu, B., Xie, Y., Li, Z., Huang, W., Yuan, J., et al. (2012). SOAPdenovo2: an empirically improved memory-efficient short-read de novo assembler. *GigaScience* 1:18. doi: 10.1186/2047-217x-1-18

MacCready, J. S., Basalla, J. L., and Vecchiarelli, A. G. (2020). Origin and evolution of carboxysome positioning systems in cyanobacteria. *Mol. Biol. Evol.* 37, 1434–1451. doi: 10.1093/molbev/msz308

Mangan, N. M., Flamholz, A., Hood, R. D., Milo, R., and Savage, D. F. (2016). pH determines the energetic efficiency of the cyanobacterial CO_2 concentrating mechanism. *Proc. Natl. Acad. Sci. U.S.A.* 113, 5354–5362. doi: 10.1073/pnas.1525145113

Melnicki, M. R., Sutter, M., and Kerfeld, C. A. (2021). Evolutionary relationships among shell proteins of carboxysomes and metabolosomes. *Curr. Opin. Microbiol.* 63, 1–9. doi: 10.1016/j.mib.2021.05.011

Mook, W. G. (2000). *Environmental Isotopes in the Hydrological Cycle - Principles and Applications*. Paris: UNESCO-IHP.

Nakamura, Y., Kaneko, T., Sato, S., Ikeuchi, M., Katoh, H., Sasamoto, S., et al. (2002). Complete genome structure of the thermophilic cyanobacterium *Thermosynechococcus elongatus* BP-1. *DNA Res.* 9, 123–130. doi: 10.1093/dnares/9.4.123

Noreña-Caro, D., and Benton, M. G. (2018). Cyanobacteria as photoautotrophic biofactories of high-value chemicals. *J. CO2 Util.* 28, 335–366. doi: 10.1016/j.jcou.2018.10.008

Olsen, M. T., Nowack, S., Wood, J. M., Becraft, E. D., LaButti, K., Lipzen, A., et al. (2015). The molecular dimension of microbial species: 3. Comparative genomics of *Synechococcus* strains with different light responses and in situ diel transcription patterns of associated putative ecotypes in the Mushroom Spring microbial mat. *Front. Microbiol.* 6:604. doi: 10.3389/fmicb.2015.00604

Omata, T. (1995). Structure, function and regulation of the nitrate transport system of the cyanobacterium *Synechococcus* sp. PCC7942. *Plant Cell Physiol.* 36, 207–213. doi: 10.1093/oxfordjournals.pcp.a078751

Omata, T., Price, G. D., Badger, M. R., Okamura, M., Gohta, S., and Ogawa, T. (1999). Identification of an ATP-binding cassette transporter involved in bicarbonate uptake in the cyanobacterium *Synechococcus* sp. strain PCC 7942. *Proc. Natl. Acad. Sci. U.S.A.* 96, 13571–13576. doi: 10.1073/pnas.96.23.13571

Omata, T., Takahashi, Y., Yamaguchi, O., and Nishimura, T. (2002). Structure, function and regulation of the cyanobacterial high-affinity bicarbonate transporter, BCT1. *Funct. Plant Biol.* 29, 151–159. doi: 10.1071/pp01215

Parks, D. H., Imelfort, M., Skennerton, C. T., Hugenholtz, P., and Tyson, G. W. (2015). CheckM: assessing the quality of microbial genomes recovered from isolates, single cells, and metagenomes. *Genom. Res.* 25, 1043–1055. doi: 10.1101/gr.186072.114

Patel, A., Matsakas, L., Rova, U., and Christakopoulos, P. (2019). A perspective on biotechnological applications of thermophilic microalgae and cyanobacteria. *Bioresour. Technol.* 278, 424–434. doi: 10.1016/j.biortech.2019.01.063

Peña, K. L., Castel, S. E., de Araujo, C., Espie, G. S., and Kimber, M. S. (2010). Structural basis of the oxidative activation of the carboxysomal γ-carbonic anhydrase, CcmM. *Proc. Natl. Acad. Sci. U.S.A.* 107, 2455–2460. doi: 10.1073/pnas.0910866107

Price, G. D. (2011). Inorganic carbon transporters of the cyanobacterial CO_2 concentrating mechanism. *Photosynth. Res.* 109, 47–57. doi: 10.1007/s11120-010-9608-y

Price, G. D., Badger, M. R., Woodger, F. J., and Long, B. M. (2007). Advances in understanding the cyanobacterial CO_2-concentrating-mechanism (CCM): functional components, Ci transporters, diversity, genetic regulation and prospects for engineering into plants. *J. Exp. Bot.* 59, 1441–1461. doi: 10.1093/jxb/erm112

Price, G. D., Woodger, F. J., Badger, M. R., Howitt, S. M., and Tucker, L. (2004). Identification of a SulP-type bicarbonate transporter in marine cyanobacteria. *Proc. Natl. Acad. Sci. U.S.A.* 101, 18228–18233. doi: 10.1073/pnas.0405211101

Pronina, N. A., Kupriyanova, E. V., and Igamberdiev, A. U. (2017). "Photosynthetic carbon metabolism and CO_2-concentrating mechanism of cyanobacteria," in *Modern Topics in the Phototrophic Prokaryotes: Metabolism, Bioenergetics, and Omics*, ed. P. C. Hallenbeck (Cham: Springer International Publishing), 271–303. doi: 10.1007/978-3-319-51365-2_8

Qin, Q., Xie, B., Zhang, X., Chen, X., Zhou, B., Zhou, J., et al. (2014). A proposed genus boundary for the prokaryotes based on genomic insights. *J. Bacteriol.* 196, 2210–2215. doi: 10.1128/jb.01688-14

Rae, B., Long, B. M., Badger, M. R., Dean, P. G., and Lei, B. (2012). Structural determinants of the outer shell of β-Carboxysomes in *Synechococcus elongatus* PCC 7942: Roles for ccmK2, K3-K4, ccmO, and ccmL. *PLoS One* 7:e43871. doi: 10.1371/journal.pone.0043871

Rae, B. D., Long, B. M., Badger, M. R., and Price, G. D. (2013). Functions, compositions, and evolution of the two types of carboxysomes: polyhedral microcompartments that facilitate CO_2 fixation in cyanobacteria and some *proteobacteria*. *Microbiol. Mol. Biol. Rev.* 77, 357–379. doi: 10.1128/MMBR.00061-12

Raven, J. A., John, B., and Patricia, S. B. (2017). The possible evolution and future of CO_2-concentrating mechanisms. *J. Exp. Bot.* 68, 3701–3716. doi: 10.1093/jxb/erx110

Sandrini, G., Matthijs, H. C. P., Verspagen, J. M. H., Muyzer, G., and Huisman, J. (2014). Genetic diversity of inorganic carbon uptake systems causes variation in CO_2 response of the cyanobacterium Microcystis. *ISME J.* 8, 589–600. doi: 10.1038/ismej.2013.179

Shih, P. M., Dongying, W., Latifi, A., Axen, S. D., Fewer, D. P., Talla, E., et al. (2013). Improving the coverage of the cyanobacterial phylum using diversity-driven genome sequencing. *Proc. Natl. Acad. Sci. U.S.A.* 110, 1053–1058. doi: 10.1073/pnas.1217107110

So, A. K.-C., and Espie, G. S. (2005). Cyanobacterial carbonic anhydrases. *Can. J. Bot.* 83, 721–734. doi: 10.1139/b05-057

Solomon, T. (2001). The Definition and Unit of Ionic Strength. *J.Chem. Educ.* 78, 1691. doi: 10.1021/ed078p1691

Soltes-Rak, E., Mulligan, M. E., and Coleman, J. R. (1997). Identification and characterization of a gene encoding a vertebrate-type carbonic anhydrase in cyanobacteria. *J. Bacteriol.* 179, 769–774. doi: 10.1128/jb.179.3.769-774.1997

Sommer, M., Cai, F., Melnicki, M., and Kerfeld, C. A. (2017). β-Carboxysome bioinformatics: identification and evolution of new bacterial microcompartment protein gene classes and core locus constraints. *J. Exp. Bot.* 68, 3841–3855. doi: 10.1093/jxb/erx115

Sommer, M., Sutter, M., Gupta, S., Kirst, H., Turmo, A., Lechno-Yossef, S., et al. (2019). Heterohexamers formed by CcmK3 and CcmK4 increase the complexity of Beta carboxysome shells. *Plant Physiol.* 179, 156–167. doi: 10.1104/pp.18.01190

Sun, N., Han, X., Xu, M., Kaplan, A., Espie, G. S., and Mi, H. (2019). A thylakoid-located carbonic anhydrase regulates CO_2 uptake in the cyanobacterium *Synechocystis* sp. PCC 6803. *New Phytol.* 222, 206–217. doi: 10.1111/nph.15575

Tang, J., Du, L., Li, M., Yao, D., Waleron, M., Waleron, K. F., et al. (2022a). Characterization of a novel hot-spring cyanobacterium *Leptodesmis sichuanensis* sp. nov. and genomic insights of molecular adaptations into its habitat. *Front. Microbiol.* 12:739625. doi: 10.3389/fmicb.2021.739625

Tang, J., Shah, M. R., Yao, D., Du, L., Zhao, K., Li, L., et al. (2022b). Polyphasic identification and genomic insights of *Leptothermofonsia sichuanensis* gen. sp. nov., a novel thermophilic cyanobacteria within Leptolyngbyaceae. *Front. Microbiol.* 13:765105. doi: 10.3389/fmicb.2022.765105

Tang, J., Du, L., Liang, Y., and Daroch, M. (2019). Complete genome sequence and comparative analysis of *Synechococcus* sp. CS-601 (SynAce01), a cold-adapted cyanobacterium from an oligotrophic Antarctic habitat. *Int. J. Mol. Sci.* 20:152. doi: 10.3390/ijms20010152

Tang, J., Jiang, D., Luo, Y., Liang, Y., Li, L., Shah, M., et al. (2018a). Potential new genera of cyanobacterial strains isolated from thermal springs of western Sichuan, China. *Algal Res.* 31, 14–20. doi: 10.1016/j.algal.2018.01.008

Tang, J., Liang, Y., Jiang, D., Li, L., Luo, Y., Shah, M. M. R., et al. (2018b). Temperature-controlled thermophilic bacterial communities in hot springs of western Sichuan, China. *BMC Microbiol.* 18:134. doi: 10.1186/s12866-018-1271-z

Tang, J., Li, L., Li, M., Du, L., Shah, M. R., Waleron, M., et al. (2021). Description, taxonomy, and comparative genomics of a novel species, *Thermoleptolyngbya sichuanensis* sp. nov., isolated from Hot Springs of Ganzi, Sichuan, China. *Front. Microbiol.* 12:696102. doi: 10.3389/fmicb.2021.696102

Tremaine, P., Zhang, K., Bénézeth, P., and Xiao, C. (2004). "Ionization equilibria of acids and bases under hydrothermal conditions," in *Aqueous Systems at Elevated Temperatures and Pressures*, eds D. A. Palmer, R. Fernández-Prini, and A. H. Harvey (London: Academic Press), 441–492. doi: 10.1016/b978-012544461-3/50014-4

Walker, B. J., Abeel, T., Shea, T., Priest, M., Abouelliel, A., Sakthikumar, S., et al. (2014). Pilon: an integrated tool for comprehensive microbial variant detection and genome assembly improvement. *PLoS One* 9:e112963. doi: 10.1371/journal.pone.0112963

Walter, J. M., Coutinho, F. H., Dutilh, B. E., Swings, J., Thompson, F. L., and Thompson, C. C. (2017). Ecogenomics and taxonomy of cyanobacteria phylum. *Front. Microbiol.* 8:2132. doi: 10.3389/fmicb.2017.02132

Woosley, R. J. (2021). Evaluation of the temperature dependence of dissociation constants for the marine carbon system using pH and certified reference materials. *Mar. Chem.* 229:103914. doi: 10.1016/j.marchem.2020.103914

Yoon, K. S., Nguyen, N. T., Tran, K. T., Tsuji, K., and Ogo, S. (2017). Nitrogen fixation genes and nitrogenase activity of the non-heterocystous cyanobacterium *Thermoleptolyngbya* sp. O-77. *Microb. Environ.* 32, 324–329. doi: 10.1264/jsme2.ME17015

Conflict of Interest: The authors declare that the research was conducted in the absence of any commercial or financial relationships that could be construed as a potential conflict of interest.

Publisher's Note: All claims expressed in this article are solely those of the authors and do not necessarily represent those of their affiliated organizations, or those of the publisher, the editors and the reviewers. Any product that may be evaluated in this article, or claim that may be made by its manufacturer, is not guaranteed or endorsed by the publisher.

frontiers | Frontiers in Microbiology

ORIGINAL RESEARCH
published: 06 May 2022
doi: 10.3389/fmicb.2022.876122

Structure Insights Into Photosystem I Octamer From Cyanobacteria

Ming Chen[1†], Yujie He[2†], Dongyang Liu[3], Lijin Tian[3], Pengqi Xu[1], Xuan Liu[1], Yihang Pan[1], Shuqi Dong[2,4], Jun He[2,4] and Ying Zhang[1]**

[1]The Seventh Affiliated Hospital, Sun Yat-sen University, Shenzhen, China, [2]Center for Cell Fate and Lineage (CCLA), Bioland Laboratory (Guangzhou Regenerative Medicine and Health Guangdong Laboratory), Guangzhou, China, [3]Photosynthesis Research Centre, Institute of Botany, Chinese Academy of Sciences (CAS), Beijing, China, [4]Center for Cell Lineage and Development, Guangzhou Institutes of Biomedicine and Health, Chinese Academy of Sciences, Guangzhou, China

The diversity of photosystem oligomers is essential to understanding how photosynthetic organisms adapt to light conditions. Due to its structural and physiological significance, the assembly of the PSI supercomplex has been of great interest recently in terms of both chloroplast and cyanobacteria. In this study, two novel photosystem I supercomplexes were isolated for the first time from the low light incubated culture of filamentous cyanobacterium *Anabaena* sp. PCC 7120. These complexes were defined as PSI hexamers and octamers through biochemical and biophysical characterization. Their 77K emission spectra indicated that the red forms of chlorophylls seemed not to be affected during oligomerization. By cryo-EM single-particle analysis, a near-atomic (7.0 Å) resolution structure of a PSI octamer was resolved, and the molecular assemblies of a stable PSI octamer were revealed.

Keywords: cyanobacteria, photosystem I, hexamer, octamer, single particle

OPEN ACCESS

Edited by:
Bao-Sheng Qiu,
Central China Normal University, China

Reviewed by:
Weimin Ma,
Shanghai Normal University, China
Haijun Liu,
Washington University in St. Louis, United States
Xiaochun Qin,
University of Jinan, China

****Correspondence:***
Jun He
he_jun@gibh.ac.cn
Ying Zhang
zhangy856@mail.sysu.edu.cn

[†]These authors have contributed equally to this work

Specialty section:
This article was submitted to Microbial Physiology and Metabolism, a section of the journal Frontiers in Microbiology

Received: *15 February 2022*
Accepted: *30 March 2022*
Published: *06 May 2022*

Citation:
Chen M, He Y, Liu D, Tian L, Xu P, Liu X, Pan Y, Dong S, He J and Zhang Y (2022) Structure Insights Into Photosystem I Octamer From Cyanobacteria. Front. Microbiol. 13:876122. doi: 10.3389/fmicb.2022.876122

INTRODUCTION

Photosystem I (PSI) is a light-driven plastocyanin: ferredoxin oxidoreductase with a quantum efficiency close to 100%—probably the most efficient photoelectron converter in nature (Amunts and Nelson, 2009). The function of this bio-macromolecule is highly conserved in cyanobacteria, algae, and plants, yet it carries complicated structural diversities, especially in cyanobacteria. It has been acknowledged for years that the chloroplast PSI-LHCI complex can only form a monomeric state. And this classic theory was challenged by an observation of the spinach thylakoid membrane with atomic force microscopy (AFM) in which PSI-LHCI complexes tend to assemble around each other to form a dimeric supercomplex in dark conditions (Wood et al., 2018). Additionally, an atomic-resolution (2.97 Å) structure of the novel dimeric PSI-LHCI supercomplex was recently resolved in low light-adapted green alga *Chlamydonomas reinhardtii* (Naschberger et al., 2021). Things are more complicated in cyanobacteria in which the PSI complex is assembled as a trimer in most species (Boekema et al., 1987; Kruip et al., 1994; Jordan et al., 2001); meanwhile, the dimer and tetramer have been identified in some heterocyst-forming cyanobacteria and their close unicellular relatives (Li et al., 2014, 2019; Watanabe et al., 2014; Zheng et al., 2019; Chen et al., 2020). Recently, high-resolution structures of PSI monomers with full physiological function were also resolved in some species of unicellular cyanobacteria (Netzer-El et al., 2018; Çoruh et al., 2021). All these studies have indicated that the dynamic oligomeric states of the PSI complex are essential to helping

photosynthetic organisms adapt to changing environments, especially under stress conditions, such as limited light energy supply.

Moreover, by using blue-native PAGE, Li and co-workers observed a possible PSI hexamer in *Chroococcidiopsis* sp. PCC 6712 upon thylakoid membrane extraction (Li et al., 2019). Before that, a projection of two associated PSI tetramers was spotted with single particle analysis in filamentous cyanobacterium *Anabaena* sp. PCC 7120 (here after *Anabaena* 7120; Watanabe et al., 2014). Due to the key role of PSI oligomer states in understanding the photosynthesis mechanism, molecular evidence and structure insights into those higher-ordered PSI oligomer complexes are of significant interest and are highly desired now. Here, two novel oligomer states of the PSI complex were isolated from the low light incubated culture of *Anabaena* 7120. The pure molecules were set into biophysical analysis, and the existence of higher-ordered PSI supercomplexes in cyanobacteria was ultimately demonstrated. By employing cryo-EM single-particle analysis, one of these PSI supercomplexes was subjected to high resolutions structure determination in which a novel molecular interface for PSI complex assembly was detected.

MATERIALS AND METHODS

Species and Growth Conditions

Filamentous cyanobacteria *Anabaena* 7120 (FACHB-418), were purchased from the Institute of Hydrobiology, Chinese Academy of Sciences. Cyanobacterial cells were cultured at 20°C–30°C in BG-II (+N) media. The liquid culture in the flask was incubated under illumination with fluorescent lamps (5–50 $\mu E\, m^{-2}\, s^{-1}$).

Membrane Protein Complexes Isolation

For membrane complex extraction, 150 ml liquid cultures at the logarithmic phase (A_{730} = 1.0–1.3) were harvested at 4,000 *g* centrifugation under 4°C, and cells were washed once in 15 ml pre-cooled buffer A (50 mM HEPES, 10 mM $MgCl_2$, 5 mM $CaCl_2$ and 15 mM NaCl). Cells were then resuspended in 10 ml buffer A and treated with a cycle of 15 min frozen in −80°C refrigerator and 10 min melting at room temperature. Treated cells were harvested at 4,000 *g* centrifugation under 4°C and resuspended in 1.5–3 ml buffer A, and 10% (w/v) of β-DDM were supplemented to the given final concentration for membrane solubilization and complex extraction. The mixture was incubated on ice for 30 min, and insolubilized materials were removed by 14,000 *g* centrifugation under 4°C for 15 min. The supernatants were harvested for supercomplex isolation. For fluorescence emission spectra samples, solubilized supernatant was subjected to sucrose gradient ultracentrifugation (10%–50% (w/v) sucrose in buffer A with 0.03% (w/v) digitonin) at 35,000 rpm (sw41 Ti rotor, Beckman Coulter) for 16 h at 4°C. The band containing PSI tetramers and lower bands were collected with a syringe and directly used for spectroscopic analysis. For single-particle samples, supercomplexes in solubilized supernatants were isolated and collected through a Blue-Native PAGE and re-extraction method.

Blue-Native PAGE and Re-extraction

BN-PAGE was performed in a cold room or a large ice bucket to maintain the low temperature (4°C) during electrophoresis. A Bio-Rad Mini-PROTEAN Tetra Cell (1658006) system was used for mini gel casting and electrophoresis running. The reagents for gel casting, the anode, and cathode native PAGE buffers were prepared according to Wittig's protocol (Wittig et al., 2006). A gradient generator was used to prepare the acrylamide gradient gel. In this study, 3%–10% (w/v) acrylamide gel was selected according to the large molecular weight of megacomplexes. In most cases, 4%–13% (w/v) gels are feasible to separate proteins with molecular weights ranging from 10 to 3,000 kDa, and 3%–13% (w/v) gels are appropriate for separating 10–10,000 kDa protein molecules. Electrophoresis power was generated using a Bio-rad PowerPac TM Basic Power Supply (1645050). In the first stage, cathode buffer B was used, and the power supply was set to 135 V for electrophoresis. Stage two involved exchanging cathode buffer B with cathode buffer B/10 when the samples were moved into a separate gel (approximately 30 min). The running was maintained at 135 V for another 1.5–2 h until acceptable separation efficiency was obtained.

For the re-extraction of proteins, target bands were excised immediately after electrophoresis and stored in an ice-cooled Eppendorf tube. Gel bands were manually homogenized with a glass rod directly into the tube to minimize the loss of protein samples. To prevent heat damage to the protein complex, 10 cycles of 30 s on and 60 s off were programmed for homogenization. The gel slurry was then mixed with re-extraction buffer (buffer A with 0.03% digitonin), and the gel debris was removed by centrifugation at 14,000 × *g* for 15 min at 4°C. The supernatant was subjected to a second run of BN-PAGE for purity and integrity check and concentrated to qualified concentration with a 100 kDa cut-off Millipore membrane filter (UFC5100BK) for single-particle analysis.

Cryo-EM and Image Processing

Three microliters of purified PSI supercomplex were applied onto glow-discharged holey carbon grids (Cu Quantifoil R1.2/1.3) at a protein concentration of approximately 2.5 mg/ml, prior to vitrification using a Vitrobot MKIV (3.0 s blot 5, 4°C, 100% humidity). The images were collected in 17 different sessions on a 200 kV FEI Titan Krios electron microscope (50 μm C2 aperture). A Gatan K3-Summit detector was used in counting mode at a magnification of 45,000 (yielding a pixel size of 0.88 Å), and a dose rate of 30 electrons per pixel per second. Exposures of 1.618 s (yielding a total dose of 63 $eÅ^{-2}$). SerialEM was used to collect a total of 23,491 images, which were fractionated into 27 movie frames with defocus values ranging from 1.5 to 2.5 μm. All datasets were processed separately by using the same procedure. Collected micrographs were corrected for local-frame movement and dose-filtered using Motioncor2 (Zheng et al., 2017). The contrast transfer function parameters were estimated using Gctf (Zhang, 2016). In total, 184,882 particles were auto picked using warp, and they were subjected to reference-free two-dimensional class averaging in Relion 3.0.8 (Zivanov et al., 2018). After 2D

classification, 100 k good particles were generated in which top-views were divided into 10 subsets. Each subset was combined with the side-view separately for the 3D map refinement in cryoSPARC (Punjani et al., 2017), yielding a map at an overall resolution of 7.0 Å. No symmetry was applied during the final processing, as it did not improve the map. The reported resolutions are based on 3D refinement by applying a 0.143 criterion on the FSC between reconstructed half-maps. All figures were generated using PyMOL (DeLano, 2002) and Chimaera X (Goddard et al., 2018). A local resolution map was generated using the cryoSPARC.

Negative Staining EM and Data Processing

The purified PSI tetramer and supercomplexes were adjusted to 0.15, 0.19, and 0.27 mg/ml protein, respectively. In all cases, 3 µl of the protein solution was loaded on the glow-discharged copper grid. The excess protein solution was blotted with filter paper. The grid was washed twice with distilled water and then stained with 0.75% (w/v) uranyl formate for 30 s. The stain solution was blotted and the grid was dried in air. The grids were examined using a Tecnai G2 Spirit electron microscopy under 120 kV accelerating voltage. Micrographs were recorded with a CCD camera at a normal magnification of 49,000× with a variation of defocus values from −1.5 to −2.5 µm, resulting in a pixel size of 4.3 Å at specimen level. In total, 34, 16, and 18 images were manually collected for the PSI tetramer, supercomplex 1 and supercomplex 2, respectively. In total, 359, 2,518, and 822 particles were manually picked and were proceeded to a reference-free two-dimensional class averaging using Relion 3.0.8.

Steady-State Fluorescence Spectroscopy

Fluorescence emission spectra were recorded on a FLS1000 Photoluminescence Spectrometer (Edinburgh). The sample OD at the maximum emission in the red region of the spectrum was adjusted 0.05 for fluorescence measurements. A bandwidth of 3 nm was used for both excitation and emission, and the step size was 1 nm. An optical long-pass filter (590 nm) was placed before the detector to remove scattered light.

RESULTS AND DISCUSSION

Discovery of Higher-Ordered PSI Complexes

Blue-native PAGE has been recognized as a powerful tool to investigate thylakoid membrane complexes (Wittig et al., 2006; Järvi et al., 2011). The bands corresponding to complexes of high molecular weight suggest the existence of higher-order oligomeric states of photosynthetic membrane complexes currently undefined, especially for PSI assembled hetero- or homo- complexes (Zhang et al., 2010; Järvi et al., 2011; Kouřil et al., 2018).

As shown in **Figure 1Aa$_1$**, two undescribed complexes (supercomplex 1 and 2), both larger than the PSI-tetramer (1,400 kDa), were extracted from *Anabaena* 7120 using 1% (w/v) β-DDM and subsequently separated on BN-PAGE gel. The naturally green color of the bands indicates that these are chlorophyll-containing complexes, most likely the PSI-assembled complexes. To verify this hypothesis, the complexes were separated and harvested through sucrose gradient ultracentrifugation. The fraction scattering in sucrose gradients (**Figure 1Aa$_2$**) is highly consistent with the gradient gel results in the BN-PAGE experiment (**Figure 1Aa$_1$**). The fractions corresponding to supercomplex 1 and supercomplex 2 were collected and subjected to low temperature (77 K) fluorescence spectra measurement under the excitation of the 430 nm, and the PSI tetramer fraction was also harvested for comparison. As shown in **Figure 1B**, the emission spectra of supercomplexes 1 and 2 peaked at ~730 nm, largely overlapping with the one of PSI tetramer. Their emission spectra showed that the lowest energy level of quantum yield of chlorophylls in PSI remained ~730 nm, indicating that the red forms of chlorophylls were not energetically altered. This fluorescence spectral characteristic strongly suggests that these two complexes are both PSI homogenous supercomplexes (Watanabe et al., 2014; Lamb et al., 2018; Chen et al., 2020).

For a closer look at the molecules, the complexes were subjected to negative staining electron microscopy (EM) analysis. While the homogeneity of particles from all three samples is acknowledged (**Figures 1Cc$_1$–c$_3$**), the remarkable diversity in particle size from different samples is also revealed by negative staining EM. We subsequently used the single particle analysis (SPA) approach to check the oligomeric states of various samples. Using the high-resolution structure of the PSI tetramer as a reference (Kato et al., 2019; Zheng et al., 2019; Chen et al., 2020), particles in micrograph **Figure 1Cc$_1$** are generated as tilted views of the PSI tetramer. Over 90% of the particles presented a top-view (yellow circles) orientation parallel to the thylakoid membrane plane, while about 9.5% of them are side views (red circles). The contribution of the top and side views is consistent with those previously reported (Watanabe et al., 2014). For the samples of supercomplex 1 and supercomplex 2, the particle morphology in the images indicated that these proteins are PSI higher-ordered oligomeric complexes (**Figures 1Cc$_2$,c$_3$**).

To further characterize the molecular architectures, three datasets were collected for the PSI tetramer, supercomplex 1, and supercomplex 2, respectively, from which particles were manually picked. Particles were then used for pre-processing and 2D classification, and the most dominant averages are shown as the enlarged part in the bottom right corner of **Figures 1Cc$_1$–c$_3$**. From these closer views, it is strongly suggested that supercomplex 1 is a PSI hexamer consisting of a tetramer and a dimer, while supercomplex 2 is a PSI octamer formed by two assembled tetramers, which agrees with the previous results (Watanabe et al., 2014). This conclusion is supported by a rigid fitting of PSI tetramer and dimer models over the 2D map of the complexes, respectively (**Figure 1D**). By comparison to the PSI tetramer, the PSI hexamer can be identified as a complex arranged with a tetramer and dimer with substantial confidence. However, it is ambiguous to identify the interface for the linkage of the PSI tetramer and dimer in such a

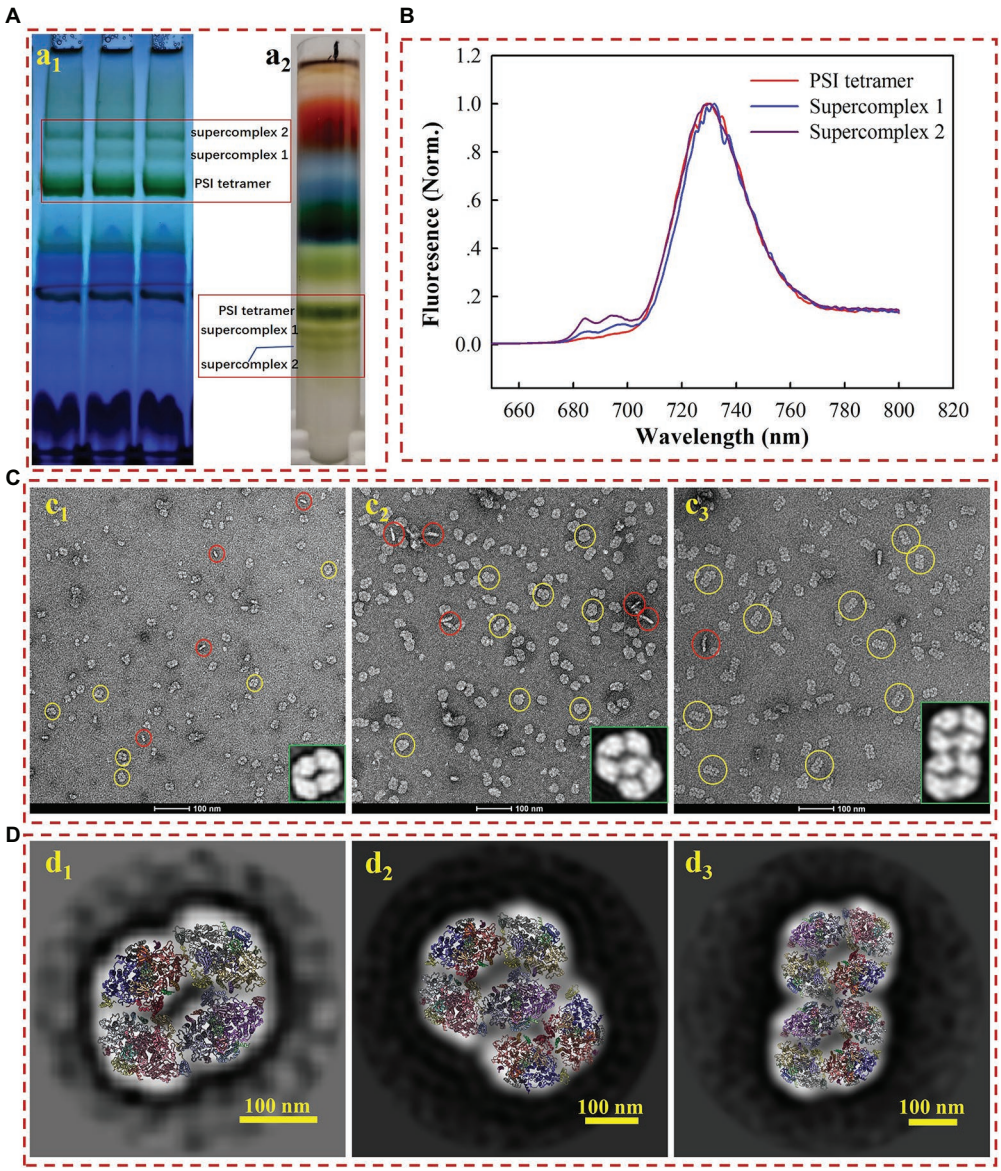

FIGURE 1 | Biochemical **(A)** and biophysical **(B–D)** characterization of the PSI tetramer, supercomplex 1, and supercomplex 2. **(a_1)** Membrane crude extracts were loaded on BN-PAGE at a total amount of 9–12 μg chlorophyll a for each lane; **(a_2)** membrane crude extracts were loaded on sucrose gradient ultracentrifugation for the separation of PSI tetramer and supercomplexes. **(B)** Low temperature (77 k) fluorescence emission detection of PSI tetramer (red line), supercomplex 1 (blue line), and supercomplex 2 (purple line). **(C)** Negative staining electron microscopy image of PSI tetramer **(c_1)** supercomplex 1 **(c_2)** and supercomplex 2 **(c_3)**. The yellow and red circles indicate the top and side views, respectively. The enlarged image in the right corner shows the 2D averages of the most contributed particles. **(D)** The average 2D model-fitted maps of the PSI tetramer **(d_1)** supercomplex 1 **(d_2)** and supercomplex 2 **(d_3)**.

low-resolution map. Furthermore, from the fitted model (**Figure 1Dd_2**), the PsaL-PsaA, PsaK-PsaK, and PsaM-PsaF interfaces should be addressed in further studies providing high-resolution details. The PSI octamer revealed in **Figure 1Dd_3** is a supercomplex assembled though a 'side by side' arrangement of two tetramers, the fitted model reveals the possible interfaces of PsaA-PsaF, PsaK-PsaK, and PsaB-PsaK. Studies providing a high-resolution structure would also be appreciated to investigate the detailed molecule basis for the intra- and inter-connection of these supercomplexes.

Cryo-EM Structure of the PSI Octamer Complex

In our experiments, the *in vitro* safety and stabilities of the PSI octamer are better than those of the hexamer; for this reason, a near-atomic resolution structure of stable PSI octamers was resolved by cryo-EM single-particle analysis in the present study. For maximal harvests and minimal destruction to the PSI octamer, the Native-PAGE-based purifying method was applied for sample purification. The whole process for concentrated pure samples preparation was completed in only

6–8 h, and the fresh molecules were then frozen immediately for cryo-EM single-particle analysis. Protein samples with a concentration of approximately 3 mg/ml were loaded onto the grids for frozen and quality evaluations. Initially, very few particles could be observed in the hole of the ice layer, while most of them clumped together around the carbon edge (**Figure 2Aa$_1$**). To help particles move into the hole, an extra detergent, fos-choline 8, was added to the sample immediately just before the blotting. A significantly improved distribution of particles in the holes was obtained, with approximately 30 particles per micrograph (**Figure 2Aa$_2$**). However, the presence of random orientations is a challenge when considering the surface charge of the complex. By optimizing the wait time between sample loading and blotting, we improved the distribution of the side view by approximately 10% (**Figure 2Aa$_3$**). The preferential orientation issue is dependent on the biological specimen, and many options may proceed on a case-by-case basis (Tan et al., 2017; Han et al., 2020; Sorzano et al., 2021). If the particles are two linked PSI tetramers, then the preferential orientation is relatively inevitable as the hydrophilic area of the top view is as large as around 1,000 nm^2, while it is less than 200 nm^2 for the side view (**Supplementary Figure 1**). Additionally, top views have a much higher probability of being absorbed and face the air-water interface when a sample is blotted and frozen (Noble et al., 2018).

As revealed in **Supplementary Figure 2**, after 2D classification and screening, about 100 k good particles were randomly separated into 10 datasets and screened for 3D reconstruction and structure determination, respectively, in cryoSPARC.

Reconstruction of this complex proceeded without applying symmetry (C1) from homogenous particle subsets. Non-uniform refinement from 12,121 particles of subset 5 generated a map at the overall resolution of 7.0 Å and the highest local resolution of 6.0 Å (**Supplementary Figure 3**). As shown in **Figure 2B**, the molecular sizes of PSI octamers are 40.6, 25.7, and 9.8 nm

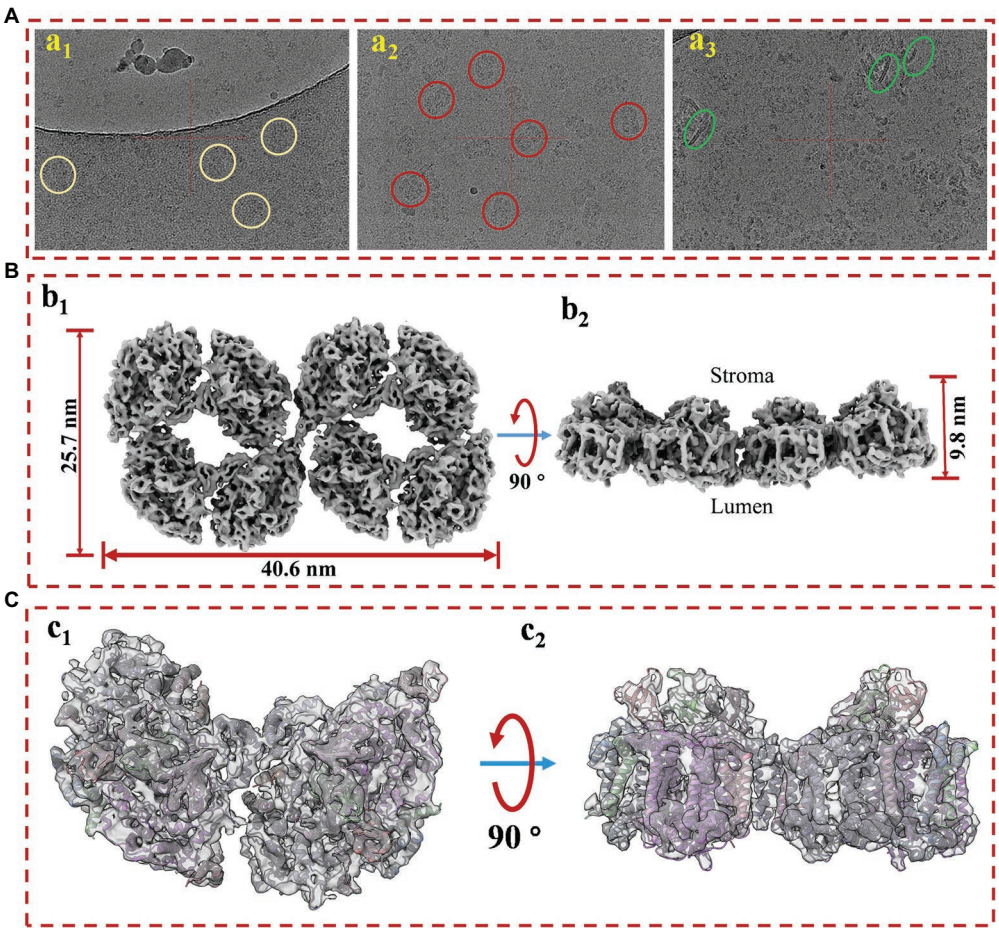

FIGURE 2 | The cryo-EM sample prep optimization and structure determination of PSI supercomplex 2. **(A)** Optimization of cryo-EM sample. **(a$_1$)** The protein particles were blotted immediately after sample loading; **(a$_2$)** detergent fos-coline-8 was supplemented into the protein sample at a final concentration of 1.0 mM around 5 s before blotting; **(a$_3$)** additional 3 s of waiting time were introduced between the loading and blotting of fos-choline-8 mixed sample. **(B)** Top **(b$_1$)** and side **(b$_2$)** views of the refined 3D density map of PSI supercomplex 2. **(C)** Model and map fitting for structure comparison of cyanobacterial PSI dimer and the supercomplex. Top **(c$_1$)** and side **(c$_2$)** views of model fitting of PSI dimer into the density map. The model used for fitting is a published PSI dimer structure (PDB code: 6K61) from *Anabaena* sp. PCC 7120.

for length, width, and height, respectively. The overall shape of the map strongly suggested that this megacomplex is a PSI oligomer synclastic arranged by two tetramers linked side by side, which first proved that the complex is a PSI octamer structurally. To verify this conclusion, a PSI dimer model was fitted into a part of the map (**Figures 2Cc_1,c_2**). The secondary structures in both the transmembrane and out membrane region (lumen and stroma sides) can be fitted perfectly into the densities.

Interestingly, a density of interface for linkage was objectively reconstructed in this map. As shown in **Supplementary Figure 4**, the density (red frame) is consistent with the threshold levels, and the firmness is stronger than the interfaces that form dimers (green frame) and tetramers (light blue frame). It is indicated that the newly identified PSI octamer is a physiologically relevant megacomplex rather than a random aggregation during sample preparation. This solid evidence was then obtained from the biochemical characterizations of PSI octamers from cells growing in changing physiological conditions. As shown in **Supplementary Figure 5**, by native-PAGE characterization of cells that incubated in different light conditions, the PSI octamer is a low-light responded supercomplex in *Anabaena* sp. PCC 7120. The result agrees with the conclusion from Wood's work published in 2018 in which tighter packing of PSI complexes was detected in the dark (Wood et al., 2018). To find the possible interfaces for the assembly of two tetramers, separated PSI tetramer models were fitted rigorously into the map with the ChimeraX program. As shown in **Figure 3**, an interaction between PsaK subunits from two linked PSI tetramers was found in the fitted model (**Figure 3A**). As revealed in **Figure 3B**, two residues, Lys52 and Phe53, of PsaK from tetramer 1 (T1) interacted with the same residues from tetramer 2 (T2) with each other. This novel interface should be a major contribution to stabilizing PSI octamer. In summary, the map is qualified to be applied to perform rigid-body fitting with an atomic model when more structural details are required to be revealed. On the other hand, this map is reconstructed with datasets collected from the 200 kV microscope, and higher resolution is expected by using a zero-loss energy filter equipped detector. The resolution can also be theoretically significantly improved with a 300 kV microscope.

Higher-ordered PSI oligomers are physiologically relevant megacomplexes rather than random aggregations during sample preparation. For instance, in this study, the PSI octamer was strongly suggested as a low-light responded

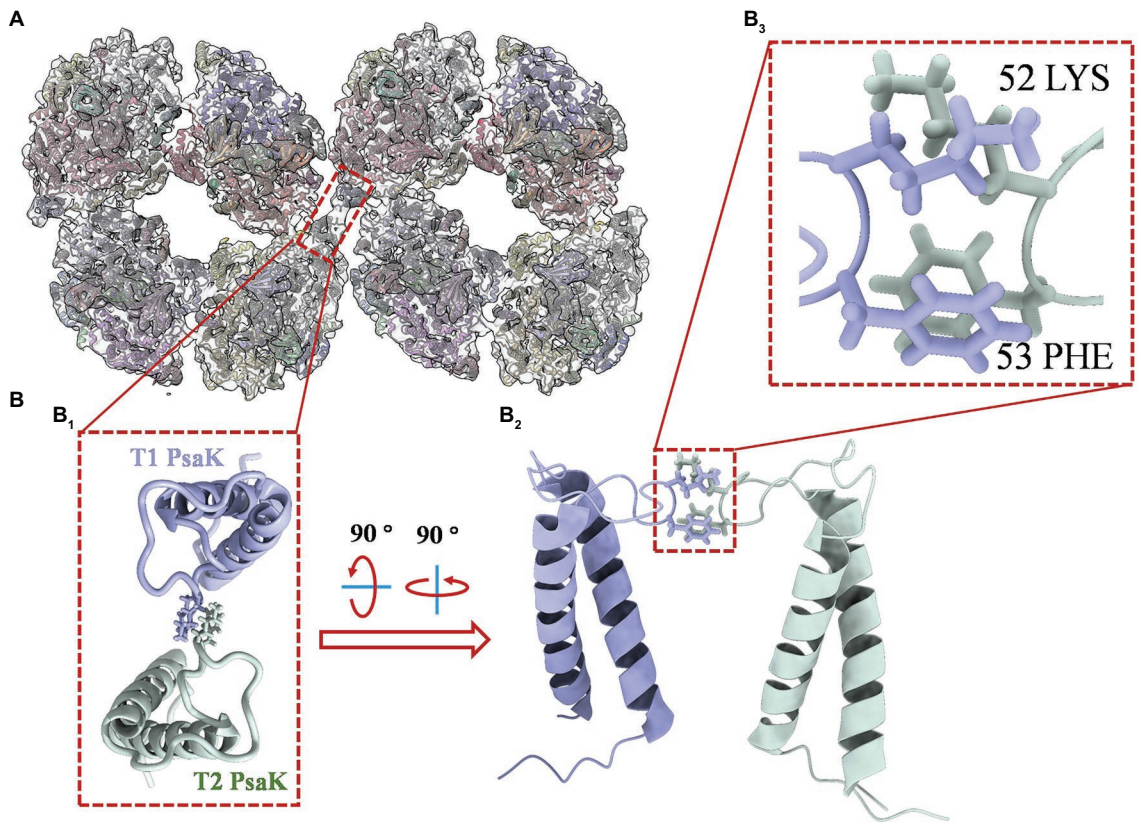

FIGURE 3 | Structure details of PsaK-PsaK interaction in PSI octamer supercomplex. **(A)** Overall view of the interface location in the complex (top view from the stromal side). The original structure applied for fitting is the PSI tetramer model (PDB code: 6TCL) from *Anabaena* sp. PCC 7120. **(B)** Close-up view of structural details indicated in **(B_1)**. The enlarged top view of two PsaK subunits from the assembled PSI tetramers (T1 and T2), the interacted amino acids were shown as stick form. **(B_2)** Tilted side view of interacted PsaK subunits. **(B_3)** The focus view of intact amino acids Lys52 and Phe53 in PsaK subunits.

super complex in *Anabaena* sp. PCC 7120 (results shown in **Supplementary Figure 5**). A similar conclusion was presented by Wood's observation through atomic force microscopy in which tighter packing of chloroplast PSI complexes is more abundant in the dark (Wood et al., 2018). And the super high-resolution structure of such a tight-packed chloroplast PSI oligomer was resolved very recently (Naschberger et al., 2021). A novel type of interface for connection between PSI monomers was structurally detected and genetically solidified. It has been demonstrated that the remodeling of photosynthetic machinery on the thylakoid membrane would happen in the low-light-adapted chloroplast (Wood et al., 2018). The dimeric PSII supercomplex has both a larger relative physical antenna size and higher relatively light-harvesting efficiency (Kirchhoff et al., 2007; Kim et al., 2020). And dimeric PSI-LHCI supercomplex was also found to be associated with higher cyclic electron transfer (Wood et al., 2018), which will help cells produce ATP more efficiently under stress. PSI-assembled heterogeneous or homogenous supercomplexes have frequently been detected biochemically in previous studies (Zhang et al., 2010; Järvi et al., 2011; Kouřil et al., 2018); here, we isolated two supercomplexes and set up biophysical characterizations of the molecules. Taking the evidence from low-temperature fluorescence and negative staining EM, we concluded that these two complexes are the PSI hexamer and PSI octamer, respectively. To our knowledge, this is the first study to isolate such higher-ordered PSI complexes in photosynthetic organisms, paving the way for a better understanding of the molecular architecture and physiological functions of each type of photosystem oligomers. Additionally, the cryo-EM structure of PSI octamer revealed a novel molecular interface (PsaK-PsaK) for PSI assembly in photosynthetic organisms.

DATA AVAILABILITY STATEMENT

The original contributions presented in the study are included in the article/**Supplementary Material**; further inquiries can be directed to the corresponding authors.

AUTHOR CONTRIBUTIONS

MC, PX, and YZ designed the research. YH, MC, DL, and QS performed the research and data curation under the supervision of LT and JH. MC wrote the manuscript with adding from YH, YP, and DL. YZ, LT, QS, and JH analyzed the data and edited the manuscript. JH and YZ supported the research with funding acquisition. All authors read and approved the manuscript.

FUNDING

This work was supported by China Postdoctoral Science Foundation (grant no. 2020T130747), National Natural Science Foundation of China (31900429), Shenzhen Sanming Project of Medicine (SZSM201911003), Shenzhen Science Technology and Innovation Commission (SZSTI) Basic Research Program (JCYJ20190809165417340) and by 100 Top Talents Program of Sun Yat-sen University (grant no. 392009).

SUPPLEMENTARY MATERIAL

The Supplementary Material for this article can be found online at: https://www.frontiersin.org/articles/10.3389/fmicb.2022.876122/full#supplementary-material

REFERENCES

Amunts, A., and Nelson, N. (2009). Plant photosystem I design in the light of evolution. *Structure* 17, 637–650. doi: 10.1016/j.str.2009.03.006

Boekema, E. J., Dekker, J. P., van Heel, M. G., Rögner, M., Saenger, W., Witt, I., et al. (1987). Evidence for a trimeric organization of the photosystem I complex from the thermophilic cyanobacterium *Synechococcus* sp. *FEBS Lett.* 217, 283–286. doi: 10.1016/0014-5793(87)80679-8

Chen, M., Perez-Boerema, A., Zhang, L., Li, Y., Yang, M., Li, S., et al. (2020). Distinct structural modulation of photosystem I and lipid environment stabilizes its tetrameric assembly. *Nat. Plants* 6, 314–320. doi: 10.1038/s41477-020-0610-x

Çoruh, O., Frank, A., Tanaka, H., Kawamoto, A., El-Mohsnawy, E., Kato, T., et al. (2021). Cryo-EM structure of a functional monomeric photosystem I from *Thermosynechococcus elongatus* reveals red chlorophyll cluster. *Commun. Biol.* 4:304. doi: 10.1038/s42003-021-01808-9

DeLano, W. L. (2002). Pymol: an open-source molecular graphics tool. *CCP4 Newsletter Pro. Crystallogr.* 40:11.

Goddard, T. D., Huang, C. C., Meng, E. C., Pettersen, E. F., Couch, G. S., Morris, J. H., et al. (2018). UCSF ChimeraX: meeting modern challenges in visualization and analysis. *Protein Sci.* 27, 14–25. doi: 10.1002/pro.3235

Han, Y., Fan, X., Wang, H., Zhao, F., Tully, C. G., Kong, J., et al. (2020). High-yield monolayer graphene grids for near-atomic resolution cryoelectron microscopy. *Proc. Natl. Acad. Sci. U. S. A.* 117, 1009–1014. doi: 10.1073/pnas.1919114117

Järvi, S., Suorsa, M., Paakkarinen, V., and Aro, E.-M. (2011). Optimized native gel systems for separation of thylakoid protein complexes: novel super- and mega-complexes. *Biochem. J.* 439, 207–214. doi: 10.1042/BJ20102155

Jordan, P., Fromme, P., Witt, H. T., Klukas, O., Saenger, W., and Krauß, N. (2001). Three-dimensional structure of cyanobacterial photosystem I at 2.5 Å resolution. *Nature* 411, 909–917. doi: 10.1038/35082000

Kato, K., Nagao, R., Jiang, T.-Y., Ueno, Y., Yokono, M., Chan, S. K., et al. (2019). Structure of a cyanobacterial photosystem I tetramer revealed by cryo-electron microscopy. *Nat. Commun.* 10:4929. doi: 10.1038/s41467-019-12942-8

Kim, E., Watanabe, A., Duffy, C. D. P., Ruban, A. V., and Minagawa, J. (2020). Multimeric and monomeric photosystem II supercomplexes represent structural adaptations to low- and high-light conditions. *J. Biol. Chem.* 295, 14537–14545. doi: 10.1074/jbc.RA120.014198

Kirchhoff, H., Haase, W., Wegner, S., Danielsson, R., Ackermann, R., and Albertsson, P. A. (2007). Low-light-induced formation of semicrystalline photosystem II arrays in higher plant chloroplasts. *Biochemistry* 39, 11169–11176. doi: 10.1021/bi700748y

Kouřil, R., Nosek, L., Semchonok, D., Boekema, E., and Ilík, P. J. S.-C. B. (2018). "Organization of plant photosystem II and photosystem I supercomplexes," in *Membrane Protein Coomplexes: Structure and Function. Subcellular Biochemistry*. eds. J. Harris and E. Boekema *Vol. 87*. (Singapore: Springer).

Kruip, J., Bald, D., Boekema, E., and Rögner, M. (1994). Evidence for the existence of trimeric and monomeric photosystem I complexes in thylakoid

membranes from cyanobacteria. *Photosynth. Res.* 40, 279–286. doi: 10.1007/BF00034777

Lamb, J. J., Røkke, G., and Hohmann-Marriott, M. F. (2018). Chlorophyll fluorescence emission spectroscopy of oxygenic organisms at 77 K. *Photosynthetica* 56, 105–124. doi: 10.1007/s11099-018-0791-y

Li, M., Calteau, A., Semchonok, D. A., Witt, T. A., Nguyen, J. T., Sassoon, N., et al. (2019). Physiological and evolutionary implications of tetrameric photosystem I in cyanobacteria. *Nat. Plants* 5, 1309–1319. doi: 10.1038/s41477-019-0566-x

Li, M., Semchonok, D. A., Boekema, E. J., and Bruce, B. D. (2014). Characterization and evolution of tetrameric photosystem I from the thermophilic cyanobacterium *Chroococcidiopsis* sp TS-821. *Plant Cell* 26, 1230–1245. doi: 10.1105/tpc.113.120782

Naschberger, A., Mosebach, L., Tobiasson, V., Kuhlgert, S., Scholz, M., Perez-Boerema, A., et al. (2021). Chloroplast photosystem I dimer and high resolution model of the complex with plastocyanin. bioRxiv [Preprint]. doi: 10.1101/2021.08.30.458224

Netzer-El, S. Y., Caspy, I., and Nelson, N. (2018). Crystal structure of photosystem I monomer from *Synechocystis* PCC 6803. *Front. Plant Sci.* 9:1865. doi: 10.3389/fpls.2018.01865

Noble, A. J., Wei, H., Dandey, V. P., Zhang, Z., Tan, Y. Z., Potter, C. S., et al. (2018). Reducing effects of particle adsorption to the air–water interface in cryo-EM. *Nat. Methods* 15, 793–795. doi: 10.1038/s41592-018-0139-3

Punjani, A., Rubinstein, J. L., Fleet, D. J., and Brubaker, M. A. (2017). cryoSPARC: algorithms for rapid unsupervised cryo-EM structure determination. *Nat. Methods* 14, 290–296. doi: 10.1038/nmeth.4169

Sorzano, C. O. S., Semchonok, D., Lin, S. C., Lo, Y. C., Vilas, J. L., Jiménez-Moreno, A., et al. (2021). Algorithmic robustness to preferred orientations in single particle analysis by CryoEM. *J. Struct. Biol.* 213:107695. doi: 10.1016/j.jsb.2020.107695

Tan, Y. Z., Baldwin, P. R., Davis, J. H., Williamson, J. R., Potter, C. S., Carragher, B., et al. (2017). Addressing preferred specimen orientation in single-particle cryo-EM through tilting. *Nat. Methods* 14, 793–796. doi: 10.1038/nmeth.4347

Watanabe, M., Semchonok, D. A., Webber-Birungi, M. T., Ehira, S., Kondo, K., Narikawa, R., et al. (2014). Attachment of phycobilisomes in an antenna–photosystem I supercomplex of cyanobacteria. *Proc. Natl. Acad. Sci. U.S.A.* 111, 2512–2517. doi: 10.1073/pnas.1320599111

Wittig, I., Braun, H.-P., and Schägger, H. (2006). Blue native PAGE. *Nat. Protoc.* 1, 418–428. doi: 10.1038/nprot.2006.62

Wood, W. H. J., MacGregor-Chatwin, C., Barnett, S. F. H., Mayneord, G. E., Huang, X., Hobbs, J. K., et al. (2018). Dynamic thylakoid stacking regulates the balance between linear and cyclic photosynthetic electron transfer. *Nat. Plants* 4, 116–127. doi: 10.1038/s41477-017-0092-7

Zhang, K. (2016). Gctf: real-time CTF determination and correction. *J. Struct. Biol.* 193, 1–12. doi: 10.1016/j.jsb.2015.11.003

Zhang, Y., Chen, M., Church, W. B., Lau, K. W., Larkum, A. W. D., and Jermiin, L. S. (2010). The molecular structure of the IsiA–photosystem I supercomplex, modelled from high-resolution, crystal structures of photosystem I and the CP43 protein. *Biochim. Biophys. Acta Bioenerg.* 1797, 457–465. doi: 10.1016/j.bbabio.2010.01.002

Zheng, L., Li, Y., Li, X., Zhong, Q., Li, N., Zhang, K., et al. (2019). Structural and functional insights into the tetrameric photosystem I from heterocyst-forming cyanobacteria. *Nat. Plants* 5, 1087–1097. doi: 10.1038/s41477-019-0525-6

Zheng, S. Q., Palovcak, E., Armache, J.-P., Verba, K. A., Cheng, Y., and Agard, D. A. (2017). MotionCor2: anisotropic correction of beam-induced motion for improved cryo-electron microscopy. *Nat. Methods* 14, 331–332. doi: 10.1038/nmeth.4193

Zivanov, J., Nakane, T., Forsberg, B. O., Kimanius, D., Hagen, W. J. H., Lindahl, E., et al. (2018). New tools for automated high-resolution cryo-EM structure determination in RELION-3. *eLife* 7:e42166. doi: 10.7554/eLife.42166

Conflict of Interest: The authors declare that the research was conducted in the absence of any commercial or financial relationships that could be construed as a potential conflict of interest.

Publisher's Note: All claims expressed in this article are solely those of the authors and do not necessarily represent those of their affiliated organizations, or those of the publisher, the editors and the reviewers. Any product that may be evaluated in this article, or claim that may be made by its manufacturer, is not guaranteed or endorsed by the publisher.

frontiers | Frontiers in Microbiology

ORIGINAL RESEARCH
published: 25 May 2022
doi: 10.3389/fmicb.2022.891895

Patterning of the Autotrophic, Mixotrophic, and Heterotrophic Proteomes of Oxygen-Evolving Cyanobacterium *Synechocystis* sp. PCC 6803

*Dorota Muth-Pawlak, Sanna Kreula, Peter J. Gollan, Tuomas Huokko, Yagut Allahverdiyeva and Eva-Mari Aro**

Laboratory of Molecular Plant Biology, Department of Life Technologies, University of Turku, Turku, Finland

OPEN ACCESS

Edited by:
Luning Liu,
University of Liverpool,
United Kingdom

Reviewed by:
Dmitry A. Los,
Timiryazev Institute of Plant Physiology (RAS), Russia
Klaas Jan Hellingwerf,
University of Amsterdam, Netherlands

****Correspondence:***
Eva-Mari Aro
evaaro@utu.fi

Specialty section:
This article was submitted to Microbial Physiology and Metabolism, a section of the journal Frontiers in Microbiology

Received: *08 March 2022*
Accepted: *25 March 2022*
Published: *25 May 2022*

Citation:
Muth-Pawlak D, Kreula S, Gollan PJ, Huokko T, Allahverdiyeva Y and Aro E-M (2022) Patterning of the Autotrophic, Mixotrophic, and Heterotrophic Proteomes of Oxygen-Evolving Cyanobacterium Synechocystis sp. PCC 6803. Front. Microbiol. 13:891895. doi: 10.3389/fmicb.2022.891895

Proteomes of an oxygenic photosynthetic cyanobacterium, *Synechocystis* sp. PCC 6803, were analyzed under photoautotrophic (low and high CO_2, assigned as ATLC and ATHC), photomixotrophic (MT), and light-activated heterotrophic (LAH) conditions. Allocation of proteome mass fraction to seven sub-proteomes and differential expression of individual proteins were analyzed, paying particular attention to photosynthesis and carbon metabolism–centered sub-proteomes affected by the quality and quantity of the carbon source and light regime upon growth. A distinct common feature of the ATHC, MT, and LAH cultures was low abundance of inducible carbon-concentrating mechanisms and photorespiration-related enzymes, independent of the inorganic or organic carbon source. On the other hand, these cells accumulated a respiratory NAD(P)H dehydrogenase I (NDH-1_1) complex in the thylakoid membrane (TM). Additionally, in glucose-supplemented cultures, a distinct NDH-2 protein, NdbA, accumulated in the TM, while the plasma membrane-localized NdbC and terminal oxidase decreased in abundance in comparison to both AT conditions. Photosynthetic complexes were uniquely depleted under the LAH condition but accumulated under the ATHC condition. The MT proteome displayed several heterotrophic features typical of the LAH proteome, particularly including the high abundance of ribosome as well as amino acid and protein biosynthesis machinery-related components. It is also noteworthy that the two equally light-exposed ATHC and MT cultures allocated similar mass fractions of the total proteome to the seven distinct sub-proteomes. Unique trophic condition-specific expression patterns were likewise observed among individual proteins, including the accumulation of phosphate transporters and polyphosphate polymers storing energy surplus in highly energetic bonds under the MT condition and accumulation under the LAH condition of an enzyme catalyzing cyanophycin biosynthesis. It is concluded that the rigor of cell growth in the MT condition results, to a great extent, by combining photosynthetic activity with high intracellular inorganic carbon conditions created upon

glucose breakdown and release of CO_2, besides the direct utilization of glucose-derived carbon skeletons for growth. This combination provides the MT cultures with excellent conditions for growth that often exceeds that of mere ATHC.

Keywords: photoautotrophy, heterotrophy, photomixotrophy, photosynthesis, carbon metabolism, environmental acclimation, proteomics

INTRODUCTION

Photosynthetic organisms use light as a source of energy for CO_2 assimilation, thereby storing light energy into chemical bonds of organic molecules. Nevertheless, several photosynthetic organisms, particularly those from aquatic environments, also possess a capacity for heterotrophic growth or for combining the photoautotrophic (hereafter autotrophic) and heterotrophic traits in a metabolic strategy known as photomixotrophy (hereafter mixotrophy). This capacity can also be used as an asset for fast acclimation of aquatic photosynthetic organisms to changes in environmental conditions, including light intensity and temperature conditions, but particularly to the availability of CO_2 and other forms of carbon that drastically modulate cell photosynthetic efficiency and growth potential. Metabolic changes that allow for flexibility in the use of carbon from the environment, thereby driving mixotrophy and/or autotrophy strategies, are still poorly understood. Despite several metabolomes (Knoop et al., 2013; Yoshikawa et al., 2013; Nakajima et al., 2014; You et al., 2014; Wan et al., 2017), proteomes (Plohnke et al., 2015; Fang et al., 2017; Toyoshima et al., 2020), and transcriptomes (Yoshikawa et al., 2013; You et al., 2015) studies with model photosynthetic microorganisms, like the prokaryotic cyanobacterium *Synechocystis* sp. PCC 6803 (hereafter *Synechocystis*) investigated here, the choice and regulation of the bioenergetic and metabolic pathways prevailing under a particular trophic mode have remained poorly understood, mainly because of the complexity of experimental questions and designs involved in the deeper elucidation of different trophic strategies. Cyanobacteria are the only prokaryotes capable of oxygenic photosynthesis, and, although the comparison of their metabolism with that of the best investigated heterotrophic bacterium *Escherichia coli* has revealed distinct differences, it has also highlighted numerous knowledge gaps concerning the functionality of cyanobacterial metabolism (Mills et al., 2020).

During the past decade, cyanobacteria have attracted special attention as potential future photosynthetic cell factories, which, *via* synthetic biology approaches, will be engineered to efficiently convert solar energy into useful chemicals and fuels (Gangl et al., 2015; Aro, 2016; Lea-Smith and Howe, 2017; Lindblad et al., 2019; Santos-Merino et al., 2019; Liu et al., 2022). The capability of cyanobacteria to adopt different trophic strategies is used as an asset in enhancing productivity in photosynthetic cell factories and different co-culture designs, for example, with yeast (Song et al., 2014; Hays et al., 2017; Ai et al., 2021). Nevertheless, the prevalence and modulations of different metabolic and bioenergetic routes under different trophic conditions have remained rather undefined. However, this knowledge is extremely relevant for the design and implementation of new biotechnology methods when endogenous cell metabolism should be fluently integrated with newly introduced metabolic traits in photosynthetic microorganisms.

Flux of energy for cellular needs is the key difference among different trophic growth modes. Autotrophic traits of harvesting and transduction of light energy in cyanobacteria are confined to the thylakoid membrane (TM), while respiratory pathways are present in both the TM and the plasma membrane (PM) (Schultze et al., 2009; Mullineaux, 2014). The extent to which these pathways are modified in different trophic modes (Plohnke et al., 2015; Huokko et al., 2017, 2019), has not been thoroughly investigated. Similarly, the carbon assimilation and hydrocarbon catabolic pathways as well as many other pathways of central metabolism are expected to be modulated depending on trophic growth condition.

Synechocystis glucose-tolerant strain is one of the most extensively investigated cyanobacterial species. In addition to autotrophic (AT) and mixotrophic (MT) growth, *Synechocystis* is capable of light-activated heterotrophic (LAH) growth in darkness, provided that cells are supplemented with a short light period every 24 h (Anderson and McIntosh, 1991). Here, we performed a comparative proteomics study to dissect proteins and corresponding pathways that are important specifically for AT, MT, and LAH strategies in support of *Synechocystis* growth at a similar OD_{750} close to 1. Additionally, the availability of inorganic carbon (C_i) as CO_2 at low (0.04%, ATLC) or high (3%, ATHC) levels was investigated under autotrophy. With respect to the general availability of carbon, the ATHC, MT, and LAH trophic conditions were collectively called carbon-rich conditions irrespective of organic or inorganic origin, whereas ATLC represented the natural low-carbon reference condition. LAH, on the contrary, was the only condition with strongly limited availability of light, whereas the other trophic strategies were provided with equivalent irradiance conditions.

MATERIALS AND METHODS

Cultivation Conditions

In this study, we used the glucose-tolerant cyanobacterial strain *Synechocystis* sp. PCC 6803. Pre-experimental cultures were grown in a BG11 medium buffered with 20 mM HEPES-NaOH (pH 7.5) under continuous white light of 50 μmol photons m^{-2} s^{-1} at 30°C, under air enriched with 3% CO_2 with agitation at 150 rpm for 3 days. Experimental cultures were inoculated at OD_{750} = 0.1 in a 100-ml fresh BG11 medium buffered with 20 mM HEPES-NaOH (pH 7.5) and agitated in 250-ml Erlenmeyer flasks at 150 rpm in AlgaeTron AG130 (PSI Instruments, Czech) cool-white LED growth chambers at 30°C. The cultures were

cultivated under four different conditions; (i) autotrophic growth at low (0.04%) CO_2 (ATLC) and continuous illumination (50 μmol photons m^{-2} s^{-1}); (ii) autotrophic growth under high (3%) CO_2 conditions (ATHC) and continuous illumination (50 μmol photons m^{-2} s^{-1}); (iii) mixotrophic growth (MT) in the presence of 10 mM glucose (Glc) at low (0.04%) CO_2, and continuous illumination (50 μmol photons m^{-2} s^{-1}); (iv) light-activated heterotrophic growth (LAH) in the presence of 10 mM Glc at low (0.04%) CO_2 in the dark, where cells were illuminated (50 μmol photons m^{-2} s^{-1}) for only 10 min every 24 h. Optical densities at 750 nm (OD_{750}) were measured using a Lambda 25 UV/VIS (PerkinElmer) spectrometer. The cultures were grown under the experimental conditions described above until $OD_{750} \approx 1$, taking 1.5 days for the MT and ATHC conditions or 3.5 days for the ATLC and LAH conditions.

To determine the influence of inoculation of experimental cultures with HC-adapted cells on the proteome of ATLC experimental cultures, the following experimental setup was used. Two types of pre-cultures were grown under the ATLC and ATHC conditions, and each of them was further inoculated in a BG11 medium and grown under ATLC conditions (as described above). The cells were collected at OD = 1 at c.a. 1.5 days.

Mass Spectrometry Data-Dependent Acquisition

For liquid chromatography-tandem mass spectrometry (LC-ESI-MS/MS) analysis, total proteins were isolated and digested as described previously (Huokko et al., 2019).

LC-ESI-MS/MS analyses were performed on a nanoflow HPLC system (Easy-nLC1200, Thermo Fisher Scientific) coupled to a Q Exactive HF mass spectrometer (Thermo Fisher Scientific) equipped with a nano-electrospray ionization source. Samples from three to four individual cultures of each condition ($n = 3$ or 4) were injected into an analytical C18 column (75 μm × 40 cm, ReproSil-Pur 1.9 μm 120 Å C18-AQ; Dr. Maisch HPLC GmbH, Ammerbuch-Entringen, Germany). The mobile phase consisted of water with 0.1% formic acid (solvent A) or acetonitrile/water [80:20 (v/v)] with 0.1% formic acid (solvent B). Peptides were separated with a two-step, 110 min gradient from 5 to 26% solvent B for over 70 min, followed by 26–49% B increase for over 30 min.

MS data were acquired automatically using the Thermo Xcalibur 3.1 software (Thermo Fisher Scientific). A data-dependent acquisition (DDA) method consisted of an Orbitrap MS survey scan of mass range 300–1,800 m/z followed by HCD fragmentation for the 12 most intense peptide ions. Spectra were registered with a resolution of 120,000 and 15,000 (at m/z 200) for full scan and for fragment ions, respectively, and normalized collision energy of 27%. Automatic gain control (AGC) was set to a maximum fill time of 100 ms and 250 ms to obtain a maximum number of 3e6 and 1e5 ions for MS and MS/MS scans, respectively.

Data Analysis

Proteins were identified and annotated according to the *Synechocystis* database retrieved from Cyanobase (Kaneko et al., 1996) (3,672 entries, 23.10.2012) using the Proteome Discoverer 2.2 software (Thermo Fisher Scientific) connected to an in-house server running the Mascot 2.6.1 (Perkins et al., 1999) algorithm (Matrix Science). Precursor value was restricted to monoisotopic mass tolerance of ±4 ppm and fragment ion mass tolerance of ±0.02 Da. Two missed cleavages were allowed, and decoy searches were performed. For validation of the identified spectra, we used a Percolator algorithm (Käll et al., 2007) with a relaxed false discovery rate (FDR) of 0.05. The original data and protein identification files are deposited in the PRIDE Archive database (Vizcaíno et al., 2016) (PXD030630). A quantitative analysis was conducted in the Progenesis (Waters) software with global normalization and using relative quantification of proteins with at least two peptides with no conflicts per protein. The statistical test ANOVA was used (with experimental setup called in Progenesis software as between subject design), assuming that the tested conditions are independent. In the analysis of different proteomic responses of *Synechocystis* upon acclimation to various trophic conditions, the practical threshold of fold change (FC) was set to 1.5 ($\log_2 1.5 = 0.58$) for upregulated proteins and -1.5 [$-\log_2(1.5) = -0.58$] for less abundant proteins. Proteins quantified in at least three replicates and at least two conditions were used for data interpretation. Data with missing points or unreliable peptides were filtered out before the quantification process.

Obtained values of protein abundance were also used to calculate the distribution of proteome mass fraction to functional categories (Jahn et al., 2018) under the four conditions: ATLC, ATHC, MT, and LAH. Proteins were grouped according to an annotation used previously (Jahn et al., 2018) (**Supplementary Table 1**).

RESULTS

Growth of *Synechocystis* Cultures Under Different Trophic Conditions

Four different growth strategies were applied to *Synechocystis* to investigate the proteome pattern of cultures upon reaching the optical density at 750 nm (OD_{750}) of ca. 1 (**Figure 1**). *Synechocystis* cells were grown autotrophically under air-level (0.04%) (ATLC) or enriched 3% CO_2 (ATHC), or mixotrophically with 10 mM Glc (MT) or under light-activated heterotrophy (LAH) with 10 mM Glc (**Figure 1A**); the latter two were also under air-level CO_2. The ATHC and MT cultures exhibited rapid growth, which was attributed to excess of available inorganic and organic carbon, respectively (**Figure 1B**). On the contrary, the slower growth of *Synechocystis* under the ATLC and LAH conditions was due to limited carbon and light for photosynthesis, respectively (**Figure 1**). Cells were harvested for proteome analysis when $OD_{750} \approx 1$ had been reached after about ≈1.5 days of growth under the ATHC and MT conditions and ca. 3.5 days under ATLC and LAH conditions (**Figure 1B**). Notably, the pre-cultures were grown under HC while the growth of experimental cultures took place at LC in the case of ATLC, MT, and LAH. This prompted us to test whether the pre-cultures grown under LC or HC influenced the proteome of ATLC to be analyzed after the OD_{750} ≈1.0 had

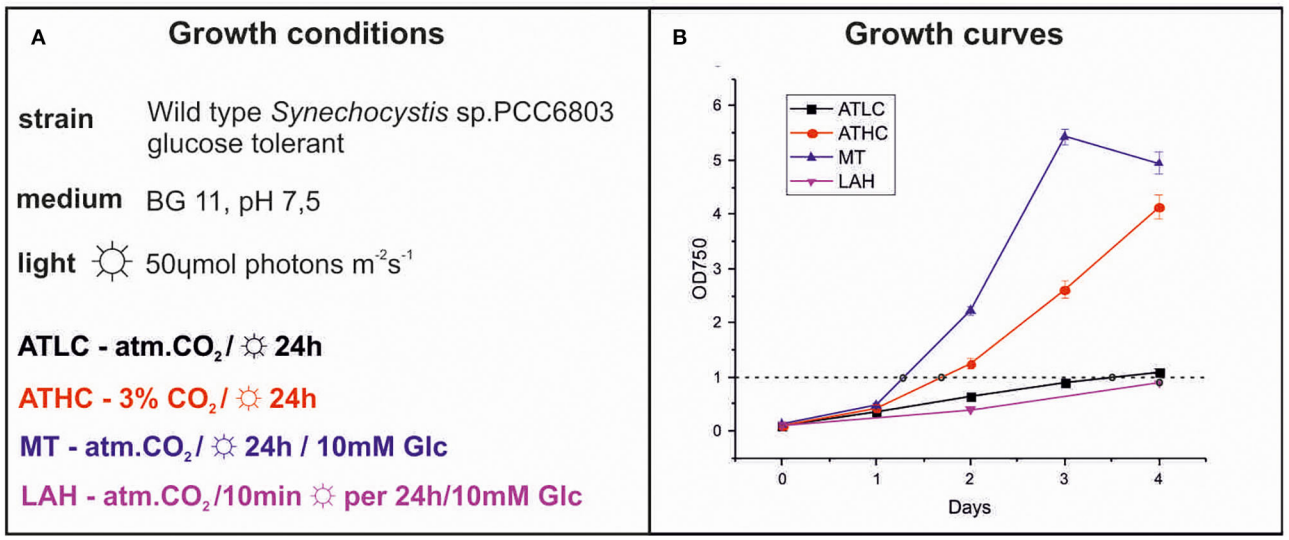

FIGURE 1 | Different growth strategies in Synechocystis cells. Growth conditions **(A)** and growth dynamics **(B)** of Synechocystis cells under photoautotrophic at low CO_2 (ATLC; black) and high CO_2 (ATHC; red), photomixotrophic (MT; blue) and light activated growth (LAH; magenta) conditions. The timing of collection of cells for proteomics, when optical density at 750 nm (OD_{750}) 1,0 is marked with black circles. Values are means ± SD; $n = 3$ biologically independent experiments.

been reached. Quantitative analysis of *Synechocystis* autotrophic proteomes from cells acclimated to the LC condition and from cells acclimated to HC and shifted to the LC condition revealed (at $OD_{750} = 1$) only minor differences (**Supplementary Table 2**). Seventy-nine proteins were differentially expressed and included glutamate-ammonia ligase (GlnN) and glutamine synthetase inactivating factors GifA and GifB as well as potassium and sulfate transporters. Notably, no differences were recorded in carbon metabolism or photosynthetic/respiratory proteins. Thus, we chose to use HC-acclimated cells for inoculations in analyses of different trophic proteomes of *Synechocystis*, keeping in mind the minor effects of the pre-culturing condition.

General View of *Synechocystis* Proteome Under the Four Growth Strategies

Overall, 2,287 proteins (62% of *Synechocystis* theoretical proteome) were identified with at least two peptides present in at least two conditions under study (**Supplementary Tables 3–7**). Of these, 1,651 proteins (45% of *Synechocystis* proteome) were identified in all the growth modes, as shown in the Venn diagram summarizing all proteins identified in this study (**Figure 2**). A total of 2,145 proteins were quantified by label-free DDA mass spectrometry represented by at least 2 peptides (ANOVA $P < 0.05$) (**Supplementary Table 1**).

Proteome Mass Fraction Analysis Revealed Growth Condition-Dependent Protein Accumulation in Different Cellular Functionalities

As the first approach, we analyzed the distribution of protein mass into different functional categories (main and subcategories as classified by Jahn et al., 2018) and calculated the fraction of

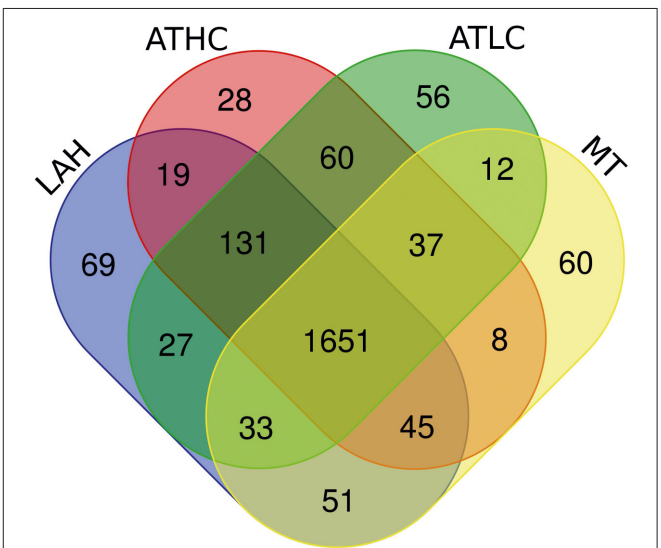

FIGURE 2 | Venn diagram showing the number of proteins identified under the four growth conditions, ATLC, ATHC, MT, and LAH.

the total proteome mass allocated to the seven main functional categories for every growth condition (ATLC, ATHC, MT, and LAH) (**Table 1**).

This analysis was conducted to reveal functionalities that either increased or decreased in the *Synechocystis* proteome under the different growth modes and thus, gave insights into the allocation of cell's energetic and material resources to the particular functional category under each cultivation strategy. The measurement of mass fraction is based on the assumption that the overall amount of proteome mass in *Synechocystis* cells

TABLE 1 | Proteome classification categories used for mass fraction analyses.

Proteins classification categories		
PSET	CYTB6F	Cytochrome b_6f
	SEC	Soluble electron carriers
	NADH	Respiartoy NDH-1 and 2
	RTO	Respiratory terminal oxidases
	HYDR	Hydrogenase
	ATPS	ATP synthase
	PSI	Photosystem I
	PSII	Photosystem II
LHC	PBS	Phycobilisome
	BSC	Biosynthesis of cofactors (chlorophyll)
CBM	TBP	Transport and binding proteins
	CCM	Carbon concentrating mechanism
	AAB	Aminocids biosynthesis
	CIM	Central intermediary metabolism
	TS	Translation
	EM	Energy metabolism
GLM	GLC	Glycolysis
	OPP	Pentose phosphate pathway
	SUGMET	Sugars
LPB	CE	Cell envelope
	BSC	Biosynthesis of cofactors (Lipoate)
	FA	Fatty acid
MAI	BSC	Biosynthesis of cofactors (others)
	PPN	Purines, pyrimidines, nucleosides and nucleotides
	CELPROC	Cellular processes
	TRANSL	Translation
	CIM	Central intermediary metabolism
	TRANSCR	Transcription
	OTHER	Other categories
	HYP	Hypothetical
	RF	Regulatory functions
	DNARP	DNA replication, restriction, modification, Recombination, and repair
	UNK	Unknown
	WDPROT	WD repeat proteins
RIB	CELPROC	Cellular processes
	TRANS	Translation (ribosomal proteins)

PSET, photosystems and photosynthetic transport; LHC, light-harvesting complex; CBM, carbon metabolism; GLM, glucose uptake and metabolism; LPB, lipid biosynthesis and membrane components; MAI, maintenance and regulation (including proteins of unknown function and hypothetical); RIB, ribosome and protein production.

does not fluctuate under the four different growth conditions when a OD_{750} of 1 had been reached (Zheng and O'Shea, 2017). **Figure 3** depicts the percentage of proteome mass fraction distribution in the main functional categories shown in **Table 1**.

As expected, the allocation of proteome mass fractions in LAH distinctively differed from those under the ATLC, MT, and ATHC conditions. In particular, the proteome mass fractions collectively allocated to photosynthetic electron transfer (PSET) and light-harvesting phycobilisomes (LHC) were reduced to 17% in LAH in comparison to the 31–35% in the remaining conditions (**Figure 3**). Conversely, LAH uniquely accumulated proteome fractions in the maintenance (MAI) category, comprising many proteins of unknown function, as well as in the carbon metabolism (CBM) category (**Supplementary Table 1**). Relatively high proteome mass fraction of the ribosome and protein production (RIB) category was a common feature for both MT and LAH (**Figure 3**). The ATHC cultures, despite rapid cell proliferation close to that of MT (**Figure 1B**), demonstrated a lower mass fraction of the RIB category (**Figure 3**). The two autotrophic conditions, ATLC and ATHC, differed by a decrease in LHC proteome fraction and accumulation of MAI and CBM proteome fractions in the slowly growing ATLC cultures, in comparison to the faster-growing ATHC cultures.

The two major functional categories, PSET and CBM, were selected for deeper analyses of proteome mass fraction accumulation into their various protein subcategories shown in **Table 1**. Differential proteome mass accumulation in the subcategories of PSET and CBM is presented in **Figures 4A,B**, respectively. In the PSET category, both photosystem II (PSII) and photosystem I (PSI) collectively accumulated to a substantially lower amount in LAH (49%) than in the ATLC (60%), ATHC (68%), or MT (69%) condition (**Figure 4A**). At the same time, ATP synthase fraction (ATPS), as well as the respiratory complexes NDH-1_{1-2} and NDH-2 proteins, increased under LAH as compared to the other conditions. The CBM category (**Figure 4B**) demonstrated relatively high proteome mass fractions allocated to the amino acid biosynthesis (AAB) in ATHC, MT, and LAH in comparison to ATLC. On the contrary, the protein mass fraction of the carbon concentration mechanism (CCM) subcategory was substantially larger in ATLC (30%) compared to the three carbon-rich growth conditions (14–17%). The allocation of protein mass into the transport and binding protein (TBP) subcategory was higher in MT (21%) than in the other growth conditions (12–14%).

TROPHIC MODE-DEPENDENT DIFFERENTIAL PROTEIN EXPRESSION

After focusing on functional categories, we analyzed the differential expression of individual proteins in *Synechocystis* in response to growth under ATHC, MT, and LAH using the protein abundance in *Synechocystis* grown autotrophically at low CO_2 (ATLC) as a reference. Results on differentially expressed (DE) proteins are presented below in **Tables 2–6**, grouping the proteins primarily according to the main functional categories (see **Table 1**).

Differential Expression of Carbon Metabolism-Related Proteins in Response to the Trophic Strategy

Proteins of the constitutively expressed C_i uptake systems (BicA and NDH-1_4 complex) were particularly abundant under all the carbon-rich conditions (ATHC, MT, and LAH) with respect to the ATLC reference condition (**Table 2**). Conversely, inducible components of inorganic CCM, such as NDH-1_3 and bicarbonate

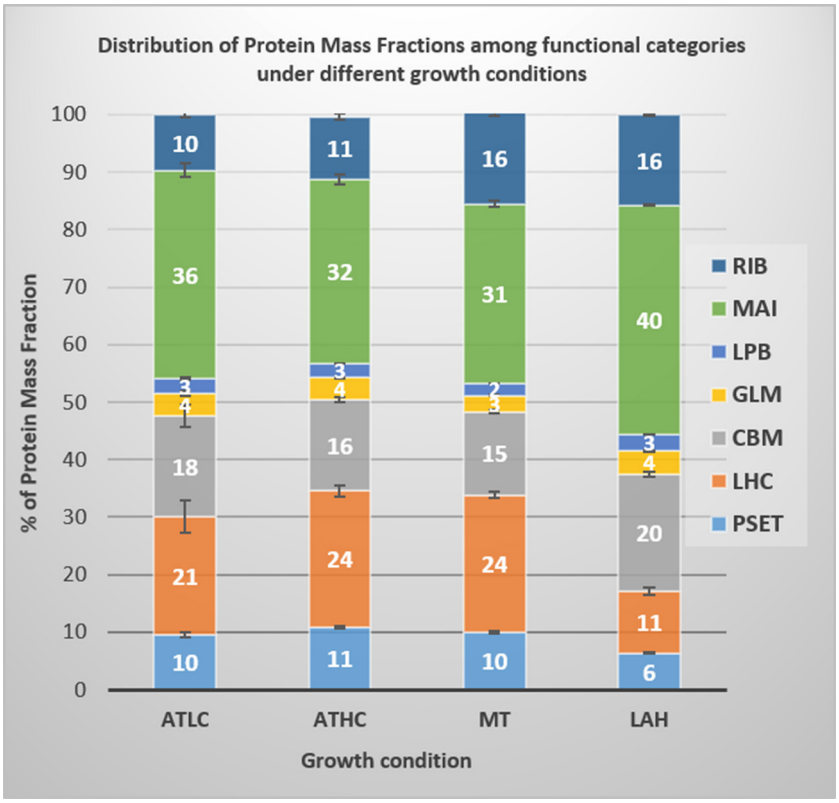

FIGURE 3 | Proteome mass fraction distribution into main categories in *Synechocystis* cells grown under the four different growth conditions, ATLC, ATHC, MT, and LAH. Functional categories: PSET, photosystems and photosynthetic transport; LHC, light-harvesting complex; CBM, carbon metabolism; GLM, glucose uptake and metabolism; LPB, lipid biosynthesis and membrane components; MAI, maintenance and regulation (including proteins of unknown function and hypothetical); RIB, ribosome and protein production. Three to four biological replicates per condition were used to calculate proteome mass fractions and corresponding standard error.

transporters BCT1 and SbtA/SbtB, had very low abundance under ATHC, MT, and LAH. Intriguingly, the porin protein PorB, a product of the *cmp* operon that encodes the BCT1 transporter, showed the lowest differential expression in ATHC. Ribulose bisphosphate carboxylase (RuBisCO) subunits, RbcS and RbcL, and structural proteins of carboxysome CcmK-N were less abundant under ATHC than under the ATLC conditions and clearly the least abundant under the LAH and MT trophic modes. Similarly, both carbonic anhydrases, the thylakoid-located EcaB (Sun et al., 2019) and CcaA, showed lower abundance under ATHC and even more so under MT and LAH. Importantly, enzymes of glycolate metabolism involved in photorespiration, particularly glyoxylate aminotransferase (Slr0006) (Eisenhut et al., 2008), showed downregulation under all the carbon-rich conditions compared to control ATLC.

Glutamate-ammonia ligase GlnN, which is the primary enzyme in nitrogen assimilation *via* the GS-GOGAT pathway, maintained a high expression level under all the carbon-rich trophic conditions, but showed downregulation under the ATLC condition (**Table 2**; **Supplementary Table 1**). Different mechanisms of nitrogen uptake, including the high-affinity nitrate/nitrite transporter NrtA-D, as well as the ammonium permeases Amt1 and Amt2, were also among the most elevated proteins under the ATHC, MT, and LAH conditions in relation to ATLC, while the urea transporter UrtA-E had highest abundance under LAH and moderately upregulated under the MT and ATHC conditions compared to ATLC. The nitrate/nitrite reductases NirA and NarB were upregulated under all the carbon-rich conditions.

Phosphate transport systems, on the other hand, showed the most differential expression under the three carbon-rich conditions in comparison to ATLC (**Table 2**). The high-velocity, low-affinity Pst1 phosphate transport system (SphX, PstS1, PstC1, PstA1, PstB1, and PstB2) encoded by the *pst1* gene cluster as well as the low-velocity, high-affinity Pst2 system encoded by a homologous *pst2* gene cluster (*slr1247–slr1250*) (Pitt et al., 2010) accumulated strongly under the MT growth condition, underwent a significant decrease in abundance under LAH, and remained unaffected by ATHC (**Table 2**). The phosphate-binding PstS homolog was found with reduced abundance under ATHC and LAH, while the exopolyphosphatase Ppx had high abundance under all the carbon-rich conditions, and polyphosphate kinase Ppk was induced under MT but decreased under LAH, all in comparison to the ATLC trophic mode.

The tricarboxylic acid (TCA) cycle oxidizes acetyl-CoA released from carbohydrates and forms 2-oxoglutarate (2-OG),

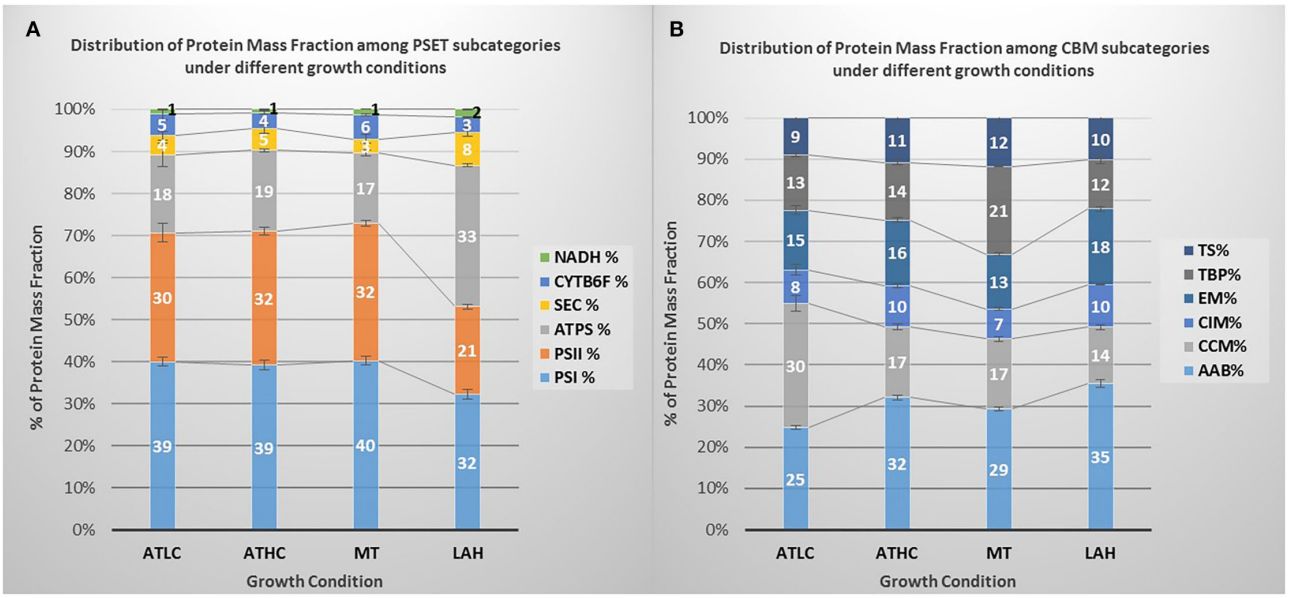

FIGURE 4 | Distribution of protein mass fraction in categories of **(A)** photosystems and photosynthetic transport (PET) and **(B)** relevant subcategories of carbon metabolism (CBM) under the different growth conditions: ATLC, ATHC, MT, and LAH. In **(A)**, PSI, photosystem I; PSII, photosystem II; ATPS, ATP synthase; SEC, soluble electron carriers, Cytb_6f-cytochrome b_6f, NADPH-dehydrogenase complex (NDH-1_1 and NDH-2); in **(B)**, AAB, amino acid biosynthesis; CCM, carbon-concentrating mechanism; CIM, central intermediary metabolism; EM, energy metabolism; TBP, transport and binding proteins; TS, translation. Three to four biological replicates per condition were used to calculate proteome mass fractions and corresponding standard error.

an intermediate metabolite that functions as a reporter of cellular carbon to nitrogen C/N balance and carbon skeleton for nitrogen assimilation (Muro-Pastor et al., 2001; Fokina et al., 2010; Huergo and Dixon, 2015). Enzymes related to the transformation of 2-OG to succinate *via* succinate-semialdehyde dehydrogenase (SSADH) bypass, including 2-OG decarboxylase (2-OGDC) and SSADH (Xiong et al., 2014), had significantly lower levels under ATHC, while both succinate dehydrogenase subunits ShdA/B and fumarase (FumC) had a low level under all the three carbon-rich conditions in comparison to ATLC (**Table 2**). At the same time, the amount of succinyl-CoA synthetase SucC/D (of the TCA cycle) was clearly reduced only under LAH. From the GABA shunt of the TCA cycle, only N-acetylornithine aminotransferase (ArgD) had significantly higher abundance under MT and even more under LAH. In addition, an N-acetylglutamate kinase (ArgB) increased in abundance under the LAH condition (at the border of practical threshold under the MT condition). At the same, time the malic enzyme (Me) from the malic shunt of the TCA cycle was slightly upregulated under the MT condition, indicating enhanced flow through the malic shunt (You et al., 2015). Furthermore, multiple enzymes involved in AAB pathways were induced under Glc supplemented conditions MT and LAH (**Table 2**).

As expected, the LAH and MT conditions enhanced the abundance of enzymes involved in glycogen catabolism, including the glycogen phosphorylase 2 (GlgP2) isoform, phosphoglucomutase (Pgm), 4-alpha-glucanotransferase (MalQ), and glycogen isoamylase (GlgX). At the same time, the other GlgP isoform (encoded by *sll1356*) was downregulated under the ATHC and LAH conditions, in line with a previous report showing the highest activity of GlgP under autotrophic conditions (Fu and Xu, 2006).

Coordinated downregulation of proteins responsible for cation transport, such as Na^+/H^+ antiporters (NhaS), Sll1263, PacL, Pma1, and SynCAX, was observed under all the carbon-rich conditions (**Table 2**). At the same time specifically potassium-transporting P-type ATPase subunits of KdpA-D were strongly induced under MT but strongly decreased under LAH and ATLC. In addition, the KchX potassium channel (Berry et al., 2003) was upregulated in MT and LAH (**Table 2**).

From other CBM category proteins of high physiological importance, a nitric oxide reductase (NorB), a protein reducing nitrogen oxide (NO) and operating in connection to the electron transport chain in TM (Büsch et al., 2002), was downregulated under the LAH condition (**Table 2**). The sulfate transporter CysA, in turn, was maintained at a low level under all the carbon-rich conditions. In contrast, iron transporters FutA1 and FutC were induced under all three carbon-rich conditions, which corresponds with upregulation of the *suf* operon (*slr0074-slr0077*) that is important for the biosynthesis of Fe-S clusters. Cysteine desulfurase (NifS2) and an ABC-transporter DevC-homolog, Sll1482, were among the most upregulated proteins in the CBM category under the LAH condition.

Trophic Strategy-Response of Glucose Uptake and Metabolism (GLM)-Related Proteins

Enzymes of the glycolytic routes, the Embden-Meyerhof-Parnas (EMP) pathway, Entner-Doudoroff (ED) pathway, and oxidative pentose phosphate (OPP) pathway, showed

TABLE 2 | Differentially expressed proteins from the carbon metabolism (CBM) category.

Complex/ Process	Protein	ORF	Log_2FC			Complex/ Process	Protein	ORF	Log_2FC		
			ATHC/ ATLC	MTLC/ ATLC	LAH/ ATLC				ATHC/ ATLC	MT/ ATLC	LAH/ ATLC
BCT1	CmpA	*slr0040*	**-4.1**	**-3.1**	**-3.8**	GS-GoGAT	GlnN	*slr0288*	**3.4**	**4.7**	**4.3**
	CmpB	*slr0041*	**-3.6**	**-2.9**	**-3.7**		BicA	*sll0834*	**2.4**	**3.7**	**3.8**
	CmpC	*slr0043*	**-4.2**	**-3.3**	**-4.2**		Sll1482	*sll1482*	**0.4**	**1.4**	**3.2**
	CmpD	*slr0044*	**-5.0**	**-3.2**	**-3.6**	NDH-1_4	NdhD4	*sll0027*	**1.3**	**1.0**	**1.1**
	PorB	*slr0042*	**-5.3**	**-2.4**	**-3.3**		CupB	*slr1302*	**1.2**	**1.4**	**0.9**
NDH-1_3	NdhF3	*sll1732*	**-6.6**	**-3.5**	**-4.2**	Nitrate transporter	NrtA	*sll1450*	**0.8**	1.9	**1.6**
	NdhD3	*sll1733*	**-3.9**	**-1.9**	**-3.8**		NrtB	*sll1451*	**1.7**	**2.4**	**2.6**
	CupA	*sll1734*	**-4.7**	**-3.2**	**-3.6**		NrtC	*sll1452*	**1.9**	**0.9**	**2.9**
	CupS	*sll1735*	**-3.9**	**-2.7**	**-2.6**		NrtD	*sll1453*	**3.3**	**2.9**	**4.1**
Sbt	SbtA	*slr1512*	**-5.3**	**-3.4**	**-4.4**	Amonium transporter	Amt1	*sll0108*	**2.8**	1.4	**2.7**
	SbtB	*slr1513*	**-3.9**	**-3.3**	**-3.6**		Amt2	*sll1017*	**0.9**	**1.3**	**1.5**
RuBisCo	RbcS	*slr0012*	**-1.3**	**-2.7**	**-1.7**	Urea transport	UrtA	*slr0447*	1.3	**-0.5**	**3.2**
	RbcL	*slr0009*	**-1.3**	**-1.6**	**-1.8**		UrtB	*slr1200*	**0.8**	**0.9**	**1.0**
Carbonic anhydrase	EcaB	*slr0051*	**-0.8**	**-1.9**	**-2.0**		UrtC	*slr1201*	0.9	0.3	**2.2**
	CcaA	*slr1347*	**-0.6**	**-0.8**	**-1.1**		UrtD	*sll0764*	**0.4**	**0.7**	**1.1**
Ccm	CcmK2	*sll1028*	**-1.0**	**-1.8**	**-1.2**		UrtE	*sll0374*	**0.7**	**1.2**	**0.9**
	CcmK1	*sll1029*	**-0.9**	**-1.3**	**-1.2**		NirA	*slr0898*	**1.1**	**0.3**	**0.7**
	CcmL	*sll1030*	**-0.9**	**-1.4**	**-1.1**		NarB	*sll1454*	**1.9**	**1.0**	0.6
	CcmM	*sll1031*	**-0.7**	**-1.4**	**-1.6**	Phosphate metabolism	Ppk	*sll0290*	0.1	**1.2**	**-0.4**
	CcmN	*sll1032*	**-0.8**	**-1.5**	**-1.7**		Ppx	*sll1546*	**0.4**	**0.6**	**0.8**
Phosphate transport	PstA1	*sll0682*	0.4	**3.8**	**-2.9**	Potassium transport	Sll0536	*sll0536*	0.4	**2.9**	**3.2**
	PstB1	*sll0683*	0.1	**4.0**	**-3.6**		KdpA	*slr1728*	**0.6**	**1.6**	**-0.5**
	PstC1	*sll0681*	0.1	**2.7**	**-3.2**		KdpB	*slr1729*	**0.9**	**2.0**	**-0.7**
	PstS1	*sll0680*	-0.5	**1.5**	**-1.6**		KdpC	*slr1730*	**0.9**	**2.0**	**-0.9**
	PstB2	*sll0684*	0.1	**4.9**	**-3.1**		KdpD	*slr1731*	0.1	**1.7**	**-1.8**
	PstS2	*slr1247*	-1.0	**2.1**	**-1.6**	Iron transporters	FutC	*sll1878*	**1.4**	**1.3**	**2.3**
	SphX	*sll0679*	-0.4	0.1	**-1.6**		FutA1	*slr1295*	0.4	**2.5**	**1.5**
	CysA	*slr1455*	**-3.6**	**-3.5**	**-4.1**	Fe-S cluster biosynthesis	SufB	*slr0074*	0.1	**0.8**	**1.5**
	NorB	*sll0450*	**-0.4**	-0.2	**-1.4**		SufC	*slr0075*	0.2	**0.7**	**1.4**
TCA	Icd	*slr1289*	0.2	**0.5**	**0.4**		SufD	*slr0076*	0.3	**0.5**	**1.3**
	2-OGDC	*sll1981*	**-0.7**	**-0.4**	**0.2**		SufE	*slr1419*	0.1	**0.7**	**0.6**
	SSADH	*slr0370*	**-0.5**	**-0.3**	0.2		SufS	*slr0077*	0.3	**1.0**	**1.6**
	SdhA	*slr1233*	**-0.6**	**-0.9**	**-0.9**		SufR	*sll0088*	-0.4	**0.8**	**1.1**
	SdhB	*sll1625*	**-0.7**	**-0.9**	**-1.3**	cysteine desulfurase	NifS	*slr0387*	**-0.6**	**0.7**	**0.6**
	FumC	*slr0018*	-0.4	**-0.7**	**-0.8**		NifS2	*sll0704*	0.4	**0.9**	**4.9**
	SucC	*sll1023*	**-0.5**	**0.3**	**-0.6**	AA biosynthesis	AroK	*sll1669*	0.2	**0.5**	**0.6**
	SucD	*sll1557*	**-0.4**	**0.7**	**-0.8**		AroH	*sll0109*	**0.4**	**1.2**	**1.0**
	Me	*slr0721*	0.0	**0.6**	**0.5**		AroA2	*sll0934*	**-0.6**	**1.9**	**1.4**
Cation transport	SynCAX	*slr1336*	0.1	**-0.6**	-0.4		HisC	*sll1713*	**0.9**	**1.0**	**1.2**
	Sll1263	*sll1263*	**-1.4**	**-1.3**	**-1.3**		HisD	*slr0682*	0.3	**0.6**	**1.1**
	NhaS1	*slr1727*	**-0.3**	**-0.7**	**-0.9**		TrpC	*slr0546*	0.2	**0.5**	**1.5**
	NhaS3	*sll0689*	**-0.7**	**-1.2**	**-1.5**		GlyA	*sll1931*	**0.7**	**1.2**	**1.7**
	NhaS5	*slr0415*	0.1	**-1.8**	0.1		GcvP	*slr0293*	0.1	**0.7**	**1.7**
	NhaS6	*sll0556*	0.0	-0.9	**-2.2**		Gad	*sll1641*	**0.1**	0.6	**-0.8**
	Pma1	*sll1614*	-0.7	**-1.7**	**-0.7**		ArgD	*slr1022*	**0.4**	**0.8**	**1.6**
	Slr0822	*slr0822*	0.6	**-0.4**	**-1.5**		ArgB	*slr1898*	**0.4**	**0.6**	**1.0**
	Sll0672	*sll0672*	**-1.0**	**-0.8**	**-1.4**		ArgG	*slr0585*	**0.2**	**0.4**	**0.8**
Glycogen catabolism	Pgm	*sll0762*	**0.8**	**1.1**	**1.8**	Glycolate metabolism	GlcD1	*sll0404*	**-0.5**	**-0.6**	**-1.0**
	GlgP	*sll1356*	**-0.5**	0.9	**-0.9**		GlcE	*sll1189*	**-0.5**	**-0.7**	**-0.5**
	GlgP2	*slr1367*	0.2	**1.4**	**1.8**		GlcF	*sll1831*	**-0.8**	-0.2	**-1.9**
	GlgX	*slr0237*	0.2	**0.7**	**0.6**		Slr0006	*sll0006*	**-4.1**	**-2.5**	**-2.0**
	MalQ	*sll1676*	0.0	**0.8**	**1.3**		Sll1359	*sll1359*	**-0.8**	NA	**-3.6**

The gradient from blue to red was applied to highlight the proteins below or above practical fold change threshold (−0.58 > log_2FC >0.58), with lowest to highest abundance, respectively, in relation to the ATLC growth condition. Statistically significant results ($p < 0.05$) are highlighted with bold font.

variance in abundance among the three different carbon-rich conditions (**Table 3**). As for individual GLM category proteins, phosphomannose isomerase (RfbM), which catalyzes the conversion of mannose-6-P to fructose-6-P, was found in higher abundance under the MT and LAH conditions, while under the ATHC condition fructose-bisphosphate aldolase

TABLE 3 | Differentially expressed proteins from the glucose uptake and metabolism (GLM) category.

Complex/ Process	Protein	ORF	Log_2FC		
			ATHC/ ATLC	MT/ ATLC	LAH/ ATLC
GalE	Slr1067	*slr1067*	**-0.8**	**-1.0**	**-1.5**
	Sll0244	*sll0244*	-0.4	-0.4	**-0.6**
Glycolisis	Pgk	*slr0394*	0.0	**-1.4**	**-1.2**
	Eno	*slr0752*	0.0	**-0.6**	**-0.6**
OPP	Pgl	*slr1349*	**-0.6**	**-0.5**	**-0.7**
	Zwf	*slr1843*	**-0.4**	**-0.2**	**-0.6**
	RpiA	*slr0194*	**0.6**	-0.2	0.0
	CfxE	*sll0807*	-0.3	**0.7**	0.1
ED / OPP	Glk	*sll0593*	**-0.5**	**-0.7**	**-0.7**
EMP	Pfk2	*sll0745*	**-0.2**	**-0.3**	**-0.6**
	Pfk1	*sll1196*	**0.6**	**0.9**	**0.8**
	FbaA	*sll0018*	**-0.3**	**-0.7**	**-0.3**
	Fda	*slr0943*	**0.6**	0.8	0.1
	Pgm	*slr1945*	**0.3**	**0.8**	**0.9**
Other	Sll1558	*sll1558*	**0.4**	**0.2**	**0.2**
	Spp	*slr0953*	0.2	**0.6**	**0.6**
	Sps	*sll0045*	**-0.4**	0.4	**0.6**
	Slr1617	*slr1617*	**-0.6**	**-0.5**	**-1.1**
	CscK	*slr1448*	**-0.9**	-0.2	0.1
	MtfB	*sll1231*	**-0.2**	-0.5	**-0.8**
	RfbD	*sll1212*	**-0.8**	**-1.2**	**-1.1**
	RfbM	*slr0493*	0.2	**1.7**	**1.5**

The gradient from blue to red was applied to highlight the proteins above the practical fold change threshold (−0.5 8> log_2FC > 0.58), with lowest to highest abundance, respectively, in relation to the ATLC growth condition. Statistically significant results ($p < 0.05$) are highlighted with bold font.

(Fda) was observed at a higher level than under ATLC. Phosphofructokinase (Pfk1) and phosphoglycerate mutase (Pgm) were among the most abundant proteins of the GLM subcategory under all the carbon-rich conditions. On the contrary, two UDP-glucose 4-epimerases (Sll0244 and Slr1067) and hypothetical protein Slr1617, as well as GDP-mannose 4,6-dehydratase (RfbD) were among the most downregulated proteins in comparison to ATLC. The enzyme glucokinase (Glk) that phosphorylates glucose to prevent its diffusion from cells, was downregulated under LAH and MT as compared to ATLC. Common enzymes leading to pyruvate production in glycolysis, such as phosphoglycerate kinase (Pgk) and enolase (Eno), were present at lower abundance in Glc-supplemented growth modes in comparison to the autotrophic ATLC and ATHC conditions.

Trophic Strategy-Dependent Expression of Photosynthetic, Respiratory, and Tetrapyrrole Biosynthesis Proteins (PSET and LHC)

All protein components of PSII and PSI as well as phycobiliproteins (PBS) demonstrated lower abundance under LAH than under the ATLC condition, with PSII subunits more strongly downregulated than PSI and PBS subunits (**Table 4**). On the contrary, under the ATHC condition, several components of PSI, PSII, and PBS complexes had higher abundance than under ATLC. Interestingly, PSII-associated proteins encoded by the *Pap* operon (*slr0144-slr0151*) showed higher abundance under all the carbon-rich trophic strategies compared to ATLC and were among the most upregulated proteins in the PSET category (**Table 4**). Similar behavior was demonstrated by a protein, BtpA, involved in the biogenesis of PSI (Bartsevich and Pakrasi, 1997). In addition, the PSII assembly factor (PSII AF) Pam68 (Rengstl et al., 2013) was elevated under the ATHC condition, while Ycf39 (Knoppová and Komenda, 2019) was downregulated under the LAH and MT conditions (**Table 4**). Abundances of Psb28-2 and phycocyanin lyase subunits (CpcE/F) were distinctively elevated under the Glc-supplemented MT and LAH conditions compared to ATLC.

Subunits of the thylakoid cytochrome (Cyt) b_6f complex (PetA-D), including the Rieske protein PetC1, were generally downregulated in Glc-supplemented conditions, more prominently under LAH than MT, while the periplasmic Rieske isoform (PetC3) decreased in abundance under all the carbon-rich conditions (**Table 4**). The NdhD1 and NdhF1 subunits of the respiratory NDH-1_1 complex had higher abundance under ATHC, MT, and LAH than under ATLC. Cytochrome bd quinol terminal oxidases (Cyd) together with some other soluble electron carriers (SEC) decreased in abundance under the LAH condition. Under the MT condition, alternative respiratory terminal oxidase (ARTO) and ferredoxin-like protein Sll1584 (Mustila et al., 2014) were downregulated, while ferredoxin Fed1 was slightly upregulated (**Table 4**). The thylakoid-localized NDH-2 protein NdbA (Huokko et al., 2019) showed the highest abundance among proteins of the PSET category under the LAH and MT conditions (**Table 4**), while the PM-localized NdbC (Huokko et al., 2017) had lower abundance under the carbon-rich conditions (**Table 4**). NdbB abundance, on the other hand, was lower under ATHC but higher under the LAH condition than under ATLC.

Hydrogenase accessory proteins (Hyp) were upregulated, to various extents, under all the carbon-rich trophic conditions in comparison to ATLC, with HypB showing the second-highest upregulation in the PSET category under MT and LAH (**Table 4**). In comparison to the ATLC condition, HypB-D proteins were strongly induced under MT. At the same time, most protein subunits of the bidirectional hydrogenase, encoded by the *hox* operon (*hoxE, hoxF, sll1222, hoxU, hoxY,* and *hoxH*) were significantly less abundant under ATHC and MT but particularly under LAH.

Chlorophyll biosynthesis proteins ChlH, ChlD, and ChlI were at an elevated level under all the carbon-rich conditions, and the subunits of the light-independent protochlorophyllide reductase complex (ChlN, ChlL) were among the most induced proteins in comparison to the ATLC condition (**Table 5**). The abundance of these proteins showed a clear increase from ATHC to MT and finally to the highest level in LAH. Heme biosynthesis proteins showed differential trends under the ATHC, MT, and LAH conditions; for example, the heme

TABLE 4 | Differential expression of photosynthetic and respiratory proteins from the photosystems and photosynthetic transport (PSET) category.

Complex	Protein	ORF	Log_2FC			Complex	Protein	ORF	Log_2FC		
			ATHC/ ATLC	MT/ ATLC	LAH/ ATLC				ATHC/ ATLC	MT/ ATLC	LAH/ ATLC
Photosynthetic proteins											
PSI	PsaA	*slr1834*	**0.3**	-0.2	**-1.1**	PSII	PsbA1	*slr1311*	**0.6**	-0.3	**-2.6**
	PsaB	*slr1835*	**0.3**	-0.8	**-1.2**		PsbB	*slr0906*	**0.7**	-0.3	**-2.6**
	PsaC	*ssl0563*	-0.3	-0.3	**-1.5**		PsbC	*sll0851*	**0.6**	-0.2	**-2.6**
	PsaD	*slr0737*	0.3	-0.2	**-1.3**		PsbD	*sll0849*	**0.6**	**-0.4**	**-2.9**
	PsaE	*ssr2831*	0.3	-0.3	**-1.0**		PsbE	*ssr3451*	**0.4**	-0.1	**-2.8**
	PsaF	*sll0819*	**0.6**	-0.3	**-1.1**		PsbL	*smr0007*	**0.7**	NA	**-2.4**
	PsaJ	*sml0008*	**1.0**	NA	**-1.3**		PsbO	*sll0427*	**0.7**	-0.5	**-0.9**
	PsaK1	*ssr0390*	**2.1**	**0.9**	1.5		PsbQ	*sll1638*	**0.5**	-0.3	**-1.4**
	PsaK2	*sll0629*	**0.3**	0.4	**-0.6**		PsbU	*sll1194*	**0.6**	-0.2	**-1.5**
	PsaL	*slr1655*	**0.4**	0.2	**-0.8**		PsbV	*sll0258*	0.2	0.6	**-2.0**
	PsaM	*smr0005*	0.7	NA	**-0.9**		PsbY	*sml0007*	0.2	NA	**-3.2**
	BtpA	*sll0634*	**0.6**	**1.0**	**1.0**	PSII Assembly Factors	Sll0933	*sll0933*	**0.9**	0.1	**0.5**
PBS	ApcA	*slr2067*	**0.7**	0.6	**-0.8**		Psb27	*slr1645*	0.2	**-0.3**	**-0.8**
	ApcC	*ssr3383*	**0.5**	**0.4**	**-1.1**		Csm6	*sll1390*	**0.2**	**-0.8**	**-0.8**
	ApcE	*slr0335*	**0.5**	0.8	**-1.0**		Psb28-1	*sll1398*	0.1	**-0.4**	**-0.7**
	ApcF	*slr1459*	**0.8**	**0.5**	**-0.6**		Psb28-2	*slr1739*	-0.6	**1.5**	**1.4**
	CpcA	*sll1578*	0.3	0.3	**-1.5**		Ycf39	*slr0399*	**0.2**	**-0.9**	**-1.1**
	CpcB	*sll1577*	**0.4**	**-0.1**	**-1.2**		Psb35	*ssl2148*	0.1	-0.2	**-0.9**
	CpcC1	*sll1580*	0.4	0.3	**-1.5**		Psb34	*ssl1498*	**0.6**	NA	**-1.6**
	CpcC2	*sll1579*	**0.5**	-0.2	**-2.3**		Psb32	*sll1390*	**0.2**	**-0.8**	**-0.8**
	CpcD	*ssl3093*	**0.6**	0.3	**-2.0**	Pap operon	Slr0144	*slr0144*	**1.7**	**1.0**	**1.5**
	CpcE	*slr1878*	0.1	**0.3**	**0.7**		Slr0145	*slr0145*	**1.0**	**1.1**	**1.1**
	CpcF	*sll1051*	**0.3**	**0.6**	**0.8**		Slr0146	*slr0146*	-0.3	**1.3**	**-1.0**
	CpcG1	*slr2051*	**0.3**	0.1	**-1.0**		Slr0147	*slr0147*	**1.3**	**1.1**	**1.1**
	CpcG2	*sll1471*	**0.7**	**-0.5**	**-3.6**		Slr0149	*slr0149*	**1.4**	**1.2**	**1.3**
Respiratory proteins											
NDH-2	NdbA	*slr0851*	0.1	**3.7**	**3.0**	ARTO	CtaCII	*sll0813*	**-0.4**	**-0.8**	**-1.4**
	NdbC	*sll1484*	**-0.4**	**-0.7**	**-0.9**		CtaDII	*slr2082*	-0.6	0.7	**-1.3**
	NdbB	*slr1743*	**-0.7**	0.3	**0.6**		CtaEII	*slr2083*	0.2	NA	**-1.3**
$NDH\text{-}1_1$	NdhD1	*slr0331*	**0.7**	**0.7**	**0.5**	Cyd	CydA	*slr1379*	**0.4**	0.4	**-0.9**
	NdhF1	*slr0844*	**0.8**	**0.7**	**0.8**		CydB	*slr1380*	0.7	NA	**-1.6**
Hyp	HypB	*sll1432*	0.1	**1.6**	**1.7**	$Cytb_6f$	PetA	*sll1317*	0.1	-0.2	**-1.0**
	HypC	*ssl3580*	**0.3**	**1.2**	**0.8**		PetB	*slr0342*	0.3	-0.3	**-1.0**
	HypD	*slr1498*	0.6	**1.5**	0.4		PetC1	*sll1316*	**0.5**	**-0.5**	**-1.2**
SEC	Sll1584	*sll1584*	0.1	**-0.9**	**-1.7**		PetC3	*sll1182*	**-0.6**	**-0.6**	**-0.4**
	PetE	*sll0199*	0.1	**-0.8**	**-0.8**		PetD	*slr0343*	**0.4**	**-0.4**	**-0.9**
	NifJ	*sll0741*	0.0	1.3	**-1.3**	Hox	HoxE	*sll1220*	**-0.7**	-0.5	**-1.9**
SEC -Fed	Fed1	*ssl0020*	0.3	**0.9**	**0.5**		HoxF	*sll1221*	**-0.6**	**-0.5**	**-1.8**
	Fed6	*ssl2559*	**-1.2**	-0.2	**-0.8**		HoxH	*sll1226*	**-0.5**	**-0.7**	**-1.4**
	Fed7	*sll0662*	-0.4	**-0.7**	0.3		HoxU	*sll1223*	**-0.8**	**-0.7**	**-2.1**
	Fed9	*slr2059*	**-0.5**	0.1	**-0.6**		HoxY	*sll1224*	**-0.5**	0.3	**-1.7**

The gradient from blue to red was applied to highlight the proteins above practical fold change threshold ($-0.58 > log_2FC > 0.58$), with lowest to highest abundance, respectively, in relation to the ATLC growth condition. Statistically significant results ($p < 0.05$) are highlighted with bold font.

oxygenase isoform (Ho1), active under aerobic conditions (Aoki et al., 2011), was upregulated under the ATHC condition and downregulated under LAH as compared to ATLC (**Table 5**). Cobyrinic acid, a c-diamide synthase (CobB) protein involved in the biosynthesis of other tetrapyrrole compounds, was induced under the LAH condition, while most of remaining enzymes from the pathway were not affected or did not decrease in abundance. The uroporghyrin-III C-methyltransferase (CysG) protein, a siroheme synthesizing enzyme, had high abundance under ATHC, MT, and LAH.

TABLE 5 | Differential expression of proteins involved in the biosynthesis of tetrapyrrole compounds, included in the PSET category.

Complex/ Process	Protein	ORF	Log_2FC		
			ATHC/ ATLC	MT/ ATLC	LAH/ ATLC
Hem	Ho1	*sll1184*	**1.2**	0.2	**-1.4**
	HemB	*sll1994*	**0.8**	**0.4**	**0.3**
	HemE	*slr0536*	**0.7**	**0.5**	0.1
	HemF	*sll1185*	**1.1**	**0.8**	**0.3**
	HemH	*slr0839*	**0.4**	-0.3	**-1.3**
	HemK	*sll1237*	**-0.9**	NA	**-0.7**
	Sll5080	*sll5080*	**-0.5**	**-0.7**	**-1.0**
Chl	ChlAI	*sll1214*	**0.9**	0.1	**-0.4**
	ChlD	*slr1777*	**0.4**	**0.9**	**0.9**
	ChlH	*slr1055*	**1.1**	**1.6**	**1.8**
	ChlI	*slr1030*	**0.4**	**0.8**	**0.8**
	ChlM	*slr0525*	**-0.6**	0.1	**-0.9**
	ChlP	*sll1091*	**1.0**	0.2	**-0.4**
	Sll1512	*sll1512*	0.1	**-0.3**	**0.8**
Chl-DPOR	ChlL	*slr0749*	**1.8**	**3.3**	**4.6**
	ChlN	*slr0750*	**1.5**	**2.6**	**3.5**
Cob&Cbi	CobA	*sll0378*	**1.8**	**3.5**	**6.2**
	CobB	*sll1501*	-0.3	0.3	**3.6**
	CobL	*slr1368*	0.1	-0.3	**-0.8**
	CobM	*slr0239*	**-1.1**	**-0.5**	**-0.5**
	CobP	*slr0216*	**-0.6**	**-0.7**	**-1.2**
	CobQ	*slr0618*	**-1.0**	**0.8**	0.2
	CobQ like	*slr1742*	**-0.3**	-0.6	0.0
	HemD	*sll0166*	**-0.6**	**-0.7**	**-0.8**
	Slr1467	*slr1467*	**-1.2**	**-0.3**	**-0.3**

The gradient from blue to red was applied to highlight the proteins above practical fold change threshold (−0.58 > log_2FC > 0.58), with lowest to highest abundance, respectively, in relation to the ATLC growth condition. Statistically significant results ($p < 0.05$) are highlighted with bold font.

TABLE 6 | Differential expression of proteins from the maintenance and regulation (MAI) category with response to trophic growth condition.

Complex/ Process	Protein	ORF	Log_2FC		
			ATHC/ ATLC	MT/ ATLC	LAH/ ATLC
Prp	Prp1	*sll2008*	**0.4**	0.3	**1.7**
	Prp2	*sll2009*	**0.5**	0.8	**2.1**
	Prp3	*sll0055*	**2.5**	**5.4**	**5.5**
Pnt	PntA	*slr1239*	**0.3**	**0.9**	**0.4**
	PntB	*slr1434*	**0.4**	**0.9**	**0.3**
Flv	Flv2	*sll0219*	**-4.8**	**-3.3**	**-4.4**
	Flv4	*sll0217*	**-4.1**	**-1.9**	**-3.9**
	Flv3	*sll0550*	**-1.8**	**-1.2**	**-1.5**
Photo protection	Frp	*slr1964*	**3.6**	**3.5**	**4.3**
	Ocp	*slr1963*	**-1.0**	**0.3**	**1.2**
	Cph2	*sll0821*	**2.0**	-0.4	**1.7**
CCM	CmpR	*sll0030*	**-4.0**	**-2.7**	**-3.8**
	NdhR	*sll1594*	**-1.6**	**-1.7**	**-1.6**
	Rre37	*sll1330*	**0.7**	**2.1**	**2.9**
Gif	GifA	*ssl1911*	**-2.9**	**-2.9**	**-4.6**
	GifB	*sll1515*	**-2.9**	**-7.7**	**-2.7**
NDH-1M	NdhA	*sll0519*	**-2.0**	**-1.5**	**-2.0**
	NdhB	*sll0223*	**-1.8**	**-2.0**	**-2.1**
	NdhE	*sll0522*	**-1.1**	**-2.0**	**-1.2**
	NdhG	*sll0521*	**-1.8**	**-1.7**	**-2.1**
	NdhH	*slr0261*	**-2.0**	**-1.7**	**-1.7**
	NdhI	*sll0520*	**-1.7**	**-1.8**	**-1.8**
	NdhJ	*slr1281*	**-1.9**	**-1.7**	**-1.8**
	NdhK	*slr1280*	**-1.9**	**-1.8**	**-1.8**
	NdhM	*slr1623*	**-1.8**	**-1.7**	**-2.0**
	NdhN	*sll1262*	**-2.0**	**-1.7**	**-2.1**
	NdhO	*ssl1690*	**-1.7**	**-1.3**	**-1.5**
PHB	PhaP	*ssl2501*	-0.4	**4.8**	**5.0**
	PhaA	*slr1993*	**-0.3**	**0.9**	**0.9**
	PhaB	*slr1994*	0.1	**0.5**	**0.6**
	Sll0783	*sll0783*	**1.6**	**1.6**	**2.9**
Cop	CopR	*sll0789*	**-3.6**	**-1.4**	**0.8**
	CopC	*slr6044*	**-0.3**	**-1.4**	**0.2**
	CopS	*sll0790*	**-0.6**	**-1.6**	**0.3**
Others	Slr1535	*slr1535*	**3.5**	**6.4**	**6.1**
	SphR	*slr0081*	**1.0**	**1.7**	0.2
	CphA	*slr2002*	**0.5**	**0.5**	**1.2**
	Slr1019	*slr1019*	**-5.3**	**-3.7**	**-5.2**

The gradient from blue to red was applied to highlight the proteins above practical fold change threshold (−0.58 > log_2FC > 0.58), with lowest to highest abundance, respectively, in relation to the ATLC growth condition. Statistically significant results ($p < 0.05$) are highlighted with bold font.

Differential Expression of Regulatory and Maintenance Proteins (MAI) in Response to Growth Strategy

The MAI category comprises a large and very heterogeneous group of proteins involved in the maintenance and regulation of cellular functions, including a plethora of proteins with hypothetical or unknown function. Nevertheless, some MAI proteins are well-characterized, and others are gradually becoming annotated, including proteins with seminal roles in regulation of photosynthesis and cellular redox homeostasis, and protein expression for central metabolism and transport. MAI proteins with most prominent differential accumulation upon growth under different trophic conditions are shortly presented below, together with their preliminarily assigned physiological functions.

Regulation of Photosynthesis

Two important proteins related to non-photochemical quenching (NPQ) in cyanobacteria were among highly differentially expressed proteins depending on trophic conditions. The fluorescence recovery protein (Frp) was among the most upregulated proteins under the ATHC, MT, and LAH conditions in comparison to ATLC (**Table 6**). The orange carotenoid protein (Ocp) (Kirilovsky and Kerfeld, 2013) was likewise significantly upregulated under LAH compared to ATLC but was less abundant under ATHC. Alternative electron acceptors from a photosynthetic electron transfer chain (PETC) and a flavodiiron (Flv) protein (Zhang et al., 2009, 2012) were

less abundant under ATHC, MT, and LAH in comparison to ATLC. The Flv2 and Flv4 proteins were identified only in ATLC samples, whereas the Flv1 and Flv3 proteins were expressed in all the growth conditions, with decreasing abundance under all the carbon-rich conditions.

Redox-Related Regulation and Signaling

Trans-2,3-dihydro-3-hydroxyanthranilate isomerase (Slr1019), involved in phenazine biosynthesis, had significantly decreased abundance under all the carbon-rich growth conditions in relation to ATLC (**Table 6**). Phenazine is an aromatic tricyclic compound that includes two nitrogen atoms in the central ring. Its function has been associated with electron transport, cellular redox state, cell signaling, and biofilm formation (Pierson and Pierson, 2010).

Master Transcriptional Regulators

Regulatory proteins were assigned to the MAI category (Jahn et al., 2018) and consist of a very central group of molecules guiding the function of various cell machineries. Two main LysR type gene expression regulators of C_i uptake, NdhR (CcmR) (Wang et al., 2004) and CmpR (Pan et al., 2016), had reduced abundance in ATHC, MT, and LAH in comparison to ATLC (**Table 6**). On the contrary, the OmpR-type transcriptional regulator Rre37, described as a regulator transferring signals from light and glucose to glycolytic genes (Tabei et al., 2007), demonstrated higher abundance under all the carbon-rich conditions as compared to ATLC (**Table 6**). The main transcriptional regulator of nitrogen metabolism, the NtcA protein, remained constant under all the different growth modes. A two-component system CopS/CopR, regulating copper assimilation was less abundant under the ATHC and MT conditions, whereas the response regulator of phosphate uptake regulon SphR was more abundant under the ATHC and MT conditions, all in comparison to ATLC.

Regulators of Central Metabolism

Glutamate synthase inactivating factors GifA and GifB, highly responsive to C_i level, were upregulated upon CO_2 step down under the ATLC condition (**Supplementary Table 2**) and maintained low abundance under all the carbon-rich conditions. The hypothetical Slr1535 and Prp3 proteins demonstrated the highest relative accumulation under the ATHC, MT, and LAH conditions (**Table 6**). Slr1535 contains a domain that specifies it as α-mannosidase, the protein involved in glycogen degradation (Spät et al., 2018), while Prp3 has been characterized as a processing metalo-peptidase with unknown target(s) (Sokolenko et al., 2002). Two other processing metalo-peptidases, Prp1 and Prp2, involved in degradation of GifA (Galmozzi et al., 2007) accumulated under the ATHC and LAH condition (**Table 6**). However, a hypothetical protein, Ssl2501, is among the most induced proteins under the MT and LAH conditions, and has been characterized as phasin (PhaP), a protein controlling the amount and size of polyhydroxybutyrate (PHB) granules (Hauf et al., 2015). Other proteins involved in PHB synthesis, such as acetyl-CoA acetyltransferase PhaA, acetoacetyl-CoA reductase PhaB, and Sll0783 (Schlebusch and Forchhammer, 2010; Hauf et al., 2015), likewise accumulated in LAH and MT (**Table 6**). Elevated abundance under MT and, to a lesser extent, under ATHC and LAH in comparison to ATLC was recorded for pyridine nucleotide transhydrogenase PntAB, responsible for adjusting NADH:NADPH ratio (Kämäräinen et al., 2017) (**Table 6**).

The common core unit NDH-1M, composed of the NdhA, B, E, G-K, and M-O subunits and present in all NDH-1_{1-4} complexes, was qualified to the MAI category in our analyses, since the NDH-1_{1-2} and NDH-1_{3-4} complexes maintain different functions in cyanobacterial cells. All common subunits had lower abundance under the three carbon-rich conditions (ATHC, MT, and LAH) compared to ATLC (**Table 6**).

DISCUSSION

Trophic Conditions Govern Growth Rates and Proteome Profiles

Aquatic photosynthetic microorganisms modulate their growth mode among autotrophy, mixotrophy, and heterotrophy by tuning the metabolic, bioenergetic, and transport pathways according to the availability of nutrients, particularly carbon, and light. However, knowledge gaps regarding pathway preferences or discrimination in different trophic conditions are numerous. This study focused on identifying metabolic pathway modulations that govern the growth and photosynthesis of *Synechocystis* cells under autotrophy at low (ATLC) or high CO_2 (ATHC), as well as under Glc-supplemented mixotrophy (MT) and light-activated heterotrophy (LAH) at low CO_2. Identical continuous irradiance conditions (50 μmol photons m^{-2} s^{-1}) were applied for the ATLC, ATHC, and MT strategies, while LAH occurred in darkness with only 10-min illumination every 24 h. With respect to the general availability of carbon, the ATHC, MT, and LAH trophic conditions were collectively denoted "carbon-rich" irrespective of organic or inorganic origin, whereas ATLC represented the natural low-carbon reference condition.

The experimental cultures exhibited different growth rates that corelated with carbon and light availability. ATHC and MT demonstrated enhanced growth due to a surplus of CO_2 and Glc, respectively (**Figure 1**). The slow growth of the ATLC and LAH cultures was due to limited CO_2 and light, respectively. Unique metabolic strategies adapted in the four growth conditions were reflected in differences in proteome mass fraction distribution (**Figures 3**, **4**). These results highlighted especially how carbon metabolism and energy production processes are adjusted to the needs of diverse trophic conditions (discussed below). More detailed information about the metabolic pathways employed under specific trophic conditions was obtained from assessing the DE of single proteins and subunits of protein complexes in the three carbon-rich growth modes with ATLC as a reference condition (**Tables 2–6**). These proteome-based observations allowed insights into physiological processes that gained or lost importance under each trophic growth strategy, as summarized in **Figures 5**, **6**.

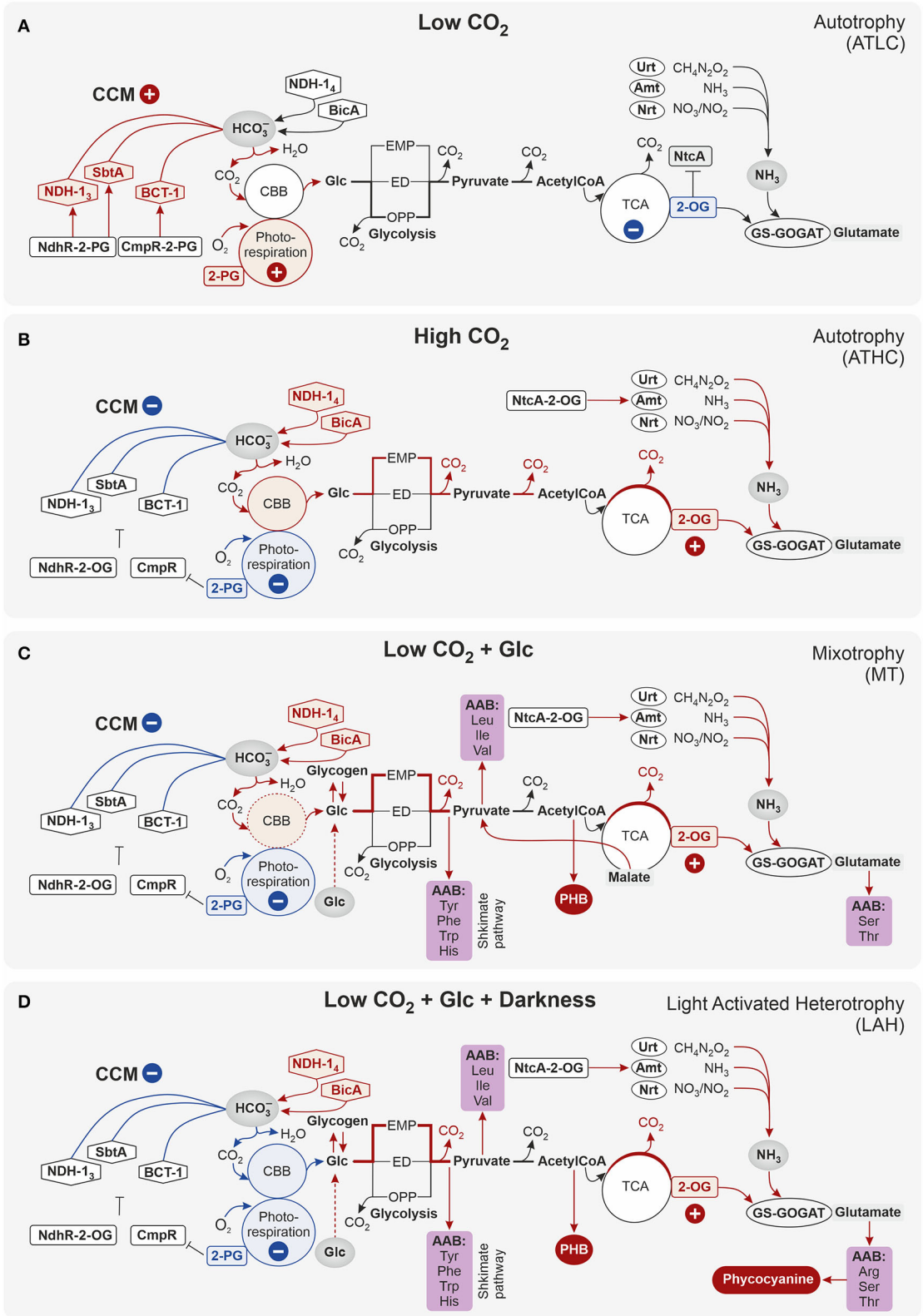

FIGURE 5 | Schematic representation of the regulation of carbon metabolism in Synechocystis sp. PCC 6803 cells grown under **(A)** low-carbon autotrophy (ATLC) and **(B–D)** carbon-rich ATHC **(B)**, MT **(C)**, LAH **(D)** conditions. The main sensors of carbon availability in the cells are 2-phosphoglycolate (2-PG), the product of photorespiration, and 2-oxoglutarate (2-OG), an intermediary product in TCA cycle. In low CO_2 autotrophy (ATLC), 2-PG is typically at high level together with CCM

(Continued)

FIGURE 5 | (red symbol), while 2-OG-regulated nitrogen assimilation is downregulated (blue symbol). Differently from (ATLC), under carbon-rich conditions, independently on the length of illumination or the source of carbon, the prevalence of 2-OG with respect to 2-PG causes downregulation of CCM (blue arrow), strengthens RuBisCo carboxylase activity (red color) and induces nitrogen transport (red arrow) that is immediately build in the 2-OG carbon skeleton to provide glutamate. The NAD(P)H/$NADP^+$ ratio in the cell is maintained by different processes depending on carbon availability.

Acquisition of Carbon/Nitrogen Balance

Sensing Carbon/Nitrogen (C/N) balance by the accumulation of 2-OG or 2-PG is an important requirement for adjusting metabolism and nutrient uptake to maintain metabolic homeostasis in cyanobacteria (for a review, see Forchhammer and Selim, 2019). The proteome of each carbon-rich trophic strategy revealed an accumulation of proteins involved in N acquisition and metabolism, including nitrate, ammonia, and urea transporters and nitrate reductases, at significantly higher levels compared to low-carbon ATLC (**Table 2**). Such high levels of N import and metabolism imply high levels of cellular 2-OG in all the carbon-rich conditions, independently of whether the carbon source was Glc or surplus CO_2 (**Figure 5**). Low-carbon conditions, on the other hand, lead to low 2-OG levels (Burnap et al., 2015), evidenced here by the low expression of proteins involved in N-assimilation-related processes (**Figure 5**). Nonetheless, the C/N balance sensing proteins P_{II} and NtcA (Forchhammer and De Marsac, 1994; Tanigawa et al., 2002; Vázquez-Bermúdez et al., 2002; Watzer et al., 2019) showed stable abundance levels among all the four growth conditions under study, providing evidence that their regulatory activity is not necessarily evidenced by the DDA data (**Supplementary Table 1**) but is rather modulated by sensing allosteric effectors 2-OG, ATP/ADP, NAGK, and PipX (Forcada-Nadal et al., 2018) or/and by post-translational modifications (PTM) (Lee et al., 2000; Watzer et al., 2019).

The carbon metabolism of cyanobacteria is highly dependent on the availability of CO_2 for carbon assimilation by the Calvin–Benson–Bassham (CBB) cycle, with CCMs playing an integral role in the capacity of cyanobacteria to thrive under low carbon conditionsby allowing for the enhancement of the carboxylation activity of RuBisCO and decreasing photorespiration (Burnap et al., 2015; Kaplan, 2017) (**Figure 5**). ATLC uniquely displayed nearly twice the mass fraction in the CCM subproteome (**Figure 4B**), particularly in its inducible components (BCT1, NDH-1_3, and StbA/B) (**Table 2**). Under these conditions, the enhanced binding of the photorespiration product (2-phosphoglycolate, 2-PG) by the two regulatory proteins, CmpR and NdhR, enables the transcription of CCM genes (Jiang et al., 2017) and, indeed, the accumulation of their encoded proteins was evident from our data sets (**Table 2**). CmpR-2-PG likely induced the transcription of genes encoding inducible HCO_3^- transporter BCT1, while NdhR-2-PG upregulated the expression of the *sbtA/B* and *ndh1*$_3$ operons and the *ndhR* gene itself (reviewed in Burnap et al., 2015) (**Figure 5**).

Under high carbon conditions, on the other hand, the accumulation NdhR-2-OG suppressor complex is known to reduce the abundance of inducible CCM proteins and NdhR itself (Jiang et al., 2017), which was clearly evident in all the carbon-rich conditions in our study (**Tables 2**, **6**). These findings are in line with the low abundance of inducible CCM proteins together with the downregulation of glycolate metabolism components (**Table 2**), thus indicative of low level of photorespiration in the presence of Glc as well as under high CO_2 (Burnap et al., 2015). Meanwhile, the constitutively expressed low affinity C_i transport systems (BicA and NDH-1_4) provided the means for C_i uptake under all the carbon-rich conditions (**Table 2**; **Figure 5**). In addition, the downregulation of both CBB cycle proteins and carboxysome-building proteins under these conditions was likely operated *via* the RbcR (Ycf30) activator of CBB genes (Carmel, 2011; Tomar et al., 2017), being slightly downregulated under all the carbon-rich conditions in comparison to ATLC (**Table 2**).

Production of Reducing Power and ATP *via* Metabolic Processes

Reducing power (NAD(P)H) and chemical energy (ATP), both necessary to run metabolic processes, are derived prevalently from photosynthesis under autotrophy and from glycolysis and respiration in darkness or upon heterotrophic growth (**Figure 5**). It has been hypothesized that the presence of three glycolytic routes in *Synechocystis*, the oxidative pentose phosphate (OPP), Entner-Doudoroff (ED), and Embden-Meyerhof-Parnas (EMP) pathways, represents different opportunities for quick acclimation to dynamic changes in nutrients and/or light availability (Chen et al., 2016; Wan et al., 2017; Makowka et al., 2020; Lucius et al., 2021). The OPP pathway has been demonstrated as the main glycolytic route and the source of NADPH in darkness but maintains only residual activity under autotrophy (Welkie et al., 2019; Makowka et al., 2020). In this study, the abundance of OPP pathway proteins was hardly affected by the trophic condition, irrespective of carbon supply or availability of light (**Table 3**). Conversely, the increased abundance of phosphofructokinase (Pfk1) and phosphoglycerate mutase (Pgm) under LAH and MT suggests enhanced flow through the EMP pathway in the presence of Glc. Notably, the essential regulator of glycolytic genes, Rre37 (Tabei et al., 2007; Azuma et al., 2011), was found upregulated under all the carbon-rich conditions in this study (**Table 6**). Despite the observed changes in abundance of some glycolytic enzymes, it remains unclear whether the measured abundance of the protein corresponds with its activity, as many glycolytic enzymes are allosterically activated (Feng et al., 2014; Nishiguchi et al., 2019, 2020). Thus, the activity of a particular glycolytic pathway is difficult to predict from the proteome data without additional protein structure analyses or metabolite screening (Feng et al., 2014). The glycolytic routes generate reduced power in the form of NADH or NADPH. The balance between these two forms is maintained by a cytoplasmic pyridine nucleotide transhydrogenase, PntAB, which, in *Synechocystis*, is specifically directed toward NADPH

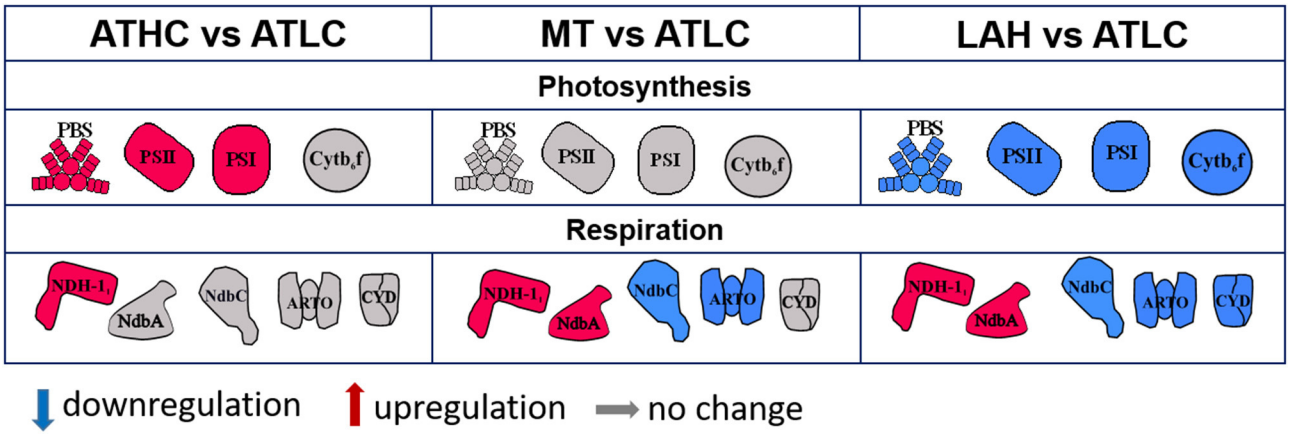

FIGURE 6 | Summary of differentially regulated complexes or proteins from photosynthesis and respiration processes under the ATHC, MT, and LAH conditions compared to the reference ATLC condition. Red color, increase ($log_2FC > 0.58$); gray color, no change ($-0.58 < log_2FC < 0.58$); blue, decrease ($-0.58 > log_2FC$) in abundance with $p < 0.05$.

(Kämäräinen et al., 2017). The increased abundance of PntAB under the MT condition (**Table 6**) implies the predominance of NADH over NADPH, possibly due to enhanced carbon flux through the EMP pathway, as compared to fully autotrophic growth mode. Some increase in PntAB abundance was also observed under ATHC and LAH due to a greater need for NADPH for CO_2 fixation and the lack of photosynthetic NADPH production, respectively.

Modulation of Photosynthetic and Respiratory Electron Transfer in Response to the Trophic Growth Strategy

The main bioenergetic hubs in cyanobacteria comprise the mixed respiratory and photosynthetic electron transfer pathways in the TM and the separate respiratory pathway(s) occurring in the PM (Mullineaux, 2014; Liberton et al., 2016; Baers et al., 2019; Liu and Zhang, 2019; Rast et al., 2019). As for respiratory complexes in the PM, no distinct differences were evident between the autotrophic conditions (ATLC and ATHC), while MT resulted in lower abundance of PM-located respiratory complexes (NdbC, ARTO, and Cyd) and even fewer were present in the LAH condition (**Figure 6**; **Table 4**). The common and specific feature in both Glc-supplemented conditions, MT and LAH, was distinct accumulation of the type 2 NAD(P)H dehydrogenase (NDH-2) protein NdbA (**Table 4**), which locates in the TM (Huokko et al., 2019) and potentially mediates electrons from NAD(P)H to the PQ pool (Howitt et al., 1999). Thus, the PM-located respiratory activity appears not to be of particular importance for growth under an organic carbon source. Instead, ATP seems to be primarily sourced from thylakoids, where NdbA is likely to act as an electron carrier from Glc degradation to the thylakoid electron transfer chain beside its other potential functions (Desplats et al., 2009; Saroussi et al., 2016). In addition, the respiratory NDH-1_1 complex accumulated in the TM, but this was not specific only for MT and LAH but also occurred under ATHC and coincided with downregulation of Flv1/3 proteins (**Table 6**). It, therefore, appears that in all the carbon-rich conditions, the availability of NADPH is not a critical factor, and that instead the cells invest in efficient ATP production *via* NDH-1 cyclic electron transfer. Flexibility between cyclic NDH-1_1 and Flv1/3 electron transfer routes in *Synechocystis* cells has been assigned also for the protection of PETC against over reduction (Nikkanen et al., 2020).

Distinct upregulation of PETC complexes takes place upon transfer of *Synechocystis* from LC to HC conditions to meet the high ATP and NADPH demands to support efficient CO_2 fixation and rapid growth under ATHC (Battchikova et al., 2010; Muramatsu and Hihara, 2012). This can also be deduced from the proteome mass fraction distribution in the PSET subcategory (**Figure 4A**). Under MT, the distribution of the proteome mass fraction for photosynthetic complexes in PSET was very similar to that in ATHC, demonstrating the importance of photosynthetic electron transport in supplement to glycolysis under mixotrophy. The extent of the role of photosynthesis in MT might be dependent on the growth state of cells and strains under examination, as attenuation of photosynthesis in *Synechocystis* grown under mixotrophy has also been reported (Solymosi et al., 2020). LAH cells, on the contrary, were severely depleted in thylakoid light-harvesting and photosynthetic electron transfer complexes PSII, PSI, and Cytb_6f in comparison to other trophic conditions (**Figures 3**, **4A** and **Table 4**). It has been shown earlier that PSII is not functional under the LAH condition (Anderson and McIntosh, 1991; Huokko et al., 2019), while PSI still remains partially functional (Barthel et al., 2013; Huokko et al., 2019). Unlike in a previous study (Plohnke et al., 2015), downregulation of all photosynthetic subunits under LAH occurred in this study (**Figures 3**, **4** and **Table 4**), indicating a low level of photosynthetic and respiratory electron transfer in the TM and reiterating strong reliance on glycogen catabolism (**Table 2**) to sustain growth. However, the induction of iron uptake as well as iron-sulfur cluster protein biosynthesis under both

glucose-supplemented conditions indicates the need for electron carriers and important cofactors to ensure redox homeostasis under LAH and MT.

Despite a general trend for downregulation of photosynthesis subunits in LAH relative to ATLC, several proteins associated with photosystems were upregulated (**Table 4**), including Psb28-2 (Sakata et al., 2013; Bečková et al., 2017) and the *pap* operon involved in PSII biogenesis (Wegener et al., 2008; Rast et al., 2016), as well as the PSI assembly protein BtpA (Bartsevich and Pakrasi, 1997; Zak et al., 1999). Additionally, the phycocyanobilin lyases CpcE and CpcF that are responsible for the attachment of bilin chromophores to apoproteins (Scheer and Zhao, 2008; Zhao et al., 2017; Kronfel et al., 2019) were induced relative to ATLC (**Table 4**). Although these proteins were also upregulated under the other trophic conditions, in comparison to ATLC, their abundance in LAH was unexpected and suggested that rapid activation of photosynthetic complexes is important to capitalize on brief daily exposure to light. Furthermore, both light-dependent and light-independent chlorophyll synthesis (LDCS and LICS respectively) pathways were induced under all the carbon-rich conditions (**Table 5**); however, LICS showed the highest increase under LAH in line with previous observations (Fang et al., 2017). It is, therefore, conceivable that the induction of two *pap* operon proteins Slr0144 and Slr0147 (**Table 4**) with a chlorophyll-binding domain in their structures (Wegener et al., 2008) transiently neutralizes the disadvantage because of free pigments under LAH where LICS proteins accumulate (**Table 5**). In addition, upregulation under LAH of two putative ferredoxins (containing Fe-S clusters) of the *pap* operon, Slr0148, and Slr0150, possibly reflects enhanced activity of LAH-specific metabolic pathways requiring these cofactors. Finally, the abundance of the Slr1051 tetratricopeptide repeat protein (TRP), previously shown to be involved in PSII repair under high light conditions (Yang et al., 2014), increased in abundance under LAH (**Table 2**). Overall, the *pap* operon proteins were strongly elevated under all the carbon-rich conditions (**Table 4**), implying their importance although still poorly understood, under the conditions of enhanced carbohydrate metabolism.

Conversely, the abundance of photoprotective Flv proteins, particularly Flv2, 3, and 4, was strongly diminished under all the carbon-rich conditions in comparison to the ATLC reference condition (**Table 6**), reflecting a balanced state of the photosynthetic apparatus that appears to be related to the availability of carbon (Zhang et al., 2009, 2012; Battchikova et al., 2010). The OCP protein was likewise downregulated under ATHC (**Table 6**) but upregulated under the LAH condition, where it may have a role in quenching excess light energy in sudden and short daily illumination periods. On the other hand, the ability of OCP to bind a chromophore may consist of a way to neutralize the potentially harmful activity of free carotenoids under the LAH condition (Melnicki et al., 2016). The strong upregulation of the OCP-inactivating protein FRP (Boulay et al., 2010) in all the carbon-rich conditions, reported also in previous proteomic studies (Kurian et al., 2006; Plohnke et al., 2015), may indicate an additional but still unknown function for FRP.

Glucose Supplementation Upregulates the Proteome for Amino Acid and Protein Synthesis

A clearly higher accumulation of protein mass in the RIB (ribosome and protein production) category was the most distinct proteome feature shared by the Glc supplemented MT- and LAH- grown *Synechocystis* cells in comparison to both AT conditions (**Figure 3**). The TCA cycle provides building blocks for biosynthesis of amino acids, the substrate for protein translational machinery. The presence of multiple branches from the TCA cycle, such as the GABA shunt, glyoxylate shunt, and OgdA/SsaD bypass, provides flexibility for cyanobacterial physiology and consequently allows for the acclimation of cells to alterations in nutrient availability (Zhang et al., 2016). The Glc-supplemented conditions of MT and LAH slightly enhanced the accumulation of Icd (*slr1289*) that catalyzes the oxidative step leading to 2-OG formation, although all other components of the TCA cycle were moderately downregulated in all the carbon-rich conditions compared to ATLC (**Table 2**). The induced flux toward 2-OG coincided with the increased efficiency of the N fixation process evidenced by the high abundance of GlnN and low contents of GifA and GifB under all the carbon-rich conditions, which also correlates with the increased N uptake discussed earlier. Furthermore, the strong downregulation in Glc-supplemented conditions and, to a lesser extent, in ATHC of enzymes, such as succinate dehydrogenase (SdhA, SdhB), succinyl-CoA synthetase (SucC and SucD), and FumC, catalyzing the consecutive reductive steps of the TCA cycle, strongly implied the redirection of carbon flow toward amino acid biosynthesis. Under the MT condition, enhanced flow through the malic shunt was evidenced by increased abundance of Me, which leads to an alternative way of pyruvate biosynthesis (**Table 2**, **Figure 5**) (You et al., 2015).

Under the LAH and MT conditions, the induced flow *via* GS-GOGATis likely directed into ornithine and AAB, as deduced from the strong accumulation of ArgB and ArgD enzymes (**Table 2**). It is conceivable that in Glc supplemented conditions, glutamate is incorporated in serine, threonine, and arginine. ArgB (NAGK) interacts with the P_{II} protein and controls arginine (Arg) synthesis *via* feedback inhibition determining the limiting step in Arg biosynthesis (Forchhammer and Selim, 2019), while ArgD is a subsequent enzyme catalyzing the reaction of N-acetylornithine biosynthesis (Xiong et al., 2014). In addition, enhanced flux toward pyruvate under Glc-supplemented conditions results in enhanced aliphatic and aromatic AA biosynthesis (**Figure 5**), evidenced by the accumulation of AroK/AroH, HisC/HisD, and TrpC (**Table 2**). Furthermore, the upregulated Sll0934 protein, predicted to encode a 3-deoxy-7-phosphoheptulonate synthase (AROA2 or DAHP) (Ogawa et al., 1994), which catalyzes one of the steps in the shikimate pathway biosynthesis (Brey et al., 2020), corroborates the enhancement of aromatic AAB.

Differential Accumulation of Pathway Enzymes for Storage Polymers Reveals Unique Strategies in Different Trophic Modes

Glycogen synthesis and degradation cycle are an important energy buffer and are recently shown to be also crucial for photosynthesis activation (Cano et al., 2018; Shinde et al., 2020). Enzymes involved in glycogen synthesis did not show differential accumulation in this study, while several glycogen catabolism enzymes diminished in abundance under Glc supplementation in MT and LAH (**Table 2**). The higher abundance of the GlgP2 isoform, as well as Pfk2 in MT and LAH, correlates with the induction of the biosynthesis of PHB, another carbon storage polymer that accumulates in *Synechocystis* under N or phosphate deprivation and functions as an important electron sink and source of building blocks for AAB (Panda et al., 2006; Panda and Mallick, 2007; Schlebusch and Forchhammer, 2010; Koch et al., 2019, 2020).

A striking difference in the accumulation of phosphate transporters (Psts) was observed for the two *Synechocystis* cultures supplemented with Glc, being strongly upregulated in MT and, conversely, downregulated in LAH, compared to the autotrophic conditions (ATLC and ATHC, **Table 2**). Induction of polyphosphate kinase Ppk together with Psts transporters in MT indicates enhanced synthesis of polyphosphates (polyPs) composed of orthophosphate residues linked with high-energy phosphoanhydride bonds (Gómez-García et al., 2003; Gomez-Garcia et al., 2013). Accumulation of polyPs granules in *Synechocystis* cells and algae grown under mixotrophy has been previously shown (Plohnke et al., 2015; Wu et al., 2021) and reflects the high cellular energy level in the MT condition due to the presence of simultaneously induced sugar catabolism and photosynthesis. Neutralization of anionic polyPs with positive charges could explain the high abundance of potassium ion channels (Kdps) observed under the MT condition (**Table 2**). Maintenance of phosphate storage in *Synechocystis* is considered as an adaptation to changes occurring in environmental conditions and energy reservoirs (Voronkov and Sinetova, 2019; Sanz-Luque et al., 2020).

The upregulation of N uptake and metabolism, including biosynthesis of N-rich AA like arginine in the LAH condition, coincided with the upregulation of cyanophycin synthetase CphA (**Table 6**). CphA is the main enzyme in the biosynthesis of cyanophycin, a polymer composed of equimolar aspartate and arginine residues, and forms granule peptide structures visible in cells grown under LAH conditions (Plohnke et al., 2015). Cyanophycin accumulates in unbalanced growth or under excess nitrogen, plays an important role in cell adaptation to different nutritional conditions, and buffers C and N availability (Watzer and Forchhammer, 2018).

Autotrophic and Heterotrophic Proteomes Are Balanced Under Mixotrophic Growth

Taken together, it is apparent that the *Synechocystis* cells benefited from both the autotrophic and heterotrophic traits in unique combinations during MT growth. As the differences between the trophic growth strategies were dependent on the quantity as well as the quality of the carbon source and on the availability of light for photosynthesis, the proteomes of *Synechocystis* cells harvested for investigation at similar OD_{750}, mostly reflected the differences in carbon acquisition and bioenergetic (photosynthesis and respiration) systems as well as in protein and amino acid biosynthesis, and accumulation of transporters and polymer storage.

The PSET proteome category, comprising the two photosystems, Cytb_6f, ATPase, NDH-1_1, and NDH-2, soluble electron carriers and ARTO, was present in surprisingly similar abundance in the total proteomes of *Synechocystis* from both autotrophic and the MT conditions. On the other hand, these proteomes distinctively but differentially diverged from the Glc-supplemented LAH proteome by a significant decrease in the accumulation of PSI and PSII as well as by increase in ATP synthase protein mass fraction (**Figure 4A**).

A common feature of ATHC, MT, and LAH was a shutdown of the energy-consuming inducible CCM (SbtA/B, BCT1, and NDH-1_3) that comprises a considerable proteome mass fraction in ATLC (**Figures 3**, **4B**). It is conceivable that the levels of accumulated 2-OG and 2-PG downregulated the inducible CCM to balance the cellular C/N ratio independently of the inorganic or organic source of carbon. It is likely that high C/N under all the carbon-rich conditions led to an enhanced flux of carbon through the GS-GOGAT pathway, which in turn enhanced N uptake and metabolism, in comparison to ATLC. Under the LAH and MT conditions, the surplus of carbon was derived from glycolysis and was incorporated into arginine and AAB, as well as converted to PHB.

The proteome data revealed strong upregulation of another respiratory NDH-2 protein, NdbA, together with the respiratory NDH-1_1 complex localized in the TMin MT and LAH strategies, and downregulation of respiratory pathways located in the PM, particularly the NDH-2 protein NdbC and ARTO, in comparison to ATHC and ATLC.

These results suggest that the respiratory electron transfer complexes in both TM and PM provide ATP for enhanced carbon fixation in the ATHC condition as compared to ATLC. Instead, respiration upon MT mode seems to primarily rely on high abundance of NdbA and the NDH-1_1 complex in the TM, while at the same time, PM respiratory components diminished in comparison to ATLC. It is also worth noting that the downregulation of auxiliary electron transfer pathways catalyzed by Flv1-4, as well as other photoprotective proteins, occurred similarly in MT and ATHC. Furthermore, the scarcity of photorespiratory proteins provides evidence that RuBisCO primarily functions in CO_2 fixation under MT conditions rather than in the oxygenation reaction that leads to photorespiration and loss of fixed carbon, thus mimicking in this respect the autotrophic ATHC condition.

In LAH, with only 10 min of daily illumination, depletion of respiratory complexes from the PM as well as the

photosynthetic and PBS proteins from the TM was evident when compared to all the other trophic conditions. However, the high level of the ATP synthase and the induction of thylakoid-localized NDH-2 (NdbA) and NDH-1_1 complexes suggest rigorous respiration and ATP synthesis primarily in the TM. Although LAH thylakoids mainly support dark respiration, they also host partially functional PSI centers (Huokko et al., 2019) that are essential during a short but obligatory diurnal illumination period that is required for *Synechocystis* growth under LAH by mechanism(s) that remains elusive.

It is concluded that upon flexible mixotrophic growth under low CO_2 and supplemental Glc (MT), *Synechocystis* relies on the use of a plethora of different physiological traits that also partially develop upon ATHC. These include downregulation of the CCM and enhanced N-metabolism. An additional feature of MT proteome, missing from all the other trophic condition proteomes, including ATHC, is profound accumulation of Psts as well as induction of the malic shunt of the TCA cycle (**Table 2** and **Figure 5**). The latter feature likely provides an invaluable asset for mixotrophic cultures to enhance their metabolism upon the availability of organic carbon. Surplus of produced energy when both autotrophic and heterotrophic growth strategies coexist is stored in polyPs granules neutralized with potassium ions. Their likely role for cyanobacteria in natural environments of low ambient CO_2 is to provide trophic flexibility in highly dynamic environments, for example, to cope with nutrient exhaustion following phytoplankton blooms. From a biotechnology viewpoint, it is clear that metabolic pathways show great plasticity according to the trophic growth mode and could be utilized as an asset for efficient production of target molecules like aromatic amino acids as an example.

DATA AVAILABILITY STATEMENT

The mass spectrometry proteomics data generated and analyzed for this study have been deposited to the ProteomeXchange Consortium *via* the PRIDE partner repository with the dataset identifier PXD030630 (http://www.ebi.ac.uk/pride/archive/projects/PXD030630).

AUTHOR CONTRIBUTIONS

DM-P, TH, YA, and E-MA made the experimental design. DM-P and TH conducted the experiments. DM-P, SK, and E-MA analyzed the proteomics data. DM-P, PG, and E-MA interpreted the data and wrote the manuscript. All authors contributed to the revision of the manuscript. All authors contributed to the article and approved the submitted version.

FUNDING

The authors acknowledge the Jane and Aatos Erkko Foundation, Turku Collegium for Science and Medicine (TCSM), and NordForskNCoE, NordAqua (Project 82845).

ACKNOWLEDGMENTS

Mass spectrometry analysis was performed at the Turku Proteomics Facility, University of Turku and Åbo Akademi University. The facility is supported by Biocenter Finland.

SUPPLEMENTARY MATERIAL

The Supplementary Material for this article can be found online at: https://www.frontiersin.org/articles/10.3389/fmicb.2022.891895/full#supplementary-material

REFERENCES

Ai, M., Zhu, Y., and Jia, X. (2021). Recent advances in constructing artificial microbial consortia for the production of medium-chain-length polyhydroxyalkanoates. *World J. Microbiol. Biotechnol.* 37, 1–14. doi: 10.1007/s11274-020-02986-0

Anderson, S. L., and McIntosh, L. (1991). Light-activated heterotrophic growth of the cyanobacterium *Synechocystis* sp. strain PCC 6803: a blue-light-requiring process. *J. Bacteriol.* 173, 2761–2767. doi: 10.1128/jb.173.9.2761-2767.1991

Aoki, R., Goto, T., and Fujita, Y. (2011). A heme oxygenase isoform is essential for aerobic growth in the cyanobacterium *Synechocystis* sp. PCC 6803: modes of differential operation of two isoforms/enzymes to adapt to low oxygen environments in cyanobacteria. *Plant Cell Physiol.* 52, 1744–1756. doi: 10.1093/pcp/pcr108

Aro, E. M. (2016). From first generation biofuels to advanced solar biofuels. *Ambio* 45, 24–31. doi: 10.1007/s13280-015-0730-0

Azuma, M., Osanai, T., Hirai, M. Y., and Tanaka, K. (2011). A response regulator Rre37 and an RNA polymerase sigma factor SigE represent two parallel pathways to activate sugar catabolism in a cyanobacterium *Synechocystis* sp. PCC 6803. *Plant Cell Physiol.* 52, 404–412. doi: 10.1093/pcp/pcq204

Baers, L. L., Breckels, L. M., Mills, L. A., Gatto, L., Deery, M., Stevens, T. J., et al. (2019). Proteome mapping of a cyanobacterium reveals distinct compartment organisation and cell-dispersed metabolism. *Plant Physiol.* 2019, 00897. doi: 10.1104/pp.19.00897

Barthel, S., Bernát, G., Seidel, T., Rupprecht, E., Kahmann, U., and Schneider, D. (2013). Thylakoid membrane maturation and PSII activation are linked in greening *Synechocystis* sp. PCC 6803 cells1. *Plant Physiol.* 163, 1037–1046. doi: 10.1104/pp.113.224428

Bartsevich, V. V., and Pakrasi, H. B. (1997). Molecular identification of a novel protein that regulates biogenesis of photosystem I, a membrane protein complex. *J. Biol. Chem.* 272, 6382–6387. doi: 10.1074/jbc.272.10.6382

Battchikova, N., Vainonen, J. P., Vorontsova, N., Keranen, M., Carmel, D., and Aro, E.-M. (2010). Dynamic changes in the proteome of *Synechocystis* 6803 in response to CO_2 limitation revealed by quantitative proteomics. *J. Proteome Res.* 9, 5896–5912. doi: 10.1021/pr100651w

Bečková, M., Gardian, Z., Yu, J., Konik, P., Nixon, P. J., and Komenda, J. (2017). Association of Psb28 and Psb27 proteins with PSII-PSI supercomplexes upon exposure of *Synechocystis* sp. PCC 6803 to High Light. *Mol. Plant* 10, 62–72. doi: 10.1016/J.MOLP.2016.08.001

Berry, S., Esper, B., Karandashova, I., Teuber, M., Elanskaya, I., Rögner, M., et al. (2003). Potassium uptake in the unicellular cyanobacterium *Synechocystis* sp. strain PCC 6803 mainly depends on a Ktr-like system encoded by slr1509 (ntpJ). *FEBS Lett.* 548, 53–58. doi: 10.1016/S0014-5793(03)00729-4

Boulay, C., Wilson, A., D'Haene, S., and Kirilovsky, D. (2010). Identification of a protein required for recovery of full antenna capacity in OCP-related photoprotective mechanism in cyanobacteria. *Proc. Natl. Acad. Sci. USA* 107, 11620–11625. doi: 10.1073/pnas.1002912107

Brey, L. F., Włodarczyk, A. J., Bang Thøfner, J. F., Burow, M., Crocoll, C., Nielsen, I., et al. (2020). Metabolic engineering of *Synechocystis* sp. PCC 6803 for the production of aromatic amino acids and derived phenylpropanoids. *Metab. Eng.* 57, 129–139. doi: 10.1016/j.ymben.2019.11.002

Burnap, R., Hagemann, M., and Kaplan, A. (2015). Regulation of CO2 Concentrating Mechanism in Cyanobacteria. *Life* 5, 348–371. doi: 10.3390/life5010348

Büsch, A., Friedrich, B., and Cramm, R. (2002). Characterization of the norB gene, encoding nitric oxide reductase, in the nondenitrifying cyanobacterium *Synechocystis* sp. strain PCC6803. *Appl. Environ. Microbiol.* 68, 668–672. doi: 10.1128/AEM.68.2.668-672.2002

Cano, M., Holland, S. C., Artier, J., Burnap, R. L., Ghirardi, M., Morgan, J. A., et al. (2018). Glycogen synthesis and metabolite overflow contribute to energy balancing in cyanobacteria. *Cell Rep.* 23, 667–672. doi: 10.1016/j.celrep.2018.03.083

Carmel, D. (2011). Novel CO_2 regulated proteins in Synechocystis *PCC* 6803. doi: 10.1006/jmbi.1993.1626

Chen, X., Schreiber, K., Appel, J., Makowka, A., Fähnrich, B., Roettger, M., et al. (2016). The Entner–Doudoroff pathway is an overlooked glycolytic route in cyanobacteria and plants. *Proc. Natl. Acad. Sci. USA* 113, 5441–5446. doi: 10.1073/pnas.1521916113

Desplats, C., Mus, F., Cuiné, S., Billon, E., Cournac, L., and Peltier, G. (2009). Characterization of Nda2, a plastoquinone-reducing type II NAD(P)H dehydrogenase in chlamydomonas chloroplasts. *J. Biol. Chem.* 284, 4148–4157. doi: 10.1074/JBC.M804546200

Eisenhut, M., Ruth, W., Haimovich, M., Bauwe, H., Kaplan, A., and Hagemann, M. (2008). The photorespiratory glycolate metabolism is essential for cyanobacteria and might have been conveyed endosymbiontically to plants. *Proc. Natl. Acad. Sci. USA* 105, 17199–17204. doi: 10.1073/pnas.0807043105

Fang, L., Ge, H., Huang, X., Liu, Y., Lu, M., Wang, J., et al. (2017). Trophic mode-dependent proteomic analysis reveals functional significance of light-independent chlorophyll synthesis in *Synechocystis* sp. PCC 6803. *Mol. Plant* 10, 73–85. doi: 10.1016/j.molp.2016.08.006

Feng, Y., De Franceschi, G., Kahraman, A., Soste, M., Melnik, A., Boersema, P. J., et al. (2014). Global analysis of protein structural changes in complex proteomes. *Nat. Biotechnol.* 32, 1036–1044. doi: 10.1038/nbt.2999

Fokina, O., Chellamuthu, V.-R., Forchhammer, K., and Zeth, K. (2010). Mechanism of 2-oxoglutarate signaling by the Synechococcus elongatus PII signal transduction protein. *Proc. Natl. Acad. Sci. USA.* 107, 19760–19765. doi: 10.1073/pnas.1007653107

Forcada-Nadal, A., Llácer, J. L., Contreras, A., Marco-Marín, C., and Rubio, V. (2018). The PII-NAGK-PipX-NtcA regulatory axis of cyanobacteria: a tale of changing partners, allosteric effectors and non-covalent interactions. *Front. Mol. Biosci.* 5, 91. doi: 10.3389/fmolb.2018.00091

Forchhammer, K., and De Marsac, N. T. (1994). The PII protein in the cyanobacterium Synechococcus sp. strain PCC 7942 is modified by serine phosphorylation and signals the cellular N-status. *J. Bacteriol.* 176, 84–91. doi: 10.1128/JB.176.1.84-91.1994

Forchhammer, K., and Selim, K. A. (2019). Carbon/nitrogen homeostasis control in cyanobacteria. *FEMS Microbiol. Rev.* 44, 33–53. doi: 10.1093/femsre/fuz025

Fu, J., and Xu, X. (2006). The functional divergence of two glgP homologues in *Synechocystis* sp. PCC 6803. *FEMS Microbiol. Lett.* 260, 201–209. doi: 10.1111/j.1574-6968.2006.00312.x

Galmozzi, C. V., Fernández-Avila, M. J., Reyes, J. C., Florencio, F. J., and Muro-Pastor, M. I. (2007). The ammonium-inactivated cyanobacterial glutamine synthetase I is reactivated *in vivo* by a mechanism involving proteolytic removal of its inactivating factors. *Mol. Microbiol.* 65, 166–179. doi: 10.1111/j.1365-2958.2007.05773.x

Gangl, D., Zedler, J. A. Z., Rajakumar, P. D., Martinez, E. M. R., Riseley, A., Włodarczyk, A., et al. (2015). Biotechnological exploitation of microalgae. *J. Exp. Bot.* 66, 6975–6990. doi: 10.1093/jxb/erv426

Gomez-Garcia, M. R., Fazeli, F., Grote, A., Grossman, A. R., and Bhayaa, D. (2013). Role of polyphosphate in thermophilic Synechococcus sp. from microbial mats. *J. Bacteriol.* 195, 3309–3319. doi: 10.1128/JB.00207-13

Gómez-García, M. R., Losada, M., and Serrano, A. (2003). Concurrent transcriptional activation of ppa and ppx genes by phosphate deprivation in the cyanobacterium *Synechocystis* sp. strain PCC 6803. *Biochem. Biophys. Res. Commun.* 302, 601–609. doi: 10.1016/S0006-291X(03)00162-1

Hauf, W., Watzer, B., Roos, N., Klotz, A., and Forchhammer, K. (2015). Photoautotrophic polyhydroxybutyrate granule formation is regulated by cyanobacterial phasin PhaP in *Synechocystis* sp. strain PCC 6803. *Appl. Environ. Microbiol.* 81, 4411–4422. doi: 10.1128/AEM.00604-15

Hays, S. G., Yan, L. L. W., Silver, P. A., and Ducat, D. C. (2017). Synthetic photosynthetic consortia define interactions leading to robustness and photoproduction. *J. Biol. Eng.* 11, 1–14. doi: 10.1186/s13036-017-0048-5

Howitt, C. A., Udall, P. K., and Vermaas, W. F. (1999). Type 2 NADH dehydrogenases in the cyanobacterium *Synechocystis* sp. strain PCC 6803 are involved in regulation rather than respiration. *J. Bacteriol.* 181, 3994–4003. 0021-9193/99/04.00+0

Huergo, L. F., and Dixon, R. (2015). The emergence of 2-oxoglutarate as a master regulator metabolite. *Microbiol. Mol. Biol. Rev.* 79, 419–435. doi: 10.1128/MMBR.00038-15/ASSET/228A3E10-FAFA-4125-A615-0C71FCFABB83/ASSETS/GRAPHIC/ZMR0041524020009.JPEG

Huokko, T., Muth-Pawlak, D., and Aro, E.-M. (2019). Thylakoid localized type 2 NAD(P)H dehydrogenase NdbA optimizes light-activated heterotrophic growth of *Synechocystis* sp. PCC 6803. *Plant Cell Physiol.* 60, 1386–1399. doi: 10.1093/pcp/pcz044

Huokko, T., Muth-Pawlak, D., Battchikova, N., Allahverdiyeva, Y., and Aro, E.-M. (2017). Role of Type 2 NAD(P)H dehydrogenase NdbC in redox regulation of carbon allocation in *Synechocystis*. *Plant Physiol.*174, 1863–1880. doi: 10.1104/pp.17.00398

Jahn, M., Vialas, V., Karlsen, J., Maddalo, G., Edfors, F., Forsström, B., et al. (2018). Growth of cyanobacteria is constrained by the abundance of light and carbon assimilation proteins. *Cell Rep.* 25, 478–486.e8. doi: 10.1016/J.CELREP.2018.09.040

Jiang, Y.-L., Wang, X.-P., Sun, H., Han, S.-J., Li, W.-F., Cui, N., et al. (2017). Coordinating carbon and nitrogen metabolic signaling through the cyanobacterial global repressor NdhR. *Proc. Natl. Acad. Sci. USA* 115, 201716062. doi: 10.1073/pnas.1716062115

Käll, L., Canterbury, J. D., Weston, J., Noble, W. S., and MacCoss, M. J. (2007). Semi-supervised learning for peptide identification from shotgun proteomics datasets. *Nat. Methods* 4, 923–925. doi: 10.1038/nmeth1113

Kämäräinen, J., Huokko, T., Kreula, S., Jones, P. R., Aro, E. M., and Kallio, P. (2017). Pyridine nucleotide transhydrogenase PntAB is essential for optimal growth and photosynthetic integrity under low-light mixotrophic conditions in *Synechocystis* sp. PCC 6803. *New Phytol.* 214, 194–204. doi: 10.1111/nph.14353

Kaneko, T., Sato, S., Kotani, H., Tanaka, A., Asamizu, E., Nakamura, Y., et al. (1996). Sequence analysis of the genome of the unicellular cyanobacterium *Synechocystis* sp. strain PCC6803. II. Sequence determination of the entire genome and assignment of potential protein-coding regions. *DNA Res.* 3, 109–36. Available online at: http://www.ncbi.nlm.nih.gov/pubmed/8905231 (accessed October 16, 2018).

Kaplan, A. (2017). On the cradle of CCM research: discovery, development, and challenges ahead. *J. Exp. Bot.* 68, 3785–3796. doi: 10.1093/jxb/erx122

Kirilovsky, D., and Kerfeld, C. A. (2013). The Orange Carotenoid Protein: a blue-green light photoactive protein. *Photochem. Photobiol. Sci.* 12, 1135. doi: 10.1039/c3pp25406b

Knoop, H., Gründel, M., Zilliges, Y., Lehmann, R., Hoffmann, S., Lockau, W., et al. (2013). Flux balance analysis of cyanobacterial metabolism: the metabolic network of *Synechocystis* sp. PCC 6803. *PLoS Comput. Biol.* 9, 1003081. doi: 10.1371/journal.pcbi.1003081

Knoppová, J., and Komenda, J. (2019). Sequential deletions of photosystem II assembly factors Ycf48, Ycf39 and Pam68 result in progressive loss of

autotrophy in the cyanobacterium Synechocystis PCC 6803. *Folia Microbiol.* 2019, 1–7. doi: 10.1007/s12223-019-00736-w

Koch, M., Berendzen, K. W., and Forchhammer, K. (2020). On the role and production of polyhydroxybutyrate (Phb) in the cyanobacterium *Synechocystis* sp. *pcc. Life* 10, 6803. doi: 10.3390/life10040047

Koch, M., Doello, S., Gutekunst, K., and Forchhammer, K. (2019). PHB is produced from glycogen turn-over during nitrogen starvation in *Synechocystis* sp. PCC 6803. *Int. J. Mol. Sci.* 20, 1942. doi: 10.3390/ijms20081942

Kronfel, C. M., Hernandez, C. V., Frick, J. P., Hernandez, L. S., Gutu, A., Karty, J. A., et al. (2019). CpeF is the bilin lyase that ligates the doubly linked phycoerythrobilin on β-phycoerythrin in the cyanobacterium *Fremyella diplosiphon*. *J. Biol. Chem.* 294, 3987–3999. doi: 10.1074/jbc.RA118.007221

Kurian, D., Jansèn, T., and Mäenpää, P. (2006). Proteomic analysis of heterotrophy in *Synechocystis* sp. PCC 6803. *Proteomics* 6, 1483–1494. doi: 10.1002/pmic.200500413

Lea-Smith, D. J., and Howe, C. J. (2017). "The Use of Cyanobacteria for Biofuel Production," in *Biofuels and Bioenergy* (New York: John Wiley and Sons) 143–155.

Lee, H. M., Flores, E., Forchhammer, K., Herrero, A., and Tandeau De Marsac, N. (2000). Phosphorylation of the signal transducer P(II) protein and an additional effector are required for the P(II)-mediated regulation of nitrate and nitrite uptake in the cyanobacterium *Synechococcus* sp. PCC 7942. *Eur. J. Biochem.* 267, 591–600. doi: 10.1046/j.1432-1327.2000.01043.x

Liberton, M., Saha, R., Jacobs, J. M., Nguyen, A. Y., Gritsenko, M. A., Smith, R. D., et al. (2016). Global proteomic analysis reveals an exclusive role of thylakoid membranes in bioenergetics of a model cyanobacterium. *Mol. Cell. Proteomics* 15, 2021–2032. doi: 10.1074/mcp.M115.057240

Lindblad, P., Fuente, D., Borbe, F., Cicchi, B., Conejero, J. A., Couto, N., et al. (2019). CyanoFactory, a European consortium to develop technologies needed to advance cyanobacteria as chassis for production of chemicals and fuels. *Algal Res.* 41, 101510. doi: 10.1016/j.algal.2019.101510

Liu, L.-N., and Zhang, Y.-Z. (2019). Cryoelectron microscopy delineates the in situ structure of the thylakoid network. *Mol. Plant* 12, 1176–1178. doi: 10.1016/J.MOLP.2019.07.005

Liu, X., Xie, H., Roussou, S., and Lindblad, P. (2022). Current advances in engineering cyanobacteria and their applications for photosynthetic butanol production. *Curr. Opin. Biotechnol.* 73, 143–150. doi: 10.1016/J.COPBIO.2021.07.014

Lucius, S., Makowka, A., Michl, K., Gutekunst, K., and Hagemann, M. (2021). The Entner-Doudoroff pathway contributes to glycogen breakdown during high to low CO_2 shifts in the cyanobacterium *Synechocystis* sp. PCC 6803. *Front. Plant Sci.* 12, 787943. doi: 10.3389/fpls.2021.787943

Makowka, A., Nichelmann, L., Schulze, D., Spengler, K., Wittmann, C., Forchhammer, K., et al. (2020). Glycolytic shunts replenish the Calvin–Benson–Bassham cycle as anaplerotic reactions in cyanobacteria. *Mol. Plant* 13, 471–482. doi: 10.1016/j.molp.2020.02.002

Melnicki, M. R., Leverenz, R. L., Sutter, M., López-Igual, R., Wilson, A., Pawlowski, E. G., et al. (2016). Structure, diversity, and evolution of a new family of soluble carotenoid-binding proteins in cyanobacteria. *Mol. Plant* 9, 1379–1394. doi: 10.1016/j.molp.2016.06.009

Mills, L. A., McCormick, A. J., and Lea-Smith, D. J. (2020). Current knowledge and recent advances in understanding metabolism of the model cyanobacterium *Synechocystis* sp. PCC 6803. *Biosci. Rep.* 40, 3325. doi: 10.1042/BSR20193325

Mullineaux, C. W. (2014). Co-existence of photosynthetic and respiratory activities in cyanobacterial thylakoid membranes. *Biochim. Biophys. Acta Bioenerg.* 1837, 503–511. doi: 10.1016/j.bbabio.2013.11.017

Muramatsu, M., and Hihara, Y. (2012). Acclimation to high-light conditions in cyanobacteria: From gene expression to physiological responses. *J. Plant Res.* 125, 11–39. doi: 10.1007/s10265-011-0454-6

Muro-Pastor, M. I., Reyes, J. C., and Florencio, F. J. (2001). Cyanobacteria perceive nitrogen status by sensing intracellular 2-oxoglutarate levels. *J. Biol. Chem.* 276, 38320–38328. doi: 10.1074/jbc.M105297200

Mustila, H., Allahverdiyeva, Y., Isojärvi, J., Aro, E. M., and Eisenhut, M. (2014). The bacterial-type [4Fe−4S] ferredoxin 7 has a regulatory function under photooxidative stress conditions in the cyanobacterium *Synechocystis* sp. PCC 6803. *Biochim. Biophys. Acta Bioenerg.* 1837, 1293–1304. doi: 10.1016/J.BBABIO.2014.04.006

Nakajima, T., Kajihata, S., Yoshikawa, K., Matsuda, F., Furusawa, C., Hirasawa, T., et al. (2014). Integrated metabolic flux and omics analysis of *Synechocystis* sp. PCC 6803 under mixotrophic and photoheterotrophic conditions. *Plant Cell Physiol.* 55, 1606–1612. doi: 10.1093/pcp/pcu091

Nikkanen, L., Santana Sánchez, A., Ermakova, M., Rögner, M., Cournac, L., and Allahverdiyeva, Y. (2020). Functional redundancy between flavodiiron proteins and NDH-1 in *Synechocystis* sp. PCC 6803. *Plant J.* 103, 1460–1476. doi: 10.1111/tpj.14812

Nishiguchi, H., Hiasa, N., Uebayashi, K., Liao, J., Shimizu, H., and Matsuda, F. (2019). Transomics data-driven, ensemble kinetic modeling for system-level understanding and engineering of the cyanobacteria central metabolism. *Metab. Eng.* 52, 273–283. doi: 10.1016/j.ymben.2019.01.004

Nishiguchi, H., Liao, J., Shimizu, H., and Matsuda, F. (2020). Novel allosteric inhibition of phosphoribulokinase identified by ensemble kinetic modeling of *Synechocystis* sp. PCC 6803 metabolism. *Metab. Eng. Commun.* 11, e00153. doi: 10.1016/j.mec.2020.e00153

Ogawa, T., Marco, E., and Orus, M. I. (1994). A gene required for carboxysome formation. *J. Bacteriol.* 176, 2374–2378.

Pan, L.-L., Onai, K., Uesaka, K., Ihara, K., Natsume, T., Takatani, N., et al. (2016). Transcriptional regulation of CmpR, the LysR family protein involved in CO2-responsive gene regulation in the cyanobacterium Synechococcus elongatus. *Biomed. Genet. Genomics* 1, 1–6. doi: 10.15761/bgg.1000123

Panda, B., Jain, P., Sharma, L., and Mallick, N. (2006). Optimization of cultural and nutritional conditions for accumulation of poly-β-hydroxybutyrate in *Synechocystis* sp. PCC 6803. *Bioresour. Technol.* 97, 1296–1301. doi: 10.1016/J.BIORTECH.2005.05.013

Panda, B., and Mallick, N. (2007). Enhanced poly-?-hydroxybutyrate accumulation in a unicellular cyanobacterium, *Synechocystis* sp. PCC 6803. *Lett. Appl. Microbiol.* 44, 194–198. doi: 10.1111/j.1472-765X.2006.02048.x

Perkins, D. N., Pappin, D. J. C., Creasy, D. M., and Cottrell, J. S. (1999). Probability-based protein identification by searching sequence databases using mass spectrometry data. *Electrophoresis* 20, 3551–3567. doi: 10.1002/(SICI)1522-2683(19991201)20:18<3551::AID-ELPS3551>3.0.CO;2-2

Pierson, L. S., and Pierson, E. A. (2010). Metabolism and function of phenazines in bacteria: Impacts on the behavior of bacteria in the environment and biotechnological processes. *Appl. Microbiol. Biotechnol.* 86, 1659–1670. doi: 10.1007/s00253-010-2509-3

Pitt, F. D., Mazard, S., Humphreys, L., and Scanlan, D. J. (2010). Functional characterization of *Synechocystis* sp. strain PCC 6803 pst1 and pst2 gene clusters reveals a novel strategy for phosphate uptake in a freshwater cyanobacterium. *J. Bacteriol.* 192, 3512–3523. doi: 10.1128/JB.00258-10

Plohnke, N., Seidel, T., Kahmann, U., Rögner, M., Schneider, D., and Rexroth, S. (2015). The proteome and lipidome of *Synechocystis* sp. PCC 6803 cells grown under light-activated heterotrophic conditions. *Mol. Cell. Proteomics* 14, 572–584. doi: 10.1074/mcp.M114.042382

Rast, A., Rengstl, B., Heinz, S., Klingl, A., and Nickelsen, J. (2016). The role of Slr0151, a tetratricopeptide repeat protein from *Synechocystis* sp. PCC 6803, during photosystem II assembly and repair. *Front. Plant Sci.* 7, 605. doi: 10.3389/fpls.2016.00605

Rast, A., Schaffer, M., Albert, S., Wan, W., Pfeffer, S., Beck, F., et al. (2019). Biogenic regions of cyanobacterial thylakoids form contact sites with the plasma membrane. *Nat. Plants* 5, 436–446. doi: 10.1038/s41477-019-0399-7

Rengstl, B., Knoppová, J., Komenda, J., and Nickelsen, J. (2013). Characterization of a Synechocystis double mutant lacking the photosystem II assembly factors YCF48 and Sll0933. *Planta* 237, 471–480. doi: 10.1007/s00425-012-1720-0

Sakata, S., Mizusawa, N., Kubota-Kawai, H., Sakurai, I., and Wada, H. (2013). Psb28 is involved in recovery of photosystem II at high temperature in *Synechocystis* sp. PCC 6803. *Biochim. Biophys. Acta Bioenerg.* 1827, 50–59. doi: 10.1016/J.BBABIO.2012.10.004

Santos-Merino, M., Singh, A. K., and Ducat, D. C. (2019). New applications of synthetic biology tools for cyanobacterial metabolic engineering. *Front. Bioeng. Biotechnol.* 7, 33. doi: 10.3389/fbioe.2019.00033

Sanz-Luque, E., Bhaya, D., and Grossman, A. R. (2020). Polyphosphate: a multifunctional metabolite in cyanobacteria and algae. *Front. Plant Sci.* 11, 938. doi: 10.3389/fpls.2020.00938

Saroussi, S. I., Wittkopp, T. M., and Grossman, A. R. (2016). The type II NADPH dehydrogenase facilitates cyclic electron flow, energy-dependent quenching, and chlororespiratory metabolism during acclimation of *Chlamydomonas reinhardtii* to nitrogen deprivation. *Plant Physiol.* 170, 1975–1988. doi: 10.1104/PP.15.02014

Scheer, H., and Zhao, K.-H. (2008). Biliprotein maturation: the chromophore attachment. *Mol. Microbiol.* 68, 263–276. doi: 10.1111/j.1365-2958.2008.06160.x

Schlebusch, M., and Forchhammer, K. (2010). Requirement of the nitrogen starvation-induced protein s110783 for polyhydroxybutyrate accumulation in *Synechocystis* sp. strain PCC 6803. *Appl. Environ. Microbiol.* 76, 6101–6107. doi: 10.1128/AEM.00484-10

Schultze, M., Forberich, B., Rexroth, S., Dyczmons, N. G., Roegner, M., and Appel, J. (2009). Localization of cytochrome b6f complexes implies an incomplete respiratory chain in cytoplasmic membranes of the cyanobacterium *Synechocystis* sp. PCC 6803. *Biochim. Biophys. Acta Bioenerg.* 1787, 1479–1485. doi: 10.1016/j.bbabio.2009.06.010

Shinde, S., Zhang, X., Singapuri, S. P., Kalra, I., Liu, X., Morgan-Kiss, R. M., et al. (2020). Glycogen metabolism supports photosynthesis start through the oxidative pentose phosphate pathway in cyanobacteria. *Plant Physiol.* 182, 507–517. doi: 10.1104/pp.19.01184

Sokolenko, A., Pojidaeva, E., Zinchenko, V., Panichkin, V., Glaser, V. M., Herrmann, R. G., et al. (2002). The gene complement for proteolysis in the cyanobacterium *Synechocystis* sp. PCC 6803 and *Arabidopsis thaliana* chlorophlasts. *Curr. Genet.* 41, 291–310. doi: 10.1007/s00294-002-0309-8

Solymosi, D., Nikkanen, L., Muth-Pawlak, D., Fitzpatrick, D., Vasudevan, R., Howe, C. J., et al. (2020). Cytochrome cM decreases photosynthesis under photomixotrophy in *Synechocystis* sp. PCC 6803. *Plant Physiol.* 183, 700–716. doi: 10.1104/PP.20.00284

Song, H., Ding, M. Z., Jia, X. Q., Ma, Q., and Yuan, Y. J. (2014). Synthetic microbial consortia: From systematic analysis to construction and applications. *Chem. Soc. Rev.* 43, 6954–6981. doi: 10.1039/c4cs00114a

Spät, P., Klotz, A., Rexroth, S., Maček, B., and Forchhammer, K. (2018). Chlorosis as a developmental program in cyanobacteria: the proteomic fundament for survival and awakening. *Mol. Cell. Proteomics* 17, 1650–1669. doi: 10.1074/MCP.RA118.000699

Sun, N., Han, X., Xu, M., Kaplan, A., Espie, G. S., and Mi, H. (2019). A thylakoid-located carbonic anhydrase regulates CO_2 uptake in the cyanobacterium *Synechocystis* sp. PCC 6803. *New Phytol.* 222, 206–217. doi: 10.1111/nph.15575

Tabei, Y., Okada, K., and Tsuzuki, M. (2007). Sll1330 controls the expression of glycolytic genes in *Synechocystis* sp. PCC 6803. *Biochem. Biophys. Res. Commun.* 355, 1045–1050. doi: 10.1016/J.BBRC.2007.02.065

Tanigawa, R., Shirokane, M., Maeda, S. I., Omata, T., Tanaka, K., and Takahashi, H. (2002). Transcriptional activation of NtcA-dependent promoters of Synechococcus sp. PCC 7942 by 2-oxoglutarate in vitro. *Proc. Natl. Acad. Sci. USA* 99, 4251–4255. doi: 10.1073/PNAS.072587199

Tomar, V., Sidhu, G. K., Nogia, P., Mehrotra, R., and Mehrotra, S. (2017). Regulatory components of carbon concentrating mechanisms in aquatic unicellular photosynthetic organisms. *Plant Cell Rep.* 36, 1671–1688. doi: 10.1007/s00299-017-2191-3

Toyoshima, M., Tokumaru, Y., Matsuda, F., and Shimizu, H. (2020). Assessment of protein content and phosphorylation level in *Synechocystis* sp. PCC 6803 under various growth conditions using quantitative phosphoproteomic analysis. *Molecules* 25, 3582. doi: 10.3390/molecules25163582

Vázquez-Bermúdez, M. F., Herrero, A., and Flores, E. (2002). 2-Oxoglutarate increases the binding affinity of the NtcA (nitrogen control) transcription factor for the *Synechococcus* glnA promoter. *FEBS Lett.* 512, 71–74. doi: 10.1016/S0014-5793(02)02219-6

Vizcaíno, J. A., Csordas, A., del-Toro, N., Dianes, J. A., Griss, J., Lavidas, I., et al. (2016). 2016 update of the PRIDE database and its related tools. *Nucleic Acids Res.* 44, D447–D456. doi: 10.1093/nar/gkv1145

Voronkov, A., and Sinetova, M. (2019). Polyphosphate accumulation dynamics in a population of *Synechocystis* sp. PCC 6803 cells under phosphate overplus. *Protoplasma* 256, 1153–1164. doi: 10.1007/s00709-019-01374-2

Wan, N., DeLorenzo, D. M., He, L., You, L., Immethun, C. M., Wang, G., et al. (2017). Cyanobacterial carbon metabolism: fluxome plasticity and oxygen dependence. *Biotechnol. Bioeng.* 114, 1593–1602. doi: 10.1002/bit.26287

Wang, H. L., Postier, B. L., and Burnap, R. L. (2004). Alterations in global patterns of gene expression in *Synechocystis* sp. PCC 6803 in response to inorganic carbon limitation and the inactivation of ndhR, a LysR family regulator. *J. Biol. Chem.* 279, 5739–5751. doi: 10.1074/jbc.M311336200

Watzer, B., and Forchhammer, K. (2018). Cyanophycin synthesis optimizes nitrogen utilization in the unicellular cyanobacterium *Synechocystis* sp. strain PCC 6803. *Appl. Environ. Microbiol.* 84. doi: 10.1128/AEM.01298-18

Watzer, B., Spät, P., Neumann, N., Koch, M., Sobotka, R., Macek, B., et al. (2019). The signal transduction protein PII controls ammonium, nitrate and urea uptake in cyanobacteria. *Front. Microbiol.* 10, 1428. doi: 10.3389/fmicb.2019.01428

Wegener, K. M., Welsh, E. A., Thornton, L. E., Keren, N., Jacobs, J. M., Hixson, K. K., et al. (2008). High sensitivity proteomics assisted discovery of a novel operon involved in the assembly of photosystem II, a membrane protein complex. *J. Biol. Chem.* 283, 27829–27837. doi: 10.1074/jbc.M803918200

Welkie, D. G., Rubin, B. E., Diamond, S., Hood, R. D., Savage, D. F., and Golden, S. S. (2019). A hard day's night: cyanobacteria in diel cycles. *Trends Microbiol.* 27, 231–242. doi: 10.1016/J.TIM.2018.11.002

Wu, Q., Guo, L., Wang, Y., Zhao, Y., Jin, C., Gao, M., et al. (2021). Phosphorus uptake, distribution and transformation with Chlorella vulgaris under different trophic modes. *Chemosphere* 285. doi: 10.1016/j.chemosphere.2021.131366

Xiong, W., Brune, D., and Vermaas, W. F. J. (2014). The γ-aminobutyric acid shunt contributes to closing the tricarboxylic acid cycle in *Synechocystis* sp. PCC 6803. *Mol. Microbiol.* 93, 786–796. doi: 10.1111/mmi.12699

Yang, H., Liao, L., Bo, T., Zhao, L., Sun, X., Lu, X., et al. (2014). Slr0151 in *Synechocystis* sp. PCC 6803 is required for efficient repair of photosystem II under high-light condition. *J. Integr. Plant Biol.* 56, 1136–1150. doi: 10.1111/jipb.12275

Yoshikawa, K., Hirasawa, T., Ogawa, K., Hidaka, Y., Nakajima, T., Furusawa, C., et al. (2013). Integrated transcriptomic and metabolomic analysis of the central metabolism of *Synechocystis* sp. PCC 6803 under different trophic conditions. *Biotechnol. J.* 8, 571–580. doi: 10.1002/biot.201200235

You, L., Berla, B., He, L., Pakrasi, H. B., and Tang, Y. J. (2014). ^{13}C-MFA delineates the photomixotrophic metabolism of *Synechocystis* sp. PCC 6803 under light- and carbon-sufficient conditions. *Biotechnol. J.* 9, 684–692. doi: 10.1002/biot.201300477

You, L., He, L., and Tang, Y. J. (2015). Photoheterotrophic fluxome in *Synechocystis* sp. strain PCC 6803 and its implications for cyanobacterial bioenergetics. *J. Bacteriol.* 197, 943–950. doi: 10.1128/JB.02149-14

Zak, E., Norling, B., Andersson, B., and Pakrasi, H. B. (1999). Subcellular localization of the BtpA protein in the cyanobacterium *Synechocystis* sp. PCC 6803. *Eur J Biochem* 261, 311–316. doi: 10.1046/j.1432-1327.1999.00281.x

Zhang, P., Allahverdiyeva, Y., Eisenhut, M., and Aro, E. M. (2009). Flavodiiron proteins in oxygenic photosynthetic organisms: photoprotection of photosystem II by FIv2 and FIv4 in *Synechocystis* sp. PCC 6803. *PLoS ONE* 4, 5331. doi: 10.1371/journal.pone.0005331

Zhang, P., Eisenhut, M., Brandt, A.-M., Carmel, D., Silen, H. M., Vass, I., et al. (2012). Operon flv4-flv2 provides cyanobacterial photosystem II with flexibility of electron transfer. *Plant Cell* 24, 1952–1971. doi: 10.1105/tpc.111.094417

Zhang, S., Qian, X., Chang, S., Dismukes, G. C., and Bryant, D. A. (2016). Natural and synthetic variants of the tricarboxylic acid cycle in cyanobacteria: introduction of the GABA Shunt into *Synechococcus* sp. PCC 7002. *Front. Microbiol.* 7, 1972. doi: 10.3389/fmicb.2016.01972

Zhao, C., Höppner, A., Xu, Q.-Z., Gärtner, W., Scheer, H., Zhou, M., et al. (2017). Structures and enzymatic mechanisms of phycobiliprotein lyases CpcE/F and PecE/F. *Proc. Natl. Acad. Sci. USA* 114, 13170–13175. doi: 10.1073/pnas.1715495114

Zheng, X., and O'Shea, E. K. (2017). Cyanobacteria maintain constant protein concentration despite genome copy-number variation. *Cell Rep.* 19, 497–504. doi: 10.1016/J.CELREP.2017.03.067

Conflict of Interest: The authors declare that the research was conducted in the absence of any commercial or financial relationships that could be construed as a potential conflict of interest.

The handling editor LL declared a past collaboration with the author TH.

Publisher's Note: All claims expressed in this article are solely those of the authors and do not necessarily represent those of their affiliated organizations, or those of the publisher, the editors and the reviewers. Any product that may be evaluated in this article, or claim that may be made by its manufacturer, is not guaranteed or endorsed by the publisher.

frontiers | Frontiers in Microbiology

ORIGINAL RESEARCH
published: 26 May 2022
doi: 10.3389/fmicb.2022.923367

Crystal Structure of an Intramolecular Mesaconyl-Coenzyme A Transferase From the 3-Hydroxypropionic Acid Cycle of *Roseiflexus castenholzii*

Zhenzhen Min[1†], Xin Zhang[1†], Wenping Wu[1], Yueyong Xin[2], Menghua Liu[1], Kangle Wang[1], Xingwei Zhang[1], Yun He[3], Chengpeng Fan[3], Zhiguo Wang[1*] and Xiaoling Xu[1,2,4*]*

[1] Department of Biochemistry and Molecular Biology, School of Basic Medical Sciences, The Affiliated Hospital of Hangzhou Normal University, Hangzhou, China, [2] Photosynthesis Research Center, College of Life and Environmental Sciences, Hangzhou Normal University, Hangzhou, China, [3] Department of Biochemistry and Molecular Biology, School of Basic Medical Sciences, Wuhan University, Wuhan, China, [4] Key Laboratory of Aging and Cancer Biology of Zhejiang Province, Hangzhou Normal University, Hangzhou, China

OPEN ACCESS

Edited by:
Weimin Ma,
Shanghai Normal University, China

Reviewed by:
Xiaoyun Ji,
Nanjing University, China
Lanfeng Wang,
Institut Pasteur of Shanghai (CAS), China
Xiaochun Qin,
University of Jinan, China

***Correspondence:**
Chengpeng Fan
chengpeng.fan@whu.edu.cn
Zhiguo Wang
zhgwang@hznu.edu.cn
Xiaoling Xu
xuxl@hznu.edu.cn

[†] These authors have contributed equally to this work and share first authorship

Specialty section:
This article was submitted to Microbial Physiology and Metabolism, a section of the journal Frontiers in Microbiology

Received: 19 April 2022
Accepted: 09 May 2022
Published: 26 May 2022

Citation:
Min Z, Zhang X, Wu W, Xin Y, Liu M, Wang K, Zhang X, He Y, Fan C, Wang Z and Xu X (2022) Crystal Structure of an Intramolecular Mesaconyl-Coenzyme A Transferase From the 3-Hydroxypropionic Acid Cycle of Roseiflexus castenholzii. Front. Microbiol. 13:923367. doi: 10.3389/fmicb.2022.923367

Coenzyme A (CoA) transferases catalyze reversible transfer of CoA groups from CoA-thioesters to free acids, playing important roles in the metabolism of carboxylic acids in all organisms. An intramolecular CoA transferase, Mesaconyl-CoA C1-C4 CoA transferase (MCT) was identified in the autotrophic CO_2 fixation pathway, 3-hydroxypropionic acid cycle of filamentous anoxygenic phototrophs (FAPs). Different from the well-known CoA transferases that catalyze CoA transfer between two distinct substrates, MCT specifically catalyzes the reversible transformation of mesaconyl-C1-CoA to mesaconyl-C4-CoA, a key reaction intermediate for carbon fixation. However, the molecular mechanism of MCT in employing one substrate is enigmatic. Here we determined the crystal structure of MCT from a chlorosome-less FAP *Roseiflexus castenholzii* at 2.5 Å resolution, and characterized the catalytic mechanisms through structural analyses and molecular dynamic simulations. The structure of *R. castenholzii* MCT consists of a Rossmann fold larger domain and a small domain that are connected by two linkers. Two MCT subunits are cross interlocked at the linker regions to form a functional dimer in solution, in which the substrate binding pockets are located at the interface of the Rossmann fold larger domain from one subunit and the small domain from the other subunit. In the simulated binding structures, both the substrate mesaconyl-C1-CoA and product mesaconyl-C4-CoA form extensive electrostatic and hydrogen bonding interactions with MCT. But some differences exist in the binding mode of these two CoA analogs, Arg314' from the second subunit of the dimer presenting dramatic conformational changes in binding with mesaconyl-C4-CoA. Together with Arg47 and one water molecule, a strictly conserved residue Asp165 are essential for catalyzing the reversible intramolecular CoA transfer reaction, through the electrostatic and hydrogen bonding interactions with the mesaconic tail of both the substrate and

product. This study revealed a previously unrecognized mechanism for the uncommon intramolecular CoA transfer reaction, which will not only broaden the knowledge on the catalytic mechanisms of CoA transferases, but also contribute to enzyme engineering or biosynthetic applications of the 3-HP cycle for synthesis of fine chemicals and important metabolites.

Keywords: filamentous anoxygenic phototrophs, 3-hydroxypropionic acid cycle, Mesaconyl-CoA transferase, *Roseiflexus castenholzii*, crystal structure

INTRODUCTION

Coenzyme A (CoA)-transferases catalyze the reversible transfer of CoA groups from CoA-thioesters to free acids, playing essential roles in the metabolism of carboxylic acids in all organisms. Based on the reaction mechanisms and amino acid sequences, these enzymes are grouped into three types. The reaction mechanisms of type I and II CoA transferases both involve the alternate formation of thioester and anhydride intermediates, but their catalytic mechanisms are quite different (Heider, 2001). The type-I enzymes catalyze CoA transfer using a ping-pong mechanism that requires formation of the CoA-thioester intermediate with a glutamate residue of the enzyme, then the enzyme-CoA intermediate reacts with a CoA-acceptor to proceed the reaction. The type-II CoA transferase usually catalyzes a partial reaction of the citrate or citramalate lyases that are comprised of a CoA-transferase (α-subunit), a lyase (β-subunit) and an acyl carrier protein (ACP, γ-subunit) (Buckel and Bobi, 1976; Subramanian et al., 1983). The catalytic mechanism involves ternary-complex formation of the enzyme, donor ACP-thioester (acetyl-ACP) and a thioester-acceptor (citrate or citramalate), without formation of covalently bound intermediates at the enzyme (Buckel et al., 1971; Buckel and Bobi, 1976; Malinin, 1977). Upon conversion of the thiol group of ACP to an acetyl-thioester, the CoA-transferase subunit catalyzes the exchange of free citrate or citramalate against the acetyl group of ACP (Dimroth and Eggerer, 1975; Buckel and Bobi, 1976; Mandal et al., 2000). Similarly, reaction of the type III CoA transferase also requires formation of a ternary complex between the enzyme and two substrates, but these enzymes employ diffusible CoA-thioester instead of ACP-thioester as substrates (Baetz and Allison, 1990; Leutwein and Heider, 1999; Dickert et al., 2000; Elssner et al., 2001; Heider, 2001; Jonsson et al., 2004; Friedmann et al., 2006).

In addition to the above-mentioned CoA transferases that catalyze CoA transfer between two distinct substrates, an intramolecular CoA transferase, Mesaconyl-CoA C1-C4 CoA transferase (MCT) was identified in the autotrophic CO_2 fixation pathway of a phototrophic bacterium *Chloroflexus aurantiacus* (Zarzycki et al., 2009). As the representative species of filamentous anoxygenic phototrophs (FAPs), *C. aurantiacus* grow heterotrophically in the dark by aerobic respiration but autotrophically in the light through photosynthesis (Pierson and Castenholz, 1974; Strauss and Fuchs, 1993). Instead of Calvin cycle, *C. aurantiacus* and many other FAPs fix carbon through a new metabolic pathway, the 3-hydroxypropionate (3-HP) cycle (Strauss and Fuchs, 1993). This cycle utilizes bicarbonate instead of CO_2 as substrate, it also assimilates small organic fermentation products even under anaerobic conditions. Most importantly, the 3-HP cycle is coupled by two cycles that ensure efficient utilization of the substrates and reaction intermediates. The first cycle catalyzes acetyl-CoA and two molecules of bicarbonate into one molecule of *(S)*-malyl-CoA, which is then cleaved to glyoxylate and acetyl-CoA. The second cycle starts from condensation of glyoxylate and propionyl-CoA to a *(2R, 3S)*-β-methylmalyl-CoA, and ends with cleavage of *(S)*-citramalyl-CoA into pyruvate and acetyl-CoA. As a result, the bicycle absorbs three molecules of bicarbonate and produces one molecule of pyruvate, with consumption of 5 molecules of ATP and 6 molecules of NADPH (Strauss and Fuchs, 1993; Zarzycki et al., 2009).

In the second cycle, conversion of *(2R, 3S)*-β-methylmalyl-CoA to *(S)*-citramalyl-CoA requires transfer of the CoA moiety from the C1 to C4 carboxyl group of the C5-dicarboxylic acid. However, neither free carboxylic acid nor free mesaconate exchange with mesaconyl-CoA was observed in the reaction. Zarzycki et al. (2009) identified and characterized a new CoA transferase that does not use acetyl-CoA or succinyl-CoA as CoA donors, nor free mesaconate, itaconate, (*R*)-/(*S*)-malate and (*R*)-/(*S*)-citrate as CoA receptors. Instead, it specifically catalyzes the intramolecular transformation of mesaconyl-C1-CoA to mesaconyl-C4-CoA, and therefore named as MCT. Sequence alignment with those of the type III CoA transferases revealed a strictly conserved aspartate residue of MCT, which seems to be capable of forming an acid anhydride with the CoA-activated acid. Reaction of this anhydride with the inhibitor compounds resulted in inactivation of the enzyme. However, MCT was partially inactivated by hydroxylamine that forms a hydroxamate at the CoA-activated glutamate residue of type I CoA transferases (White and Jencks, 1976; Mack and Buckel, 1995; Selmer and Buckel, 1999). Additionally, the enzymatic activity of MCT was nearly not affected by sodium borohydride that reduces the glutamyl-CoA (Mack and Buckel, 1995; Zarzycki et al., 2009), indicating that the active site conformation and catalytic mechanism of MCT are probably different from other CoA transferases. Especially, in comparison with the enzymes that transfer CoA between two different substrates, the molecular mechanism of MCT in catalyzing the intramolecular CoA transfer of only one substrate is enigmatic.

Abbreviations: CoA, Coenzyme A; MCT, mesaconyl-CoA C1-C4 CoA transferase; FAP, filamentous anoxygenic phototroph; *C. aurantiacus*, *Chloroflexus aurantiacus*; *R. castenholzii*, *Roseiflexus castenholzii*; 3-HP, 3-hydroxypropionate; MD, molecular dynamics; RMSD, root-mean-square deviation; RMSF, root-mean-square fluctuation; SAD, single-wavelength anomalous dispersion.

Here, we report the crystal structure of MCT from *Roseiflexus castenholzii*, a chlorosome-less FAP that is closely related to *C. aurantiacus*, wherein MCT was first identified and characterized (Hanada et al., 2002; Zarzycki et al., 2009). Although no substrate or analog has been detected in the structure, the binding modes of CoA, mesaconyl-C1-CoA and mesaconyl-C4-CoA were obtained through structural superimpositions and molecular dynamics (MD) simulations. Based on the crystal structure of apo-MCT and the characterized binding features of these CoA analogs, we proposed a molecular mechanism of *R. castenholzii* MCT in catalyzing the intramolecular CoA-transfer reaction. The results of this study provide structural basis for understanding the catalytic mechanism of intramolecular CoA transfer reactions, it will contribute to the diversity and molecular evolutions of CoA transferases, and their applications in synthesis of 3-HP and other important fine chemicals.

MATERIALS AND METHODS

Protein Expression and Purification

The gene sequence encoding Mesaconyl-CoA transferase from *R. castenholzii* strain DSM 13941 (NC_009767) was inserted into pEASY-E1 expression vector at *Nhe*I and *Sac*I restriction site to construct a N-terminal 6 × His-tagged recombinant expression vector. After DNA sequencing, the plasmid with the correct insert was transformed into *Escherichia coli* BL21 (DE3) cells, the cells were grown in 1 L Luria-Bertani broth containing 100 mg mL^{-1} Ampicillin at 37°C until the OD_{600} reached 0.6–0.8. The gene expression was then induced with 0.1 mM isopropyl-β-D-thiogalactopyranoside (IPTG) overnight at 25°C.

Cells were harvested by centrifugation at 6,000 r.p.m. for 15 min at 4°C, and resuspended in 40 mL wash buffer containing 25 mM Tris–HCl pH 8.0, 300 mM NaCl, 10 mM imidazole, 0.01% Triton X-100 and 0.1 mM phenylmethylsulfonylfluoride (PMSF) prior to the homogenization with a high-pressure homogenizer (Union, People's Republic of China). The insoluble cell debris was removed by centrifugation at 15,000 rpm for 40 min at 4°C. The supernatant containing crude soluble proteins was loaded onto a Ni^{2+}-chelating affinity chromatography column (GE Healthcare, United States) and was rinsed with 100 mL binding buffer (25 mM Tris–HCl pH 8.0, 300 mM NaCl, 20–50 mM imidazole) to remove non-specifically bound proteins. The bound MCT protein was eluted with the binding buffer containing 200 mM imidazole. The eluates were further purified by a HiLoad 16/600 Superdex 200 PG size exclusion column (GE Healthcare, United States) with buffer containing 25 mM Tris–HCl pH 8.0, 150 mM NaCl to 95% purity.

Crystallization of the Apo-Mesaconyl-Coenzyme A Transferase and Heavy Atom Soaking of the Crystals

The purified MCT protein was concentrated to 20 mg mL^{-1} at 4°C using an Amicon Ultra centrifugal filter device (10 kDa molecular-weight cutoff; Millipore, Germany). Protein concentration was determined using a NanoDrop (Thermo Scientific, United States) to measure the absorption at 280 nm. Crystallization was performed using the hanging-drop vapor diffusion method, with 1.5 μL of protein sample mixed with an equal volume of the reservoir solution, and then the drop was equilibrated against 200 μL reservoir solution. Hexagonal shaped crystals were obtained at 14 mg mL^{-1} with the reservoir solution (14% PEG4000, 0.1M Li_2SO_4, 0.1M Sodium Citrate) at 16°C. In order to determine the phase using single-wavelength anomalous dispersion data, heavy atom soaking of the crystals was performed. The purified MCT sample was mixed with various heavy atom derivatives from the heavy atom screen kit (Hampton Research, United States) at different concentrations. The homogeneity and binding properties of the mixed samples were analyzed by Native-PAGE. Then the derivatives represent the higher homogeneity with the MCT protein were selected for soaking. Finally, the native-MCT crystals were transferred and soaked in a solution containing 14% PEG4000, 0.1M Li_2SO_4, 0.1 M Sodium Citrate, 2.5 mM phenylmercury acetate, or 2.5 mM ethylmercurithiosalicylic acid, sodium salt for soaking.

Crystal Data Collection, Structure Determination, and Refinement

The optimized native-MCT crystals and Hg-soaked derivative crystals were cryo-protected by adding 25% glycerol to the reservoir solution and flash-frozen with liquid nitrogen, respectively. A 2.5 Å resolution dataset of native-MCT was collected at SSRF beamline BL19U1 with a 400 mm crystal-to-detector distance at wavelength of 0.97892 Å. 360 diffraction frames were collected with 1° oscillation per image. The crystal belongs to space group *C2* with unit cell dimensions a = 364.413 Å, b = 210.118 Å, c = 73.476 Å, α = 90°, β = 95.812°, γ = 90°. The diffraction data of Hg-soaked derivative crystal was also collected at SSRF BL19U1 with a 400 mm crystal-to-detector distance at wavelength of 0.87250 Å and 720 diffraction frames were collected with 0.5° oscillation per image. A 2.9 Å dataset was collected belonging to space group *C2* with unit cell dimensions a = 363.824 Å, b = 209.727 Å, c = 73.479 Å, α = 90°, β = 95.535°, γ = 90° (**Table 1**).

Diffraction data were processed, integrated, and scaled with HKL3000R software (Minor et al., 2006). The data quality was assessed using SFCHECK (Vaguine et al., 1999), and the solvent content was calculated using MATTHEWS_COEF from CCP4 (Matthews, 1968; Collaborative Computational Project, 1994). The dataset of Hg-soaked derivative crystal was used for phasing by single-wavelength anomalous dispersion (SAD) method, the positions of Hg-atoms were determined and the initial model was automatically built by AutoSol program (Terwilliger et al., 2009) and initially refined by Phenix-Refine (Afonine et al., 2012). Then the structure model was built using Coot (Emsley and Cowtan, 2004) and refined against the native dataset to 2.5 Å resolution using Refmac5 (Murshudov et al., 1997) from CCP4 package (Collaborative Computational Project, 1994) and the Phenix (Liebschner et al., 2019; **Table 1**).

TABLE 1 | Data collection and processing statistics of *R. castenholzii* MCT.

Crystal sample	Native MCT	Hg-derivative of MCT
Diffraction source	BL19U1, SSRF	BL19U1, SSRF
Wavelength (Å)	0.97892	0.87250
Temperature (K)	100	100
Detector	Pilatus3 6M	Pilatus3 6M
Crystal-to-detector distance (mm)	400	400
Rotation range per image (°)	1	0.5
Total rotation range (°)	360	360
Exposure time per image (s)	0.2	0.3
Space group	*C2*	*C2*
Cell parameters (Å)	*a* = 364.413, *b* = 210.118, *c* = 73.476 α = 90°, β = 95.812°, γ = 90°	*a* = 363.824, *b* = 209.727, *c* = 73.479 α = 90°, β = 95.535°, γ = 90°
Resolution range (Å)	50–2.50 (2.54-2.50)	50–2.90 (2.95-2.90)
Total no. of reflections	1300633	994583
No. of unique reflections	188922 (9443)	120126 (5862)
Completeness (%)	99.7 (99.2)	98.8 (95.9)
Redundancy	6.9 (6.6)	8.3 (7.8)
$<I/\sigma(I)>$	15.82 (3.95)	9.83 (2.17)
$CC_{1/2}$	0.956 (0.902)	0.950 (0.864)
R_{merge} (%)	14.7 (45.4)	17.6 (67.7)
Overall *B* factors from Wilson plot (Å^2)	24.43	26.63
Matthews coefficient		
V_M (Å^3 Da^{-1})	5.08	4.95
Solvent content (%)	75.81	75.15

R_{merge} = Σ_{hkl} Σ_i|I_i(hkl)-<I(hkl)>|/Σ_{hkl} Σ_i I_i(hkl), where I_i(hkl) is the intensity of the ith measurement of reflection hkl and <I(hkl)> is the mean intensity of all symmetry related reflection.

Gel Filtration and Sedimentation Velocity Analytical Ultracentrifugation

Gel filtration and sedimentation velocity analytical ultracentrifugation (AUC) were performed to check the oligomerization state of MCT in solution. The purified MCT sample was loaded on a Superdex 200 10/300 GL size exclusion column (GE Healthcare, United States) and eluted with buffer containing 25 mM Tris–Cl pH 8.0, 150 mM NaCl at 0.5 mL min^{-1}. Sedimentation experiments were performed on a Beckman Coulter ProteomeLab XL-I ultracentrifuge (Beckman Coulter, Indianapolis, United States) using a 4-hole An-60Ti rotor. Samples with an initial absorbance at 280 nm of approximately 0.5–0.8 were equilibrated for 2 h at 20°C under a vacuum prior to sedimentation. The absorbance at 280 nm was measured using a continuous scan mode during sedimentation at 55,000 rpm in 12 mm double-sector cells. The data were analyzed using sedfit (Schuck, 2000).

Molecular Dynamics Simulation and Binding Free Energy Calculations

The binding structure of MCT and CoA was constructed through structure superimposition with the formyl-CoA transferase from *Oxalobacter formigenes* (FRC, PDB ID: 1P5R) (Ricagno et al., 2003), a member of the type III CoA transferase. Based on the complex structure of MCT-CoA, the binding structures of mesaconyl-C1-CoA and mesaconyl-C4-CoA were generated under criteria that the mesaconyl-C1 and mesaconyl-C4 groups form as much as possible electrostatic and hydrogen bonding interactions with the surrounding amino acid residues of MCT. Structure superimposition and editing were accomplished by using the UCSF Chimera software (Pettersen et al., 2004).

Molecular dynamics (MD) simulations were performed by using the AMBER 12 software (Case et al., 2005). The CoA, mesaconyl-C1-CoA and mesaconyl-C4-CoA bound MCT structures were individually immersed into the center of a truncated octahedron box of TIP3P water molecules with a margin distance of 10.0 Å. The environmental sodium counterions were added to keep the system in electric neutrality. The AMBER ff14SB force field was applied for MCT (Maier et al., 2015). For the CoA, mesaconyl-C1-CoA and mesaconyl-C4-CoA, structure optimization was firstly performed with Gaussian 03 at the level of DFT B3LYP/6-31G(d) (Wang et al., 2022), then their atomic partial charges were calculated using the restricted electrostatic potential (RESP) method with a basis set of HF/6-31G(d) (Bayly et al., 1993). The other force field parameters of CoA analogs were generated from the Generalized Amber Force field (GAFF) with the Antechamber module of Amber Tools (Wang et al., 2004). Finally, by following the same procedure in our previous report (Wang et al., 2019), MD simulations were conducted with varied time scales, i.e., 200 ns for MCT-CoA and 300 ns for MCT-mesaconyl-C1-CoA/mesaconyl-C4-CoA binding structures.

Upon the equilibrium of MD simulations, the binding free energies (ΔG_{bind}) between MCT and the bound CoA analogs were obtained through the molecular mechanics/generalized Born surface area (MM/GBSA) calculation approach (Kollman et al., 2000):

$$\Delta G_{bind} = G_{complex} - (G_{protein} + G_{ligand}) \quad (1)$$

$$\Delta G_{bind} = \Delta H - T\Delta S \approx \Delta E_{MM} + \Delta G_{solv} - T\Delta S \quad (2)$$

$$\Delta E_{MM} = \Delta E_{vdW} + \Delta E_{ele} + \Delta E_{ini} \quad (3)$$

$$\Delta G_{solv} = \Delta G_{GB} + \Delta G_{SA} \quad (4)$$

where E_{MM} is the gas phase interaction energy comprising van der Waals energy (E_{vdW}) and electrostatic energy (E_{ele}). Internal strain energy difference (ΔE_{int}) equals zero since no contribution difference of bond, angle and torsion takes place. G_{solv} is the solvation free energy, including the contributions form a polar part (G_{GB}) and a non-polar part (G_{SA}). ΔG_{GB} was estimated using the generalized Born model with the interior and exterior dielectric constants set to 4 and 80, respectively (Liu et al., 2018). ΔG_{SA} was estimated using the LCPO algorithm: $\Delta G_{SA} = \gamma\Delta SASA + \beta$, where γ and β were set to 0.0072 and 0, respectively (Weiser et al., 1999). 200 snapshots were evenly extracted from the last 40 ns of each MD trajectory for the calculations of ΔE_{vdW}, ΔE_{ele}, ΔG_{GB} and ΔG_{SA}. The solute entropy term TΔS is sometimes approximated by normal mode entropy (Genheden and Ryde, 2015), but such treatment rarely

leads to improvement in the correlation with experiments (Deng et al., 2019). In this work we do not include the solute entropy term in estimating ΔG_{bind}.

RESULTS

Overall Structure of Mesaconyl-Coenzyme A Transferase From *Roseiflexus castenholzii*

To investigate the catalytic mechanism of MCT, we determined the crystal structure of apo-MCT using the single wavelength anomalous dispersion (Hendrickson et al., 1985; Rice et al., 2000) data from the crystals soaked with Hg-derivatives. The final model was refined to an R_{work} of 15.9% and an R_{free} of 19.2% at 2.5 Å resolution (**Tables 1**, **2**). The structure covers the full-length enzyme (Met1–Glu407) that consists of a Rossmann fold larger domain (Residues M1-N216 and F340-E407) and a small domain (Residues F231-P319), which are joined together by two linker regions (Residues D217-A230 for linker 1 and Y320-M339 for linker 2) (**Figure 1A** and **Supplementary Figure 1**). Two MCT subunits are cross interlocked at the linker regions, wherein α5 (D135-L142), α7 (A163-T186), and α8 (L196-L207) from each subunit are symmetrically interacted in the center, with two small domains and two Rossmann fold larger domains distributed at the top and bottom sides, respectively (**Figure 1B**). The dimer interface is stabilized by extensive hydrogen bonding and salt bridge interactions with amino acid pairs Arg324–Asp219 (3.0 Å), Arg324–Asp217 (3.3 Å), Tyr320-Asn158 (2.6 Å), Asp330-Lys197 (2.8 Å), and so on, as well as hydrophobic interactions involve side chains of Tyr136-Tyr320-Leu227, Ile166-Val167, and Met171 and so on (**Supplementary Figure 2A**). Both gel filtration and ultracentrifugation analyses showed that *R. castenholzii* MCT exists as a dimer in solution (**Supplementary Figures 2B,C**), which is consistent with previous biochemical evidences that the type III CoA transferases function as a dimer.

The *C2* crystal of apo-MCT contains a hexamer of three dimers in one asymmetric unit. The small domains of three dimers are closely associated with each other at α11 (T263-L273) and α12 (E280-A300) helices that are related by a threefold rotational axis (**Supplementary Figure 3A**). The loop regions (T148-A163) between α6 and α7 of six subunits are directing into the center, forming a cavity with a diameter about 14 Å at the threefold axis. At the interface, the guanidine side chains of Arg285 and the main chain oxygen of Ala300 form weak hydrogen bonding interactions, and π-π stacking interactions are formed between the guanidine and imidazole side chains of Arg288 and His299 (**Supplementary Figure 3B**). The PISA analyses (Krissinel and Henrick, 2007) revealed a CSS core of 1.0 and an average interface area of 6675.8 $Å^2$ for the basic dimer unit as shown in **Figure 1B**, which are contributed by the interactions from 74 hydrogen bonds and 43 salt bridges. Theoretical calculations predict a free energy of interaction (ΔG^{int}) of -94.0 kcal mol^{-1} and dissociation (ΔG^{diss}) of 115.9 kcal mol^{-1} for the dimer. Whereas the average interface area of other dimer forms ranged from 88.5 to 392.1 $Å^2$, with a CSS score from 0.011 to 0.044 (**Supplementary Table 1**). Therefore, the basic unit of dimer assembly shown in **Figure 1B** represents the stable biological assembly, and the hexamer assembly is formed due to the crystal packing.

Superimposition of the MCT dimer with that of the type III CoA-transferases reveals high structural similarity at the Rossmann fold larger domains, whereas the conformations of the small domain are dramatically different (**Figure 2A**). This is consistent with the multiple sequence alignment that showed considerable amino acid sequence conservation in the Rossman fold larger domains but less conservation in the small domains (**Supplementary Figure 1**). Compared to the formyl-CoA transferase from *O. formigenes* (FRC, PDB ID: 2VJQ) (Ricagno et al., 2003) that contain much longer linker 1 loop (Residues E226-V251), the corresponding loop are shorter in the formyl-CoA: oxalate-CoA transferase from *Acetobacter aceti* (FCOCT, PDB ID: 3UBM) (Mullins et al., 2012) and the formyl-CoA transferase from *E. coli* (YfdW, PDB ID: 1PT5) (Gogos et al., 2004; Toyota et al., 2008; **Figure 2B**; **Supplementary Figure 1**). In contrast, absence of this loop in MCT leads to the removal of a glycine-rich loop (G258-G261) that points directly into the active site pocket of FRC and Yfdw, as well as the shorter glycine-rich loop in FCOCT, creating a relatively larger substrate binding pocket of MCT (**Figure 2C**).

TABLE 2 | Structural refinement statistics of *R. castenholzii* MCT.

Resolution (Å)	50–2.5
No. of unique reflections	188472 (18766)
Reflections used for R_{free}	9360 (876)
R_{work} (%)	15.9
R_{free} (%)	19.2
No. of atoms	20538
macromolecules	18792
ligands	0
solvent	1746
Protein residues	2435
R.M.S. deviations	
bonds (Å)	0.008
angles (°)	1.02
Ramachandran favored (%)	98.39
Ramachandran allowed (%)	1.61
Ramachandran outliers (%)	0.00
Rotamer outliers (%)	1.04
Clashscore	3.22
Average B-factor ($Å^2$)	30.53
macromolecules	30.17
solvent	34.39

Alternative Conformations of *Roseiflexus castenholzii* Mesaconyl-Coenzyme A Transferase in Binding With Different Coenzyme A Analogs

Attempts to obtain the substrate-bound structure of *R. castenholzii* MCT were not successful, by either co-crystallization or soaking the crystals with various CoA analogs (succinyl-CoA, acetyl-CoA, propionyl-CoA, malonyl-CoA),

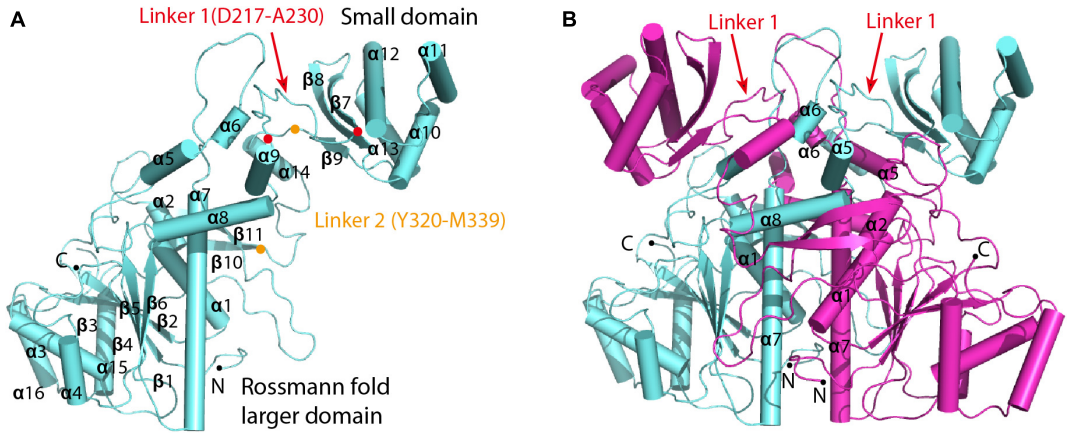

FIGURE 1 | Overall crystal structure of *R. castenholzii* MCT. **(A)** Overall structure of the subunit that comprises a dimer of MCT. Each subunit consists of a Rossmann fold larger domain and a small domain, which are joined together by two linker regions (Residues D217-A230 for linker 1 and Y320-M339 for linker 2). The N- and C-terminus, and amino acid residues located at the two ends of the linker are indicated as dots. **(B)** The conformation of the dimer. Two subunits are cross interlocked at the linker regions, wherein α5, α6, α7, and α8 from each subunit symmetrically interacted in the center of the dimer interface.

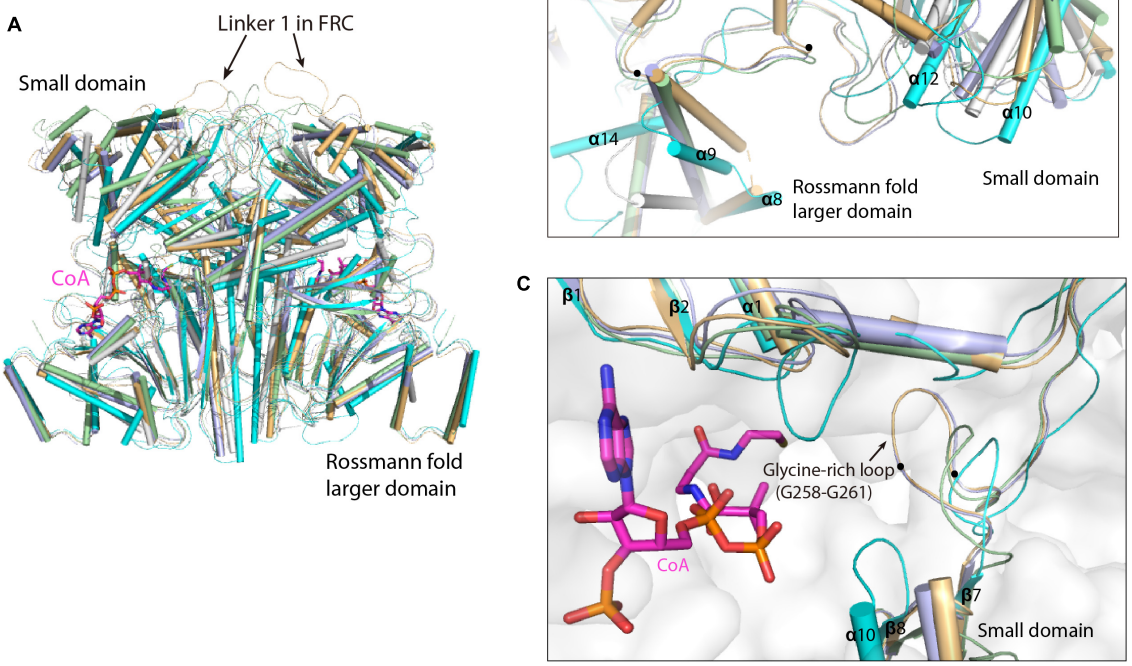

FIGURE 2 | Superimposition of *R. castenholzii* MCT dimer with that of the type III CoA-transferases. **(A)** Overall structure superimposition of MCT dimer with the dimers of formyl-CoA transferase from *Oxalobacter formigenes* (FRC, PDB ID: 2VJQ, yellow orange); formyl-CoA transferase from *E. coli* (YfdW, PDB ID: 1PT5, light blue); CoA transferase III from *Mycobacterium tuberculosis* (Rv3272, PDB ID: 5YIT, white); formyl-CoA: oxalate-CoA transferase from *Acetobacter aceti* (FCOCT, PDB ID: 3UBM, light green). The structures are aligned at the Rossman fold larger domain. The linker 1 in FRC is indicated with arrows. The CoA molecules bound in FCOCT are shown as stick models in magenta. **(B)** Comparison of the small domains and linker 1 loops in MCT and some type III CoA-transferases. The linker 1 loop in FRC is indicated with dots at the two ends of the loop and labeled. **(C)** Comparison of the substrate binding pocket of MCT with that of the type III CoA-transferases. The glycine-rich loop in FRC is indicated with dots at the two ends of the loop and labeled.

or the reaction intermediate mesaconic acid. To explore the catalytic mechanism of MCT, the binding structures of MCT with substrate analog CoA, the reaction substrate mesaconyl-C1-CoA and product mesaconyl-C4-CoA were generated, and their binding features were characterized through molecular dynamics (MD) simulations. No drastic fluctuations occurred at the root-mean-square deviation (RMSD) values during MD simulations, indicating the conformations of these complex structures are rather stable (**Supplementary Figures 4A–C**). In addition, the root-mean square fluctuation (RMSF) profiles of the binding complexes showed overall consistent pattern to that of the crystal structure of apo-MCT, indicating binding of the substrate analogs did not cause drastic conformational changes to MCT (**Supplementary Figure 4D**). Two CoA molecules were initially docked into the dimer of MCT through structural superimposition with the (FRC, PDB ID: 1P5R) (Ricagno et al., 2003), which gives a main chain RMSD of 2.378 and results in binding of the CoA molecules at the interface of the Rossmann fold larger domain from one subunit and the small domain from the other subunit (**Figure 3A**).

In the equilibrated binding structures derived from MD simulations, the adenine ring of the CoA is buried in a pocket formed by several loop regions connecting α3-β3, α2-β2, α1-β1 from top and α4-β4 at the bottom, wherein it is surrounded by the side chains of Pro38, Phe36, Ile72, Trp106, and Phe101 (**Figures 3A,B**). The phosphate moiety is hydrogen bonded with Arg75 NH2 (2.9 Å) and Arg104 NH2 (2.8 Å), respectively. The CoA pantetheine O1 and O4 atoms are hydrogen bonded with the NH2 atoms of Arg314' (2.7 Å) and Asn252' (2.9 Å) from the small domain of the other subunit. On the other side, the pantetheine tail is directing into the cavity formed by β1-α1, β5-α5, and α6-α7, wherein it is stabilized by hydrogen bonding interactions with the NH2 of Asn100 (2.8 Å), the hydroxyl group of Ser132 (2.7 Å), and the main chain oxygen of Glu133 (3.2 Å). At the end of CoA, the thiol group forms one hydrogen bond with Asp165 OD2 (3.0 Å).

In the equilibrated mesaconyl-C1-CoA bound structure, the adenine ring adopts similar spatial environment as CoA. The ribose oxygen forms hydrogen bond with Arg75 NH2 (2.9 Å), the phosphate O7 (3.0 Å), and O8 (2.9 Å) form hydrogen bonds with the guanidine side chain of Arg104 (**Figures 3C,D**). The pantetheine tail of mesaconyl-C1-CoA is hydrogen bonding with NH2 of Asn100 (2.8 Å), and main chain nitrogen (3.2 Å) and oxygen (2.9 Å) of Glu133. Importantly, the mesaconic end is positioned into a slit formed by loop regions connecting α6-α7 and β7'-α9', wherein it is coordinated by hydrogen bonding interactions with Arg47 NH1 (2.7 Å) and electrostatic interaction between the carbonyl C and Asp165 OD2 (3.4 Å) (**Figures 3C,D** and **Supplementary Figure 5A**).

In the equilibrated binding structure with mesaconyl-C4-CoA (**Figure 3E**), the guanidine side chains of Arg104, Arg314', and Ser132 undergo conformational changes as compared to the mesaconyl-C1-CoA bound MCT (**Figures 4A,B**). The adenine ring of mesaconyl-C4-CoA is coordinated in same conformation as mesaconyl-C1-CoA, except an additional hydrogen bond between the adenosine N6 atom and Asp37 OD2 (3.5 Å) (**Figure 3F**). Hydrogen bonding interactions are observed between the ribose oxygen and Arg75 NH2 (3.1 Å), the ribose phosphate oxygens with Arg104 NH1 of (2.8 Å) and NH2 (2.7 Å). Notably, the guanidine group of Arg314' dramatically flipped toward the pantetheine tail of mesaconyl-C4-CoA and hydrogen bonded with O9 (2.8 Å). Additionally, the pantetheine tail are hydrogen bonded with the main chain oxygen (2.9 Å) and nitrogen (2.9 Å) of Glu133. Although the conformation of mesaconyl-C4-CoA changes in comparison with mesaconyl-C1-CoA, the mesaconic end maintains a similar binding mode with the surrounding Asp165 (2.7 Å) and Arg47 (2.9 Å) residues (**Figure 3F**).

Binding Features Characterized From Molecular Dynamics Simulation

To further explore the binding characteristics of MCT with the CoA analogs, the binding affinities were evaluated based on the widely recognized molecular mechanics/generalized Born surface area (MM/GBSA) calculation (Kollman et al., 2000). As shown in **Table 3**, mesaconyl-C1-CoA exhibited the highest binding free energies to MCT ($\Delta G = -90.33$ kcal mol^{-1}), whereas CoA and mesaconyl-C4-CoA showed comparable binding free energies, indicating mesaconyl-C1-CoA is more favorable for binding to MCT. It is noted that electrostatic interaction (ΔE_{ele}) and polar solvation effect (ΔG_{GB}) contributed negatively and positively to the binding with CoA, respectively (**Table 3**). In contrast, the binding free energies of mesaconyl-C1-CoA and mesaconyl-C4-CoA were both contributed by a positive ΔE_{ele} and a negative ΔG_{GB}. Considering the adenine ring and pantetheine tail of these CoA analogs are basically immobilized with similar hydrophobic and hydrogen bonding interactions (**Figures 3B,D,F**), these reverse effects are probably resulted from the ligated mesaconic groups.

The binding free energy was further decomposed to identify the per-residue contribution (**Figure 5**). Phe16 contributed to the binding through hydrophobic interactions with the alkyl groups linked to the S atom of CoA analogs, more extensive hydrophobic contacts resulted in increased contribution of free energies to the binding of mesaconyl-C1-CoA and mesaconyl-C4-CoA with MCT (**Figures 5A–C**). Through electrostatic interactions with the phosphate group of CoA analogs, Arg75 and Arg104 made significant contributions to free energies that resulted in stable binding of the three analogs. The largest per-residue contribution came from Phe101, which forms parallel π-π interactions with the adenine ring of all the three CoA analogs. Notably, Arg47 made considerable contributions to the binding of mesaconyl-C1-CoA and mesaconyl-C4-CoA, but almost no contribution to the binding of CoA (**Figures 5A–C**). This agreed well with the observations that no electrostatic and hydrogen bonding interactions exist between Arg47 and the terminal thiol group of CoA, due to lack of the ligated mesaconic groups (**Figures 3B,D,F**). In contrast to the bindings of CoA and mesaconyl-C4-CoA, Arg314' from the other subunit of the dimer showed negligible contribution to the binding of mesaconyl-C1-CoA, which is also consistent with the characterized binding conformations (**Figures 3B,D,F**, **5**). Therefore, Arg47, Arg75, Phe101, and Arg104 are both essential for the binding of

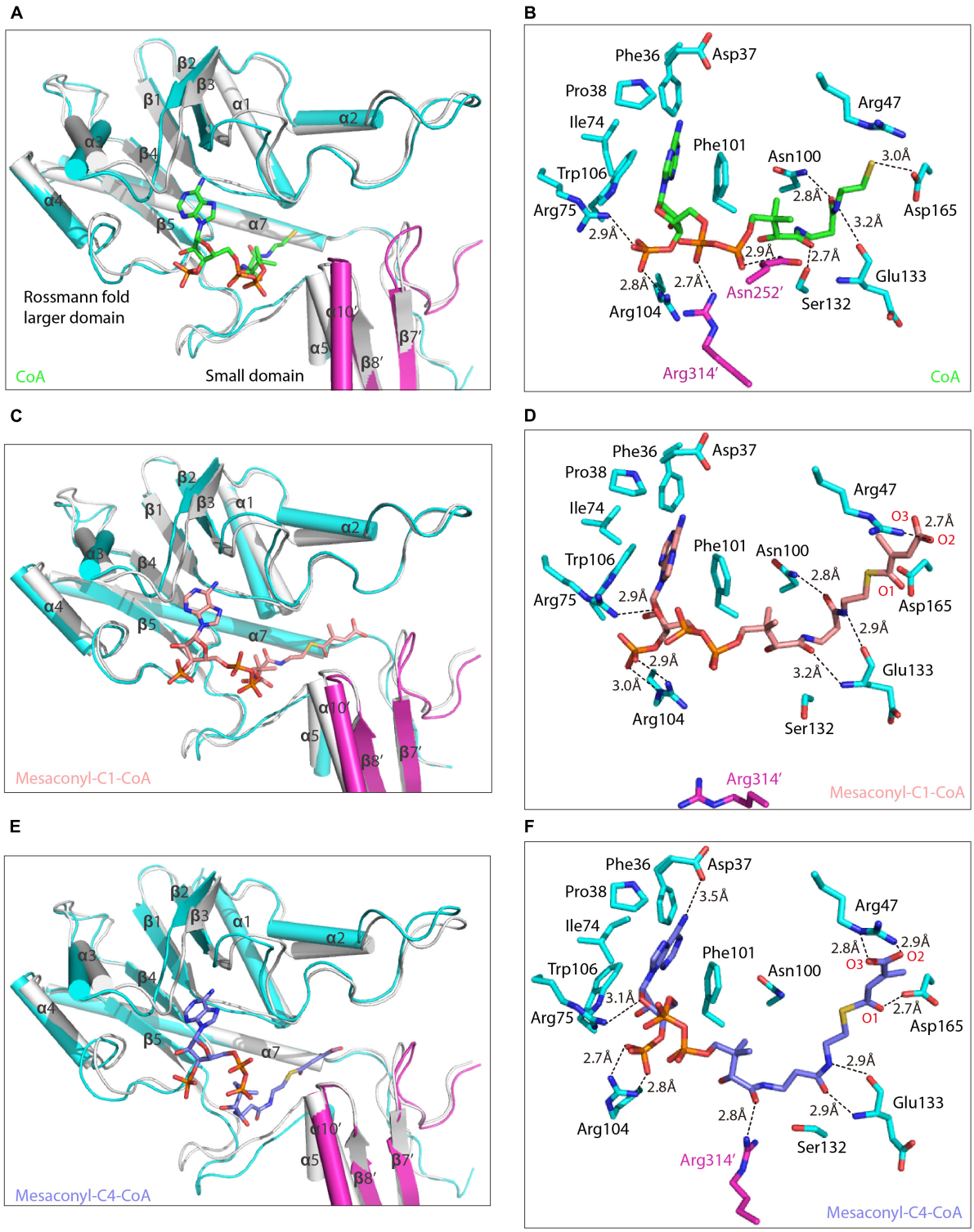

FIGURE 3 | Alternative conformations of the substrate binding pocket in binding with different CoA analogs. **(A,C,E)** The equilibrated binding structures of MCT in complex with CoA (**A**, green), mesaconyl-C1-CoA (**C**, salmon), and mesaconyl-C4-CoA (**E**, blue) are superimposed with the crystal structure of apo-MCT (the two subunits of the binding structures are colored in cyan and magenta). The secondary structures that form the substrate binding pocket of MCT are shown in ribbon and labeled, and the CoA analogs are shown in stick models. **(B,D,F)** Coordination of three CoA analogs with the substrate binding pocket of MCT. Amino acid residues essential for coordinating the CoA (**B**, green), mesaconyl-C1-CoA (**D**, salmon), and mesaconyl-C4-CoA (**F**, blue) are shown as stick models, the hydrogen bonding interactions are shown as dashed lines with distances labeled.

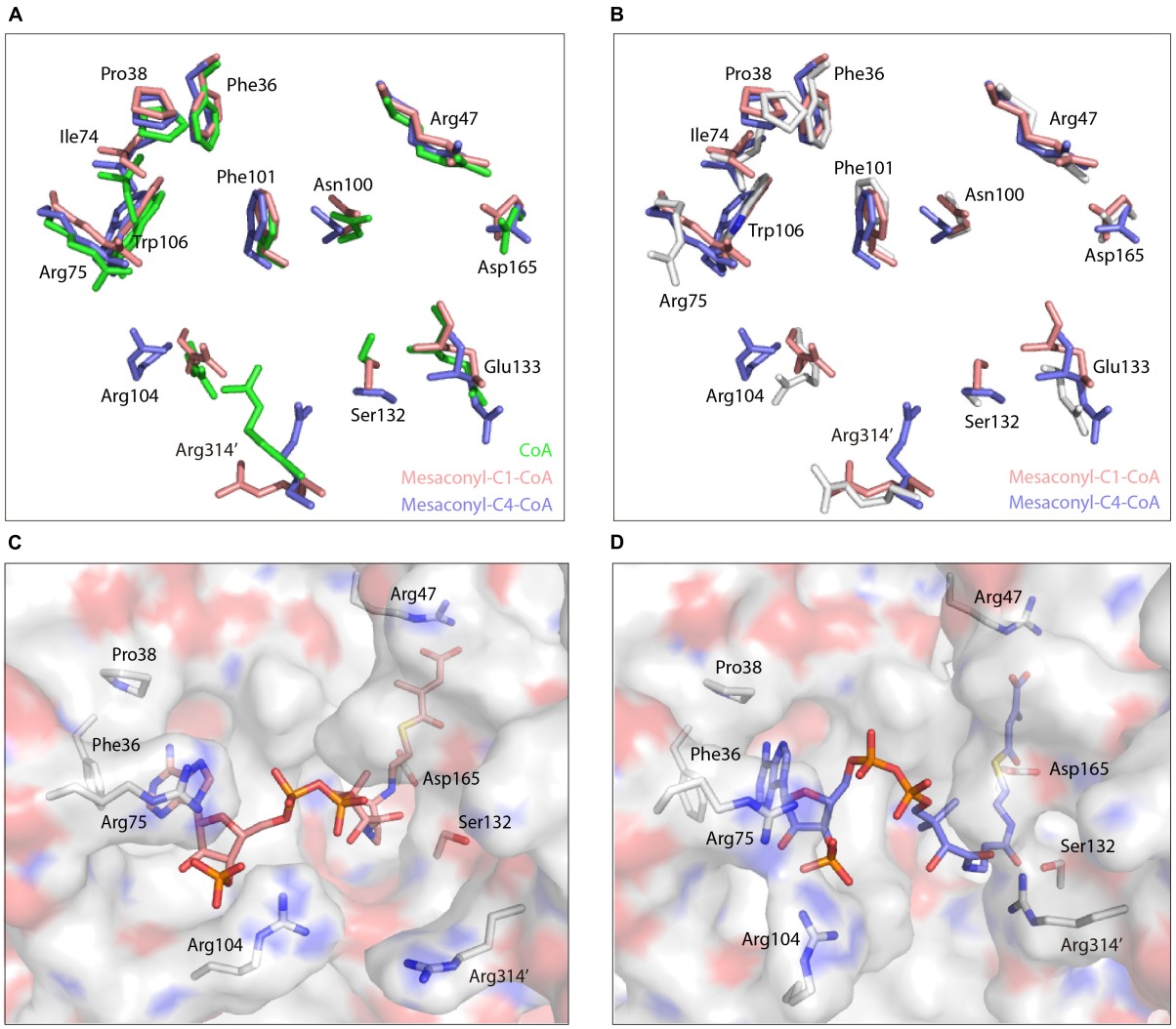

FIGURE 4 | Conformational changes of the substrate binding pocket in binding with different CoA analogs. **(A)** Superimpositions of the amino acid residues that are necessary for coordinating the CoA (green), mesaconyl-C1-CoA (salmon), and mesaconyl-C4-CoA (blue). **(B)** Superimpositions of the amino acid residues that are necessary for coordinating mesaconyl-C1-CoA (salmon) and mesaconyl-C4-CoA (blue) with the apo-MCT (white). **(C,D)** The binding mode of mesaconyl-C1-CoA **(C)**, mesaconyl-C4-CoA **(D)**, and the surface electrostatic potentials of MCT that are represented with positive, negative, and neutral charged residues colored in blue, red, and white, respectively. The key amino acid residues for coordinating the CoA analogs are shown in stick models.

TABLE 3 | Binding free energies calculated using the MM/PBSA approach.

Binding complex	Energy component[a]				
	ΔE_{ele}	ΔE_{vdW}	ΔG_{GB}	ΔG_{SA}	ΔG
MCT-CoA	−20.45 ± 5.63	−68.66 ± 4.93	12.61 ± 3.41	−10.25 ± 0.24	−86.76 ± 4.29
MCT-mesaconyl-C1-CoA	40.37 ± 8.593	−77.72 ± 4.88	−40.92 ± 8.64	−12.06 ± 0.32	−90.33 ± 5.07
MCT-mesaconyl-C4-CoA	23.05 ± 7.69	−68.82 ± 4.83	−27.76 ± 7.09	−11.49 ± 0.24	−85.02 ± 3.90

[a]*Energies are in kcal mol*$^{-1}$.

mesaconyl-C1-CoA and mesaconyl-C4-CoA, and the interaction with Arg314' is pivotal for discriminating these two analogs.

Further superimposition analyses revealed that the side chains of Arg104 and Arg314' undergo dramatic conformational changes in binding with the three CoA analogs (**Figures 4A,B**). Compared to the structure of apo-MCT, the guanidine side chain of Arg75 and Arg104 was flipped toward the substrate binding pocket to stabilize the ribose and phosphate group of the CoA analogs through hydrogen bonding interactions (**Figures 3B,D,F**, **Figure 4B**). For the binding of mesaconyl-C4-CoA, the guanidine

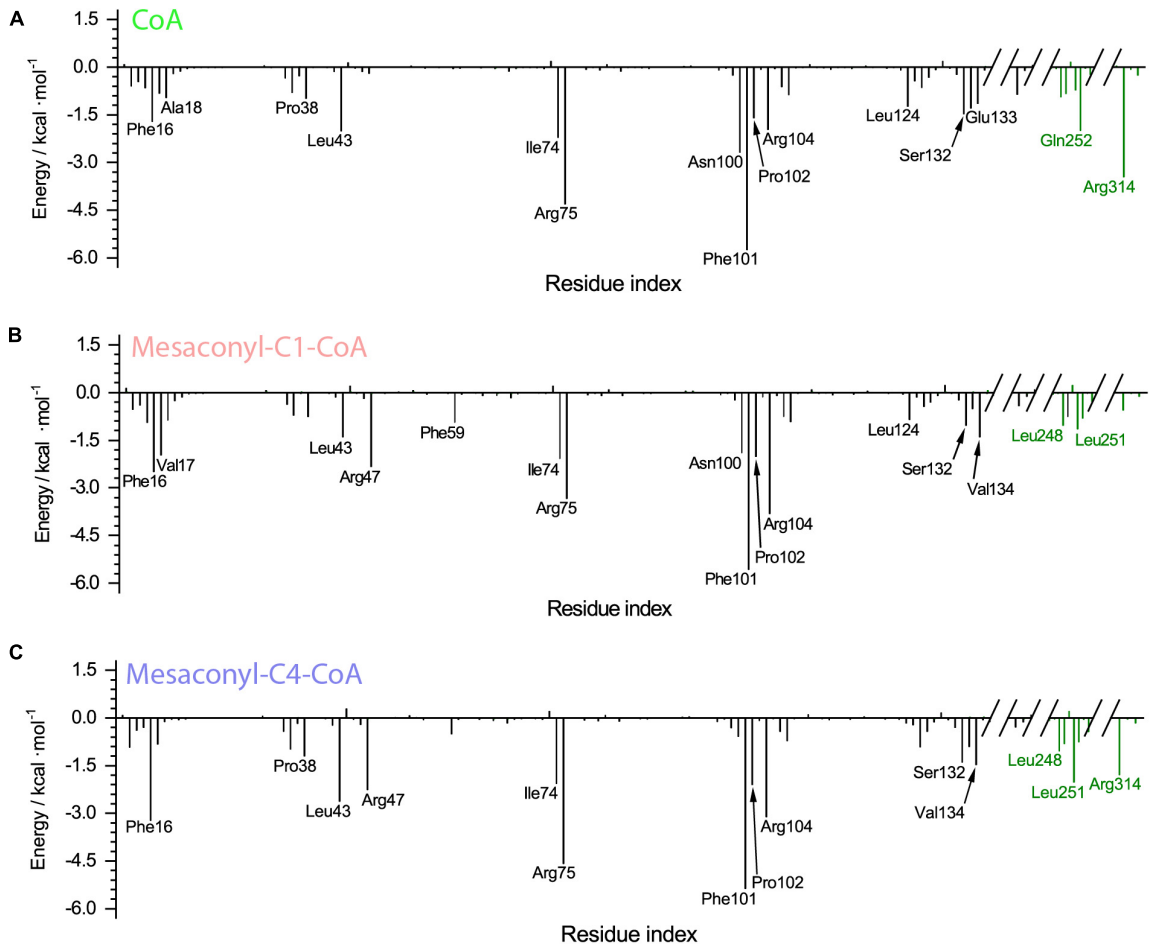

FIGURE 5 | The per-residue decomposition of the binding free energies of *R. castenholzii* MCT in binding with CoA **(A)**, mesaconyl-C1-CoA **(B)**, and mesaconyl-C4-CoA **(C)**. The binding free energy values (kcal mol^{-1}) are plotted against the amino acid numbers to show their contributions.

group of Arg314' was oscillated approximately 60° toward the pantetheine tail, the guanidine group of Arg104 was concomitantly flipped about 40° outward, these conformational changes together broaden the substrate entrance located in between the guanidine groups of Arg104 and Arg314' (**Figures 4B–D**). In addition, binding of mesaconyl-C1-CoA and mesaconyl-C4-CoA also resulted in distinct conformations and surface electron potentials of the substrate binding pocket. Mesaconyl-C1-CoA was fitted into the substrate binding pocket with pantetheine tail and phosphate group exposed, whereas the pantetheine tail of mesaconyl-C4-CoA was completely buried within the pocket (**Figures 4C,D**).

Molecular Mechanism of *Roseiflexus castenholzii* Mesaconyl-Coenzyme A Transferase Catalyzed Intramolecular Coenzyme A Transfer

The mesaconic end of mesaconyl-C1-CoA and mesaconyl-C4-CoA were stabilized by hydrogen bonding interactions with Asp165 and Arg47 (**Figures 3D,F**). In the equilibrated binding structure with mesaconyl-C1-CoA, no hydrogen bonding but electrostatic interaction was observed between the carbonyl C1 atom and the hydroxyl group (OD2) of Asp165 (3.4 Å), providing a prerequisite for hydrophilic attack at the C1 atom. On the other side, the O2 atom of the mesaconic end was immobilized in a chain of hydrogen bonding interactions with Arg47 NH1 (2.7 Å) and a water molecule (2.8 Å) (**Supplementary Figure 5A**). Similar hydrogen bonding interactions were also observed for the O2 atom of mesaconyl-C4-CoA. In contrast, mesaconyl-C4-CoA was accommodated with a longer distance between the C4 atom and Asp165 OD2 (3.7 Å) (**Supplementary Figure 5B**). Considering the strictly conservation of Asp165 with the catalytic aspartate residues of type III CoA-transferases, Asp165 and Arg47 residues are essential for catalyzing the CoA transfer reaction.

Based on the crystal structure of apo-MCT and the characterized binding features with mesaconyl-C1/C4-CoA, we proposed a catalytic mechanism for the intramolecular CoA transfer reaction (**Figures 6A,B**). At the close-to-neutral pH environment of the cell, both Asp165 and mesaconyl-C1-CoA are deprotonated, and Arg47 is protonated. Initially, the negatively charged carboxyl oxygen of Asp165 launches a nucleophilic

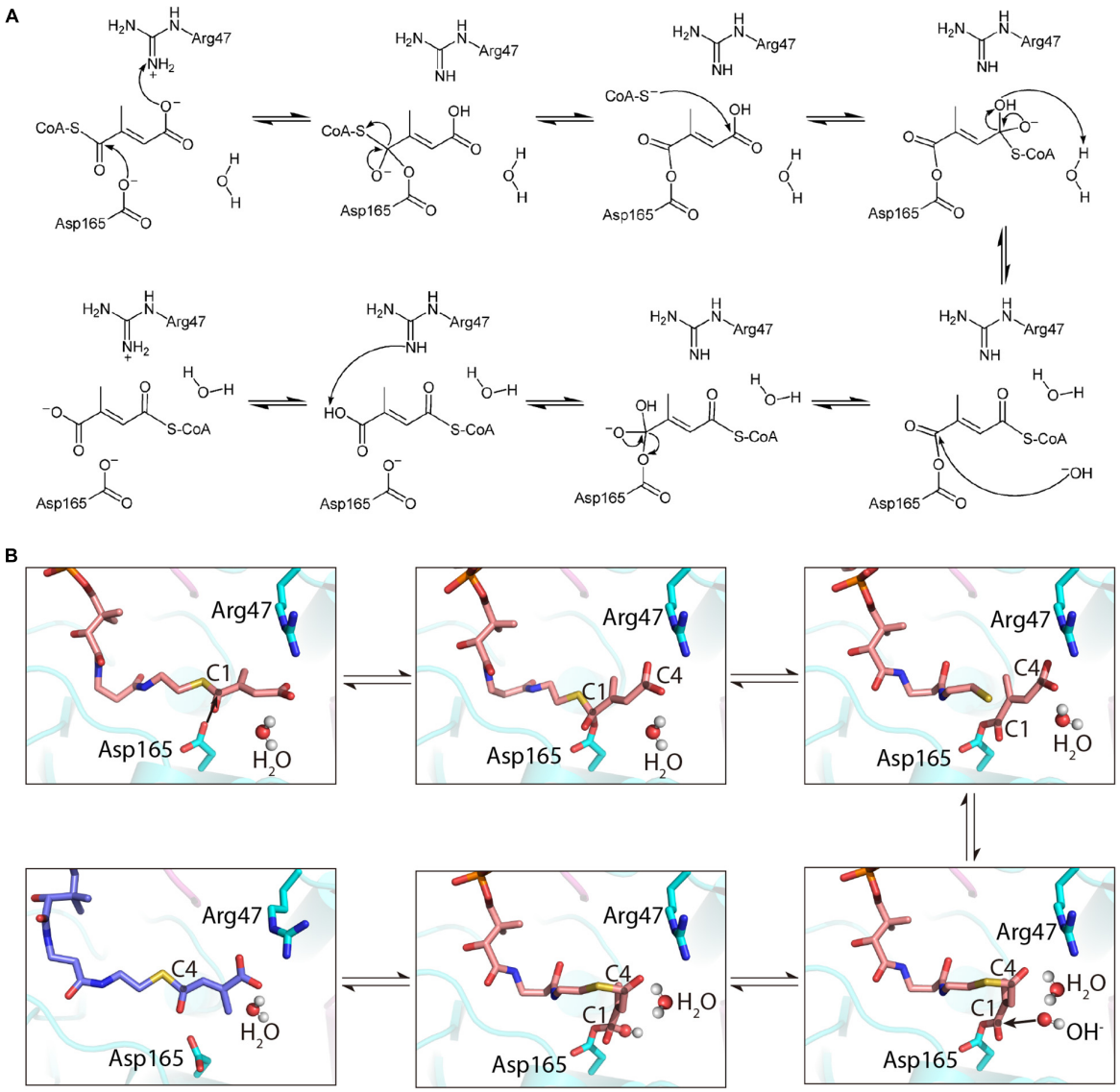

FIGURE 6 | Illustration of the proposed mechanism of *R. castenholzii* MCT as an intramolecular CoA-transferase. **(A)** The proposed mechanism of MCT in catalyzing the reversible CoA transfer between mesaconyl-C1-CoA and mesaconyl-C4-CoA. **(B)** Cartoon presentation of the mechanism of MCT in catalyzing the intramolecular CoA transfer reaction. Mesaconyl-C1-CoA (salmon), mesaconyl-C4-CoA (blue), and the key amino acid residues Arg47 and Asp165 are shown in stick models, and the water molecules are shown as spheres.

attack at the carbonyl C1 atom of mesaconyl-C1-CoA, and a proton involved in the electrostatic and hydrogen bonding interactions at the reactant state is concomitantly extracted from the guanidine group of Arg47 to the terminal carboxyl group of mesaconyl-C1-CoA. Subsequent intramolecular electron reorganization releases the $CoAS^-$ and forms an enzyme-bound anhydride. The liberated $CoAS^-$ anion is then engaged in a second nucleophilic attack at the carboxyl C4 atom of mesaconyl-C1-CoA. With involvement of a water molecule, the resultant tetrahedral intermediate is further converted to an enzyme (Asp165)-bound CoA-thioester, generating hydroxide ion and a new water. Subsequently, the released hydroxide ion initiates a third nucleophilic attack at the carbonyl C1 atom of the enzyme-bound CoA-thioester, then the electron rearrangement dissociates Asp165 from the CoA-thioester to its original deprotonated state. Finally, mesaconyl-C4-CoA is formed when a proton is extracted by the deprotonated guanine sidechain of Arg47 (**Figures 6A,B**).

DISCUSSION

Coenzyme A transferases are essential enzymes for the metabolism of carboxylic acids in all organisms, wherein they catalyze the reversible CoA transfer reactions with broad substrate specificity. In this study, we determined the

crystal structure of a novel intramolecular CoA transferase, Mesaconyl-CoA C1-C4 CoA transferase (MCT) from a green non-sulfur photosynthetic bacteria *R. castenholzii*, and characterized its catalytic mechanisms through structural analyses and MD simulations. The basic dimer unit observed in the crystal structure is consistent with the findings that *R. castenholzii* MCT exists as a dimer in solution. The substrate mesaconyl-C1-CoA and product mesaconyl-C4-CoA are coordinated at the interface between the Rossman fold larger domain from one subunit and the small domain from the other subunit of the dimer. In the equilibrated structures, Arg47 made considerable contributions to the binding of mesaconyl-C1-CoA and mesaconyl-C4-CoA, whereas Arg314' from the other subunit undergo dramatic conformational changes in binding with mesaconyl-C4-CoA. Together with Arg47 and one water molecule, a strictly conserved Asp165 residue are essential for catalyzing the reversible intramolecular CoA transfer reaction, through electrostatic and the hydrogen bonding interactions with the mesaconic tail of both the substrate and product.

Mesaconyl-coenzyme A transferase was originally identified in the 3-hydroxypropionic acid (3-HP) cycle of *C. aurantiacus* (Pierson and Castenholz, 1974), the representative bacteria of filamentous anoxygenic phototrophs (FAPs). FAPs are phylogenetically distant from other anoxygenic photosynthetic bacterium and form the deepest branch of photosynthetic bacteria (Oyaizu et al., 1987). This type of organism has acquired a "chimeric" photosynthetic system during evolution, with their reaction center and associated antenna resembling that of purple bacteria, whereas the light harvesting apparatus is similar as that of green sulfur bacteria (Blankenship, 2010; Hohmann-Marriott and Blankenship, 2011; Tang et al., 2011). Notably, FAPs evolved a new type carbon fixation pathway 3-hydroxypropionic acid bicycle, instead of Calvin cycle during evolution. This autotrophic pathway directly generates acetyl-CoA and pyruvate, and assimilates small organic fermentation products, such as acetate, propionate, or succinate even under anaerobic conditions. Notably, the byproduct 3-HP is an intermediate for the metabolism of dimethylsulfoniopropionate (Ansede et al., 1999; Sunda et al., 2002; Yoch, 2002), a ubiquitous osmoprotectant and antioxidant of algae (Todd et al., 2007; Johnston et al., 2008). Therefore, investigation of the enzymes in 3-HP cycle is necessary for understanding the autotrophic carbon fixation mechanisms of early branch prokaryotic phototrophs.

Multiple sequence alignment of *R. castenholzii* MCT with the type III CoA-transferases showed considerable amino acid sequence conservation in the Rossman fold larger domains but less conservation in the small domains, which is consistent with the structural superimposition analyses (**Figure 2** and **Supplementary Figure 1**). These type III CoA-transferases are mostly involved in anaerobic biochemical pathways, wherein they play essential roles for activating specific organic acids for subsequent decarboxylation, β-oxidation or elimination of α- or β-hydroxy groups (Heider, 2001). The reaction mechanism of type III CoA transferases requires formation of covalently bound substrate intermediates with a conserved aspartate residue of the enzyme (Gruez et al., 2003; Ricagno et al., 2003; Gogos et al., 2004; Stenmark et al., 2004; Toyota et al., 2008). In the reaction of butyrobetainyl-CoA:(*R*)-carnitine-CoA transferase (CaiB), Asp169 initiates a nucleophilic attack at the substrate γ-butyrobetaine-CoA to form a covalently bound intermediate and release the $CoAS^-$. Subsequently, the second substrate carnitine reacts with the covalent intermediate to form a reactant state, in which carnitine is also covalently bound to Asp169. This reactant state is stabilized by the release of γ-butyrobetaine. Then the $CoAS^-$ anion launches a second nucleophilic attack at the enzyme-anhydride intermediate to produce carnityl-CoA and regenerate the deprotonated Asp 169 (Stenmark et al., 2004). In *R. castenholzii* MCT, the catalytic residue Asp165 is strictly conserved with CaiB (Stenmark et al., 2004), the formyl-CoA transferase from *O. formigenes* (FRC) and *E. coli* (YfdW) (Gogos et al., 2004; Toyota et al., 2008), as well as formyl-CoA: oxalate-CoA transferase from *A. aceti* (FCOCT) (Mullins et al., 2012) and a CoA transferase III from *Mycobacterium tuberculosis* (Rv3272) (Karade et al., 2019; **Supplementary Figure 1**), indicating MCT probably adopts a similar reaction mechanism as the type III CoA-transferase.

However, MCT catalyzes the reversible transformation of mesaconyl-C1-CoA to mesaconyl-C4-CoA, the only difference of the substrate and product of this reaction is the position of a methyl group. Compared to FRC that contain a much longer linker 1 loops, absence of this region in MCT leads to the removal of a glycine-rich loop that points directly into the active site pocket of FRC, YfdW, and FCOCT, results in a larger substrate binding pocket of MCT (**Figures 2B,C**), which could provide enough space for the intramolecular CoA transfer reactions. Based on the MD simulations, mesaconyl-C1-CoA exhibited higher binding free energies, indicating mesaconyl-C1-CoA is more favorable for binding to MCT. In the equilibrated structures, the mesaconic tails of both mesaconyl-C1-CoA and mesaconyl-C4-CoA were stabilized by a chain of hydrogen bonding interactions with Arg47 NH1 and one water molecule (**Supplementary Figures 5A,B**). Particularly, electrostatic interactions between the carbonyl C1 atom and Asp165 OD2 provided a prerequisite for hydrophilic attack of the reaction. Therefore, we proposed a previously unrecognized catalytic mechanism that involves formation of covalently bound intermediates with Asp165, and the participation of the less conserved Arg47 and water molecule. In this reaction mechanism, the water molecule takes place the role of the second substrate in type III CoA-transferases, providing protons for the enzyme-bound CoA-thioester and launching a nucleophilic attack to release the Asp165 and generate mesaconyl-C4-CoA. Therefore, the close proximities of the catalytic triad Asp165, Arg47, and a water molecule inside the active site pocket ensured occurrence of the reversible CoA-transfer reaction within only one substrate.

In conclusion, this study revealed the catalytic mechanism of an uncommon intramolecular CoA-transfer reaction in the 3-HP cycle of FAPs. As ancient anoxygenic photosynthetic bacteria, FAPs evolved an autotrophic bicycle to ensure sufficient utilization of the reaction intermediates for metabolism. Additionally, many multi-functional enzymes constitute an efficient carbon fixation system of the 3-HP cycle, in total 19 reactions are catalyzed by only 13 enzymes. Therefore, the intramolecular CoA transfer

activity of MCT is also an economical and energy saving approach for efficient CoA shift of this autotrophic carbon fixation pathway. Besides the physiological importance, the mechanism of MCT in catalyzing intramolecular CoA transfer reaction can be applied to enzyme engineering or manipulations of the 3-HP cycle for synthesis of fine chemicals and important metabolites in the future.

DATA AVAILABILITY STATEMENT

The datasets presented in this study can be found in online repositories. The names of the repository/repositories and accession number(s) can be found in the article/ **Supplementary Material**.

AUTHOR CONTRIBUTIONS

XX initiated the project and supervised all experiments. ZM and XZ performed expression, purification, crystallization, and data collection of *Roseiflexus castenholzii* MCT. CF and WW determined and refined the crystal structure. YX constructed the plasmid for recombinant expression of MCT. ZW performed the MD simulation and free energy calculations. ML and KW performed the gel filtration and AUC analyses. YH performed the PISA analyses. XX, ZW, and XWZ analyzed the data and wrote the manuscript. All authors contributed to the article and approved the submitted version.

FUNDING

This work was supported by grants from the National Natural Science Foundation of China (31870740, 32171227, and 31570738) and Zhejiang Provincial Natural Science Foundation of China under Grant No. LR22C020002 to XX.

ACKNOWLEDGMENTS

We thank the staff of the beamline BL19U at Shanghai Synchrotron Radiation Facility for assistance during crystal diffraction data collection.

SUPPLEMENTARY MATERIAL

The Supplementary Material for this article can be found online at: https://www.frontiersin.org/articles/10.3389/fmicb.2022.923367/full#supplementary-material

REFERENCES

Afonine, P. V., Grosse-Kunstleve, R. W., Echols, N., Headd, J. J., Moriarty, N. W., Mustyakimov, M., et al. (2012). Towards automated crystallographic structure refinement with phenix.refine. *Acta Crystallogr. D Biol. Crystallogr.* 68, 352–367. doi: 10.1107/S0907444912001308

Ansede, J. H., Pellechia, P. J., and Yoch, D. C. (1999). Metabolism of acrylate to beta-hydroxypropionate and its role in dimethylsulfoniopropionate lyase induction by a salt marsh sediment bacterium, Alcaligenes faecalis M3A. *Appl. Environ. Microbiol.* 65, 5075–5081. doi: 10.1128/AEM.65.11.5075-5081.1999

Baetz, A. L., and Allison, M. J. (1990). Purification and characterization of formyl-coenzyme A transferase from Oxalobacter formigenes. *J. Bacteriol.* 172, 3537–3540. doi: 10.1128/jb.172.7.3537-3540.1990

Bayly, C. I., Cieplak, P., Cornell, W., and Kollman, P. A. (1993). A well-behaved electrostatic potential based method using charge restraints for deriving atomic charges: the RESP model. *J. Phys. Chem.* 97, 10269–10280. doi: 10.1021/j100142a004

Blankenship, R. E. (2010). Early evolution of photosynthesis. *Plant Physiol.* 154, 434–438. doi: 10.1104/pp.110.161687

Buckel, W., and Bobi, A. (1976). The enzyme complex citramalate lyase from Clostridium tetanomorphum. *Eur. J. Biochem.* 64, 255–262. doi: 10.1111/j.1432-1033.1976.tb10295.x

Buckel, W., Buschmeier, V., and Eggerer, H. (1971). [The action mechanism of citrate lyase from Klebsiella aerogenes]. *Hoppe Seylers Z. Physiol. Chem.* 352, 1195–1205.

Case, D. A., Cheatham, T. E. III, Darden, T., Gohlke, H., Luo, R., Merz, K. M. Jr., et al. (2005). The Amber biomolecular simulation programs. *J. Comput. Chem.* 26, 1668–1688. doi: 10.1002/jcc.20290

Collaborative Computational Project (1994). The CCP4 suite: programs for protein crystallography. *Acta Crystallogr. D Biol. Crystallogr.* 50, 760–763. doi: 10.1107/S0907444994003112

Deng, N., Xia, J., Wickstrom, L., Lin, C., Wang, K., He, P., et al. (2019). Ligand Selectivity in the Recognition of Protoberberine Alkaloids by Hybrid-2 Human Telomeric G-Quadruplex: binding Free Energy Calculation, Fluorescence Binding, and NMR Experiments. *Molecules* 24:1574. doi: 10.3390/molecules24081574

Dickert, S., Pierik, A. J., Linder, D., and Buckel, W. (2000). The involvement of coenzyme A esters in the dehydration of (R)-phenyllactate to (E)-cinnamate by Clostridium sporogenes. *Eur. J. Biochem.* 267, 3874–3884. doi: 10.1046/j.1432-1327.2000.01427.x

Dimroth, P., and Eggerer, H. (1975). Isolation of subunits of citrate lyase and characterization of their function in the enzyme complex. *Proc. Natl. Acad. Sci. U. S. A.* 72, 3458–3462. doi: 10.1073/pnas.72.9.3458

Elssner, T., Engemann, C., Baumgart, K., and Kleber, H. P. (2001). Involvement of coenzyme A esters and two new enzymes, an enoyl-CoA hydratase and a CoA-transferase, in the hydration of crotonobetaine to L-carnitine by *Escherichia coli*. *Biochemistry* 40, 11140–11148. doi: 10.1021/bi0108812

Emsley, P., and Cowtan, K. (2004). Coot: model-building tools for molecular graphics. *Acta Crystallogr. D Biol. Crystallogr.* 60, 2126–2132. doi: 10.1107/S0907444904019158

Friedmann, S., Alber, B. E., and Fuchs, G. (2006). Properties of succinyl-coenzyme A:D-citramalate coenzyme A transferase and its role in the autotrophic 3-hydroxypropionate cycle of Chloroflexus aurantiacus. *J. Bacteriol.* 188, 6460–6468. doi: 10.1128/JB.00659-06

Genheden, S., and Ryde, U. (2015). The MM/PBSA and MM/GBSA methods to estimate ligand-binding affinities. *Expert Opin. Drug Discov.* 10, 449–461. doi: 10.1517/17460441.2015.1032936

Gogos, A., Gorman, J., and Shapiro, L. (2004). Structure of *Escherichia coli* YfdW, a type III CoA transferase. *Acta Crystallogr. D Biol. Crystallogr.* 60, 507–511. doi: 10.1107/S0907444904000034

Gruez, A., Roig-Zamboni, V., Valencia, C., Campanacci, V., and Cambillau, C. (2003). The crystal structure of the *Escherichia coli* YfdW gene product reveals a new fold of two interlaced rings identifying a wide family of CoA transferases. *J. Biol. Chem.* 278, 34582–34586. doi: 10.1074/jbc.C300282200

Hanada, S., Takaichi, S., Matsuura, K., and Nakamura, K. (2002). Roseiflexus castenholzii gen. nov., sp. nov., a thermophilic, filamentous, photosynthetic bacterium that lacks chlorosomes. *Int. J. Syst. Evol. Microbiol.* 52, 187–193. doi: 10.1099/00207713-52-1-187

Heider, J. (2001). A new family of CoA-transferases. *FEBS Lett.* 509, 345–349.

Hendrickson, W. A., Smith, J. L., and Sheriff, S. (1985). Direct phase determination based on anomalous scattering. *Methods Enzymol.* 115, 41–55. doi: 10.1016/0076-6879(85)15006-8

Hohmann-Marriott, M. F., and Blankenship, R. E. (2011). Evolution of photosynthesis. *Annu. Rev. Plant Biol.* 62, 515–548. doi: 10.1146/annurev-arplant-042110-103811

Johnston, A. W., Todd, J. D., Sun, L., Nikolaidou-Katsaridou, M. N., Curson, A. R., and Rogers, R. (2008). Molecular diversity of bacterial production of the climate-changing gas, dimethyl sulphide, a molecule that impinges on local and global symbioses. *J. Exp. Bot.* 59, 1059–1067. doi: 10.1093/jxb/erm264

Jonsson, S., Ricagno, S., Lindqvist, Y., and Richards, N. G. (2004). Kinetic and mechanistic characterization of the formyl-CoA transferase from Oxalobacter formigenes. *J. Biol. Chem.* 279, 36003–36012. doi: 10.1074/jbc.M404873200

Karade, S. S., Pandey, S., Ansari, A., Das, S., Tripathi, S., Arora, A., et al. (2019). Rv3272 encodes a novel Family III CoA transferase that alters the cell wall lipid profile and protects mycobacteria from acidic and oxidative stress. *Biochim. Biophys. Acta Proteins Proteom.* 1867, 317–330. doi: 10.1016/j.bbapap.2018.10.011

Kollman, P. A., Massova, I., Reyes, C., Kuhn, B., Huo, S., Chong, L., et al. (2000). Calculating structures and free energies of complex molecules: combining molecular mechanics and continuum models. *Acc. Chem. Res.* 33, 889–897. doi: 10.1021/ar000033j

Krissinel, E., and Henrick, K. (2007). Inference of macromolecular assemblies from crystalline state. *J. Mol. Biol.* 372, 774–797. doi: 10.1016/j.jmb.2007.05.022

Leutwein, C., and Heider, J. (1999). Anaerobic toluene-catabolic pathway in denitrifying Thauera aromatica: activation and beta-oxidation of the first intermediate, (R)-(+)-benzylsuccinate. *Microbiology* 145, 3265–3271. doi: 10.1099/00221287-145-11-3265

Leutwein, C., and Heider, J. (2001). Succinyl-CoA:(R)-benzylsuccinate CoA-transferase: an enzyme of the anaerobic toluene catabolic pathway in denitrifying bacteria. *J. Bacteriol.* 183, 4288–4295. doi: 10.1128/JB.183.14.4288-4295.2001

Liebschner, D., Afonine, P. V., Baker, M. L., Bunkoczi, G., Chen, V. B., Croll, T. I., et al. (2019). Macromolecular structure determination using X-rays, neutrons and electrons: recent developments in Phenix. *Acta Crystallogr. D Struct. Biol.* 75, 861–877. doi: 10.1107/S2059798319011471

Liu, N., Zhou, W., Guo, Y., Wang, J., Fu, W., Sun, H., et al. (2018). Molecular Dynamics Simulations Revealed the Regulation of Ligands to the Interactions between Androgen Receptor and Its Coactivator. *J. Chem. Inf. Model.* 58, 1652–1661. doi: 10.1021/acs.jcim.8b00283

Mack, M., and Buckel, W. (1995). Identification of glutamate beta 54 as the covalent-catalytic residue in the active site of glutaconate CoA-transferase from Acidaminococcus fermentans. *FEBS Lett.* 357, 145–148. doi: 10.1016/0014-5793(94)01351-z

Maier, J. A., Martinez, C., Kasavajhala, K., Wickstrom, L., Hauser, K. E., and Simmerling, C. (2015). ff14SB: improving the Accuracy of Protein Side Chain and Backbone Parameters from ff99SB. *J. Chem. Theory Comput.* 11, 3696–3713. doi: 10.1021/acs.jctc.5b00255

Malinin, G. L. (1977). Stable sudanophilia of "bound" lipids in tissue culture cells is a staining artifact. *J. Histochem. Cytochem.* 25, 155–156. doi: 10.1177/25.2.65419

Mandal, M. N., Santha, I. M., Lodha, M. L., and Mehta, S. L. (2000). Cloning of acyl-acyl carrier protein (ACP) thioesterase gene from Brassica juncea. *Biochem. Soc. Trans.* 28, 967–969.

Matthews, B. W. (1968). Solvent content of protein crystals. *J. Mol. Biol.* 33, 491–497.

Minor, W., Cymborowski, M., Otwinowski, Z., and Chruszcz, M. (2006). HKL-3000: the integration of data reduction and structure solution–from diffraction images to an initial model in minutes. *Acta Crystallogr. D Biol. Crystallogr.* 62, 859–866. doi: 10.1107/S0907444906019949

Mullins, E. A., Starks, C. M., Francois, J. A., Sael, L., Kihara, D., and Kappock, T. J. (2012). Formyl-coenzyme A (CoA):oxalate CoA-transferase from the acidophile Acetobacter aceti has a distinctive electrostatic surface and inherent acid stability. *Protein Sci.* 21, 686–696. doi: 10.1002/pro.2054

Murshudov, G. N., Vagin, A. A., and Dodson, E. J. (1997). Refinement of macromolecular structures by the maximum-likelihood method. *Acta Crystallogr. D Biol. Crystallogr.* 53, 240–255. doi: 10.1107/S0907444996012255

Oyaizu, H., Debrunner-Vossbrinck, B., Mandelco, L., Studier, J. A., and Woese, C. R. (1987). The green non-sulfur bacteria: a deep branching in the eubacterial line of descent. *Syst. Appl. Microbiol.* 9, 47–53.

Pettersen, E. F., Goddard, T. D., Huang, C. C., Couch, G. S., Greenblatt, D. M., Meng, E. C., et al. (2004). UCSF Chimera–a visualization system for exploratory research and analysis. *J. Comput. Chem.* 25, 1605–1612. doi: 10.1002/jcc.20084

Pierson, B. K., and Castenholz, R. W. (1974). A phototrophic gliding filamentous bacterium of hot springs, Chloroflexus aurantiacus, gen. and sp. nov. *Arch. Microbiol.* 100, 5–24.

Ricagno, S., Jonsson, S., Richards, N., and Lindqvist, Y. (2003). Formyl-CoA transferase encloses the CoA binding site at the interface of an interlocked dimer. *EMBO J.* 22, 3210–3219. doi: 10.1093/emboj/cdg333

Rice, L. M., Earnest, T. N., and Brunger, A. T. (2000). Single-wavelength anomalous diffraction phasing revisited. *Acta Crystallogr. D Biol. Crystallogr.* 56, 1413–1420. doi: 10.1107/s0907444900010039

Schuck, P. (2000). Size-distribution analysis of macromolecules by sedimentation velocity ultracentrifugation and lamm equation modeling. *Biophys. J.* 78, 1606–1619. doi: 10.1016/S0006-3495(00)76713-0

Selmer, T., and Buckel, W. (1999). Oxygen exchange between acetate and the catalytic glutamate residue in glutaconate CoA-transferase from Acidaminococcus fermentans. Implications for the mechanism of CoA-ester hydrolysis. *J. Biol. Chem.* 274, 20772–20778. doi: 10.1074/jbc.274.30.20772

Stenmark, P., Gurmu, D., and Nordlund, P. (2004). Crystal structure of CaiB, a type-III CoA transferase in carnitine metabolism. *Biochemistry* 43, 13996–14003. doi: 10.1021/bi048481c

Strauss, G., and Fuchs, G. (1993). Enzymes of a novel autotrophic CO2 fixation pathway in the phototrophic bacterium Chloroflexus aurantiacus, the 3-hydroxypropionate cycle. *Eur. J. Biochem.* 215, 633–643.

Subramanian, S., Basu, A., and SivaRaman, C. (1983). The presence of essential arginine residues at the active sites of citrate lyase complex from Klebsiella aerogenes. *Biochem. Biophys. Res. Commun.* 111, 490–497. doi: 10.1016/0006-291x(83)90333-9

Sunda, W., Kieber, D. J., Kiene, R. P., and Huntsman, S. (2002). An antioxidant function for DMSP and DMS in marine algae. *Nature* 418, 317–320. doi: 10.1038/nature00851

Tang, K. H., Barry, K., Chertkov, O., Dalin, E., Han, C. S., Hauser, L. J., et al. (2011). Complete genome sequence of the filamentous anoxygenic phototrophic bacterium Chloroflexus aurantiacus. *BMC Genomics* 12:334. doi: 10.1186/1471-2164-12-334

Terwilliger, T. C., Adams, P. D., Read, R. J., McCoy, A. J., Moriarty, N. W., Grosse-Kunstleve, R. W., et al. (2009). Decision-making in structure solution using Bayesian estimates of map quality: the PHENIX AutoSol wizard. *Acta Crystallogr. D Biol. Crystallogr.* 65, 582–601. doi: 10.1107/S0907444909012098

Todd, J. D., Rogers, R., Li, Y. G., Wexler, M., Bond, P. L., Sun, L., et al. (2007). Structural and regulatory genes required to make the gas dimethyl sulfide in bacteria. *Science* 315, 666–669. doi: 10.1126/science.1135370

Toyota, C. G., Berthold, C. L., Gruez, A., Jonsson, S., Lindqvist, Y., Cambillau, C., et al. (2008). Differential substrate specificity and kinetic behavior of *Escherichia coli* YfdW and Oxalobacter formigenes formyl coenzyme A transferase. *J. Bacteriol.* 190, 2556–2564. doi: 10.1128/JB.01823-07

Vaguine, A. A., Richelle, J., and Wodak, S. J. (1999). SFCHECK: a unified set of procedures for evaluating the quality of macromolecular structure-factor data and their agreement with the atomic model. *Acta Crystallogr. D Biol. Crystallogr.* 55, 191–205. doi: 10.1107/S0907444998006684

Wang, J., Wolf, R. M., Caldwell, J. W., Kollman, P. A., and Case, D. A. (2004). Development and testing of a general amber force field. *J. Comput. Chem.* 25, 1157–1174. doi: 10.1002/jcc.20035

Wang, Y., Li, G., Meng, T., Qi, L., Yan, H., and Wang, Z. (2022). Molecular insights into the selective binding mechanism targeting parallel human telomeric G-quadruplex. *J. Mol. Graph. Model.* 110:108058. doi: 10.1016/j.jmgm.2021.108058

Wang, Z., Chen, Z., Li, J., Huang, J., Zheng, C., and Liu, J. P. (2019). Combined 3D-QSAR, molecular docking and molecular dynamics study on the benzimidazole inhibitors targeting HCV NS5B polymerase. *J. Biomol. Struct. Dyn.* 38, 1071–1082. doi: 10.1080/07391102.2019.1593244

Weiser, J., Shenkin, P. S., and Still, W. C. (1999). Approximate solvent-accessible surface areas from tetrahedrally directed neighbor densities. *Biopolymers* 50, 373–380. doi: 10.1002/(SICI)1097-0282(19991005)50:4<373::AID-BIP3<3.0.CO;2-U

White, H., and Jencks, W. P. (1976). Properties of succinyl-CoA:3-ketoacid coenzyme A transferase. *J. Biol. Chem.* 251, 1708–1711.

Yoch, D. C. (2002). Dimethylsulfoniopropionate: its sources, role in the marine food web, and biological degradation to dimethylsulfide. *Appl. Environ. Microbiol.* 68, 5804–5815. doi: 10.1128/AEM.68.12.5804-5815.2002

Zarzycki, J., Brecht, V., Muller, M., and Fuchs, G. (2009). Identifying the missing steps of the autotrophic 3-hydroxypropionate CO2 fixation cycle in Chloroflexus aurantiacus. *Proc. Natl. Acad. Sci. U. S. A.* 106, 21317–21322. doi: 10.1073/pnas.0908356106

Conflict of Interest: The authors declare that the research was conducted in the absence of any commercial or financial relationships that could be construed as a potential conflict of interest.

frontiers | Frontiers in Microbiology

PERSPECTIVE
published: 16 June 2022
doi: 10.3389/fmicb.2022.928046

Preparation of Photo-Bioelectrochemical Cells With the RC-LH Complex From *Roseiflexus castenholzii*

*Jinsong Du[1], Jiyu Xin[1,2], Menghua Liu[1], Xin Zhang[1], Huimin He[1], Jingyi Wu[1] and Xiaoling Xu[1,2]**

[1] Photosynthesis Research Center, Hangzhou Normal University, Hangzhou, China, [2] Department of Biochemistry and Molecular Biology, School of Basic Medical Sciences, The Affiliated Hospital of Hangzhou Normal University, Hangzhou, China

Roseiflexus castenholzii is an ancient green non-sulfur bacteria that absorbs the solar energy through bacteriochlorophylls (BChls) bound in the only light harvesting (LH) complex, and transfers to the reaction center (RC), wherein primary charge separation occurs and transforms the energy into electrochemical potentials. In contrast to purple bacteria, *R. castenholzii* RC-LH (*rc*RC-LH) does not contain an H subunit. Instead, a tightly bound tetraheme cytochrome *c* subunit is exposed on the P-side of the RC, which contains three BChls, three bacteriopheophytins (BPheos), two menaquinones, and one iron for electron transfer. These novel structural features of the *rc*RC-LH are advantageous for enhancing the electron transfer efficiency and subsequent photo-oxidation of the *c*-type hemes. However, the photochemical properties of *rc*RC-LH and its applications in developing the photo-bioelectrochemical cells (PBECs) have not been characterized. Here, we prepared a PBEC using overlapped fluorine-doped tin oxide (FTO) glass and Pt-coated glass as electrodes, and *rc*RC-LH mixed with varying mediators as the electrolyte. Absence of the H subunit allows *rc*RC-LH to be selectively adhered onto the hydrophilic surface of the front electrode with its Q-side. Upon illumination, the photogenerated electrons directly enter the front electrode and transfer to the counter electrode, wherein the accepted electrons pass through the exposed *c*-type hemes to reduce the excited P^+, generating a steady-state current of up to 320 nA/cm^2 when using 1-Methoxy-5-methylphenazinium methyl sulfate (PMS) as mediator. This study demonstrated the novel photoelectric properties of *rc*RC-LH and its advantages in preparing effective PBECs, showcasing a potential of this complex in developing new type PBECs.

Keywords: photo-bioelectrochemical cell, reaction center, light harvesting complex, photosynthetic bacteria, electron transfer

OPEN ACCESS

Edited by:
Weimin Ma,
Shanghai Normal University, China

Reviewed by:
Lijin Tian,
Key Laboratory of Photobiology, Institute of Botany (CAS), China
Wenda Wang,
Institute of Botany (CAS), China
Qiang Wang,
Henan University, China

***Correspondence:**
Xiaoling Xu
xuxl@hznu.edu.cn

Specialty section:
This article was submitted to Microbial Physiology and Metabolism, a section of the journal Frontiers in Microbiology

Received: *25 April 2022*
Accepted: *30 May 2022*
Published: *16 June 2022*

Citation:
Du J, Xin J, Liu M, Zhang X, He H, Wu J and Xu X (2022) Preparation of Photo-Bioelectrochemical Cells With the RC-LH Complex From Roseiflexus castenholzii. Front. Microbiol. 13:928046. doi: 10.3389/fmicb.2022.928046

INTRODUCTION

Photosynthesis is the process that converts solar energy into electrochemical energy and supports almost all life on Earth. It originated from bacteria, and gradually appeared in algae and higher plants through genetic transfer. Diverse photosynthetic systems have evolved to achieve higher energy transformation efficiency. The membrane-bound protein-pigment complexes in these

systems are capable of catalyzing the photochemical charge separation with a quantum efficiency of close to 100% (Blankenship et al., 2011; Singh et al., 2018), which has inspired the exploration and development of the third-generation solar cells (O'Regan and Grätzel, 1991; Wang et al., 2020, 2021). The third-generation solar cells prepared by plant and bacterial photosynthetic complexes are collectively known as photo-bioelectrochemical cells (PBECs) (Feng et al., 2016; Sekar et al., 2016; Musazade et al., 2018; Zhou et al., 2019; Lee et al., 2020).

In contrast to algae, cyanobacteria and higher plants that have evolved oxygenic photosynthesis, anoxygenic phototrophs are prokaryotes with primitive photosynthetic systems. In the model organism purple bacteria, light energy is absorbed by bacteriochlorophyll (BChl) B880 bound in the light harvesting complex 1 (LH1) either directly or from the peripheral antenna LH2 and transferred to the reaction center (RC), where charge separation occurs and transforms the energy into electrochemical potentials. The RC is composed of L, M subunits that each contains five transmembrane helices, and the H subunit comprising a cytoplasmic globular domain anchored to the membrane by an N-terminal transmembrane helix (**Supplementary Figures 1A,B**). The RC accommodates a special pair (P) of BChls, two accessary BChls and two bacteriopheophytins (BPheos), as well as an iron and two ubiquinone (UQ) molecules for electron transfer (**Supplementary Figures 1C,D**). Excitation of the special pair (a dimer of coupled BChls that are arranged in a slipped face-to-face π-π-stacking, which acts as primary donor in the initial steps of the charge separation) on the P-side of the RC initiates transfer of an electron along the A-branch BChl (B_A), BPheo (H_A), Q_A quinone, and iron to Q_B quinone. Two electrons transferred from the charge separation fully reduces the quinone to hydroquinone, which diffuses into the membrane pool and initiates cyclic electron transfer between the RC and cytochrome bc_1 to build up a proton motive force for ATP synthesis. This highly stable and relatively simple RC-LH1 complex of purple bacteria has been extensively studied to develop new type of PBECs (Ravi and Tan, 2015).

To prepare an efficient PBEC, the photosynthetic complexes are required to constantly generate electrons and continuously inject these photogenerated electrons into electrodes (Paul et al., 2020; Buscemi et al., 2021). The efficiency of the photoelectric conversion is correlated with the transfer path of electrons inside the PBEC. In most PBECs prepared from purple bacteria RC-LH1, the RC is attached to the front electrode with its P-side, which enables the Q-side and cytoplasmic domain of the H subunit exposed in the mediator. The photogenerated electrons are transferred through the mediator to the counter electrode, wherein the accepted electrons pass through an external circuit to the front electrode to reduce the excited P^+ and form a steady-state current (**Supplementary Figure 1E**). However, transfer of the photogenerated electrons with a mediator often decreases the electron transfer efficiency and results in loss of the photocurrent (Takshi et al., 2010). To address this problem, Masaharu et al. connected the H subunit of RC to the electrode using a connector N-(1-Pyrenyl) Iodoacetamide, which allowed the photogenerated electrons flow out of Q_B and be directly transferred into the electrode (Trammell et al., 2006). Unfortunately, presence of the relatively thick H subunit (24Å) and the connector (4Å) increased the actual distance between Q_B and the electrode to 28Å, which resulted in a relatively low electron transfer efficiency of this system.

Beatty et al. then shortened the distance between Q_B and the electrode by genetically truncating the H subunit of *Rhodobacter sphaeroides*. The shortest mutant (45M RC) contains 45 amino acids left at the N-terminal of H subunit, it retained the main function of charge separation (formation of P^+ and Q_A^-) but lacked a bound quinone at Q_B site. When the H-truncated RC (45M-M229Q_B^-) was attached to a gold electrode *via* a Cys engineered near the Q_A site, the steady-state currents increased to 200 nA/cm^2 when using 20 mM hydroquinone as the sole mediator (Jun et al., 2018). The photocurrents were increased and decreased in about 0.2 s, a rate that is one or two orders of magnitude faster than previously reported values obtained using soluble mediators (Trammell et al., 2006; Terasaki et al., 2009). However, truncation of the H subunit increased the conformational or electrostatic changes of the quinone binding pockets and decreased the binding affinity of Q_B (Sun et al., 2015), causing the photogenerated electrons transferred only from Q_A to the electrode (**Supplementary Figure 1F**; Jun et al., 2018). Notably, complete removal of the H subunit from an intact RC severely reduced the electron transfer from Q_A to Q_B by approximately 10^2 to 10^3-fold, the resultant LM RC retained 95 ± 3% electron transfer to the primary Q_A (Debus et al., 1985). Consistently, the electron transfer rate from H_A^- to Q_A was decreased by approximately 4-fold in the LM dimer (Sun et al., 2016). Therefore, a RC-LH that lacks the H subunit but maintains intact electron transfer capacity is required to enhance the electron transfer efficiency of the PBECs.

Roseiflexus castenholzii (*R. castenholzii*) is an ancient green non-sulfur bacteria that contains a unique photosynthetic system. In contrast to purple bacteria, *R. castenholzii* does not contain a peripheral LH2. It contains only one LH that encircles the L, M, and cyt *c* subunits composed RC to form an opened elliptical ring (Yamada et al., 2005; Majumder et al., 2016; Xin et al., 2018). Especially, *R. castenholzii* RC-LH (*rc*RC-LH) lacks the H subunit, it tightly associates a cytochrome (cyt) *c* subunit through a novel transmembrane helix (c-TM), with the tetraheme binding domain protruding into the periplasmic space, which can accept electrons transferred from the periplasmic electron donors. The c-TM further inserts into the gap of the LH ring, in together with a newly identified transmembrane helix X to form a quinol shuttling channel (**Figure 1A** and **Supplementary Figure 2A**). The RC contains three BChls and three BPheos (Collins et al., 2010), instead of four BChls and two BPheos in purple bacteria. Additionally, two menaquinone-11 (MQ) molecules have been identified within the RC, instead of the UQs bound in purple bacteria RC (**Figures 1A,B** and **Supplementary Figures 1A–D**). These novel structural features of *rc*RC-LH are beneficial for enhancing the electron transfer efficiency and subsequent photo-oxidation of the *c*-type hemes (Deisenhofer and Michel, 1989). Importantly, absence of the H subunit in *rc*RC-LH provides a prerequisite for direct transfer of the photogenerated electrons from the

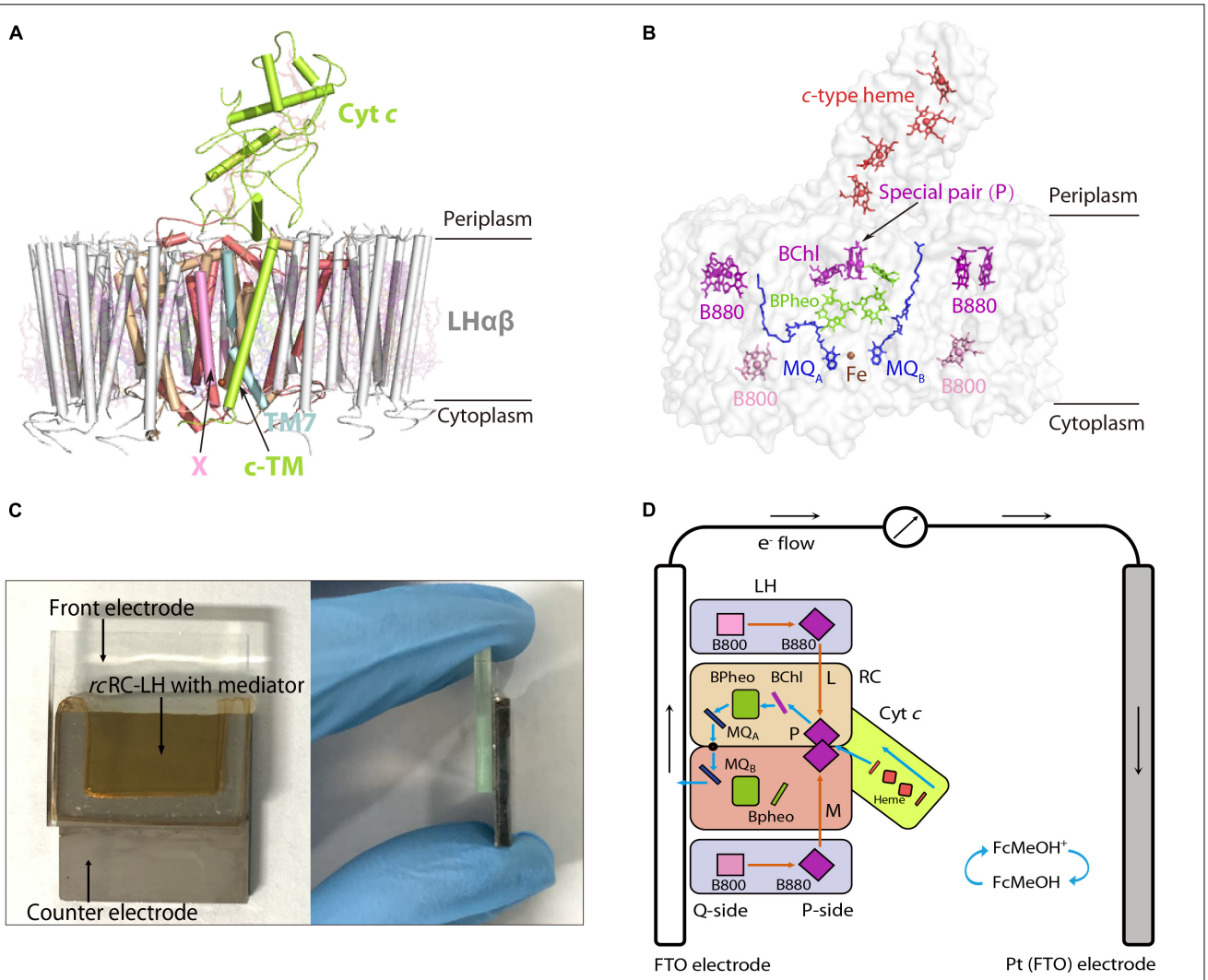

FIGURE 1 | Preparation of an FTO-Pt PBEC using the RC-LH from *R. castenholzii (rcRC-LH) rc*. **(A)** Overall structure of the *rc*RC-LH (PDB ID: 5YQ7) is shown at the side view. The light harvesting (LH) complex (white) is composed of 15 LHαβ heterodimers in the form of an opened elliptical ring, which encircles the L (wheat), M (salmon), and cyt *c* subunit (limon) composed RC. The tetraheme (red sticks) binding domain of the cyt *c* subunit is exposed at the periplasmic side. Especially, a novel transmembrane helix of the cyt *c* (c-TM) inserts into the gap of the LH ring, and form a quinol shuttling channel in together with a newly identified X subunit (pink). An unassigned TM7 transmembrane helix (light cyan) is identified near the transmembrane helices of the L and M subunits in the RC. All the cofactors are shown as stick models with a transparency at 80%. **(B)** Spatial organization of the pigments and electron carriers in the *rc*RC-LH. Each LHαβ non-covalently binds two B880s (purple) at the periplasmic side, one B800 (pink) at the cytoplasmic side. The RC accommodates a special pair of BChls (P, purple), an accessary BChl (purple), and three BPheos (chartreuse), as well as an iron (brown sphere) and two menaquinone-11 (MQ, blue) molecules. The four *c*-type hemes bound in the cyt *c* subunit are exposed in the periplasmic side. All the cofactors except the iron are shown as stick models. **(C)** Construction of the *rc*RC-LH based FTO-Pt PBEC. The PBEC is composed of a FTO glass as the front electrode and a Pt-coated FTO glass as the counter electrode, a mixed solution of *rc*RC-LH with the mediator is injected into the cavity between the two electrodes as the electrolyte. A front (left) and side (right) view of the apparatus is shown. **(D)** Diagram of the operating mechanism of the *rc*RC-LH prepared FTO-Pt PBEC. The electron donor FcMeOH (hydroxymethylferrocene) was used as the mediator. Orange arrows indicate the route of light energy transfer, and blue arrows indicate the route of electron transfer. The P-side represents the direction of the *rc*RC-LH wherein the special pair (P) is located, and the direction where the MQ_A and MQ_B located is named the Q-side. The photogenerated electrons released from the excited P^+ are transferred along the accessary BChl, BPheo to Q_A, an iron, then to Q_B. The electrons at the Q_B directly enter the front electrode (FTO) and are transferred to the counter electrode (Pt), wherein the accepted electrons pass through the *c*-type hemes *via* the mediator to reduce the excited P^+ and form a steady-state current.

Q-side to the electrodes. However, the photochemical properties of *rc*RC-LH and its applications in developing PBECs have not been characterized.

In this study, we made the first attempt to prepare a PBEC using the *rc*RC-LH complex (**Figures 1C,D**). The extracted *rc*RC-LH showed excellent photoreduction activity in catalyzing the reduction of the electron acceptor methylviologen (MV^{2+}). The PBEC was prepared using an overlapped fluorine-doped tin oxide (FTO) glass as the front electrode, a Pt-coated glass as the counter electrode, and the purified *rc*RC-LH mixed with a mediator as the electrolyte. Photoelectric measurements characterized the immobilization of *rc*RC-LH on the electrode, the electron transfer

path, and photocurrent intensities of the PBECs using different mediators. The results of this study revealed the photochemical properties and potentials of *rc*RC-LH in preparing an effective PBEC, and will contribute to the development of new type PBECs in the future.

MATERIALS AND METHODS

Extraction and Purification of the *rc*RC-LH Complex

The *rc*RC-LH complex was extracted and purified from photoheterotrophically grown *R. castenholzii* as previous reported (Xin et al., 2018). The homogeneity and purity of the complex was monitored at each stage of the preparation by recording the absorption spectrum from 250–900 nm. The final 880 nm to 280 nm absorption ratio for the purified *rc*RC-LH complex was above 1.25.

Measurement of the Stability and Photoreduction Activity of the *rc*RC-LH Complex

To test the stability of the purified *rc*RC-LH complex, light energy was simulated with a 200 W incandescent lamp. The freshly prepared *rc*RC-LH complex was placed 40 cm away from the light source and exposed under light for 12 h at 25 °C. Then, the absorption spectrum over the range 700–1000 nm before and after the illumination was measured *via* UV-Vis spectrometry (Mapada P6, China). The photoreduction activity of the *rc*RC-LH was measured by mixing the *rc*RC-LH complex (20 μM) with 20 mM methylviologen (Aladdin Chemical Reagent Co., Ltd., United States), 0.2 mM polyvinyl pyrrolidone (Macklin Biochemical Co., Ltd., United States), 35 mM L-Lysine (Biosharp Life Sciences Co., Ltd., China), and 500 mM 2-Hydroxy-1-ethanethiol (Aladdin Chemical Reagent Co., Ltd., United States) to a final volume of 1 mL. Using deionized water as a negative control group, the absorbance of the mixed solution at 605 nm was recorded with and without light exposure. All the measurements were performed independently three times. The average and standard deviations of the values were calculated.

Preparation of an FTO-Pt PBEC Using the *rc*RC-LH Complex

We prepared the FTO-Pt PBECs according to previous literatures (Tan et al., 2012a,b). The FTO conducting glass (TEC 7 ohm/sq, 20 mm square × 2.2 mm thick; Shangzhuo Technology Co., Ltd., China) was dipped into acetone and isopropanol successively for 30 min and dried to serve as the front electrode. The counter electrode was comprised of a second piece of FTO conducting glass covered with a layer of 25 nm-thick Pt that was deposited by magnetron sputtering technology (MSP-300C, China). The conductive film of the two electrodes was checked with scanning electron microscope (Hitachi S-4800, Japan), and the water contact angles of the surfaces were measured using Drop Shape Analyser (Kruss DSA100, Germany). The two electrodes were then connected by a hot melt adhesive film (300 μm-thick; Xingxia Polymer Products Co., Ltd., China) to form a cavity of about 1 cm^2 between the boundaries of the two electrodes. A 30 μL electrolyte solution containing 40 μM of the *rc*RC-LH complex and varying mediators (each at 250 μM concentration) such as hydroxymethylferrocene (FcMeOH), methylviologen, N, N, N′, N′-Tetramethyl-p-phenylene-diamine dihydrochloride (TMPD), and 1-Methoxy-5-methylphenazinium methyl sulfate (PMS) (Aladdin Chemical Reagent Co., Ltd., United States) was injected into the cavity. Finally, the opening was sealed by hot glue gun.

Characterizations of the Photoelectric Properties of the FTO-Pt PBEC

To measure the photostability of the prepared FTO-Pt PBEC, light energy was simulated with a 200 W incandescent lamp. The FTO-Pt PBEC was placed 40 cm away from the light source and exposed under light for 12 h at 25 °C. Then, the absorption spectrum of *rc*RC-LH in FTO-Pt PBEC over the range 700–1000 nm before and after the illumination was measured *via* UV-Vis spectrometry. The prepared FTO-Pt PBEC was exposed to a light source that was simulated using a 200 W incandescent lamp at a distance of 40 cm. The photocurrent intensities in the cell were measured by an electrochemical workstation (Lanlink LK2005A, China), with an applied voltage at 0 mV and the current intensity in the dark environment as the baseline. Since the active areas of the cells were slightly different, an opaque mask with a 0.1 cm^2 hole was placed on the outer surface of front electrode before measurement, which ensured that the intensity of the incident light in each cell reached approximately 1.5 mW/cm^2.

RESULTS

The Cofactors Arrangement and Electron Transfer Routes in the *rc*RC-LH Complex

In our previously reported cryo-EM structure of *rc*RC-LH (Xin et al., 2018), the only LH is composed of 15 LHαβ heterodimers in the form of an opened elliptical ring. Each LHαβ non-covalently binds two B880s at the periplasmic side, one B800 at the cytoplasmic side, and one keto-γ-carotene spanning the interface between LHαβ for light harvesting and transfer (**Figure 1A** and **Supplementary Figures 2A,B**). The L and M subunits of RC accommodate a special BChl dimer P (B865), a BChl (B818), and three BPheos, as well as an iron and two MQ-11 molecules that are positioned within 14Å of each other (**Figure 1B** and **Supplementary Figure 3A**), a distance necessary for efficient electron orbital coupling and energy resonance (Osyczka et al., 2004). The distance between the special pair (P) and the nearest *c*-type heme is approximately 10.4Å (**Supplementary Figure 3A**), which is adequate for the subsequent reduction of the excited P^+, through accepting the electrons transferred back from the four *c*-type hemes.

The light energy absorbed by the coupled pigments (B800, B880, and keto-γ-carotene) in LH are transferred to the special pair (P) of the RC. Once excited, the state P^+ is stabilized by transferring an electron to the primary electron acceptor, BChl,

within several picoseconds, and then passed through BPheo, MQ_A, and iron to MQ_B ($P^+Q_B^-$) (**Supplementary Figure 3B**). P^+ can be reduced by electrons transferred back from the *c*-type hemes. Transfer of two electrons from the photochemical charge separation forms $P^+Q_A^-Q_B^-$, which is fully reduced to hydroquinone (QH_2) after accepting the second photogenerated electron and incorporating two protons from the cytoplasm (**Supplementary Figure 3B**). The tightly bound tetraheme cyt *c* subunit endows the *R. castenholzii* RC a much higher efficiency for the energy transfer and photo-oxidation of the *c*-type hemes, which is significantly different from the soluble and monoheme cyt *c* in purple bacteria.

The Stability and Photoreduction Activity of the *rc*RC-LH Complex

The *rc*RC-LH complex was extracted and purified from the heterotrophically grown *R. castenholzii*. Spectroscopic analyses revealed typical Qy bands of the LH-bound BChls at 800 nm (B800) and 880 nm (B880), and a Qx band of BChls at 594 nm. The RC-bound BPheos were determined at 760 nm, and the carotenoids showed absorption at 457, 482, and 519 nm. Near this region, an absorption peak corresponding to the oxidized cyt *c* was observed at 410 nm, as well as the split peaks of BChls at 374 nm (**Supplementary Figure 4A**). The absorption spectrum of *rc*RC-LH barely changed after exposure to simulated light energy for 12 h, indicating the excellent photo-thermal stability of the complex (**Supplementary Figure 4B**).

Methylviologen (MV^{2+}) is an electron acceptor that can be easily reduced to MV^+ upon accepting a single electron (Wang et al., 2021). Using 2-Hydroxy-1-ethanethiol as the electron donor and MV^{2+} as the electron acceptor, we measured the photochemical activity of *rc*RC-LH through recording the absorbance of MV^+ at 605 nm (**Figure 2A**). In presence of the *rc*RC-LH, the absorbance of MV^+ at 605 nm continually increased under illumination and kept constant when the illumination was turned off. Once re-exposed to the simulated light, the absorbance quickly increased, indicating that the *rc*RC-LH was excited by the light energy to initiate charge separation and subsequent electron transfer, releasing electrons to reduce MV^{2+} to MV^+. Therefore, the extracted *rc*RC-LH possessed considerable photoreduction activity *in vitro*.

Preparation of an FTO-Pt PBEC Using the *rc*RC-LH Complex

To prepare PBECs, the photosynthetic complex is often fixed to the working electrode by physical adsorption or chemical coupling after a long period of incubation with the electrode (Tan et al., 2012a). Before preparation, the working electrode usually needs to be pre-processed by high-temperature sensitization, chemical coupling, or modification of the surfaces (Lebedev et al., 2008; Terasaki et al., 2009). Here, a piece of FTO conducting glass deposited with a 350 nm-thick conductive film of fluorine-doped tin oxide was dipped into acetone and isopropanol successively for 30 min, then dried to serve as the front electrode. The surface of the FTO-glass is roughly textured (**Supplementary Figure 5A**), as a result of the low symmetric tetragonal crystal structures of fluorine-doped tin oxide (Zhang et al., 2018). This structure is similar to the wrinkles on the surface of the bacterial plasma membrane, which facilitates attachment of the photosynthetic complexes (Csiki et al., 2018).

The counter electrode is comprised of a second piece of FTO conducting glass covered with a layer of 25 nm-thick Pt, which can evenly cover the surface of the FTO-glass without affecting its electrical conductivity (**Supplementary Figure 5B**). Moreover, coating of the Pt layer also enabled the two electrodes to show distinct wettability (**Supplementary Figures 5C,D**). Notably, the surface of the front electrode is hydrophilic with a water contact angle of 45.1°, whereas the Pt surface of the counter electrode is more hydrophobic (with a contact angle of 91.6°), which would affect the attachment of the *rc*RC-LH onto the electrodes. An electrolyte containing 40 μM *rc*RC-LH and alternative mediator was injected into the cavity formed between the two electrodes to prepare the FTO-Pt PBEC (**Figures 1C,D**). The absorption spectrum of the *rc*RC-LH stored in the FTO-Pt PBEC were barely changed after exposure to the simulated light energy for 12 h (**Supplementary Figure 4C**), indicating a moderate photostability of the FTO-Pt PBEC.

By constructing a PBEC containing two electrodes with distinct wettability, the *rc*RC-LH was expected to selectively adhere to the hydrophilic surface of the front electrode (Tan et al., 2013). To test which electrode the *rc*RC-LH was attached to, we constructed two PBECs using the electron donor hydroxymethylferrocene (FcMeOH) as the mediator. One PBEC was constructed using FTO-glass for both electrodes (FTO-FTO), and the other was constructed with FTO-glass as the front electrode only (FTO-Pt). The current intensities of the two PBECs were measured *via* an electrochemical workstation under illumination. Without illumination, the current intensities of both FTO-FTO and FTO-Pt were zero. However, the photogenerated current of the FTO-Pt was much higher than that of FTO-FTO under illumination (**Figure 2B**), indicating the *rc*RC-LH was selectively adhered to the hydrophilic surface of the FTO glass, and that it was active in catalyzing the photochemical conversion reactions to generate electrons at the front electrode under illumination. In the FTO-FTO PBEC, the photogenerated electrons were probably being neutralized, due to the comparable binding capacity of the *rc*RC-LH complex onto the two electrodes with the same wettability. Therefore, we successfully immobilized the *rc*RC-LH complex onto the hydrophilic front electrode of the FTO-Pt PBEC through controlling the wettability of the surfaces instead of utilizing a complicated pre-processing procedure, thus eliminating a time- and resource-consuming step.

Photoelectric Characterizations of the FTO-Pt PBEC

When using electron donor FcMeOH as the mediator, a reverse current spike was generated once the PBEC was exposed to illumination (**Figure 2B**), indicating the photogenerated electrons were flowing out of the front electrode. The current spike was then deflected to form a steady-state current after about a 5 s illumination (**Figure 2B**), indicating the electrons

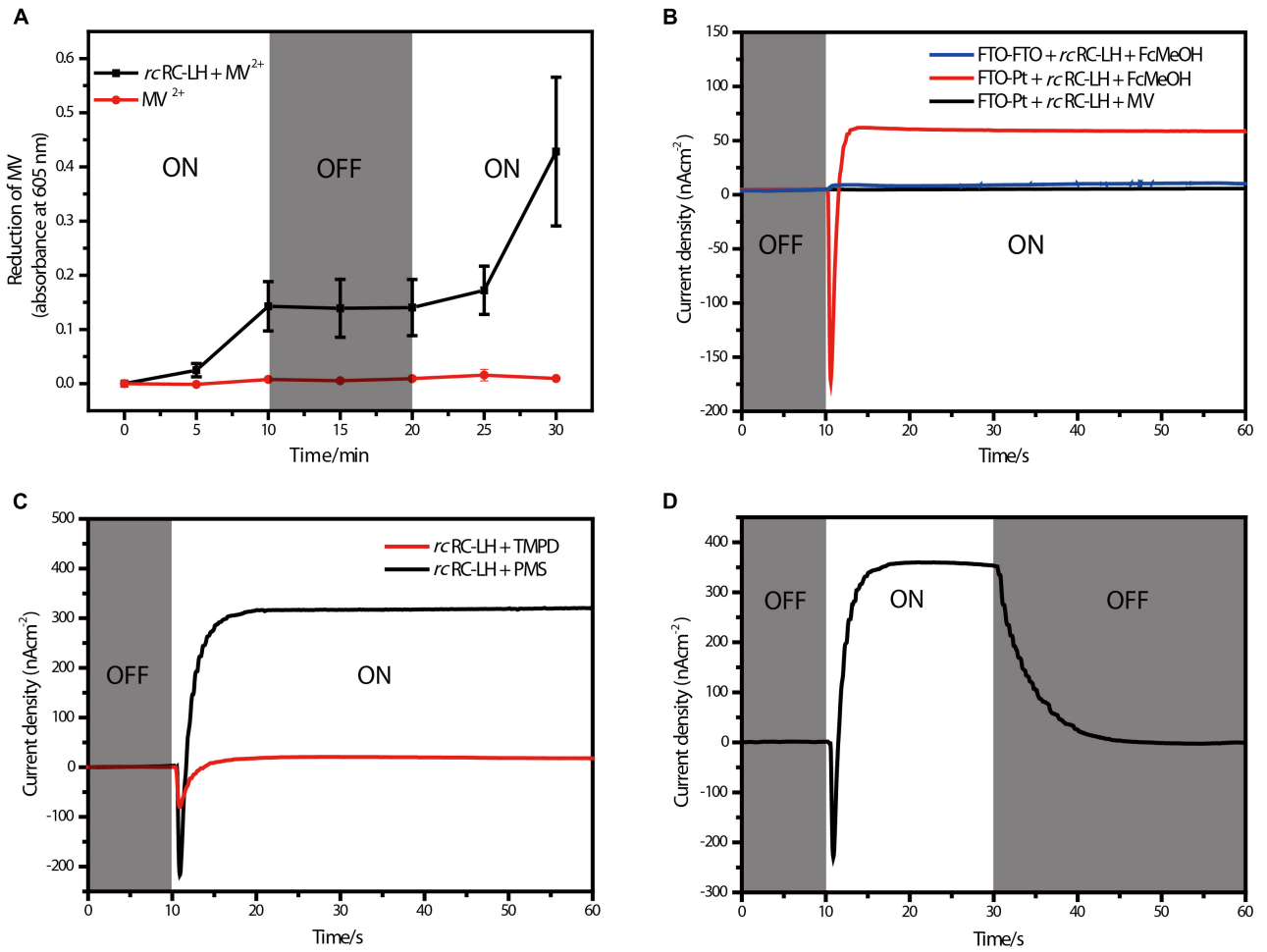

FIGURE 2 | Photoelectric characterizations of the FTO-Pt PBEC. **(A)** Photoreduction activity of the *rc*RC-LH complex measured by using MV^{2+} as the electron acceptor, the absorbance of MV^{+} at 605 nm was recorded in the presence and absence of the *rc*RC-LH. The illumination period is indicated in the white sections of graph, and the dark period is indicated in gray. **(B)** Measurements of the photocurrent intensities of alternative PBECs. The photocurrent intensities were plotted over time with (white background) or without (gray background) illumination. One PBEC was prepared using FTO-glass as both electrodes (FTO-FTO), the other PBEC was prepared with only FTO-glass as the front electrode (FTO-Pt). FcMeOH (hydroxymethylferrocene) and MV (methylviologen) were used as the mediators in these PBECs. **(C)** Comparison of the photocurrent intensities of the FTO-Pt PBECs prepared using TMPD and PMS as the mediators. White graph background indicates a period of illumination, gray represents the period of darkness. **(D)** Changes of the photocurrent intensities of the PMS FTO-Pt PBEC upon alternating illumination conditions. White graph background indicates a period of illumination, gray represents the period of darkness.

were flowing into the front electrode from the *rc*RC-LH. The appearance of the reverse current spike was intriguing, as in the PBECs prepared from purple bacteria RC-LH1, the reduction rate of P^{+} is usually thousands of times higher than the oxidation rate of Q_B^{-} (Agalidis and Velthuys, 1986; Tan et al., 2012a). During photochemical electron transfer of the *rc*RC-LH prepared FTO-Pt PBEC, the excited P^{+} is reduced by the electrons transferred from the four *c*-type hemes *via* the mediator FcMeOH (**Figure 1D**). As the rate of electrons flow more quickly into the P-side than out of the Q-side, the electron carriers in the RC serve as an electron sink. The over-oxidized FcMeOH extracts electrons from the front electrode, generating a reverse current spike. When the electron carriers in the RC are fully occupied and $FcMeOH^{+}$ is spreading inside the PBEC to reach an equilibration, the photogenerated electrons continuously flow into the front electrode to form a steady-state current (**Figure 1D**).

To allow the photogenerated electrons directly flow into the electrode, the Q_B of the RC are required to face the electrode (Page et al., 1999; Winkler and Gray, 2014; Jun et al., 2018). Therefore, attachment orientation of the RC-LH on the electrode is essential for direct electron transfer into the front electrode. In the PBECs prepared by connecting the P-side of RC-LH1 to the front electrode (**Supplementary Figure 1E**), the mediator MV^{2+} accepted the photogenerated electrons from the Q-side, and transferred the electrons to the counter electrode to form a steady-state current (Kondo et al., 2007). To check the attachment direction of *rc*RC-LH on the electrodes, we replaced the electron donor FcMeOH with electron acceptor MV^{2+}. As shown in **Figure 2B**, when using MV^{2+} as a mediator, the

FTO-Pt PBEC did not generate a current under illumination, indicating that no photogenerated electrons were transferred to the counter electrode *via* MV^{2+}. Since the tetraheme binding domain of the cyt *c* subunit is exposed on the P-side of the *rc*RC-LH, if it is attached to the front electrode with the P-side, Q_B^- would reduce the electron acceptor MV^{2+} to ensure continuous photocurrent generation. Therefore, lost of the photocurrent indicated that the *rc*RC-LH complex was selectively attached to the front FTO electrode with its Q-side. In contrast to the previously reported PBECs, the photogenerated electrons in our FTO-Pt PBEC can directly enter the front electrode without assistance of a mediator, avoiding the current losses that result from mediated electron transport.

The mediator also plays a significant role in the electron transfer of the PBECs, as it continuously supplies electrons to the excited P^+ through the *c*-type hemes, in order to ensure continuous photocurrent generations (**Figure 1D**). Both N, N, N′, N′-Tetramethyl-p-phenylene-diamine dihydrochloride (TMPD) and 1-Methoxy-5-methylphenazinium methyl sulfate (PMS) can serve as electron donors for the *rc*RC-LH. The vacuum potentials of TMPD and cyt *c* are −4.7 eV, whereas PMS, with a vacuum potential of −4.5 eV, is more favorable to provide electrons for the cyt *c* (Yaghoubi et al., 2014). As shown in **Figure 2C**, when TMPD and PMS were used as mediators, a steady-state current was generated in 10 s after illumination. The efficiency of the solar cell is strongly dependent on the short-circuit photocurrent density (J_{SC}) and the associated open-circuit voltage (V_{OC}). Specifically, the PMS PBEC could reach a steady-state J_{SC} of 320 nA/cm^2 and V_{OC} of 50 mV, which is much higher than that generated by the TMPD PBEC. These results indicated that the photocurrent intensities of the PBEC can be increased by changing the vacuum potentials of the mediator. In addition, the photocurrent of PMS PBEC started to decrease and gradually reached 0 nA/cm^2 when the light was turned off (**Figure 2D**). The gradual decrease of the photocurrent was a result of the flowing of the stored photogenerated electrons into the electron carriers of the RC, when the reduction rate of P^+ is much higher than the oxidation rate of Q_B^-.

DISCUSSION AND FUTURE PERSPECTIVE

In this study, we prepared a PBEC using the RC-LH complex from an ancient green non-sulfur bacteria *R. castenholzii*, which are phylogenetically distant from other anoxygenic photosynthetic bacteria. Different from the well-studied purple bacteria, *R. castenholzii* does not have a peripheral antenna LH2, instead it contains only one LH, which is composed of 15 αβ-polypeptides to form an opened elliptical ring. The open conformation of the LH ring structurally resembles that of the purple bacteria LH1, which also contain an LH1 ring with gap produced by PufX, protein-W, or special transmembrane helices (Qian et al., 2021a,b; Swainsbury et al., 2021). However, the c-TM and the newly identified X in *rc*RC-LH share no sequence identity and spatial organizations with any of these proteins. Compared to the monomeric RC-LH1 of *Rba. Sphaeroides*, both c-TM and X are located at different positions with distinct conformations (**Figure 1A** and **Supplementary Figures 1A,B**). Specifically, the c-TM and X are almost parallel with the LHαβ heterodimers, whereas the PufX is tilted with the LHαβs at approximately 60°, and the protein-U is formed by two transmembrane helices in a U-shape (**Figure 1A** and **Supplementary Figures 1A,B**; Qian et al., 2021b). Besides, incorporation of the B800s at the cytoplasmic side of *rc*LH combines the spectroscopic properties of purple bacteria LH1 and LH2, which are beneficial for enhancing the light harvesting efficiency of the *rc*RC-LH.

Compared to the LH that contains different compositional and structural features, the core components of the RC, including the L, M-subunits and cofactors are structurally conserved with that of purple bacteria (**Supplementary Figures 1A–D, 2A,B**). Notably, purple bacteria usually contain an H subunit that is important for regulating the assembly and electron transfer of the RC (Debus et al., 1985; Sun et al., 2015; Sun, 2017; Cao et al., 2022). However, presence of the H subunit often increased the distance between Q-side of the RC and the electrode, and decreased the electron transfer efficiency in PBECs. In contrast, absence of the H subunit allows the *rc*RC-LH to be selectively adhered to the hydrophilic surface of the front electrode with its Q-side, then the photogenerated electrons directly enter the electrode without assistance from any mediators (**Figure 1D**). Moreover, *R. castenholzii* RC contains a membrane-bound cyt *c* subunit that is tightly associated with the L and M subunits, with its tetraheme binding domain exposed at the P-side (**Figure 1A** and **Supplementary Figure 2A**). Exposure of the tetraheme binding domain endows *rc*RC-LH a higher photo-oxidation rate of the *c*-type hemes, which accepted the electrons transferred from the counter electrode and reduced the excited P^+ to form a continuous photocurrent (**Figure 1D**). Therefore, the novel structural features of *rc*RC-LH provide a prerequisite for constructing effective PBECs.

The PBEC in this study was prepared using overlapped FTO glass and Pt-coated glass as electrodes, and the *rc*RC-LH mixed with a mediator as the electrolyte. As shown in **Figure 2C**, when using PMS as the mediator, the PBEC produced continuous photocurrent in 10 s after illumination (**Figure 2C**). A steady-state J_{SC} of up to 320 nA/cm^2 was generated with V_{OC} at 50 mV and the incident light intensities at 1.5 mW/cm^2. In the FTO-Pt PBEC prepared using *Rba. sphaeroides* RC-LH1 (**Supplementary Figure 1E**), generation of the steady-state current took about 20 s after illumination. However, the steady-state J_{SC} of this PBEC could reach 900 nA/cm^2 for the fresh PMS, with a V_{OC} of 80 mV and the incident light intensities at 10 mW/cm^2 (Tan et al., 2012b). In respect to the power conversion efficiency that is calculated from the product of the V_{OC} and J_{SC} divided by the incident light intensities, a higher power conversion efficiency of 1.07×10^{-3}% was obtained for the *rc*RC-LH based PBEC than that prepared by *Rba. sphaeroides* RC-LH1 (7.2×10^{-4}%). Therefore, although the *rc*RC-LH prepared FTO-Pt PBEC generated lower V_{OC} and J_{SC}, but it achieved a relatively faster and higher power conversion efficiency than the RC-LH1 based FTO-Pt PBEC.

Difference of the power conversion efficiency are mainly resulted from the distinct structural features and attachment orientations of the *rc*RC-LH and RC-LH1. It has been shown that removal of the H subunit from purple bacteria RC results in enhanced exposure of the semiquinone sites in the LM dimer (Sun, 2017), indicating the cytoplasmic domain of the H subunit shields the internal quinones of the RC-LH1. Therefore, presence of the H subunit hindered electron transfer from the Q-side of the RC to the electrode and decreased the electron transfer efficiency in the RC-LH1 prepared PBECs, no matter the RC-LH1 was attached to the electrode with its P-side or Q-side (**Supplementary Figures 1E,F**). Genetic truncation of the cytoplasmic domain of the H subunit indeed shortened the distance between Q_B and electrode to about 12Å, a steady-state J_{SC} of up to 200 nA/cm^2 was generated when using hydroquinone as the mediator (Jun et al., 2018). However, the photogenerated electrons were transferred only from Q_A to the electrode (**Supplementary Figure 1F**), since the Q_B binding affinity was dramatically decreased due to truncation of the H subunit (Sun et al., 2015). In contrast, the *rc*RC-LH is a natural protein complex bound with endogenous menaquinones, the conformations of the quinone binding pockets were not affected during preparation of the PBECs. As a result, the photogenerated electrons could transfer from the excited P^+ to both the Q_A and Q_B in the PBECs. Therefore, absence of the H subunit in *rc*RC-LH is an advantageous structural feature that not only effectively exposes the Q-side of the RC for direct electron transfer to the electrode, but also enhances the power conversion efficiency of the PBECs.

However, the steady-state V_{OC} and J_{SC} of the *rc*RC-LH prepared FTO-Pt PBEC are relatively low, as compared with the dye-sensitized solar cells that commonly generate V_{OC} at several hundreds of mV and J_{SC} in mA/cm^2 range. The redox potential difference between the electrolyte and the photo-oxidized BChls in the RC (P/P^+) is a major determinant of the V_{OC}. In *Rba. Sphaeroides* RC-LH1 prepared PBEC, the V_{OC} scaled approximately linear with the measured potential of the electrolyte. On the other side, the J_{SC} was also increased by the vacuum potentials of the mediator. The FTO-Pt PBECs containing fresh TMPD (−4.73 eV) typically produced steady V_{OC} of approximately 7 mV and J_{SC} of 150 nA/cm^2, which are much lower than that generated by the fresh PMS (−4.51 eV) (Tan et al., 2012b). Consistently, both the V_{OC} and J_{SC} of the *rc*RC-LH prepared PBEC were remarkably increased when PMS was used as the mediator (**Figure 2C**). Therefore, it is possible to increase the V_{OC} and J_{SC} of the *rc*RC-LH based PBECs by simple manipulation of the electrolyte or alternating the potential of the coupled P/P^+ through engineering of the RC. In addition, the photocurrent output can also be improved by optimizing the coverage and assemble form of the photoactive proteins on the electrode, exploiting the use of different electrode materials, fabrication procedures, and alternative incident light intensities of these PBECs. Besides, the electrolyte in our FTO-Pt PBEC could still have the loss of volatilization during long-time exposure to the light. Therefore, a more stable electrolyte with minimal volatilization rate also needs to be investigated in the future.

CONCLUSION

We prepared a novel FTO-Pt PBEC that converts the simulated light energy into steady-state current, using the natural *rc*RC-LH complex as the photovoltaic module. In contrast to the purple bacteria RC-LH1, the *rc*RC-LH does not contain the H subunit. Instead, a tightly bound tetraheme cyt *c* subunit is exposed on the P-side of the RC, which allows the *rc*RC-LH to selectively adhere onto the hydrophilic surface of the front electrode with its Q-side. As a result, the photogenerated electrons can directly enter the front electrode without assistance of a mediator, avoiding decrease of the electron transfer efficiency and loss of the photocurrent. Additionally, the photocurrent intensities of this FTO-Pt PBEC can be enhanced by changing vacuum potentials of the mediators. A steady-state current of up to 320 nA/cm^2 was generated in the presence of PMS as the mediator. The results of this study provide a new perspective for preparing new type PBECs using the unique structural features of the *rc*RC-LH complex.

DATA AVAILABILITY STATEMENT

The original contributions presented in this study are included in the article/**Supplementary Material**, further inquiries can be directed to the corresponding author.

AUTHOR CONTRIBUTIONS

XX initiated the project and supervised all experiments. JD prepared the PBECs and characterized its photoelectrical properties. JX and ML purified the RC-LH complex from *R. castenholzii*. XZ, HH, and JW assisted in measurement of the photoelectric properties of the *rc*RC-LH based PBECs. XX and JD analyzed the data and wrote the manuscript. All authors contributed to the article and approved the submitted version.

FUNDING

This work was supported by grants from the National Natural Science Foundation of China (32171227, 31870740, and 31570738) and Zhejiang Provincial Natural Science Foundation of China under Grant No. LR22C020002 to XX.

ACKNOWLEDGMENTS

We thank Hualan Wang at the College of Material, Chemistry and Chemical Engineering for assistance during characterization of the photoelectric property of FTO-Pt PBEC.

SUPPLEMENTARY MATERIAL

The Supplementary Material for this article can be found online at: https://www.frontiersin.org/articles/10.3389/fmicb.2022.928046/full#supplementary-material

REFERENCES

Agalidis, I., and Velthuys, B. R. (1986). Oxidation of QA- and of QB- of photosynthetic reaction centers by an artificial acceptor. *FEBS Lett.* 197, 263–266. doi: 10.1016/0014-5793(86)80339-8

Blankenship, R. E., Tiede, D. M., Barber, J., Brudvig, G. W., Fleming, G., Ghirardi, M., et al. (2011). Comparing photosynthetic and photovoltaic efficiencies and recognizing the potential for improvement. *Science* 332, 805–809. doi: 10.1126/science.1200165

Buscemi, G., Vona, D., Ragni, R., Comparelli, R., Trotta, M., Milano, F., et al. (2021). Polydopamine/ethylenediamine nanoparticles embedding a photosynthetic bacterial reaction center for efficient photocurrent generation. *Adv. Sustain. Syst.* 5:2000303. doi: 10.1002/adsu.202000303

Cao, P., Bracun, L., Yamagata, A., Christianson, B. M., Negami, T., Zou, B., et al. (2022). Structural basis for the assembly and quinone transport mechanisms of the dimeric photosynthetic RC-LH1 supercomplex. *Nat. Commun.* 13:1977. doi: 10.1038/s41467-022-29563-3

Collins, A. M., Qian, P., Tang, Q., Bocian, D. F., Hunter, C. N., and Blankenship, R. E. (2010). Light-harvesting antenna system from the phototrophic bacterium *Roseiflexus castenholzii*. *Biochemistry* 49, 7524–7531. doi: 10.1021/bi101036t

Csiki, R., Drieschner, S., Lyuleeva, A., Cattani-Scholz, A., Stutzmann, M., and Garrido, J. A. (2018). Photocurrent generation of biohybrid systems based on bacterial reaction centers and graphene electrodes. *Diam. Relat. Mater.* 89, 286–292. doi: 10.1016/j.diamond.2018.09.005

Debus, R. J., Feher, G., and Okamura, M. Y. (1985). LM complex of reaction centers from *Rhodopseudomonas sphaeroides* R-26: characterization and reconstitution with the H subunit. *Biochemistry* 24, 2488–2500. doi: 10.1021/bi00331a015

Deisenhofer, J., and Michel, H. (1989). The photosynthetic reaction center from the purple bacterium *Rhodopseudomonas viridis*. *Science* 245, 1463–1473. doi: 10.1126/science.245.4925.1463

Feng, H. J., Liang, Y. X., Guo, K., Li, N., Shen, D. S., Cong, Y. Q., et al. (2016). Hybridization of photoanode and bioanode to enhance the current production of bioelectrochemical systems. *Water Res.* 102, 428–435. doi: 10.1016/j.watres.2016.06.061

Jun, D., Dhupar, H. S., Mahmoudzadeh, A., Duong, F., Madden, J. D. W., and Beatty, J. T. (2018). In vivo assembly of a truncated H subunit mutant of the *Rhodobacter sphaeroides* photosynthetic reaction centre and direct electron transfer from the Q(A) quinone to an electrode. *Photosynth. Res.* 137, 227–239. doi: 10.1007/s11120-018-0493-0

Kondo, M., Nakamura, Y., Fujii, K., Nagata, M., Suemori, Y., Dewa, T., et al. (2007). Self-assembled monolayer of light-harvesting core complexes from photosynthetic bacteria on a gold electrode modified with alkanethiols. *Biomacromolecules* 8, 2457–2463. doi: 10.1021/bm070352z

Lebedev, N., Trammell, S. A., Tsoi, S., Spano, A., Kim, J. H., Xu, J., et al. (2008). Increasing efficiency of photoelectronic conversion by encapsulation of photosynthetic reaction center proteins in arrayed carbon nanotube electrode. *Langmuir* 24, 8871–8876. doi: 10.1021/la8011348

Lee, J., Cho, H., and Kim, S. (2020). Enhanced photocurrent generation from a single-mediated photo-bioelectrochemical cell using wild-type *Anabaena Variabilis* dispersed in solution. *ChemElectroChem* 7, 4075–4083. doi: 10.1002/celc.202001026

Majumder, E. L., Olsen, J. D., Qian, P., Collins, A. M., Hunter, C. N., and Blankenship, R. E. (2016). Supramolecular organization of photosynthetic complexes in membranes of *Roseiflexus castenholzii*. *Photosynth. Res.* 127, 117–130. doi: 10.1007/s11120-015-0179-9

Musazade, E., Voloshin, R., Brady, N., Mondal, J., Atashova, S., Zharmukhamedov, S. K., et al. (2018). Biohybrid solar cells: fundamentals, progress, and challenges. *J. Photochem. Photobiol. C Photochem. Rev.* 35, 134–156. doi: 10.1016/j.jphotochemrev.2018.04.001

O'Regan, B., and Grätzel, M. (1991). A low-cost, high-efficiency solar cell based on dye-sensitized colloidal TiO2 films. *Nature* 353, 737–740. doi: 10.1038/353737a0

Osyczka, A., Moser, C. C., Daldal, F., and Dutton, P. L. (2004). Reversible redox energy coupling in electron transfer chains. *Nature* 427, 607–612. doi: 10.1038/nature02242

Page, C. C., Moser, C. C., Chen, X., and Dutton, P. L. (1999). Natural engineering principles of electron tunnelling in biological oxidation–reduction. *Nature* 402, 47–52. doi: 10.1038/46972

Paul, N., Suresh, L., Vaghasiya, J. V., Yang, L., Zhang, Y., Nandakumar, D. K., et al. (2020). Self-powered all weather sensory systems powered by *Rhodobacter sphaeroides* protein solar cells. *Biosens. Bioelectron.* 165:112423. doi: 10.1016/j.bios.2020.112423

Qian, P., Croll, T. I., Hitchcock, A., Jackson, P. J., Salisbury, J. H., Castro-Hartmann, P., et al. (2021a). Cryo-EM structure of the dimeric *Rhodobacter sphaeroides* RC-LH1 core complex at 2.9 A: the structural basis for dimerisation. *Biochem. J.* 478, 3923–3937. doi: 10.1042/BCJ20210696

Qian, P., Swainsbury, D. J. K., Croll, T. I., Salisbury, J. H., Martin, E. C., Jackson, P. J., et al. (2021b). Cryo-EM structure of the monomeric *Rhodobacter sphaeroides* RC-LH1 core complex at 2.5 A. *Biochem. J.* 478, 3775–3790. doi: 10.1042/BCJ20210631

Ravi, S. K., and Tan, S. C. (2015). Progress and perspectives in exploiting photosynthetic biomolecules for solar energy harnessing. *Energy Environ. Sci.* 8, 2551–2573. doi: 10.1039/c5ee01361e

Sekar, N., Jain, R., Yan, Y., and Ramasamy, R. P. (2016). Enhanced photo-bioelectrochemical energy conversion by genetically engineered cyanobacteria. *Biotechnol. Bioeng.* 113, 675–679. doi: 10.1002/bit.25829

Singh, V. K., Ravi, S. K., Ho, J. W., Wong, J. K. C., Jones, M. R., and Tan, S. C. (2018). Biohybrid photoprotein-semiconductor cells with deep-lying redox shuttles achieve a 0.7 V Photovoltage. *Adv. Funct. Mater.* 28:1703689. doi: 10.1002/adfm.201703689

Sun, C. (2017). Removal of the H subunit results in enhanced exposure of the semiquinone sites in the LM dimer from *Rhodobacter sphaeroides* to oxidation by ferricyanide and by O2. *Photosynth. Res.* 133, 371–377. doi: 10.1007/s11120-017-0404-9

Sun, C., Carey, A. M., Gao, B. R., Wraight, C. A., Woodbury, N. W., and Lin, S. (2016). Ultrafast electron transfer kinetics in the LM dimer of bacterial photosynthetic reaction center from *Rhodobacter sphaeroides*. *J. Phys. Chem. B* 120, 5395–5404. doi: 10.1021/acs.jpcb.6b05082

Sun, C., Taguchi, A. T., Beal, N. J., O'malley, P. J., Dikanov, S. A., and Wraight, C. A. (2015). Regulation of the primary quinone binding conformation by the H subunit in reaction centers from *Rhodobacter sphaeroides*. *J. Phys. Chem. Lett.* 6, 4541–4546. doi: 10.1021/acs.jpclett.5b01851

Swainsbury, D. J. K., Qian, P., Jackson, P. J., Faries, K. M., Niedzwiedzki, D. M., Martin, E. C., et al. (2021). Structures of *Rhodopseudomonas palustris* RC-LH1 complexes with open or closed quinone channels. *Sci. Adv.* 7:eabe2631. doi: 10.1126/sciadv.abe2631

Takshi, A., Madden, J. D. W., Mahmoudzadeh, A., Saer, R., and Beatty, J. T. (2010). A photovoltaic device using an electrolyte containing photosynthetic reaction centers. *Energies* 3, 1721–1727. doi: 10.3390/en3111721

Tan, S. C., Crouch, L. I., Jones, M. R., and Welland, M. (2012a). Generation of alternating current in response to discontinuous illumination by photoelectrochemical cells based on photosynthetic proteins. *Angew. Chem. Int. Ed. Engl.* 51, 6667–6671. doi: 10.1002/anie.201200466

Tan, S. C., Crouch, L. I., Mahajan, S., Jones, M. R., and Welland, M. E. (2012b). Increasing the open-circuit voltage of photoprotein-based photoelectrochemical cells by manipulation of the vacuum potential of the electrolytes. *ACS Nano* 6, 9103–9109. doi: 10.1021/nn303333e

Tan, S. C., Yan, F., Crouch, L. I., Robertson, J., Jones, M. R., and Welland, M. E. (2013). Superhydrophobic carbon nanotube electrode produces a near-symmetrical alternating current from photosynthetic protein-based photoelectrochemical cells. *Adv. Funct. Mater.* 23, 5556–5563. doi: 10.1002/adfm.201301057

Terasaki, N., Yamamoto, N., Hiraga, T., Yamanoi, Y., Yonezawa, T., Nishihara, H., et al. (2009). Plugging a molecular wire into photosystem I: reconstitution of the photoelectric conversion system on a gold electrode. *Angew. Chem. Int. Ed. Engl.* 48, 1585–1587. doi: 10.1002/anie.200805748

Trammell, S. A., Spano, A., Price, R., and Lebedev, N. (2006). Effect of protein orientation on electron transfer between photosynthetic reaction centers and carbon electrodes. *Biosens. Bioelectron.* 21, 1023–1028. doi: 10.1016/j.bios.2005.03.015

Wang, X., Liu, C., Shi, Z., Pan, M., and Yu, D. (2020). Protein-encapsulated chlorophyll a molecules for biological solar cells. *Mater. Des.* 195:108983. doi: 10.1016/j.matdes.2020.108983

Wang, X., Pan, M., Shi, Z., Yu, D., and Huang, F. (2021). Protein nanobarrel for integrating chlorophyll a molecules and its photochemical performance. *ACS Appl. Bio Mater.* 4, 399–405. doi: 10.1021/acsabm.0c00208

Winkler, J. R., and Gray, H. B. (2014). Long-range electron tunneling. *J. Am. Chem. Soc.* 136, 2930–2939. doi: 10.1021/ja500215j

Xin, Y., Shi, Y., Niu, T., Wang, Q., Niu, W., Huang, X., et al. (2018). Cryo-EM structure of the RC-LH core complex from an early branching photosynthetic prokaryote. *Nat. Commun.* 9:1568. doi: 10.1038/s41467-018-03881-x

Yaghoubi, H., Li, Z., Jun, D., Lafalce, E., Jiang, X. M., Schlaf, R., et al. (2014). Hybrid Wiring of the *Rhodobacter sphaeroides* reaction center for applications in bio-photoelectrochemical solar cells. *J. Phys. Chem. C* 118, 23509–23518. doi: 10.1021/jp507065u

Yamada, M., Zhang, H., Hanada, S., Nagashima, K. V., Shimada, K., and Matsuura, K. (2005). Structural and spectroscopic properties of a reaction center complex from the chlorosome-lacking filamentous anoxygenic phototrophic bacterium *Roseiflexus castenholzii*. *J. Bacteriol.* 187, 1702–1709. doi: 10.1128/JB.187.5.1702-1709.2005

Zhang, J., Lou, Y., Liu, M., Zhou, H., Zhao, Y., Wang, Z., et al. (2018). High-performance dye-sensitized solar cells based on colloid–solution deposition planarized fluorine-doped tin oxide substrates. *ACS Appl. Mater. Interfaces* 10, 15697–15703. doi: 10.1021/acsami.8b01737

Zhou, X., Gai, P. P., Zhang, P. B., Sun, H., Lv, F. T., Liu, L. B., et al. (2019). Conjugated polymer enhanced photoelectric response of self-circulating photosynthetic bioelectrochemical cell. *ACS Appl. Mater. Interfaces* 11, 38993–39000. doi: 10.1021/acsami.9b12560

Conflict of Interest: The authors declare that the research was conducted in the absence of any commercial or financial relationships that could be construed as a potential conflict of interest.

Publisher's Note: All claims expressed in this article are solely those of the authors and do not necessarily represent those of their affiliated organizations, or those of the publisher, the editors and the reviewers. Any product that may be evaluated in this article, or claim that may be made by its manufacturer, is not guaranteed or endorsed by the publisher.

frontiers | Frontiers in Microbiology

REVIEW
published: 01 July 2022
doi: 10.3389/fmicb.2022.933160

Cyanobacterial NDH-1 Complexes

*Mi Hualing**

National Key Laboratory of Plant Molecular Genetics, CAS Center for Excellence in Molecular Plant Sciences, Institutes of Plant Physiology and Ecology, Shanghai, China

Light reaction of photosynthesis is efficiently driven by protein complexes arranged in an orderly in the thylakoid membrane. As the 5th complex, NAD(P)H dehydrogenase complex (NDH-1) is involved in cyclic electron flow around photosystem I to protect plants against environmental stresses for efficient photosynthesis. In addition, two kinds of NDH-1 complexes participate in CO_2 uptake for CO_2 concentration in cyanobacteria. In recent years, great progress has been made in the understanding of the assembly and the structure of NDH-1. However, the regulatory mechanism of NDH-1 in photosynthesis remains largely unknown. Therefore, understanding the regulatory mechanism of NDH-1 is of great significance to reveal the mechanism of efficient photosynthesis. In this mini-review, the author introduces current progress in the research of cyanobacterial NDH-1. Finally, the author summarizes the possible regulatory mechanism of cyanobacterial NDH-1 in photosynthesis and discusses the research prospect.

Keywords: cyanobacteria (blue-green algae), NAD(P)H dehydrogenase complex, photosynthesis, cyclic electron transport around photosystem I, CO_2 uptake and concentrating mechanism

OPEN ACCESS

Edited by:
Weimin Ma,
Shanghai Normal University, China

Reviewed by:
Lianwei Peng,
Shanghai Normal University, China
Mei Li,
Institute of Biophysics (CAS), China
Guangye Han,
Institute of Botany (CAS), China
Toshiharu Shikanai,
Kyoto University, Japan

***Correspondence:**
Mi Hualing
mihl@cemps.ac.cn
orcid.org/0000-0003-1021-8372

Specialty section:
This article was submitted to Microbial Physiology and Metabolism, a section of the journal Frontiers in Microbiology

Received: *30 April 2022*
Accepted: *24 May 2022*
Published: *01 July 2022*

Citation:
Hualing M (2022) Cyanobacterial NDH-1 Complexes. Front. Microbiol. 13:933160. doi: 10.3389/fmicb.2022.933160

INTRODUCTION

Cyanobacteria belong to prokaryotic photosynthetic organisms. Like other green plants, the light reaction of photosynthesis is carried out with the participation of two photosystems (photosystem I and II, PSI and PSII). Light energy absorbed by antenna pigments is transferred to the photosystem reaction centers and is converted to assimilative power (ATP and NADPH) *via* a series of electron transporters. Electron transport between PSI and PSII is mediated by the cytochrome *b6f* complex (Cyt *b6f*), coupling the translocation of protons across the thylakoid membranes. The resulting proton concentration difference (ΔpH) and membrane potential difference ($\Delta\psi$) between inside and outside the thylakoid membrane drive ATP synthase (ATPase) to synthesize ATP. The electron transfer in this process is known as linear electron transport (LET). In addition, the donation of electrons from the PSI reduction side to the electron carriers between two photosystems to form circle electron transport is known as cyclic electron transport around PSI (CET-PSI). CET-PSI is also coupled with the formation of ATP, but there is no accumulation of NADPH or other reducing substances. NADPH and ATP produced by the light reaction are used for CO_2 fixation (carbon assimilation). Compared with carbon assimilation, the light energy utilization efficiency in the light reaction is higher. The light reaction is driven by protein complexes arranged orderly on the thylakoid membrane. The protein complexes involved in LET include PSI, PSII, cytochrome *b6/f* complex, and ATPase, while the complexes involved in CET-PSI include thylakoid membrane-bound NAD(P)H dehydrogenase-like complex (chloroplast NDH or cyanobacterial NDH-1). Studies have demonstrated that NDH/NDH-1 mediated CET-PSI (Mi et al., 1992, 1994, 1995) can protect plants from photoinhibition caused by various stress environmental conditions (Endo et al., 1999; Mi et al., 2001; Wang et al., 2006) for efficient photosynthesis (Munekaga et al., 2004).

Cyanobacteria equip a series of environmental adaptations to efficiently fixate inorganic carbon (Ci) under CO_2-limited conditions. All these adaptations, including the active uptake of Ci, the subsequent localized elevation of CO_2 around the primary CO_2-fixing enzyme, ribulose 1,5-bisphosphate carboxylase/oxygenase (Rubisco), and the partitioning of Rubisco into the carboxysome, are collectively considered as the carbon concentrating mechanism (CCM) (Badger et al., 2002; Badger and Price, 2003; Raven, 2003; Giordano et al., 2005). CCM requires the coordination of two systems, an inorganic carbon transporter system and the carboxysome containing Rubisco. To date, five inorganic carbon transporters have been found, including two Na^+-dependent HCO_3^- transporters (BicA and SbtA), one ATPase-dependent HCO_3^- transporter (BCT1), and two CO_2-uptake NDH-1 (type 1 NDH) complexes in *Synechocystis* sp. PCC 6803 (hereafter *Syne*6803) and other cyanobacterial strains (Ogawa and Kaplan, 2003; Ogawa and Mi, 2007; Price, 2011). Therefore, cyanobacterial NDH-1 complexes function not only in light reactions but also in carbon assimilation as an important regulator. This mini-review summarizes the recent research progress of characterization and functions of cyanobacterial NDH-1 in photosynthesis and prospects for the future research direction.

COMPOSITION AND STRUCTURAL CHARACTERISTICS OF NDH-1 COMPLEX IN CYANOBACTERIA

Through the genome comparison of chloroplast and cyanobacteria, 15 highly homologous *ndh* genes, namely *NdhA-O*, were found in cyanobacteria (Kaneko et al., 1996) and the corresponding homologous proteins (NdhA-O) were identified (Friedrich and Scheide, 2000; Prommeenate et al., 2004; Rumeau et al., 2005). An additional 4 proteins NdhP, NdhQ, NdhS, and NdhV were successively identified (Battchikova et al., 2011a; Nowaczyk et al., 2011; Chen et al., 2016). In contrast to the crystal structure of Complex I (Baradaran et al., 2013), cyanobacterial NDH-1 is speculated to possess an oxygenic photosynthesis-specific (OPS) domain (Birungi et al., 2010) comprised of NdhL-NdhQ, -NdhS, -NdhV. NdhL is necessary for the docking of hydrophilic subcomplex to hydrophobic subcomplex in both cyanobacteria (Battchikova et al., 2005) and plants (Shimizu et al., 2008). Deletion of NdhL lowered CET-PSI activity in cyanobacteria (Mi et al., 1992). By studying NDH-1 mutants and protein-protein interaction of multiple subunits, our group found that NdhM locates in the core of the NDH-1 hydrophilic arm of cyanobacteria and plays a key role in the assembly and activity of the NDH-1 hydrophilic arm (He et al., 2016). NdhN also affects the assembly and activity of NDH-1 (He and Mi, 2016). In contrast, although the little contribution of NdhO to CET-PSI activity, it plays an important role in respiratory metabolism under the condition of limited inorganic carbon (He and Mi, 2016). NdhV is a subunit which functions in regulation of NDH-1 activity. Mutation of *NdhV* resulted in the instability and decrease of NDH activity in Arabidopsis (Fan et al., 2015), loss of the upregulation of NDH-1 level and activity induced at high light (Chen et al., 2016), and causing heat sensitivity (Gao et al., 2016) in cyanobacteria. *E. coli* NDH-1 complex is the mode of complex I with the smallest components of protein subunits, composed of 14 subunits from NuoA to NuoN. This smallest module carries out the most basic energy conversion reaction (Friedrich and Scheide, 2000). Comparing the NDH composition of *E. coli*, cyanobacteria and chloroplasts indicate that NdhA-K is a conserved component of NDH-1 in prokaryotes and eukaryotes. However, the homologous proteins of three subunits NuoE, NuoF, and NuoG involved in NADH oxidation in *E. coli* were not found in chloroplasts and cyanobacteria. Since these three subunits contain NADH-binding sites, cofactor FMN, and iron-sulfur clusters, whether thylakoid membrane NDH-1 can directly oxidize NADH, or NADPH remains to be confirmed. Experiment using thylakoid membranes has demonstrated that ferredoxin (Fd) can donate an electron to PQ *via* cyanobacterial NDH-1 (Mi et al., 1995). At present, it is believed that the electron donor of chloroplast NDH is Fd rather than NAD (P) H (Shikanai, 2014), which is based on their laboratory study that the C-terminal of CRR31 (NdhS) subunit from Arabidopsis (Yamamoto et al., 2011; Yamamoto and Shikanai, 2013) and cyanobacterium *Syne* 6803 (Battchikova et al., 2011a), contains SH3 (Src homology 3) domain-like fold, which serves as Fd docking site. In addition, *in vitro* experiments have proved that the reduction of PQ is required for binding Fd and catalytic activity (Yamamoto et al., 2011). The C-terminal of NdhS of cyanobacteria is conserved, indicating that the electron donor element of thylakoid membrane NDH is conserved (Battchikova et al., 2011b). It was also demonstrated that thermophilic cyanobacterial Fd can interact with NDH-1 probably *via* the interaction of NdhS with NdhH or NdhI by using surface plasmon resonance (SPR) (He et al., 2015). Recently, cyanobacterial NDH-1 structures provided strong evidence that Fd binds with cyanobacterial NDH-1 *via* extensive contact with NdhI and NdhH (Pan et al., 2020; Zhang et al., 2020).

Proteomic analysis of cyanobacterial NDH-1 complexes has revealed the presence of three complexes NDH-1L/-1L' (large size), NDH-1M (medium size), and NDH-1S (small size) in *Synechosystis* PCC 6803 (Herranen et al., 2004). NDH-1L/-1L' is composed of NDH-1M, NdhD1/D2, NdhF1, NdhP, and NdhQ, which are involved in respiration and CET-PSI, while NDH-MS is composed of NDH-1M and NDH-1S (including NdhD3, NdhF3, CupA, and CupS) and NDH-MS' composed of NDH-1M and NDH-1S' (including NdhD3, NdhF3, CupB, and CupS') participate in CO_2 uptake (Ogawa and Mi, 2007). Three types of cyanobacteria NDH-1 complexes contain NDH-1M as a skeleton. The expression of NDH-1L is stable under different growth conditions; however, the NDH-1L' has not been detected on the protein level (Zhang et al., 2004). Similar to bacterial complex I, NDH-1L forms an L-shaped architecture by analysis of the complex isolated from *Thermosynechococcus elongatus* strain earlier with electron microscopy in low resolution (Arteni et al., 2006) and recently with cryo-EM in high resolution: the previous two structures contained no NdhV (Laughlin et al., 2019; Schuller et al., 2019) and the latter two structures contained

NdhV and Fd (Pan et al., 2020; Zhang et al., 2020). NDH-1MS is inducible at limiting inorganic carbon conditions and has a high uptake affinity for CO_2, which is easily dissociated into NDH-1M and NDH-1S (Herranen et al., 2004). The NDH-1MS complex has been isolated from a *Thermosynechococcus elongatus* strain in which the C terminus of NdhL has been tagged with 6-His. This complex is easily dissociated into NDH-1M and NDH-1S complexes (Zhang et al., 2005). Single-particle electron microscopy analysis of purified thylakoid membrane components indicated that NDH-1MS had a U-shaped structure (Arteni et al., 2006). CupA is responsible for the formation of a U-shape by binding at the tip of the membrane-bound arm of NDH-1MS in both *T. elongatus* and *Syne 6803* (Folea et al., 2008). The structure of NDH-1MS has also been resolved by cryo-EM (Schuller et al., 2020). NDH-1MS' is involved in the complex of constitutive CO_2 uptake, and its key gene *CupB* is homologous with *CupA* (Madsen et al., 2002; Shibata et al., 2002). CupB protein is dependent on NdhD4 to locate on the thylakoid membrane, and a 450 kDa NDH-1MS' complex was identified by isolation and purification (Xu et al., 2008).

The plastid coding subunits of NDH in terrestrial plant chloroplast are highly homolog to NDH-1L in cyanobacteria. In addition, plant chloroplast NDH contains at least 18 nucleus-encoded subunits formed from different subcomplexes (Ifuku et al., 2011; Ueda et al., 2012). Chloroplast NDH can form a supercomplex with a PSI core *via* two minor light-harvesting complexes I (LHCI) subunits, Lhca5 and Lhca5, for the association of PSI-LHCI (Kouril et al., 2014; Otani et al., 2018). Recently, two research works have reported the structure of chloroplast PSI-NDH supercomplex that the PSI-NDH is composed of two copies of the PSI-LHCI subcomplex, one NDH complex, and two monomeric LHCI proteins, Lhca5 and Lhca6, mediate the binding of two PSI complexes to NDH (Shen et al., 2022; Su et al., 2022).

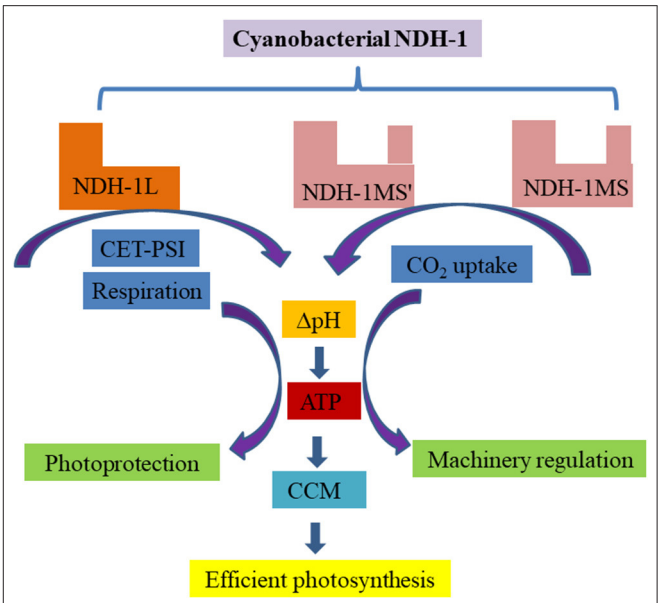

FIGURE 1 | A schematic representation of the possible mechanism of cyanobacterial NDH-1 in photosynthesis. As NDH-1L is involved in CET-PSI and respiratory pathways, NDH-1MS' and NDH-MS participate in CO_2 uptake. These pathways couple the generation of trans-thylakoid membrane proton gradient to synthesize ATP for photoprotection, photosynthetic machinery regulation, and energy supply for carbon assimilation, especially under changing environments.

POSSIBLE MECHANISM OF NDH-1

As the fifth complex, chloroplast NDH only participates in CET-PSI and cyanobacterial NDH-1 is also involved in CCM, playing important role in regulating photosynthesis. **Figure 1** summarizes the possible mechanism of NDH-1 based on a series of research works.

Supplement ATP for Effective Carbon Assimilation

Cyanobacteria could survive in a low CO_2 environment in water due to their CCMs, which can increase the CO_2 concentration around the active site of Rubisco, the key enzyme of photosynthetic carbon assimilation, and overcome their low affinity for CO_2, thereby effectively assimilating CO_2 (Price et al., 1998; Kaplan and Reinhold, 1999). The CCMs and inorganic carbon transport of cyanobacteria are ATP-consuming processes. The *Syne*6803 mutant defective in NdhB (Ogawa, 1991a), NdhH, NdhJ, NdhN, or NdhM (He and Mi, 2016; He et al., 2016) completely lost CET-PSI activity mediated by HDH-1 and could not survive in the concentration of air CO_2. The mutants lost partial NDH-1 activity and grew slower in air CO_2 (Ogawa, 1991b; He and Mi, 2016). Klughammer et al. (Klughammer et al., 1999) used *NdhD3*-, *NdhF3*-mutants of *Synechococcus* PCC7002, to study the CO_2 uptake efficiency. They observed that these mutants could neither induce efficient CO_2 uptake nor efficient carbonate transport. They proposed that NDH-1 special subunits encoded by *NdhD3* and *NdhF* participate in high-affinity CO_2 uptake. Ogawa's group proposed the involvement of NDH-1 in energy conduction and induction of a high-affinity inorganic carbon transport by studying mutants involved in CCM (Ohkawa et al., 2000). Further research indicated that deletion of NdhDs suppressed the building up of the trans-thylakoidal ΔpH resulting in the loss of the CO_2 uptake function (Han et al., 2017). Therefore, cyanobacterial NDH-1 would provide ATP for CCM.

As the assimilation force, ATP and NADPH produced in photoreaction are used for CO_2 assimilation. According to theoretical calculations, the ratio of ATP/NADPH required to assimilate each molecule of CO_2 is 1.5. However, in C3 plants, due to the existence of photorespiration, the required theoretical value of ATP/NADPH increases to 1.66. When plants are in various developmental stages with different energy requirements or facing environmental changes, the fixed proportion of ATP and NADPH produced by LET often could not meet the needs of CO_2 assimilation. Since CET-PSI only produces ATP, additional ATP can be provided (Shikanai, 2007) to meet the needs of ATP for photosynthetic carbon assimilation. In

*Syne*6803, deletion of *NdhV* caused a decrease in a trans-thylakoid membrane ΔpH and loss of the upregulation of CET-PSI activity at high light (Chen et al., 2016). Also, the mutant that deleted either NdhD3 or NdhD4 significantly lowered the trans-thylakoid membrane's proton gradient (Han et al., 2017) and could not survive under CO_2 conditions. Therefore, the ΔpH generated by NDH-1 drives the ATPase to synthesize ATP for active CO_2 uptake and regulation of pH in the cytosol.

Hibino et al. reported that the expression of *NdhK* and *NdhI* genes was increased under high salt concentration, and CET-PSI mediated by NDH-1 was accordingly promoted (Hibino et al., 1996). Under the shock of a high concentration of salt, the *ndhB* deletion mutant could not restore its photosynthetic ability (Tanaka et al., 1997). Therefore, it is considered that CET-PSI mediated by NDH-1 is essential for cyanobacteria to adapt to salt-stressed condition. Based on plants, adapting to stressed conditions is an energy-consuming process; it is suggested that CET-PSI mediated by NDH-1 might provide extra ATP for cells to adapt to these energy-consuming reactions. The demand and proportion of ATP and NADPH in cyanobacteria and higher plants vary with the change in the photosynthetic environment or developmental stages. When the CO_2 concentration becomes low, it is necessary to concentrate CO_2 by consuming energy, to increase the demand for ATP. The proportion of ATP and NADPH produced by LET is certain and could not be adjusted. However, through CET-PSI, it is possible to adjust the proportion of ATP and NADPH.

Regulation of Photosynthetic Machinery

In studying the kinetics of NADPH fluorescence (blue-green fluorescence), we observed that when the inhibitor of Calvin cycle iodoacetic acid (IAA) was added, the amplitude of rapid NADP reduction is approximately doubled in wild-type but not in the *ndhB* gene deletion mutant M55 cells. Apparently, in wild-type cells, the rate of the Calvin cycle is sufficiently high to prevent full NADP reduction even upon the onset of saturating illumination. This is possible only if there is a correspondingly high ATP supply. On the other hand, in M55 cells, full NADP reduction is obtained. This suggests that in M55 cells, ATP limits the activity of the Calvin cycle due to the lack of CET-PSI phosphorylation (Mi, 2000).

The redistribution of excitation energy between the two light systems (state transitions) is mainly to adjust the excitation imbalance of the two photosystems. It is a mechanism for plants to resist the light damage caused by excessive excitation energy. In cyanobacteria, it has been reported that NDH-1 participates in state transitions of excitation energy between PS I and II by CET-PSI. NDH-1 inactivated mutants, M55, lost the function of state transitions and were locked in state 1 (Schreiber et al., 1995). The mobility of the major accessory's light-harvesting complex phycobilisome (PBS) is related to state transitions, CET-PSI, and respiration. The immobilization of PBS at PSII inhibited the increase in CET-PSI and decrease in respiration that occurred during the movement of PBS from PSII to PSI. In contrast, the immobilization of PBS at PSI inhibited the increase in respiration and decrease in CET-PSI that occurred when PBS moved from PSI to PSII (Ma et al., 2007). State transitions in cyanobacteria, dependent on "spillover" and membrane fluidity, are induced by redox changes in the PQ pool. The light-induced state transitions induced by PBS movement caused redox poise of the PQ pool. A protein kinase known as Stt7/Stn7 has been implicated in state transitions by acting as the LHC II kinase, it seems necessary to assume that a bifurcated redox signaling pathway carries information from the PQ pool (Allen et al., 2011). NDH-I-mediated CET-PSI might participate in the redistribution of excitation energy by affecting the redox state of plastoquinone (Ma et al., 2007, 2008). However, how the redox state is sensed in cyanobacterial state transition is not clear. Plants balance their redox system by regulating CET-PSI or respiratory electron transport so that it will not be over oxidized or over-reduced. Under normal physiological conditions, when the Calvin cycle is fully active, the reduction is mainly caused by LET, and the proportion of CET-PSI is small enough to be ignored. However, when CO_2 assimilation is decreased, NADPH and reduced ferredoxin will accumulate too much, and CET-PSI would be promoted under stressed conditions. We observed that when dark-adapted *Syne*6803 cells were moved to light, NDH-1 expression was significantly induced, and NDH-1 mediated CET-PSI and respiratory electron transport were upregulated (Mi et al., 2001). Therefore, it is suggested that NDH-1 mediated CET-PSI might co-operate with respiratory alternative oxidase transfer electrons to O_2, thereby avoiding the over-reduction of the PQ pool under various stresses.

Our group found that the CO_2 uptake systems NDH-1MS and NDH-1MS' are associated with a carbonic anhydrase EcaB, which catalyzes the conversion of CO_2 into HCO_3^- in response to high pH values, high light, or low CO_2 concentrations, thereby helping to balance the redox state of inter photosystem electron carriers and maintain efficient photosynthesis (Sun et al., 2019).

Photoprotection

Photosynthesis needs light energy, but the excess excitation energy would cause photoinhibition and even cause photodamage of PSII. The CET-PSI is involved in eliminating excess light energy through the mechanism of heat dissipation to protect plants from light damage caused by strong light. CET-PSI can also reduce photoinhibition by downstream regulation of PSII by generating transmembrane proton gradient (Heber, 1992). We found that the deletion of *ndhc-j-k* in tobacco leads to the accumulation of reactive oxygen species under low or high-temperature stresses (Wang et al., 2006). In addition, a low concentration of $NaHSO_3$ promotes CET-PSI in *Syne*6803 (Wang et al., 2003) and tobacco under the condition of dark-light transition, alleviating photooxidative damage and improving photosynthesis by promoting photosynthetic phosphorylation mediated by NDH-1 (Wu et al., 2011, 2012).

CONCLUSION REMARKS

The NDH-1 plays an important role in the regulation of efficient operation of photosynthetic apparatus under changed environmental conditions. Structure bases have been made in NDH-1L and NDH-1MS. It is not clear whether there is a cross-talk between NDH-1L mediated CET-PS I and NDH-1MS/NDH-1MS' involvement in CO_2 uptake. How does NDH-1 function in coordination with light reaction and carbon assimilation? In the future, we may use a high-resolution cryo-EM to observe and analyze active forms and states of NDH-1, and deeply study the dynamic regulation mechanism of NDH-1. With the development of molecular biology, proteomics, metabolomics, computational biology, and structural biology, it is possible to reveal the complicated regulatory network of NDH-1 in photosynthesis.

AUTHOR CONTRIBUTIONS

MH wrote this manuscript.

FUNDING

This work was supported by funds from Synthesis Biology [2019YFA0904602] and the Strategic Priority Research Program of CAS [XDB27020106].

REFERENCES

Allen, J. F., Santabarbara, S., Allen, C. A., and Puthiyaveetil, S. (2011). Discrete redox signaling pathways regulate photosynthetic light-harvesting and chloroplast gene transcription. *PLoS ONE* 6, e026372. doi: 10.1371/journal.pone.0026372

Arteni, A. A., Zhang, P. P., Battchikova, N., Ogawa, T., Aro, E. M., and Boekema, E. J. (2006). Structural characterization of NDH-1 complexes of Thermosynechococcus elongatus by single particle electron microscopy. *Biochimica Et Biophysica Acta-Bioenergetics* 1757, 1469–1475. doi: 10.1016/j.bbabio.2006.05.042

Badger, M. R., Hanson, D., and Price, G. D. (2002). Evolution and diversity of CO2 concentrating mechanisms in cyanobacteria. *Funct. Plant Biol.* 29, 161–173. doi: 10.1071/PP01213

Badger, M. R., and Price, G. D. (2003). CO2 concentrating mechanisms in cyanobacteria: molecular components, their diversity and evolution. *J. Exp. Bot.* 54, 609–622. doi: 10.1093/jxb/erg076

Baradaran, R., Berrisford, J. M., Minhas, G. S., and Sazanov, L. A. (2013). Crystal structure of the entire respiratory complex I. *Nature* 494, 443–448. doi: 10.1038/nature11871

Battchikova, N., Eisenhut, M., and Aro, E.-M. (2011b). Cyanobacterial NDH-1 complexes: Novel insights and remaining puzzles. *Biochim. Biophys. Acta-Bioenerg.* 1807, 935–944. doi: 10.1016/j.bbabio.2010.10.017

Battchikova, N., Wei, L., Du, L., Bersanini, L., Aro, E.-M., and Ma, W. (2011a). Identification of novel Ssl0352 protein (NdhS), essential for efficient operation of cyclic electron transport around photosystem I, in NADPH:plastoquinone oxidoreductase (NDH-1) complexes of synechocystis sp. PCC 6803. *J. Biol. Chem.* 286, 36992–37001. doi: 10.1074/jbc.M111.263780

Battchikova, N., Zhang, P. P., Rudd, S., Ogawa, T., and Aro, E. M. (2005). Identification of NdhL and Ssl1690 (NdhO) in NDH-1L, and NDH-1M complexes of Synechocystis sp PCC 6803. *J. Biol. Chem.* 280, 2587–2595. doi: 10.1074/jbc.M410914200

Birungi, M., Folea, M., Battchikova, N., Xu, M., Mi, H. L., Ogawa, T., et al. (2010). Possibilities of subunit localization with fluorescent protein tags and electron microscopy examplified by a cyanobacterial NDH-1 study. *Biochim. Biophys. Acta-Bioenergetics* 1797, 1681–1686. doi: 10.1016/j.bbabio.2010.06.004

Chen, X., He, Z., Xu, M., Peng, L., and Mi, H. (2016). NdhV subunit regulates the activity of type-1 NAD(P)H dehydrogenase under high light conditions in cyanobacterium Synechocystis sp PCC 6803. *Sci. Rep.* 6:2016. doi: 10.1038/srep28361

Endo, T., Shikanai, T., Takabayashi, A., Asada, K., and Sato, F. (1999). The role of chloroplastic NAD(P)H dehydrogenase in photoprotection. *FEBS Lett.* 457, 5–8. doi: 10.1016/S0014-5793(99)00989-8

Fan, X., Zhang, J., Li, W., and Peng, L. (2015). The NdhV subunit is required to stabilize the chloroplast NADH dehydrogenase-like complex in Arabidopsis. *Plant J.* 82, 221–231. doi: 10.1111/tpj.12807

Folea, I. M., Zhang, P., Nowaczyk, M. M., Ogawa, T., Aro, E.-M., and Boekema, E. J. (2008). Single particle analysis of thylakoid proteins from Thermosynechococcus elongatus and Synechocystis 6803: Localization of the CupA subunit of NDH-1. *FEBS Lett.* 582, 246–251. doi: 10.1016/j.febslet.2007.12.012

Friedrich, T., and Scheide, D. (2000). The respiratory complex I of bacteria, archaea and eukarya and its module common with membrane-bound multisubunit hydrogenases. *FEBS Lett.* 479, 1–5. doi: 10.1016/S0014-5793(00)01867-6

Gao, F., Zhao, J., Wang, X., Qin, S., Wei, L., and Ma, W. (2016). NdhV is a subunit of NADPH dehydrogenase essential for cyclic electron transport in synechocystis sp strain PCC 6803. *Plant Physiol.* 170, 752–760. doi: 10.1104/pp.15.01430

Giordano, M., Beardall, J., and Raven, J. A. (2005). CO2 concentrating mechanisms in algae: mechanisms, environmental modulation, and evolution. *Annu. Rev. Plant Biol.* 56, 99–131. doi: 10.1146/annurev.arplant.56.032604.144052

Han, X., Sun, N., Xu, M., and Mi, H. (2017). Co-ordination of NDH and Cup proteins in CO2 uptake in cyanobacterium Synechocystis sp PCC 6803. *J. Exp. Bot.* 68, 3869–3877. doi: 10.1093/jxb/erx129

He, Z., and Mi, H. (2016). Functional characterization of the subunits N, H, J, and O of the NAD(P)H dehydrogenase complexes in synechocystis sp strain PCC 6803. *Plant Physiol.* 171, 1320–1332. doi: 10.1104/pp.16.00458

He, Z., Xu, M., Wu, Y., Lv, J., Fu, P., and Mi, H. (2016). NdhM is required for the stability and the function of NAD(P)H dehydrogenase complexes involved in CO_2 uptake in *Synechocystis* sp. strain PCC 6803. *J. Biol. Chem.* 2016, 5902–5912. doi: 10.1074/jbc.M115.698084

He, Z., Zheng, F., Wu, Y., Li, Q., Lv, J., Fu, P., et al. (2015). NDH-1L interacts with ferredoxin via the subunit NdhS in Thermosynechococcus elongatus. *Photosyn. Res.* 126, 341–349. doi: 10.1007/s11120-015-0090-4

Heber, U. (1992). Concerning a dual function of coupled cyclic electro-transport in leaves. *Plant Physiol. Plant Physiology* 100, 1261–1264. doi: 10.1104/pp.100.4.1621

Herranen, M., Battchikova, N., Zhang, P. P., Graf, A., Sirpio, S., Paakkarinen, V., et al. (2004). Towards functional proteomics of membrane protein complexes in Synechocystis sp PCC 6803. *Plant Physiol.* 134, 470–481. doi: 10.1104/pp.103.032326

Hibino, T. L. B., Rai, A. K., Ishikawa, H., Kojima, H., Tawada, M., Shimoyama, H., et al. (1996). Salt enhances photosystem I content and cyclic electron flow via NAD(P)H dehydrogenase in halotolerant cyanobacterium Aphanothece halophytica. *Aust J Plant Physilol* 23, 321–330. doi: 10.1071/PP9960321

Ifuku, K., Endo, T., Shikanai, T., and Aro, E.-M. (2011). Structure of the chloroplast NADH dehydrogenase-like complex: nomenclature for nuclear-encoded subunits. *Plant Cell Physiol.* 52, 1560–1568. doi: 10.1093/pcp/pcr098

Kaneko, T., Sato, S., Kotani, H., Tanaka, A., Asamizu, E., Nakamura, Y., et al. (1996). Sequence analysis of the genome of the unicellular cyanobacterium Synechocystis sp. strain PCC6803. II. Sequence determination of the entire genome and assignment of potential protein-coding regions (supplement). *DNA Res.* 3, 185–209. doi: 10.1093/dnares/3.3.185

Kaplan, A., and Reinhold, L. (1999). CO2 concentrating mechanisms in photosynthetic microorganisms. *Annu. Rev. Plant Physiol. Plant Mol. Biol.* 50:539. doi: 10.1146/annurev.arplant.50.1.539

Klughammer, B., Sultemeyer, D., Badger, M. R., and Price, G. D. (1999). The involvement of NAD(P)H dehydrogenase subunits, NdhD3 and NdhF3, in

high-affinity CO2 uptake in Synechococcus sp PCC7002 gives evidence for multiple NDH-1 complexes with specific roles in cyanobacteria. *Mol. Microbiol.* 32, 1305–1315. doi: 10.1046/j.1365-2958.1999.01457.x

Kouril, R., Strouhal, O., Nosek, L., Lenobel, R., Chamrad, I., Boekema, E. J., et al. (2014). Structural characterization of a plant photosystem I and NAD(P)H dehydrogenase supercomplex. *Plant J.* 77, 568–576. doi: 10.1111/tpj.12402

Laughlin, T. G., Bayne, A. N., Trempe, J.-F., Savage, D. F., and Davies, K. M. (2019). Structure of the complex I-like molecule NDH of oxygenic photosynthesis. *Nature* 566, 411–414. doi: 10.1038/s41586-019-0921-0

Ma, W., Ogawa, T., Shen, Y., and Mi, H. (2007). Changes in cyclic and respiratory electron transport by the movement of phycobilisomes in the cyanobacterium Synechocystis sp strain PCC 6803. *Biochimica Et Biophysica Acta-Bioenergetics* 1767, 742–749. doi: 10.1016/j.bbabio.2007.01.017

Ma, W. M., Deng, Y., and Mi, H. L. (2008). Redox of plastoquinone pool regulates the expression and activity of NADPH dehydrogenase supercomplex in Synechocystis sp strain PCC 6803. *Curr. Microbiol.* 56, 189–193. doi: 10.1007/s00284-007-9056-x

Madsen, T. V., Olesen, B., and Bagger, J. (2002). Carbon acquisition and carbon dynamics by aquatic isoetids. *Aquat. Bot.* 73, 351–371. doi: 10.1016/S0304-3770(02)00030-X

Mi, H., Endo, T., Schreiber, U., Ogawa, T., and Asada, K. (1994). Nad(P)H dehydrogenase-dependent cyclic electron flow around photosystem-i in the cyanobacterium synechocystis PCC-6803 - a study of dark-starved cells and spheroplastS. *Plant Cell Physiol.* 35, 163–173.

Mi, H. K. C. (2000). Schreiber U Light-induced dynamic changes of NADPH fluorescence in *Synechocystis* PCC 6803 and its *ndh*B-defective mutant M55. *Plant Cell Physiol.* 41, 1129–1135. doi: 10.1093/pcp/pcd038

Mi, H. L., Deng, Y., Tanaka, Y., Hibino, T., and Takabe, T. (2001). Photo-induction of an NADPH dehydrogenase which functions as a mediator of electron transport to the intersystem chain in the cyanobacterium Synechocystis PCC6803. *Photosyn. Res.* 70, 167–173. doi: 10.1023/A:1017946524199

Mi, H. L., Endo, T., Ogawa, T., and Asada, K. (1995). Thylakoid membrane-bound, nadph-specific pyridine-nucleotide dehydrogenase complex mediates cyclic electron-transport in the cyanobacterium synechocystis SP PCC-68038. *Plant Cell Physiol.* 36, 661–668.

Mi, H. L., Endo, T., Schreiber, U., Ogawa, T., and Asada, K. (1992). Electron donation from cyclic and respiratory flows to the photosynthetic intersystem chain is mediated by pyridine-nucleotide dehydrogenase in the cyanobacterium synechocystis PCC-6803. *Plant Cell Physiol.* 33, 1233–1237.

Munekaga, Y., Hashimoto, M., Miyaka, C., Tomizawa, K. I., Endo, T., Tasaka, M., et al. (2004). Cyclic electron flow around photosystem I is essential for photosynthesis. *Nature* 429, 579–582. doi: 10.1038/nature02598

Nowaczyk, M. M., Wulfhorst, H., Ryan, C. M., Souda, P., Zhang, H., Cramer, W. A., et al. (2011). NdhP and NdhQ: two novel small subunits of the cyanobacterial NDH-1 complex. *Biochemistry* 50, 1121–1124. doi: 10.1021/bi102044b

Ogawa, T. (1991a). A gene homologous to the subunit-2 gene of nadh dehydrogenase is essential to inorganic carbon transport of synechocystis PCC6803. *Proc. Natl. Acad. Sci. U.S.A.* 88, 4275–4279. doi: 10.1073/pnas.88.10.4275

Ogawa, T. (1991b). Cloning and inactivation of a gene essential to inorganic carbon transport of synechocystis PCC6803. *Plant Physiol.* 96, 280–284. doi: 10.1104/pp.96.1.280

Ogawa, T., and Kaplan, A. (2003). Inorganic carbon acquisition systems in cyanobacteria. *Photosyn. Res.* 77, 105–115. doi: 10.1023/A:1025865500026

Ogawa, T., and Mi, H. (2007). Cyanobacterial NADPH dehydrogenase complexes. *Photosyn. Res.* 93, 69–77. doi: 10.1007/s11120-006-9128-y

Ohkawa, H., Price, G. D., Badger, M. R., and Ogawa, T. (2000). Mutation of ndh genes leads to inhibition of CO2 uptake rather than HCO3- uptake in Synechocystis sp strain PCC 6803. *J. Bacteriol.* 182, 2591–2596. doi: 10.1128/JB.182.9.2591-2596.2000

Otani, T., Kato, Y., and Shikanai, T. (2018). Specific substitutions of light-harvesting complex I proteins associated with photosystem I are required for supercomplex formation with chloroplast NADH dehydrogenase-like complex. *Plant J.* 94, 122–130. doi: 10.1111/tpj.13846

Pan, X., Cao, D., Xie, F., Xu, F., Su, X., Mi, H., et al. (2020). Structural basis for electron transport mechanism of complex I-like photosynthetic NAD(P)H dehydrogenase. *Nat. Commun.* 11:14456. doi: 10.1038/s41467-020-14456-0

Price, G. D. (2011). Inorganic carbon transporters of the cyanobacterial CO2 concentrating mechanism. *Photosyn. Res.* 109, 47–57. doi: 10.1007/s11120-010-9608-y

Price, G. D., Sultemeyer, D., Klughammer, B., Ludwig, M., and Badger, M. R. (1998). The functioning of the CO2 concentrating mechanism in several cyanobacterial strains: a review of general physiological characteristics, genes, proteins, recent advances. *Canad. J. Botany-Revue Canadienne De Botanique* 76, 973–1002. doi: 10.1139/cjb-76-6-973

Prommeenate, P., Lennon, A. M., Markert, C., Hippler, M., and Nixon, P. J. (2004). Subunit composition of NDH-1 complexes of Synechocystis sp PCC 6803 - Identification of two new ndh gene products with nuclear-encoded homologues in the chloroplast Ndh complex. *J. Biol. Chem.* 279, 28165–28173. doi: 10.1074/jbc.M401107200

Raven, J. A. (2003). Inorganic carbon concentrating mechanisms in relation to the biology of algae. *Photosyn. Res.* 77, 155–171. doi: 10.1023/A:1025877902752

Rumeau, D., Becuwe-Linka, N., Beyly, A., Louwagie, M., Garin, J., and Peltier, G. (2005). New subunits NDH-M, -N, and -O, encoded by nuclear genes, are essential for plastid Ndh complex functioning in higher plants. *Plant Cell* 17, 219–232. doi: 10.1105/tpc.104.028282

Schreiber, U. E. T., Mi, H. L., and Asada, K. (1995). Quenching analysis of chlorophyll fluorescence by the saturation pulse method: prticular aspects relating to the study of eukayotic algae and cyanobacteria. *Plant Cell Physiol.* 36, 873–882. doi: 10.1093/oxfordjournals.pcp.a078833

Schuller, J. M., Birrell, J. A., Tanaka, H., Konuma, T., Wulflhorst, H., Cox, N., et al. (2019). Structural adaptations of photosynthetic complex I enable ferredoxin-dependent electron transfer. *Science* 363:257. doi: 10.1126/science.aau3613

Schuller, J. M., Saura, P., Thiemann, J., Schuller, S. K., Gamiz-Hernandez, A. P., Kurisu, G., et al. (2020). Redox-coupled proton pumping drives carbon concentration in the photosynthetic complex I. *Nat. Commun.* 11:494. doi: 10.1038/s41467-020-14347-4

Shen, L., Tang, K., Wang, W., Wang, C., Wu, H., Mao, Z., et al. (2022). Architecture of the chloroplast PSI–NDH supercomplex in Hordeum vulgare. *Nature* 601, 649–654. doi: 10.1038/s41586-021-04277-6

Shibata, M., Ohkawa, H., Katoh, H., Shimoyama, M., and Ogawa, T. (2002). Two CO2 uptake systems in cyanobacteria: four systems for inorganic carbon acquisition in Synechocystis sp strain PCC6803. *Funct. Plant Biol.* 29, 123–129. doi: 10.1071/PP01188

Shikanai, T. (2007). Regulation of photosynthesis via PSI cyclic electron transport. *Photosyn. Res.* 91:PS141. doi: 10.1007/978-1-4020-6709-9_214

Shikanai, T. (2014). Central role of cyclic electron transport around photosystem I in the regulation of photosynthesis. *Curr. Opin. Biotechnol.* 26, 25–30. doi: 10.1016/j.copbio.2013.08.012

Shimizu, H., Peng, L., Myouga, F., Motohashi, R., Shinozaki, K., and Shikanai, T. (2008). CRR23/NdhL is a subunit of the chloroplast NAD(P)H dehydrogenase complex in Arabidopsis. *Plant Cell Physiol.* 49, 835–842. doi: 10.1093/pcp/pcn058

Su, X., Cao, D., Pan, X., Shi, L., Liu, Z., Dall'OSto, L., et al. (2022). NADH dehydrogenase-like complex with photosystem I from Arabidopsis thaliana. *Mol. Plant* 15, 454–467. doi: 10.1016/j.molp.2022.01.020

Sun, N., Han, X., Xu, M., Kaplan, A., Espie, G. S., and Mi, H. (2019). A thylakoid-located carbonic anhydrase regulates CO2 uptake in the cyanobacterium Synechocystis sp. PCC 6803. *New Phytol.* 222, 206–217. doi: 10.1111/nph.15575

Tanaka, Y. K. S., Ishikawa, H., Ogawa, T., and Takabe, T. (1997). Electron flow from NADPH dehydrogenase to photosystem I is required for adaptation to shalt shock in the cyanobacterium *Synechocystis* sp. PCC 6803. *Plant Cell Physiol.* 38, 1311–1318. doi: 10.1093/oxfordjournals.pcp.a029123

Ueda, M., Kuniyoshi, T., Yamamoto, H., Sugimoto, K., Ishizaki, K., Kohchi, T., et al. (2012). Composition and physiological function of the chloroplast NADH dehydrogenase-like complex in Marchantia polymorpha. *Plant J.* 72, 683–693. doi: 10.1111/j.1365-313X.2012.05115.x

Wang, H. W., Mi, H. L., Ye, J. Y., Deng, Y., and Shen, Y. K. (2003). Low concentrations of NaHSO3 increase cyclic photophosphorylation and photosynthesis in cyanobacterium Synechocystis PCC6803. *Photosyn. Res.* 75, 151–159. doi: 10.1023/A:1022813402265

Wang, P., Duan, W., Takabayashi, A., Endo, T., Shikanai, T., Ye, J. Y., et al. (2006). Chloroplastic NAD(P)H dehydrogenase in tobacco leaves functions in alleviation of oxidative damage caused by temperature stress. *Plant Physiol.* 141, 465–474. doi: 10.1104/pp.105.070490

Wu, Y., He, W., Ma, W., Shen, Y., and Mi, H. (2012). Low concentrations of NaHSO3 enhance NAD(P)H dehydrogenase-dependent cyclic photophosphorylation and alleviate the oxidative damage to improve photosynthesis in tobacco. *Chin. Sci. Bull.* 57, 3872–3877. doi: 10.1007/s11434-012-5309-6

Wu, Y., Zheng, F., Ma, W., Han, Z., Gu, Q., Shen, Y., et al. (2011). Regulation of NAD(P)H dehydrogenase-dependent cyclic electron transport around PSI by NaHSO(3) at low concentrations in tobacco chloroplasts. *Plant Cell Physiol.* 52, 1734–1743. doi: 10.1093/pcp/pcr109

Xu, M., Ogawa, T., Pakrasi, H. B., and Mi, H. (2008). Identification and localization of the CupB protein involved in constitutive CO(2) uptake in the cyanobacterium, Synechocystis sp strain PCC 6803. *Plant Cell Physiol.* 49, 994–997. doi: 10.1093/pcp/pcn074

Yamamoto, H., Peng, L., Fukao, Y., and Shikanai, T. (2011). An Src homology 3 domain-like fold protein forms a ferredoxin binding site for the chloroplast NADH dehydrogenase-like complex in arabidopsis. *Plant Cell* 23, 1480–1493. doi: 10.1105/tpc.110.080291

Yamamoto, H., and Shikanai, T. (2013). In planta mutagenesis of Src homology 3 domain-like fold of NdhS, a ferredoxin-binding subunit of the chloroplast NADH dehydrogenase-like complex in arabidopsis A conserved ARG-193 plays a critical role in ferredoxin binding. *J. Biol. Chem.* 288, 36328–36337. doi: 10.1074/jbc.M113.511584

Zhang, C., Shuai, J., Ran, Z., Zhao, J., Wu, Z., Liao, R., et al. (2020). Structural insights into NDH-1 mediated cyclic electron transfer. *Nat. Commun.* 11:14732. doi: 10.1038/s41467-020-14732-z

Zhang, P. P., Battchikova, N., Jansen, T., Appel, J., Ogawa, T., and Aro, E. M. (2004). Expression and functional roles of the two distinct NDH-1 complexes and the carbon acquisition complex NdhD3/NdhF3/CupA/Sll1735 in Synechocystis sp PCC 6803. *Plant Cell* 16, 3326–3340. doi: 10.1105/tpc.104.026526

Zhang, P. P., Battchikova, N., Paakkarinen, V., Katoh, H., Iwai, M., Ikeuchi, M., et al. (2005). Isolation, subunit composition and interaction of the NDH-1 complexes from Thermosynechococcus elongatus BP-1. *Biochem. J.* 390, 513–520. doi: 10.1042/BJ20050390

Conflict of Interest: The author declares that the research was conducted in the absence of any commercial or financial relationships that could be construed as a potential conflict of interest.

frontiers | Frontiers in Microbiology

ORIGINAL RESEARCH
published: 13 July 2022
doi: 10.3389/fmicb.2022.956578

Genome-Wide Insights Into the Organelle Translocation of Photosynthetic NDH-1 Genes During Evolution

Jie Yu, Zhaoxing Ran, Jingsong Zhang, Lanzhen Wei and Weimin Ma**

College of Life Sciences, Shanghai Normal University, Shanghai, China

Translocation of chloroplast-located genes to mitochondria or nucleus is considered to be a safety strategy that impedes mutation of photosynthetic genes and maintains their household function during evolution. The organelle translocation strategy is also developed in photosynthetic NDH-1 (pNDH-1) genes but its understanding is still far from complete. Here, we found that the mutation rate of the conserved pNDH-1 genes was gradually reduced but their selection pressure was maintained at a high level during evolution from cyanobacteria to angiosperm. By contrast, oxygenic photosynthesis-specific (OPS) pNDH-1 genes had an opposite trend, explaining the reason why they were transferred from the reactive oxygen species (ROS)-enriched chloroplast to the ROS-barren nucleus. Further, genome-wide sequence analysis supported the possibility that all conserved pNDH-1 genes lost in chloroplast genomes of Chlorophyceae and Pinaceae were transferred to the ROS-less mitochondrial genome as deduced from their truncated pNDH-1 gene fragments. Collectively, we propose that the organelle translocation strategy of pNDH-1 genes during evolution is necessary to maintain the function of the pNDH-1 complex as an important antioxidant mechanism for efficient photosynthesis.

Keywords: organelle translocation, photosynthetic NDH-1, mitochondrial NDH-1, evolutionary events, plant evolution

OPEN ACCESS

Edited by:
Hui Wu,
East China University of Science and Technology, China

Reviewed by:
Guangye Han,
Institute of Botany (CAS), China
Hualing Mi,
Center for Excellence in Molecular Plant Sciences (CAS), China

****Correspondence:***
Lanzhen Wei
weilz@shnu.edu.cn
Weimin Ma
wma@shnu.edu.cn

Specialty section:
This article was submitted to Microbial Physiology and Metabolism, a section of the journal Frontiers in Microbiology

Received: *30 May 2022*
Accepted: *20 June 2022*
Published: *13 July 2022*

Citation:
Yu J, Ran Z, Zhang J, Wei L and Ma W (2022) Genome-Wide Insights Into the Organelle Translocation of Photosynthetic NDH-1 Genes During Evolution. Front. Microbiol. 13:956578. doi: 10.3389/fmicb.2022.956578

INTRODUCTION

During evolution of photosynthetic organisms, the rise of O_2 and environmental stress inevitably results in the production of reactive oxygen species (ROS), which can trigger the mutation of genes under the low selection pressure (Ishikawa et al., 2008; Otten and Smeets, 2015). It is well known that in eukaryotic photosynthetic organisms, genes are located in the genomes of chloroplast, mitochondria, and nucleus. Considering the O_2 content, the ROS concentrations of chloroplast, mitochondria, and nucleus under environmental stresses are assumed to be relatively abundant, less, and barren, respectively (Allen and Raven, 1996; Martin and Herrmann, 1998; Adams and Palmer, 2003; Foyer and Noctor, 2003; Laloi et al., 2004; Zhao et al., 2020). As a consequence,

Abbreviations: d_N, non-synonymous substitution rate; d_S, synonymous substitution rate; K_c, amino acid conservative substitution; OPS, oxygenic photosynthesis-specific; pNDH-1, photosynthetic NDH-1; rNDH-1, respiratory NDH-1; ROS, reactive oxygen species.

the organelle translocation is considered to be an important safety strategy that impedes mutation of photosynthetic genes and maintains their household function during evolution.

Complete sequencing of the chloroplast genomes of *Marchantia polymorpha* and *Nicotiana tabacum* unexpectedly demonstrates the presence of photosynthetic NDH-1 (pNDH-1) (hereafter referred to as pNDH-1) genes (Ohyama et al., 1986; Shinozaki et al., 1986). All complexes of pNDH-1 are involved in cyclic electron transfer around photosystem I (Bernát et al., 2011), which is an important antioxidant mechanism that balances the ATP/NADPH ratio required for the Calvin–Benson cycle and reduces the ROS production (Arnon, 1971; Kramer and Evans, 2011). They consist of conserved subunits (NdhA to NdhK) and oxygenic photosynthesis-specific (OPS) subunits (such as NdhL to NdhQ, NdhS, and NdhV) (Laughlin et al., 2019; Schuller et al., 2019, 2020; Pan et al., 2020; Zhang et al., 2020; Shen et al., 2022). It is found that these conserved genes of pNDH-1 reside in chloroplast genome (Ohyama et al., 1986; Shinozaki et al., 1986) but its OPS genes are translocated to the nucleus genome (Rumeau et al., 2005; Ishikawa et al., 2008; Shimizu et al., 2008; Suorsa et al., 2009; Yamamoto et al., 2011; Fan et al., 2015). However, little is known regarding the reason why these OPS pNDH-1 genes are translocated to the nucleus genome. In addition, genome-wide sequence analysis of pNDH-1 genes in Chlorophyceae and Pinaceae indicates that OPS pNDH-1 genes reside also in the nucleus genome, but all conserved pNDH-1 genes are lost entirely in the chloroplast and nucleus genomes (Wakasugi et al., 1994; Maul et al., 2002; Nystedt et al., 2013; Neale et al., 2014; Ranade et al., 2016; Lin et al., 2017). However, as yet, whether all these conserved pNDH-1 genes have been lost entirely or transferred to the mitochondrial genome remains a mystery.

Here, we calculated and analyzed the mutation frequency and selection pressure, explaining the reason why these OPS pNDH-1 genes were transferred from chloroplast to the nucleus. Further, we found the presence of conserved pNDH-1 gene fragments in mitochondrial genomes of Chlorophyceae and Pinaceae, implying that these conserved pNDH-1 genes lost in chloroplast genomes of Chlorophyceae and Pinaceae were transferred to their mitochondrial genomes. Collectively, our data provide new insights into the organelle translocation of pNDH-1 genes during evolution from cyanobacteria to angiosperm.

MATERIALS AND METHODS

Phylogenetic Analysis

Phylogenetic tree was constructed based on *rbcL* gene of Methanogen, Cyanobacteria, Chlorophyceae, Bryophyta, Pinaceae, Monocots, and Dicots. The gene sequences of *rbcL* from different species were obtained from the National Center for Biotechnology Information (NCBI[1]). The names of the selected species and their GenBank accession numbers are listed in **Supplementary Table 1**. Sequence alignments were performed using MUSCLE (Edgar, 2004). The aligned dataset was analyzed in Data Analysis in Molecular Biology and Evolution (DAMBE) version 7 (Xia, 2018), and was converted into MEGA format. Unrooted phylogenetic trees were created using MEGA version 7 (Kumar et al., 2016) and maximum likelihood method (Felsenstein, 1981) with the bootstrap support of 1,000 replicates. Creating the phylogenetic tree, the parameters used were: complete deletion of gaps/missing data, distance model set to applying the nucleotide kimura-2-parameter, homogeneous pattern among lineages and uniform rates among sites and using the maximum composite likelihood model. The FigTree (v1.3.1[2]) was used for the unrooted phylogenetic tree visualization.

Calculation of Synonymous Substitution Rate and Non-synonymous Substitution Rate

The values of synonymous substitution rate (d_S) and non-synonymous substitution rate (d_N) were calculated using DNAsp6 software (Rozas et al., 2017). We first removed the terminators of each sequence and then used MUSCLE for sequence alignment, and the alignments of all these genes of pNDH-1 and rNDH-1 were converted into a codon alignment using TranslatorX (Abascal et al., 2010). The ambiguously aligned regions were excluded using trimAl v1.2 (Capella-Gutiérrez et al., 2009) and the results were exported as a Fasta file. Having opened the exported file with DNAsp6, we set the genomic state and chromosomal location, assigned the coding regions, and calculated the d_S and d_N values. The average values were calculated using SigmaPlot 14.0.

Calculation of Amino Acid Conservative Substitution

Calculation of amino acid conservative substitution (K_c) was carried out with the aid of a pipeline SAMEM v.0.83.[3] The SAMEM package (Gunbin et al., 2011) has a major path for the gene evolution analysis. We divided these 20 amino acids into two groups according to their physicochemical properties, such as volume (RQEHILKMFWYV ANDCGPST), which are related to protein function. Amino acid substitutions within groups are called conservative substitutions (Hanada et al., 2007). The general step and method of calculating K_c are as follows: translation of nucleic acid sequence into amino acid sequence by Transeq, multiple alignment of amino acid sequences by the Mafft 6.717 algorithm (Katoh and Toh, 2008) using the BLOSUM 62 matrix (Henikoff and Henikoff, 1992), and models of amino acid substitutions were calculated based on multiple alignment using the Modelestimator algorithm (Arvestad, 2006), phylogenetic trees were calculated on the basis of the replacement model using FastTree 2.1.1 (Price et al., 2010), ancestral gene sequences are reconstructed based on gapless alignments of codons using FASTML (Pupko et al., 2002), calculation of K_c using Zhang's (2000) method (the HON-NEW program). For each of 531 properties (Kawashima et al., 2008), amino acids are divided into classes by k-means clustering using R.

[1] http://www.ncbi.nlm.nih.gov/

[2] http://tree.bio.ed.ac.uk/software/figtree

[3] http://pixie.bionet.nsc.ru/samem/

Sequence Analysis

Homology search was performed by comparing amino acid sequences with sequences in local nucleotide databases (TBLASTN). Eleven *Arabidopsis thaliana* pNDH-1 gene sequences were used as templates for TBLASTN searches of Chlorophyceae and Pinaceae mitochondrial genomes. The TBLASTN expectation value threshold E was altered to 10 to allow for a less stringent alignment search.

Data Availability

The data underlying this article are available within the NCBI GenBank database,[4] and all GenBank accession numbers are listed in **Supplementary Table 1**. The alignments analyzed in this study are available in the article's online **Supplementary Figures 2–4**.

RESULTS

Phylogenetic Tree Marks These Important Evolutionary Events of Photosynthetic NDH-1

Genome-wide sequence analysis suggests that pNDH-1 originates from a group 4 membrane-bound [NiFe] hydrogenase (Böhm et al., 1990; Peltier et al., 2016) and evolves from archaea (gray tree branches in **Figure 1**) to prokaryote (blue tree branches in **Figure 1**) and to eukaryotic photosynthetic organisms (green tree branches in **Figure 1**). In eukaryotic photosynthetic organisms except Chlorophyceae, Pinaceae and Orchidaceae, conserved pNDH-1 genes reside in chloroplast genome, whereas OPS pNDH-1 genes are transferred to the nucleus genome (Rumeau et al., 2005; Ishikawa et al., 2008; Shimizu et al., 2008; Suorsa et al., 2009; Yamamoto et al., 2011; Fan et al., 2015). In addition, in eukaryotic Chlorophyceae and Pinaceae (red species name in **Figure 1**), OPS pNDH-1 genes reside also in the nucleus genome, but all conserved pNDH-1 genes are lost entirely in their chloroplast and nucleus genomes (Wakasugi et al., 1994; Maul et al., 2002; Lin et al., 2017). The below investigations will try to explain the reason why these OPS pNDH-1 genes in eukaryotic photosynthetic organisms except Chlorophyceae, Pinaceae, and Orchidaceae were transferred from chloroplast genome to the nucleus genome and unravel the mystery whether conserved pNDH-1 genes of Chlorophyceae and Pinaceae have been lost entirely or transferred to the mitochondrial genome.

An Evolutionary Trend of Conserved and Oxygenic Photosynthesis-Specific Photosynthetic NDH-1 Genes

During the evolution process from cyanobacteria to dicots, we found that the mutation rate of conserved pNDH-1 genes was gradually decreased, as deduced from the results of d_S (**Figures 2A–F**). This was supported by the data of K_c (**Supplementary Figure 1**). As a consequence, the mutation rate of conserved pNDH-1 genes has a trend of gradual decrease during evolution.

To fully understand the trend of conserved pNDH-1 genes during evolution, we calculated the ratio of d_N to d_S. Our data indicated that all d_N/d_S ratios of conserved pNDH-1 genes were less than 1 (**Figures 3A–F**), indicating that the evolutional rate of all these conserved pNDH-1 genes was relatively slow and under the purifying selection (Endo et al., 1997; Messier and Stewart, 1997). Further, under the purifying selection, the magnitude of d_N/d_S values could reflect the selection pressure of these conserved pNDH-1 genes (Berg and Kurland, 2000). If the d_N/d_S ratio was more close to 0, the selection pressure was higher, whereas if the ratio was more close to 1, the selection pressure was lower. We found that the selection pressure of conserved pNDH-1 genes was increased during evolution from cyanobacteria to dicots, as deduced from the results of d_N/d_S values (**Figures 3A–F**). Collectively, we propose that conserved pNDH-1 genes have an evolutionary trend that the mutation rate was gradually decreased but the selection pressure was maintained at a relatively high level.

Unexpectedly, the mutation rate of OPS pNDH-1 genes was increased and kept at a high level during evolution from cyanobacteria to dicots, as deduced from the d_S values (**Figures 2A–F**). Meanwhile, the selection pressure of OPS pNDH-1 genes was deceased during evolution from cyanobacteria to dicots, as deduced from the data of d_N/d_S values (**Figures 3A–F**). Taking all these results together, we can clearly find that OPS and conserved pNDH-1 genes have a distinctly different trend of their mutation rate and selection pressure during evolution.

Presence of Photosynthetic NDH-1 Gene Fragments in the Mitochondrial Genomes of Chlorophyceae and Pinaceae

To unravel the mystery whether these conserved pNDH-1 genes have been lost entirely or transferred to the mitochondrial genome, we conducted the sequence searches in the mitochondrial genomes of Chlorophyceae and Pinaceae using pNDH-1 sequences of *Arabidopsis thaliana* as templates. Our results revealed that the fragments of conserved pNDH-1 genes lost in the chloroplast genomes of Chlorophyceae and Pinaceae were found to be in their mitochondrial genomes (**Figure 4** and **Supplementary Figures 2–4**). Collectively, we propose that these conserved pNDH-1 genes lost in the chloroplast genomes of Chlorophyceae and Pinaceae were transferred to their mitochondrial genomes.

A Trend of Respiratory NDH-1 Genes During Evolution

Consistent with the conserved pNDH-1 genes, the mutation rate of respiratory NDH-1 (rNDH-1) genes was gradually decreased but their selection pressure was maintained at a relatively high level during evolution from methanogen to dicots (pink in **Figures 5A,B**). However, the mutation rate and selection pressure of rNDH-1 genes in Chlorophyceae and Pinaceae

[4]https://www.ncbi.nlm.nih.gov/genbank

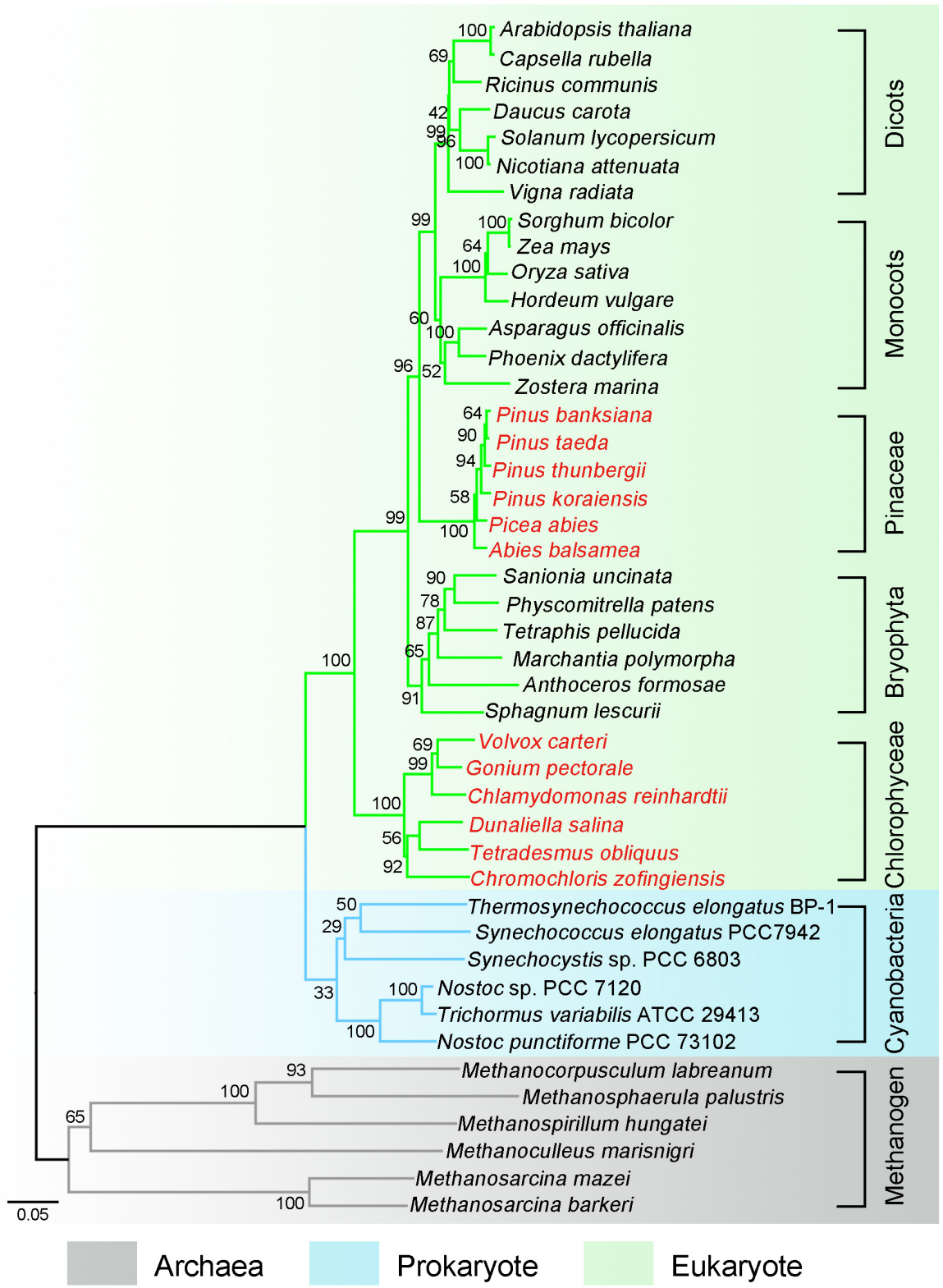

FIGURE 1 | Phylogenetic tree marks these important events of photosynthetic NDH-1 (pNDH-1) during evolution from archaea to eukaryote. Phylogenetic tree was constructed based on marker gene *rbcL*. The pNDH-1 originates from a group 4 membrane-bound [NiFe] hydrogenase and evolves from archaea (gray tree branches) to prokaryote (blue tree branches) and to eukaryotic photosynthetic organisms (green tree branches). In chloroplast, the species with pNDH-1 are represented by black letters, and the species without pNDH-1 are represented by red letters.

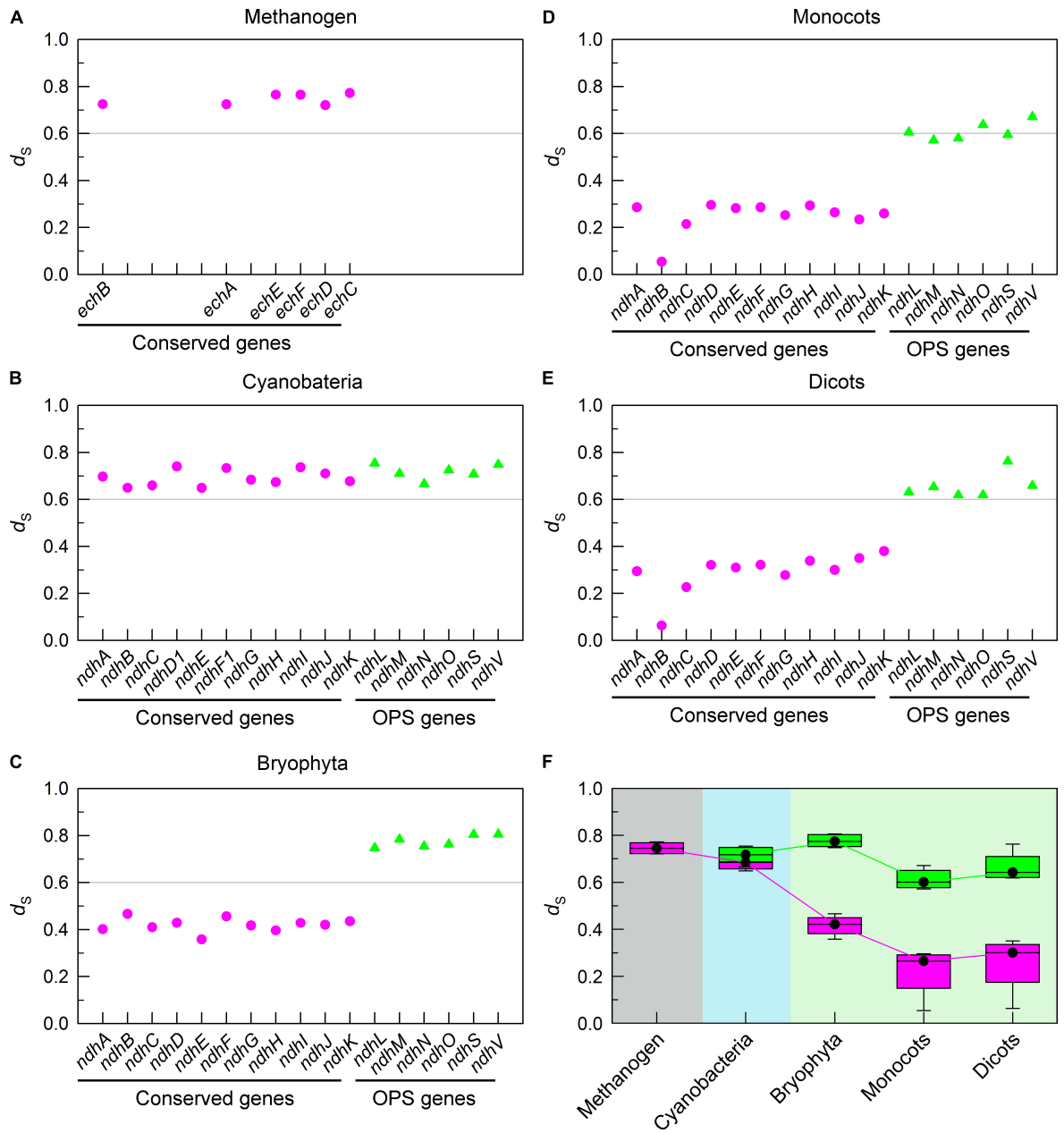

FIGURE 2 | The trend of mutation rate of pNDH-1 genes during evolution from cyanobacteria to dicots. The mutation rate is deduced from the values of synonymous substitution rate (d_S). The Scatter plot shows the respective d_S values of conserved genes and oxygenic photosynthesis-specific (OPS) genes of pNDH-1 in methanogen **(A)**, cyanobacteria **(B)**, bryophyta **(C)**, monocots **(D)**, and dicots **(E)**. The pink dots represent conserved genes and the green triangles represent OPS genes. Box plot shows the average d_S values of conserved genes and OPS genes of pNDH-1 in methanogen, cyanobacteria, bryophyta, monocots, and dicots **(F)**. The box represents the values between the quartiles and the black lines inside the box represent the median value.

did not follow the trend of rNDH-1 during evolution from methanogen to dicots (red in **Figures 5A,B**). It is reasonable to infer that the transfer of chloroplast pNDH-1 genes of Chlorophyceae and Pinaceae to their mitochondrial genomes results in mitochondrial DNA rearrangement, thereby increasing the mutation rate of rNDH-1 genes and relatively decreasing their selection pressure. This supports the conclusion that these conserved pNDH-1 genes lost in chloroplast genomes of Chlorophyceae and Pinaceae were transferred to their mitochondrial genomes.

DISCUSSION

During the evolution from prokaryotic cyanobacteria to eukaryotic angiosperm, organelle translocation is considered

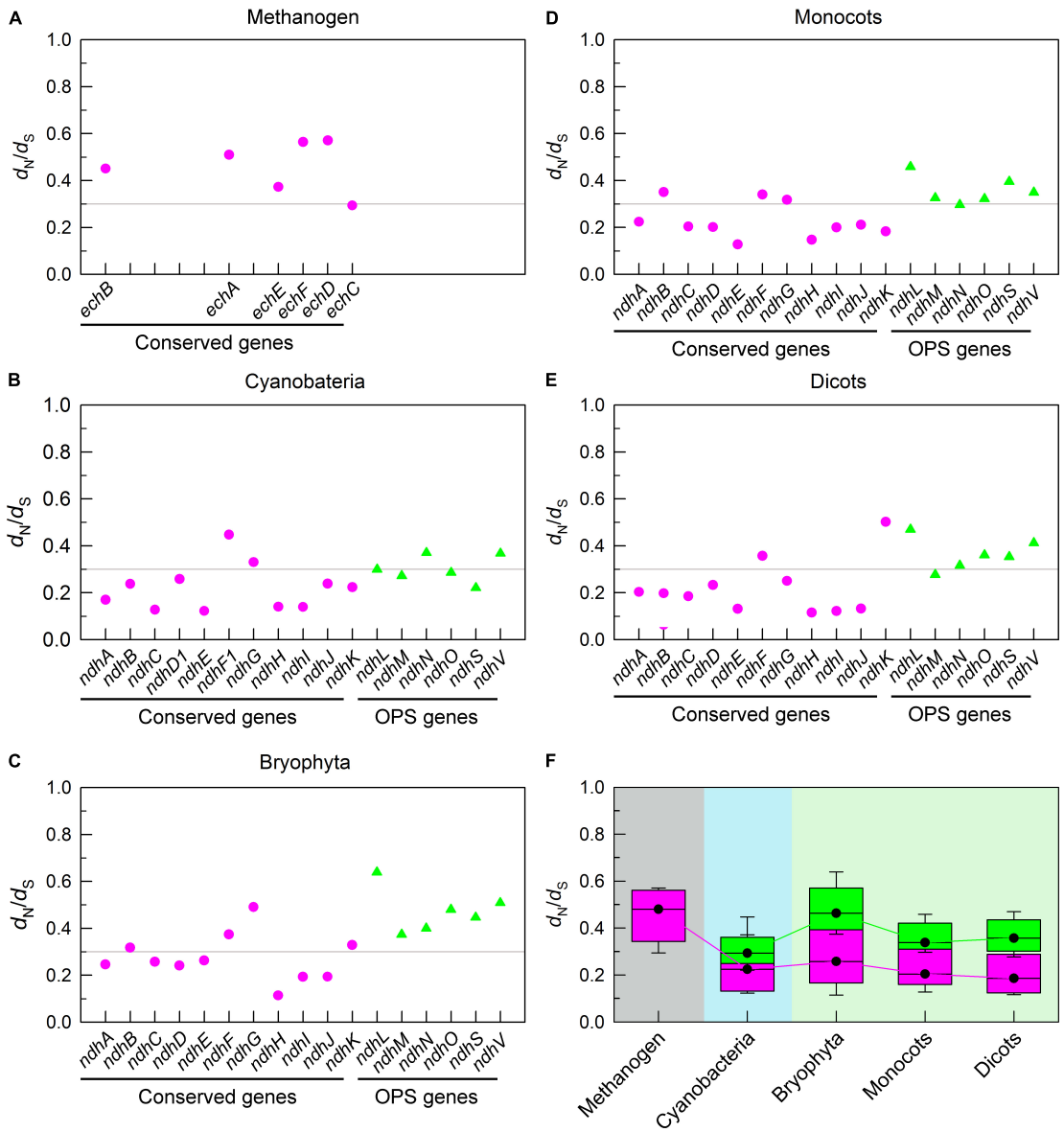

FIGURE 3 | The trend of selection pressure of pNDH-1 genes during evolution from cyanobacteria to dicots. The selection pressure is deduced from the values of non-synonymous substitution rate (d_N)/d_S. Scatter plot shows the respective d_N/d_S values of conserved genes and OPS genes of pNDH-1 in methanogen **(A)**, cyanobacteria **(B)**, bryophyta **(C)**, monocots **(D)**, and dicots **(E)**. The pink dots represent conserved genes and the green triangles represent OPS genes. Box plot shows the average d_N/d_S values of conserved genes and OPS genes of pNDH-1 in methanogen, cyanobacteria, bryophyta, monocots, and dicots **(F)**. The box represents the values between the quartiles and the black lines inside the box represent the median value.

to be an important safety strategy that impedes mutation of photosynthetic genes and maintain their household function (Baldauf and Palmer, 1990; Gantt et al., 1991; Martin et al., 1998; Adams and Palmer, 2003; Rokka et al., 2005). Such organelle translocation is also found to be a universal safety strategy, for example, the mitochondrial genome contains between 1 and 10% of chloroplast sequences in different seed plants (Stern and Lonsdale, 1982; Joyce and Gray, 1989; Wang et al., 2007, 2012). In eukaryotic photosynthetic organisms except Chlorophyceae, Pinaceae, and Orchidaceae, OPS pNDH-1 genes are found to transfer from chloroplast genome to the nucleus genome during evolution (Rumeau et al., 2005; Ishikawa et al., 2008; Shimizu et al., 2008; Suorsa et al., 2009; Yamamoto et al., 2011; Fan et al., 2015), although conserved pNDH-1 genes still reside in chloroplast genome (Ohyama et al., 1986; Shinozaki et al., 1986).

The results of this study found that two distinctly different strategies have been developed by conserved and OPS pNDH-1 genes to impede their mutations and maintain their functions (**Figures 2**, **3** and **Supplementary Figure 1**). Conserved pNDH-1 genes develop a safety strategy *via* decreasing their mutation

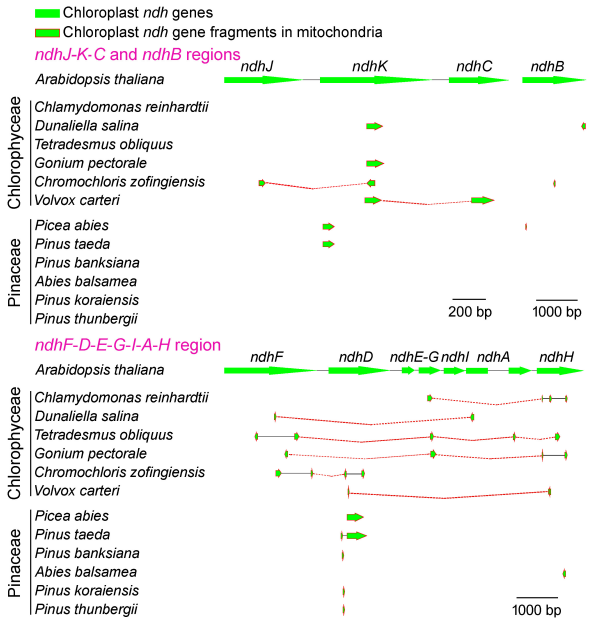

FIGURE 4 | Comparison of Chlorophyceae and Pinaceae mitochondrial genomes with *Arabidopsis thaliana* chloroplast pNDH-1 genes. The arrows indicate coding regions. The arrowheads indicate the direction of the genes.

rate and increasing their selection pressure, while OPS pNDH-1 genes develop another safety strategy *via* transferring them from the chloroplast genome to a relatively safe nucleus genome (**Figures 2**, **3** and **Supplementary Figure 1**). It is worthy of note that according to Mahler's ratchet effect (Muller, 1964), gene recombination is lacked in chloroplast because of no sexual reproduction. When a gene is successfully transferred from chloroplast to nuclear, in other words, from asexual to sexual, gene recombination is restored and provides a chance to get rid of the fate crisis of gene mutation, reinforcing the conclusion that the nucleus is much safer than the chloroplast. Collectively, during evolution of photosynthetic organisms, these two distinctly different strategies jointly maintain the function of pNDH-1 as an important antioxidant mechanism for efficient photosynthesis through impeding mutation of its conserved and OPS genes.

Consistent with the previously reported Orchidaceae (Lin et al., 2015, 2017), these conserved pNDH-1 genes lost in Chlorophyceae and Pinaceae were transferred from chloroplast genome to the mitochondrial genome as deduced from their common gene fragments (**Figure 4** and **Supplementary Figures 2–4**) and the abnormal mutation rate and selection pressure of rNDH-1 genes (**Figure 5**). It has been reported that Chlorophyceae green algae frequently meet with various environmental challenges, such as fluctuations in nutrient, light availability, and temperature, in their natural habitat (Varshney et al., 2015). Consistent with this situation, the chloroplast DNA and mitochondrial DNA of Chlorophyceae underwent substantial changes in their architecture (such as gene losses and genome expansion in the case of mitochondrial DNA) during evolution (Turmel et al., 2002; Wodniok et al., 2011). Under this background, it is reasonable to infer that these conserved pNDH-1 genes of Chlorophyceae are lost in chloroplast and are transferred to the mitochondrial genome.

Compared with the land plants, Bryophyta and Pteridophyte, the trees in Pinaceae grow quite high (Graham et al., 1995), implying that they have an efficient photosynthesis and produce more O_2. Consistent with the hypothesis, Pinaceae underwent an O_2-rise phase (Savard et al., 1994; Berner, 2006) and may produce abundant ROS in chloroplast but less ROS in mitochondria under environmental stresses (Foyer and Noctor, 2003; Laloi et al., 2004; Zhao et al., 2020). As a consequence, it appears plausible that pNDH-1 genes lost in Pinaceae are transferred from O_2-enriched chloroplast to the O_2-less mitochondria as oxygen-consuming organelle.

Based on the aforementioned analysis, we propose that translocation of pNDH-1 genes from chloroplast genome to the nucleus genome or mitochondrial genome is important

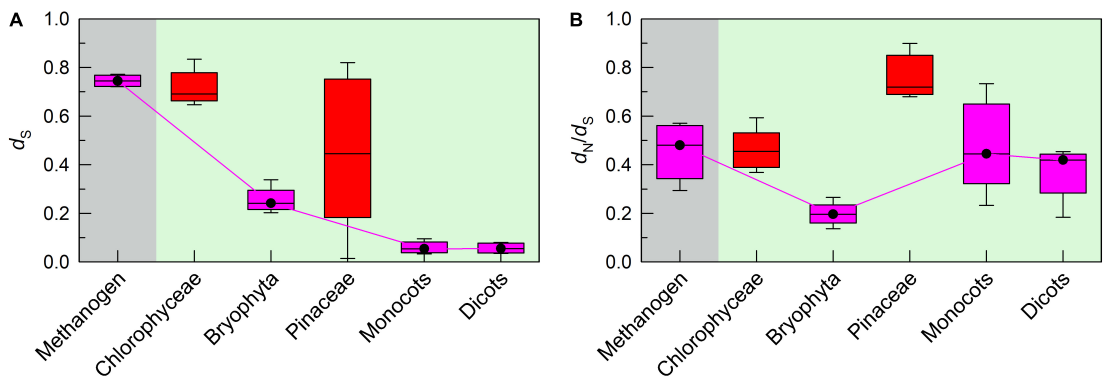

FIGURE 5 | The trends of mutation rate and selection pressure of rNDH-1 genes during evolution from chlorophyceae to dicots. The mutation rate and selection pressure are deduced from the values of d_S and d_N/d_S, respectively. Boxplots show the average d_S **(A)** and d_N/d_S **(B)** values of rNDH-1 in methanogen, Chlorophyceae, bryophyta, Pinaceae, monocots, and dicots. The box represents the values between the quartiles and the black lines inside the box represent the median value.

to maintain the architecture and household function of pNDH-1 during evolution. As a consequence, the function of pNDH-1 as an important antioxidant mechanism can reduce ROS production necessary for the survival of eukaryotic photosynthetic organisms in aerobic environment.

DATA AVAILABILITY STATEMENT

The raw data supporting the conclusions of this article will be made available by the authors, without undue reservation.

AUTHOR CONTRIBUTIONS

WM conceived and designed the project. JY and JZ performed the bioinformatics analysis. JY, ZR, LW, and WM interpreted the data and wrote the manuscript. All authors read and approved the final manuscript.

FUNDING

This work was supported by the National Natural Science Foundation of China (grant nos. 32170257, 32070381, and 31770259), and Shanghai Science and Technology Committee (grant nos. 22010503500 and 20ZR1441300).

SUPPLEMENTARY MATERIAL

The Supplementary Material for this article can be found online at: https://www.frontiersin.org/articles/10.3389/fmicb.2022.956578/full#supplementary-material

REFERENCES

Abascal, F., Zardoya, R., and Telford, M. J. (2010). TranslatorX: multiple alignment of nucleotide sequences guided by amino acid translations. *Nucleic Acids Res.* 38, W7–W13. doi: 10.1093/nar/gkq291

Adams, K. L., and Palmer, J. D. (2003). Evolution of mitochondrial gene content: gene loss and transfer to the nucleus. *Mol. Phylogenet. Evol.* 29, 380–395. doi: 10.1016/s1055-7903(03)00194-5

Allen, J. F., and Raven, J. A. (1996). Free-radical-induced mutation vs redox regulation: costs and benefits of genes in organelles. *J. Mol. Evol.* 42, 482–492. doi: 10.1007/BF02352278

Arnon, D. I. (1971). The light reactions of photosynthesis. *Proc. Natl. Acad. Sci. U.S.A.* 68, 2883–2892. doi: 10.1073/pnas.68.11.2883

Arvestad, L. (2006). Efficient methods for estimating amino acid replacement rates. *J. Mol. Evol.* 62, 663–673. doi: 10.1007/s00239-004-0113-9

Baldauf, S. L., and Palmer, J. D. (1990). Evolutionary transfer of the chloroplast *tufA* gene to the nucleus. *Nature* 344, 262–265. doi: 10.1038/344262a0

Berg, O. G., and Kurland, C. G. (2000). Why mitochondrial genes are most often found in nuclei. *Mol. Biol. Evol.* 17, 951–961. doi: 10.1093/oxfordjournals.molbev.a026376

Bernát, G., Appel, J., Ogawa, T., and Rögner, M. (2011). Distinct roles of multiple NDH-1 complexes in the cyanobacterial electron transport network as revealed by kinetic analysis of $P700^+$ reduction in various *ndh*-deficient mutants of *Synechocystis* sp. strain PCC6803. *J. Bacteriol.* 193, 292–295. doi: 10.1128/JB.00984-10

Berner, R. A. (2006). GEOCARBSULF: a combined model for Phanerozoic atmospheric O_2 and CO_2. *Geochim. Cosmochim. Acta* 70, 5653–5664. doi: 10.1016/j.gca.2005.11.032

Böhm, R., Sauter, M., and Böck, A. (1990). Nucleotide sequence and expression of an operon in *Escherichia coli* coding for formate hydrogen lyase components. *Mol. Microbiol.* 4, 231–243. doi: 10.1111/j.1365-2958.1990.tb00590.x

Capella-Gutiérrez, S., Silla-Martínez, J. M., and Gabaldón, T. (2009). trimAl: a tool for automated alignment trimming in large-scale phylogenetic analyses. *Bioinformatics* 25, 1972–1973. doi: 10.1093/bioinformatics/btp348

Edgar, R. C. (2004). MUSCLE: multiple sequence alignment with high accuracy and high throughput. *Nucleic Acids Res.* 32, 1792–1797. doi: 10.1093/nar/gkh340

Endo, T., Imanishi, T., Gojobori, T., and Inoko, H. (1997). Evolutionary significance of intra-genome duplications on human chromosomes. *Gene* 205, 19–27. doi: 10.1016/S0378-1119(97)00478-2

Fan, X., Zhang, J., Li, W., and Peng, L. (2015). The NdhV subunit is required to stabilize the chloroplast NADH dehydrogenase-like complex in *Arabidopsis*. *Plant J.* 82, 221–231. doi: 10.1111/tpj.12807

Felsenstein, J. (1981). Evolutionary trees from DNA sequences: a maximum likelihood approach. *J. Mol. Evol.* 17, 368–376. doi: 10.1007/bf01734359

Foyer, C. H., and Noctor, G. (2003). Redox sensing and signalling associated with reactive oxygen in chloroplasts, peroxisomes and mitochondria. *Physiol. Plant* 119, 355–364. doi: 10.1034/j.1399-3054.2003.00223.x

Gantt, J. S., Baldauf, S. L., Calie, P. J., Weeden, N. F., and Palmer, J. D. (1991). Transfer of *rpl22* to the nucleus greatly preceded its loss from the chloroplast and involved the gain of an intron. *EMBO J.* 10, 3073–3078. doi: 10.1002/j.1460-2075.1991.tb07859.x

Graham, J. B., Aguilar, N. M., Dudley, R., and Gans, C. (1995). Implications of the late Palaeozoic oxygen pulse for physiology and evolution. *Nature* 375, 117–120. doi: 10.1038/375117a0

Gunbin, K. V., Suslov, V. V., Genaev, M. A., and Afonnikov, D. A. (2011). Computer system for analysis of molecular evolution modes (SAMEM): analysis of molecular evolution modes at deep inner branches of the phylogenetic tree. *In Silico Biol.* 11, 109–123. doi: 10.3233/ISB-2012-0446

Hanada, K., Shiu, S. H., and Li, W. H. (2007). The nonsynonymous/synonymous substitution rate ratio versus the radical/conservative replacement rate ratio in the evolution of mammalian genes. *Mol. Biol. Evol.* 24, 2235–2241. doi: 10.1093/molbev/msm152

Henikoff, S., and Henikoff, J. G. (1992). Amino acid substitution matrices from protein blocks. *Proc. Natl. Acad. Sci. U.S.A.* 89, 10915–10919. doi: 10.1073/pnas.89.22.10915

Ishikawa, K., Takenaga, K., Akimoto, M., Koshikawa, N., Yamaguchi, A., Imanishi, H., et al. (2008). ROS-generating mitochondrial DNA mutations can regulate tumor cell metastasis. *Science* 320, 661–664. doi: 10.1126/science.1156906

Joyce, P. B., and Gray, M. W. (1989). Chloroplast-like transfer RNA genes expressed in wheat mitochondria. *Nucleic Acids Res.* 17, 5461–5476. doi: 10.1093/nar/17.14.5461

Katoh, K., and Toh, H. (2008). Recent developments in the MAFFT multiple sequence alignment program. *Brief. Bioinform.* 9, 286–298. doi: 10.1093/bib/bbn013

Kawashima, S., Pokarowski, P., Pokarowska, M., Kolinski, A., Katayama, T., and Kanehisa, M. (2008). AAindex: amino acid index database, progress report 2008. *Nucleic Acids Res.* 36, D202–D205. doi: 10.1093/nar/gkm998

Kramer, D. M., and Evans, J. R. (2011). The importance of energy balance in improving photosynthetic productivity. *Plant Physiol.* 155, 70–78. doi: 10.1104/pp.110.166652

Kumar, S., Stecher, G., and Tamura, K. (2016). MEGA7: molecular evolutionary genetics analysis version 7.0 for bigger datasets. *Mol. Biol. Evol.* 33, 1870–1874. doi: 10.1093/molbev/msw054

Laloi, C., Apel, K., and Danon, A. (2004). Reactive oxygen signalling: the latest news. *Curr. Opin. Plant Biol.* 7, 323–328. doi: 10.1016/j.pbi.2004.03.005

Laughlin, T. G., Bayne, A. N., Trempe, J. F., Savage, D. F., and Davies, K. M. (2019). Structure of the complex I-like molecule NDH of oxygenic photosynthesis. *Nature* 566, 411–414. doi: 10.1038/s41586-019-0921-0

Lin, C. S., Chen, J. J. W., Chiu, C. C., Hsiao, H. C. W., Yang, C. J., Jin, X. H., et al. (2017). Concomitant loss of NDH complex-related genes within chloroplast and nuclear genomes in some orchids. *Plant J.* 90, 994–1006. doi: 10.1111/tpj.13525

Lin, C. S., Chen, J. J. W., Huang, Y. T., Chan, M. T., Daniell, H., Chang, W. J., et al. (2015). The location and translocation of *ndh* genes of chloroplast origin in the Orchidaceae family. *Sci. Rep.* 5, 1–10. doi: 10.1038/srep09040

Martin, W., and Herrmann, R. G. (1998). Gene transfer from organelles to the nucleus: how much, what happens, and why? *Plant Physiol.* 118, 9–17. doi: 10.1104/pp.118.1.9

Martin, W., Stoebe, B., Goremykin, V., Hansmann, S., Hasegawa, M., and Kowallik, K. V. (1998). Gene transfer to the nucleus and the evolution of chloroplasts. *Nature* 393, 162–165. doi: 10.1038/30234

Maul, J. E., Lilly, J. W., Cui, L., dePamphilis, C. W., Miller, W., Harris, E. H., et al. (2002). The *Chlamydomonas reinhardtii* plastid chromosome: islands of genes in a sea of repeats. *Plant Cell* 14, 2659–2679. doi: 10.1105/tpc.006155

Messier, W., and Stewart, C. B. (1997). Episodic adaptive evolution of primate lysozymes. *Nature* 385, 151–154. doi: 10.1038/385151a0

Muller, H. J. (1964). The relation of recombination to mutational advance. *Mutat. Res.* 1, 2–9. doi: 10.1016/0027-5107(64)90047-8

Neale, D. B., Wegrzyn, J. L., Stevens, K. A., Zimin, A. V., Puiu, D., Crepeau, M. W., et al. (2014). Decoding the massive genome of loblolly pine using haploid DNA and novel assembly strategies. *Genome Biol.* 15:R59. doi: 10.1186/gb-2014-15-3-r59

Nystedt, B., Street, N. R., Wetterbom, A., Zuccolo, A., Lin, Y. C., Scofield, D. G., et al. (2013). The Norway spruce genome sequence and conifer genome evolution. *Nature* 497, 579–584. doi: 10.1038/nature12211

Ohyama, K., Fukuzawa, H., Kohchi, T., Shirai, H., Sano, T., Sano, S., et al. (1986). Chloroplast gene organization deduced from complete sequence of liverwort *Marchantia polymorpha* chloroplast DNA. *Nature* 322, 572–574. doi: 10.1038/322572a0

Otten, A. B., and Smeets, H. J. (2015). Evolutionary defined role of the mitochondrial DNA in fertility, disease and ageing. *Hum. Reprod. Update* 21, 671–689. doi: 10.1093/humupd/dmv024

Pan, X., Cao, D., Xie, F., Xu, F., Su, X., Mi, H., et al. (2020). Structural basis for electron transport mechanism of complex I-like photosynthetic NAD(P)H dehydrogenase. *Nat. Commun.* 11:610. doi: 10.1038/s41467-020-14456-0

Peltier, G., Aro, E. M., and Shikanai, T. (2016). NDH-1 and NDH-2 plastoquinone reductases in oxygenic photosynthesis. *Annu. Rev. Plant Biol.* 67, 55–80. doi: 10.1146/annurev-arplant-043014-114752

Price, M. N., Dehal, P. S., and Arkin, A. P. (2010). FastTree 2–approximately maximum-likelihood trees for large alignments. *PLoS One* 5:e9490. doi: 10.1371/journal.pone.0009490

Pupko, T., Pe'er, I., Hasegawa, M., Graur, D., and Friedman, N. (2002). A branch-and-bound algorithm for the inference of ancestral amino-acid sequences when the replacement rate varies among sites: application to the evolution of five gene families. *Bioinformatics* 18, 1116–1123. doi: 10.1093/bioinformatics/18.8.1116

Ranade, S. S., Garcia-Gil, M. R., and Rossello, J. A. (2016). Non-functional plastid *ndh* gene fragments are present in the nuclear genome of Norway spruce (*Picea abies* L. Karsch): insights from in silico analysis of nuclear and organellar genomes. *Mol. Genet. Genomics* 291, 935–941. doi: 10.1007/s00438-015-1159-7

Rokka, A., Suorsa, M., Saleem, A., Battchikova, N., and Aro, E. M. (2005). Synthesis and assembly of thylakoid protein complexes: multiple assembly steps of photosystem II. *Biochem. J.* 388, 159–168. doi: 10.1042/BJ20042098

Rozas, J., Ferrer-Mata, A., Sanchez-DelBarrio, J. C., Guirao-Rico, S., Librado, P., Ramos-Onsins, S. E., et al. (2017). DnaSP 6: DNA sequence polymorphism analysis of large data sets. *Mol. Biol. Evol.* 34, 3299–3302. doi: 10.1093/molbev/msx248

Rumeau, D., Becuwe-Linka, N., Beyly, A., Louwagie, M., Garin, J., and Peltier, G. (2005). New subunits NDH-M, -N, and -O, encoded by nuclear genes, are essential for plastid NDH complex functioning in higher plants. *Plant Cell* 17, 219–232. doi: 10.1105/tpc.104.028282

Savard, L., Li, P., Strauss, S. H., Chase, M. W., Michaud, M., and Bousquet, J. (1994). Chloroplast and nuclear gene sequences indicate late Pennsylvanian time for the last common ancestor of extant seed plants. *Proc. Natl. Acad. Sci. U.S.A.* 91, 5163–5167. doi: 10.1073/pnas.91.11.5163

Schuller, J. M., Birrell, J. A., Tanaka, H., Konuma, T., Wulfhorst, H., Cox, N., et al. (2019). Structural adaptations of photosynthetic complex I enable ferredoxin-dependent electron transfer. *Science* 363, 257–260. doi: 10.1126/science.aau3613

Schuller, J. M., Saura, P., Thiemann, J., Schuller, S. K., Gamiz-Hernandez, A. P., Kurisu, G., et al. (2020). Redox-coupled proton pumping drives carbon concentration in the photosynthetic complex I. *Nat. Commun.* 11:494. doi: 10.1038/s41467-020-14347-4

Shen, L., Tang, K., Wang, W., Wang, C., Mao, J., Zhou, T., et al. (2022). Architecture of the chloroplast PSI–NDH supercomplex in *Hordeum vulgare*. *Nature* 601, 649–654. doi: 10.1038/s41586-021-04277-6

Shimizu, H., Peng, L., Myouga, F., Motohashi, R., Shinozaki, K., and Shikanai, T. (2008). CRR23/NdhL is a subunit of the chloroplast NAD(P)H dehydrogenase complex in *Arabidopsis*. *Plant Cell Physiol.* 49, 835–842. doi: 10.1093/pcp/pcn058

Shinozaki, K., Ohme, M., Tanaka, M., Wakasugi, T., Hayashida, N., Matsubayashi, T., et al. (1986). The complete nucleotide sequence of the tobacco chloroplast genome: its gene organization and expression. *EMBO J.* 5, 2043–2049. doi: 10.1002/j.1460-2075.1986.tb04464.x

Stern, D. B., and Lonsdale, D. M. (1982). Mitochondrial and chloroplast genomes of maize have a 12-kilobase DNA sequence in common. *Nature* 299, 698–702. doi: 10.1038/299698a0

Suorsa, M., Sirpio, S., and Aro, E. M. (2009). Towards characterization of the chloroplast NAD(P)H dehydrogenase complex. *Mol. Plant* 2, 1127–1140. doi: 10.1093/mp/ssp052

Turmel, M., Otis, C., and Lemieux, C. (2002). The chloroplast and mitochondrial genome sequences of the charophyte *Chaetosphaeridium globosum*: insights into the timing of the events that restructured organelle DNAs within the green algal lineage that led to land plants. *Proc. Natl. Acad. Sci. U.S.A.* 99, 11275–11280. doi: 10.1073/pnas.162203299

Varshney, P., Mikulic, P., Vonshak, A., Beardall, J., and Wangikar, P. P. (2015). Extremophilic micro-algae and their potential contribution in biotechnology. *Bioresour. Technol.* 184, 363–372. doi: 10.1016/j.biortech.2014.11.040

Wakasugi, T., Tsudzuki, J., Ito, S., Nakashima, K., Tsudzuki, T., and Sugiura, M. (1994). Loss of all *ndh* genes as determined by sequencing the entire chloroplast genome of the black pine *Pinus thunbergii*. *Proc. Natl. Acad. Sci. U.S.A.* 91, 9794–9798. doi: 10.1073/pnas.91.21.9794

Wang, D., Rousseau-Gueutin, M., and Timmis, J. N. (2012). Plastid sequences contribute to some plant mitochondrial genes. *Mol. Biol. Evol.* 29, 1707–1711. doi: 10.1093/molbev/mss016

Wang, D., Wu, Y. W., Shih, A. C. C., Wu, C. S., Wang, Y. N., and Chaw, S. M. (2007). Transfer of chloroplast genomic DNA to mitochondrial genome occurred at least 300 MYA. *Mol. Biol. Evol.* 24, 2040–2048. doi: 10.1093/molbev/msm133

Wodniok, S., Brinkmann, H., Glöckner, G., Heidel, A. J., Philippe, H., Melkonian, M., et al. (2011). Origin of land plants: do conjugating green algae hold the key? *BMC Evol. Biol.* 11:104. doi: 10.1186/1471-2148-11-104

Xia, X. (2018). DAMBE7: new and improved tools for data analysis in molecular biology and evolution. *Mol. Biol. Evol.* 35, 1550–1552. doi: 10.1093/molbev/msy073

Yamamoto, H., Peng, L., Fukao, Y., and Shikanai, T. (2011). An Src homology 3 domain-like fold protein forms a ferredoxin binding site for the chloroplast NADH dehydrogenase-like complex in *Arabidopsis*. *Plant Cell* 23, 1480–1493. doi: 10.1105/tpc.110.080291

Zhang, C., Shuai, J., Ran, Z., Zhao, J., Wu, Z., Liao, R., et al. (2020). Structural insights into NDH-1 mediated cyclic electron transfer. *Nat. Commun.* 11:888. doi: 10.1038/s41467-020-14732-z

Zhang, J. (2000). Rates of conservative and radical nonsynonymous nucleotide substitutions in mammalian nuclear genes. *J. Mol. Evol.* 50, 56–68. doi: 10.1007/s002399910007

Zhao, Y., Yu, H., Zhou, J. M., Smith, S. M., and Li, J. (2020). Malate circulation: linking chloroplast metabolism to mitochondrial ROS. *Trends Plant Sci.* 25, 446–454. doi: 10.1016/j.tplants.2020.01.010

Conflict of Interest: The authors declare that the research was conducted in the absence of any commercial or financial relationships that could be construed as a potential conflict of interest.

Publisher's Note: All claims expressed in this article are solely those of the authors and do not necessarily represent those of their affiliated organizations, or those of the publisher, the editors and the reviewers. Any product that may be evaluated in this article, or claim that may be made by its manufacturer, is not guaranteed or endorsed by the publisher.

frontiers | Frontiers in Microbiology

TYPE Original Research
PUBLISHED 04 August 2022
DOI 10.3389/fmicb.2022.933404

OPEN ACCESS

EDITED BY
Bao-Sheng Qiu,
Central China Normal University, China

REVIEWED BY
Hope A. Johnson,
California State University, Fullerton, United States
Anthony William Larkum,
University of Technology Sydney, Australia
Nathan Soulier,
TriLink BioTechnologies, United States

*CORRESPONDENCE
Daniela Billi
billi@uniroma2.it

SPECIALTY SECTION
This article was submitted to Microbial Physiology and Metabolism, a section of the journal Frontiers in Microbiology

RECEIVED 30 April 2022
ACCEPTED 28 June 2022
PUBLISHED 04 August 2022

CITATION
Billi D, Napoli A, Mosca C, Fagliarone C, de Carolis R, Balbi A, Scanu M, Selinger VM, Antonaru LA and Nürnberg DJ (2022) Identification of far-red light acclimation in an endolithic *Chroococcidiopsis* strain and associated genomic features: Implications for oxygenic photosynthesis on exoplanets. *Front. Microbiol.* 13:933404. doi: 10.3389/fmicb.2022.933404

Identification of far-red light acclimation in an endolithic *Chroococcidiopsis* strain and associated genomic features: Implications for oxygenic photosynthesis on exoplanets

Daniela Billi[1]*, Alessandro Napoli[1,2], Claudia Mosca[1], Claudia Fagliarone[1], Roberto de Carolis[1], Amedeo Balbi[3], Matteo Scanu[1], Vera M. Selinger[4], Laura A. Antonaru[4] and Dennis J. Nürnberg[4]

[1]Department of Biology, University of Rome Tor Vergata, Rome, Italy, [2]Ph.D. Program in Cellular and Molecular Biology, Department of Biology, University of Rome Tor Vergata, Rome, Italy, [3]Department of Physics, University of Rome Tor Vergata, Rome, Italy, [4]Department of Physics, Biochemistry and Biophysics of Photosynthetic Organisms, Freie Universität Berlin, Berlin, Germany

Deserts represent extreme habitats where photosynthetic life is restricted to the lithic niche. The ability of rock-inhabiting cyanobacteria to modify their photosynthetic apparatus and harvest far-red light (near-infrared) was investigated in 10 strains of the genus *Chroococcidiopsis*, previously isolated from diverse endolithic and hypolithic desert communities. The analysis of their growth capacity, photosynthetic pigments, and *apcE2*-gene presence revealed that only *Chroococcidiopsis* sp. CCMEE 010 was capable of far-red light photoacclimation (FaRLiP). A total of 15 FaRLiP genes were identified, encoding paralogous subunits of photosystem I, photosystem II, and the phycobilisome, along with three regulatory elements. CCMEE 010 is unique among known FaRLiP strains by undergoing this acclimation process with a significantly reduced cluster, which lacks major photosystem I paralogs *psaA* and *psaB*. The identification of an endolithic, extremotolerant cyanobacterium capable of FaRLiP not only contributes to our appreciation of this phenotype's distribution in nature but also has implications for the possibility of oxygenic photosynthesis on exoplanets.

KEYWORDS

FaRLiP, desert cyanobacteria, *Chroococcidiopsis*, astrobiology, biosignature

Introduction

The discovery of cyanobacteria capable of harvesting far-red light (near-infrared, wavelengths > 700 nm) has changed the paradigm that oxygenic photosynthesis is only driven by visible light and exclusively by chlorophyll *a* (Chl *a*) (Chen et al., 2012; Loughlin et al., 2013; Gan et al., 2014). The red limit of photosynthesis is of particular interest to astrobiology. M-stars, the most common type of star in the galaxy, have a light spectrum that peaks in the far-red and infrared. Some may be orbited by Earth-like planets, and any photosynthetic life potentially inhabiting them would likely use these wavelengths (Cockell et al., 2009). Furthermore, it is well known that pigments involved in oxygenic photosynthesis exhibit a sharp increase in reflectance at near-infrared wavelengths, a feature usually termed "red edge," that can be used as a remote indication of life on rocky planets occurring in the so-called habitable zone (see, e.g., Hegde and Kaltenegger, 2013).

On Earth, far-red light photosynthesis occurs in cyanobacteria living in environments where visible light is strongly attenuated, for instance, by competing for photosynthetic organisms or by physical conditions (Larkum and Kühl, 2005; Gan and Bryant, 2015). This creates selective pressure for using photons that are normally too low in energy to drive water splitting. There are two known types of far-red oxygenic photosynthesis: A constitutive adaptation that uses a majority of chlorophyll *d* and is restricted to a single genus (*Acaryochloris*), and an acclimation response (far-red light photoacclimation, or FaRLiP), which is present in phylogenetically diverse cyanobacteria (Gan and Bryant, 2015; Averina et al., 2018; Antonaru et al., 2020). The latter uses ∼10% chlorophyll *f*, alongside a majority of chlorophyll *a* and traces of chlorophyll *d* (Gan et al., 2014; Nürnberg et al., 2018). Both chlorophylls *f* and *d* are substituted, spectrally red-shifted variants of chlorophyll *a*.

Chlorophyll *d* was first discovered > 40 years ago (Manning and Strain, 1943), and recent 16S rRNA and pigment analysis data suggest a potential global distribution (see, e.g., Kashiyama et al., 2008; Behrendt et al., 2014; Zhang et al., 2019). In contrast, the first Chl *f*-containing species, *Halomicronema hongdechloris*, has been isolated only within the last decade from stromatolites in Shark Bay, Western Australia (Chen et al., 2012). Since then, more Chl *f*-producing cyanobacteria have been found growing under selective far-red light samples collected from caves, lakes, beach rocks, hot spring mats, and subtropical forests (Akutsu et al., 2011; Behrendt et al., 2015; Trampe and Kühl, 2016; Ohkubo and Miyashita, 2017; Goìmez-Lojero et al., 2018; Zhang et al., 2019; Kühl et al., 2020). In addition, a wealth of data has come from sequence-based searches. Many of the known Chl *f*-producing cyanobacteria were identified by searching publicly available genomes for a gene cluster associated with far-red light photoacclimation (FaRLiP) (Gan et al., 2014, 2015). In addition, insights into the distribution of Chl *f*-photosynthesis at a global scale were later provided by screening environmental metagenomic data with a single far-red gene as a marker (Antonaru et al., 2020). This sequence (*apcE2*) encodes the core-membrane linker of the far-red phycobilisome. Overall, the FaRLiP cluster consists of ∼19 genes encoding paralogous subunits of the photosystem I (PSI), photosystem II (PSII), and the phycobilisome (PBS), along with three *rfp* genes encoding master control elements (Gan et al., 2014, 2015; Zhao et al., 2015; Wiltbank and Kehoe, 2019). A highly divergent PSII paralog, *chlF*, also known as *psbA4*, is involved in chlorophyll *f* synthesis (Ho et al., 2016; Trinugroho et al., 2020). These genes are most commonly found together but may occasionally be split into two subclusters (Gan et al., 2015; Sheridan et al., 2020).

The FaRLiP capacity of rock-inhabitant cyanobacteria in extreme environments has been poorly investigated. There has been one report focusing on the subject (Murray et al., 2022), together with one report on the far-red *apcE2* gene being present in the metagenome of endolithic communities from the Atacama Desert (Antonaru et al., 2020). In fact, in hot and cold deserts, cyanobacteria take refuge in or under rocks, where the transmitted light is still sufficient for photosynthesis (Cockell et al., 2009). Different rock substrates have different light transmissions, for instance, calcite is more translucent than granite, gypsum, and ignimbrite, although they all have a higher transmission of red wavelengths compared to blue (Smith et al., 2014; Meslier et al., 2018). Depending on the mineralogical composition, cyanobacterial colonization can be endolithic, including beneath the rock surface within pores (cryptoendoliths) or in cracks or fissures (chasmoendoliths), but also hypolithic, at the rock–soil interface (Wierzchos et al., 2011). Recently, chlorophylls *d* and *f* were reported for endolithic communities from gypsum, calcite, and sandstone from the Atacama and Namib deserts (Murray et al., 2022), but these pigments were not detected in hypolithic communities from quartz pebbles in the latter desert (Gwizdala et al., 2021). Red-shift carotenoids were also reported for endolithic communities (primarily composed of *Chroococcidiopsis* cyanobacteria) in ignimbrite rocks from the Atacama Desert (Vítek et al., 2017). Moreover, a red-shifted emission spectrum of the photosynthetic pigments was reported for *Chroococcidiopsis* cells occurring in hypolithic communities in quartz, carbonate, and talc from the Mojave Desert (Smith et al., 2014). This raises the possibility that FaRLiP may be significantly present.

In this study, the FaRLiP capacity of rock-inhabiting cyanobacteria was investigated in 10 strains of *Chroococcidiopsis* isolated from endolithic and hypolithic communities collected from five deserts worldwide. The selected strains were grown under far-red light (FRL) and white light (WL) and tested for growth, photosynthetic pigment features (as revealed by confocal laser scanning microscopy), and the presence of the far-red *apcE2* gene (by polymerase chain reaction). Among the

10 investigated strains, only *Chroococcidiopsis* sp. CCMEE 010 showed a FaRLiP response. Therefore, the Oxford Nanopore and Illumina platforms were used to obtain the whole-genome sequence of this strain, and a bioinformatics search was performed to identify FaRLiP-relevant genes. Finally, to evaluate the Chl *f* detectability as a far-red shifted signature of life on exoplanets, the reflectance spectrum of dried cells of this far-red positive *Chroococcidiopsis* strain was measured and compared to that of a negative far-red *Chroococcidiopsis* strain.

Materials and methods

Strains and growth conditions

A total of 10 *Chroococcidiopsis* strains were obtained from the Culture Collection of Microorganisms from Extreme Environments (CCMEE) established by E. Imre and Roseli Ocampo-Friedmann and currently maintained at the Department of Biology, University of Tor Vergata (**Table 1**). White light (WL) was provided by cool white fluorescent bulbs and FRL by 750 nm LEDs (Epitex; L750-01AU). Triplicates were grown for 14 days in liquid BG-11 medium at 25°C under permanent WL and FRL illumination with a photon flux density of approximately 40 μmol m^{-2} s^{-1} for both light sources. After a 14-day incubation, the growth was evaluated by measuring the optical density (OD) at 730 nm using a spectrophotometer.

Confocal laser scanning microscopy

Culture aliquots of the selected 10 *Chroococcidiopsis* strains grown for 14 days under WL and FRL were immobilized onto a BG-11 medium containing 1.5% agarose and examined with a Confocal Laser Scanning Microscopy System (CLSM; Olympus Fluoview 1000). CLSM lambda scans were obtained by using a 488 nm excitation laser (and collecting the emission from 550 to 800 nm). Curve plotting was performed using the GraphPad Prism program (GraphPad Software, San Diego, CA). Fluorescence images of *Chroococcidiopsis* sp. CCMEE 010 cells were acquired with a Leica SP8 inverted CLSM by exciting the immobilized cells with a 488 nm laser and acquiring the fluorescence emission from 650 to 680 nm for phycobilisomes and Chl *a,* and from 720 to 750 nm for Chl *f*.

TABLE 1 List of *Chroococcidiopsis* strains used in this study.

CCMEE strain	Sampling site	Rock substrate/ colonization type
06	Negev Desert, Israel	Sandstone/cryptoendolithic
07	Negev Desert, Israel	Granite/cryptoendolithic
010	Negev Desert, Israel	Granite/chasmoendolithic
019	Negev Desert, Israel	Calcite/chasmoendolitic
046	Negev Desert, Israel	Limestone/hypolithic
053	Sinai Desert, Egypt	Granite/chasmoendolitic
064	Sinai Desert, Egypt	Stone pavement/hypolithic
078	Mojave Desert, California	Granite/chasmoendolitic
088	Sonora Desert, Mexico	Granite/chasmoendolithic
313	Broken Hill Desert, Australia	Granite/hypolithic

Reflectance measurement

Liquid-culture aliquots of *Chroococcidiopsis* were immobilized on 0.2-μm polycarbonate filters (Millipore, Burlington, MA, United States), dried under a laminar flow hood for 24 h, and then stored at RT in the dark. Reflectance spectra were acquired with an Agilent Cary 60 Remote Diffuse Reflectance Accessory connected to an Agilent Cary 60 UV/Vis spectrometer.

PCR amplification of far-red specific genes

The genomic DNA of the ten *Chroococcidiopsis* sp. strains was extracted using a PowerWater DNA Isolation Kit (MO BIO Laboratories, Carlsbad, CA, United States) and quantified using the NanoDrop Lite Spectrophotometer (Thermo Fisher Scientific, Waltham, MA, United States). Amplification of *apcE2* was performed by using 12 ng of genomic DNA in 12 μl PCR reaction mixtures containing 6 μl of Phusion High-Fidelity PCR Master Mix with HF Buffer (New England Biolabs, Ipswich, MA, United States) and F-apcE2M and R-apcE2M primers as described (Antonaru et al., 2020). The resulting amplicons were loaded onto a 1.5% agarose gel containing 0.5 mg ml^{-1} ethidium bromide and, after electrophoresis, visualized with a transilluminator.

For *psaA2* and *psaB2*, PCR involved 50 ng of gDNA in 25 μl reactions, using a Q5 High-Fidelity 2X Master Mix (New England Biolabs, Ipswich, MA, United States). Primers are listed in **Supplementary Table 1**. Thermocycling conditions were as reported above, except for a 1 min extension time, and a gradient annealing temperature as described below. The results were visualized on a 1.5% agarose gel stained with ROTI GelStain Red (Carl Roth GmbH, Karlsruhe, Germany).

Identification of far-red genes in CCMEE 010's genome

Genomic DNA of *Chroococcidiopsis* sp. CCMEE 010 was sequenced using Illumina MiSeq and Oxford Nanopore MinION. Illumina libraries were prepared using the Kapa Hyperplus library kit (Roche Molecular System Inc.) following

the manufacturer's instructions. The final pooled library was quantified by qPCR and sequenced using the MiSeq Reagent Kit V3. The Oxford Nanopore libraries were prepared following the manufacturer's instructions. Samples were first labeled using a rapid barcoding kit (SQK-RBK004) and then sequenced through the ligation kit LSK-SQK109. Base calls were performed using the guppy software 4.4.1.[1] Illumina and Nanopore reads were assembled together using Unicycler version 0.4.8 (Wick et al., 2017), a hybrid assembly pipeline for bacterial genomes. The assembly yielded a circular genome (length 5,449,630 bp, mean coverage ~113x, with a minimum of 41x) that was annotated with PROKKA version 1.14.5 (Seemann, 2014) through the interface provided by Galaxy (Afgan et al., 2018). Putative FaRLiP genes were recovered and confirmed by using BLAST, e.g., against the NCBI nr database (Johnson et al., 2008; Sayers et al., 2021).

Multiple sequence alignment

Cyanobacterial far-red genes were downloaded from GenBank (National Centre for Biotechnology Information, NCBI) and Uniprot databases (Uniprot, 2021), and multiple alignments were obtained by using Clustal Omega (Sievers and Higgins, 2014). Sequence alignments were displayed graphically using JalView 2.10.5 (Waterhouse et al., 2009).

Confirmation of gene absence by PCR

Initial searches revealed the absence of far-red *psaA* and *psaB* paralogs in both assembled and unassembled data. Due to the fragmented nature of the latter, short (19–22 aa), FaRLiP-specific motifs were used as queries (*psaA*: AQPLGDVFGGVRGIELSGLGTT; *psaB*: LVWAHEKTPLSFGYWRDKP). For the validation of the gene loss, PCR primers were developed that could preferentially amplify these genes from genomic material. Both the conserved motifs and the primers targeting them were built by comparing far-red *psaA* and *psaB* sequences using the species dataset from Antonaru et al. (2020) with standard, white-light paralogs (recovered by BLAST from NCBI). To build the motifs, 60–70 sequences were used per paralog per gene. Primers were built using the Multiple Primer Analyzer web tool (Thermo Fisher Scientific, Waltham, MA, United States). The variation within FaRLiP sequences, combined with the high sequence similarity to standard paralogs, limits the usefulness of these primers to closely related clades (Chroococcidiopsidales and some heterocyst-forming cyanobacteria). For *psaA*, primers could not accurately distinguish between FaRLiP and WL paralogs. Nevertheless, the amplicons could be distinguished by size. A 70–80 bp insertion is specific to FaRLiP *psaA* in all sequences studied apart from the distantly related *Leptolyngbya* sp. JSC-12. Amplicons were checked by sequencing (Microsynth, Balgach, Switzerland).

1 www.nanoporetech.com

Results

Chroococcidiopsis CCMEE 010 has the capacity for far-red light photoacclimation

A total of 10 *Chroococcidiopsis* strains isolated from endolithic and hypolithic communities from five different deserts (**Table 1**) were grown under WL and FRL (**Figure 1A**). After 14 days of FRL incubation, only strain CCMEE 010 showed an increase in cell density compared to time zero. No increase in cell density was observed in the other nine strains, namely, CCMEE 06, 07, 019, 046, 053, 064, 078, 088, and 313 (**Figure 1A**). All the ten strains showed increased cell densities when grown under white light (**Figure 1B**).

When the 10 *Chroococcidiopsis* strains were screened for the presence of the far-red marker gene *apcE2*, a PCR amplicon of the expected size of ~1.2 kbp was obtained only for CCMEE 010 (**Figure 1B**).

Chroococcidiopsis CCMEE 010 shows spectral features associated with Chl *f* formation

All *Chroococcidiopsis* strains under study showed fluorescence emission peaks in the range of 645–680 nm under white light. This can be attributed to phycobiliproteins and Chl *a*-containing photosystems. Nine of these strains (namely, CCMEE 06, 07, 019, 046, 053, 064, 078, 088, and 313) also maintained this emission range under far-red light but showed some variation in the intensity associated with a change in phycobilisome and photosystem content (**Figure 2**). A single strain, *Chroococcidiopsis* sp. CCMEE 010 (**Figure 2**), showed an additional peak around 715–725 nm under FRL. This is a characteristic of the red-shifted Chl *f*, and it has been previously used to identify cyanobacteria capable of FaRLiP (Chen et al., 2012). The slightly shifted fluorescence emission of Chl *f* to shorter wavelengths and the reduction in the overall fluorescence intensity in comparison to previous studies might be caused by the decreased sensitivity of the detector above 700 nm, in fact, the fluorescence in the region from 720 to 750 nm is shown in **Figure 3B**.

The difference in fluorescence emission spectra was also used for CLSM imaging. *Chroococcidiopsis* sp. CCMEE 010 cells grown under FRL showed the emission of phycobilisomes

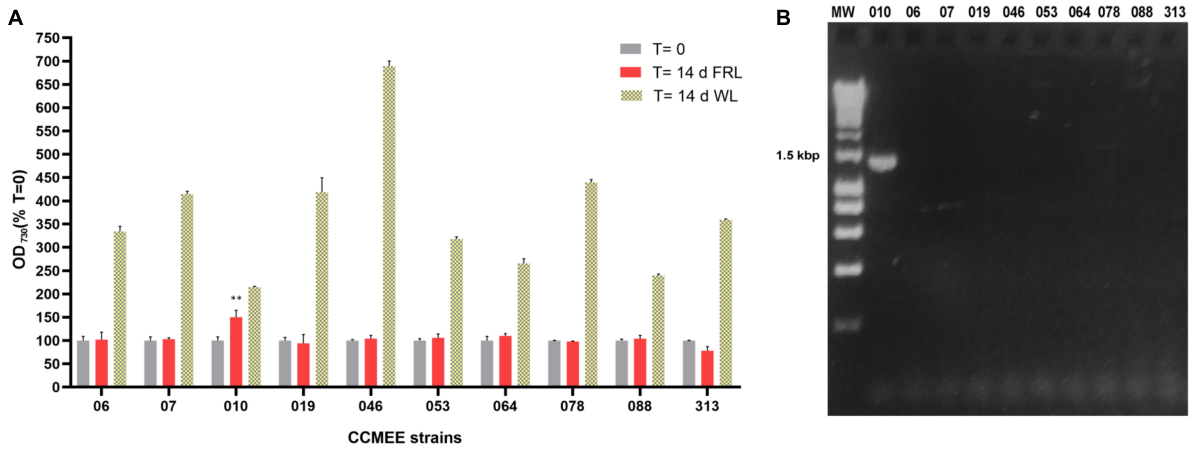

FIGURE 1
Capacity for photosynthesis under far-red light in 10 desert *Chroococcidiopsis* strains. **(A)** Cell densities after 14-day incubation under WL or FRL; values at time zero are set as 100. All WL cultures showed a significant increase in OD_{730} (p-value < 0.001, not shown) after 14 days under FRL a significant increase in OD_{730} occurred only in CCMEE 010 (**p-value < 0.01). **(B)** PCR amplification of the far-red *apcE2* gene. MW, molecular weight (HyperLadder 1 kb, Bioline Inc., MA, United States).

and Chl *a* (Figure 3A, 650–680 nm) as well as of Chl *f* (Figure 3B, 720–750 nm). In contrast, WL-grown cells showed Chl *a* emission (Figure 3C) but lacked the Chl *f* emission (Figure 3D), similar to what was observed for closely related *Chroococcidiopsis thermalis* PCC 7203 (MacGregor-Chatwin et al., 2022).

Spectral differences are also evident in reflectance measurements. Dried samples of FRL-grown cells of *Chroococcidiopsis* sp. CCMEE 010 had a spectrum extended by 50 nm into the far red and a reduced signal in the blue range when compared to FaRLiP negative *Chroococcidiopsis* sp. CCMEE 088 (Figure 3E). The shift in the so-called "red edge" indicated a different pigment composition and the presence of far-shifted Chl *f* occurring after 14 days of FRL incubation in CCMEE 010 cells (Figure 3E).

Unusual genetic basis of far-red light photoacclimation

Out of nineteen FaRLiP genes expected, fifteen were identified in the genome assembly of CCMEE 010 by using homology and synteny information (Table 2). These include two PSI paralogs (*psaF* and *psaJ*), three components of a phytochrome signaling cascade (*rfpA*/*B*/*C*), five genes encoding for phycobilisome components (*apcE2*, *apcD2*/*3*/*5*), and five PSII paralogs (*psbA3*, *psbA4*, *psbB2*, *psbC2*, and *psbD3*). Of the latter, *psbA4*, also known as *chlF* or super-rogue, is a highly divergent D1 gene, which does not form an oxygen-evolving PSII complex but rather is involved in Chl *f* synthesis (Ho et al., 2016; Trinugroho et al., 2020). All these genes were found in a single cluster (Figure 4).

Four photosystem I paralogs, present in all other strains known to be capable of FaRLiP, are absent from the CCMEE 010 cluster. These include major components *psaA* (~2,350 bp) and *psaB* (~2,225 bp), as well as minor components *psaL* (~550 bp) and *psaI* (~150 bp). They were not found by BLAST searches in the rest of the assembled contigs. As it is not unusual for paralogs to break assemblies, conserved far-red motifs for *psaA* and *psaB* were also used to search unassembled data, but unsuccessfully. Genes *psaI* and *psaL* were considered too small and variable for this task.

The high coverage of the assembly made it unlikely that the genes had been missed in the sequencing. As such, variable primers were built to test for the presence of far-red *psaA* and *psaB* in genomic DNA (Supplementary Figure 1A). Far-red specific amplicons were obtained from the related strain *Chroococcidiopsis thermalis* PCC 7203, as well as the less-closely related heterocyst-forming cyanobacterium *Chlorogloeopsis fritschii* PCC 6912 (Supplementary Figure 1B). However, they were absent from CCMEE 010. No amplicons at all were recovered with *psaB* FaRLiP-specific primers from CCMEE 010 or from the negative control *Acaryochloris marina* MBIC11017 (which lacks FaRLiP). Only a standard WL *psaA* amplicon was recovered from CCMEE 010 using the *psaA* primers.

Conserved far-red light molecular markers

A total of two *apcE* phycobilisome-membrane linker sequences were recovered from the assembly. To confirm which of them is the FaRLiP version, they were translated and aligned with FR (ApcE2) and standard WL (ApcE1) sequences

10.3389/fmicb.2022.933404

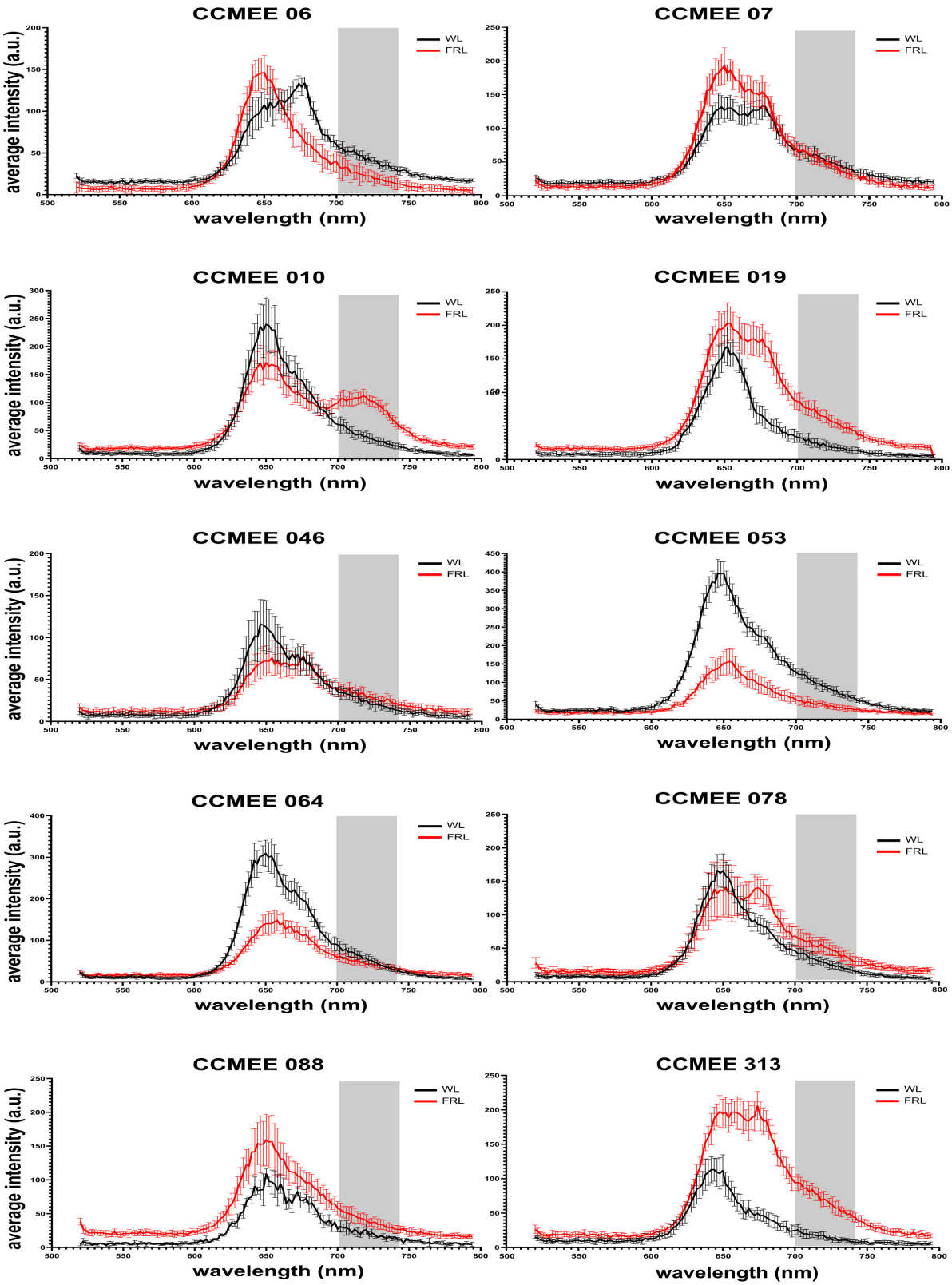

FIGURE 2
CSLM spectral scans of individual cells of FaRLiP negative *Chroococcidiopsis* spp. CCMEE strains grown for 14 days under white or far-red illumination.

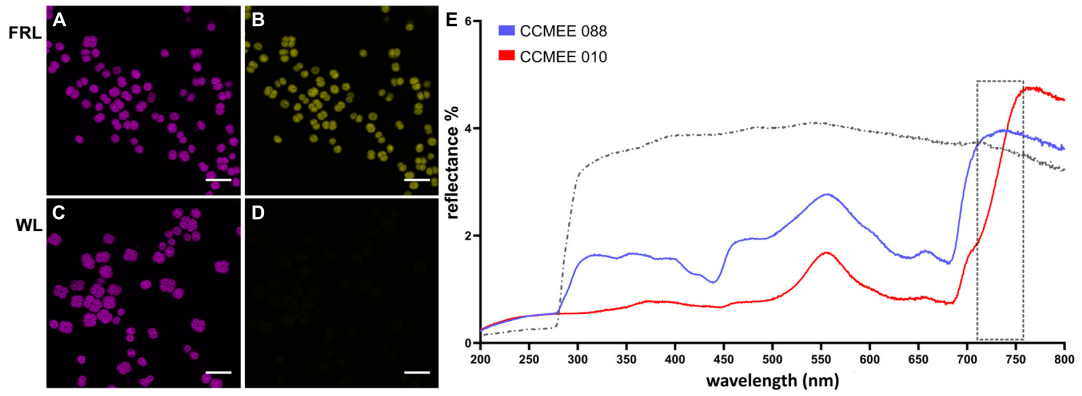

FIGURE 3
Spectral characteristics of far-red light photoacclimation. CSLM images of *Chroococcidiopsis* sp. CCMEE 010 grown for 14 days under FRL **(A)** or WL **(C)** in the 650–680 nm emission range. Red-shifted Chl *f* presence in FRL-acclimated cells in the 720–750 nm emission range **(B)** and absence in WL cells **(D)**. Scale bars 20 μm. Reflectance spectra **(E)** of the FaRLiP positive *Chroococcidiopsis* sp. CCMEE 010 (red line) and FaRLiP negative *Chroococcidiopsis* sp. CCMEE 088 (blue line) dried on polycarbonate filters (gray line).

from *Halomicronema hongdechloris* C2206, *Leptolyngbyaceae* cyanobacterium JSC-12, and *Chlorogloeopsis fritschii* PCC 6912 (**Figure 5**). Standard paralogs are characterized by an ENACS-like motif that includes phytochrome-binding cysteine, while the FaRLiP proteins bind the phytochrome non-covalently using a VIPEDV-like motif (Gan et al., 2015; Antonaru et al., 2020). The FaRLiP sequence from *Chroococcidiopsis* sp. CCMEE 010 is present in the FaRLiP cluster, with the additional version being characteristic of WL. As previously observed for other strains, the FaRLiP sequence is considerably shorter than the WL one (774 aa as opposed to 1,133 aa), due to the presence of only two (as opposed to four) REP domains (Gan et al., 2015).

It could be argued that a more direct marker for FaRLiP is *chlF* (super rogue/*psbA4)*, the synthase for red-shifted chlorophyll *f* (Ho et al., 2016; Trinugroho et al., 2020). In particular, two amino acids (the QD site) were shown to be fully conserved, as well as necessary and sufficient for this synthase function (Trinugroho et al., 2020). The *chlF* sequence from *Chroococcidiopsis* sp. CCMEE 010 showed this site (**Figure 6**, residues 150–151). In addition, the ChlF of *Chroococcidiopsis* sp. CCMEE 010 lacked key residues required for binding the Mn_4CaO_5 cluster for water oxidation as previously reported (Murray, 2012; Ho et al., 2016), which were conversely present in the PsbA3 paralog (**Figure 6**). This protein is encoded by the gene adjacent to *chlF* in the FaRLiP cluster and contains residues for key cofactor binding for water oxidation and charge separation under FRL conditions (**Figure 4**).

Discussion

Out of ten *Chroococcidiopsis* strains, isolated from varied microenvironments in five different deserts, only strain CCMEE 010 was capable of FaRLiP. It showed a far-red shift in the emission spectrum of its photosynthetic pigments under far-red illumination. Furthermore, PCR showed the presence of the far-red *apcE* gene, used as a marker for chlorophyll *f*-producing cyanobacteria (Antonaru et al., 2020).

This prompted a more in-depth analysis by whole-genome sequencing. A total of 15 FaRLiP genes were identified in a cluster. Their sequence similarity with homologous FaRLiP sequences, together with the fact that they include conserved far-red associated motifs, suggests they are functional. However, in terms of gene arrangement, the *Chroococcidiopsis* sp. CCMEE 010 far-red cluster is distinct not only from the cluster in the related *Chroococcidiopsis thermalis* PCC 7203 but also from clusters in more distantly related strains such as the heterocyst-forming cyanobacteria (**Supplementary Figure 2**). A *Chroococcidiopsis*-associated cluster recovered from an Atacama metagenome also did not show these changes (Murray et al., 2022). Notably, *psaF* and *psaJ* were inserted between *psbC* and *psbB*, which has not been observed in any other FaRLiP clusters (Gan et al., 2014, 2015; Chen et al., 2019; Sheridan et al., 2020). In addition, the orientation of the phytochrome cascade genes (*rfpA/B/C*) has been reversed (**Supplementary Figure 2**).

Furthermore, photosystem I paralogs *psaA2*, *psaB2*, *psaL2*, and *psaI2* are missing. Although a few FaRLiP strains exist where some PSI genes are relocated to other genomic areas, e.g., *psaF2* and *psaJ2* in *Chroococcidiopsis thermalis* PCC 7203, or *psaA2/B2/L2/I2* in *Calothrix* sp. NIES-3974 (Gan et al., 2014, 2015; Sheridan et al., 2020), our combined bioinformatics and molecular biology approach supports this as a genuine gene loss. This represents a novel FaRLiP cluster. It would have structural implications for photoacclimation in far-red light, showing that FR photosynthesis may occur with a red-shifted PSII connected with a less red-shifted PSI or that the incorporation of chlorophyll *f* into a standard (WL) PSI might be sufficient to support far-red photosynthesis,

which has been observed when expressing *chlF* in a non-FaRLiP cyanobacterium (Tros et al., 2020). Future studies using isolated PSI from FRL-grown *Chroococcidiopsis* sp. CCMEE 010 will reveal the composition of this unusual complex. Far-red paralog *psbH2* was also not detected, but it is an optional gene not present in all strains. It is possible, though highly unlikely, that some of the small (<560 bp) genes were simply missed by the genome analysis and will be revealed by future transcriptomics/proteomics studies.

It is puzzling that strains isolated from the same microenvironment, the same desert (or neither) as the FaRLiP positive CCMEE 010 (chasmoendolithic on granite, Negev desert), were FaRLiP negative in this study. Such a low FaRLiP occurrence among desert strains of *Chroococcidiopsis* suggested that this photoacclimation mechanism might not be common among rock-inhabiting cyanobacteria. Enrichment cultures may nevertheless reveal it, for instance, in samples from Negev sandstone or the Atacama Desert (Murray et al., 2022). It is possible that intense abiotic stress could result in reduced competition from other photosynthetic organisms (Lacap-Bugler et al., 2017) and, consequently, a decreased evolutionary pressure to maintain a complex acclimation response. Reduced selective pressure might also explain the unusual level of FaRLiP gene rearrangement. Synteny and gene orientation tend to be highly conserved for genes in the FaRLiP cluster, in some cases, across high-level taxonomic groups such as orders (Gan et al., 2014, 2015; Sheridan et al., 2020); changes between closely related species tend to be minor (e.g., insertions of non-FaRLiP genes or split clusters). This hints at co-regulation at a transcriptional level and suggests that a cluster showing high levels of rearrangement might, in contrast, be under relaxed selection.

TABLE 2 Far-red cluster genes in *Chroococcidiopsis* sp. CCMEE 010's genome (in red missing genes).

FaRLiP genes	Gene product according to PROKKA annotation	GenBank accession number
PSI		
psaF2	Photosystem I reaction center subunit III	OM156478
psaJ2	Photosystem I reaction center subunit IX	OM156479
psaA2	Chlorophyll *a* apoprotein A1	
psaB2	Chlorophyll *a* apoprotein A2	
psaI2	Photosystem I reaction center subunit VIII	
psaL2	Photosystem I reaction center subunit IX	
PSII		
psbA4 (*chlF*)	Chlorophyll *f* synthase	OM156469
psbA3	Photosystem II protein D1	OM156470
psbD3	Photosystem II protein D2	OM156476
psbC2	CP43 reaction center protein	OM156477
psbB2	CP47 reaction center protein	OM156480
psbH2	Photosystem II peripheral protein H*	
PBS		
apcD5	Allophycocyanin subunit alpha-B	OM156471
apcB2	Allophycocyanin beta chain	OM156472
apcD2	Allophycocyanin subunit alpha-B	OM156473
apcE2	Phycobiliprotein core-membrane linker	OM156474
apcD3	Allophycocyanin subunit alpha-B	OM156475
Master control		
rfpA	Knotless phytochrome with a kinase domain	OM156467
rfpB	Transcriptional activator	OM156466
rfpC	Response regulatory protein	OM156468

**Not present in all cyanobacteria.*

The discovery of a FaRLiP-positive *Chroococcidiopsis* strain isolated from an extreme, dry environment nevertheless supports the habitability of exoplanets orbiting stars that are poor in visible light but rich in far-red/near infra-red light. In a previous study, three FaRLiP cyanobacteria, namely, *Chlorogloeopsis fritschii* PCC 6912 from thermal springs, *Chroococcidiopsis thermalis* PCC 7203 from a forest soil sample and *Synechococcus* sp. PCC 7335 from snail shells in the intertidal zone, were shown to grow under an M-dwarf simulated spectrum (Claudi et al., 2021). Although the non-FaRLiP *Synechocystis* sp. PCC 6803 also grew (by using the visible part of the simulated spectrum), it is likely that in environments more complex than unialgal cultures, oxygenic photosynthesis above 700 nm could provide a competitive advantage and therefore be more likely to evolve. Anoxygenic near-infrared photosynthesis/phototrophy would also be favored.

If far-red photosynthesis occurs on exoplanets, it might be possible to detect it. The reflectance spectrum of dried cells of *Chroococcidiopsis* sp. CCMEE 010 showed a significant shift (approximately 50 nm) of the "red edge" with respect to a non-FaRLiP *Chroococcidiopsis* strain. This might in principle serve as a diagnostic of the prevalent type of photosynthetic pigment acting on another planet, provided that it covers a large fraction of the surface (Hegde et al., 2015). In fact, dried microbial samples were reported to have higher reflectance than hydrated ones, suggesting that the reflectance signal could be more intense for exoplanets and moons drier than on Earth (Coelho et al., 2022). Nevertheless, a large percentage of planets orbiting within the habitable zone of small-mass M-class stars are predicted to be tidally locked (Barnes, 2017). With one side of the planet permanently facing the sun and intense storms caused by temperature differences, life might be restricted to the "twilight zone" and, therefore, surface signatures might be challenging to detect.

Furthermore, the habitability of planets orbiting active M-stars is placed at risk by strong UV and ionizing radiation.

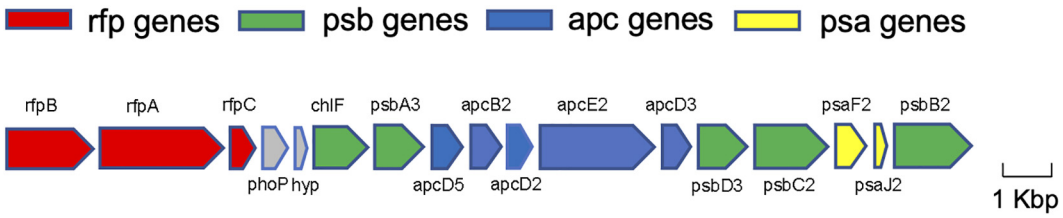

FIGURE 4
Far-red genes of *Chroococcidiopsis* sp. CCMEE 010. Color-coding for genes: *psa* genes for subunits of PSI (yellow); *psb* genes of PSII (green); *apc* genes of PBS (blue); *rfp* genes for the knotless phytochrome (RfpA) and response regulators RfpB and RfpC (red); genes presumed unrelated to photosynthesis are shown in gray. The figure was built using Gene Graphics (Harrison et al., 2018).

```
                                                        *
ApcE1  Halomicronema hongdechloris                KSLRDLSWFLRYVTYAIVAGDPNIISVNVRGLREIIETACSGSATLVALQTMQQSSLRYF 217
       Leptolyngbyaceae cyanobacterium JSC-12     KSLRDLSWFLRYTTYAIVAGDPNIIAVNTRGLREIIERACSGEATIVALQKMKAAALSYF 218
       Chroococcidiopsis sp. 010                  KSLRDLSWFLRYVTYAIVAGDPNIIAVNTRGLREIIENACSGEATIVALQEMRQAALSYF 215
       Chlorogloeopsis fritschii                  KSLRDLSWFLRYATYAIVAGDPNIIAVNTRGLREIIENACSGEATIVALQEMKAAALSYF 218
ApcE2  Leptolyngbyaceae cyanobacterium JSC-12     KSMRDIAWFLRYVIYAIVAGDSSILTVNVRGLRGVIPENV-TAATVVAMQTLKWKSLSYF 227
       Halomicronema hongdechloris                RSMRDLDWFLRYTTYAIVAGDTNILSVNVRGLRGVIPEDV-TLATVVALQEMQWKAAQYV 221
       Chroococcidiopsis sp. 010                  RSMRDLSWFLRYITYAIIAGDSSILSVNVRGLRGVIPEDV-TEATVVALREMRRKSLSYF 226
       Chlorogloeopsis fritschii                  RSMRDLAWFLRYITFAIVAGDTSILSANARGLRGVIPEDV-TDATVVALKEMQRQSLSYF 227
```

FIGURE 5
Alignment of ApcEs from *Chroococcidiopsis* sp. CCMEE 010 with homologs from FaRLiP cyanobacteria. Conserved ENACS-motif of ApcE1 is shaded yellow, asterisk (*) shows phytochrome-binding cysteine, VIPEDV-motif of ApcE2 is shaded light red according to Antonaru et al. (2020). UniProtKB: A0A1Z3HIK5_9CYAN, A0A1Z3HPW3_9CYAN; K8GCZ7_9CYAK, K8GJS2_9CYAN; A0A3S0YF90_CHLFR, A0A433NA38_CHLFR.

```
Chroococcidiopsis sp. 010;psbA3       YGNNIITAAV VPMSNAVGLH FYPIWEAASM DEWLYNGGPY QMIGFHYIPA LACYMGREWE   132
Chroococcidiopsis sp. 010;chlF        SGNNLITAAV VPTSAAIGLH FYPIWEAASL DEWLYNGGPY QLIVLHFLIG IICYQDREWE   155
Synechococcus sp. PCC 7335;chlF       DGNNLITAAV VPTSAAIGLH FYPIWEAASL DEWLINGGPY QLIVLHFIIG IISYQDREWE   176
Halomicronema hongdechloris;chlF      HGNNLITGAV VPTSAAIGLH FYPIWEAASL QEWLTNGGPY QLIVLHFLIG IICYQDREWE   157
Chlorogloeopsis fritschii;chlF        SGNNIITAAV VPTSAAIGLH FYPIWEAASI DEWLYNGGPY QLIVLHFLIG IIAYQDREWE   154

Chroococcidiopsis sp. 010;psbA3       LSYRLGMRPW IAVAYSAPFV ATTSVFLIYP IGQGSFSDGL PMGISGTFNF MFVFQAEHNI   192
Chroococcidiopsis sp. 010;chlF        LSYRLGMRPW ISLAFSAPVA ASVSIFLIYP IGQGSFSAAM PLGISGTFNF MLLFQANHNI   215
Synechococcus sp. PCC 7335;chlF       LSYRLKMRPW ISLAFTAPVA ASVSVLLVYP VGQGGFASGM PLGISGTFTF MMQFQADHNI   236
Halomicronema hongdechloris;chlF      LSYRLGMRPW ISLAFTAPVA AATSVLLIYP VGQGSFSAGM PLGISGTFTF MLQFQADHNI   217
Chlorogloeopsis fritschii;chlF        LSYRLGMRPW ISLAFTAPVA ASVSVLLIYP VGQGSLSAGM PLGISGTFHF MLQFQADHNI   214

Chroococcidiopsis sp. 010;psbA3       LMHPFHMLGV AGVLGGSLFC AMHGSLVTSS LIRET--TES ESQ----NYG YKFGQEQETY   246
Chroococcidiopsis sp. 010;chlF        VMSPFHQLGV IGVLGGAFLS AMHGSLVTST LIRTN-NSEH ESI----NAG YKLGQKQPTY   270
Synechococcus sp. PCC 7335;chlF       LASPLHQMGV IGVLGGALLC AVHGSLVTST VCRAPAQ-TM ALTTTKTGTD RQKPKKAKTY   295
Halomicronema hongdechloris;chlF      LANPFHQLGV IGVFGGALFC AAHGSLVTSA LFRRGPSRTS GWV-----KP AWARESEGTY   272
Chlorogloeopsis fritschii;chlF        LMSPLHQLGV IGVLGGAFAA AMHGSLVTST LIRSHNHSES ESI----NKG YKLGQQHPTY   270

Chroococcidiopsis sp. 010;psbA3       NIVAAHGYFG RLIFQYASFN NSRSLHFFLA AWPVVCIWAT ALGICVMAFN LNGFNFNNSV   306
Chroococcidiopsis sp. 010;chlF        SFRSAQVYLW QLVWQRASFP NSRKLHFFLA AFPVAGIWSA ALGVDIAAFN FDEFNFNQPA   330
Synechococcus sp. PCC 7335;chlF       SFEHAQAYQQ TLLWRGAKFN SSRAVHFCLA ALPVAGIWSA AIGVDLAAFD FDRLSFELPS   355
Halomicronema hongdechloris;chlF      SFEHIQVNQQ KLFWRGMSFR SSRSLHFCLA AFPVAGIWSA ALGVDMAAFG FDPSSG---A   329
Chlorogloeopsis fritschii;chlF        NFRSAQVYLW HLIWQRVSFP NSRKLHFFLA ALPVAGIWSA ALGVDIAAFD FDYLQFHQPE   330

Chroococcidiopsis sp. 010;psbA3       LDSQGR---- VLNTWADVLN RANLGFEVMH ERNAHNFPLD LACGEAVPVS FQAPAISG--   360
Chroococcidiopsis sp. 010;chlF        IKCRDRDVAC NVPTWVDIIN RADLGIAEIG DRRIHNFPGG LATSEPVLLR LTAPALEDCV   390
Synechococcus sp. PCC 7335;chlF       HISVRK---T VVPTWSDVVN QANLGIHTVG EKTPPKFSES GF-PEFKLSE FVEPIAE--D   409
Halomicronema hongdechloris;chlF      NSYLQQ---T TVPTWIDLVT QVNLGIQAIE DQPTAQQ--- -F-PLVL-G- -EEPEEDNAL   378
Chlorogloeopsis fritschii;chlF        LKSQGQ---- IIHTWADTID WASLGIKVLD ERHIYDFPEN LTAGEVVPWK ----------   376
```

FIGURE 6
Alignment of ChlF from *Chroococcidiopsis* sp. CCMEE 010 with homologs from FaRLiP cyanobacteria. ChlFs lack ligands to the Mn4CaO5 oxygen-evolving center shaded blue in the PsbA3 sequence of CCMEE 010 and show the conserved QD residues shaded yellow. Photosynthetic reaction center proteins signature (PROSITE entry PS00244) is shaded green. UniProtKB: P0DOC9 (CHLF_CHLFP); B4WP19 (CHLF_SYNS7); A0A1Z3HIN9 (A0A1Z3HIN9_9CYAN).

Thus, microbial phototrophs might take refuge under the surface, resulting in a cryptic photosynthesis, undetectable in a planetary reflectance spectrum (Cockell et al., 2009; Cockell, 2014). Nevertheless, the discovery of a FaRLiP-positive *Chroococcidiopsis* strain supports the possibility of oxygenic photosynthetic life on exoplanets. Desert strains of *Chroococcidiopsis* are resistant to UV and gamma radiation (Billi et al., 2000; Baqué et al., 2013), on a similar order of magnitude as the well-known radioresistant bacterium *Deinococcus radiodurans* (Slade and Radman, 2011). UVC-absorbing pigments such as scytonemin (Cockell, 1998), or possible alternative UV-protective mechanisms such as biofluorescence, could also be involved (O'Malley-James and Kaltenegger, 2019). Responsiveness to multiple parts of the solar spectrum is not unusual. Notably, the genes for the synthesis of UV-protectant mycosporine—like amino acids were reported to be upregulated in FRL-grown cells of *Chlorogloeopsis fritschii* PCC 6912 (Llewellyn et al., 2020). Therefore, microbial life might endure on exoplanetary surfaces highly irradiated by an M-type star long enough to complete its life cycle if it possessed radioresistance and a capacity for far-red photosynthesis.

Data availability statement

The datasets presented in this study can be found in online repositories. The names of the repository/repositories and accession number(s) can be found in the article/**Supplementary material**.

Author contributions

CM, CF, LA, VS, and RC carried out the laboratory culturing, CLSM analysis, and PCR assays. AN and LA performed the bioinformatics analysis. MS participated in the genome sequence analysis. DB and DN conceived and coordinated the study. DB, DN, and LA wrote the manuscript. AB contributed to the writing. All authors discussed the results and commented on the manuscript.

Funding

This research was supported by the Italian Space Agency (ASI, DC-VUM-2017-034, Grant no. 2019-3 U.0 Life in Space to DB and AB), by ASI/INAF (Agreement no. 2013-056-R.0 to AB), and by the Deutsche Forschungsgemeinschaft (Emmy Noether project award no. NU 421/1 to DN). LA was supported by a postdoctoral fellowship from the Freie Universität Berlin.

Acknowledgments

We would like to thank Dr. Alessandro Cestaro (Centro di Ricerca Interdipartimentale, Fondazione Edmund Mach, Trento, Italy) for helping with the bioinformatic analysis.

Conflict of interest

The authors declare that the research was conducted in the absence of any commercial or financial relationships that could be construed as a potential conflict of interest.

Publisher's note

All claims expressed in this article are solely those of the authors and do not necessarily represent those of their affiliated organizations, or those of the publisher, the editors and the reviewers. Any product that may be evaluated in this article, or claim that may be made by its manufacturer, is not guaranteed or endorsed by the publisher.

Supplementary material

The Supplementary Material for this article can be found online at: https://www.frontiersin.org/articles/10.3389/fmicb.2022.933404/full#supplementary-material

References

Afgan, E., Baker, D., Batut, B., van den Beek, M., Bouvier, D., Cech, M., et al. (2018). The galaxy platform for accessible, reproducible and collaborative biomedical analyses: 2018 update. *Nucleic Acids Res.* 46, 537–544. doi: 10.1093/nar/gky379

Akutsu, S., Fujinuma, D., Furukawa, H., Watanabe, T., Ohnishi-Kameyama, M., Ono, H., et al. (2011). Pigment analysis of a chlorophyll f- containing cyanobacterium strain KC1 isolated from Lake Biwa. *Photochem. Photobiol.* 33, 35–40.

Antonaru, L. A., Cardona, T., Larkum, A. W. D., and Nürnberg, D. J. (2020). Global distribution of a chlorophyll f cyanobacterial marker. *ISME J.* 14, 2275–2287. doi: 10.1038/s41396-020-0670-y

Averina, S., Velichko, N., Senatskaya, E., and Pinevich, A. (2018). Far-red light photoadaptations in aquatic cyanobacteria. *Hydrobiologia* 813, 1–17. doi: 10.1007/s10750-018-3519-x

Baqué, M., Scalzi, G., Rabbow, E., Rettberg, P., and Billi, D. (2013). Biofilm and planktonic lifestyles differently support the resistance of the desert cyanobacterium *Chroococcidiopsis* under space and Martian simulations. *Orig. Life Evol. Biosph.* 43, 377–389. doi: 10.1007/s11084-013-9341-6

Barnes, R. (2017). Tidal locking of habitable exoplanets. *Celest. Mech. Dyn. Astr.* 129, 509–536. doi: 10.1007/s10569-017-9783-7

Behrendt, L., Nielsen, J. L., Sørensen, S. J., Larkum, A. W., Winther, J. R., and Kühl, M. (2014). Rapid TaqMan-based quantification of chlorophyll d-containing

cyanobacteria in the genus *Acaryochloris*. *Appl. Environ. Microbiol.* 80, 3244–3249. doi: 10.1128/AEM.00334-14

Behrendt, L., Brejnrod, A., Schliep, M., Sørensen, S. J., Larkum, A. W., and Kühl, M. (2015). Chlorophyll f-driven photosynthesis in a cavernous cyanobacterium. *ISME J.* 9, 2108–2111. doi: 10.1038/ismej.2015.14

Billi, D., Friedmann, E. I., Hofer, K. G., Caiola, M. G., and Ocampo-Friedmann, R. (2000). Ionizing-radiation resistance in the desiccation-tolerant cyanobacterium *Chroococcidiopsis*. *Appl. Environ. Microbiol.* 6, 1489–1492. doi: 10.1128/AEM.66.4.1489-1492.2000

Chen, M., Li, Y., Birch, D., and Willows, R. D. (2012). A cyanobacterium that contains chlorophyll f-a red-absorbing photopigment. *FEBS Lett.* 586, 3249–3254. doi: 10.1016/j.febslet.2012.06.045

Chen, M., Hernandez-Prieto, M. A., Loughlin, P. C., Li, Y., and Willows, R. D. (2019). Genome and proteome of the chlorophyll f-producing cyanobacterium Halomicronema hongdechloris: adaptative proteomic shifts under different light conditions. *BMC Genomics* 20:207. doi: 10.1186/s12864-019-5587-3

Claudi, R., Alei, E., Battistuzzi, M., Cocola, L., Erculiani, M. C., Pozzer, A. C., et al. (2021). Super-earths, M dwarfs, and photosynthetic organisms: habitability in the lab. *Life* 11:10. doi: 10.3390/life11010010

Coelho, L. F., Madden, J., Kaltenegger, L., Zinder, S., Philpot, W., Esquível, M. G., et al. (2022). Color catalogue of life in ice: surface biosignatures on icy worlds. *Astrobiology* 22, 313–321. doi: 10.1089/ast.2021.0008

Cockell, C. S. (1998). Biological effects of high ultraviolet radiation on early earth – a theoretical evaluation. *J. Theor. Biol.* 193, 717–729. doi: 10.1006/jtbi.1998.0738

Cockell, C. S. (2014). Habitable worlds with no signs of life. *Philos. Trans. A Math. Phys. Eng. Sci.* 372:20130082. doi: 10.1098/rsta.2013.0082

Cockell, C. S., Kaltenegger, L., and Raven, J. A. (2009). Cryptic photosynthesis – extrasolar planetary oxygen without a surface biological signature. *Astrobiology* 9, 623–636. doi: 10.1089/ast.2008.0273

Gan, F., Zhang, S., Rockwell, N. C., Martin, S. S., Lagarias, J. C., and Bryant, D. A. (2014). Extensive remodeling of a cyanobacterial photosynthetic apparatus in far-red light. *Science* 345, 1312–1317. doi: 10.1126/science.1256963

Gan, F., and Bryant, D. A. (2015). Adaptive and acclimative responses of cyanobacteria to far-red light. *Environ. Microbiol.* 17, 3450–3465. doi: 10.1111/1462-2920.12992

Gan, F., Shen, G., and Bryant, D. A. (2015). Occurrence of far-red light photo-acclimation (FaRLiP) in diverse cyanobacteria. *Life* 5, 4–24. doi: 10.3390/life5010004

Goìmez-Lojero, C., Leyva-Castillo, L., Herrera-Salgado, P., Barrera-Rojas, J., Ríos-Castro, E., and Gutiérrez-Cirlos, E. B. (2018). Leptolyngbya CCM 4, a cyanobacterium with far-red photoacclimation from Cuatro Cieìnegas Basin, Meìxico. *Photosynthetica* 56, 342–353. doi: 10.1007/s11099-018-0774-z

Gwizdala, M., Lebre, P. H., Maggs-Kölling, G., Marais, E., Cowan, D. A., and Krüger, T. P. J. (2021). Sub-lithic photosynthesis in hot desert habitats. *Environ. Microbiol.* 23, 3867–3880. doi: 10.1111/1462-2920.15505

Harrison, K. J., Crécy-Lagard, V., and Zallot, R. (2018). Gene graphics: a genomic neighborhood data visualization web application. *Bioinformatics* 34, 1406–1408. doi: 10.1093/bioinformatics/btx793

Hegde, S., and Kaltenegger, L. (2013). Colors of extreme exo-earth environments. *Astrobiology* 13, 47–56. doi: 10.1089/ast.2012.0849

Hegde, S., Paulino-Lima, I. G., Kent, R., Kaltenegger, L., and Rothschild, L. (2015). Surface biosignatures of exo-earths: Remote detection of extraterrestrial life. *Proc. Natl. Acad. Sci. U.S.A.* 112, 3886–3891.

Ho, M. Y., Shen, G., Canniffe, D. P., Zhao, C., and Bryant, D. A. (2016). Light-dependent chlorophyll f synthase is a highly divergent paralog of PsbA of photosystem II. *Science* 26:aaf9178. doi: 10.1126/science.aaf9178

Johnson, M., Zaretskaya, I., Raytselis, Y., Merezhuk, Y., McGinnis, S., Madden, T. L., et al. (2008). NCBI BLAST: a better web interface. *Nucleic Acids Res.* 36, W5–W9. doi: 10.1093/nar/gkn201

Kashiyama, Y., Miyashita, H., Ohkubo, S., Ogawa, N. O., Chikaraishi, Y., Takano, Y., et al. (2008). Evidence of global chlorophyll d. *Science* 321:658. doi: 10.1126/science.1158761

Kühl, M., Trampe, E., Mosshammer, M., Johnson, M., Larkum, A. W., Frigaard, N. U., et al. (2020). Substantial near-infrared radiation-driven photosynthesis of chlorophyll f-containing cyanobacteria in a natural habitat. *Elife* 9:e50871. doi: 10.7554/eLife.50871

Lacap-Bugler, D. C., Lee, K. K., Archer, S., Gillman, L. N., Lau, M. C. Y., Leuzinger, S., et al. (2017). Global diversity of desert hypolithic cyanobacteria. *Front. Microbiol.* 8:867. doi: 10.3389/fmicb.2017.00867

Larkum, A. W., and Kühl, M. (2005). Chlorophyll d: the puzzle resolved. *Trends Plant Sci.* 10, 355–357. doi: 10.1016/j.tplants.2005.06.005

Llewellyn, C. A., Greig, C., Silkina, A., Kultschar, B., Hitchings, M. D., and Farnham, G. (2020). Mycosporine-like amino acid and aromatic amino acid transcriptome response to UV and far-red light in the cyanobacterium *Chlorogloeopsis fritschii* PCC 6912. *Sci. Rep.* 10:20638. doi: 10.1038/s41598-020-77402-6

Loughlin, P., Lin, Y., and Chen, M. (2013). Chlorophyll d and *Acaryochloris marina*: current status. *Photosynth. Res.* 116, 277–293. doi: 10.1007/s11120-013-9829-y

MacGregor-Chatwin, C., Nürnberg, D. J., Jackson, P. J., Vasilev, C., Hitchcock, A., Ho, M. Y., et al. (2022). Changes in supramolecular organization of cyanobacterial thylakoid membrane complexes in response to far-red light photoacclimation. *Sci. Adv.* 8:eabj4437. doi: 10.1126/sciadv.abj4437

Manning, W. M., and Strain, H. H. (1943). Chlorophyll d: a green pigment in red algae. *J. Biol. Chem.* 151, 1–19. doi: 10.1016/S0021-9258(18)72109-1

Meslier, V., Casero, M. C., Dailey, M., Wierzchos, J., Ascaso, C., Artieda, O., et al. (2018). Fundamental drivers for endolithic microbial community assemblies in the hyperarid Atacama Desert. *Environ. Microbiol.* 20, 1765–1781. doi: 10.1111/1462-2920.14106

Murray, J. W. (2012). Sequence variation at the oxygen-evolving centre of photosystem II: a new class of "rogue" cyanobacterial D1 proteins. *Photosynth. Res.* 110, 177–184. doi: 10.1007/s11120-011-9714-5

Murray, B., Ertekin, E., Dailey, M., Soulier, N. T., Shen, G., Bryant, D. A., et al. (2022). Adaptation of cyanobacteria to the endolithic light spectrum in hyper-arid deserts. *Microorganisms* 10:1198. doi: 10.3390/microorganisms10061198

Nürnberg, D. J., Morton, J., Santabarbara, S., Telfer, A., Joliot, P., Antonaru, L. A., et al. (2018). Photochemistry beyond the red limit in chlorophyll f-containing photosystems. *Science* 360, 1210–1213. doi: 10.1126/science.aar8313

O'Malley-James, J. T., and Kaltenegger, L. (2019). Lessons from early earth: UV surface radiation should not limit the habitability of active M star systems. *Mon. Notices Royal Astron. Soc.* 485, 5598–5603. doi: 10.1093/mnras/stz724

Ohkubo, S., and Miyashita, H. (2017). A niche for cyanobacteria producing chlorophyll f within a microbial mat. *ISME J.* 11, 2368–2378. doi: 10.1038/ismej.2017.98

Sayers, E. W., Cavanaugh, M., Clark, K., Pruitt, K. D., Schoch, C. L., Sherry, S. T., et al. (2021). GenBank. *Nucleic Acids Res.* 49, D92–D96. doi: 10.1093/nar/gkaa1023

Seemann, T. (2014). Prokka: rapid prokaryotic genome annotation. *Bioinformatics* 30, 2068–2069. doi: 10.1093/bioinformatics/btu153

Sheridan, K. J., Duncan, E. J., Eaton-Rye, J. J., and Summerfield, T. C. (2020). The diversity and distribution of D1 proteins in cyanobacteria. *Photosynth. Res.* 145, 111–128. doi: 10.1007/s11120-020-00762-7

Sievers, F., and Higgins, D. G. (2014). Clustal omega, accurate alignment of very large numbers of sequences. *Methods Mol. Biol.* 1079, 105–116. doi: 10.1007/978-1-62703-646-7_6

Slade, D., and Radman, M. (2011). Oxidative stress in *Deinococcus radiodurans*. *Microbiol. Mol. Biol. Rev.* 75, 133–191. doi: 10.1128/MMBR.00015-10

Smith, H. D., Baquei, M., Duncan, A. G., Lloyd, C. R., McKay, C. P., and Billi, D. (2014). Comparative analysis of cyanobacteria inhabiting rocks with different light transmittance in the Mojave Desert: a Mars terrestrial analogue. *Int. J. Astrobiol.* 13, 271–277. doi: 10.1017/S1473550414000056

Trampe, E., and Kühl, M. (2016). Chlorophyll f distribution and dynamics in cyanobacterial beachrock biofilms. *J. Phycol.* 52, 990–996. doi: 10.1111/jpy.12450

Trinugroho, J. P., Beèková, M., Shao, S., Yu, J., Zhao, Z., Murray, J. W., et al. (2020). Chlorophyll f synthesis by a super-rogue photosystem II complex. *Nat. Plants* 6, 238–244. doi: 10.1038/s41477-020-0616-4

Tros, M., Bersanini, L., Shen, G., Ho, M. Y., van Stokkum, I. H. M., Bryant, D. A., et al. (2020). Harvesting far-red light: functional integration of chlorophyll f into photosystem I complexes of *Synechococcus* sp. PCC 7002. *Biochim. Biophys. Acta Bioenerg.* 1861:148206. doi: 10.1016/j.bbabio.2020.148206

Uniprot, C. (2021). UniProt: the universal protein knowledgebase in 2021. *Nucleic Acids Res.* 49, D480–D489.

Vítek, P., Ascaso, C., Artieda, O., Casero, M. A., and Wierzchos, J. (2017). Discovery of carotenoid red-shift in endolithic cyanobacteria from the Atacama Desert. *Sci. Rep.* 7:11116. doi: 10.1038/s41598-017-11581-7

Waterhouse, A. M., Procter, J. B., Martin, D. M., Clamp, M., and Barton, G. F. (2009). Jalview Version 2 – a multiple sequence alignment editor and analysis workbench. *Bioinformatics* 25, 1189–1191. doi: 10.1093/bioinformatics/btp033

Wick, R. R., Judd, L. M., Gorrie, C. L., and Holt, K. E. (2017). Unicycler: resolving bacterial genome assemblies from short and long sequencing reads. *PLoS Comput. Biol.* 13:e1005595. doi: 10.1371/journal.pcbi.1005595

Wierzchos, J., Cámara, B., de Los Ríos, A., Davila, A. F., Sánchez Almazo, I. M., Artieda, O., et al. (2011). Microbial colonization of Ca-sulfate crusts in the hyperarid core of the Atacama Desert: implications for the search for life on Mars. *Geobiology* 9, 44–60. doi: 10.1111/j.1472-4669.2010.00254.x

Wiltbank, L. B., and Kehoe, D. M. (2019). Diverse light responses of cyanobacteria mediated by phytochrome superfamily photoreceptors. *Nat. Rev. Microbiol.* 17, 37–50. doi: 10.1038/s41579-018-0110-4

Zhang, Z.-C., Li, Z.-K., Yin, Y.-C., Li, Y., Jia, Y., Chen, M., et al. (2019). Widespread occurrence and unexpected diversity of red-shifted chlorophyll producing cyanobacteria in humid subtropical forest ecosystems. *Environ. Microbiol.* 21, 1497–1510. doi: 10.1111/1462-2920.14582

Zhao, C., Gan, F., Shen, G., and Bryant, D. A. (2015). RfpA, RfpB, and RfpC are the master control elements of far-red light photoacclimation (FaRLiP). *Front. Microbiol.* 6:1303. doi: 10.3389/fmicb.2015.01303

frontiers | Frontiers in Microbiology

TYPE Original Research
PUBLISHED 08 August 2022
DOI 10.3389/fmicb.2022.956554

OPEN ACCESS

EDITED BY
Haichun Gao,
Zhejiang University, China

REVIEWED BY
Jing-Hua Chen,
Zhejiang University, China
Shin-Ichiro Ozawa,
Okayama University, Japan
Jean-David Rochaix,
Université de Genève, Switzerland

*CORRESPONDENCE
Deqiang Duanmu
duanmu@mail.hzau.edu.cn

SPECIALTY SECTION
This article was submitted to Microbial Physiology and Metabolism, a section of the journal Frontiers in Microbiology

RECEIVED 30 May 2022
ACCEPTED 07 July 2022
PUBLISHED 08 August 2022

CITATION
Zhang W, Deng R, Shi W, Li Z, Larkin RM, Fan Q and Duanmu D (2022) Heme oxygenase-independent bilin biosynthesis revealed by a *hmox1* suppressor screening in *Chlamydomonas reinhardtii*. *Front. Microbiol.* 13:956554. doi: 10.3389/fmicb.2022.956554

Heme oxygenase-independent bilin biosynthesis revealed by a *hmox1* suppressor screening in *Chlamydomonas reinhardtii*

Weiqing Zhang[1], Rui Deng[1], Weida Shi[1], Zheng Li[1], Robert M. Larkin[2], Qiuling Fan[1] and Deqiang Duanmu[1,3]*

[1]State Key Laboratory of Agricultural Microbiology, College of Life Science and Technology, Shenzhen Institute of Nutrition and Health, Huazhong Agricultural University, Wuhan, China, [2]Key Laboratory of Horticultural Plant Biology, Ministry of Education, Huazhong Agricultural University, Wuhan, China, [3]Shenzhen Branch, Guangdong Laboratory for Lingnan Modern Agriculture, Genome Analysis Laboratory of the Ministry of Agriculture, Agricultural Genomics Institute at Shenzhen, Chinese Academy of Agricultural Sciences, Shenzhen, China

Bilins are open-chain tetrapyrroles synthesized in phototrophs by successive enzymic reactions catalyzed by heme oxygenases (HMOXs/HOs) and ferredoxin-dependent biliverdin reductases (FDBRs) that typically serve as chromophore cofactors for phytochromes and phycobiliproteins. *Chlamydomonas reinhardtii* lacks both phycobiliproteins and phytochromes. Nonetheless, the activity and stability of photosystem I (PSI) and the catalytic subunit of magnesium chelatase (MgCh) named CHLH1 are significantly reduced and phototropic growth is significantly attenuated in a *hmox1* mutant that is deficient in bilin biosynthesis. Consistent with these findings, previous studies on *hmox1* uncovered an essential role for bilins in chloroplast retrograde signaling, maintenance of a functional photosynthetic apparatus, and the direct regulation of chlorophyll biosynthesis. In this study, we generated and screened a collection of insertional mutants in a *hmox1* genetic background for suppressor mutants with phototropic growth restored to rates observed in wild-type 4A+ *C. reinhardtii* cells. Here, we characterized a suppressor of *hmox1* named *ho1su1* with phototrophic growth rates and levels of CHLH1 and PSI proteins similar to 4A+. Tetrad analysis indicated that a plasmid insertion co-segregated with the suppressor phenotype of *ho1su1*. Results from TAIL-PCR and plasmid rescue experiments demonstrated that the plasmid insertion was located in exon 1 of the *HMOX1* locus. Heterologous expression of the bilin-binding reporter *Nostoc punctiforme* NpF2164g5 in the chloroplast of *ho1su1* indicated that bilin accumulated in the chloroplast of *ho1su1* despite the absence of the HMOX1 protein. Collectively, our study reveals the presence of an alternative bilin biosynthetic pathway independent of HMOX1 in the chloroplasts of Chlamydomonas cells.

KEYWORDS

heme oxygenase, heme, bilin, suppressor screening, insertional mutagenesis

Introduction

The chloroplast is a vital organelle in photosynthetic eukaryotes that performs photosynthesis and synthesizes important metabolites such as fatty acids, vitamins, amino acids, and tetrapyrroles (Jarvis and López-Juez, 2013). The nucleus uses the process of anterograde signaling to precisely control the gene expression, and the structure and function of chloroplasts (Berry et al., 2013; Singh et al., 2015). Meanwhile, the chloroplast is frequently confronted with endogenous developmental cues and environmental challenges (Li and Kim, 2021; Woodson, 2022). The chloroplast communicates its functional status to the nucleus by emitting signals, namely chloroplast retrograde signals. These signals regulate the expression of nuclear genes that are essential for chloroplast biogenesis, maintenance, and stress responses (Chan et al., 2016; Mielecki et al., 2020). The molecular mechanism of chloroplast retrograde signaling was extensively characterized through the study of *genomes uncoupled* (*gun*) mutants in *Arabidopsis thaliana* (Susek et al., 1993; Larkin, 2014). Among six identified *GUN* genes, *GUN2-GUN6* encode enzymes and regulatory proteins involved in tetrapyrrole biosynthesis, indicating the important roles of tetrapyrrole intermediates as chloroplast retrograde signals (Susek et al., 1993; Wu and Bock, 2021).

Tetrapyrroles are a class of cyclic and linear molecules containing four pyrrole rings that are widely distributed in animals, plants, and microbes. Tetrapyrroles commonly serve as cofactors for proteins involved in important biological processes, such as photosynthesis and respiration (Tanaka and Tanaka, 2007; Mochizuki et al., 2010). Tetrapyrroles are made from glutamate in the plastid of photosynthetic eukaryotes and are converted to 5-aminolevulinic acid (ALA)—the universal precursor of tetrapyrroles—and are further converted to protoporphyrin IX (PPIX) (Tanaka et al., 2011; Brzezowski et al., 2015). Magnesium chelatase (MgCh) synthesizes Mg-PPIX from PPIX by inserting a Mg^{2+} ion into PPIX, which is a precursor for chlorophyll. Ferrochelatase (FeCh) synthesizes heme from PPIX by inserting a Fe^{2+} ion into PPIX (Busch and Montgomery, 2015). Heme oxygenases (HMOXs/HOs) convert heme into biliverdin IXα (BV), which is subsequently reduced to various types of bilins by a class of ferredoxin-dependent biliverdin reductases (FDBRs) with regiospecificities for BV reduction in phototrophs (Nagahatenna et al., 2015; Rockwell and Lagarias, 2017).

Bilins generally serve as cofactors for phytochromes and phycobiliproteins, which contribute to light perception and light harvesting in oxygenic phototrophs (Adir et al., 2020; Fushimi and Narikawa, 2021). Despite the absence of both phytochromes and phycobiliproteins, the model photosynthetic organism *Chlamydomonas reinhardtii* contains HMOX1 and PCYA1 (phycocyanobilin ferredoxin oxidoreductase) that enable phycocyanobilin (PCB) production in the chloroplast (Duanmu et al., 2013; Rockwell et al., 2014). Previous studies on a Chlamydomonas *hmox1* mutant revealed that bilin is a promising chloroplast retrograde signal that regulates the expression of genes associated with the detoxification of reactive oxygen species (ROS) that are essential to alleviate oxidative stress during the diurnal dark-to-light transition (Duanmu et al., 2013, 2017). Bilin also functions in the chloroplast to maintain the stability of photosystem I (PSI) and to sustain a robust photosynthetic apparatus during photo-acclimation (Wittkopp et al., 2017). Additionally, bilin regulates chlorophyll biosynthesis in *C. reinhardtii* by promoting the activity of MgCh and the stability of the catalytic subunit of MgCh (CHLH1) by binding GUN4, a key regulator of MgCh that interacts with CHLH1 (Zhang et al., 2021). These studies reveal the critical role of bilin signaling in photo-acclimation and maintenance of photosynthesis.

The bilin signal transduction pathway has not been elucidated. Identification of key regulatory components involved in bilin signaling and characterization of their biological functions are essential for understanding the mechanistic details of bilin signaling. We employed a plasmid-based method for random insertional mutagenesis to identify *hmox1* suppressors and aimed to isolate components related to bilin signaling. This study describes one such *hmox1* suppressor named *ho1su1*, which grew similar to wild-type *C. reinhardtii* cells in the light. The loss of CHLH1 and PSI-related proteins LHCA1 and PSAD was fully rescued in *ho1su1*, and bilin was surprisingly found to accumulate in *ho1su1* despite the absence of HMOX1. Our study, therefore, reveals the presence of an HMOX1-independent bilin biosynthetic pathway in Chlamydomonas cells.

Materials and methods

Chlamydomonas strains and growth conditions

C. reinhardtii strains 4A+ (wild-type, mating type plus, mt+), *hmox1* (mt+), *ho1*C2 (genetically complemented strain of *hmox1*), and *hmox2* were described previously (Duanmu et al., 2013). The 4A− (wild-type, mating type minus, mt-) was ordered from the Chlamydomonas Resource Center. The *hmox1* suppressor *ho1su1* (mt+) was generated in this study. All Chlamydomonas strains were maintained on Tris-acetate-phosphate (TAP) plates at 22–25°C in a 20-h dark/4-h light cycle (∼10 μmol photons m^{-2} s^{-1}). For growth comparisons, similar numbers of cells resuspended in Tris-phosphate (TP) medium were spotted in TAP medium (mixotrophic growth) or TP medium (phototrophic growth) containing agar and were grown in different light intensities. For total protein extraction and protein accumulation (HMOX1, PSI-related proteins,

and CHLH1) analysis, cells were grown in a TAP medium under white light (~30 μmol photons m^{-2} s^{-1}) until they reached a logarithmic phase and were then harvested for protein extraction.

Generation of *hmox1* suppressors

The *hmox1* cells were resistant to paromomycin due to the insertion of a pBC1 plasmid into the genome (Duanmu et al., 2013) and were cultured in a TAP medium in white light (~30 μmol photons m^{-2} s^{-1}) until they reached a cell density of ~3 × 10^6 cells/mL and were harvested by centrifugation at 2,000 *g* for 5 min at 4°C. The cells were resuspended in a TAP medium supplemented with 60 mM sucrose to a density of ~10^8 cells/mL and maintained at 4°C for 15 min. Aliquots of 250 μL of cells were transformed with 200–500 ng of *Kpn*I-linearized pHyg3 plasmid containing a hygromycin resistance cassette using electroporation with the BTX Gemini X2 System (1,575 Ω resistance, 50 μF capacitance, and 800 V voltage). Cells were transferred to a TAP medium containing 60 mM sucrose and recovered for 24 h in dim light. Chlamydomonas cells were selected on a solid TP medium supplemented with 10 μg/mL hygromycin in high-intensity light (~400 μmol photons m^{-2} s^{-1}). Survival of transformants containing both hygromycin and paromomycin cassettes accumulated LHCA1, PSAD, and CHLH1 and were also insensitive to high-intensity light were regarded as *hmox1* suppressors.

Genetic analysis of suppressor *ho1su1*

The *ho1su1* (mt+) was crossed to 4A− (mt−) to generate complete tetrads for genetic analysis and for evaluating the cosegregation of the suppression phenotype with the pHyg3 insertion. In brief, gametes from *ho1su1* and 4A− were induced and mated to form zygotes as described previously (Zhang et al., 2021). Zygotes were transferred to a solid TAP medium in white light (~30 μmol photons m^{-2} s^{-1}) to germinate. The four progeny of the germinating zygote (tetrad) were observed with an inverted microscope and separated using a glass needle. Progeny from complete tetrads were grown on a solid TAP medium and used for phenotypic and genetic analyses.

Thermal asymmetric interlaced polymerase chain reaction

TAIL-PCR was used to identify genomic sequences flanking the linearized-pHyg3 insertion in *ho1su1* (Dent et al., 2005; Wang et al., 2014). Specific primers (DP4/DP3/DP2 and UP4/UP3/UP2) were designed to amplify the sequences that flank the linearized-pHyg3, both downstream and upstream of the hygromycin resistance gene cassette (see **Supplementary Figure 3A**) and used along with the degenerate primer RMD227 for primary, secondary, and tertiary rounds of TAIL-PCR reactions. Primers used in this study are listed in **Supplementary Table 1**. In brief, 20–50 ng genomic DNA from *ho1su1* were used as DNA templates for primary reactions with GoTaq green master mix (Promega, Madison, WI, United States), containing 0.2 μM of specific primer (DP4 or UP4), 1 μM of degenerate primer RMD227, and 10% DMSO. For the second round reaction, the 50-fold diluted primary reaction products were used as DNA templates with GoTaq green master mix, containing 0.2 μM DP3 or UP3, 1 μM RMD227, and 10% DMSO. Then, 1 μL of the 50-fold diluted secondary TAIL-PCR product was used for the tertiary round reactions with GoTaq green master mix, containing 0.2 μM DP2 or UP2, 1 μM RMD227, and 10% DMSO. Parameters for three rounds of TAIL-PCR reactions were set up as previously reported (Dent et al., 2005; Wang et al., 2014). Agarose gel electrophoresis was used for separating TAIL-PCR products. DNA fragments that were extracted from agarose gels were sequenced.

Plasmid rescue

The plasmid rescue method was also used to identify genomic sequences flanking the linearized-pHyg3 insertion in *ho1su1*. In brief, genomic DNA from *ho1su1* was digested with *Pst*I. Then, the digested genomic DNA was self-ligated using T4 DNA ligase (Thermo Fisher Scientific, Waltham, MA, United States). Competent *E. coli* Tans1-T1 (TransGen, Beijing, China) was transformed with the products of the ligation reaction. Transformants were selected on Luria-Bertani (LB) plates supplemented with 100 μg/mL ampicillin. Single bacterial colonies were cultured and plasmids were extracted and compared using agarose gel electrophoresis and DNA sequence analyses.

Reverse transcription-PCR

Total RNA was extracted from 4A+, *hmox1,* and *ho1su1* using the TransZol plant kit as recommended by the manufacturer (Transgen, Beijing, China). Contaminating genomic DNA was removed using a DNaseI treatment. RNA was reverse transcribed using an oligo dT primer (Zhang et al., 2018) and the M-MLV reverse transcriptase (Takara, Kusatsu, Shiga, Japan). cDNA obtained from the reverse transcription reaction was used as a template for the amplification of the coding sequence of *HMOX1* using the primers detailed in **Supplementary Table 1**.

Rapid amplification of cDNA ends

5′RACE assays were performed to amplify the 5′-end of *HMOX1* transcripts from 4A+, *hmox1,* and *ho1su1* as recommended by a previously published method (Scotto-Lavino et al., 2006). In brief, DNaseI-treated total RNA, primer G1 targeting exon2 of *HMOX1,* and M-MLV reverse transcriptase were used for the reverse transcription of the 5′-end of the *HMOX1* mRNA. The product was ligated to poly(G) at the 5′-end and then used as a template for the 1st round of amplification with primers Qo, Qc, and gene-specific primer G2 targeting exon2 of *HMOX1*. The PCR product was diluted 10-fold and used as a template for further PCR amplification (2nd round) with primer Qi and gene-specific primer G3 spanning exon1 and exon2 of *HMOX1*. The final PCR product was analyzed using agarose gel electrophoresis and sequenced. Alternatively, the final PCR product was ligated into the pEASY-T5 Zero cloning vector (Transgen, Beijing, China) and introduced into competent *E. coli* Tans1-T1. Colonies that yielded PCR products larger than 250 bp when they were analyzed with M13F and M13R primers were used for plasmid extraction. Plasmids were sequenced to confirm they contained cDNA sequences derived from various types of *HMOX1* transcripts from 4A+, *hmox1,* and *ho1su1*.

Chloroplast expression of a bilin-binding reporter

To evaluate the accumulation of PCB in *hmox1* and *ho1su1*, the cyanobacterial bilin reporter NpF2164g5 from *Nostoc punctiforme* was fused with a twin-strep tag (STII) and inserted into the p322-PsbDp-AtpAp.aadA vector (Duanmu et al., 2013). The resulting plasmid was used for chloroplast transformation experiments with *hmox1* and *ho1su1* using particle bombardment with the PDS-1000/He system (BioRad, California, United States). The bombarded cells were transferred to a solid TAP medium containing 400 μg/mL spectinomycin. Positive transformants that expressed NpF2164g5-STII were identified using PCR and immunoblotting analyses and were further selected with at least 4∼5 rounds of growth on solid TAP medium supplemented with 400 μg/mL spectinomycin to achieve chloroplast DNA homoplasmy. Transgenic lines were named *hmox1:NpF2164g5-STII* and *ho1su1:NpF2164g5-STII*, respectively. NpF2164g5-STII purification was performed using Strep-tag II magnetic beads (Beaver, Suzhou, China) following the protocol recommended by the manufacturer. Purified NpF2164g5-STII protein was concentrated and used for zinc-dependent fluorescence assays to evaluate the presence or absence of covalently bound PCB as described previously (Zhang et al., 2018).

Expression of truncated HMOX1 and HMOX2 in *hmox1*

The coding region of the truncated *HMOX1* (HMOX1ΔTP, amino acids 61–263, without the predicted chloroplast transit peptide) was fused with the STII tag and cloned into the PsaD-Ble vector. The full-length *HMOX2* genomic DNA was inserted into the pHSP70/RbcS2-Ble vector. The resulting plasmids were digested with *Not*I and *Kpn*I and were introduced into *hmox1* cells using electroporation. Transformants were selected on TAP plates supplemented with 10 μg/mL zeocin. Positive transformants accumulating truncated HMOX1 and HMOX2 were named *hmox1:HMOX1ΔTP-STII* and *hmox1:HMOX2*, respectively.

Protein extraction and immunoblotting analyses

Extraction of total protein from Chlamydomonas and immunoblotting analyses were performed as previously described (Duanmu et al., 2013). Anti-LHCA1 (PHY2510S), anti-STII (PHY1926A), and anti-CHLH1 (PHY5508S) antibodies were obtained from PhytoAB (San Jose, CA, United States). Anti-CP29 and anti-D1 antibodies were obtained from Dr. Jean-David Rochaix (University of Geneva). Anti-HMOX1 and anti-HMOX2 were produced previously (Duanmu et al., 2013). Anti-PSAD (AS09 461) antibodies was purchased from Agrisera (Vännäs, Sweden). All antibodies were used at 1,000-fold dilutions.

Determination of intracellular reactive oxygen species content in chlamydomonas cells

Chlamydomonas cells were grown under continuous low light (∼30 μmol photons m^{-2} s^{-1}) until reaching a logarithmic phase. Then, cells were diluted in TAP medium to a density around 1∼2 × 10^6 cells/mL and incubated in dark for 24 h. About 2 mL of cell culture were collected by centrifugation and resuspended in an equal volume of TAP medium supplemented with 10 μM 2′,7′-dichlorofluorescein diacetate (DCFH-DA, Sigma Aldrich). Half of the cell cultures were grown in the dark for 30 min, while the other half of the cell cultures were exposed to light (∼200 μmol photons m^{-2} s^{-1}) for 30 min. Cells were then washed three times with TAP medium and resuspended in 500 μL of TAP medium. The fluorescence of dichlorofluorescein (DCF) was detected by a microplate reader (Tecan, Männedorf, Switzerland; excitation at 485 nm and emission at 530 nm). Two biological replicates were performed.

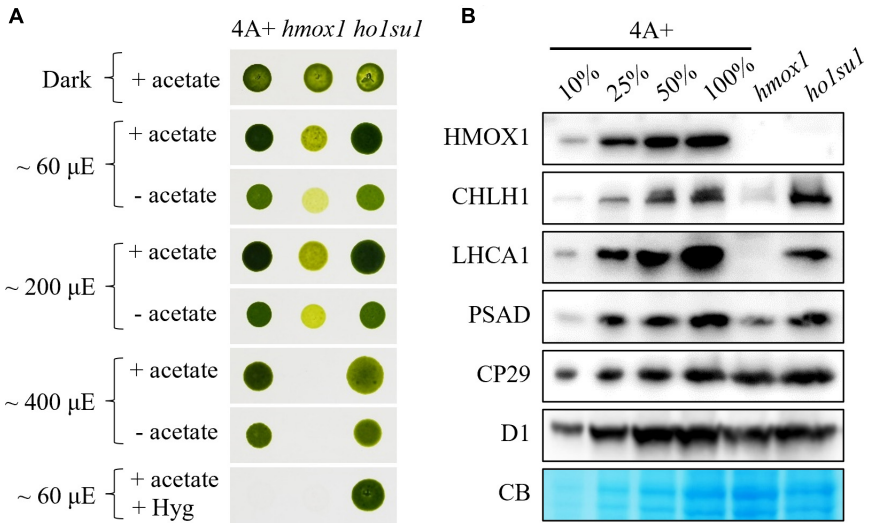

FIGURE 1
Phenotypic analysis of the *hmox1* suppressor *ho1su1*. **(A)** Mixotrophic (+ acetate) and phototrophic (– acetate) growth of 4A+, *hmox1,* and *ho1su1* in different light intensities. Hyg, hygromycin. **(B)** Immunoblotting analysis of HMOX1, the catalytic subunit of MgCh (CHLH1), representative proteins from PSI (LHCA1 and PSAD) and PSII (CP29 and D1) in 4A+, *hmox1,* and *ho1su1* using specific antibodies. Coomassie blue staining (CB) was used to test for equal loading. Similar amounts of protein were loaded for each genotype. A dilution series (10, 25, and 50%) of total protein from wild-type 4A+ (100%) is provided to help evaluate protein abundance.

Results

Isolation of *hmox1* suppressors

To identify key components of a bilin-activated retrograde signaling mechanism, collections of plasmid-based random insertion mutants were screened for mutants with partially or completely recovered phototrophic growth in the photosynthesis-deficient *hmox1* mutant background. As reported previously, phototrophic growth and the accumulation of the catalytic subunit of MgCh and the PSI reaction center and antenna proteins were significantly reduced in *hmox1* relative to wild-type (Duanmu et al., 2013; Wittkopp et al., 2017; Zhang et al., 2021). Indeed, *hmox1* was unable to survive in light intensity of approximately 400 µmol photons m^{-2} s^{-1} (**Figure 1A**). To screen *hmox1* suppressors, the *Kpn*I-linearized pHyg3 plasmid containing a hygromycin resistance gene cassette was introduced into *hmox1* cells using electroporation, and transformants were selected using phototrophic growth conditions (i.e., TP medium without acetate) at a lethal light intensity for *hmox1* (i.e., approximately 400 µmol photons m^{-2} s^{-1}) (**Supplementary Figure 1**). Transformants that grew in these selective conditions were regarded as candidate suppressors.

Eight candidate *hmox1* suppressors were obtained and characterized. We found that the mixotrophic (with acetate) and phototrophic (without acetate) growth rates of these suppressors in different light intensities were similar to wild-type 4A+. In contrast, increasing light intensities inhibited the growth rate of *hmox1* (**Supplementary Figure 2**). However, most of these suppressors (i.e., *ho1su2* to *ho1su8*) were not resistant to hygromycin, which indicated that these candidate suppressors lost the hygromycin cassette. The loss of hygromycin resistance was probably due to the low selective concentration of hygromycin, or the instability of hygromycin under this specific harsh condition used for suppressor screening. Only *ho1su1* was resistant to hygromycin and, therefore, presumably contains an intact hygromycin resistance gene in its genome (**Supplementary Figure 2** and **Figure 1A**).

Rescue of phototrophic growth in *ho1su1*

We next assessed the effect of the suppressor mutation in *ho1su1* on the stability of PSI, photosystem II (PSII), and the catalytic subunit of MgCh (CHLH1). Consistent with previous observations (Wittkopp et al., 2017; Zhang et al., 2021), the levels of CHLH1, the antenna protein (LHCA1), and the reaction center protein (PSAD) of PSI were dramatically reduced in *hmox1* (**Figure 1B**). In contrast, in *ho1su1*, these proteins accumulated to levels that were similar to wild-type 4A+ (**Figure 1B**). Furthermore, there were no obvious differences in the levels of the PSII antenna protein CP29 and the core subunit D1 in 4A+, *hmox1,* and *ho1su1* (**Figure 1B**). These data indicated that the disruption of *HMOX1* and the second site mutations in *ho1su1* had no impact on the accumulation of PSII proteins. These results demonstrate that the phototrophic

10.3389/fmicb.2022.956554

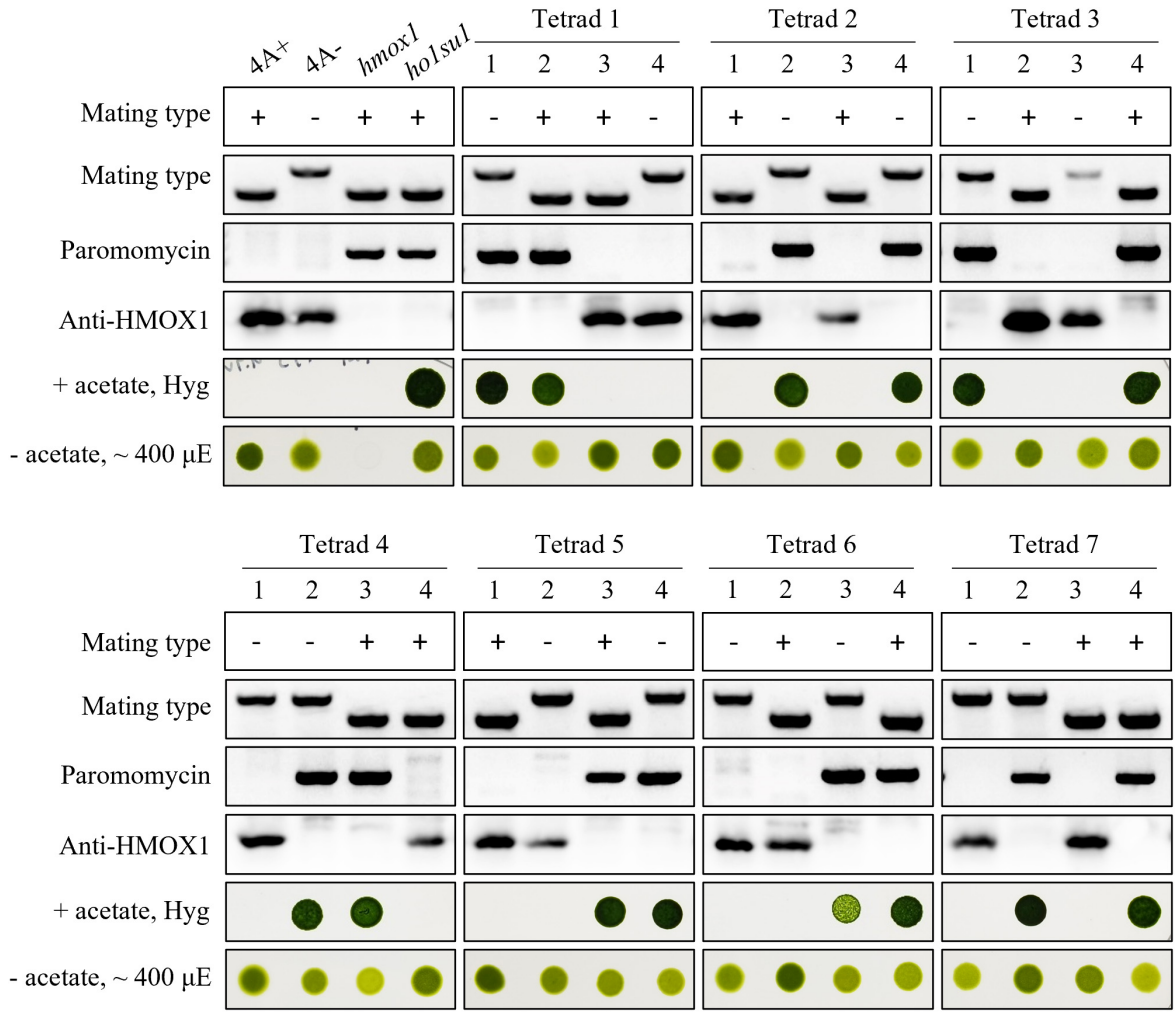

FIGURE 2
Genetic analyses of *ho1su1*. Progeny from seven complete tetrads derived from crosses between 4A− (mt−) and *ho1su1* (mt+) were used for genetic linkage analysis. Mating type, antibiotic resistance against paromomycin and hygromycin (Hyg), accumulation of HMOX1, and photoautotrophic growth (− acetate) in light intensity of approximately 400 µE were analyzed. PCR amplification of specific DNA fragments was used to test mating type and to test for the presence of the paromomycin resistance gene cassette.

growth phenotypes of *ho1su1* and 4A+ are indistinguishable and indicate that the suppressor mutation fully restored the photosynthetic deficiency of *hmox1*.

Co-segregation of the plasmid insert with the suppressor phenotype

Tetrad analysis was performed to evaluate the genetic linkage between the pHyg3 insertion and the suppressor phenotype in *ho1su1*. Seven complete tetrads from the *ho1su1* (mt+) × 4A− (mt−) cross were isolated and analyzed (Figure 2). Surprisingly, each tetrad contained two progeny that were antibiotic sensitive and two progeny that were resistant to both hygromycin and paromomycin. These data indicate that the pHyg3 insertion and the *HMOX1* gene were located on the same chromosome (Figure 2). Notably, the phototropic growth phenotype of the progeny from these tetrads was similar to wild-type (4A+, 4A−) and *ho1su1*, regardless of the presence or absence of the HMOX1 protein (Figure 2). These results indicate that the pHyg3 insertion is genetically linked to the suppressor phenotype of *ho1su1*.

Mapping of plasmid insertion sites in *ho1su1*

To identify genomic sequences flanking the pHyg3 insert in *ho1su1*, TAIL-PCR was performed with primers targeting downstream (DP4, DP3, and DP2) and upstream (UP4, UP3,

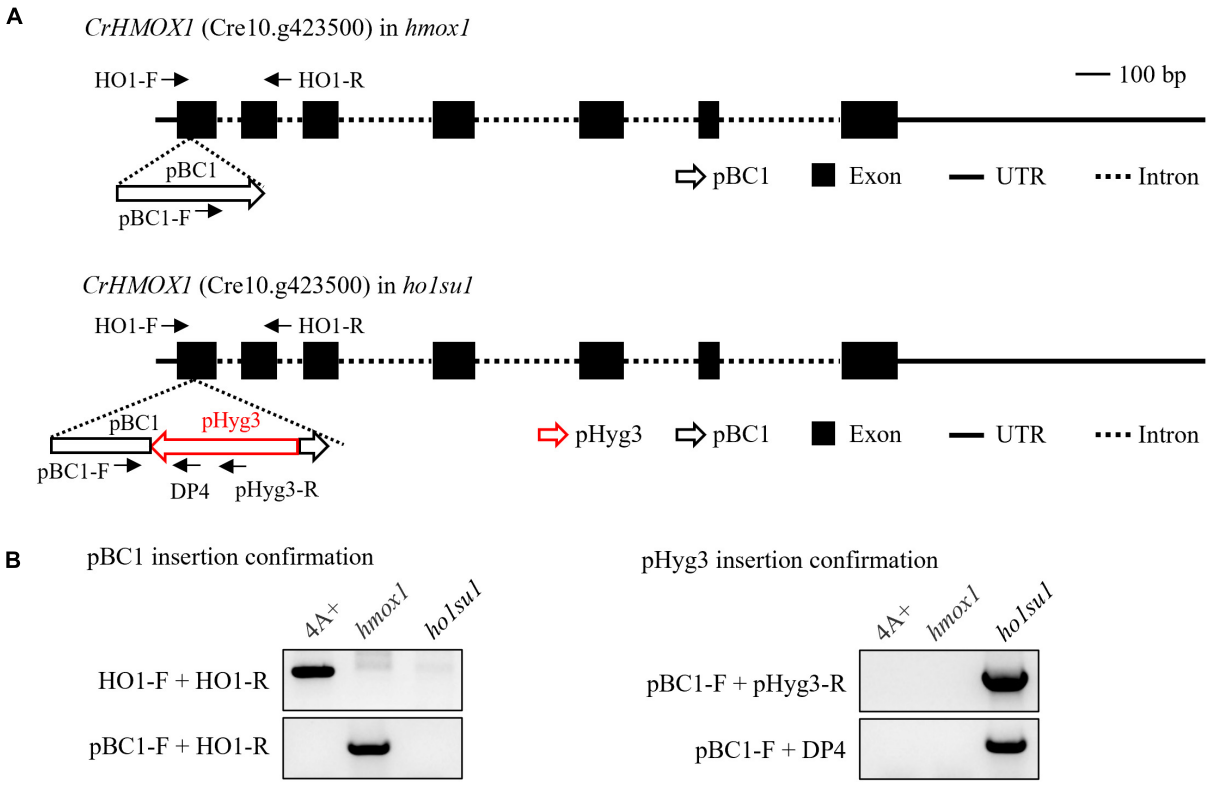

FIGURE 3
Identification of the pHyg3 insertion site in *ho1su1*. **(A)** Schematic diagram of the paromomycin resistance gene cassette (pBC1) and the hygromycin resistance gene cassette (pHyg3) insertion sites in *hmox1* (upper) and *ho1su1* (lower). The arrows represent primers used for plasmid insert analysis. **(B)** Analysis of pBC1 and pHyg3 insertion sites in *hmox1* and *ho1su1* using PCR and primers depicted in **(A)**.

and UP2) regions of the hygromycin resistance gene cassette (**Supplementary Figure 3A**). We obtained a PCR product downstream of pHyg3 but could not amplify the upstream flanking sequences (**Supplementary Figure 3B**). The TAIL-PCR product was sequenced and found to match the sequence of the pBC1 insert (i.e., the paromomycin resistance gene cassette) that disrupts *HMOX1* in the *hmox1* mutant (**Figure 3A**). Indeed, we found that in *ho1su1*, the linearized pHyg3 is inserted exactly in the pBC1 cassette.

Plasmid rescue was also used to determine the genomic sequences flanking the pHyg3 insert in *ho1su1*. The *Pst*I-digested genomic DNA of *ho1su1* was self-ligated and used to transform competent *E. coli* cells (**Supplementary Figure 3C**). Plasmids were extracted from the five colonies. These plasmids were digested using *Pst*I and plasmid backbones were sequenced (**Supplementary Figure 3D**). We found that the flanking sequences from these five backbones all matched the sequences from pHyg3 and pBC1, which indicates the presence of both hygromycin and paromomycin cassettes in these plasmids. These data were also confirmed using PCR analyses (**Supplementary Figure 3E**). These results revealed that the pHyg3 cassette in *ho1su1* was inserted into the pBC1 cassette located in exon 1 of *HMOX1* (**Figure 3A**). These data were also confirmed using PCR analyses with pBC1- and pHyg3-specific primer pairs (**Figure 3B**).

HMOX1 transcripts in *hmox1* and *ho1su1*

Due to the genetic linkage between the pHyg3 insert and the suppression phenotype of *ho1su1*, we hypothesized that the pHyg3 insertion might create a specific form of the HMOX1 protein and this specific HMOX1 protein could rescue the phototrophic growth of *hmox1*. To this end, we used RT-PCR to test whether *HMOX1* was transcribed in *hmox1* and *ho1su1*. In contrast to 4A+, the full-length *HMOX1* transcript was absent in *hmox1* and *ho1su1* as indicated with PCR assays that utilized the primer pairs F1 + R1. However, truncated *HMOX1* transcripts were found to be present in *hmox1* and *ho1su1* as indicated with PCR assays that utilized the primer pairs F2 + R1 and F3 + R1 (**Supplementary Figures 4A,B**). The truncated form of the *HMOX1* transcript in *ho1su1* might be translated *in vivo* and accumulated as an enzymatically active protein that rescues the phototrophic-deficient phenotype of *hmox1*.

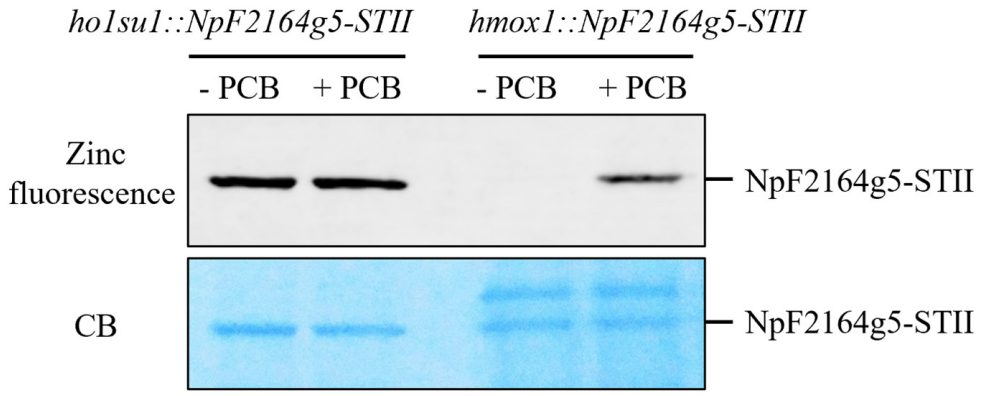

FIGURE 4
Bilin biosynthesis in *ho1su1*. Cyanobacterial NpF2164g5, a PCB binding reporter, was expressed in the chloroplasts of *hmox1* and *ho1su1*. Affinity purified NpF2164g5-STII protein was assembled with (+ PCB) or without PCB (– PCB) *in vitro* and detected using a zinc-dependent fluorescence assay to test whether a covalently bound PCB was present. Upper panel, zinc fluorescence; lower panel, Coomassie blue staining (CB). The Zinc-dependent fluorescent signal indicates that PCB is covalently bound to the NpF2164g5-STII protein.

Reactivated bilin synthesis in *ho1su1*

It was previously demonstrated that the *hmox1* mutant could not synthesize bilins in the chloroplast and, therefore, was deficient in phototrophic growth (Duanmu et al., 2013; Wittkopp et al., 2017). To determine whether the suppressor phenotype of *ho1su1* was caused by reactivated bilin biosynthesis in the chloroplast, the bilin-binding reporter NpF2164g5 from *Nostoc punctiforme* was expressed in the chloroplast of *hmox1* and *ho1su1*. Affinity-purified NpF2164g5 protein from *hmox1* and *ho1su1* were assembled with or without PCB *in vitro* and tested for the presence or absence of covalently bound PCB using a zinc-dependent fluorescence assay. Consistent with a previous report on the deficiency of PCB biosynthesis in *hmox1* (Duanmu et al., 2013), a fluorescence signal was not detected from the NpF2164g5 protein that was purified from *hmox1* unless exogenous PCB was added to the assay. These data indicate that PCB was absent in the NpF2164g5 protein from *hmox1* (**Figure 4**). In contrast, we detected fluorescence from the NpF2164g5 protein that was purified from *ho1su1* regardless of whether exogenous PCB was added to the assay (**Figure 4**). These data indicate that NpF2164g5 binds PCB in *ho1su1* and, therefore, that PCB is synthesized in *ho1su1*.

Overexpression of HMOX2 and truncated HMOX1 could not rescue the phototrophic growth phenotype of *hmox1*

The accumulation of PCB in *ho1su1* indicates that its precursor BV IXα is synthesized in *ho1su1*. *C. reinhardtii* contains two enzymes that catalyze the conversion of heme to BV IXα, including chloroplastic HMOX1 and cytosolic HMOX2 (Duanmu et al., 2013). Because *HMOX1* was still transcribed in *hmox1* and *ho1su1*, we performed 5′RACE to determine the 5′-end sequences of *HMOX1* transcripts in these two strains (**Supplementary Figure 4C**). Most of the *HMOX1* cDNA sequences prepared from *hmox1* and *ho1su1* were the same as the *HMOX1* cDNA prepared from 4A+ (shown as black letters in **Supplementary Figure 4D**), with the exception of approximately 140 bp from the 5′ end (shown as red letters in **Supplementary Figure 4D**). There was approximately 30 bp that was different at the 5′ end of *HMOX1* in *ho1su1* relative to *hmox1*. Three types of *HMOX1* transcript sequences were confirmed in 4A+, *hmox1*, and *ho1su1* using PCRs with the F0 and R1 primers (**Supplementary Figures 4E, 5**). Based on the sequences of these transcripts, the only possible open reading frame (ORF) encoding an active heme oxygenase in *ho1su1* might be translated into a truncated HMOX1 protein that contains amino acids 61–263 relative to the HMOX1 protein from 4A+ (shown as black letters on a yellow background in **Supplementary Figure 4D**) and, therefore, lacks the putative chloroplast transit peptide (i.e., amino acids 1–30).

To test whether the putative-truncated HMOX1 protein could rescue the phototrophic-deficient phenotype of *hmox1*, we expressed the truncated HMOX1 protein containing amino acids 61–263 (hereafter referred to as HMOX1ΔTP) in *hmox1* and selected three independent lines that expressed HMOX1ΔTP (**Figure 5A**). Growth comparisons showed that expression of truncated HMOX1 could not complement the light-sensitive phototrophic growth deficiency of *hmox1* (**Figure 5C**).

HMOX2 protein abundance is very low in 4A+ and *hmox1* and is undetectable in immunoblotting assays as previously reported (Duanmu et al., 2013). We used the HSP70/RbcS2

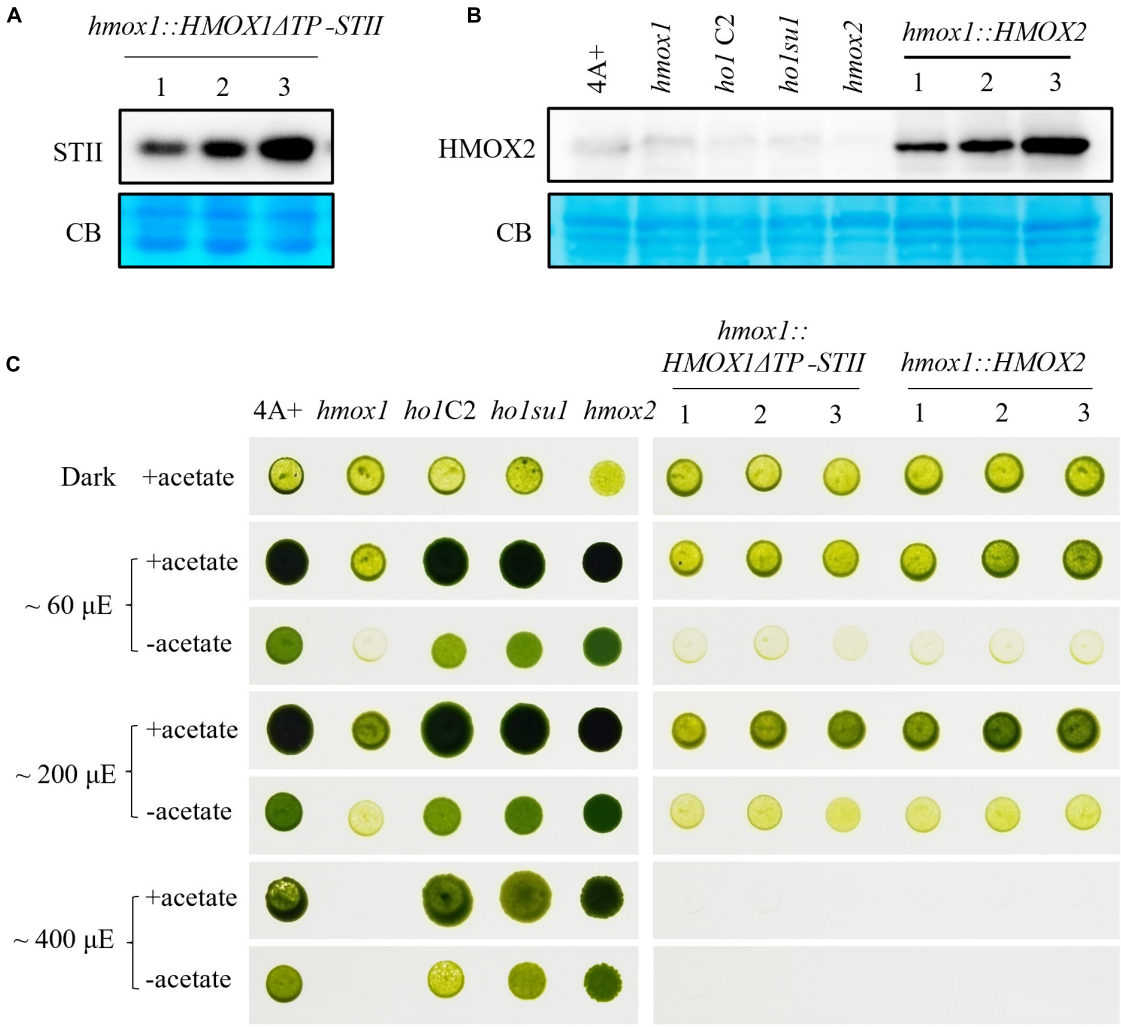

FIGURE 5
Characterization of *hmox1* expressing either HMOX2 or truncated HMOX1. **(A)** Immunoblotting analysis of *hmox1* expressing HMOX1ΔTP-STII. An anti-STII tag antibody was used. **(B)** Immunoblotting analysis of different strains expressing the HMOX2 protein. Equal amounts of protein extracted from 4A+, *hmox1*, *ho1C2* (*hmox1* cDNA complemented line), *ho1su1*, *hmox2*, and *hmox1::HMOX2* (HMOX2 overexpression lines in *hmox1*) were analyzed using immunoblotting. Anti-HMOX2 antibodies were used. **(C)** Growth of 4A+, *hmox1*, *ho1C2*, *ho1su1*, *hmox2*, *hmox1::HMOX1ΔTP-STII*, and *hmox1::HMOX2*. The strains were grown on TAP (with acetate) or TP (without acetate) media at different fluence rates of light.

chimeric promoter to constitutively overexpress HMOX2 in *hmox1*. An immunoblotting analysis using HMOX2 antibodies indicated that all three independent *hmox1*::HMOX2 lines accumulated significantly elevated levels of HMOX2 protein (Figure 5B). However, all three lines demonstrated similar degrees of phototrophic growth deficiencies as *hmox1*. These data indicate that the overexpression of HMOX2 could not rescue the *hmox1* phenotype (Figure 5C).

These results ruled out the possibility that the restored bilin biosynthesis and rescued phototrophic growth of *ho1su1* were associated with the overexpression of HMOX2 or the accumulation of a truncated HMOX1. Since HMOX1 and HMOX2 are the only two heme oxygenases that are known to convert heme to BV in *C. reinhardtii*, we conclude that our data have uncovered the existence of an alternative bilin biosynthesis pathway that does not require classical heme oxygenases.

Discussion

The cyclic tetrapyrrole molecule heme is present in almost all organisms (Larkin, 2016; Sugishima et al., 2019). Heme serves as a cofactor for hemoproteins (cytochromes, hemoglobin, myoglobin, etc.) and performs essential functions in various biological processes (Shimizu et al., 2019; Ryter, 2021). Many organisms utilize heme as an iron source and use heme

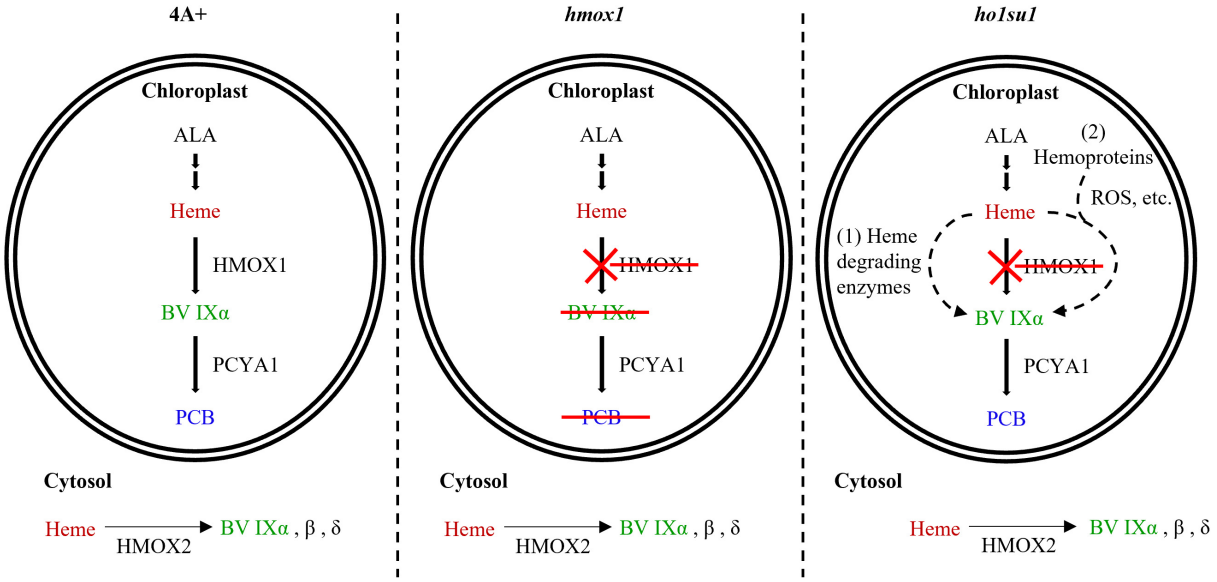

FIGURE 6
Model for bilin biosynthesis in *ho1su1*. In wild-type 4A+, heme is catabolized by HMOX1 and PCYA1 to yield BV IXα and PCB, respectively (left). In *hmox1*, BV IXα and PCB are not synthesized in the chloroplast due to the disruption of *HMOX1*, although PCYA1 still accumulates (middle). The cytosolic BV IXα produced by overexpressing HMOX2 or truncated HMOX1 is insufficient to support bilin biosynthesis in the chloroplast of *hmox1*. In *ho1su1*, PCB is produced in the absence of HMOX1 (right). Alternative pathways for bilin biosynthesis in *ho1su1* may include (1) the conversion of heme to BV IXα by unknown heme degrading enzymes and (2) reactive oxygen species (ROS) or other metabolites (e.g., ascorbic acid) attacking heme or hemoproteins to produce BV IXα. ALA, 5-aminolevulinic acid.

degrading enzymes to convert heme into pyrrole products, with the concomitant release of iron and carbon monoxide (Kikuchi et al., 2005; Mahawar and Shekhawat, 2018). Several groups of heme oxygenases (HMOXs/HOs) with distinct structures and regiospecificities for heme cleavage have been well-documented (Lyles and Eichenbaum, 2018). When the HO-1 family members (e.g., HMOX1, HemO, and HmuO) degrade heme, they generally yield BV IXα (Wilks and Ikeda-Saito, 2014). In contrast to HO-1, the IsdG family of HOs converts heme to a mixture of formaldehyde and staphylobilin rather than biliverdins (Matsui et al., 2013). PigA and the HO groups containing the HemS motif convert heme into β and δ isoforms of BV (Friedman et al., 2004; Onzuka et al., 2017; Li et al., 2021). Additionally, the HO group belonging to the FMN binding-like superfamily, such as HugZ, HutZ, and HupZ, also converts heme to either β or δ isoforms of BV (Lyles and Eichenbaum, 2018). Among the products formed by the oxidative cleavage of heme, BV IXα is further converted to bilirubin by biliverdin reductase (BVR) in mammals and other types of bilins by FDBRs in aerobic photosynthetic organisms (Tenhunen et al., 1970; Sugishima et al., 2019).

Bilin biosynthesis is of great importance for photosynthetic organisms because of the essential roles of bilins in light sensing, photon capture, and photoacclimation (Rockwell et al., 2014; Duanmu et al., 2017; Bachy et al., 2022). The Chlamydomonas *hmox1* mutant is deficient in bilin biosynthesis due to the disruption of *HMOX1*, although the PCYA1 protein accumulates at similar levels relative to wild-type 4A+ (Duanmu et al., 2013). The generation of PCB in *ho1su1* indicates that *ho1su1* synthesizes BV IXα from heme. *C. reinhardtii* employs three types of heme oxygenases for heme metabolism, including the chloroplast-localized HMOX1 (Cre10.g423500) that converts heme into BV IXα, the cytosolic HMOX2 (Cre11.g467753) that converts heme into α, β, and δ isoforms of BV, and the IsdG family protein LFO1 (Cre07.g312300) that converts heme into products structurally different from BV (Duanmu et al., 2013; Lojek et al., 2017). BV IXα could be used as a substrate for chloroplast-localized PCYA1 to synthesize PCB. Overexpression of the truncated HMOX1 and HMOX2 could not rescue the phototrophic growth deficiency of *hmox1* (**Figure 5**), which indicates that the cytosolic BV IXα produced by either the hypothetical truncated HMOX1 or HMOX2 was insufficient to activate the PCB production in the chloroplast. These results provide evidence for an alternative bilin biosynthetic pathway possibly supported by uncharacterized heme degrading enzyme(s) in *C. reinhardtii* (**Figure 6**).

A previous study demonstrated that Arabidopsis HOZ (At3g03890)—a protein homologous to HugZ—is chloroplast localized and structurally related to non-canonical HMOX and possesses heme degrading activity that yields BV *in vitro* (Wang et al., 2020). The biological function of HOZ in tetrapyrrole metabolism in Arabidopsis requires further characterization.

Additionally, there are two proteins that are homologous to HOZ (Cre12.g520200 and Cre02.g098250) in *C. reinhardtii* that may contribute to the degradation of heme and bilin biosynthesis. However, these two genes are not associated with the same chromosome as *HMOX1*. Based on genetic linkage analysis, we excluded the possibility of these two proteins functioning in BV IXα and bilin biosynthesis in *ho1su1*.

In addition to enzyme-catalyzed heme metabolism, heme could also be subjected to non-enzymatic degradation (Nagababu and Rifkind, 2004; Kikuchi et al., 2005). ROS and other metabolites (i.e., ascorbic acid) can catalyze the conversion of heme into various pyrrole products, including BV (Nagababu and Rifkind, 2004). It was reported that hydrogen peroxide (H_2O_2) could degrade ferric heme to yield carbon monoxide and BV IXα (Jones et al., 1973). Ascorbic acid randomly attacks the methene bridges of heme and hemoproteins to generate mixtures of four BV isomers (α, β, γ, and δ) (Bonnett and McDonagh, 1973). Our data showed that the *hmox1* mutant contained a much higher level of ROS than 4A+, whereas the ROS content in *ho1su1* is intermediate between *hmox1* and 4A+ (**Supplementary Figure 6**). Therefore, it is reasonable to hypothesize that heme or hemoproteins in the chloroplast probably undergoes a non-enzymatic degradation process to produce BV IXα, which is further utilized by PCYA1 to generate PCB in *ho1su1* (**Figure 6**). Further identification of the suppressor gene(s) and investigation of the interactions between its protein product and ROS accumulation and/or heme degradation should be the focus of future work.

Tetrapyrrole biosynthesis and regulation are elegantly controlled to meet the demands of critical cellular processes (Mochizuki et al., 2010). Our study demonstrates that an alternative HMOX1-independent bilin biosynthetic pathway is probably fulfilled by an unknown heme degrading enzyme(s) or non-enzymatic degradation process(es). Identification of genes associated with this alternative pathway should provide deeper insights into elucidating bilin biosynthesis and the regulatory networks of retrograde bilin signaling, which is essential to sustain robust photosynthesis in *C. reinhardtii*.

Data availability statement

The raw data supporting the conclusions of this article will be made available by the authors, without undue reservation.

Author contributions

WZ, QF, and DD designed the research and analyzed the results. WZ, RD, WS, and ZL performed the experiments. WZ, RL, and DD wrote and edited the manuscript. All authors read and approved the manuscript.

Funding

This research was funded by the National Natural Science Foundation of China (Grant No. 32070268), the China Postdoctoral Science Foundation (Grant No. 2021M701347), the Fundamental Research Funds for the Central Universities Program 2662020SKPY007, HZAU-AGIS Cooperation Fund (SZYJY2022005), the Postdoctoral Creative Research Position of Hubei Province of China (2021), and the Bai Chuan fellowship of College of Life Science and Technology, Huazhong Agricultural University.

Acknowledgments

We thank J. Clark Lagarias (University of California, Davis) for helpful suggestions for this study.

Conflict of interest

The authors declare that the research was conducted in the absence of any commercial or financial relationships that could be construed as a potential conflict of interest.

Publisher's note

Supplementary material

The Supplementary Material for this article can be found online at: https://www.frontiersin.org/articles/10.3389/fmicb.2022.956554/full#supplementary-material

References

Adir, N., Bar-Zvi, S., and Harris, D. (2020). The amazing phycobilisome. *Biochim. Biophys. Acta Bioenerg.* 1861:148047. doi: 10.1016/j.bbabio.2019.07.002

Bachy, C., Wittmers, F., Muschiol, J., Hamilton, M., Henrissat, B., and Worden, A. Z. (2022). The Land-Sea Connection: Insights Into the Plant Lineage from a Green Algal Perspective. *Annu. Rev. Plant Biol.* 73, 585–616. doi: 10.1146/annurev-arplant-071921-100530

Berry, J. O., Yerramsetty, P., Zielinski, A. M., and Mure, C. M. (2013). Photosynthetic gene expression in higher plants. *Photosynth. Res.* 117, 91–120. doi: 10.1007/s11120-013-9880-8

Bonnett, R., and McDonagh, A. F. (1973). The meso-reactivity of porphyrins and related compounds. VI. Oxidative cleavage of the haem system. The four isomeric biliverdins of the IX series. *J. Chem. Soc. Perkin 1.* 9, 881–888. doi: 10.1039/p19730000881

Brzezowski, P., Richter, A. S., and Grimm, B. (2015). Regulation and function of tetrapyrrole biosynthesis in plants and algae. *Biochim. Biophys. Acta* 1847, 968–985. doi: 10.1016/j.bbabio.2015.05.007

Busch, A. W., and Montgomery, B. L. (2015). Interdependence of tetrapyrrole metabolism, the generation of oxidative stress and the mitigative oxidative stress response. *Redox Biol.* 4, 260–271. doi: 10.1016/j.redox.2015.01.010

Chan, K. X., Phua, S. Y., Crisp, P., Mcquinn, R., and Pogson, B. J. (2016). Learning the Languages of the Chloroplast: Retrograde Signaling and Beyond. *Annu. Rev. Plant Biol.* 67, 25–53. doi: 10.1146/annurev-arplant-043015-111854

Dent, R. M., Haglund, C. M., Chin, B. L., Kobayashi, M. C., and Niyogi, K. K. (2005). Functional genomics of eukaryotic photosynthesis using insertional mutagenesis of Chlamydomonas reinhardtii. *Plant Physiol.* 137, 545–556. doi: 10.1104/pp.104.055244

Duanmu, D., Casero, D., Dent, R. M., Gallaher, S., Yang, W., Rockwell, N. C., et al. (2013). Retrograde bilin signaling enables Chlamydomonas greening and phototrophic survival. *Proc. Natl. Acad. Sci. U.S.A.* 110, 3621–3626. doi: 10.1073/pnas.1222375110

Duanmu, D., Rockwell, N. C., and Lagarias, J. C. (2017). Algal light sensing and photoacclimation in aquatic environments. *Plant Cell Environ.* 40, 2558–2570. doi: 10.1111/pce.12943

Friedman, J., Lad, L., Li, H., Wilks, A., and Poulos, T. L. (2004). Structural basis for novel delta-regioselective heme oxygenation in the opportunistic pathogen *Pseudomonas aeruginosa*. *Biochemistry* 43, 5239–5245. doi: 10.1021/bi049687g

Fushimi, K., and Narikawa, R. (2021). Phytochromes and Cyanobacteriochromes: Photoreceptor Molecules Incorporating a Linear Tetrapyrrole Chromophore. *Adv. Exp. Med. Biol.* 1293, 167–187. doi: 10.1007/978-981-15-8763-4_10

Jarvis, P., and López-Juez, E. (2013). Biogenesis and homeostasis of chloroplasts and other plastids. *Nat. Rev. Mol. Cell Biol.* 14, 787–802. doi: 10.1038/nrm3702

Jones, P., Prudhoe, K., and Robson, T. (1973). Oxidation of deuteroferrihaem by hydrogen peroxide. *Biochem. J.* 135, 361–365. doi: 10.1042/bj1350361

Kikuchi, G., Yoshida, T., and Noguchi, M. (2005). Heme oxygenase and heme degradation. *Biochem. Biophys. Res. Commun.* 338, 558–567. doi: 10.1016/j.bbrc.2005.08.020

Larkin, R. M. (2014). Influence of plastids on light signalling and development. *Philos. Trans. R. Soc. Lond. B. Biol. Sci.* 369:20130232. doi: 10.1098/rstb.2013.0232

Larkin, R. M. (2016). Tetrapyrrole Signaling in Plants. *Front. Plant Sci.* 7:1586. doi: 10.3389/fpls.2016.01586

Li, M., and Kim, C. (2021). Chloroplast ROS and stress signaling. *Plant Commun.* 3:100264. doi: 10.1016/j.xplc.2021.100264

Li, S., Isiorho, E. A., Owens, V. L., Donnan, P. H., Odili, C. L., and Mansoorabadi, S. O. (2021). A noncanonical heme oxygenase specific for the degradation of c-type heme. *J. Biol. Chem.* 296:100666. doi: 10.1016/j.jbc.2021.100666

Lojek, L. J., Farrand, A. J., Wisecaver, J. H., Blaby-Haas, C. E., Michel, B. W., Merchant, S. S., et al. (2017). Chlamydomonas reinhardtii LFO1 Is an IsdG Family Heme Oxygenase. *mSphere* 2:e176–e117. doi: 10.1128/mSphere.00176-17

Lyles, K. V., and Eichenbaum, Z. (2018). From Host Heme To Iron: The Expanding Spectrum of Heme Degrading Enzymes Used by Pathogenic Bacteria. *Front. Cell Infect. Microbiol.* 8:198. doi: 10.3389/fcimb.2018.00198

Mahawar, L., and Shekhawat, G. S. (2018). Haem oxygenase: a functionally diverse enzyme of photosynthetic organisms and its role in phytochrome chromophore biosynthesis, cellular signalling and defence mechanisms. *Plant Cell Environ.* 41, 483–500. doi: 10.1111/pce.13116

Matsui, T., Nambu, S., Ono, Y., Goulding, C. W., Tsumoto, K., and Ikeda-Saito, M. (2013). Heme degradation by Staphylococcus aureus IsdG and IsdI liberates formaldehyde rather than carbon monoxide. *Biochemistry* 52, 3025–3027. doi: 10.1021/bi400382p

Mielecki, J., Gawroński, P., and Karpiński, S. (2020). Retrograde Signaling: Understanding the Communication between Organelles. *Int. J. Mol. Sci.* 21:6173. doi: 10.3390/ijms21176173

Mochizuki, N., Tanaka, R., Grimm, B., Masuda, T., Moulin, M., Smith, A. G., et al. (2010). The cell biology of tetrapyrroles: a life and death struggle. *Trends Plant Sci.* 15, 488–498. doi: 10.1016/j.tplants.2010.05.012

Nagababu, E., and Rifkind, J. M. (2004). Heme degradation by reactive oxygen species. *Antioxid. Redox Signal.* 6, 967–978. doi: 10.1089/ars.2004.6.967

Nagahatenna, D. S., Langridge, P., and Whitford, R. (2015). Tetrapyrrole-based drought stress signalling. *Plant Biotechnol. J.* 13, 447–459. doi: 10.1111/pbi.12356

Onzuka, M., Sekine, Y., Uchida, T., Ishimori, K., and Ozaki, S. I. (2017). HmuS from Yersinia pseudotuberculosis is a non-canonical heme-degrading enzyme to acquire iron from heme. *Biochim. Biophys. Acta Gen. Subj.* 1861, 1870–1878. doi: 10.1016/j.bbagen.2017.04.003

Rockwell, N. C., and Lagarias, J. C. (2017). Ferredoxin-dependent bilin reductases in eukaryotic algae: ubiquity and diversity. *J. Plant Physiol.* 217, 57–67. doi: 10.1016/j.jplph.2017.05.022

Rockwell, N. C., Lagarias, J. C., and Bhattacharya, D. (2014). Primary endosymbiosis and the evolution of light and oxygen sensing in photosynthetic eukaryotes. *Front. Ecol. Evol.* 2:66. doi: 10.3389/fevo.2014.00066

Ryter, S. W. (2021). Significance of Heme and Heme Degradation in the Pathogenesis of Acute Lung and Inflammatory Disorders. *Int. J. Mol. Sci.* 22:5509. doi: 10.3390/ijms22115509

Scotto-Lavino, E., Du, G., and Frohman, M. A. (2006). 5' end cDNA amplification using classic RACE. *Nat. Protoc.* 1, 2555–2562. doi: 10.1038/nprot.2006.480

Shimizu, T., Lengalova, A., Martínek, V., and Martínková, M. (2019). Heme: emergent roles of heme in signal transduction, functional regulation and as catalytic centres. *Chem. Soc. Rev.* 48, 5624–5657. doi: 10.1039/c9cs00268e

Singh, R., Singh, S., Parihar, P., Singh, V. P., and Prasad, S. M. (2015). Retrograde signaling between plastid and nucleus: a review. *J. Plant Physiol.* 181, 55–66. doi: 10.1016/j.jplph.2015.04.001

Sugishima, M., Wada, K., Unno, M., and Fukuyama, K. (2019). Bilin-metabolizing enzymes: site-specific reductions catalyzed by two different type of enzymes. *Curr. Opin. Struct. Biol.* 59, 73–80. doi: 10.1016/j.sbi.2019.03.005

Susek, R. E., Ausubel, F. M., and Chory, J. (1993). Signal transduction mutants of Arabidopsis uncouple nuclear CAB and RBCS gene expression from chloroplast development. *Cell* 74, 787–799. doi: 10.1016/0092-8674(93)90459-4

Tanaka, R., and Tanaka, A. (2007). Tetrapyrrole biosynthesis in higher plants. *Annu. Rev. Plant Biol.* 58, 321–346. doi: 10.1146/annurev.arplant.57.032905.105448

Tanaka, R., Kobayashi, K., and Masuda, T. (2011). Tetrapyrrole Metabolism in Arabidopsis thaliana. *Arabidopsis Book* 9:e0145. doi: 10.1199/tab.0145

Tenhunen, R., Ross, M. E., Marver, H. S., and Schmid, R. (1970). Reduced nicotinamide-adenine dinucleotide phosphate dependent biliverdin reductase: partial purification and characterization. *Biochemistry* 9, 298–303. doi: 10.1021/bi00804a016

Wang, J., Guo, Q., Li, X., Wang, X., and Liu, L. (2020). The Arabidopsis locus AT3G03890 encodes a dimeric beta-barrel protein implicated in heme degradation. *Biochem. J.* 477, 4785–4796. doi: 10.1042/BCJ20200712

Wang, L., Yamano, T., Kajikawa, M., Hirono, M., and Fukuzawa, H. (2014). Isolation and characterization of novel high-CO2-requiring mutants of Chlamydomonas reinhardtii. *Photosynth. Res.* 121, 175–184. doi: 10.1007/s11120-014-9983-x

Wilks, A., and Ikeda-Saito, M. (2014). Heme utilization by pathogenic bacteria: not all pathways lead to biliverdin. *Acc. Chem. Res.* 47, 2291–2298. doi: 10.1021/ar500028n

Wittkopp, T. M., Schmollinger, S., Saroussi, S., Hu, W., Zhang, W., Fan, Q., et al. (2017). Bilin-Dependent Photoacclimation in Chlamydomonas reinhardtii. *Plant Cell* 29, 2711–2726. doi: 10.1105/tpc.17.00149

Woodson, J. D. (2022). Control of chloroplast degradation and cell death in response to stress. *Trends Biochem. Sci.* S0968-0004(22)00069-X. doi: 10.1016/j.tibs.2022.03.010

Wu, G. Z., and Bock, R. (2021). GUN control in retrograde signaling: how GENOMES UNCOUPLED proteins adjust nuclear gene expression to plastid biogenesis. *Plant Cell* 33, 457–474. doi: 10.1093/plcell/koaa048

Zhang, W., Willows, R. D., Deng, R., Li, Z., Li, M., Wang, Y., et al. (2021). Bilin-dependent regulation of chlorophyll biosynthesis by GUN4. *Proc. Natl. Acad. Sci. U.S.A.* 118:e2104443118. doi: 10.1073/pnas.2104443118

Zhang, W., Zhong, H., Lu, H., Zhang, Y., Deng, X., Huang, K., et al. (2018). Characterization of Ferredoxin-Dependent Biliverdin Reductase PCYA1 Reveals the Dual Function in Retrograde Bilin Biosynthesis and Interaction With Light-Dependent Protochlorophyllide Oxidoreductase LPOR in Chlamydomonas reinhardtii. *Front. Plant Sci.* 9:676. doi: 10.3389/fpls.2018.00676

Frontiers in Microbiology

Explores the habitable world and the potential of microbial life The largest and most cited microbiology journal which advances our understanding of the role microbes play in addressing global challenges such as healthcare, food security, and climate change.

Discover the latest Research Topics

See more →

Frontiers

Avenue du Tribunal-Fédéral 34
1005 Lausanne, Switzerland
frontiersin.org

Contact us

+41 (0)21 510 17 00
frontiersin.org/about/contact